Joint Meeting

The Belgian and Italian Sections of The Combustion Institute

45th Meeting of the Italian Section of The Combustion Institute

Florence

May 28-31, 2023

PROCEEDINGS

edited by

Antonio Andreini, Mario Commodo, Gianluigi De Falco, Ward De Paepe, Alessandro Parente, Giancarlo Sorrentino, Antonio Tregrossi

Joint Meeting

of the Belgian and Italian Sections of The Combustion Institute

45th Meeting of the Italian Section of The Combustion Institute

PROCEEDINGS

Florence
May, 28-31, 2023

edited by
Antonio Andreini, Mario Commodo, Gianluigi De Falco, Ward De Paepe,
Alessandro Parente, Giancarlo Sorrentino, Antonio Tregrossi

Joint Meeting of the Belgian and Italian Sections of The Combustion Institute
45th Meeting of the Italian Section of The Combustion Institute
Proceedings
ISBN ISBN 978-88-88104-27-0

Editors:
Antonio Andreini, Mario Commodo, Gianluigi De Falco, Ward De Paepe,
Alessandro Parente, Giancarlo Sorrentino, Antonio Tregrossi

ASICI - Associazione Sezione Italiana del Combustion Institute
P. Tecchio, 80, 80125 Napoli
Napoli, May, 2018

The Italian Section of The Combustion Institute
www.combustion-institute.it


THE COMBUSTION INSTITUTE
1954


THE COMBUSTION INSTITUTE
1954

SUMMARY

SESSION I: Propulsion and engines including detonation and supersonic combustion

SESSION II: Novel concepts including multi-physics phenomena

SESSION III: Reaction kinetics including pollutant emission predictions

SESSION IV: Biomass and waste thermochemical processing, recycling, and valorization

SESSION V: Turbulent Combustion

SESSION VI: Fuel synthesis, upgrading, and CCUS processes

SESSION VII: Numerical Combustion

SESSION VIII: Pollutants formation, monitoring and control including nanomaterials and large molecules

SESSION IX: Low-carbon fuels and low-emission stationary combustion concepts

SESSION X: Gas turbine combustion

WORK IN PROGRESS POSTERS


THE COMBUSTION INSTITUTE
1954

SESSION I

PROPULSION AND ENGINES INCLUDING DETONATION AND SUPERSONIC COMBUSTION


THE COMBUSTION INSTITUTE
1954

Heavy duty opposed piston free piston engine simulation using 0D/1D modeling.

A. Maiello*, R. Saviano*, C. Beatrice*
armando.maiello@stems.cnr.it
*CNR-STEMS, Istituto di Scienze e Tecnologie per L'Energia e La Mobilità Sostenibili, Via G. Marconi 4, 80125, Napoli, Italy

Abstract
The use of free piston engine linear generators (FPELGs) could be a solution to overcome difficulties related to new legislation Euro 7 that will enter effect from 2025. FPELGs does not feature crankshaft kinematics as they rely on an alternative linear movement to produce electric power using an electric generator to power an electric motor or feed a battery. Lacking the crankshaft kinematics, these systems have reduced friction, can work with different compression ratio and show improved combustion efficiency since the expansion stroke is faster resulting in a combustion closer to a constant volume combustion. The absence of the crankshaft also brings to a reduction of possible points of failure and to a lower occurrence of wear and reduced maintenance required for optimal operation. On the other hand, the lack of a crankshaft requires an optimal control system to avoid malfunctions such as piston hitting the cylinder head resulting in engine failure.
This work introduces a new methodology for simulating FPELGs using coupled simulations between Simulink and GT-Power. Simulink produces the output of position of the engine as a linear length, port opening, combustion, electric force, and control logic; GT-Power is used to simulate the flow through ducts and ports and heat transfer.
Results concerning a supercharged heavy duty 2 strokes FPELG will be shown to demonstrate the potential of both the developed methodology, the implemented control strategy and the analysed system.

FPEGs Configurations and State of Art
Different configurations are possible for FPELGs [1,2]:
The single-piston configuration (Figure 1a) consists of a combustion cylinder (CC), a Linear Electric Machine (LEM), and a rebound device (RD). When combustion occurs, the movement of the piston causes an energy storage in the RD which returns the piston to the Top Dead Center (TDC). In this phase, LEM works as an electric motor to push the piston to TDC. During the expansion stroke, current flows through the coils of the LEM and electrical power is generated.
Dual piston (Figure 1b) consists of a single rod on which a linear generator is mounted and at the ends of the rod there are the two CCs which determine the movement of the system. This configuration is particularly prone to misfire problems

since motion is driven solely by combustion and there is no RD. The electric machine can also act as a motor and normal operation can be restored in the event of a fault with specific control logics.
The opposed piston configuration can be schematized as two single pistons sharing either the CC or the RD. In the first case (Figure 1c) the head of one piston represents the cylinder head of the other and vice versa. There are two LEMs and two RDs. In the second case (Figure 1d) there is a common RD connected to two rods with two LEMs and two CCs.

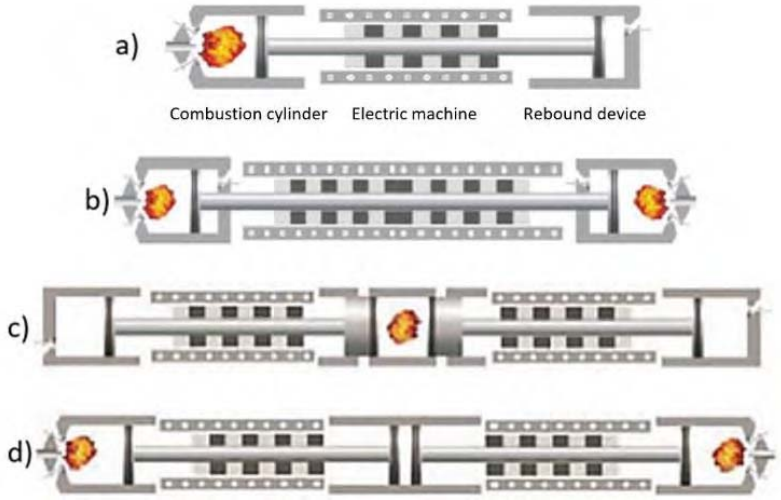

Figure 1. FRELGs configurations: a) single piston, b) dual piston, c) opposed with central CC, d) opposed with central RD.

In [3] Jia et al. compared the friction of a conventional engine with a single piston FPELG of similar size. The total frictional loss is nearly half those of a conventional engine because of the lack of the crankshaft.
In [4] a complete review of the studied control strategies was provided. The authors carried out a statistical analysis which also classifies the control strategies present in the literature. They suggested that this could help future research activities.

Simulation Environments and Simulation Methodology

The aim of the present work is to introduce a new methodology of simulation that pairs the simplicity of 0D models with the accuracy of thermodynamic calculation of GT-Power that captures gas dynamics through 1D computational fluid dynamic. The piston position dynamics, port opening, combustion, electric machine force and control strategy have been modelled in Simulink; while the flow through the ducts and ports and heat transfer have been modelled in GT-Power.
In Figure 2 is shown the Simulink scheme of an opposed piston with central CC. Definition of many sub-assemblies allows to model different configurations with minimal effort.
Piston position is calculated solving the equation of the piston dynamic that is:

$$F_p + F_e + F_f = m * a \tag{1}$$

Where F_p is the total force calculated from the cylinder pressure and the rebound device pressure, F_e is the electric force and F_a is the friction force.
Port opening and combustion are modelled using a linear correlation between linear piston position and crank angle calculated in GT-Power. This was necessary because GT-Power uses the engine speed to convert time in crank angles but for FPELG it is only possible to define an average frequency that is not the same during the whole cycle.

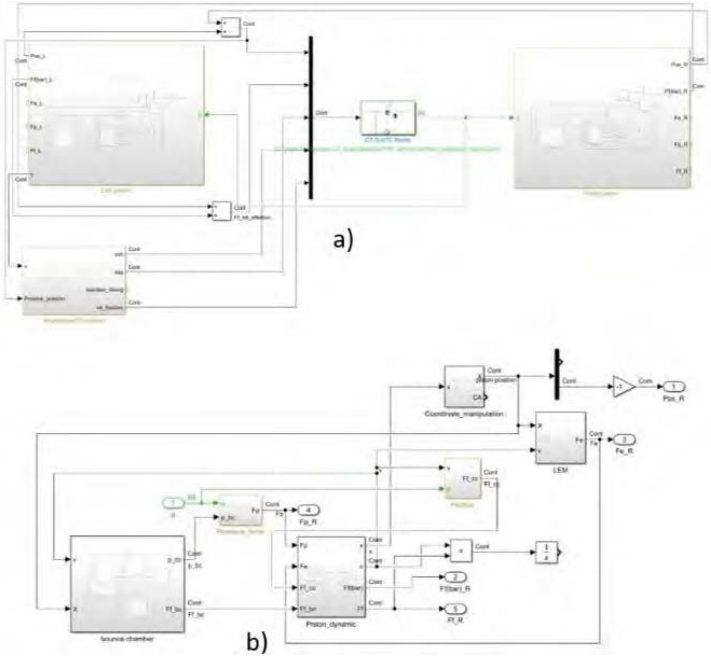

Figure 2. Simulink model: a) opposed piston configuration, b) left piston detail.

The electric machine is modelled according to [5,6]. The equations used are:

$$F_{em} = \frac{3\pi}{2\tau}\psi_f * i \tag{2}$$

$$F_{eg} = -c * v \tag{3}$$

Where F_{em} is the electric force when the machine is working as motor, F_{eg} is the electric force when the machine is working as generator, ψ_f is the flux produced by the permanent magnet, i is the current flowing into the coils, τ is the pole-pitch, c is the generator constant and v is the piston velocity.
The control strategy implemented uses a PID to control the electric force when LEM is in motor operation that is based on the piston position and uses the TDC position as target to be reached. A control based on the piston velocity determines the switch of LEM from motor to generator operation. In this condition the control is absent since the force exerted from the generator depends only on the velocity of the piston.
The GT SUITE Model block allows for data exchange with GT-Power.
A scheme of the GT-Power model is reported in Figure 3. The system is modelled

using the templates provided in the software and using a "Simulink Harness" block that allows for data exchange with Simulink. As suggested from the manual of the software, only one cylinder block is used to better reproduce the fluid dynamic of the gasses inside the cylinder.
Simulations were run using Simulink as master software, so the solver was chosen by Simulink in an automatic way as defined in the model settings. This also allowed to use "Scope" block to create graphs to see the output while simulation was ongoing.

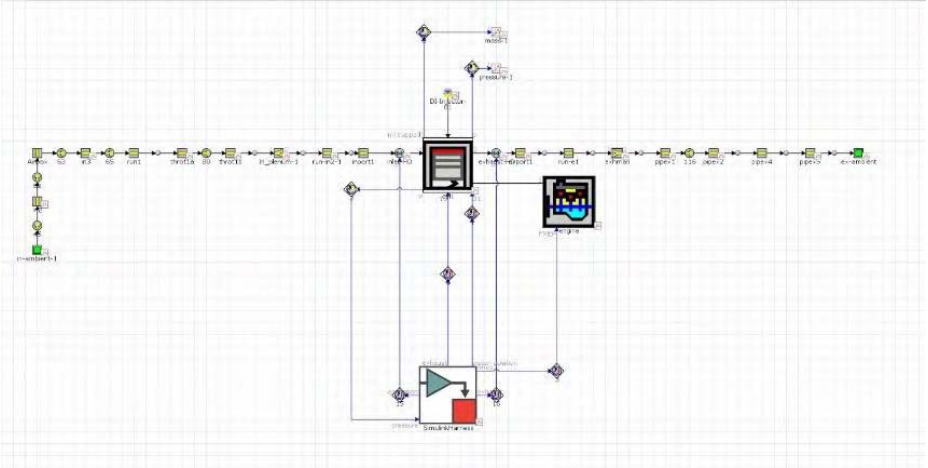

Figure 3. GT-Power model.

Comparison of Opposed Configuration with Central Combustion Cylinder and Central Rebound Device

When running a simulation in GT-Power the piston position is expected to be a value between 0 (TDC position) and -s (BDC position), with s being the stroke of the engine. The main critical issue faced during simulations run was a failure of the simulation if piston position exceeded this range. To overcome such issue, position has been limited to be in this range of values when integrating equation (1). To be sure whether the limitation has been actuated or not, a logical bit can be checked.
Some of the main parameters of the model can be found in Table 1.

Table 1. Main parameters of the models.

Description	Value
Bore (mm)	120
Maximum stroke (mm)	288
Compression ratio (-)	14
Piston mass (kg)	7
ψ_f (Wb)	0.444
τ (mm)	40
c (ks/s)	150

Results in terms of piston position and piston velocity are shown in Figure 4. Piston

position is effectively controlled to reach the TDC and BDC position without any limitation being actuated. Piston velocity values are in a realistic range considering the inertia of the piston and it is visible that velocity is higher during expansion stroke since combustion has occurred with a sudden increase of pressure in the CC. The effective compression ratio is lower than the one expected from the input in GT-Power but it is still close enough to the value expected.

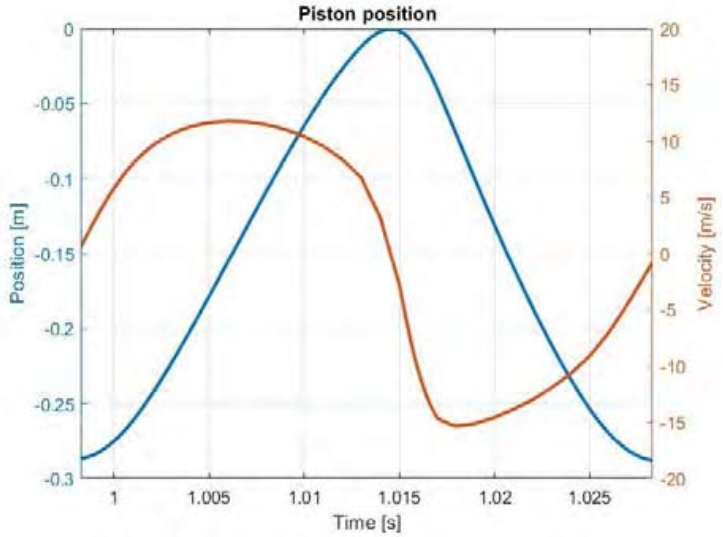

Figure 4. Piston position and piston velocity for both models.

Cylinder pressure values (Figure 5) are lower than those expected in an engine of similar displacement and compression ratio but are correctly aligned with the piston position. This could be due to the necessity of an optimization of the scavenging and combustion processes.

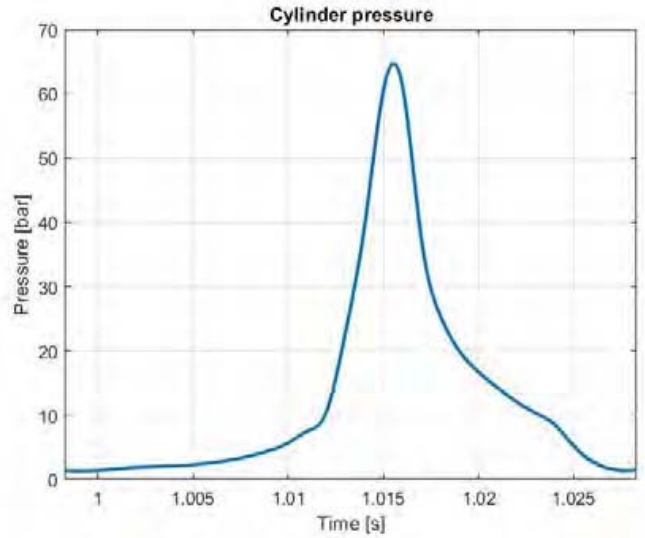

Figure 5. Pressure and heat transfer comparison for both models.

Output values of volumetric efficiency, indicated efficiency and electric power per cycle are reported in Table 2. They could be improved with an optimization of the design of the model.

Table 2. Main energetic models' output.

Description	Value
Volumetric efficiency (-)	0.86
Indicated efficiency (%)	41.7
Electric power generated per cycle (kW/cycle)	17.3

Conclusions and future developments

The developed simulation methodology can be successfully used to study FPELGs with good accuracy and limited computational effort without occurring in simulation failure or piston exceeding the dead center positions.
The energy outputs give positive results that could be improved with an optimization of the system developed so far. Energetic balance between rebound device and LEM as well as the switching moment between motor and generator operation can be studied more in detail to find the best design to ensure correct operation and best efficiency of the system. Further analysis can involve the thermal engine considering port timing, spark timing, ecc.
Simulations at different frequency and partial load will be considered as well to determine the flexibility of the system, how efficiency is affected when changing the operating point of the system and how the control strategy reacts to such changes.

References

[1] A. Heron and F. Rinderknecht, "Comparison of range extender technologies for battery electric vehicles," 2013 Eighth International Conference and Exhibition on Ecological Vehicles and Renewable Energies (EVER), Monte Carlo, Monaco, 2013, pp. 1-6, doi: 10.1109/EVER.2013.6521579.
[2] Schneider, S., & Friedrich, H. E. (2016). Experimental Investigation and Analysis of Homogeneous Charge Compression Ignition in a Two-Stroke Free-Piston Engine. SAE International Journal of Engines, 9(1), 365–373. http://www.jstor.org/stable/26284819
[3] Jia, B., Mikalsen, R., Smallbone, A., & Roskilly, A. P. (2018). A study and comparison of frictional losses in free-piston engine and crankshaft engines. *Applied Thermal Engineering*, *140*, 217-224.
[4] Raheem, A. T., Aziz, A. R. A., Zulkifli, S. A., Rahem, A. T., & Ayandotun, W. B. (2022). A review of free piston engine control literature—taxonomy and techniques. *Alexandria Engineering Journal*.
[5] Sun, P., Zhang, C., Chen, J., Zhao, F., Liao, Y., Yang, G., & Chen, C. (2017). Hybrid system modeling and full cycle operation analysis of a two-stroke free-piston linear generator. *Energies*, *10*(2), 213.

[6] Mao, J., Zuo, Z., Li, W., & Feng, H. (2011). Multi-dimensional scavenging analysis of a free-piston linear alternator based on numerical simulation. *Applied Energy*, *88*(4), 1140-1152.

Sensitivity analysis of the Partially Stirred Reactor in a scramjet combustion chamber

Alessandro Piscopo*,, Matteo Savarese*,**, Salvatore Iavarone*, Mehdi Riis*, Ward De Paepe**, Alessandro Parente***

Alessandro.Parente@ulb.be

*Université Libre de Bruxelles and Vrije Universiteit Brussel, Brussels Institute for Thermal-Fluid Systems and Clean Energy (BRITE), Brussels, Belgium.

**Univesity of Mons, Thermal Engineering & Combustion Unit, Mons, Belgium.

Abstract

Scramjet engines represent one of the most promising alternatives to power hypersonic vehicles, although the peculiarities of supersonic combustion raise many challenges. Computational Fluid Dynamics (CFD) simulations can be used to model highly turbulent reactive flows in such complex configurations and avoid expensive experimental campaigns. A particularly challenging aspect when dealing with numerical simulations of turbulent combustion is accurately modelling the interactions between chemistry and turbulence. These interactions can play a significant role in supersonic flows and require an appropriate closure since the conditions encountered in supersonic flows differ from those of conventional combustion devices. For this reason, an assessment of the role of turbulence-chemistry interactions in supersonic combustion is needed. This work evaluates the performance of the Partially Stirred Reactor (PaSR) closure of the mean chemical source term by performing Reynolds-Averaged Navier-Stokes (RANS) simulations of the German Aerospace Centre (DLR) scramjet. The PaSR approach requires the definitions of two important quantities: mixing and chemical time scales. While the chemical time scale is related to finite-rate chemistry, supersonic flow conditions can affect the correct definition of the mixing time scale. For these reasons, several formulations of the mixing and chemical time scales are assessed in this work. The results are validated against experimental data and compared with results from a Large Eddy Simulation (LES) of the DLR scramjet. The two chemical time scales formulations investigated provide quite different results, with the Fastest Formation Rate (FFR) approach showing its shortcoming in accurately describing the supersonic combustion process. However, the Slowest Formation Rate (SFR) method consistently delivers satisfactory results in temperature prediction at the three different axial locations, with the integral mixing time formulation performing the best.

Introduction

The interest in supersonic flight kept growing in the last decades for different end uses, such as faster access to space, military development, and commercial air travail. Even though scramjets show a more straightforward design with respect to other configurations, the governing physical phenomena are complex to handle, involving numerous shocks, compressibility effects and ignition issues [1]. The main advantage scramjets have on ramjets is the avoidance of strong flow deceleration from a supersonic to subsonic regime [2]. Numerical simulations help investigate the performances of such engines while avoiding the repetition of experimental tests, which can be expensive and difficult to set up. Computational Fluid Dynamics (CFD) is undoubtedly the most employed tool for numerical simulations of turbulent reactive flows in complex geometries. Large Eddy Simulations (LES) are often employed to simulate supersonic combustors as they offer superior performances compared to a lower-fidelity approach such as Reynolds-Averaged Navier-Stokes (RANS) simulations. Studies based on LES [3], [4] showed the ability of this approach to capture the peculiarities of the experimental data, such as bimodal curves in the velocity and temperature profiles. Moreover, finite-rate chemistry effects and turbulence-chemistry interactions (TCI) can have a significant role in supersonic conditions [5], [6]. In this context, RANS simulations represent a more cost-effective alternative to LES. In line with that, the extension to the supersonic combustion of the PaSR model, which has already proven its effectiveness in different regimes [7]–[13], is investigated in this work, performing RANS simulations of the DLR combustion chamber. The results are validated with the available experimental data and compared to the LES results presented in [3].

Numerical approach

This work presents RANS simulations performed on the commercial software ANSYS Fluent R2022 R1. The chemical source reaction rate term was closed with the implementation of the PaSR model via a User Defined Function (UDF). Several formulations were employed for the definition of the chemical and mixing time scales. The PaSR model considers fine structure, where reactions occur, occupying a fraction of the computational cell. Each cell is separated into a reactive and non-reactive part. The former is characterised by the reactive volume fraction γ, which is a function of both mixing (τ_m) and chemical (τ_c) time scales [13],

$$\gamma = \frac{\tau_c}{\tau_c + \tau_m} \tag{1}$$

The Damkölher (dimensionless) number, $Da = \tau_m/\tau_c$, comparing the mixing and the chemical time scales, is a good indicator for the importance of turbulence-chemistry interactions. The mean chemical reaction rate for a species *k* is expressed as follows:

$$\overline{\dot{\omega}_k} = \gamma \frac{\overline{\rho}(Y_k^* - \widetilde{Y_k})}{\tau^*}, \tag{2}$$

where τ_m is the residence time within the fine structures, $\widetilde{Y_k}$ is the mean mass fraction of the *k*-th species, and Y_k^* is its mass fraction in the fine structure. The latter is obtained by modelling the reactive zone as a Plug Flow Reactor (PFR) evolving from $Y_k^0 \approx \widetilde{Y_k}$ over the residence time τ^*, chosen as the minimum between the mixing and the chemical time scale.

A key challenge of the PaSR model is accurately estimating the chemical and mixing time scales. Different formulations, already presented in the literature [14], were assessed in this work. Two formation rates were considered for the chemical time scale, namely the slowest and the fastest formation rates. The former approach retains the Slowest Formation Rate (SFR), after removing the N_D dormant species (i.e., species that are not reacting), as the leading scale,

$$\tau_c^{SFR} = \max_{i=[1,N_S-N_D]} \left(\frac{Y_i^*}{\left| \frac{\partial Y_i^*}{\partial t} \right|} \right). \tag{3}$$

The second approach consists in selecting the Fastest Formation Rate (FFR) as follows:

$$\tau_c^{FFR} = \min_{i=[1,N_S-N_D]} \left(\frac{Y_i^*}{\left| \frac{\partial Y_i^*}{\partial t} \right|} \right). \tag{4}$$

Four different mixing time formulations were employed in this work. The first formulation expresses the mixing time as a fraction of the integral time scale ($\tau_{m,I}$), related to the eddy break-up time,

$$\tau_{m,I} = C_{mix}\tau_I = C_{mix}\frac{k}{\epsilon}, \tag{5}$$

where C_{mix} is a constant parameter, k is the turbulent kinetic energy and ϵ its dissipation rate. Another possibility consists in clipping the smallest scale in the energy cascade model, i.e., the Kolmogorov time scale (τ_K), to the mixing time as follows:

$$\tau_{m,K} = \sqrt{\frac{\nu}{\epsilon}}, \tag{6}$$

where ν is the kinematic viscosity. By taking the geometric mean of the integral and Kolmogorov scales, the last static formulation can be written as:

$$\tau_{m,G} = \sqrt{\tau_I \cdot \tau_K}. \tag{7}$$

Finally, a local formulation was investigated, based on the work of Ferrarotti et al. [15]. This model needs the definition of a scalar time as the ratio between the scalar variance $\widetilde{\phi''^2}$ and the scalar dissipation rate $\widetilde{\epsilon_\phi} = 2D_m\left(\frac{\partial\widetilde{\phi''}}{\partial x_i}\right)^2$, where $\tilde{\phi}$ is a generic scalar quantity, and D_m is the molecular diffusion coefficient. The local mixing time can thus be defined as:

$$\tau_{m,L} = \tau_\phi = \frac{\widetilde{\phi''^2}}{\widetilde{\epsilon_\phi}}. \tag{8}$$

Following [16], the mixture fraction is chosen as a scalar quantity, and two additional transport equations for its variance and scalar dissipation rate must be solved:

$$\frac{D\overline{\rho}\widetilde{Z''^2}}{Dt} = \frac{\partial}{\partial x_j}\left(\rho(D_m + D_t)\frac{\partial\widetilde{Z''^2}}{\partial x_j}\right) + 2\rho D_t\left(\frac{\partial\tilde{Z}}{\partial x_j}\right)^2 - \overline{\rho}\tilde{\chi} \tag{9}$$

$$\frac{D\rho\tilde{\chi}}{Dt} = \frac{\partial}{\partial x_j}\left(\rho(D_m + D_t)\frac{\partial\tilde{\chi}}{\partial x_j}\right) - C_{d1}\overline{\rho}\frac{\widetilde{\chi^2}}{\widetilde{Z''^2}} - C_{d2}\overline{\rho}\frac{\widetilde{\chi\epsilon}}{\tilde{k}} + C_{p1}\frac{\tilde{\chi}}{\widetilde{Z''^2}}P_f + C_{p2}\frac{\tilde{\chi}}{\tilde{k}}P_k \tag{10}$$

where D_t is the turbulent diffusivity, $P_f = -2\overline{\rho}\widetilde{u_k''Z''}\left(\frac{\partial\tilde{Z}}{\partial x_k}\right)$ is the production of the scalar fluctuation and $P_k = -\overline{\rho}\widetilde{u_k''u_i''}\left(\frac{\partial\widetilde{U_i}}{\partial x_k}\right)$ is the production of turbulent kinetic energy. The scalar dissipation rates coefficients are fixed following Musonge et al. [17] such that $C_{p1} = 1.7, C_{p2} = 1.45, C_{d1} = 1$ and $C_{d2} = 0.9$. The kinetic mechanism used was the Li mechanism involving 9 species and 21 reactions [18]. The SST k-ω model was selected for modelling turbulence, including compressibility effects. A density-based solver with an implicit formulation, characterized by a broader stability range with respect to the explicit formulation, was used. The flow field was initialized with the Full Multi-Grid Initialisation and the second-order upwind scheme was employed for spatial discretization, as well as for the turbulent kinetic energy and the dissipation rate. Turbulent Prandtl and Schmidt numbers were fixed to 0.9 [19].

DLR scramjet case study

The DLR scramjet test engine experimental campaign was presented by Waidmann et al. [20]. The fuel, hydrogen, is injected parallel to the air stream through 15 holes, 2.4 mm distant from each other, with a diameter of 1 mm at the base of a wedge with a half angle of 6°, as illustrated in Figure 1. The upper wall presents a 3° angle divergence to compensate for the boundary layer growth from x = 58 mm. The total length of the combustor is 340 mm, with a width of 40 mm and an inlet height of 50 mm. The strut injector helps in solving the well-known ignition problems in scramjet engine. The flame holder length is 32 mm, and its height is 6 mm [3].

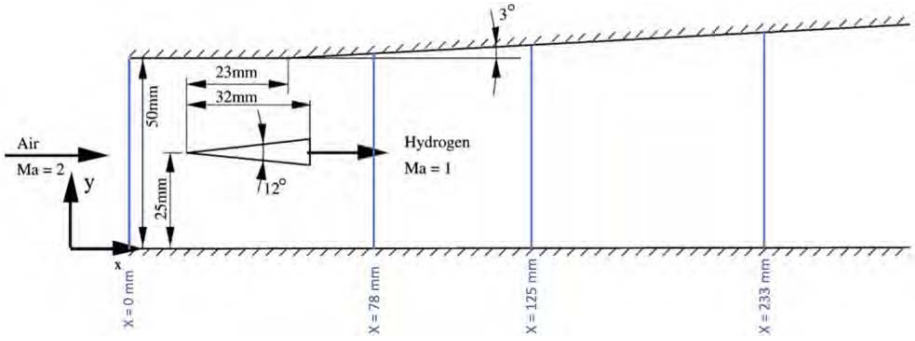

Figure 1. Sketch of the DLR scramjet combustor chamber adapter from [21].

The inlet conditions of air and hydrogen are summarized in Table 1. To reduce the computational cost, a smaller domain was kept with symmetrical boundary conditions imposed in the horizontal plane of injection. At the walls, no-slip boundary conditions were imposed. A flux-based pressure far-field boundary condition was chosen for the outlet.

Table 1. Inlet conditions of air and fuel

	T [K]	M [/]	Y_{H_2}	Y_{O_2}	Y_{H_2O}	p [atm]
Inlet Air	340	2	/	0.232	0.032	1
Inlet Fuel	250	1	1	/	/	1

The available experimental data include the velocity profiles, collected via Laser Doppler Velocimetry (LDV), and the static temperature measurements, measured by Coherent Stokes Raman Spectroscopy (CARS), at different axial locations. In addition, Particle Image Velocimetry (PIV) was used for flow visualization [20]. These experimental data were used to validate the results obtained by simulations.

Results and discussions

In this section, the temperature profiles obtained with the different mixing time formulations are presented for both chemistry time calculation methods (i.e., SFR and FFR). It must be mentioned that a preliminary validation of the CFD was performed on the available inert flow field measurements of velocity and temperature, although it is not shown here. Figure 2 shows the temperature profiles obtained with the four different mixing time formulations, with the SFR chemical time scale, at three axial locations (emphasized in Fig.1). Seemingly, two pairs of similar profiles can be observed, a first one with the integral ($\tau_{m,I}$) and the geometric mean ($\tau_{m,G}$) formulations and the other one with the Kolmogorov ($\tau_{m,K}$) and the local formulations ($\tau_{m,L}$). The trends can be explained by looking at the mixing time along the centerline, where the integral and geometric mean formulations estimate similar profiles. It can be observed that the local formulation firstly estimates a mixing time like the integral formulation, near the strut injector, then switches to the Kolmogorov time scale. This is due to the important recirculation zone present near the injector. At x=78 mm (2a), in the high-intensity turbulence region, the PaSR model is not able to catch the bimodal curve while the reference LES does. Nevertheless, the results in the other locations are satisfactory, with $\tau_{m,I}$ performing the best. At x=125 mm (2b), in the combustion region, the simulation predicts a wider reaction zone than what is observed in the experiments and estimated with LES. At x=233 mm (2c), the simulations profiles, mainly with $\tau_{m,I}$ and $\tau_{m,G}$, gets closer to the experimental data.

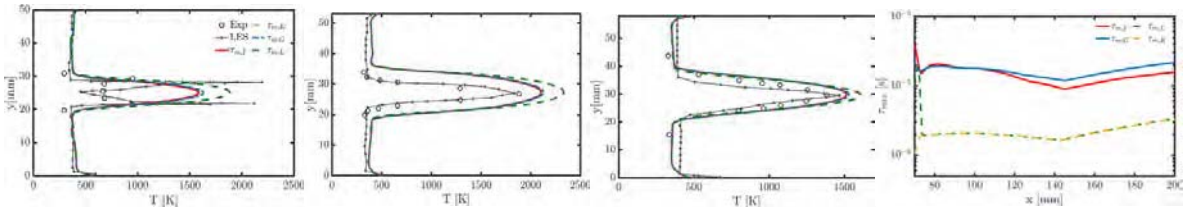

(a) (b) (c) (d)

Figure 2. Temperature profiles at three different axial locations: (a) 78 mm, (b) 125mm and (c) 233mm and (d) τ_{mix} along the centerline. Different PaSR mixing time scale τ_m are considered with the SFR formulation for τ_c. A $C_{mix} = 0.1$ was used to compute $\tau_{m,I}$. The LES results from [3] are also reported.

In Fig. 3, the results with the FFR formulation for the computation of τ_c are shown. The reported τ_{mix} remain like the one showed in Fig. 2. Nevertheless, slight changes can be identified in the results from integral and geometric mean mixing time scales as they both indicate extinction. Still, the temperature profiles predicted with the Kolmogorov and the local formulations are very similar to those obtained with the SFR approach.

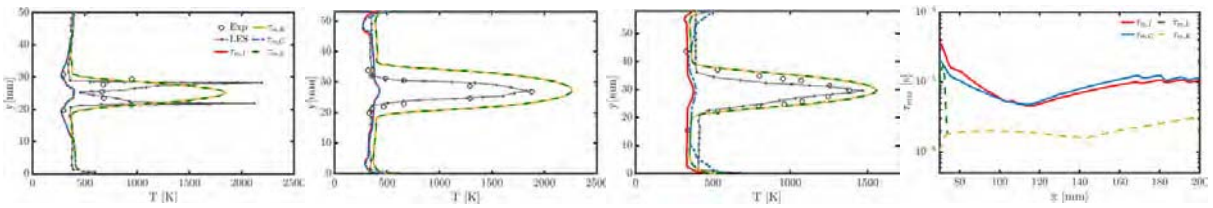

(a) (b) (c) (d)

Figure 3. Temperature profiles at three different axial locations: (a) 78mm, (b) 125mm and (c) 233mm and (d) τ_{mix} along the centerline. Different PaSR mixing time scale τ_m are considered with the FFR formulation for τ_c. $C_{mix} = 0.1$ was used to compute $\tau_{m,I}$.

Figure 4 gives some hints on the reasons why the combustion does not occur with $\tau_{m,I}$ and $\tau_{m,G}$. The chemical time scale with the two different approaches is reported, for the different mixing time formulations, along the centerline. Taking the FFR as leading scale (4a) results in a chemical time scale estimation around two orders of magnitude lower than the SFR approach (4b), as shown by the $\tau_{m,K}$ and $\tau_{m,L}$ profiles. However, the consequence of this decrease in τ_c is that the leading chemical scale becomes too fast compared to the mixing time, thus γ (Eq. 1) becomes very low, resulting in low reaction rates. Eventually the PaSR models with $\tau_{m,I}$ and $\tau_{m,G}$ provide an extinguished flame and the resulting τ_c is fixed to the maximum value set in the UDF (i.e., 10 s). On the contrary, all the mixing time formulations can predict a stable flame with the SFR approach.

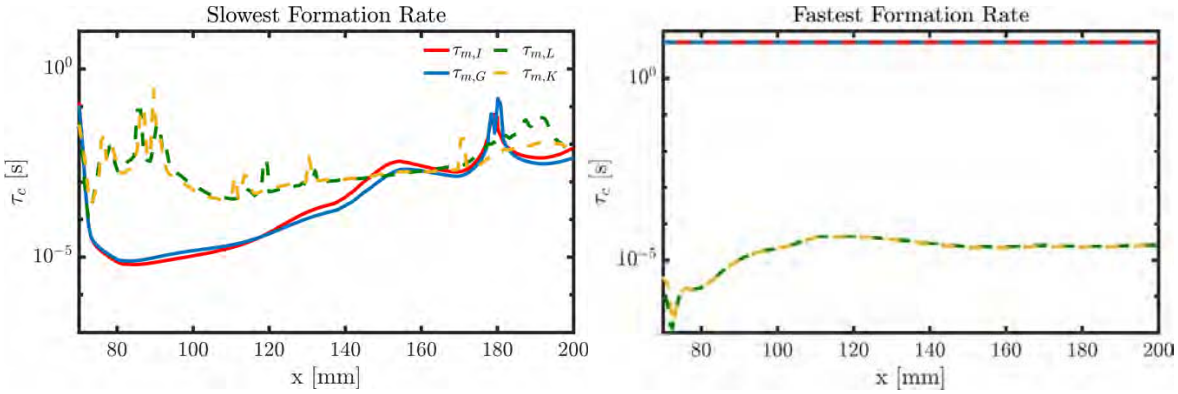

(a) (b)

Figure 4. Chemical time scale for SFR (a) and FFR formulations (b) on the centerline y=25mm.

Conclusions

In the present work, a sensitivity analysis of four mixing time scale formulations and two chemical time scale formulations for the PaSR model was conducted in a supersonic combustion chamber. The PaSR models employing the first chemical time scale approach, namely the SFR, and the two largest mixing times ($\tau_{m,I}$ and $\tau_{m,G}$) reproduce the temperature profiles better, with similar predictions. Nevertheless, the reactor-based model is not able to capture the bimodal shape in the vicinity of the injector (i.e., in the high intensity turbulence region). The Kolmogorov and local formulations, showing very similar performances, both overpredict the temperature, mainly when getting closer to the center of the engine. In contrast, the PaSR models employing the FFR approach, with either the integral or the geometric mean formulation, are not able to predict a stable flame, while the model versions using the Kolmogorov and local approaches do. This is explained by the gap between the τ_m and τ_c and its impact on the reaction rate. It may indicate the important correlation between τ_c and τ_m, highlighting the fact that the two quantities should rather be considered together than individually, mostly for the FFR approach.

References

[1] V. A. Sabelnikov and V. V Vlasenko, 'Combustion in Supersonic Flows and Scramjet Combustion Simulation', in *Modeling and Simulation of Turbulent Combustion*, S. De, A. K. Agarwal, S. Chaudhuri, and S. Sen, Eds., Singapore: Springer Singapore, 2018, pp. 585–660. doi: 10.1007/978-981-10-7410-3_20.

[2] R. J. Weber and J. S. Mackay, 'An analysis of ramjet engines using supersonic combustion', Sep. 1958.
[3] M. Berglund, N. Wikström, and C. Fureby, 'Numerical Simulation of Scramjet Combustion', 2005.
[4] F. Génin and S. Menon, 'Simulation of Turbulent Mixing Behind a Strut Injector in Supersonic Flow', *AIAA Journal*, vol. 48, no. 3, pp. 526–539, Mar. 2010, doi: 10.2514/1.43647.
[5] A. Mura, A. Techer, and G. Lehnasch, 'Analysis of high-speed combustion regimes of hydrogen jet in supersonic vitiated airstream', *Combust Flame*, vol. 239, p. 111552, 2022, doi: https://doi.org/10.1016/j.combustflame.2021.111552.
[6] N. Swaminathan, 'Physical Insights on MILD Combustion From DNS', *Front Mech Eng*, vol. 5, Oct. 2019, doi: 10.3389/fmech.2019.00059.
[7] Z. Li, A. Cuoci, A. Sadiki, and A. Parente, 'Comprehensive numerical study of the Adelaide Jet in Hot-Coflow burner by means of RANS and detailed chemistry', *Energy*, vol. 139, pp. 555–570, 2017, doi: https://doi.org/10.1016/j.energy.2017.07.132.
[8] S. Iavarone, A. Péquin, Z. X. Chen, N. A. K. Doan, N. Swaminathan, and A. Parente, 'An a priori assessment of the Partially Stirred Reactor (PaSR) model for MILD combustion', *Proceedings of the Combustion Institute*, vol. 38, no. 4, pp. 5403–5414, 2021, doi: https://doi.org/10.1016/j.proci.2020.06.234.
[9] R. Amaduzzi, M. Ferrarotti, and A. Parente, 'Strategies for Hydrogen-Enriched Methane Flameless Combustion in a Quasi-Industrial Furnace', *Front Energy Res*, vol. 8, Jan. 2021, doi: 10.3389/fenrg.2020.590300.
[10] M. Ferrarotti, M. Fürst, E. Cresci, W. De Paepe, and A. Parente, 'Key Modeling Aspects in the Simulation of a Quasi-industrial 20 kW Moderate or Intense Low-oxygen Dilution Combustion Chamber', *Energy and Fuels*, vol. 32, no. 10, pp. 10228–10241, Oct. 2018, doi: 10.1021/acs.energyfuels.8b01064.
[11] R. Amaduzzi, A. Bertolino, A. Özden, R. M. Galassi, and A. Parente, 'Impact of scalar mixing uncertainty on the predictions of reactor-based closures: Application to a lifted methane/air jet flame', *Proceedings of the Combustion Institute*, 2022, doi: https://doi.org/10.1016/j.proci.2022.06.028.
[12] S. Iavarone, M. Cafiero, M. Ferrarotti, F. Contino, and A. Parente, 'A multiscale combustion model formulation for NOx predictions in hydrogen enriched jet flames', *Int J Hydrogen Energy*, vol. 44, no. 41, pp. 23436–23457, 2019, doi: https://doi.org/10.1016/j.ijhydene.2019.07.019.
[13] Z. Li, A. Cuoci, A. Sadiki, and A. Parente, 'Finite-rate chemistry modelling of non-conventional combustion regimes', *Energy Procedia*, vol. 142, pp. 1570–1576, 2017, doi: https://doi.org/10.1016/j.egypro.2017.12.608.
[14] A. Péquin, S. Iavarone, R. Malpica Galassi, and A. Parente, 'The partially stirred reactor model for combustion closure in large eddy simulations: Physical principles, sub-models for the cell reacting fraction, and open challenges', *Physics of Fluids*, vol. 34, no. 5, p. 055122, May 2022, doi: 10.1063/5.0090970.
[15] M. Ferrarotti, Z. Li, and A. Parente, 'On the role of mixing models in the simulation of MILD combustion using finite-rate chemistry combustion models', *Proceedings of the Combustion Institute*, vol. 37, no. 4, pp. 4531–4538, 2019, doi: https://doi.org/10.1016/j.proci.2018.07.043.
[16] M. Ferrarotti, Z. Li, and A. Parente, 'On the role of mixing models in the simulation of MILD combustion using finite-rate chemistry combustion models', *Proceedings of the Combustion Institute*, vol. 37, no. 4, pp. 4531–4538, 2019, doi: https://doi.org/10.1016/j.proci.2018.07.043.
[17] I. K. Ye, 'Investigation of the scalar variance and scalar dissipation rate in URANS and LES', University of Waterloo, 2011.
[18] J. Li, Z. Zhao, A. Kazakov, and F. L. Dryer, 'An updated comprehensive kinetic model of hydrogen combustion', *Int J Chem Kinet*, vol. 36, no. 10, pp. 566–575, Oct. 2004, doi: https://doi.org/10.1002/kin.20026.
[19] Z. Gao, J. Wang, C. Jiang, and C. Lee, 'Application and theoretical analysis of the flamelet model for supersonic turbulent combustion flows in the scramjet engine', *Combustion Theory and Modelling*, vol. 18, no. 6, pp. 652–691, Nov. 2014, doi: 10.1080/13647830.2014.962617.
[20] W. Waidmann, J. Sender, and M. Oschwald, 'Experimental investigation of the combustion process in a supersonic combustion ramjet', Hardthausen, 1994.
[21] M. Oevermann, 'Numerical investigation of turbulent hydrogen combustion in a SCRAMJET using flamelet modeling', *Aerosp Sci Technol*, vol. 4, pp. 463–480, 2000.

PREDICTION OF KNOCK IN HEAVY-DUTY METHANOL ENGINES WITH NEURAL NETWORK DRIVEN IGNITION DELAY CALCULATIONS

W. Suijs*, J. Dierickx*, Y. Pu*, S. Verhelst*
ward.suijs@ugent.be
*Ghent University, Belgium

Abstract
Knock limits in heavy duty spark ignited engines can be overthrown by working with alternative fuels such as methanol. By comparing the actual residence time of the cylinder gases to the ignition delay time, one can make accurate predictions of the possible occurrence of end-gas autoignition (knock). The ignition delay times of methanol at conditions relevant to heavy duty engines were calculated using chemical kinetics. To accommodate for large bore engines, lean to stoichiometric mixtures were considered ($\lambda \in [1-4]$), a high fraction of residual gases ($f \in [0-50]$ vol%), in-cylinder pressures between $1-250$ bar, and unburned gas temperatures of $500-2000$ K. A *wide* neural network model was trained with the tabulated data and coupled to the Livengood and Wu knock integral. The methanol knock model was calibrated and validated on a small light-duty CFR engine. Afterwards, the sensitivity of the model to increasing bore sizes was studied. A proposed scaling law of the calibration constant to bore size shows the exponentially increasing relationship between calculated and calibrated ignition delay times.

Introduction
The heavy-duty (HD) industry is diligently looking for sustainable alternatives to phase out the diesel engines which they currently (heavily) rely on for both transportation as power generation. Methanol, produced as a bio- or electrofuel, can be the renewable alternative fuel the industry needs. Whereas spark-ignited (SI) gasoline engines are known to be restricted to light-duty operation due to engine knock, the strong knock-resistive properties of methanol [1] can make HD SI operation possible. A well-known method to predict the autoignition of unburned mixture in SI engines is by means of the Livengood and Wu knock integral (KI) [2], see Eq. 1, where τ_{ID} is the instantaneous ignition delay time, t_{IVC} and t_{KO} the time at intake valve closure and knock onset respectively. m is the calibration constant.

$$\mathrm{KI} = \int_{t_{IVC}}^{t_{KO}} \frac{dt}{m \cdot \tau_{ID}(t)} = 1 \tag{1}$$

If the closed engine cycle ends before the integral reaches unity, no knock is expected. The ignition delay time varies during every instant as function of in-cylinder pressure, unburned gas temperature and mixture composition. Since the methanol ignition delay times were never calculated for HD SI engine conditions, this paper focusses on their calculation and prediction using a wide neural network model. Moreover, since the heavy-duty engine industry spans a large range of engine sizes, the sensitivity of the calibration constant to engine bore size is discussed.

Lookup Table

Since the ignition delay time needs to be known at each crank angle during the combustion process, an accurate data set is needed spanning the entire range of conditions relevant to heavy duty SI-engines. The open source chemical kinetics software toolkit Cantera 2.6.0 was used to simulate the ignition process. Three different kinetic mechanisms were studied for methanol combustion [3, 4, 5]. Comparison of the simulated data with an experimental RCM dataset [6] showed that the highest accuracy could be achieved with a homogeneous 0-D ideal gas control-volume reactor model, and the ignition delay time defined as the point where the pressure rise rate maximized. In order to choose the best kinetic mechanism, the mean relative error (MRE) between the simulated and experimental values [6] was first calculated over the entire dataset for all three schemes. Evaluated by the MRE parameter, the mechanism of Li et al. [5] outperformed the other two slightly.

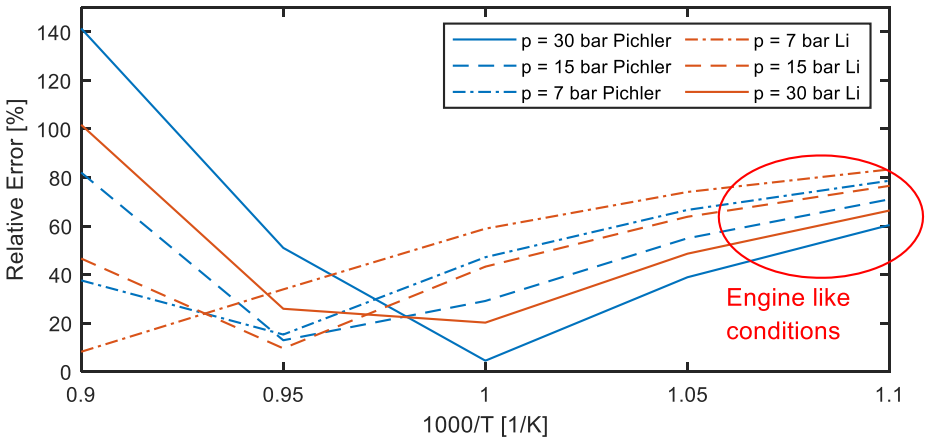

Figure 1. Comparison of kinetic mechanisms (Pichler [4] vs. Li [5]) by means of MRE for different pressures and temperatures.

However, when looking at Figure 1, for typical engine-like conditions, it is actually Pichler's scheme which is slightly better at all pressures. The large discrepancy at high temperatures makes a decisive difference leading to the higher MRE. Followed by this observation, and strengthened by the knowledge that Pichler's scheme was developed for SI-engine conditions [4], the choice was made to continue with the latter. The chemical kinetic model was used to generate ignition delay lookup tables for the operating range shown in Table 1 with intervals of 5 bar, 50 K, 0.1 and 10 vol% for pressure, temperature, lambda and residual fraction respectively. The

ranges were chosen large enough to accommodate for the various operating conditions of heavy-duty engines.

Table 1. Application range of ignition delay time calculations.

Method	P [bar]	T [K]	λ [-]	f [vol%]
Chemical kinetics	1-250	500-2000	1-4	0-50

Machine Learning methods

To overcome the large calculation time when interpolating to the exact in-cylinder conditions in the lookup table, this work explored the possibility to train an artificial neural network (ANN) model with the calculated τ_{ID} dataset. 80% of the data was selected randomly and used as training data to feed the ANN model. The remaining 20% was used as test data to evaluate its performance. In order to help choosing the best performing ANN model, and to avoid over- or underfitting the model with algorithms that are either too complex or too simple; five-fold cross validation has been applied to the training data set. Finally, due to the large range of ignition delay times, $\log_{10}(\tau_{ID})$ was used as response value rather than τ_{ID} itself.

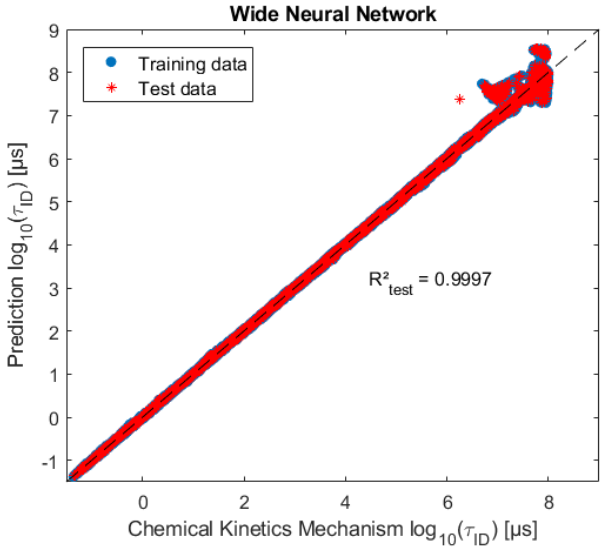

Figure 2. ANN prediction of methanol-air-residuals mixture ignition delay time versus chemical kinetics calculations.

Figure 2 shows the good agreement between the ANN predictions and the chemical kinetics calculations. The clutter at the top right corner is due to a runtime limit at very large ignition delay time values. After validation, the model was then coupled to the knock prediction model explained in Eq. 1.

Experimental data

The newly developed knock model and the sensitivity of the calibration constant to its prediction performance was evaluated on test data of three different engines

running entirely or partially on methanol fuel. The reference engine was a single cylinder port fuel injected CFR engine operated at a constant speed of 600 rpm [7]. The other two engines, a Scania D12 [8] and ABC 8-DZD [9], were specifically chosen for their progressively increasing bore size, in an attempt to cover most engine sizes in the medium to high speed heavy duty engine size range. Their main characteristics are summarized in Table 2. In-cylinder pressure data was available for all three engines at a sampling resolution of 0.1 °ca. Unburned gas temperatures and residual gas fractions were determined with a three pressure analysis (TPA) in GT-Power.

Table 2. Engine specifications [7, 8, 9].

Engine	**CFR**	**D12**	**8-DZD**
Bore [mm]	82.55	127	256
Stroke [mm]	114.2	154	310
Swept Volume [dm³/cylinder]	0.6112	1.951	15.956
Compression Ratio [-]	9-11:1	13:1	14:1
Speed [rpm]	600	1200	1000
Operating mode	SI	SI	DF
Fuel	Methanol	Methanol	Methanol + Diesel

Results

In the next chapter, the effect of the engine's bore size on the calibration constant of the model is analyzed. The intention of the knock model is for it to be used as a constraint during the design process of an entire range of dedicated heavy duty methanol engines. Since the displacement volume of the engine will be a design choice, a robust knock model is required which does not need to be calibrated for each design. Hence after discussing the results of our three reference engines, a preliminary scaling law is proposed which scales the calibration constant with the size of the engine.

CFR engine

The performance of the knock model was first tested and validated on the CFR engine dataset. Since the latter was constructed using a design of experiments (DOE) technique, it contained a central point (Condition A) which lied directly in the middle of the investigated parameter space. This point was used as an initial guess for the optimal calibration point and the results can be seen in Figure 3. In general, the model behaves adequately. The sensitivity of knock to ignition timing is higher for the knock model than for the experiments. Both for the calibration point as for condition B, knock onset advances more drastically as function of IT and, for some points, knock is even predicted while no actual knock was measured.

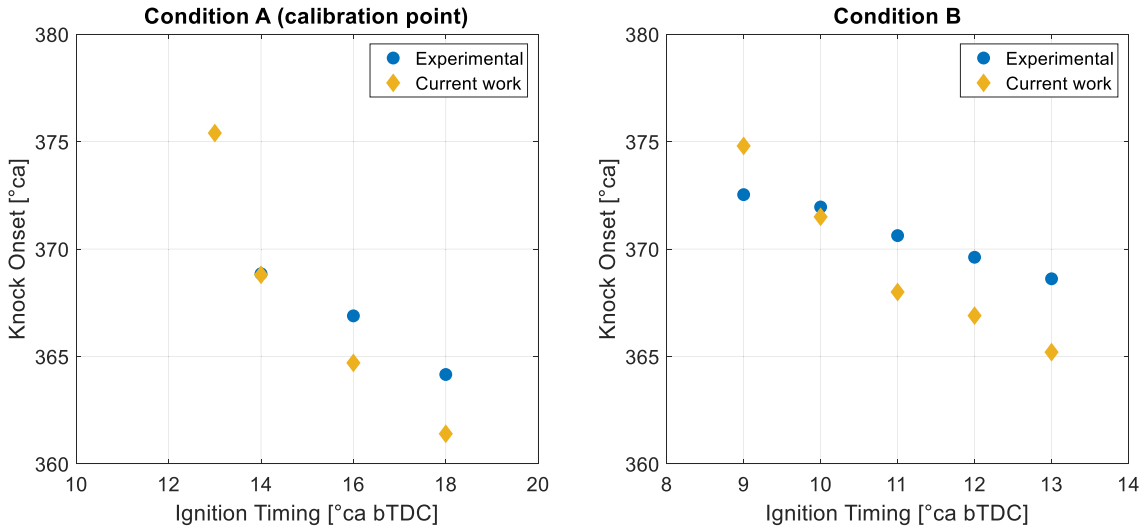

Figure 3. Ignition timing sweep for two different operating points on the CFR engine.

In order to optimize the calibration constant to the entire CFR dataset (91 points), its value was multiplied with multiples of ten and its influence on the prediction capabilities was studied. The model can be either very conservative, meaning that it classifies all points as knocking points, or not conservative at all, meaning that no knock is predicted under any circumstances. The former happens for low and high values of the calibration constant respectively.

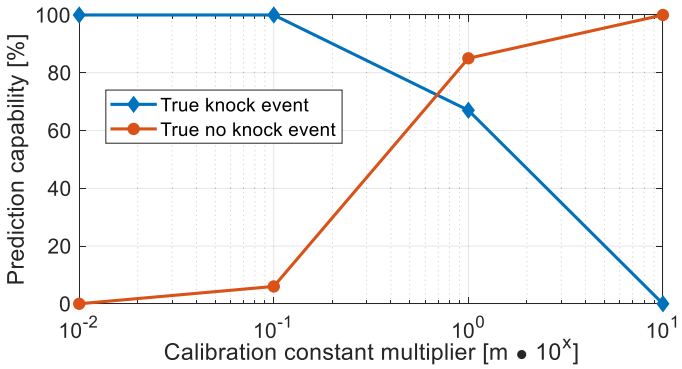

Figure 4. Sensitivity analysis on calibration constant CFR engine data set.

Figure 4 shows that the initial calibration point already favors a less conservative outcome. Since knock can be very detrimental to the engine, it is best to take a smaller value of the calibration constant. The point of intersection between both curves is currently used as 'sweet spot', with a value of $m_{CFR} = 0.86 \cdot m_A = 0.0214$.

Scaling law

The same procedure can be used for the other two engines as well. The resulting values for the calibration constant are visualized in Figure 5. Since the three

reference engines span the entire range of medium to high speed HD engines, a scaling law is proposed fitted on the curve connecting the three points. Bore size is used as size metric since knock will happen around TDC where the stroke of the combustion chamber is of less importance.

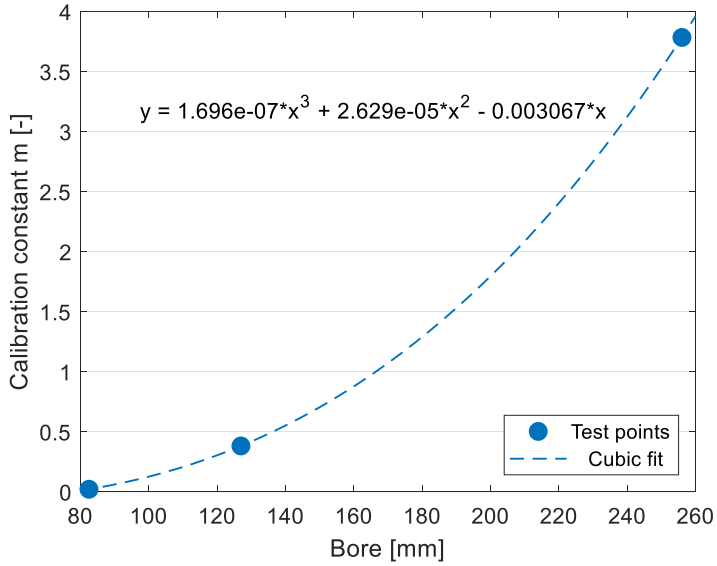

Figure 5. Proposed scaling law for calibration constant as function of engine bore size.

An exponential increase of the calibration constant with engine bore size is visible. A value close to unity means that the assumptions made in the ignition delay modelling properly portray the reality of the combustion process. The very small values for small bore diameters mean that e.g. the assumption of homogeneity of the mixture needs to be reassessed and that the actual ignition delay times are much shorter than originally calculated. Additionally, it should be noted that the different operating conditions and knock intensity levels of each dataset can result in an offset on the calibration constant. Since knock intensity values are generally calculated using in-cylinder energy or peak levels, both of which are function of the size of the engine, a dimensionless knock intensity parameter should be sought after in order to compare the different engines one-to-one and finetune the scaling law as proposed in Figure 5.

Summary

This paper enables the study of knock in large bore methanol engines by developing a neural network model of ignition delay times at conditions relevant to HD SI engines. The model was calibrated and validated on a small light-duty CFR engine. However, when looking at the sensitivity of the calibration constant to knock in bigger sized engines, an exponential increase in actual ignition delay time was noted. As bore size increases, the assumptions made for the model (e.g. homogeneity) should be carefully examined.

References

[1] S. Verhelst, J. W. Turner, L. Sileghem and J. Vancoillie, "Methanol as a fuel for internal combustion engines," *Progress in Energy and Combustion Science,* no. 70, pp. 43-88, 2019.

[2] J. Livengood and P. Wu, "Correlation of autoignition phenomena in internal combustion engines and rapid compression machines," in *Symposium (International) on Combustion 5(1)*, 1955.

[3] U. Burke, W. K. Metcalfe, S. M. Burke, K. A. Heufer, P. Dagaut and H. J. Curran, "A detailed chemical kinetic modeling, ignition delay time and jet-stirred reactor study of methanol oxidation," *Combustion and Flame,* no. 165, pp. 125-136, 2016.

[4] P. Christoffer, N. Elna J K and C. Pichler, "Reduced Kinetic Mechanism for Methanol Combustion in Spark-Ignition Engines," *Energy Fuels,* no. 32, pp. 12805-12813, 2018.

[5] J. Li, Z. Zhao, A. Kazakov, M. Chaos, F. L. Dryer and J. J. Scire, "A comprehensive Kinetic Mechanism for CO, CH2O, and CH3OH Combustion," *International Journal of Chemical Kinetics,* no. 39 (3), pp. 109-136, 2007.

[6] K. Kumar and C.-J. Sung, "Autoignition of Methanol: Experiments and Computations," *International Journal of Chemical Kinetics,* pp. 175-184, 2011.

[7] J. Vancoillie, L. Sileghem and S. Verhelst, "Development and Validation of a Knock Prediction Model for Methanol-Fuelled SI Engines," *SAE International ,* 2013.

[8] S. K. Mahendar, T. Larsson and A. C. Erlandsson, "Alcohol lean burn in heavy duty engines: Achieving 25 bar IMEP with high efficiency in spark ignited operation," *International Journal of Engine Research,* pp. 1-12, 2020.

[9] Anglo Belgian Corporation, "abc-engines," [Online]. Available: https://www.abc-engines.com/uploads/files/Data-sheet-dual-fuel_ENG.pdf. [Accessed 17 April 2023].

Heavy duty opposed piston free piston engine simulation using 0D/1D modeling.

A. Maiello*, R. Saviano*, C. Beatrice*
armando.maiello@stems.cnr.it
*CNR-STEMS, Istituto di Scienze e Tecnologie per L'Energia e La Mobilità Sostenibili, Via G. Marconi 4, 80125, Napoli, Italy

Abstract
The use of free piston engine linear generators (FPELGs) could be a solution to overcome difficulties related to new legislation Euro 7 that will enter effect from 2025. FPELGs does not feature crankshaft kinematics as they rely on an alternative linear movement to produce electric power using an electric generator to power an electric motor or feed a battery. Lacking the crankshaft kinematics, these systems have reduced friction, can work with different compression ratio and show improved combustion efficiency since the expansion stroke is faster resulting in a combustion closer to a constant volume combustion. The absence of the crankshaft also brings to a reduction of possible points of failure and to a lower occurrence of wear and reduced maintenance required for optimal operation. On the other hand, the lack of a crankshaft requires an optimal control system to avoid malfunctions such as piston hitting the cylinder head resulting in engine failure.
This work introduces a new methodology for simulating FPELGs using coupled simulations between Simulink and GT-Power. Simulink produces the output of position of the engine as a linear length, port opening, combustion, electric force, and control logic; GT-Power is used to simulate the flow through ducts and ports and heat transfer.
Results concerning a supercharged heavy duty 2 strokes FPELG will be shown to demonstrate the potential of both the developed methodology, the implemented control strategy and the analysed system.

FPEGs Configurations and State of Art
Different configurations are possible for FPELGs [1,2]:
The single-piston configuration (Figure 1a) consists of a combustion cylinder (CC), a Linear Electric Machine (LEM), and a rebound device (RD). When combustion occurs, the movement of the piston causes an energy storage in the RD which returns the piston to the Top Dead Center (TDC). In this phase, LEM works as an electric motor to push the piston to TDC. During the expansion stroke, current flows through the coils of the LEM and electrical power is generated.
Dual piston (Figure 1b) consists of a single rod on which a linear generator is mounted and at the ends of the rod there are the two CCs which determine the movement of the system. This configuration is particularly prone to misfire problems

since motion is driven solely by combustion and there is no RD. The electric machine can also act as a motor and normal operation can be restored in the event of a fault with specific control logics.
The opposed piston configuration can be schematized as two single pistons sharing either the CC or the RD. In the first case (Figure 1c) the head of one piston represents the cylinder head of the other and vice versa. There are two LEMs and two RDs. In the second case (Figure 1d) there is a common RD connected to two rods with two LEMs and two CCs.

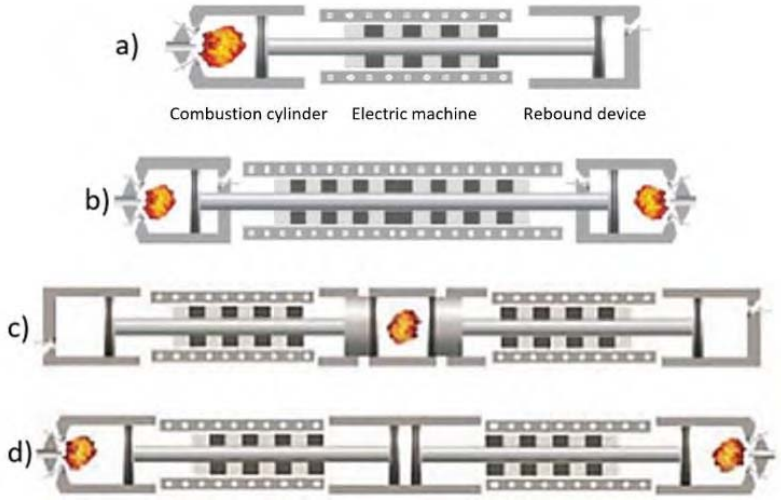

Figure 1. FRELGs configurations: a) single piston, b) dual piston, c) opposed with central CC, d) opposed with central RD.

In [3] Jia et al. compared the friction of a conventional engine with a single piston FPELG of similar size. The total frictional loss is nearly half those of a conventional engine because of the lack of the crankshaft.
In [4] a complete review of the studied control strategies was provided. The authors carried out a statistical analysis which also classifies the control strategies present in the literature. They suggested that this could help future research activities.

Simulation Environments and Simulation Methodology

The aim of the present work is to introduce a new methodology of simulation that pairs the simplicity of 0D models with the accuracy of thermodynamic calculation of GT-Power that captures gas dynamics through 1D computational fluid dynamic. The piston position dynamics, port opening, combustion, electric machine force and control strategy have been modelled in Simulink; while the flow through the ducts and ports and heat transfer have been modelled in GT-Power.
In Figure 2 is shown the Simulink scheme of an opposed piston with central CC. Definition of many sub-assemblies allows to model different configurations with minimal effort.
Piston position is calculated solving the equation of the piston dynamic that is:

$$F_p + F_e + F_f = m * a \tag{1}$$

Where F_p is the total force calculated from the cylinder pressure and the rebound device pressure, F_e is the electric force and F_a is the friction force.
Port opening and combustion are modelled using a linear correlation between linear piston position and crank angle calculated in GT-Power. This was necessary because GT-Power uses the engine speed to convert time in crank angles but for FPELG it is only possible to define an average frequency that is not the same during the whole cycle.

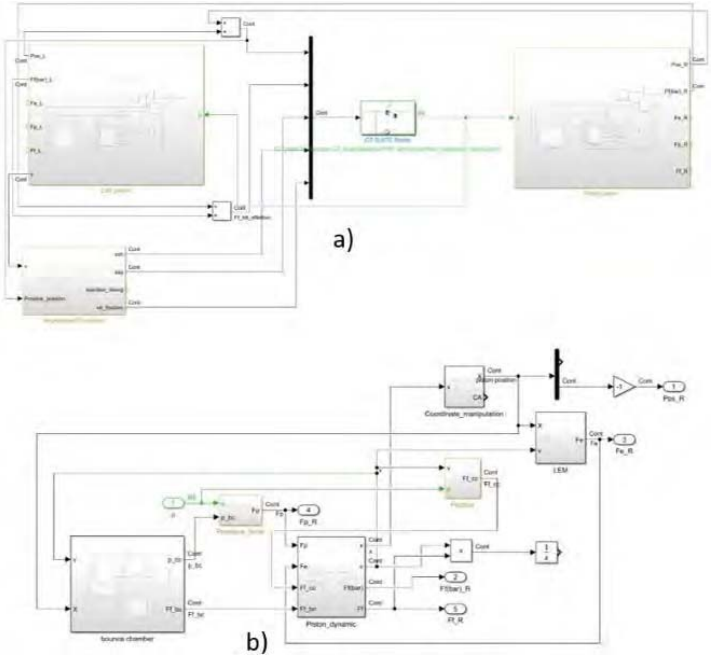

Figure 2. Simulink model: a) opposed piston configuration, b) left piston detail.

The electric machine is modelled according to [5,6]. The equations used are:

$$F_{em} = \frac{3\pi}{2\tau}\psi_f * i \tag{2}$$

$$F_{eg} = -c * v \tag{3}$$

Where F_{em} is the electric force when the machine is working as motor, F_{eg} is the electric force when the machine is working as generator, ψ_f is the flux produced by the permanent magnet, i is the current flowing into the coils, τ is the pole-pitch, c is the generator constant and v is the piston velocity.
The control strategy implemented uses a PID to control the electric force when LEM is in motor operation that is based on the piston position and uses the TDC position as target to be reached. A control based on the piston velocity determines the switch of LEM from motor to generator operation. In this condition the control is absent since the force exerted from the generator depends only on the velocity of the piston.
The GT SUITE Model block allows for data exchange with GT-Power.
A scheme of the GT-Power model is reported in Figure 3. The system is modelled

using the templates provided in the software and using a "Simulink Harness" block that allows for data exchange with Simulink. As suggested from the manual of the software, only one cylinder block is used to better reproduce the fluid dynamic of the gasses inside the cylinder.
Simulations were run using Simulink as master software, so the solver was chosen by Simulink in an automatic way as defined in the model settings. This also allowed to use "Scope" block to create graphs to see the output while simulation was ongoing.

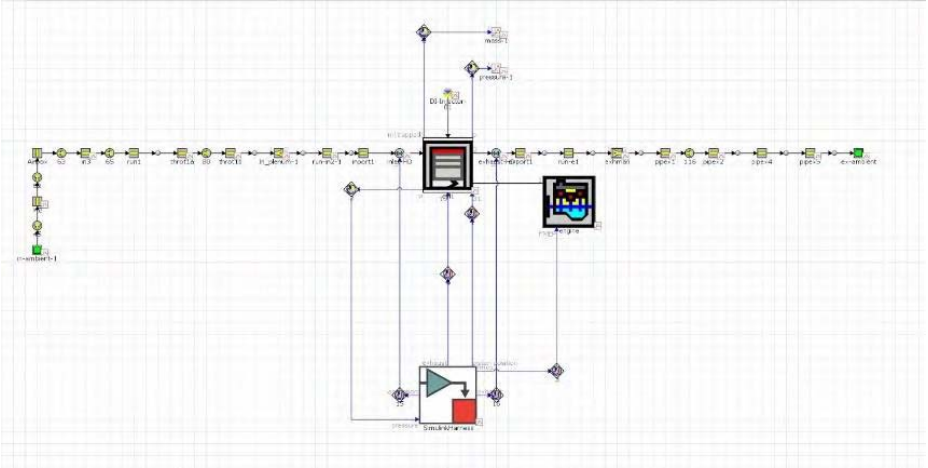

Figure 3. GT-Power model.

Comparison of Opposed Configuration with Central Combustion Cylinder and Central Rebound Device

When running a simulation in GT-Power the piston position is expected to be a value between 0 (TDC position) and -s (BDC position), with s being the stroke of the engine. The main critical issue faced during simulations run was a failure of the simulation if piston position exceeded this range. To overcome such issue, position has been limited to be in this range of values when integrating equation (1). To be sure whether the limitation has been actuated or not, a logical bit can be checked.
Some of the main parameters of the model can be found in Table 1.

Table 1. Main parameters of the models.

Description	Value
Bore (mm)	120
Maximum stroke (mm)	288
Compression ratio (-)	14
Piston mass (kg)	7
ψ_f (Wb)	0.444
τ (mm)	40
c (ks/s)	150

Results in terms of piston position and piston velocity are shown in Figure 4. Piston

position is effectively controlled to reach the TDC and BDC position without any limitation being actuated. Piston velocity values are in a realistic range considering the inertia of the piston and it is visible that velocity is higher during expansion stroke since combustion has occurred with a sudden increase of pressure in the CC. The effective compression ratio is lower than the one expected from the input in GT-Power but it is still close enough to the value expected.

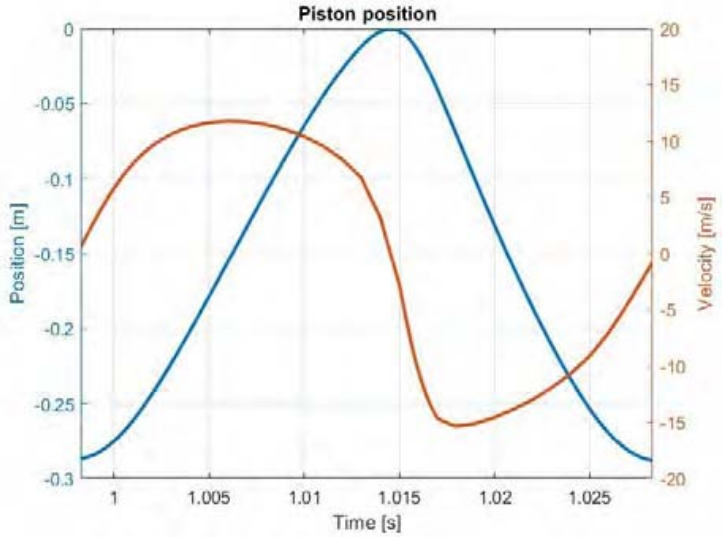

Figure 4. Piston position and piston velocity for both models.

Cylinder pressure values (Figure 5) are lower than those expected in an engine of similar displacement and compression ratio but are correctly aligned with the piston position. This could be due to the necessity of an optimization of the scavenging and combustion processes.

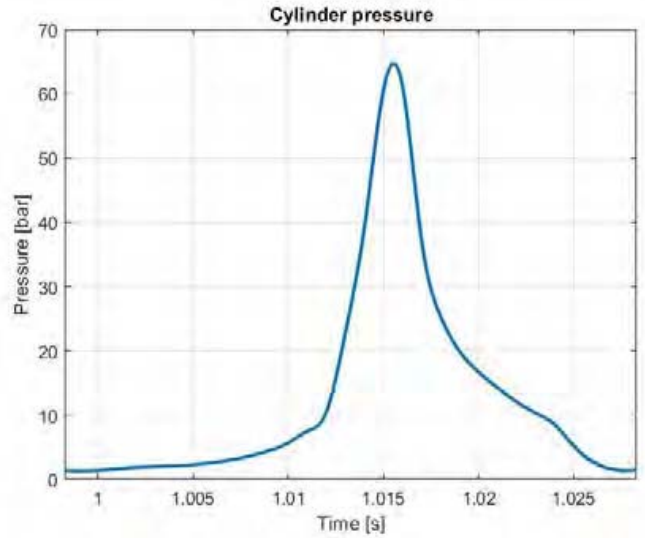

Figure 5. Pressure and heat transfer comparison for both models.

Output values of volumetric efficiency, indicated efficiency and electric power per cycle are reported in Table 2. They could be improved with an optimization of the design of the model.

Table 2. Main energetic models' output.

Description	Value
Volumetric efficiency (-)	0.86
Indicated efficiency (%)	41.7
Electric power generated per cycle (kW/cycle)	17.3

Conclusions and future developments

The developed simulation methodology can be successfully used to study FPELGs with good accuracy and limited computational effort without occurring in simulation failure or piston exceeding the dead center positions.
The energy outputs give positive results that could be improved with an optimization of the system developed so far. Energetic balance between rebound device and LEM as well as the switching moment between motor and generator operation can be studied more in detail to find the best design to ensure correct operation and best efficiency of the system. Further analysis can involve the thermal engine considering port timing, spark timing, ecc.
Simulations at different frequency and partial load will be considered as well to determine the flexibility of the system, how efficiency is affected when changing the operating point of the system and how the control strategy reacts to such changes.

References

[1] A. Heron and F. Rinderknecht, "Comparison of range extender technologies for battery electric vehicles," 2013 Eighth International Conference and Exhibition on Ecological Vehicles and Renewable Energies (EVER), Monte Carlo, Monaco, 2013, pp. 1-6, doi: 10.1109/EVER.2013.6521579.
[2] Schneider, S., & Friedrich, H. E. (2016). Experimental Investigation and Analysis of Homogeneous Charge Compression Ignition in a Two-Stroke Free-Piston Engine. SAE International Journal of Engines, 9(1), 365–373. http://www.jstor.org/stable/26284819
[3] Jia, B., Mikalsen, R., Smallbone, A., & Roskilly, A. P. (2018). A study and comparison of frictional losses in free-piston engine and crankshaft engines. *Applied Thermal Engineering*, *140*, 217-224.
[4] Raheem, A. T., Aziz, A. R. A., Zulkifli, S. A., Rahem, A. T., & Ayandotun, W. B. (2022). A review of free piston engine control literature—taxonomy and techniques. *Alexandria Engineering Journal*.
[5] Sun, P., Zhang, C., Chen, J., Zhao, F., Liao, Y., Yang, G., & Chen, C. (2017). Hybrid system modeling and full cycle operation analysis of a two-stroke free-piston linear generator. *Energies*, *10*(2), 213.

[6] Mao, J., Zuo, Z., Li, W., & Feng, H. (2011). Multi-dimensional scavenging analysis of a free-piston linear alternator based on numerical simulation. *Applied Energy*, *88*(4), 1140-1152.


THE COMBUSTION INSTITUTE
1954

SESSION II

NOVEL CONCEPTS INCLUDING MULTI-PHYSICS PHENOMENA


THE COMBUSTION INSTITUTE
1954

A NOVEL MACHINE LEARNING BASED LUMPING APPROACH FOR THE REDUCTION OF LARGE KINETIC MECHANISMS FOR PLASMA-ASSISTED COMBUSTION APPLICATIONS

G. Rekkas-Ventiris*, A. Duarte Gomez, N. Deak**, N. Kincaid***, P. Pepiot***, F. Bisetti**, A. Bellemans***

corresponding author: georgios.rekkas.ventiris@vub.be
*Faculty of Engineering, Thermo and Fluid Dynamics (FLOW), VUB, Belgium
**Department of Aerospace Engineering and Engineering Mechanics, UT Austin, USA
***Sibley School of Mechanical and Aerospace Engineering, Cornell University, USA

Abstract

This work focuses on the reduction of a detailed isooctane plasma-assisted combustion (PAC) mechanism, consisting of 2805 species and 18457 reactions, by combining two techniques. Using the well-established plasma-specific direct relation graph with error propagation (P-DRGEP) method, a reduced mechanism of 415 species and 4716 reactions is produced. The mechanism has excellent predictive capabilities over a wide range of initial conditions for: initial pressure equal to 10 atm, temperatures from 750 K to 1200 K and equivalence ratios from 0.75 to 1.50. In addition, a plasma-specific isomer lumping approach is proposed and its viability and accuracy demonstrated. With the gradient boosting machine learning method and data from 0D reactor simulations that employ the reduced mechanism, predictive regression models are trained, which are found to describe accurately the lumped reaction rate coefficients. A lumped mechanism is developed, which contains 300 species and 3827 reactions. Two variations of this method are presented: one with models that use just gas temperature as input feature and another with two-input models, which apart from gas temperature also employ one of the radicals O, H or OH as a second input feature. In the former approach and over the broad range of initial conditions used to test the reduced mechanism, absolute errors fall within 6% on time to ignition, when compared to simulations with the detailed mechanism. The latter approach produces even lower errors, which do not exceed 3%.

Activation of Highly Stable Molecules in Atmospheric Pressure Plasmas for Power-to-Chemical Conversion

L. M. Martini, F. Spadoni, P. Tosi
luca.martini.1@unitn.it
Department of Physics, University of Trento, 38123 Trento, Italy

Abstract
The decarbonization of society requires replacing fossil with renewable resources as a source of fuels and chemicals. One could use widely available molecules, such as CO_2, N_2, and H_2O, to obtain this, provided an efficient method exists to activate these highly stable molecules.
Ideally, the process should direct renewable energy toward molecular dissociation while minimizing the waste of energy in gas heating. To this purpose, the plasma approach utilizes the unique non-equilibrium properties of gaseous discharges. However, it is crucial to have control over the dissociation mechanism and to be able to monitor it to obtain the desired efficiency. We have exploited the adjustable pulsing schemes of nanosecond repetitively pulsed (NRP) discharges to control both the conversion and the efficiency of the activation process of CO_2 and N_2. Our recent contributions in this area will be presented during the workshop.

Introduction
The successful and widespread use of gas discharges is due to the possibility of inducing out-of-the-equilibrium conditions that promote highly endothermic chemical reactions in mild conditions (i.e., close to atmospheric pressure and room temperature). Non-thermal plasmas can promote the activating of highly-stable molecules, and potential applications are a) carbon dioxide conversion into molecules with higher enthalpies as a way for storing (renewable) energy in C-neutral chemicals; [1, 2, 3], b) sustainable nitrogen fixation as an alternative to the energy-intensive Haber-Bosch process for ammonia production [4].
The challenge of making the plasma technology commercially viable lies in finding the right tradeoff between bulk conversion and overall energy efficiency. A new approach to studying plasma chemistry is required beyond merely measuring the reaction products that exit the reactor. Local, time-resolved diagnostics must be developed to gain insight into the plasma at the appropriate time scale [5, 6]. In the present contribution, we present our recent developments in understanding the mechanisms of plasma dissociation of CO_2 in the sub μs time scale. In some cases, like N_2/H_2 conversion to ammonia, the plasma alone shows modest performances, and adding a catalytic stage coupled with the discharge is needed. Due to the filamentary nature of the discharge, the choice of the proper catalytic support is crucial. Our preliminary investigation on the optimal catalytic support to be coupled

with an NRP discharge for converting N_2 and H_2 into NH_3 is presented.

Materials and methods

The CO_2 reduction and N_2/H_2 conversion were carried out in two different discharge reactors, as reported in Figures 1(a) and 1(b). The two reactors shared the same electrode geometry and inlet/outlet ports for the gas flows.

Discharge apparatus. The electrodes were arranged in a pin-to-pin configuration and placed inside a vessel with optical access for spectroscopic investigations. The high voltage (HV) electrode serves as the gas inlet and the grounded as the gas outlet. The inter-electrode gap was set at 5 mm. An HV power supply was employed to produce the HV pulses, with a full width at half maximum of about 10 ns. Both reactors were operated at atmospheric pressure (950 mbar). Mass flow controllers (MFC) were used to feed the process gas inside the discharge chambers. In the case of the CO_2 reduction experiment, a trace amount of water or nitrogen was added to the gas stream as a precursor of OH or for spectroscopic thermometry respectively. Voltage and current probes were used to measure the energy dissipated in the discharge. The specific input energy (SEI) was calculated as the power dissipated by the discharge divided by the reactant standard flow.

Effluent gas analysis. A micro gas chromatograph (μGC) equipped with a thermal conductivity detector was placed in the exhaust gas line for in-line quantification of CO_2, CO, O_2, N_2, and H_2. A Fourier transform infrared (FTIR) spectrometer is used to quantify NH_3.

Spectroscopic apparatus and methods. The time evolution of the gas temperature in the CO_2 reduction experiment was derived from the optical emission of the second positive system (SPS) of N_2 [6]:

$$N_2(C^3\Pi_u, v'=0) \rightarrow N_2(B^3\Pi_g, v=0) \quad (1)$$

For this purpose, 5% of N_2 was added to the CO_2 stream. The emission was collected by a 300 mm focal length spectrograph equipped with a gated intensified-CCD (ICCD) camera. The time evolution of the CO_2 conversion was determined using the collisional energy transfer laser induced fluorescence methodology [7]. A frequency-doubled tunable dye laser produced the OH(A), and the fluorescence was detected with the same apparatus used to record the N_2 SPS emission. As described in detail in [8, 9], energy-transfer collisions with the background molecules modify the population of the laser-excited OH(A) state and influence the fluorescence spectra. Thus, LIF outcomes recorded various times after the discharge pulse carry information on gas composition and CO_2 dissociation.

(a)

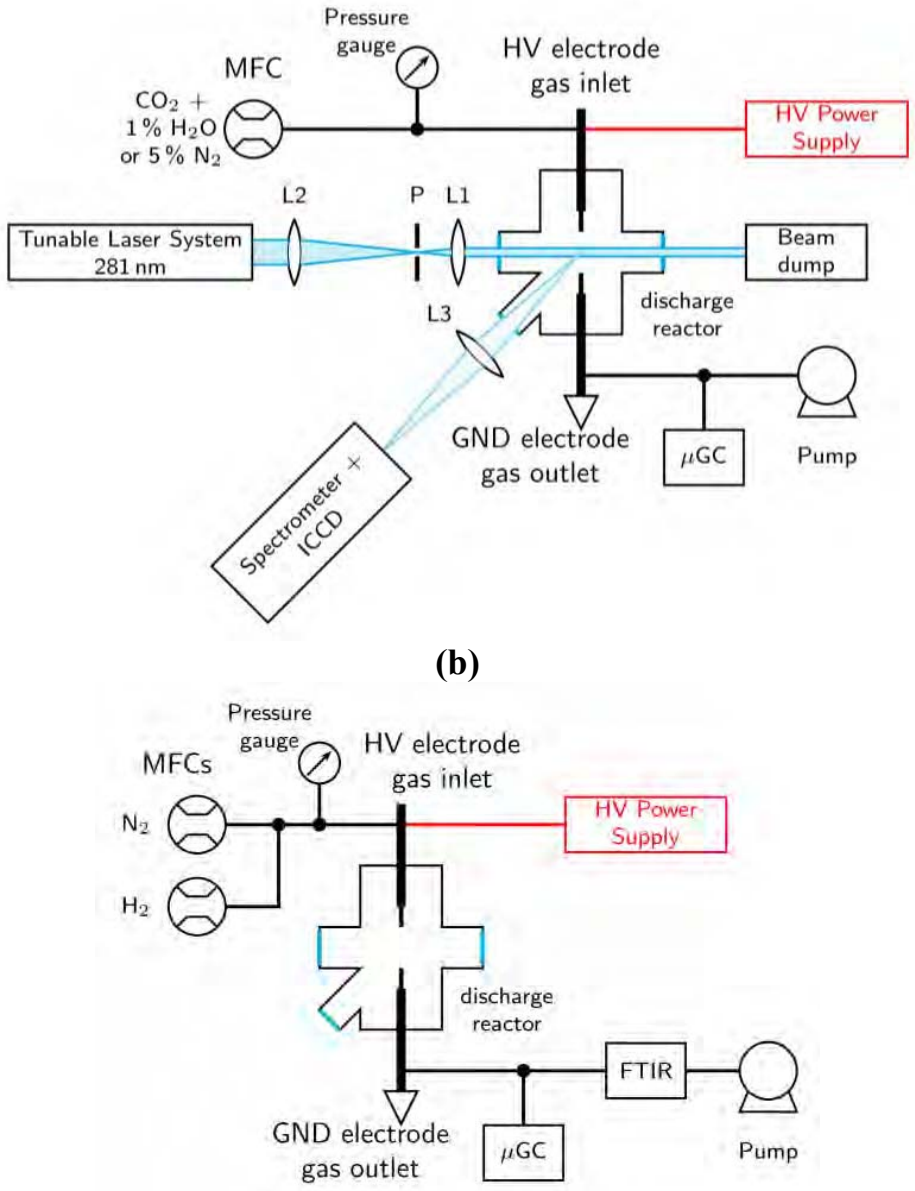

Figure 1. Simplified diagram of the experimental setups for **(a)** CO2 reduction experiment and **(b)** ammonia production.

Results and Discussion

CO_2 reduction The time evolution of the gas temperature (T_g) and CO_2 conversion (C_{CO2}) [10] are presented in Figure 2. The CO_2 conversion in the first 80 ns does not increase significantly (C_{CO2} < 8 %), despite most of the energy (around 85%) has been already dissipated in the first 20 ns after the breakdown. Also, T_g does not exceed 1200 K in this first phase. Higher values of gas temperature and CO_2 conversion are observed around 3-5 us with a subsequent decrease of both. At longer delays, C_{CO2} reaches values similar to those measured at the reactor exit with the μGC (around 10% conversion, 3.5 kJ dm^{-3} of SEI). The progressive rise of the CO_2 conversion after the breakdown hints that the direct excitation to a dissociative state by electron impact of the CO_2 molecule might not be the primary cause of the

dissociation, which can be most likely attributed to an indirect mechanism mediated by CO_2 excitation [10, 11].

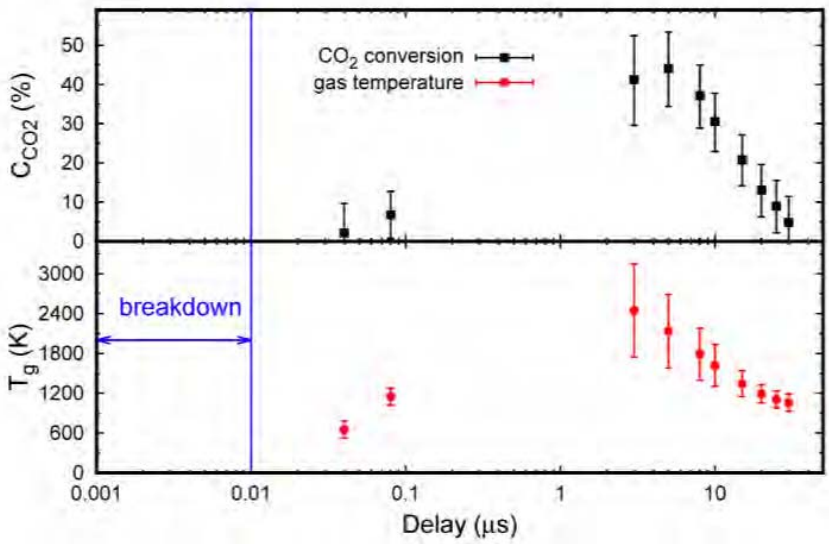

Figure 2. CO_2 conversion (C_{CO2}) and gas temperature (T_g) as a function of the delay with respect to the HV pulse. Data adapted from [10]

Ammonia Synthesis. Typical values of NH_3 concentration, energy yield (EY - the energy spent for producing a gram amount of NH_3) as a function of the gas composition, and the support material are presented in Table 1. The NH_3 production as a function of the specific input energy is similar to the values reported in the literature [4]. We observed that the H_2:N_2 ratio could influence NH_3 production and, consequently, the EY. The presence of the selected substrates for catalytic materials does not significantly affect the NH_3 conversion. The poor performances of the plasma processes without catalysts highlight the importance of identifying appropriate materials to exploit the synergy between plasma and catalysis.

Table 1. Typical values of ammonia concentration and energy yield as a function of the gas composition and the support material.

Support	H2:N2 ratio	SEI (kJ dm^{-3})	[NH_3] (ppm)	EY (g kWh^{-1})
none	9:1	5.0(5)	127(4)	$6.9(7)\cdot10^{-2}$
none	2:3	5.6(5)	67(2)	$3.2(3)\cdot10^{-2}$
SiO_2 cylinder	2:3	6.0(5)	72(2)	$3.2(3)\cdot10^{-2}$
quartz wool cylinder	2:3	6.7(5)	95(3)	$3.8(4)\cdot10^{-2}$

Conclusions

We reported a delay of hundreds of nanoseconds between the discharge breakdown and the time when most of the CO_2 dissociation occurs in an NRP discharge. This result indicates that the primary mechanism of CO_2 dissociation is mainly caused by molecular-excitation kinetics.
The ammonia synthesis in an N_2/H_2 NRP discharge presents EY in line with other discharge types. Understanding the influence of the substrate and the coupling of the plasma with the catalyzer is an essential step toward more efficient plasma NH_3 synthesis.

References

[1] Montesano, C., Quercetti, S., Martini, L.M., Dilecce, G., Tosi, P., "The effect of different pulse patterns on the plasma reduction of CO2 for a nanosecond discharge", *J. CO2 Utiliz.* 39: 101157 (2020)

[2] Montesano, C., Faedda, M., Martini, L.M., Dilecce, G., Tosi, P., "CH4 reforming with CO2 in a nanosecond pulsed discharge. The importance of the pulse sequence", *J. CO2 Utiliz.* 49: 101556 (2021)

[3] Delikonstantis, E., Scapinello, M., Singh, V., Poelman, H., Montesano, C., Martini, L.M., Tosi, P., Marin, G.B., Geem, K.M.V., Galvita, V.V., Stefanidis, G.D. "Exceeding Equilibrium CO2 Conversion by Plasma-Assisted Chemical Looping", *ACS Energy Lett.* 7:1896–1902 (2022)

[4] Rouwenhorst, K.H.R., Engelmann, Y., van 't Veer, K., Postma, R.S., Bogaerts. A., Lefferts, L., "Plasma-driven catalysis: green ammonia synthesis with intermittent electricity," *Green Chem.* 22: 6258–6287 (2020)

[5] Martini, L.M., Lovascio, S., Dilecce, G., Tosi, P., "Time-Resolved CO2 Dissociation in a Nanosecond Pulsed Discharge", *Plasma Chem. Plasma Process.* 38: 707–718 (2020)

[6] Ceppelli, M., Salden, T.P.W., Martini, L.M., Dilecce, G., Tosi, P., "Time-resolved optical emission spectroscopy in CO_2 nanosecond pulsed discharges", *Plasma Sources Sci. Technol.* 30: 115010 (2021)

[7] Martini, L.M., Gatti, N., Dilecce, G., Scotoni, M., Tosi, P. "Laser induced fluorescence in nanosecond repetitively pulsed discharges for CO_2 conversion", *Plasma Phys. Control. Fusion* 60: 014016 (2018)

[8] Ceppelli, M., Martini, L.M., Dilecce, G., Scotoni, M., Tosi, P., "Non-thermal rate constants of quenching and vibrational relaxation in the OH ($A^2\Sigma^+$, v=0,1) manifold", *Plasma Sources Sci. Technol.* 29: 065019 (2020)

[9] Dilecce, G., Martini, L.M., Ceppelli, M., Scotoni, M., Tosi, P. "Progress on laser induced fluorescence in a collisional environment: the case of OH molecules in ns pulsed discharges", *Plasma Sources Sci. Technol.* 28: 025012 (2019)

[10] Montesano, C., Salden, T.P.W., Martini, L.M., Dilecce, G., Tosi, P.,

"CO_2 Reduction by Nanosecond-Plasma Discharges: Revealing the Dissociation's Time Scale and the Importance of Pulse Sequence", accepted by *J. Phys. Chem. C* (2023)

[11] Heijkers, S., Martini, L.M., Dilecce, G., Tosi, P., Bogaerts, A., "Nanosecond Pulsed Discharge for CO_2 Conversion: Kinetic Modeling To Elucidate the Chemistry and Improve the Performance" *J. Phys. Chem. C* 123: 12104–12116 (2019)

SOLAR FUELS FROM CHEMICAL LOOPING CYCLES WITH PEROVSKITE CATALYST IN AN INNOVATIVE FLUIDIZED BED REACTOR

S. Padula*, C. Tregambi,***, M. Troiano*,**, A. Di Benedetto*, P. Salatino*, G. Landi**, R. Solimene****
gianluca.landi@stems.cnr.it, roberto.solimene@stems.cnr.it
*Dipartimento di Ingegneria Chimica dei Materiali e della Produzione Industriale (DICMaPI), Università degli Studi di Napoli Federico II, Napoli, Italy
**Istituto di Scienze e Tecnologie per l'Energia e la Mobilità Sostenibili (STEMS), Consiglio Nazionale delle Ricerche, Napoli, Italy
***Dipartimento di Ingegneria, Università degli Studi del Sannio, Benevento, Italy

Abstract
The production of solar fuels with renewable energy sources is considered a fundamental cornerstone to reach the goal of net-zero emissions by 2050. Water splitting through Chemical Looping cycles sustained by Concentrated Solar Thermal (CST) energy can be a valuable alternative to electrolysis. In the transitional phase toward a carbon-free industry model, Chemical Looping cycles can combine the use of natural or bio- gas to reduce energy requirements. The research in this field follows two parallel lines: the optimization of oxygen carriers and the development of solar reactors. In this study, a laboratory synthesized perovskite is tested in an innovative solar reactor based on fluidized bed technology.

Introduction
Concentrated Solar Thermal (CST) technology uses solar radiation as a heat source, by concentrating solar rays with an array of sun-tracking mirrors (heliostats) [1]. In the last decade the application of CST to power generation has spread over the world, reaching a total capacity of 6.2 GW in 2020 [2]. The application of CST to the production of solar fuels would mark a significant progress, leading to the decarbonization of different industrial sectors.
Chemical Looping cycles generally involve a metal oxide, that is cyclically reduced and oxidized, acting as an oxygen carrier [3]. Solar energy can sustain the endothermic reduction step, by which oxygen (O_2) is released:

$$MO_x \rightarrow MO_{x-y} + y/2\ O_2 \quad (1)$$

Then, the reduced oxide reacts with water vapor (H_2O) or carbon dioxide (CO_2), producing hydrogen (H_2) or carbon monoxide (CO) and getting oxidized back:

$$MO_{x-y} + y\ H_2O \rightarrow MO_x + y\ H_2 \quad (2)$$

$$MO_{x-y} + y\ CO_2 \rightarrow MO_x + y\ CO \quad (3)$$

By summing the two reaction steps, the overall result is the decomposition of $H_2O\backslash CO_2$. The reduction step typically occurs at temperatures of 1000-1500°C that can technically be reached in a solar reactor. Extremely low O_2 partial pressures are required, usually obtained by vacuum pumping or inert gas sweeping. By introducing methane (CH_4) in the reduction step, the reaction temperature can be lowered below 1000°C and no energy needs to be spent to keep a low O_2 partial pressure:

$$MO_x + y\ CH_4 \rightarrow MO_{x-y} + 2y\ H_2 + y\ CO \quad (4)$$

The overall process, known as Chemical Looping Reforming, is endothermic [4]. Compared to traditional steam/dry reforming, the reaction heat is supplied by CST energy rather than by the combustion of a fuel, so it yields an energy gain. An additional advantage is that the oxidation step produces a pure stream of H_2 or CO (Eq. (2–3)), ready for any use without need of downstream gas conditioning operations.

The research of suitable oxygen carriers is a key aspect in the development of this process. Feasible reduction temperatures, high re-oxidation rates and good stability over cycles are generally desired properties [5]. Perovskites are non-stoichiometric oxides characterized by the presence of two cations and represented with the formula ABO_3. They have excellent properties, due to a stable crystal phase that keeps unchanged throughout the process. Besides, redox properties can be suitably modified by partial substitution of the A and B cations [6].

The development of solar reactors is a complementary key aspect [7]. Recently a lanthanum (La) – iron (Fe) perovskite, in which strontium (Sr) partially replaces La, has been tested for Chemical Looping Reforming under both fixed and fluidized bed conditions [8]. A high selectivity toward partial oxidation of CH_4 was obtained. Fluidized bed experiments showed faster kinetics, but $9\%_w$ of the bed mass was lost probably due to fragmentation and elutriation.

In this study, the same perovskite is tested in an innovative Directly Irradiated Fluidized Bed Reactor (DIFBR) [9] and the results are compared with those obtained in a conventional fluidized bed. The effects of a support of γ-allumina are also investigated with the aim of optimizing the mechanical properties of the oxygen carrier.

Experimental methods

The experimental apparatus, outlined in Fig. 1, is the same used in previous studies [9] with some modifications. The reactor is made of stainless steel and thermally insulated with multiple layers of rock wool blanket. It is composed by two coaxial tubes connected at the bottom of a conical receiver (upper diameter 120 mm). A fluidizing gas stream is fed to the inner tube (riser, internal diameter 10 mm), through a nozzle and lifts the solid reactant up to the receiver. The solid falls in the outer tube

(the annulus) and then is recycled to the riser through four holes drilled in the riser wall.

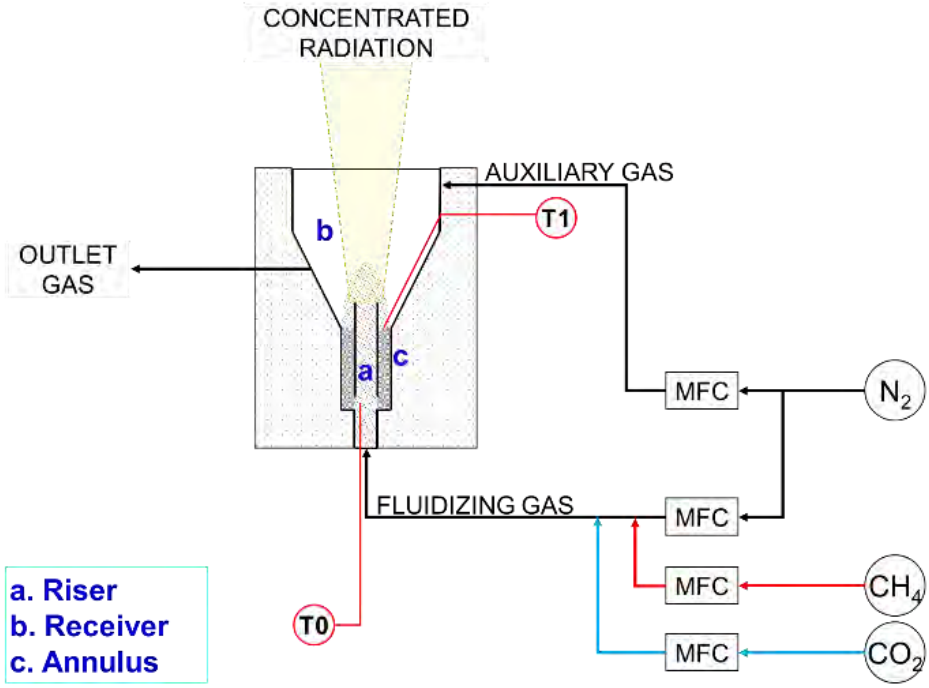

Figure 1. Experimental set-up.

The top of the receiver is sealed by a transparent quartz window, to let in solar radiation. An auxiliary stream can be fed to the receiver through a lateral tube for the protection of the window. The reactor is operated with a bed inventory of 10 g of sand-like particles. The fluidizing and reacting gases are fed from gas cylinders through mass flow controllers. Bed temperature is measured with two K-type thermocouples: one located inside the riser at the same height of the four orifices (T0), the other in the receiver at the inlet of the annulus (T1). A LabView application sets the mass flow controllers, monitors and records reactor temperatures. A high-flux solar simulator directly radiates the particles in the receiver. The power of the lamp can be varied within 2–7 kW_e with 1 kW_e steps.

The synthetized perovskite material has chemical formula $La_{0.6}Sr_{0.4}FeO_3$. A pure sample is prepared starting from an aqueous solution of nitrate salts by evaporation and calcination at 1000°C. Another perovskite sample is also prepared on a support of γ-allumina (Al_2O_3) by impregnation, evaporation and calcination at 920°C. The mass fraction of the perovskite in the supported catalyst is about 30%.

The performance of the two samples is investigated by carrying out several cycles for different inlet gas velocities. A reaction cycle consists of three steps: reduction with methane (CH_4), oxidation with carbon dioxide (CO_2) and then with oxygen (O_2). The lamp power is regulated in order to keep the T1 temperature in the range 880-900°C during the reaction steps. The supported sample is tested also in an electrically heated conventional fluidized bed for comparison. Fluidized bed tests were conducted in a 10 mm quartz tube at a temperature of 850°C taken as the mean between the T0 and T1 temperature and a gas velocity of 0.5 m/s.

Results

Figure 2 shows the temperature and gas concentration profiles during a typical reaction cycle performed in the DIFBR. The favored products of the reduction step are H_2 and CO, except for an initial peak of CO_2 and for carbon (C) that forms as perovskite full conversion is achieved. The oxygen carrier is totally re-oxidized after the steps with CO_2 and O_2, and cycles are repeatable showing no decrease in reactivity.

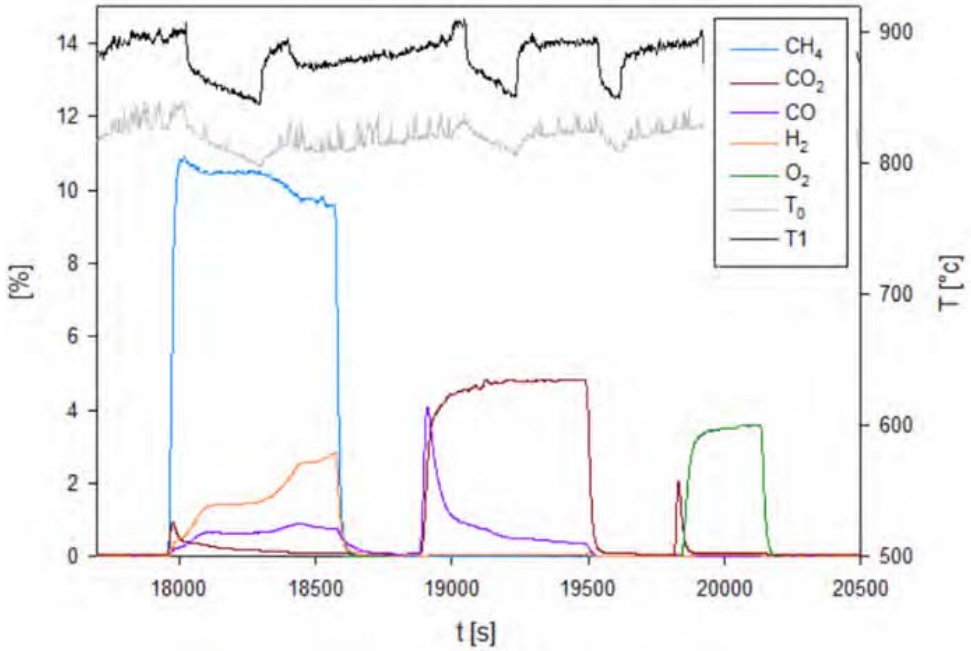

Figure 2. Concentration profiles of main gaseous species, and temperature, during a typical reaction cycle.

The maximum conversion degree of CH_4 mainly depends on the contact time (τ) between the reacting solid and the fluidizing gas (Fig. 3):

$$\tau = m_{perovskite} / Q \tag{5}$$

where $m_{perovskite}$ is the mass of perovskite in the fluidized bed and Q is the fluidizing gas flowrate. Contact times with the supported perovskite are lower than with the pure perovskite because it contains less reacting material for an equal bed inventory. Conversion degrees are coherently lower. On the other hand, the pure perovskite is very fragile and a mass loss of up to 30%$_w$ is reported for the test in DIFBR, whereas no significant loss of mass is reported for the supported perovskite.

Apparently, conversion degrees in the conventional fluidized bed are higher. However, if contact times in the solar reactor are recalculated by considering only the mass inside the riser (i.e., that effectively in contact with the gas), the data appear closer as shown in Fig. 4.

Finally, Figure 5 compares the maximum selectivity toward CO for the studied cases. Selectivity is higher for the solar reactor than for the conventional fluidized bed.

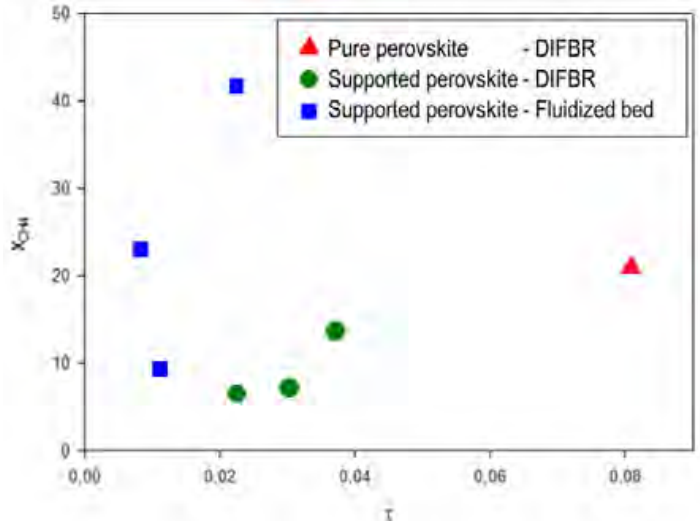

Figure 3. Maximum conversion of CH_4 (X_{CH4}) vs. contact time (τ [g h NL^{-1}]), considering the whole bed inventory for DIFBR.

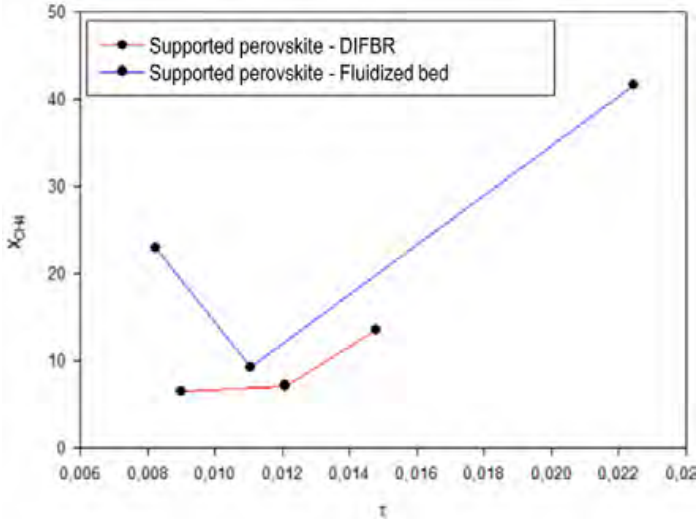

Figure 4. Maximum conversion of CH_4 (X_{CH4}) vs. contact time (τ [g h NL^{-1}]), considering only the riser inventory for DIFBR.

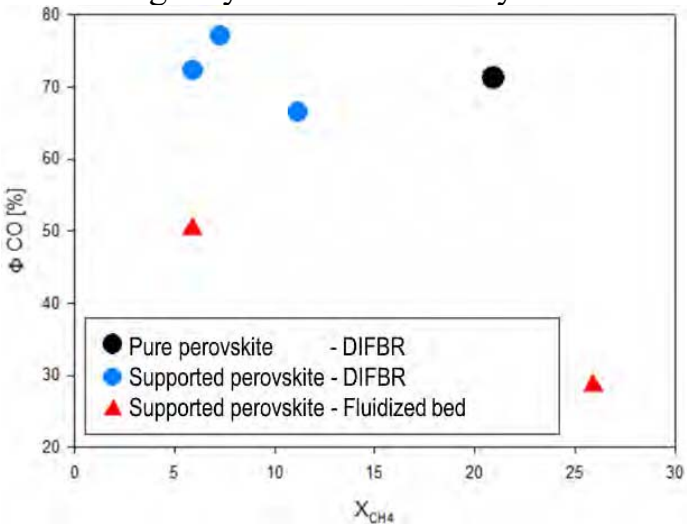

Figure 5. Maximum selectivity toward CO (Φ CO) vs. maximum conversion of CH_4 (X_{CH4}).

Conclusions

The $La_{0.6}Sr_{0.4}FeO_3$ perovskite is tested for Chemical Looping Reforming of CH_4 under simulated solar radiation in an innovative solar reactor. The results confirm that catalyst has a good stability and a good selectivity toward synthesis gas. The use of an alumina support improves the mechanical strength of the oxygen carrier and can be advised for use in fluidized bed reactors. On the other hand, the contact time must be optimized to improve CH_4 conversion. Selectivity toward synthesis gas is found to be higher for the solar reactor than for a conventional fluidized bed under equivalent operating conditions.

References

[1] Pitz-Paal, R., "Concentrating solar power" in *Future Energy: Improved, Sustainable and Clean Options for Our Planet*, Elsevier Ltd, 2020, pp. 413–430.

[2] REN21, "Renewables 2021 Global status report." (2021).

[3] C. Agrafiotis, M. Roeb, C. Sattler, "A review on solar thermal syngas production via redox pair-based water/carbon dioxide splitting thermochemical cycles", *Renewable and Sustainable Energy Reviews* 42:254–285 (2015).

[4] P. T. Krenzke, J. R. Fosheim, J. H. Davidson, "Solar fuels via chemical-looping reforming", *Solar Energy* 156:48–72 (2017).

[5] J. R. Scheffe, A. Steinfeld, "Oxygen Exchange Materials for Solar Thermochemical Splitting of H_2O and CO_2: A Review" *Materials Today* 17:341–348 (2014).

[6] G. Luciani, G. Landi, A. Aronne, A. Di Benedetto, "Partial substitution of B cation in $La_{0.6}Sr_{0.4}MnO_3$ perovskites: A promising strategy to improve the redox properties useful for solar thermochemical water and carbon dioxide splitting", *Solar Energy* 171:1–7 (2018).

[7] G. Zsembinszki, A. Solé, C. Barreneche, C. Prieto, A. I. Fernández and- L. F. Cabeza, "Review of Reactors with Potential Use in Thermochemical Energy Storage in Concentrated Solar Power Plants", *Energies* 11:2358 (2018).

[8] S. Padula, C. Tregambi, M. Troiano, A. Di Benedetto, P. Salatino, G. Landi, R. Solimene, "Chemical Looping Reforming with Perovskite based Catalysts for Thermochemical Energy Storage", *Energies* 15:8556 (2022).

[9] C. Tregambi, S. Padula, M. Galbusieri, G. Coppola, F. Montagnaro, P. Salatino, M. Troiano, R. Solimene, "Directly irradiated fluidized bed reactor for thermochemical energy storage and solar fuels production", *Powder Technology* 366:460–469 (2020).

Electric field-assisted flame synthesis of Carbon Nanoparticle films

A. Parisi*, G. De Falco*, M. Commodo, M. Sirignano*, P. Darvehi, **, B. Apicella**, C. Russo**, R. Griffo***, C. Carotenuto***, P. Minutolo**, F. Di Natale***

e-mail of corresponding author: arianna.parisi@unina.it

*Dipartimento di Ingegneria Chimica, dei Materiali e della Produzione Industriale, Università di Napoli Federico II, P.le V. Tecchio 80, 80125 Napoli (Italy)

**Istituto di Scienze e Tecnologie per l'Energia e la Mobilità Sostenibili, Consiglio Nazionale delle Ricerche, P.le Tecchio 80, 80125 Napoli, Italy

*** Dipartimento di Ingegneria, Università della Campania L. Vanvitelli, Via Roma 29, 81031 Aversa, Caserta (Italy)

Abstract

This work summarises the main findings of a joint research activity, carried out within the Italian PRIN Project MagicDust, which couples dedicated experimental campaigns and physical-mathematical modelling to exploit the main features of the electric field-assisted flame synthesis of Carbon NanoParticles (CNPs). The experimental and model results reveal that the new flame synthesis method can produce films with features very different from those obtained by conventional thermophoretic deposition, opening new possibilities in the production of CNP films with tunable properties.

Introduction

Carbon black (CB) is a fascinating material that is successfully adopted in various industrial applications thanks to its nano-sized dimensions, large specific area, chemical stability, mechanical strength, reasonable cost, good electrical conductivity and superhydrophobic properties [1,2]. In the last years, the scientific discovery of the many special features of nanometric particles promoted a new interest in the production of carbon nanoparticle (CNP) films. The CNPs are often manufactured following a top-bottom approach starting from carbon black particles that are processed using different treatments to reduce their sizes to the nanoscale [3,4].

However, combustion science and technology provide sufficient scientific and technological know-how to produce CNPs with virtually tunable size and properties following a more efficient and greener bottom-up approach: using a gaseous fuel with low molecular weight to sustain a highly controlled flame condition, and with accurate positioning and geometry of the CNP collector inside the flame, it is possible to drive the chemical processes that regulate the formation of aromatic structures, so to achieve CNPs with tunable size and properties [5–8]. Furthermore, the process involves a highly efficient combustion process with minimal creation of harmful by-products and the additional benefit of energy production. This bottom-

up approach is known as flame synthesis. Usually, the film formation process is based on the use of thermophoretic forces to deposit particles on a cold substrate immersed in the flame [9,10]. Thereinafter we will refer to this process as FS-Th. Most of the research available in the pertinent literature is based on the production of inorganic films [11–13] and its application to CNPs is the subject of few studies [14,15]. By working at carbon-to-oxygen ratios slightly higher than stoichiometric ones (C/O=0.33 ethylene-air flames), or placing the collector at a very low distance above the burner, it is possible to produce CNPs having sizes close to 10-20 nm, that are very similar to the primary particles obtained from carbon black but have a higher oxygen content that makes them more hydrophilic, a unique property that can be used for several applications alternative to those normally covered by CBs. However, in this flame, both the particle concentration and the thermophoretic deposition rate are low, undermining the process productivity.

The longstanding experience in the field of particle filtration by electrostatic forces suggested that the presence of an electric field in the flame – a plasma characterized by the presence of positive ions, electrons and charged particles – can fasten the deposition rate of CNPs overcoming the limitations of conventional thermophoretic flame synthesis [16,17].

This new process, named Electric field-assisted flame synthesis (FS-eTh in the following), is the topic of this work, which presents a summary of the main results obtained on the production of CNPs in a slightly sooting C/O ethylene-air flame. This study is based on experimental and modelling analysis and compares the characteristics of FS-eTh and FS-Th films and of their parent nanoparticles and agglomerates.

Materials and Methods

CNP films were produced in a flat laminar premixed ethylene-air flame stabilized on a water-cooled McKenna burner. Cold gas velocity was 9.8 cm/s, and the carbon-to-oxygen ratio (C/O) was set to 0.67, which corresponds to a slightly sooting flame. A sketch of the complete setup for CNP film deposition is shown in Figure 1.

CNP film was obtained on different substrates, namely a mica disk, a glass plate, and a glass plate with printed gold electrodes, which were rapidly inserted in the flame. Up to 600 insertions per test were used, the insertion time was 100 ms, and the height above the burner, HAB, was 15 mm. The probe containing the substrate was kept at a fixed electric potential, while the burner was grounded. The electric potential on the substrate was varied from 0 kV up to -3 kV, below the onset of corona discharge, which occurred at -4 kV. In this work, only negative electric potentials were tested, since in the presence of positive polarities, instabilities and flame extinctions were observed, leading to a more complex interpretation of the experimental and model results.

The experimental results consist of an extensive and brand-new set of data on the characteristics of aged CNP films and agglomerates obtained after the dissolution of the CNP films in N-Methyl-2-pyrrolidone: UV-Vis light absorption, Optical band

gaps, Raman spectra, fluorescence, AFM analysis on the morphology of the agglomerates, surface texture, wettability and conductivity measurements were carried out for both FS-Th and FS-eTh processes, allowing highlighting the similitudes and the differences of the produced films and the parent CNP agglomerates.

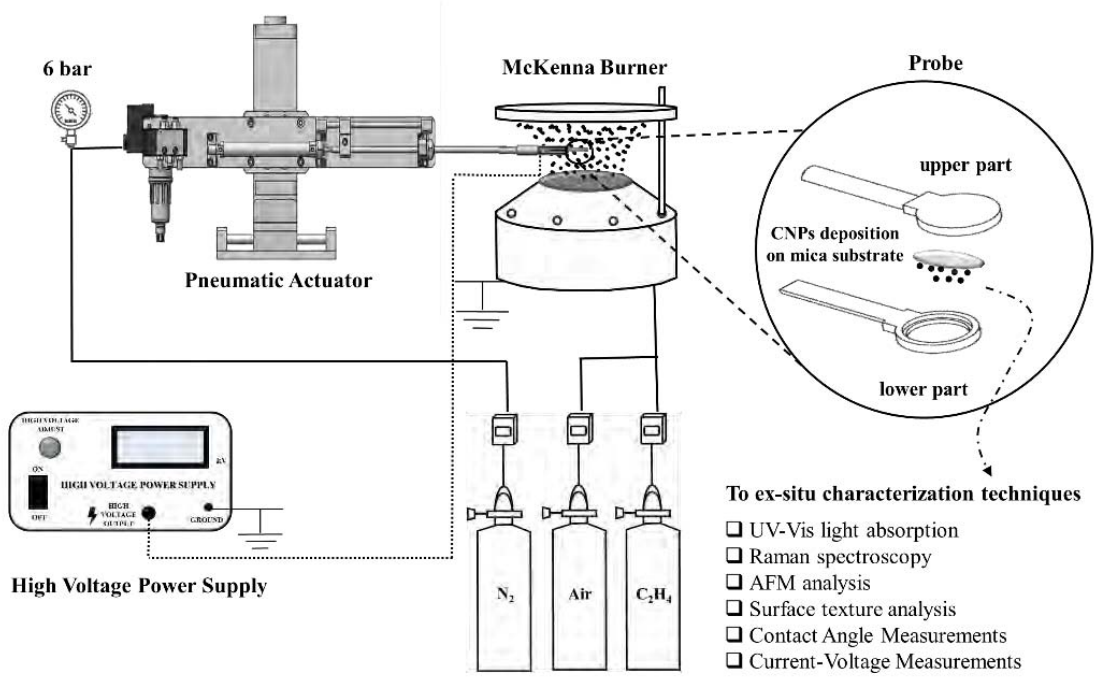

Figure 1. Sketch of the electrophoretic-thermophoretic film deposition setup.

Results and Discussion

To investigate the dynamics of particle deposition under the effect of the electric field, a mathematical model has been developed on the bases of the Langevin equation for momentum balance over a single particle and extensive knowledge of the flame properties in the investigated conditions [18]. The application of the electric field ignites the onset of two other forces in addition to the hydrodynamic and thermal Brownian motion which characterize the conventional thermophoretic deposition: the Coulomb and the electrophoretic forces, acting on charged particles, and the image and dielectrophoretic forces acting on uncharged particles. Indeed, electrophoretic forces also act between charged particles and grounded collectors in the conventional FS-Th process, but they are less relevant than the dominating thermophoretic forces.

The model reveals that the Coulomb electrophoretic force dwarfs the thermophoretic force and gives rise to faster and more perpendicular impacts of the charged particles with the collector. The dielectrophoretic force is relevant only for particles larger than 20 nm, but they represent a negligible fraction of the total CNPs found in the test flame, thus becoming irrelevant in the investigated conditions. Since the fraction of charged particles becomes appreciable only above 5 nm, the electric field-assisted

flame synthesis is more effective for these kinds of particles than for the finer ones [18]. The different impact conditions lead to produce more stable and compact films, not necessarily with a more uniform mesoscale morphology due to local polarization effects. Table 1 summarizes the similarities and differences between CNP films and their parent CNP agglomerates produced by FS-Th and FS-eTh.

Table 1. Overview of the CNP films and agglomerates properties, produced by conventional FS-Th and FS-eTh.

	FS-Th	**FS-eTh**
Length of aromatic islands	~1.36 nm	~1.36 nm
Film growth rate	2.9 nm/s	16.8 nm/s
Selective harvesting?	No	Yes, CNPs larger than 5 nm favoured
Surface texture/Roughness	Low both on nano and mesoscale, with uniform peaks and valleys.	Very high, with irregularities both on nano and mesoscale (flat valleys and many high spiked peaks).
	Volmer-Weber growth mode	Stranski-Krastanov growth mode
Fluorescence	Higher	Lower
CNP agglomerates	Small and unstable	Larger, stable with higher compactness
	Van der Waals's cohesive forces dominant	Electrostatic forces and polarization effects dominant
Optical band gap	~0.5 eV	Thickness-dependent, from ~0.5 eV to ~0 eV
Electrical conductivity	Low and temperature-dependent	Higher and temperature-independent
	$\sim 10^{-3}$ S/cm at 25°C	$\sim 10^{-1}$ S/cm
Wettability/ Contact Angle	Hydrophilic	Transition, Hydrophilic
	CA~13°	CA<40°

The experimental data confirm the model predictions and shed new light on the process dynamics. The Raman spectra indicate that the average size of the graphitic crystallites of the CNPs is unaffected by the presence of the electric field, confirming that the chemistry of CNP formation is not modified by the electric field applied to the sampling probe. The AFM and the surface texture analysis indicate that the morphology is more irregular than that observed for pure thermophoretic deposition, with the formation of large mesoscopic structures of micrometric or submicrometric sizes: while under thermophoretic flame synthesis, the film grows following the Volmer-Weber model, the electric field-assisted flame synthesis produces films which grow following the Stranski-Krastanov model [19]. This result is probably related to the onset of polarization effects in the agglomeration phenomena that gives rise to a preferential orientation of particles in the direction of the electric field,

which is often observed for the deposition of charged particles in electrets.
The AFM and the UV-Vis spectra indicate faster deposition rates, which are consistent with the model predictions. The conductivity and the optical band gap data prove the higher compactness of the deposits formed by FS-eTh as predicted from the CNPs deposition model: the analysis of agglomerates UV-Vis spectra indicates that they are on average much larger and stable for the FS-eTh and their optical band gap is lower than that of pure FS-Th. Besides, the optical band gap of the FS-eTh films indicates that its compactness greatly contributes to the conductivity of the deposits. Another indirect proof of the higher compactness of the FS-eTh deposits comes from the wettability tests, where the presence of large and stable agglomerates moving on the free surface of the droplets is observed. Indirectly, the higher stability of the agglomerates indicates that the FS-eTh is probably less useful for the production of CNPs suspension compared with the conventional thermophoretic flame synthesis.
The experiments also indicate that the hydrophilic character of the FS-Th films is preserved also in the FS-eTh films, which, despite their larger roughness, showed a fast transition from a Cassie-Baxter hydrophobic behavior to a hydrophilic one. On the other hand, this roughness is also representative of a higher surface area of the deposits that is beneficial for several technological applications.

Conclusion

Electric field-assisted flame synthesis emerges as a process useful to overcome the limits of conventional flame synthesis methods and add new degrees of freedom in synthesizing nanoparticles and thin films with unique and tunable properties. The process allows a faster deposition of CNPs and the production of more stable deposits with larger agglomerates, which allows a higher electric conductivity, and an irregular structure with large surface area and hydrophilic properties.
For its advantages in terms of enhanced productivity and the possibility to exploit new features compared with conventional carbon black particles, FS-eTh is worth future investigation and further technological development.

Acknowledgements

This is part of the PRIN 2017 MAGIC DUST project funded by the Italian Ministry of the University and the Research.

References

[1] D. Saini, N. Gunture, J. Kaushik, R. Aggarwal, K.M. Tripathi, S.K. Sonkar, Carbon Nanomaterials Derived from Black Carbon Soot: A Review of Materials and Applications, ACS Appl Nano Mater. 4 (2021) 12825–12844.
[2] R. Kumar, E. Joanni, R.K. Singh, D.P. Singh, S.A. Moshkalev, Recent advances in the synthesis and modification of carbon-based 2D materials for application in energy conversion and storage, Prog Energy Combust Sci. 67 (2018) 115–157.

[3] W. Lian, H. Song, X. Chen, L. Li, J. Huo, M. Zhao, G. Wang, The transformation of acetylene black into onion-like hollow carbon nanoparticles at 1000 °C using an iron catalyst, Carbon N Y. 46 (2008) 525–530.

[4] S. Hu, Y. Dong, J. Yang, J. Liu, S. Cao, Simultaneous synthesis of luminescent carbon nanoparticles and carbon nanocages by laser ablation of carbon black suspension and their optical limiting properties, J Mater Chem. 22 (2012) 1957–1961.

[5] M. Sirignano, C. Russo, A. Ciajolo, One-step synthesis of carbon nanoparticles and yellow to blue fluorescent nanocarbons in flame reactors, Carbon N Y. 156 (2020) 370–377.

[6] J.W. Martin, M. Salamanca, M. Kraft, Soot inception: Carbonaceous nanoparticle formation in flames: Soot inception, Prog Energy Combust Sci. 88 (2022).

[7] P. Minutolo, M. Commodo, A. D'Anna, Optical properties of incipient soot, Proceedings of the Combustion Institute. (2022).

[8] M. Commodo, G. de Falco, P. Minutolo, A. D'Anna, Structure and size of soot nanoparticles in laminar premixed flames at different equivalence ratios, Fuel. 216 (2018) 456–462.

[9] F. Zheng, Thermophoresis of spherical and non-spherical particles: a review of theories and experiments, Adv Colloid Interface Sci. 97 (2002) 255–278.

[10] C. Russo, B. Apicella, A. Tregrossi, M.M. Oliano, A. Ciajolo, Thermophoretic sampling of large PAH (C ≥ 22–24) formed in flames, Fuel. 263 (2020).

[11] G. De Falco, A. Porta, A.M. Petrone, P. del Gaudio, A. el Hassanin, M. Commodo, P. Minutolo, A. Squillace, A. D'Anna, Antimicrobial activity of flame-synthesized nano-TiO2 coatings, Environ Sci Nano. 4 (2017) 1095–1107.

[12] E.D. Tolmachoff, A.D. Abid, D.J. Phares, C.S. Campbell, H. Wang, Synthesis of nano-phase TiO2 crystalline films over premixed stagnation flames, Proceedings of the Combustion Institute. 32 II (2009) 1839–1845.

[13] Y. Zhang, L. Shuiqing, S. Deng, Q. Yao, S.D. Tse, Direct synthesis of nanostructured TiO2 films with controlled morphologies by stagnation swirl flames, J Aerosol Sci. 44 (2012) 71–82.

[14] G. De Falco, M. Commodo, M. Barra, F. Chiarella, A. D'Anna, A. Aloisio, A. Cassinese, P. Minutolo, Electrical characterization of flame-soot nanoparticle thin films, Synth Met. 229 (2017) 89–99.

[15] G. De Falco, F. Carbone, M. Commodo, P. Minutolo, A. D'Anna, Exploring nanomechanical properties of soot particle layers by atomic force microscopy nanoindentation, Applied Sciences (Switzerland). 11 (2021).

[16] H.F. Calcote, R.N. Pease, Electrical properties of flames. Burner Flames in Longitudinal Electric Fields, Ind Eng Chem. 18 (2021) 2726–2731.

[17] P.T. Sardari, H. Rahimzadeh, G. Ahmadi, D. Giddings, Nano-particle deposition in the presence of electric field, J Aerosol Sci. 126 (2018) 169–179.

[18] A. Parisi, G. De Falco, M. Sirignano, P. Minutolo, M. Commodo, C. Carotenuto, F. Di Natale, Modelling the electrophoretically-enhanced in-flame deposition of carbon nanoparticles, J Aerosol Sci. 172 (2023).

[19] H.Q. Ta, D.J. Perello, D.L. Duong, G.H. Han, S. Gorantla, V.L. Nguyen, A. Bachmatiuk, S. V. Rotkin, Y.H. Lee, M.H. Rümmeli, Stranski-Krastanov and Volmer-Weber CVD Growth Regimes to Control the Stacking Order in Bilayer Graphene, Nano Lett. 16 (2016) 6403–6410.


THE COMBUSTION INSTITUTE
1954

SESSION III

REACTION KINETICS INCLUDING POLLUTANT EMISSION PREDICTIONS


THE COMBUSTION INSTITUTE
1954

EXPERIMENTAL AND MODELING STUDY OF NH_3-NO INTERACTION AT LOW-INTERMEDIATE TEMPERATURE

M. V. Manna*, K. P. Shrestha, F. Mauß**, R. Ragucci*, M. de Joannon*, P. Sabia***

mariavirginia.manna@stems.cnr.it

* Institute of Science and Technology for Sustainable Energy and Mobility - Consiglio Nazionale delle Ricerche, Napoli, Italy

** Thermodynamics and Thermal Process Engineering - Brandenburg University of Technology, Cottbus, Germany

Abstract

In this work, the oxidation of NH_3 and NH_3 mixtures doped with NO (450, 800 ppm) was experimentally studied in a Jet Stirred Flow Reactor (JSFR), changing the inlet temperature in the range 900-1350 K, at nearly atmospheric pressure and equivalence ratio. The results show that NO concentration is controlled by DeNOx reactions in the temperature range 1100-1250 K, while no remarkably sensitizing effect is observed for the NH_3-NO mixtures. A detailed kinetic model was developed by declaring new reactions for N_2H_2 isomers (cis and trans) and tuning the rate constants of the most sensitive reactions, according to recent literature suggestions. A third body efficiency for ammonia was declared in the three-body reactions.

The proposed mechanism well reproduces target species, in particular NO and H_2 profiles. Updated DeNOx chemistry was crucial for reproducing NO profiles for NH_3-NO mixtures, while NH_2 recombination reactions were found to be essential for predicting the formation of H_2. The inclusion of the ammonia third-body efficiency showed sensitivity to model predictions, in particular for the reaction $H+O_2(+M)=HO_2(+M)$, that was crucial to predict NO formation via the NH_2+HO_2 pathway.

Introduction

The compelling requirement to reduce greenhouse gases emissions has led the scientific community to explore alternative energy sources, in particular energy vectors with a minor impact on the environment [1]. In this context, the processes of thermo-conversion of ammonia as a hydrogen carrier and as a fuel itself are currently research subject matter. In particular, recent studies [2] have demonstrated that MILD combustion processes can ensure a stable combustion conditions of NH_3 with low NOx emissions. Due to the internal or external recirculation of hot-gases, the interaction between fuel and NO has to be carefully addressed, as such species can have a sensitizing effect on fuel oxidation chemistry itself. In addition, MILD combustion working temperatures are compatible with DeNOx chemistry [3].

Therefore, the interaction between NH_3 and NO becomes a crucial aspect to investigate for both fuel oxidation and NO formation/reduction chemistry. Nevertheless, despite recent scientific contributions [4,5], the NH_3 oxidation, NO formation/reduction chemistry and the NH_3-NO interaction are still not properly addressed, especially under low temperatures (<1400K), as demonstrated by authors previous works [6,7].
In this framework, the aim of the present paper is to provide for new experimental insight into NH_3-NO oxidation chemistry in a JSFR and develop an updated kinetic mechanism, optimizing the model by Shrestha et al. [8] on the basis of the new and experimental literature data.

Experimenal setup

Experimental data were collected using a fused-silica JSFR (volume 113 cm3). Experiments were performed for NH_3-NO/O_2 mixtures diluted in N_2 at 86% as a function of the inlet temperature (T_{in}) in the range 900-1350 K, under nearly atmospheric pressure (1.4 atm) and a fixed residence time (τ) equal to 0.21s.
Experiments were performed for pure NH_3, as reference case, then they were repeated for NH_3-NO mixtures, with initial contents of NO equal to 450 and 800 ppm.
Experimental results were simulated using the PSR code of LOGEresearch [9] and the model provided by Shrestha et al. in [8]. Then, the reference kinetic scheme was optimized to improve the mechanism prediction for the current data and JSFR data from previous works by Sabia et al. [7] and Manna et al. [6]. The mechanism was further validated against literature data.

Kinetic modeling updating

The main changes to the kinetic mechanism by Shrestha et al. are summarized below.
To improve the prediction of NO formation from pure ammonia and NO doped mixtures, the rate constants of the DeNOx reactions (NH_2+NO=NNH+OH, NH_2+NO=N_2+H_2O) were updated on the basis of shock tube experiments by Song et al. [10]. Also the rate constants for the reactions between NH_2 and NO_2 to H_2NO+NO or N_2O+H_2O were modified, according to the values suggested by the theoretical work of Glarborg et al. [11].
The reaction H_2NO+O_2=HNO+HO_2 has been recognized as crucial for the low-temperature chemistry of ammonia. In the present study its rate constants is adopted from the recent theoretical work by Cañas et al. [12], with rate constants recommended for temperatures in the range 500-1700K.
Some of the reactions of the HNO sub-mechanism (i.e. HNO=H+NO, HNO+OH=NO+H_2O and HNO+NO_2=HNO_2+NO) were adopted from a recent work by Stagni et al. [20].
The effect of diazene (HNNH) chemistry on mechanism prediction was investigated, by including the diazene reaction sub-mechanism proposed by Marshall et al. [13], including its isomers (trans N_2H_2 and cis cN_2H_2), with their relative thermodynamic

coefficients. The reaction $NH_3+NH_2=N_2H_3+H_2$ revealed to be a fundamental to correctly predict both H_2 and NO profiles, under the conditions explored in this work. The rate constant from the work of Dove and Nip [14] was adopted here and increased by a factor of 2 to achieve reasonable agreement with experimental results of this study. Furthermore, NH_3 and N_2H_x third-body collisional efficiencies were also declared for all third-body reactions.

Results and discussion

The concentration profiles of main species (O_2, NO, H_2) for pure NH_3 (black symbols) and NH_3-NO oxidation (green symbols NO=450 ppm, red symbols NO=800 ppm) are reported in Fig.1. Both model predictions using the updated mechanism (solid lines) and the original Shrestha model (dashed lines) are shown. Results are reported as a function of temperature at steady state conditions (T).

In general, O_2 concentration starts decreasing for T=1100K and the complete O_2 conversion is observed for T>1300K. Doping the mixture with NO does not alter significantly the system reactivity. It can be noticed that both the Shrestha and the updated model reproduce the experimental trend. However, the former model predicts higher reactivity compared to the latter one for inlet temperature in the range 1200-1280K. Conversely, the updated model reproduces better experimental data above 1300K. The NO trend in Fig. 1b (semilogarithmic scale) for pure NH_3 is peculiarly non-monotonic at low temperatures, in agreement with authors previous findings [6,7].

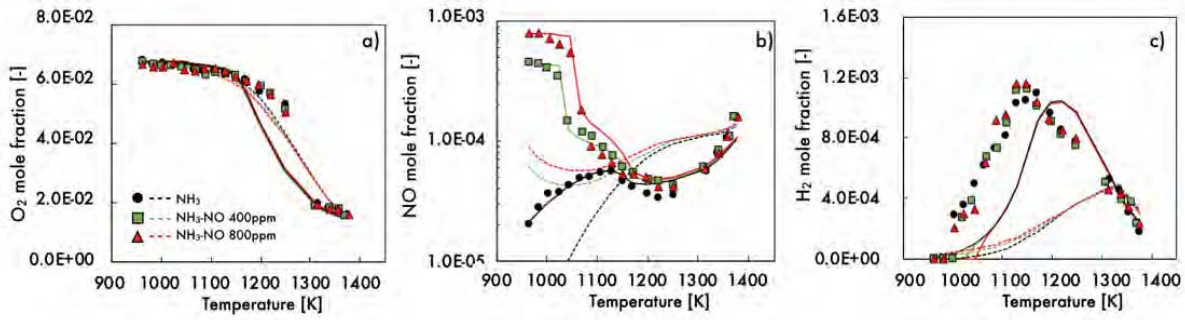

Figure 1. Experimental (symbols) and model predictions (lines) species profiles for NH_3 and NH_3-NO mixtures oxidations. Solid lines: updated model. Dashed lines: Shrestha model.

It can be observed that the updated mechanism satisfactorily predicts the non-monotonic NO experimental trend, in contrast to Shrestha model.

For mixtures doped with NO, the concentration of NO remains equal to the initial value for T<1000K, while it abruptly decreases for T close to 1100K, independently of NO initial concentration, suggesting the occurrence of fast DeNOx reactions. For T>1150K, regardless of the initial NO concentration in the mixture, NO profiles almost overlap. DeNOx reactions are less favored at higher temperatures, thus NO

formation routes overcome, determining a NO increase. The proposed mechanism well reproduces these NO trends.

Hydrogen concentration for pure NH_3 and NO-doped mixtures are almost the same. It can be observed that Shrestha model predicts a lower hydrogen net-production with respect to the experimental data, while the updated model more reasonably captures the conspicuous H_2 formation, due to the update and inclusion of new reactions, particularly involving NH_2 and N_2H_x species.

In order to identify the controlling reactions of NH_3 and NH_3-NO oxidation, flux diagrams were performed using the updated model, for three temperatures, namely 1080, 1250 and 1350K (Fig. 2). Line thickness is proportional to the reaction rate (shown in round brackets). Dashed arrows are relative to reactions more markedly affected by NO as an inlet species.

In case of pure NH_3, diagrams show that, at low temperatures, the formation of H_2NO via reaction $NH_2+NO_2=H_2NO+NO$ is the main NH_2 consumption route. Secondarily, NH_2 is involved in DeNOx reactions. Specifically, at low temperatures, the terminating reaction $NH_2+NO=N_2+H_2O$ is faster than the propagating one, $NH_2+NO=NNH+OH$. The H_2NO is involved in NO formation according to the pathway $H_2NO \rightarrow HNO \rightarrow NO$.

H_2 formation is very sensitive to the N_2H_x pathway, in particular the reaction $NH_3+NH_2=N_2H_3+H_2$ is responsible of the H_2 production at low-intermediate temperatures.

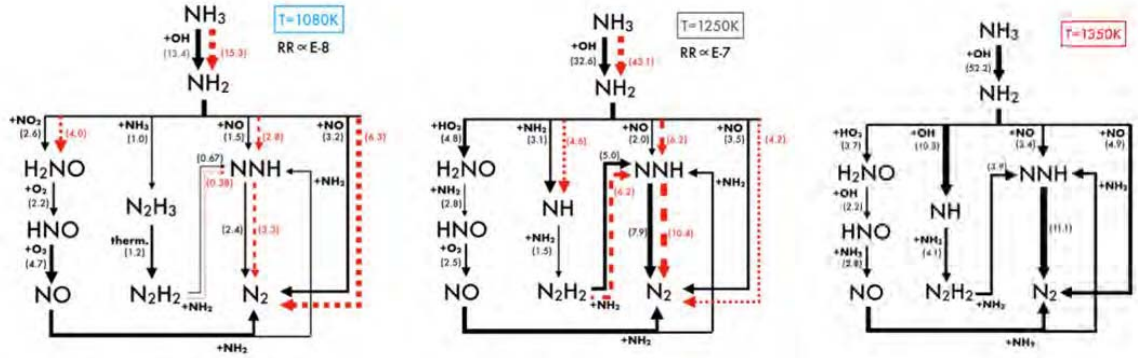

Figure 2. Flux diagram analyses for NH_3 and NH_3-NO oxidation. Solid lines: main pathways for pure NH_3. Dashed lines: effect of 800 ppm NO addition on the main pathways.

H_2 consumption through the typical H_2/O_2 oxidation chemistry is partially inhibited by NH_3 itself, since its third body efficiency enhances the role of the chain break reaction $H+O_2(+M)=HO_2(+M)$.

At=1250K NH_2 is mainly involved in NH formation, that subsequently recombines to N_2H_2. The pathway $NH \rightarrow N_2H_2 \rightarrow NNH \rightarrow N_2$ promotes the formation of H_2 and H radicals, that enhance the system reactivity. Moreover, the reactions NH_2+NO become predominant compared to $NH_2+HO_2=H_2NO+OH$. As a consequence, NO formation is slowed down in favor of its consumption, resulting in a net NO decrease.

For higher temperatures (T=1350K), the H_2/O_2 branching mechanism boosts OH formation, thus the high temperature reactivity is dominated by the conversion of NH_2 to NH, according to the reaction $NH_2+OH=NH+H_2O$, while the H_2NO formation and the DeNOx reactions play a secondary role. Therefore, NH is mainly consumed through the recombination pathway to N_2H_2. In addition, the NH paths also contribute to NO formation, along with the H_2NO/HNO reactions.

Conclusions

The present paper deals with an experimental and modelling study on the oxidation of NH_3 and NH_3-NO mixtures. Experiments were performed in a Jet Stirred Flow Reactor, for temperatures in the range 900-1350K, for mixtures diluted in N_2 at 86%, doped with 450 and 800 ppm of NO. For NH_3 and NH_3-NO mixtures, NO concentrations are controlled by DeNOx reactions in the temperature range 1100-1250K, while NH_3-NO interaction does not develop through a sensitizing effect, as suggested by O_2 and H_2 profiles. Based on the these measurements, a detailed kinetic mechanism was developed updating the Shrestha et al. [15] model, systematically considering recently updated rate constants and declaring new reactions subsets. Numerical analyses show the low-temperature chemistry of ammonia is predominately controlled by the H_2NO formation and consumption pathways. However, at high temperatures, the decomposition route of NH_2 controls the system reactivity which leads to the formation of H_2 and H radicals, enhancing the system reactivity. Moreover, the role of the NH_2+NO reactions becomes marginal at high temperature, and therefore the oxidation process is not affected by the NO addition. The improvement in model predictions are mainly ascribable to updated rate constants of $DeNO_x$ reactions, while the proper description of H_2 concentration relies on the declaration of new reactions relative to NH_2 recombination to N_2H_x species and their relative decomposition. Significantly, the role of ammonia as strong collider has been included, declaring a high collisional efficiency in third-body reactions.

References

[1] Dreizler A, Pitsch H, Scherer V, Schulz C, Janicka J. The role of combustion science and technology in low and zero impact energy transformation processes. Appl Energy Combust Sci 2021;7:100040. https://doi.org/10.1016/j.jaecs.2021.100040.

[2] Sorrentino G, Sabia P, Bozza P, Ragucci R, de Joannon M. Low-NOx conversion of pure ammonia in a cyclonic burner under locally diluted and preheated conditions. Appl Energy 2019;254:1–7. https://doi.org/10.1016/j.apenergy.2019.113676.

[3] Asghar U, Rafiq S, Anwar A, Iqbal T, Ahmed A, Jamil F, et al. Review on the progress in emission control technologies for the abatement of CO2, SOx and NOx from fuel combustion. J Environ Chem Eng 2021;9:106064. https://doi.org/10.1016/j.jece.2021.106064.

[4] Dagaut P. On the Oxidation of Ammonia and Mutual Sensitization of the Oxidation of No and Ammonia: Experimental and Kinetic Modeling. Combust Sci Technol 2019;00:1–13. https://doi.org/10.1080/00102202.2019.1678380.

[5] Alzueta MU, Ara L, Mercader VD, Delogu M, Bilbao R. Interaction of NH3 and NO under combustion conditions. Experimental flow reactor study and kinetic modeling simulation. Combust Flame 2021:111691. https://doi.org/10.1016/j.combustflame.2021.111691.

[6] Manna MV, Sabia P, Ragucci R, de Joannon M. Oxidation and pyrolysis of ammonia mixtures in model reactors. Fuel 2020;264:116768. https://doi.org/10.1016/j.fuel.2019.116768.

[7] Sabia P, Manna MV, Cavaliere A, Ragucci R, de Joannon M. Ammonia oxidation features in a Jet Stirred Flow Reactor. The role of NH2 chemistry. Fuel 2020;276:118054. https://doi.org/10.1016/j.fuel.2020.118054.

[8] Shrestha KP, Lhuillier C, Barbosa AA, Brequigny P, Contino F, Mounaïm-Rousselle C, et al. An experimental and modeling study of ammonia with enriched oxygen content and ammonia/hydrogen laminar flame speed at elevated pressure and temperature. Proc Combust Inst 2021;38:2163–74. https://doi.org/10.1016/j.proci.2020.06.197.

[9] LOGEresearch: combustion and chemical kinetics simulation software. 2021.

[10] Song S, Hanson RK, Bowman CT, Golden DM, Chavarrio Cañas JE, Monge-Palacios M, et al. Shock tube determination of the overall rate of NH2 + NO → products at high temperatures. Proc Combust Inst 2022;32:2163–74. https://doi.org/10.1016/j.combustflame.2021.111708.

[11] Glarborg P, Miller JA, Ruscic B, Klippenstein SJ. Modeling nitrogen chemistry in combustion. Prog Energy Combust Sci 2018;67:31–68. https://doi.org/10.1016/j.pecs.2018.01.002.

[12] Chavarrio Cañas JE, Monge-Palacios M, Zhang X, Sarathy SM. Probing the gas-phase oxidation of ammonia: Addressing uncertainties with theoretical calculations. Combust Flame 2021:111708. https://doi.org/10.1016/j.combustflame.2021.111708.

[13] Marshall P, Rawling G, Glarborg P. New reactions of diazene and related species for modelling combustion of amine fuels. Mol Phys 2021;119:17–8. https://doi.org/10.1080/00268976.2021.1979674.

[14] Dove JE, Nip WS. A shock-tube study of ammonia pyrolysis. Can J Chem 1979;57:689–701.

[15] Shrestha KP, Vin N, Herbinet O, Seidel L, Battin-Leclerc F, Zeuch T, et al. Insights into nitromethane combustion from detailed kinetic modeling – Pyrolysis experiments in jet-stirred and flow reactors. Fuel 2020;261:116349. https://doi.org/10.1016/j.fuel.2019.116349.

AUTOMATIC VALIDATION AND OPTIMIZATION OF A KINETIC MODEL FOR ALCOHOLS COMBUSTION

T. Dinelli, A. Pegurri, H. Tej, A. Stagni, M. Pelucchi
matteo.pelucchi@polimi.it
Department of Chemistry, Materials, and Chemical Engineering "G. Natta",
Politecnico di Milano, Milano, 20133, Italy

Abstract
Reliable solutions are urgently required to reduce emissions in the transportation sector. In this scenario, alcohols could be a valid choice as fuels or additives. Kinetic models for their combustion are essential to accelerate their possible adoption with existing infrastructures. After a long-lasting effort in developing and validating kinetic mechanisms for alcohols pyrolysis and oxidation, the strong push towards data-driven science is highlighting some major benefits in automatizing the critical steps of data analysis. The SciExpeM framework, in this context, collects experimental data and kinetic mechanisms. The most evident advantage is the possibility to run simulations of large datasets with different mechanisms simultaneously to assess and compare their performances. An unbiased and solid evaluation is ensured by an innovative analysis approach called Curve Matching. This score is an improvement of the classic quantifications of the curves' distances (e.g., sum of squared errors) because it also considers their differences in shape and possible shifts over the dependent variable. From the systematic deviations highlighted by this automated and quantitative validation, a constrained model optimization can be performed to further improve the performance.

Introduction
The ongoing energy transition requires immediate solutions to cut emissions while ensuring social development. Alcohol fuels can be a temporary sustainable alternative in this scenario. These chemicals indeed show ignition properties that are suitable for spark and compression engines already available. Methanol, ethanol, and linear C_3-C_5 alcohols present RON and MON values close to those of commercial gasoline, whereas longer linear alcohols have cetane numbers like that of commercial diesel [1]. Moreover, they can be derived from biological residues via thermochemical or biochemical processes, reducing thus the CO_2 footprint.
To be successfully adopted as additives or fuels, however, it is mandatory to know the products of their combustion. For this reason, detailed kinetic mechanisms have been developed. These are complex networks of elementary reactions involving all the species taking part in the combustion process, along with their thermodynamic and transport properties. Each reaction is described by 3 kinetic parameters (i.e.,

modified Arrhenius equation). It is crucial to carefully tune these parameters to make the model as precise as possible. Achieving this can be a tedious task since the model results must be extensively compared with experimental data such as ignition delay times in shock tubes or speciations in jet stirred (JSR) or flow reactors (FR). The comparison is time-consuming and often unreliable since it is usually based on incomplete evaluation parameters (e.g., sum of quadratic errors). Hence, an objective assessment tool called Curve Matching (CM) was introduced [2,3].
The CM approach quantifies the differences between the model and the experimental data curves through a set of indexes, without neglecting their differences in shape. Moreover, an innovative framework called SciExpeM [4] has been developed to accelerate the validation. With the OpenSMOKE++ solver [5] and the CM methodology it embeds, SciExpeM assesses the performance of multiple kinetic mechanisms simultaneously against the wide database of experiments it stores. In the following paragraphs, a kinetic model for alcohol combustion is presented, and a description is provided of how the SciExpeM platform was exploited to validate and optimize it.

Kinetic mechanism

Given the potential applications of alcohols, a kinetic mechanism to describe their pyrolysis and oxidation has been recently developed following the concepts of hierarchy and modularity. Pelucchi et al. [6] extensively applied the rate rules and reaction class technique. The kinetic parameters were obtained by merging the well-known n-alkanes rate rules with the characteristics of the alcohol functional group. This method was successfully applied to other oxygenated fuels like n-C_4-C_6 aldehydes [7] and n-C_4-C_5 organic acids [8]. The influence of the moiety (i.e., the hydroxyl group) becomes negligible beyond the carbon located in the β-position [6], therefore only reaction paths relevant to alcohols were investigated. A group of 20 reaction classes was identified as essential to describe pyrolysis and oxidation. The low-temperature oxidation pathways involve many intermediates (e.g., peroxy radicals ($R\dot{O}_2$), hydroperoxy alkyl radicals ($\dot{Q}OOH$), C_n enols, C_n epoxy alcohols, etc.), so the model was further simplified with a skeletal reduction and the lumping approach.

Validation

A set of dissimilarity indexes is used to calculate the CM score [3]. The CM ranges from 0, for total dissimilarity, to 1, for perfect agreement. The first dissimilarity index d_{L2}^{0} is the continuous equivalent of the sum of squared errors. The second one d_{L2}^{1} asserts that two curves are similar if they only differ by a vertical translation. The Pearson-based indicators quantify the difference in shape between the curves: for d_P^0 two functions are similar if they only differ by a vertical dilation, while for d_P^1 they are such if they differ by a vertical affine transformation. Finally, the shift index S computes the horizontal distance between the curves. The CM score is

calculated according to Equation (1). A CM score close to 1 means that the model well predicts the considered dataset.

$$CM_{score} = (d_{L2}{}^{0} + d_{L2}{}^{1} + d_{P}{}^{0} + d_{P}{}^{1} + 2S) / 6 \quad (1)$$

Table 1. Literature mechanisms investigated in this work.

Author	Adopted name
Sarathy et al. [1]	C1C5_alcohols
Johnson et al. [9]	C1C3_alcohols_NUIG
Black et al. [10]	C4_alcohols_NUIG

The CRECK kinetic model was compared to other literature mechanisms [1,9,10] reported in Table 1. SciExpeM [4] collects a structured database of combustion experiments performed in diverse reactors for various fuels, and new measurements can be easily uploaded. The platform also offers features to investigate and improve kinetic models. For instance, a sensitivity analysis can be performed to determine the most impacting reactions, while ROPA (Rate of Production Analysis) identifies which ones consume or produce a certain species. Quick comparisons between different models can be visualized as heat maps, where the CM scores of the mechanisms allow the identification of the operating conditions in which a specific model fails. Figure 1 exemplifies this with a set of propanol experiments, where the models, particularly C1C5_alcohols [1], do not perform well on simulation #2198 [9] (shock tube at T = 1450-2050 K, P = 1 atm, φ = 2.0).

Figure 1. Heat map of the Curve Matching scores for a set of propanol experiments for 3 different kinetic mechanisms [1,6,9].

Experimental data covering a wide range of pressures and temperatures were collected on SciExpeM to test the alcohols kinetic mechanism. Specifically, shock tube ignition delay times for methanol, ethanol, propanol, n-butanol, n-pentanol, and n-hexanol, JSR speciation measurements for propanol, n-butanol, n-pentanol, and n-hexanol, and FR concentration measurements for methanol were considered. In Figure 3, the operating conditions of the experiments are represented in the variables space.

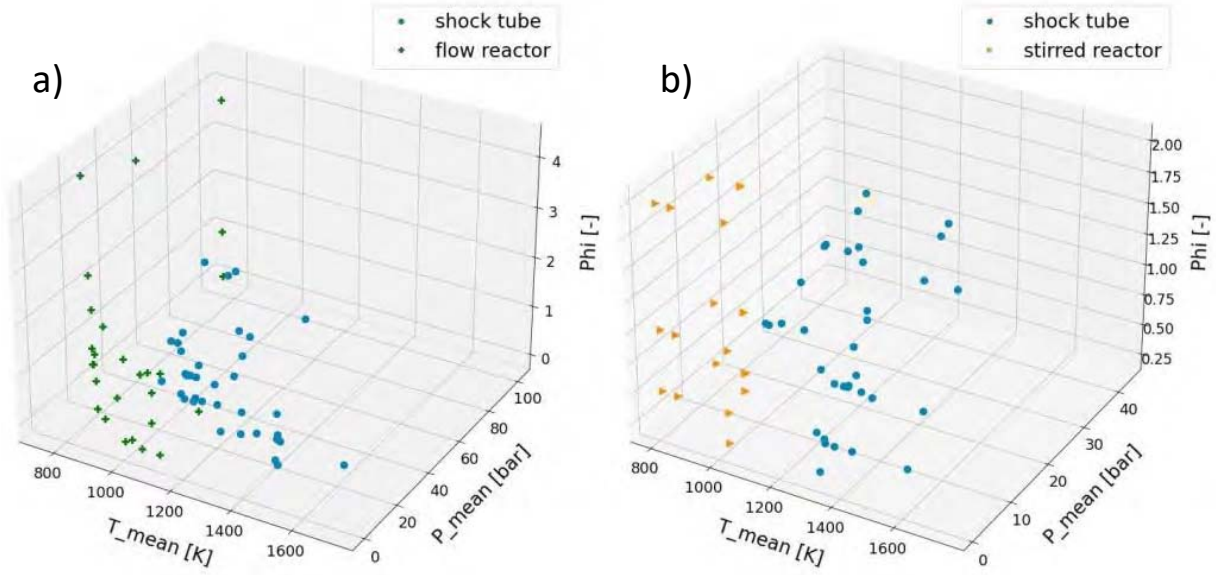

Figure 3. Operating conditions for validation of methanol (a) and longer linear alcohols (b).

Table 2 collects the CM scores of the investigated mechanisms. Despite having generally higher scores, the CRECK model performs slightly worse in the shock tubes. In the JSR, the CRECK model proved to be the most accurate to predict species concentrations. All mechanisms show rather poor performance in FR, thus calling for further study to improve the modeling in those conditions.

Table 2. Average Curve Matching scores of the investigated mechanisms.

	ST		JSR		PFR	
Kinetic mechanism	**CM_{score}**	**Error**	**CM_{score}**	**Error**	**CM_{score}**	**Error**
CRECK_alcohols	0.7932	0.0065	0.9123	0.0018	0.6592	0.0023
C1C5_alcohols	0.7954	0.0066	0.9009	0.0019	0.6323	0.0025
C1C3_alcohols_NUIG	0.7968	0.0059	0.8811	0.0021	0.6571	0.0023
C4_alcohols_NUIG	0.7904	0.0066	0.8809	0.0019	0.6591	0.0024

Optimization

The CRECK kinetic mechanism performed very well in the considered conditions, but still presented some deviations from the experimental measurements. An optimization process was then carried out using OptiSMOKE++ [11], an optimization toolbox based on evolutionary algorithms. The adopted objective function is based on the CM score and includes bootstrap variations to account for the uncertainty of the experimental measurements. The kinetic rates are expressed in a linear form to increase the algorithm's stability. The parameters to optimize are the pre-exponential factor A, the temperature exponent β, and the activation energy Ea of the modified-Arrhenius equation. A penalty function increases the value of the objective function when the combination of these parameters does not respect the

non-linear uncertainty constraints of the kinetic constant $k_{min} \leq k \leq k_{max}$. The boundaries k_{min} and k_{max} are determined by the uncertainty factor f, defined as:

$$f = \log(k_{max}) - \log(k_0) = \log(k_0) - \log(k_{min}) \quad (3)$$

where k_0 is the nominal rate constant. In this work, an uncertainty factor equal to 0.5 is adopted, which corresponds to a maximum variation of the optimized rate with respect to the original value of a factor ~3.2. A set of 8 reaction classes was consistently optimized, using the concentrations of main species in JSR as optimization targets.

The optimized model was then tested again on SciExpeM. The improvements were noticeable in the species whose previous concentration profiles had considerable deviations from the experimental points. For instance, the low-temperature prediction of n-pentanal production from n-pentanol oxidation in a JSR (P = 1 atm, φ = 1.0) [12] is more accurate, as displayed in Figure 4 (a). A large improvement is also observed in the low-temperature combustion of n-hexanol, where the nominal model overestimated reactivity whereas the optimized mechanism better predicts the concentration of products. This can be seen in Figure 4 (b), where the concentration of acetaldehyde in a JSR (P = 1 bar, φ = 0.5) [13] is reported.

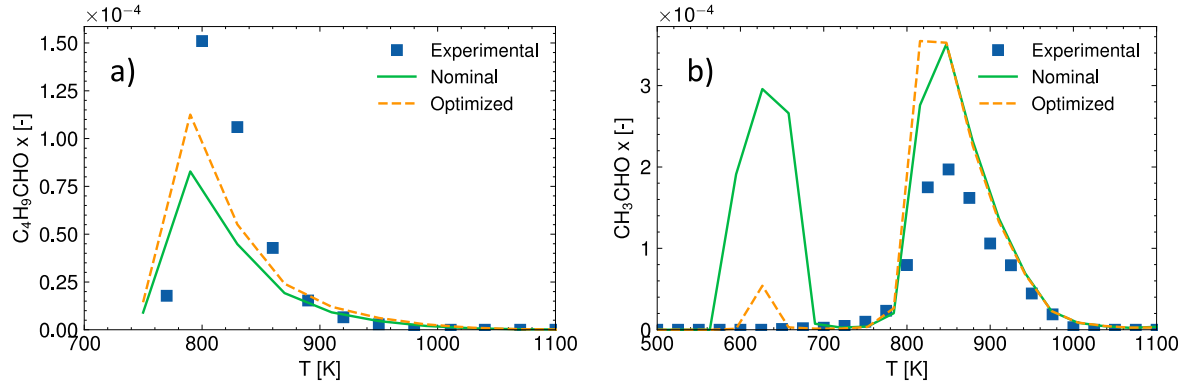

Figure 4. Concentration profiles of n-pentanal from n-pentanol (P = 10 atm, φ = 1.0) [12] (a) and acetaldehyde from n-hexanol (P = 1 bar, φ = 0.5) [13] (b).

Conclusions

In this work, a kinetic mechanism describing linear alcohols oxidation and pyrolysis was presented. The model was validated against large sets of experimental data, compared to other mechanisms from the literature, and optimized to enhance its predictions. The combination of SciExpeM with the CM approach and the OptiSMOKE++ tool resulted in a solid and automatic workflow. The model performance is excellent compared to other literature mechanisms, but predictions in the FR conditions investigated can still be improved. Also, new modules could be added to include other alcohols of interest (e.g., non-linear ones). SciExpeM is continuously evolving and, for example, an outliers-detection algorithm can be integrated to limit human error in the assessment phase.

References

[1] S.M. Sarathy, P. Oßwald, N. Hansen, K. Kohse-Höinghaus, Alcohol combustion chemistry, *Prog. Energy Combust. Sci.* 44 (2014) 40–102.

[2] M.S. Bernardi, M. Pelucchi, A. Stagni, et al., Curve matching, a generalized framework for models/experiments comparison: An application to n-heptane combustion kinetic mechanisms, *Combust. Flame*. 168 (2016) 186–203.

[3] M. Pelucchi, A. Stagni, T. Faravelli, Addressing the complexity of combustion kinetics: Data management and automatic model validation, in: Comput. Aided Chem. Eng., 2019: pp. 763–798.

[4] E. Ramalli, T. Dinelli, A. Nobili, et al., Automatic validation and analysis of predictive models by means of big data and data science, *Chem. Eng. J.* 454 (2023) 140149.

[5] A. Cuoci, A. Frassoldati, T. Faravelli, E. Ranzi, OpenSMOKE++: An object-oriented framework for the numerical modeling of reactive systems with detailed kinetic mechanisms, *Comput. Phys. Commun.* 192 (2015) 237–264.

[6] M. Pelucchi, S. Namysl, E. Ranzi, et al., Combustion of n-C 3 −C 6 Linear Alcohols: An Experimental and Kinetic Modeling Study. Part I: Reaction Classes, Rate Rules, Model Lumping, and Validation, (2020).

[7] M. Pelucchi, S. Namysl, E. Ranzi, et al., An experimental and kinetic modelling study of n-C4C6 aldehydes oxidation in a jet-stirred reactor, *Proc. Combust. Inst.* 37 (2019) 389–397.

[8] S. Namysl, M. Pelucchi, O. Herbinet, et al., A first evaluation of butanoic and pentanoic acid oxidation kinetics, *Chem. Eng. J.* 373 (2019) 973–984.

[9] M. V Johnson, S.S. Goldsborough, Z. Serinyel, et al., A Shock Tube Study of n-and iso-Propanol Ignition, (n.d.).

[10] G. Black, H.J. Curran, S. Pichon, J.M. Simmie, V. Zhukov, Bio-butanol: Combustion properties and detailed chemical kinetic model, *Combust. Flame*. 157 (2010) 363–373.

[11] M. Fürst, A. Bertolino, A. Cuoci, et al., OptiSMOKE++: A toolbox for optimization of chemical kinetic mechanisms, *Comput. Phys. Commun.* 264 (2021) 107940.

[12] C. Togbé, F. Halter, F. Foucher, C. Mounaim-Rousselle, P. Dagaut, Experimental and detailed kinetic modeling study of 1-pentanol oxidation in a JSR and combustion in a bomb, *Proc. Combust. Inst.* 33 (2011) 367–374.

[13] M. Pelucchi, S. Namysl, E. Ranzi, et al., Combustion of n-C 3 −C 6 Linear Alcohols: An Experimental and Kinetic Modeling Study. Part II: Speciation Measurements in a Jet-Stirred Reactor, Ignition Delay Time Measurements in a Rapid Compression Machine, Model Validation, and Kinetic Analysis, (2020).

LAMINAR BURNING VELOCITY AND KINETIC MODELS EVALUATION OF SYNGAS CO/H_2, CO/H_2/CH_4, CO/H_2/CO_2 AT NORMAL AND ELEVATED TEMPERATURE

Muhammad Zubair Qureshi*, Carlo Caligiuri*, Massimiliano Renzi*, Marco Baratieri*
MQureshi@unibz.it
*Faculty of Engineering, Free University of Bolzano, piazza Università 1, 39100, Bolzano, Italy

Abstract
In this work, chemical kinetic simulations of equimolar (CO:H_2=1:1) based forestry residual syngas were systematically performed adapting the laminar premixed flame model in open source CANTERA, solver. Three detailed kinetic models i.e., newly released FFCM-2, USC mech II, and modified GRI mech III were incorporated to report accurate flame parameters. The objective of the study is to evaluate kinetic models and present fresh insights on the effects of varying syngas mixtures such as CO/H_2, CO/H_2/CO_2 and CO/H_2/CH_4 on Laminar Burning Velocity (LBV) and peak LBV location ($\Phi_{LBV=max}$) at normal and elevated temperatures. On comparing the results with experiments, FFCM-2 is emerged as good kinetic model for ternary syngas mixtures CO/H_2/CH_4 in a wide range of equivalence ratios, especially for mixture containing limited share of methane. The USC mech II performed well for CO/H_2, CO/H_2/CO_2, while modified GRI mech III model gave agreeable predictions for CO/H_2/CH_4 mixture having rich methane content. The progressive CO_2 dilution and CH_4 addition reduced the peak LBV and moved the peak LBV locations to lean conditions; however, only the latter effect was enhanced at elevated initial temperature. The shift of peak LBV locations and their enhancement at elevated temperature also open the research path to study the underlying impacts on the flame modes/regimes and flame structure, especially CO emissions pathways in syngas with CH_4 and CO_2 additions.

Introduction
Since the interest and the production of biomass derived syngas fuels increased [1], more efforts are being devoted to adopt these low calorific syngas in combustors in an efficient way. Therefore, the interest to explore syngas Laminar Burning Velocity (LBV) and flame structure, has increased. Several laminar flame studies have been conducted in the last two decades relevant to industrial burners at standard thermodynamic conditions. For example, Andrade et al. [2] found higher LBV of eucalyptus wood derived producer gas (CO/H_2/CH_4), than methane. Bouvet et al. [3]

carried out measurement of LBV's of various binary syngas (H_2/CO) mixtures. Liu et al. [4] evaluated the effects of adding the H_2 and CO of syngas and reported LBV increment and extended lean flammability limits of syngas with H_2 and CO additions. Burbano et al. [5] reported lower flame speed with inert gas dilutions. However, few syngas combustion investigations have been done at elevated temperatures of complex syngas (H_2/CO/CH_4) mixtures. Also, CH_4 and CO_2 addition impacts on syngas mixture at elevated thermal conditions are rarely investigated, therefore understanding is ambiguous. In this work, laminar premixed flame kinetic simulations of varying syngas compositions such as, CO/H_2, CO/H_2/CO_2 and CO/H_2/CH_4 have been performed for investigation and promotion of forestry syngas in industrial burners. Equimolar (CO:H_2=1:1) based forestry syngas was obtained experimentally from a small-scale open top gasifier fed with forestry residues at Free University of Bolzano, Italy [6]. To this end, the objective of the work is two-fold: (i) to provide the comparison regarding predictability of recently released detailed kinetic model FFCM-2, a well-recognized USC II, and modified GRI III model for the sake of achieving accurate flame parameters; (ii) to provide deeper understanding of adjusting/controlling syngas-air volumetric flowrates or local equivalence ratio settings required with respect to varying syngas mixtures with CH_4 and CO_2 additions at different initial mixture temperatures.

Numerical method, kinetic models, and validation

Laminar premixed syngas flame model was developed using open-source solver, CANTERA using flat flame method and validated at both the standard and elevated temperature conditions. A systematic syngas flame investigation was performed using various syngas mixtures based on CO:H_2 =1, corresponding to our forestry syngas.

Table 1. Syngas-air mixtures and detailed reaction mechanisms

Mixture	CO/H2 Ratio	CO	H2	CH4	CO2	Kinetic Model(s)
BS50	1	50	50	0	0	USC mech II
						FFCM-2
BS45C10	1	45	45	0	10	USC mech II
BS40C20	1	40	40	0	20	FFCM-2
TS47.5	1	47.5	47.5	5	0	Modified - GRI III
TS45	1	45	45	10	0	USC II
TS40	1	40	40	20	0	FFCM-2

The considered binary (BS) and ternary (TS) mixtures and their composition are reported in Table 1. Detailed multi-component transport-based simulations were performed using three kinetic models such as, FFCM-2 (96 species, 1024 reactions) [7], USC mech II (111 species, 784 reactions) [8], and modified GRI mech III (53 species, 325 reactions) in which the reaction rate parameters of 11 reactions are updated, as suggested in reference Vu et al. [9]. A fit grid of around 500 grid points

was used to completely resolve the flame thickness. Moreover, kinetic simulations of BS (H_2:CO=1:1) mixtures at atmospheric conditions are validated with experimental data on similar operating conditions, available from McLean et al. [10], Prathap et al. [11], Burbano et al. [5], Natarajan et al. [12] while, Lapalme et al. [13] is used for ternary syngas (H_2:CO:CH_4=1:1:0.5). Moreover, experimental data for mixtures at elevated temperature conditions (300 K ≤ Temperature ≤ 500 K), have been taken from Han et al. [14], Natrajan et al. [12] and Singh et al. [15] studies.

Results and discussion

As shown in **Errore. L'origine riferimento non è stata trovata.** (right), a very good agreement was achieved between present numerical studies and reported experimental data for BS50 at lean fuel equivalence ratios (ER's) from $\boldsymbol{\Phi}$=0.6 up to, $\boldsymbol{\Phi}$=1.5 for both the USC II, as well as FFCM-2 kinetic model (with percentage less than ±8% difference). However, FFCM-2 slightly overpredicted the LBV's of BS50 as compared to USC II kinetic model along rich ER range ($\boldsymbol{\Phi}$=1.5 - 3.5) [3]. LBV of BS mixtures increases at low values

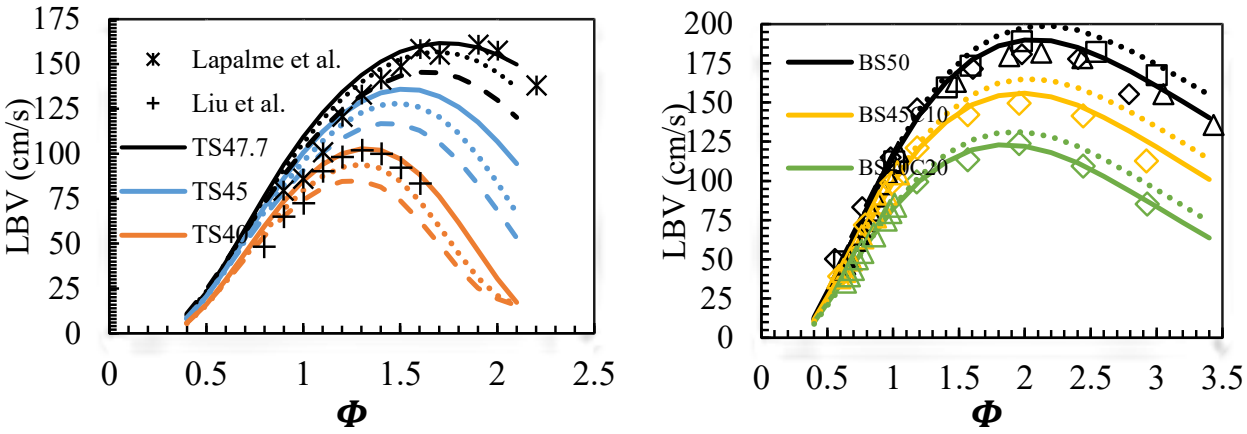

Figure 1. (Left) - Syngas mixtures TS47.5, TS45, TS40. **(Right) -** BS50, BS45C10, BS40C20 at 1bar and 300 K (Doted line- FFCM-2, Solid line- USC II, Dash line- Modified GRI III, Symbols- Experiments)

of $\boldsymbol{\Phi}$, reach a maximum of 190 cm/sec at $\boldsymbol{\Phi}$=2.2 and finally decreases onwards. As concerns TS mixtures, as shown in **Errore. L'origine riferimento non è stata trovata.** (left), LBV increases initially, peaks at $\Phi_{LBV=max}$ and then decreases rapidly due to lower flammability limit of methane. More importantly, peak LBV locations were observed to move towards leaner ER conditions with a significant change in ER i.e., from $\Phi_{LBV=max} = 1.7$ *to* $\Phi_{LBV=max} = 1.3$, due to CH_4 additions. Furthermore, limited investigations were found in literature to account the effects of CO_2 dilutions on the rich ER range of syngas mixtures. As shown in **Errore. L'origine riferimento non è stata trovata.** (right), the forecasting performance remained equally good for the syngas mixtures. It is unveiled that

progressive addition of CO_2 dilution species lowered the LBV moderately with a linear trend. Simulations were compared with experimental studies of Prathap et al. [16] and Han et al. [14] with good agreement. A sensitivity analysis is also performed to check the influence of intermediate reactions upon adding CH_4 and CO_2 species progressively. The reaction H + CH_3 (+M) <=> CH_4 (+M) is important for CH_4 additions, while CO + OH <=> CO_2 + H, H + O_2 (+M) <=> HO_2 (+M) were found responsible for CO_2 dilutions.

To the best of the authors' knowledge, few kinetic investigations of syngas mixtures have been performed at elevated temperature conditions. Also, minor predictive discrepancies of kinetic model at elevated temperature condition were observed. For instance, the FFCM-2 model deviations tend to increase from TS47.5 to TS40 mixtures. The influence of elevated temperatures was observed at a wide range of

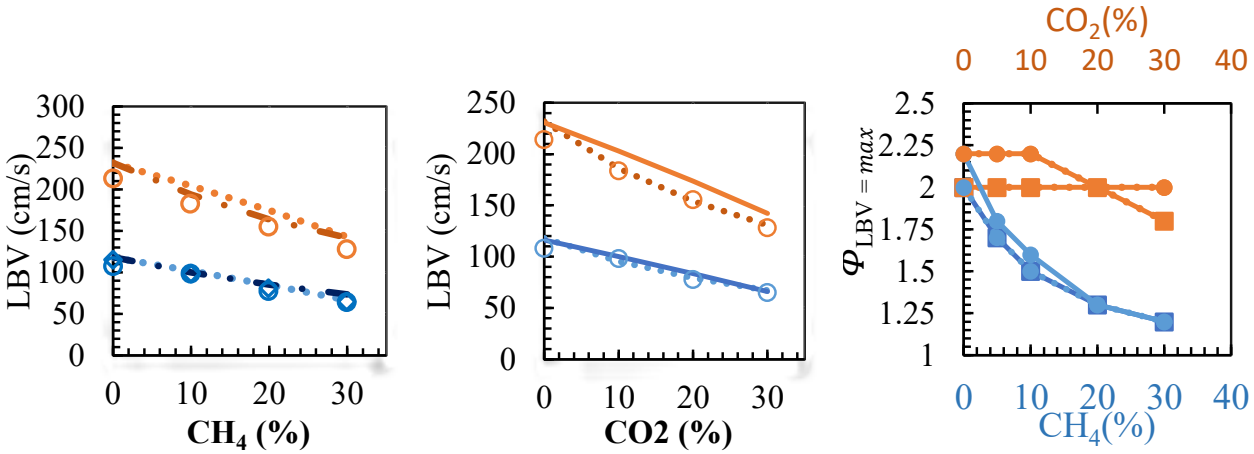

Figure 2.(Left) - Effect of CH_4 addition. **(Center) -** Effect of CO_2 addition. Temperatures, Blue (300K), Brown (450 K), ER, Φ=1, Doted line- FFCM-2, Solid line- USC II, Dash line- Modified GRI III, Symbols- Experiments. **(Right) -** Effect of CH_4 and CO_2 on peak LBV locations, Line with circular markers (300 K), Line with square markers (450 K)

ER to account the effect on location of peak LBV's. As expected, LBV of BS mixtures uplifted mainly due to increased adiabatic and raised up to maximum LBV at Φ=2.2, and then decreased gradually; however, no change in location of peak LBV's was observed. In addition, a sensitivity analysis was conducted to recognize the leading intermediate reactions which affected the LBVs during the changing temperature conditions. H_2 + OH <=> H + H_2O and H + O_2 (+M) <=> HO_2 (+M) reactions were found important to cause increment of LBV. On the other hand, similar trend was observed for TS mixtures, TS47.5, TS45, and TS40 upon elevating the temperature level. Moreover, the effects of reducing the LBV due to CH_4 and CO_2 additions were investigated with fixed ER, Φ=1, at temperatures 300 K and 450 K, as shown in Figure 2 (left and center). It was observed that temperature does not affect the peak LBV locations which only depends on the share of CH_4 and CO_2. Furthermore, it was revealed that CH_4 addition immediately affected the peak LBV

locations; when CO_2 is added, the peak started to shift after 20% CO2 dilution. The movements of peak LBV locations were enhanced at elevated temperature as shown in Figure 2 (right).

Conclusions

In conclusion, FFCM-2 proved to be a good kinetic model for ternary syngas mixtures, $CO/H_2/CH_4$ at 300 K and 450 K for composition having small methane. The progressive CO_2 dilution and CH_4 addition reduced the peak LBV and moved the peak LBV locations to lean conditions significantly; however, only the latter effect was enhanced at elevated initial temperature. The normalized sensitivity analysis was also performed: the reactions such as $H_2 + OH <=> H + H_2O$, $H + O_2 (+M) <=> HO_2 (+M)$ were found responsible to increase the LBV at elevated temperature. LBV peaks of CO/H_2 and $CO/H_2/CO_2$ mixture towards fuel rich conditions were moderately decreased as compared to $CO/H_2/CH_4$. Moreover, it was revealed that CH_4 addition shifts the peak LBV locations immediately; conversely, when CO_2 is added, the peak started to shift after 20% CO_2 dilution. Also, the effects on peak LBV locations were increased at elevated temperature. The underlying impact of this shifting can be studied further to see the effect on fame structure, more importantly the CO emissions.

References

[1] D. S. Bajwa, T. Peterson, N. Sharma, J. Shojaeiarani, and S. G. Bajwa, “A review of densi fi ed solid biomass for energy production,” *Renew. Sustain. Energy Rev.*, vol. 96, no. November 2017, pp. 296–305, 2018, doi: 10.1016/j.rser.2018.07.040.

[2] R. V. Andrade *et al.*, “Assessment of laminar flame velocity of producer gas from biomass gasification using the Bunsen burner method,” *Int. J. Hydrogen Energy*, vol. 45, no. 20, pp. 11559–11568, 2020, doi: 10.1016/j.ijhydene.2020.02.082.

[3] N. Bouvet, C. Chauveau, I. Gökalp, and F. Halter, “Experimental studies of the fundamental flame speeds of syngas (H 2/CO)/air mixtures,” *Proc. Combust. Inst.*, vol. 33, no. 1, pp. 913–920, 2011, doi: 10.1016/j.proci.2010.05.088.

[4] J. Liu, X. Zhang, T. Wang, X. Hou, J. Zhang, and S. Zheng, “Numerical study of the chemical, thermal and diffusion effects of H2 and CO addition on the laminar flame speeds of methane-air mixture,” *Int. J. Hydrogen Energy*, vol. 40, no. 26, pp. 8475–8483, 2015, doi: 10.1016/j.ijhydene.2015.04.133.

[5] H. J. Burbano, J. Pareja, and A. A. Amell, “Laminar burning velocities and flame stability analysis of H 2/CO/air mixtures with dilution of N2 and CO2,” *Int. J. Hydrogen Energy*, vol. 36, no. 4, pp. 3232–3242, 2011, doi:

10.1016/j.ijhydene.2010.11.089.

[6] D. Antolini, B. Brianti, C. Caligiuri, R. Borooah, F. Patuzzi, and M. Baratieri, "Energy valorization of forestry residues through a small-scale open top gasifier," *Eur. Biomass Conf. Exhib. Proc.*, no. July, pp. 407–410, 2020.

[7] G. P. S. and H. W. Y. Zhang, W. Dong, L. Vandewalle, R. Xu, "Foundational Fuel Chemistry Model Version 2.0 (FFCM-2)." https://web.stanford.edu/group/haiwanglab/FFCM2/pages/FFCM2.html, 2023.

[8] H. Wang *et al.*, "USC Mech Version II. High-temperature combustion reaction model of H2/CO/C1-C4 compounds," *URL http//ignis. usc. edu/USC_Mech_II. htm*, 2007.

[9] T. M. Vu, W. S. Song, J. Park, D. S. Bae, and H. S. You, "Measurements of propagation speeds and flame instabilities in biomass derived gas-air premixed flames," *Int. J. Hydrogen Energy*, vol. 36, no. 18, pp. 12058–12067, 2011, doi: 10.1016/j.ijhydene.2011.06.082.

[10] I. C. MCLean, D. B. Smith, and S. C. Taylor, "THE USE OF CARBON MONOXIDE/HYDROGEN BURNING VELOCITIES TO EXAMINE THE RATE OF THE CO + OH REACTION," *Symp. Combust. Combust. Inst.*, pp. 749–757, 2000.

[11] C. Prathap, A. Ray, and M. R. Ravi, "Investigation of nitrogen dilution effects on the laminar burning velocity and flame stability of syngas fuel at atmospheric condition," *Combust. Flame*, vol. 155, no. 1–2, pp. 145–160, 2008, doi: 10.1016/j.combustflame.2008.04.005.

[12] J. Natarajan, T. Lieuwen, and J. Seitzman, "Laminar flame speeds of H2/CO mixtures: Effect of CO2 dilution, preheat temperature, and pressure," *Combust. Flame*, vol. 151, no. 1–2, pp. 104–119, 2007, doi: 10.1016/j.combustflame.2007.05.003.

[13] D. Lapalme and P. Seers, "Influence of CO2, CH4, and initial temperature on H2/CO laminar flame speed," *Int. J. Hydrogen Energy*, vol. 39, no. 7, pp. 3477–3486, 2014, doi: 10.1016/j.ijhydene.2013.12.109.

[14] M. Han, Y. Ai, Z. Chen, and W. Kong, "Laminar flame speeds of H2/CO with CO2 dilution at normal and elevated pressures and temperatures," *Fuel*, vol. 148, pp. 32–38, 2015, doi: 10.1016/j.fuel.2015.01.083.

[15] D. Singh, T. Nishiie, S. Tanvir, and L. Qiao, "An experimental and kinetic study of syngas/air combustion at elevated temperatures and the effect of water addition," *Fuel*, vol. 94, pp. 448–456, 2012, doi: 10.1016/j.fuel.2011.11.058.

[16] C. Prathap, A. Ray, and M. R. Ravi, "Effects of dilution with carbon dioxide on the laminar burning velocity and flame stability of H 2-CO mixtures at atmospheric condition," *Combust. Flame*, vol. 159, no. 2, pp. 482–492, 2012, doi: 10.1016/j.combustflame.2011.08.006.

BENZENE FLAMMABILITY LIMITS: KINETIC MODELING AND EXPERIMENTAL VALIDATION

A. Frassoldati, A. Stagni, A. Nobili, A. Cuoci, T. Faravelli

alessio.frassoldati@polimi.it
CRECK Modeling Lab, Department of Chemistry, Materials, and Chemical Engineering, Politecnico di Milano (Italy)

Abstract
It is well known that soot is crucial not only for its role in flame chemistry under rich conditions, but also for its influence on radiation, thus affecting the flammable region of hydrocarbons. An extensive collection of experimental data from literature has revealed notable uncertainty in characterizing the UFL experimentally. This study focuses on predicting the flammable range of benzene/air mixtures using a freely-propagating flame method, where soot radiation is modeled using an optically-thin approximation. The investigation explores the impact of dilution by inert gases (steam). Initially, the kinetic model employed for flame propagation is compared to flame speed measurements. To address the substantial formation of soot during benzene combustion near the Upper Flammability Limit (UFL), the kinetic model for benzene combustion is coupled with a recently developed soot kinetic mechanism from the CRECK Modeling Lab at Politecnico di Milano. This mechanism has been validated against a vast database of sooting flames, encompassing various hydrocarbons, including benzene. The model predictions align well with experimental data available in the literature concerning the Lower Flammability Limit (LFL) and some of the experimental measurements for the UFL. The comprehensive model predictions enable differentiation among the various UFL datasets for benzene.

Introduction
The utilization of a significant amount of flammable, explosive, toxic, and corrosive hazardous chemicals in industrial production processes poses significant challenges to safety management throughout various stages, including processing, production, storage, transportation, and distribution. Numerous accidents have occurred throughout the history of petrochemical and chemical process industries, prompting extensive research on evaluating and analyzing the risks associated with fires and explosions [1,2]. Thus, chemicals flammability is a topic of the uttermost importance in fire safety engineering [3]. Benzene is one of critical chemical raw materials and solvents widely used in various industries. These chemicals pose significant risks due to their high flammability and strong toxicity [4]. Multiple sources have published data on the flammability limits of benzene across different temperatures,

ranging from ambient to elevated levels. However, due to variations in measurement methods and accuracy, the aforementioned literature exhibits some experimental data discrepancies, particularly concerning the UFLs. Since adding diluents is one of common methods to prevent explosions and extinguish fires, different authors also investigated the effect of common diluents such as N_2, CO_2, and steam (H_2O) [4,5]. Preventing these accidents is necessarily associated to the capability of anticipating the occurrence of such events, which implies their understanding at a fundamental level. This is done in this paper via chemical kinetics and flame simulations.

Kinetic model and numerical simulations

The kinetic mechanism developed at the CRECK Modeling group at Politecnico di Milano [6] is used to describe the chemistry of benzene combustion. The accuracy of this mechanism in predicting speciation data and flame speed for a large number of fuels and fuel mixtures and different operating conditions had been previously demonstrated [7][8]. The study was carried out using the OpenSMOKE++ Suite framework [9] and adopting a comprehensive kinetic model, including 327 species and 13417 reactions. The OpenSMOKE++ Suite is adopted to calculate the flammability limits (LFL, UFL) using a 1-D system modelled as a non-adiabatic freely-propagating flame (FPF), as described in detail in [3]. A 10 cm computational domain was adopted, with a large number of grid-points (up to 1,000) to ensure accurate and grid-insensitive results. In this study, a radiative term ($\dot{Q}_{rad}$) is considered in the energy conservation equation to account for the flame heat losses. The model incorporates the optically thin gas approximation, which is mathematically expressed by the following equation:

$$\dot{Q}_{rad} = 4\sigma \left[\sum_{k=1}^{N_S} p_k \alpha_k + \delta \right] (T^4 - T_{env}^4)$$

where σ is the Stefan–Boltzmann constant, p_k and α_k the partial pressure and the Planck mean absorption coefficient for the k^{th} species, respectively, and δ is soot emissivity. The radiative properties of gases are based on the RADCAL model [10]. In this work, since the predictions of the UFL require the simulation of a rich flame, a soot emissivity model was included, according to the following equation:

$$\delta = C f_v T$$

where T is the temperature, f_v is the soot volumetric fraction, and C is a fitting constant whose value (C = 2370 [1/m/K]) was estimated by Widmann [11].

Kinetic model validation

The kinetic model capability to accurately predict the combustion parameters relevant to the evaluation of benzene flammability limits is hereafter examined, with reference to laminar flame velocity and soot precursors formation in benzene flames.

Flame speed

Figure 1 shows a comparison between model predictions and flame speed measurements for benzene/air flames measured by different authors at different initial temperatures. The agreement between model predictions and experimental results is remarkable in the entire range of conditions investigated.

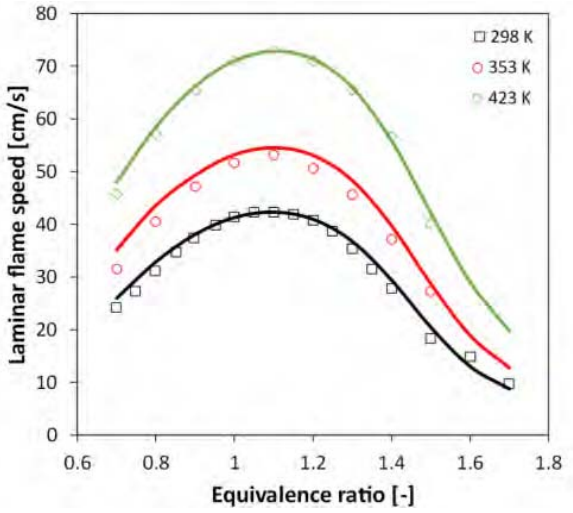

Figure 1. Benzene/air flame speed as a function of the initial temperature: 298 K [12], 353 K [13], and 423 K [13].

Benzene sooting flames

Model simulations are then compared in Figure 2 with speciation data measured by Tregrossi et al. [14] in a sooting benzene/O_2/Ar flames, at both φ=1.80 and 1.93.

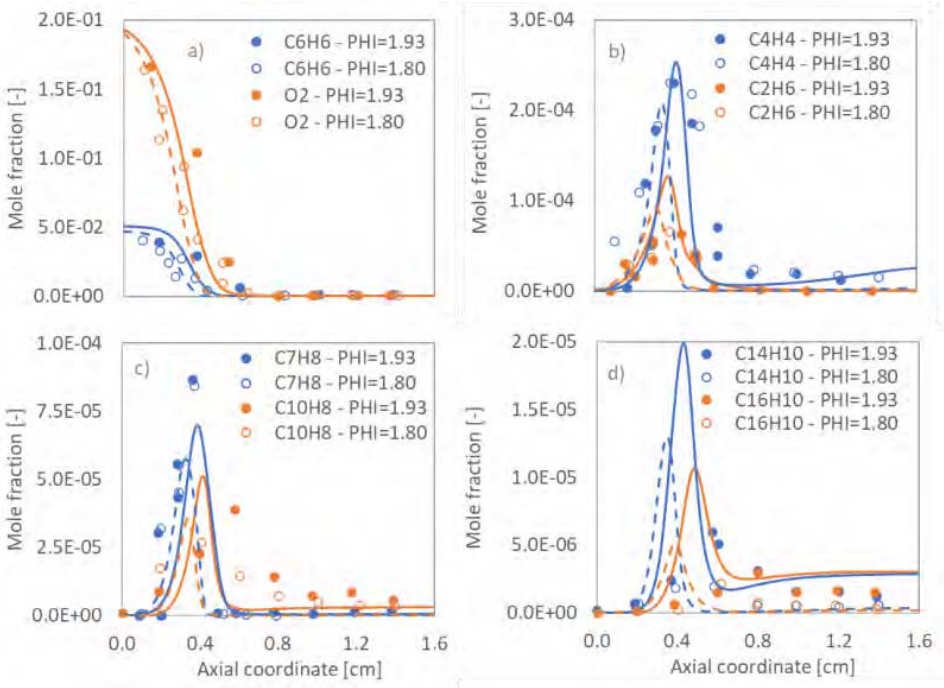

Figure 2. Atmospheric benzene/O_2/Ar flames for φ=1.80 and 1.93. Comparison between model predictions and experimental measurements [14].

Experimental temperature profiles are imposed to the simulations. As the equivalence ratio (φ) increases, T_{max} moves from 1850 to 1750 K, while fuel conversion and intermediates formation shift downstream. The model well captures this shift as well as the consumption of fuel and oxygen (Fig. 2a), and the formation of small hydrocarbons (C_2H_6 and C_4H_4 in Fig. 2b). As expected, the increase of the equivalence ratio (φ from 1.80 to 1.93) leads to larger mole fractions of all hydrocarbon intermediates. Mono- and poly-cylic aromatic hydrocarbons (C_7H_8 and $C_{10}H_8$ in Fig. 2c and $C_{14}H_{10}$ and $C_{16}H_{10}$ in Fig. 2d), which are key precursors of soot, are also satisfactorily predicted despite small discrepancies with the measurements. The model overestimation of phenanthrene ($C_{14}H_{10}$) and pyrene ($C_{16}H_{10}$) is due to the lumping of three and four ring-PAHs applied in the present model.

Prediction of Benzene flammability limits

The FPF model employs a detailed kinetic mechanism to describe the structure of a laminar flame, which is steady, non-adiabatic, 1-D and planar, resulting in an accurate description of the phenomena involved in flame propagation and extinction [3]. Starting from stoichiometric conditions, the FPF flame model dynamically solves the evolving flame structure when the equivalence ratio is slowly increased or decreased until flame extinction is observed. In this way, the UFL and LFL limits are calculated. The impact of oxidizer composition (a blend of O_2/N_2) on the flammability limits of benzene at 423 K and 1 atm is depicted in Figure 3.

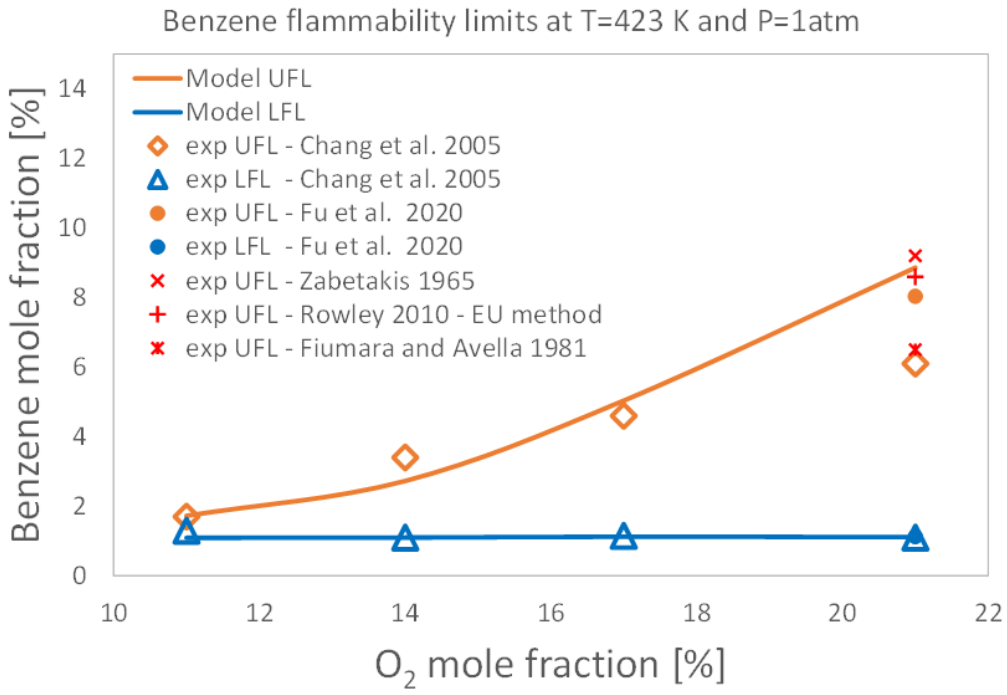

Figure 3. Benzene/O_2/N_2 flammable range. Comparison between model predictions and experimental measurements [2,4,5,15,16].

Various authors have reported different measured values for the air (21% O_2) case, underscoring the inherent uncertainty of this type of experimental measurements for

the UFL. In these conditions the model is more in line with the UFL measured by the US Bureau of Mines [5]. The model effectiveness in predicting the anticipated negligible effect of oxidizer composition on the LFL and substantial impact on the UFL is evident.

Figure 4 highlights the effect of steam dilution on the flammability limits of atmospheric benzene/air mixtures. With an increasing quantity of steam, the UFL of benzene decreases, whereas the LFL exhibits minimal sensitivity. Once the amount of steam exceeds a certain threshold, the UFL of benzene experiences a significant reduction, while the LFL shows a slight increase. The critical flammability is achieved when the LFL becomes equal to the UFL, specifically when the steam content in the diluted fuel mixture reaches ~0.97 (v/v). Figure 4 shows that also in this case the agreement between model predictions and experimentally measured flammability limits is satisfactory, although the UFL is slightly underestimated by the model at high steam dilutions.

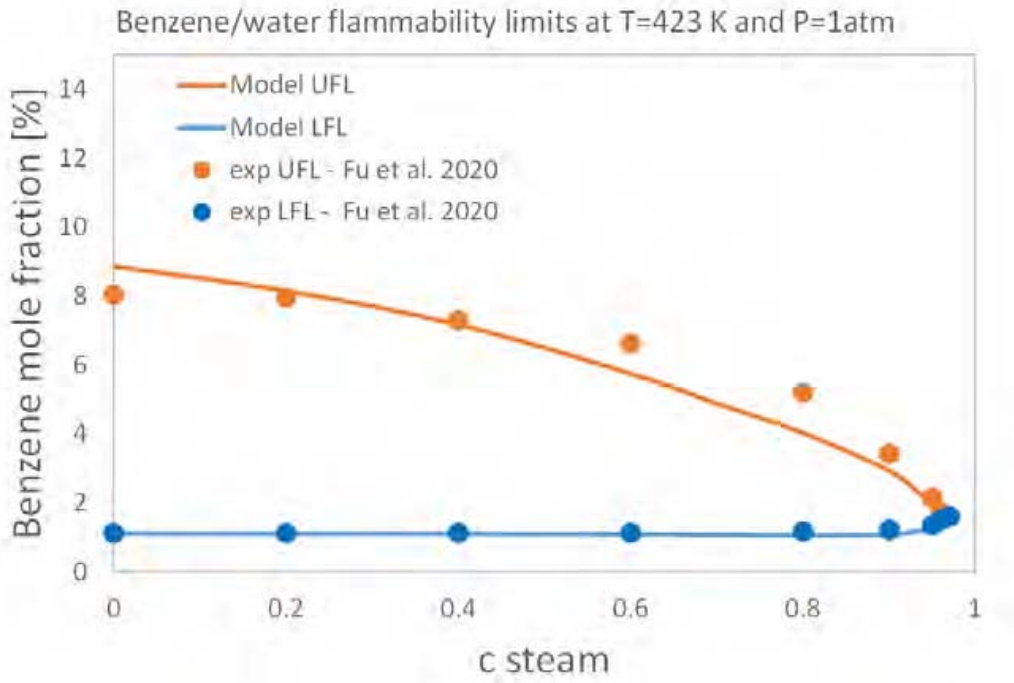

Figure 4. Benzene/Air/H_2O flammable range. Comparison between model predictions and experimental measurements [4].

Conclusion and Future insights

In this study, the Freely Propagating Flame (FPF) approach was employed to predict the flammability limits of benzene/air mixtures, considering the impact of inert dilution and the influence of soot on radiation and subsequent extinction. The propagation of flames is greatly affected by radiation due to the low reactivity exhibited by limit mixtures. Previous research has demonstrated the importance of incorporating a soot sub-mechanism and radiation model for the Upper Flammability Limit (UFL), which is particularly relevant for benzene flames even at atmospheric

pressures. However, it is anticipated to play a more significant role at higher pressures. The model accurately predicted the flammable range not only for benzene/air mixtures, but also for mixtures diluted with steam.

References

[1] Zabetakis, M.G., Fire and Explosion Hazards at Temperature and Pressure Extremes, *AIChE-IChemE Symp. Ser.* 2:99–104 (1965)
[2] Chang, Y.M., Tseng, J.M., Shuand, C.M., Hu, K.H., Flammability studies of benzene and methanol with various vapour mixing ratios at 150 °C, *Korean J. Chem. Eng.* 803–812 (2005)
[3] Bertolino A., Stagni A., Cuoci A., Faravelli T., Parente A., Frassoldati A., Prediction of flammable range for pure fuels and mixtures using detailed kinetics, *Combustion and Flame* 207:120–133 (2019)
[4] Fu W., Zhang K., Wu J., Flammability limits of benzene, toluene, xylenes from 373 K to 473 K and flame-retardant effect of steam on benzene series, P*rocess Safety and Environmental Protection* 137:328–339 (2020)
[5] Zabetakis, M.G., Flammability Characteristics of Combustible Gases and Vapors (No. BULL-627), Bureau of Mines, Washington DC (1965)
[6] http://creckmodeling.chem.polimi.it/
[7] Ranzi E., Frassoldati A., Grana R., Cuoci A., Faravelli T., Kelley A.P., Law C.K., Hierarchical and comparative kinetic modeling of laminar flame speeds of Hydrocarbon and Oxygenated fuels, *Prog. Energy Combust. Sci.* 38:468–501 (2012)
[8] Ramalli E., Dinelli T., Nobili A., Stagni A., Pernici B., Faravelli T., Automatic validation and analysis of predictive models by means of big data and data science, *Chem. Eng. Journal* 454:140149 (2023)
[9] Cuoci A., Frassoldati A., Faravelli T., Ranzi E., OpenSMOKE++: An object-oriented framework for the numerical modeling of reactive systems with detailed kinetic mechanisms, *Comput. Phys. Commun.* 192:237–264 (2015)
[10] Grosshandler W.L., RADCAL: a narrow-band model for radiation calculations in a combustion environment, 1993 NIST Technical Note, 1402, NIST
[11] Widmann J.F., Evaluation of the Planck Mean Absorption coefficients for radiation transport through smoke, *Combust. Sci. Technol.* 175:2038–2299 (2003)
[12] Davis S.G., Law C.K., Determination of and fuel structure effects on laminar flame speeds of C1 to C8 hydrocarbons, *Combust. Sci. Technol.* 140:427–449 (1998)
[13] Wang G., Li Y., Yuan W., Zhou Z., Wang Y., Wang Z., Investigation on laminar burning velocities of benzene, toluene, and ethylbenzene up to 20 atm, *Combustion and Flame* 184:312–323 (2017)
[14] Tregrossi A., Ciajolo A., Barbella R., The combustion of benzene in rich premixed flames at atmospheric pressure, *Combust. Flame*, 117 (1999), pp. 553-561
[15] Rowley, J. R., Flammability Limits, Flash Points, and Their Consanguinity: Critical Analysis, Experimental Exploration, and Prediction, Theses and Dissertations, Brigham Young University (Provo) (2010)
[16] Fiumara, A., Avella, F., Sull'infiammabilità di Benzene, Toluene e Xileni, *La Rivista Dei Combustibili*, Vol. XXXV, Fasc. 2-3:118-125 (1981)

EXPERIMENTAL AND NUMERICAL KINETICS STUDY OF OME_1 AND OME_2 COMBUSTION IN STOICHIOMETRIC LOW-PRESSURE LAMINAR FLAME

Yanan Huo, Véronique Dias, Hervé Jeanmart
yanan.huo@uclouvain.be
*Institute of Mechanics, Materials and Civil Engineering. (iMMC), Université catholique de Louvain, Louvain-la-Neuve, Belgium

Abstract
The combustion chemistry of OME_1 and OME_2 was studied in stoichiometric laminar flames at low pressure, 50 mbar, by carrying out flame structure measurements with molecular-beam mass spectrometry (MBMS). The kinetic modeling has been performed under the same conditions, and the simulated results were compared with experimental results. A new detailed kinetic sub-mechanism for OME_2 will be developed and added to the previous UCL mechanism.

Introduction
The urgency of reducing the emission of greenhouse gases and achieving a circular carbon economy encourages research on renewable energy systems. The alternative synthetic fuels (power to liquids) could be high-potential energy carriers for long-distance transportation and long-term storage [1][2]. Oxymethylene ethers (OME_s), formally known as polyoxyethylene dimethyl ethers, with the structural formula of $CH_3O(CH_2O)_nCH_3$, are regarded as a potential asset to the energy transition and one of the valuable candidates for power to liquids benefiting from its high energy density [3,4].
A deep understanding of oxidation kinetics of OME_s remains a prerequisite for optimizing their combustion and for a comprehensive assessment of the future engine application potential of OME_s. As the simplest OME_s, the combustion kinetics of OME_1, which is also named as dimethoxymethane (DMM), have been studied extensively with experimental and numerical methods [5–12]. Lean and rich premixed $OME_1/O_2/Ar$ flames were studied in our previous work with a new sub-mechanism of OME_1 in UCL mechanism [5]. Alzueta et al. [9,10] investigated OME_1 oxidation in a flow reactor at high and atmospheric pressures, from fuel-lean to rich conditions. Few detailed studies have been conducted on longer-chain OMEs (OME_n, n>1) [13-16]. In the recent work from Wang et al. [11], pyrolysis of OME_{1-3} was studied in a jet-stirred reactor (JSR) at around atmospheric pressure (1.03 atm) and temperatures of 450-1080 K. Using JSR, they further investigated the low-temperature (500-950 K) oxidation kinetics of OME_{1-3} [12]. Gaiser et al. [16] recently studied fuel-rich (equivalence ratio of 1.7) premixed flames of OME_{0-4} with

electron ionization (EI) MBMS at 40 mbar with the help of kinetic modeling with the mechanism from Kathrotia et al. [17] for interpretation, making the conclusion that oxygenated species dominate the combustion process and the observed species pool is nearly independent of the chain length of the respective OME_s. The purpose of this work is to investigate the kinetics of OME_1 and to report the combustion chemistry of OME_2 under low-pressure and stoichiometric conditions to understand the effects of ($-CH_2O$) chain length and be ready for the studies on higher OME_s in the future. The measurement and calibration of OME_1 and OME_2 stoichiometric flame have been performed. This paper focuses on the investigation of detailed kinetics of OME_1 premixed flame.

Experimental methods

The MBMS flame setup was used for measurements of both OME_1 and OME_2 stoichiometric, premixed laminar flames at low pressures. Table 1 shows the inlet composition of the flames. Before mixing with oxygen and argon, the liquid fuel is evaporated in the Controlled Evaporation Mixing (CEM) system. The vaporizer temperature was set to 333.15 K for OME_1 and 383.15 K for OME_2. To prevent condensation, the gaseous mixture passes through a pipe, which is heated up to 473.15 K. The flames are stabilized at 50 mbar on a Spalding-Botha burner, 8 cm in diameter. Parallel to the burner surface, a quartz cone (0.1 mm orifice) allows direct sampling from the flame with a distance range of 0-30 mm (precision 0.1 mm). To minimize interferences either from fragmentation during the electron impact or from overlapping species with similar masses, the ionization potentials were chosen specifically for the species detected with the precision of 0.01 eV. For OME_n ($n>0$), it is difficult to form stable molecular ions in the MBMS. The signal of molecular $C_3H_7O_2$ is regarded as OME_1, and of molecular $C_4H_9O_3$ is regarded as OME_2. An internal calibration procedure was used to calibrate the major species, such as OME_1, OME_2, O_2, CO_2, CO, H_2, and H_2O, with uncertainties lower than 6%. Direct calibration was used to determine CH_4 and C_2H_2 mole fraction profiles with uncertainties around 5-10%. Estimating ionization cross-sections for unstable species calibration resulted in higher uncertainties (10-20%). The flame temperature profiles will be measured in the next step. The one used for the simulations for the current procedure is based on the calculation of experimental temperature profile measured in the $OME_1/O_2/Ar$ fuel-rich flame in [5].

Table 1. Stoichiometric flames inlet composition (slm at 273 K; 1013 mbar). With D_t (total flow rate), and italics in the brackets are mole fractions.

	Fuel (g/h)	O_2 (slm)	Ar (slm)	D_t (slm)
OME_1	70 (0.07)	1.72 (0.24)	4.0 (0.70)	5.72
OME_2	55 (0.04)	1.10 (0.17)	4.4 (0.79)	5.72

Numerical Modeling

In this work, two mechanisms were used for chemical kinetic modeling. The UCL

mechanism was established by Dias et al. [5]. It has been developed to predict lean and rich premixed $OME_1/O_2/Ar$ flames and will be extended by building sub-mechanisms for OME_2 and OME_3 combustion. 480 elementary reactions and 90 chemical species are included in the UCL mechanism with detailed illustrations in the previous paper [5]. At the same time, the mechanism from Kathrotia et al. [17], which includes ethers from OME_0 to OME_5 with 1814 reactions and 238 species. It is named Kath- mechanism in the following discussion. The numerical modeling is performed using OpenSMOKE++ [18].

Results and Discussion

Figures 1-2 show experimental (symbols) and simulated (lines) mole fraction profiles of the chemical species measured. In the following section, we discuss the consumption of OME_1 and the formation of chemical species produced from OME_1. The primary and secondary radicals produced by H-abstraction of OME_1 are denoted as DMM_1 ($CH_2OCH_2OCH_2$) and DMM_2 ($CH_2OCHOCH_3$).

Figure 1 presents experimental and calculated mole fraction profiles of the reactants and products in the stoichiometric flame of $OME_1/O_2/Ar$ mixture. The results show good agreement between experimental results and simulated ones from both mechanisms. In Figure 1(a), the experimental results show that OME_1 was consumed earlier and faster than that estimated by the two mechanisms, probably caused by the shift of flames due to the sampling nozzle. In Figure 1(b), the experimental mole fractions of H_2 and CO are lower than the numerical results from both mechanisms. According to the research performed by Dias et al. [5] and Gaiser et al. [16], which showed the excellent prediction of the mechanisms, the deviation here might be from the estimated temperature profile used in the modeling. Unlike modeling results of the other three species, the mole fraction profile of H_2 from the Kath-mechanism is higher than that from the UCL-mechanism. From the results of simulations, H abstraction by OH and H dominates the consumption of OME_1. Among these, the reaction $OME_1+H=DMM_1+H_2$ shows the highest reaction rate in UCL-mechanism. However, the reaction $OME_1+OH=DMM_1+H_2O$ is the fastest in the Kath-mechanism. The second most crucial consumption pathway for the UCL-mechanism is H abstraction by OH to produce DMM_1 and DMM_2, with identical reaction rates, followed by the reaction with the O radical. The reactions with H are the second most important consumption pathway in the Kath-mechanism. The last consumption of OME_1 is with CH_3 in both mechanisms.

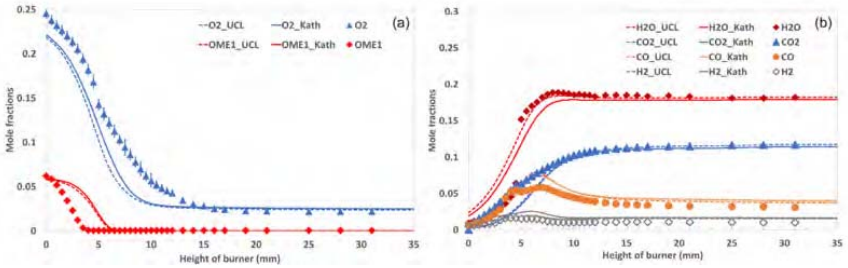

Figure 1. Experimental (symbols) and simulated mole (lines) fraction profiles of major species.

Figure 2 shows the mole fraction profiles of other important intermediates from experiments and simulations. In Figure 2(a), the two mechanisms underestimate the mole fraction of CH_3 and overestimate that of CH_2O, but with good agreement on peak positions and trends. In Figure 2(b), the simulated results almost overlap and underestimate the mole fraction of HCO on the peak position. UCL-mechanism shows a good agreement on peak value against the experimental mole fraction of HO_2, while the Kath-mechanism underestimates it. In Figure 2(c), the apparent deviation of C_2H_4 from both simulated results is observed. It has been found that Kath-mechanism showed underestimation of C_2H_4 in work from Gaiser et al. under fuel-rich OME_1 flame [16].

The two mechanisms were used for OME_1, and only Kath-mechanism was used for OME_2 to analyze the reaction pathway of OME_1 and OME_2 consumption and the formation of essential intermediates, as shown in Figure 3. The main pathway of OME_1 consumption in both mechanisms is similar to the conclusion from our previous work on the fuel-rich flame of OME_1 [5]. The red dashed pathway denotes the reactions that show the largest contributions in the UCL-mechanism while being less critical in the Kath-mechanism, and the blue dashed line shows the dominant reactions in Kath-mechanism while that being less important in UCL-mechanism. The consumption reactions of HCO in the UCL-mechanism might explain the lower predicted mole fraction of HCO, as shown in Figure 2(b). Similarly, the conversion of CH_3OCO to CH_3 might directly result in a higher simulated mole fraction of CH_3. Under stoichiometric condition, the consumption pathway of OME_2 is consistent with that of OME_1 once the primary and secondary radicals are produced, which are named as OME_2*1 and OME_2*2 separately. It is worthwhile mentioning that, expecting to form the fuel radicals, OME_2 preferentially forms DMM_1 by unimolecular decomposition.

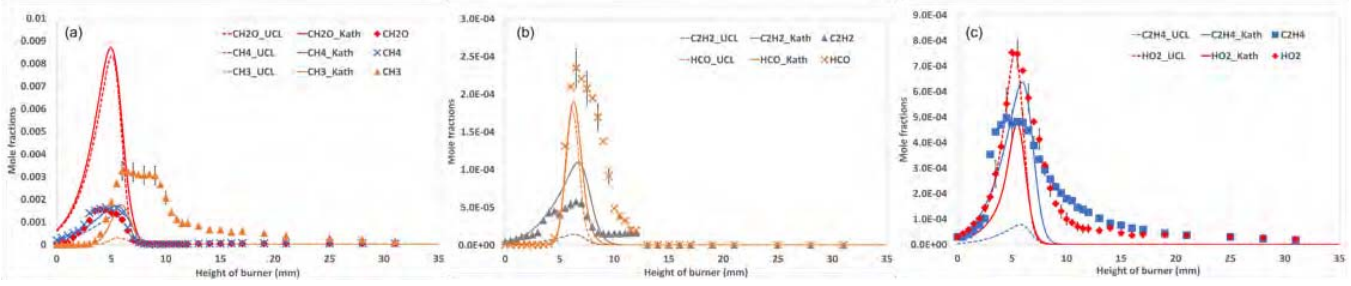

Figure 2. Experimental (symbols) and simulated mole (lines) fraction profiles of OME_1 flame.

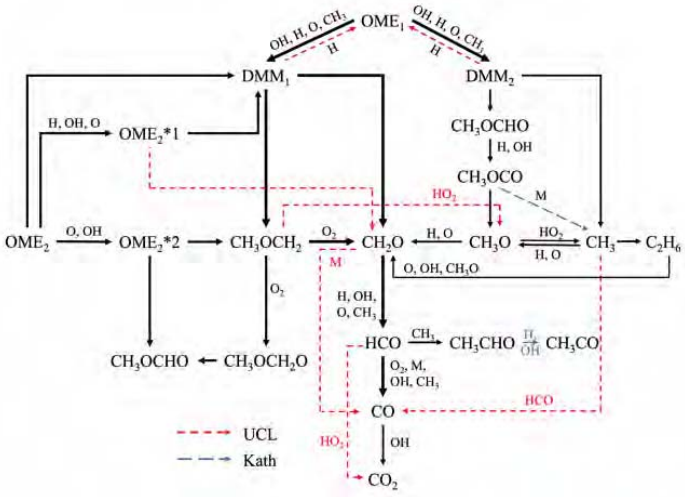

Figure 3. Reaction pathway of OME_1 and OME_2 stoichiometric flames.

Conclusion

In this work, the stoichiometric flame of $OME_1/O_2/Ar$ and $OME_2/O_2/Ar$ were measured by molecular-beam mass spectrometry at 50 mbar. The mole fraction profiles of the main species of OME_1 flame, especially the reactive intermediates, were measured and presented. Numerical modeling was performed with the UCL-mechanism and the Kath-mechanism. The comparison of the experimental results of OME_1 flame verified the experimental measurements and showed good agreement. From both mechanisms, OME_1 consumption is dominated by H-abstraction reactions. It follows two main pathways, with the first one being the fastest at the stoichiometric condition: $OME_1 \Rightarrow CH_3OCH_2OCH_2 \Rightarrow CH_3OCH_2 \Rightarrow CH_2O$ (Route 1) and $OME_1 \Rightarrow CH_3OCHOCH_3 \Rightarrow CH_3OCHO \Rightarrow CH_3OCO \Rightarrow CH_3O \Rightarrow CH_2O$ (Route 2). The new sub-mechanism of OME_2 flame will be used for modeling, evaluated against the experimental results, and expanded to the combustion of OME_3. These results will guide future work on combustion chemistry OME_3 stoichiometric flame and $OME_{1\text{-}3}$ flames under fuel-lean conditions.

References

[1] K. De Ras, R. Van de Vijver, V. V. Galvita, G. B. Marin, and K. M. Van Geem, Carbon capture and utilization in the steel industry: challenges and opportunities for chemical engineering, *Current Opinion in Chemical Engineering* 26, 81 (2019), ISSN 2211-3398, energy, Environment Sustainability: Sustainability Modeling Reaction engineering and catalysis: Green Reaction Engineering.

[2] L. E. Hombach, L. Dore, K. Heidgen, H. Maas, T. J. Wallington, and G. Walther, Economic and environmental assessment of current (2015) and future (2030) use of e-fuels in light-duty vehicles in germany, *Journal of Cleaner Production* 207, 153 (2019), ISSN 0959-6526.

[3] Y. Fenard and G. Vanhove, A mini-review on the advances in the kinetic understanding of the combustion of linear and cyclic oxymethylene ethers, *Energy & Fuels* 35, 14325 (2021).

[4] H. Liu, Z. Wang, J. Zhang, J. Wang, and S. Shuai, Study on combustion and emission characteristics of polyoxymethylene dimethyl ethers/diesel blends in light-duty and heavy-

duty diesel engines, *Applied Energy* 185, 1393 (2017), ISSN 0306-2619, clean, Efficient and Affordable Energy for a Sustainable Future.

[5] V. Dias, X. Lories, and J. Vandooren, Lean and rich premixed dimethoxymethane/oxygen/argon flames: Experimental and modeling, *Combustion Science and Technology* 182, 350 (2010).

[6] W. A. Kopp, L. C. Kro¨ger, M. Do¨ntgen, S. Jacobs, U. Burke, H. J. Curran, K. Alexander Heufer, and K. Leonhard, Detailed kinetic modeling of dimethoxymethane. part i: Ab initio thermochemistry and kinetics predictions for key reactions, *Combustion and Flame* 189, 433 (2018), ISSN 0010-2180.

[7] F. H. Vermeire, H.-H. Carstensen, O. Herbinet, F. Battin-Leclerc, G. B. Marin, and K. M. V. Geem, Experimental and modeling study of the pyrolysis and combustion of dimethoxymethane, *Combustion and Flame* 190, 270 (2018).

[8] C. A. Daly, J. M. Simmie, P. Dagaut, and M. Cathonnet, Oxidation of dimethoxymethane in a jet-stirred reactor, *Combustion and Flame* 125, 1106 (2001), ISSN 0010-2180.

[9] L.Marrodan, F. Monge, Angela Millera, R. Bilbao, and M. U. Alzueta, Dimethoxymethane oxidation in a flow reactor, *Combustion Science and Technology* 188, 719 (2016).

[10] L. Marroda´n, E. Royo, Millera, R. Bilbao, and M. U. Alzueta, High pressure oxidation of dimethoxymethane, *Energy & Fuels* 29, 3507 (2015).

[11] X. Zhong, H. Wang, Q. Zuo, Z. Zheng, J. Wang, W. Yin, and M. Yao, Experimental and kinetic modeling studies of polyoxymethylene dimethyl ether (pode) pyrolysis in jet stirred reactor, *Journal of Analytical and Applied Pyrolysis* 159, 105332 (2021), ISSN 0165-2370.

[12] H. Wang, Z. Yao, X. Zhong, Q. Zuo, Z. Zheng, Y. Chen, and M. Yao, Experimental and kinetic modeling studies on low-temperature oxidation of polyoxymethylene dimethyl ether (dmm1-3) in a jet-stirred reactor, *Combustion and Flame* 245, 112332 (2022), ISSN 0010-2180.

[13] T. He, Z. Wang, X. You, H. Liu, Y. Wang, X. Li, and X. He, A chemical kinetic mechanism for the low- and intermediate-temperature combustion of polyoxymethylene dimethyl ether 3 (PODE3), *Fuel* 212, 223 (2018).

[14] L. Cai, S. Jacobs, R. Langer, F. vom Lehn, K. A. Heufer, and H. Pitsch, Auto-ignition of oxymethylene ethers (OMEn, n = 2–4) as promising synthetic e-fuels from renewable electricity: shock tube experiments and automatic mechanism generation, *Fuel* 264, 116711 (2020).

[15] W. Sun, G. Wang, S. Li, R. Zhang, B. Yang, J. Yang, Y. Li, C. K. Westbrook, and C. K. Law, Speciation and the laminar burning velocities of poly(oxymethylene) dimethyl ether 3 (POMDME3) flames: An experimental and modeling study, *Proceedings of the Combustion Institute* 36, 1269 (2017).

[16] N. Gaiser, H. Zhang, T. Bierkandt, S. Schmitt, J. Zinsmeister, T. Kathrotia, P. Hemberger, S. Shaqiri, T. Kasper, M. Aigner, et al., Investigation of the combustion chemistry in laminar, low-pressure oxymethylene ether flames (ome0–4), *Combustion and Flame* 112060 (2022), ISSN 0010-2180.

[17] T. Kathrotia, P. Oßwald, J. Zinsmeister, T. Methling, and M. Kohler, Combustion kinetics of alternative jet fuels, part-III: Fuel modeling and surro- gate strategy, *Fuel* 302, 120737 (2021).

[18] A. Cuoci, A. Frassoldati, T. Faravelli, and E. Ranzi, Opensmoke++: An object-oriented framework for the numerical modeling of reactive systems with detailed kinetic mechanisms, *Computer Physics Communications* 192, 237 (2015), ISSN 0010-4655.

DERIVATION AND VALIDATION OF AN ARRHENIUS-BASED REDUCED GLOBAL MECHANISM FOR HYDROGEN-AIR FLAMES

F. G. Schiavone*, M. Torresi*, S. M. Camporeale*, D. Laera*
f.schiavone11@phd.poliba.it
*Department of Mechanics, Mathematics and Management, Polytechnic University of Bari, Via Orabona 4, Bari 70125, Italy

Abstract
A best-fitting methodology is applied in this work to derive an explicit, analytical dependence of reaction rate constant parameters on equivalence ratio, system pressure, and unburned gas temperature for an Arrhenius-based reduced one-step kinetics in the case of hydrogen-air combustion. A classic Pre-Exponential Adjustment (PEA) approach has been extended to capture both the equivalence ratio and pressure dependence of the laminar burning rate. A correction has also been introduced for temperature profile in the flame reaction region, improving the flame thermal thickness predictions. Both irreversible and reversible global reaction steps have been considered, and it has been observed that a backward path must be included to preserve the flame structure and adiabatic flame temperature near stoichiometry. Particular attention has been posed in separating the dependence on thermodynamic state and composition in the definition of the Pre-Exponential Adjustment laws, to reduce the numerical stiffness of the reduced chemistry scheme. Computations of one-dimensional unstrained/strained laminar flames have been performed for a wide range of pressures ([1; 30] atm), unburned gas temperature ([300; 800] K), and equivalence ratio ([0.4; 6.0]), showing a good agreement of the reduced mechanism with respect to detailed kinetics.

Introduction
Despite the full kinetics of hydrogen oxidation being well-known and studied, its integration into CFD calculations is challenging, with simplified chemistry mechanism becoming necessary, if not mandatory, to reduce the computational cost of simulations, especially in cases with complex geometries at high-pressure conditions. Three main pathways can be followed to reduce hydrogen kinetics. We first recall tabulated chemistry (e.g. [1]); this approach however makes strong assumptions on the combustion regime and raises multiple challenges on its applicability for multi-regime flames, often characterizing hydrogen systems (e.g., see the HYLON flame [2]). The inclusion of both premix and diffusion flames may result in tables with a size that may no longer be acceptable or require the use of expensive algorithms for storing and searching out data [3]. A second route is based on an analytical derivation of the reaction rate by means of first principles-derived approaches, as the quasi-

steady-state (QSS) approximation; in this context, we recall the model proposed in [4], based on the QSS approximation for all radicals, including H. This kind of approach, albeit formally rigorous and correct only for certain flame conditions, can nevertheless be difficult to implement in existing numerical codes, due to the non-Arrhenius-based reaction rate expression. Finally, a third approach relies on a "best-fit" targeting of reaction rate parameters to match detailed kinetics or experimental result. Some applications of this approach for hydrogen/air chemistry could be found in [5, 6], where stoichiometry-dependent Arrhenius-based reaction rate parameters for an overall irreversible reaction were defined for specific mixture conditions under unity Lewis number approach. While all mentioned works provide reasonably good descriptions of hydrogen oxidation for the specific flame conditions for which they were conceived, there is a lack in literature for an Arrhenius-based global mechanism able to capture hydrogen flames main properties in a sufficiently wide range of conditions. Based on these considerations, the present work, albeit recognizing the importance of complex chemistry and the consequent limit in accuracy of global description, aims at filling this gap, by exploiting the numerical simplicity of the best-fitting approach to define a one-step reduced mechanism describing, with sufficient accuracy, the main properties of hydrogen-air flames for several reactants' states. This may be used for preliminary calculations within CFD codes, for fast yet effective simulations prior of the introduction of detailed kinetics.

Derivation of the one-step scheme

Despite combustion being an irreversible process, hence described by a global irreversible reaction, the consequent assumption of complete combustion is not suitable to describe flame structure and temperature in the case of hydrogen combustion, especially in the near-stoichiometry region. Consequently, the global one-step reaction adopted in the proposed scheme is the reversible reaction $2\ H_2 + O_2 \rightleftharpoons 2\ H_2O$. The reaction rate constants are here expressed in the form of a modified Arrhenius equation for the forward reaction (k_f), and of a standard Arrhenius equation for the backward step (k_b), with Pre-Exponential Adjustment (PEA) laws adopted for the pre-exponential factors A_f and A_b to capture pressure- and composition-dependent behaviors. Based on [7, 8], pressure-dependent activation energies $E_{a,f}$, and $E_{a,b}$, and reaction orders n_{H2}, n_{O2} and n_{H2O} have been introduced. The temperature exponent of the forward reaction has been evaluated as $\beta = n/2 - 1$, with n being the overall reaction order. The pressure dependence for these parameters allows for a self-consistency of the reaction rate definition, and of the PEA law, at different system pressures, preserving the structure of the model over a wider range of initial conditions. For the forward Pre-Exponential Factor, the PEA is given by the product

$$A_f = A_f^*(p) f(\phi) g(\phi, p)\ , \qquad (1)$$

where A_f* represents the value of Pre-Exponential Factor matching the burning rate at stoichiometry and is linearly dependent on system pressure. The function f,

dependent only on equivalence ratio, has been defined to capture the impact of stoichiometry on the burning rate at normal temperature and pressure, and assumes the form

$$f(\phi) = \psi_0 + \psi_1 \exp\left[-\psi_2 \left(\frac{\phi-\varphi_0}{\psi_3}\right)^2\right] - \psi_4 \tanh(\phi-\varphi_1)\,. \tag{2}$$

Being the impact of pressure different on lean and rich flames, the function g has been introduced, to extend the model on a wider range of pressure:

$$g(\phi, p) = [\xi_0 + \xi_1 \tanh(\phi - \varphi_2)]^{[\xi_2 \ln(p/p^0)]}\,. \tag{3}$$

The pressure exponent allows for the scalability of the model, at least in the range of system pressures tested in the present study. Being it a logarithmic term, the condition $g(\phi, p) \equiv 1$ for $p = p^0 = 1$ atm is automatically imposed. For the backward reaction, the Pre-Exponential Factor is computed from the one of the forward reaction by taking into account equilibrium. These explicit functions allow, at least in the considered range of states, a computationally cheap prediction of laminar burning velocity of premixed hydrogen flames.
Together with flame speed, flame thermal thickness is another important parameter for CFD codes since it defines mesh resolution constraints. Under the assumption of constant non-unity Lewis number [9, 10], an additional function has been introduced to adjust the diffusion parameters, so that flame thickness is properly predicted. In particular, Prandtl and Schmidt numbers, as well as A_f and A_b, are divided by a Flame Thickness Adjustment (FTA) term:

$$FTA(\phi) = \frac{\sigma_1}{1+\exp\left(-\frac{\phi+\sigma_2-\sigma_3/2}{\sigma_4}\right)}\left[1-\frac{1}{1+\exp\left(-\frac{\phi+\sigma_2+\sigma_3/2}{\sigma_5}\right)}\right] - \sigma_6\,. \tag{4}$$

Validation of the one-step scheme
The validity of the reduced one-step scheme 1S_H2AIR_REV_FGS has been assessed by performing flamelet calculations involving hydrogen-air mixtures and comparing with experimental results or reference calculations based on the San Diego (UCSD) [11], the Konnov [12], and the H2_NOX_15_94_TC [10] mechanisms. A comparison of the laminar flame speeds predicted by the reduced mechanism with the reference schemes and experimental data is shown in Fig. 1. It can be observed that the proposed scheme is able to capture with elevated accuracy the burning rate at all system pressures of interest, with a maximum relative percentage error with respect to the UCSD scheme of 6% in the whole range of pressures considered.

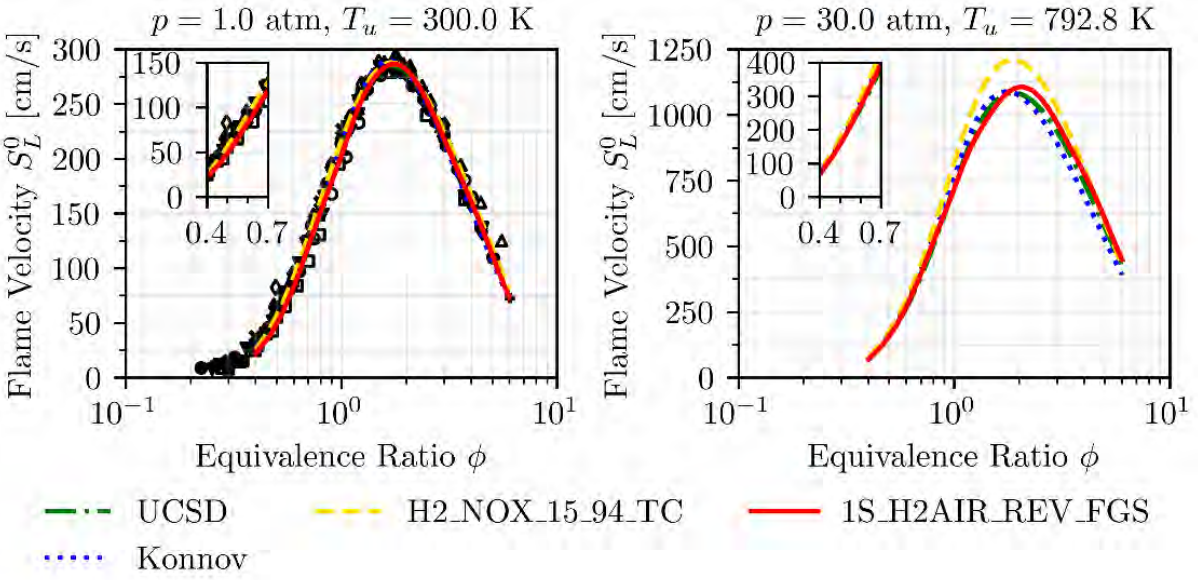

Figure 1. Laminar flame speed of H_2/air at 1 atm (left) and 30 atm (right) versus equivalence ratio, with a focus on the lean regime for $0.4 \leq \phi \leq 0.7$. Comparison between experimental measurements (symbols) taken from [3] and references therein, and numerical integrations with reduced and reference schemes.

The importance of the *FTA* function is proved in Fig. 2, where flame thickness results are shown, with the modification of diffusion coefficients allowing to adjust the temperature gradient of the reduced scheme. Interestingly, although the thickness value range varies significantly with pressure, the scaling factor between the detailed chemistry and the reduced scheme remains almost unaffected.
Finally, stretch response has been analyzed by considering consumption speeds in a counterflow premixed flame configuration, with this quantity defined as in [9]:

$$S_c = -\frac{1}{\rho_u \left(Y_F^u - Y_F^b\right)} \int_{-\infty}^{+\infty} \dot{\omega}_F \, d\mathbf{n} \tag{5}$$

As shown in Fig. 3, a very good agreement can be observed for lean flames, which are of the utmost interest for industrial applications. Reasonable results are found also for rich flames, while the most significant differences are obtained for a stoichiometric flame. In this case, the imposition of a constant value for Lewis numbers, which directly impact stretch response, in the simplified transport model adopted for the reduced schemes, can be at the origin of such limitation. In future work, the *FTA* function may be adapted to dynamically vary the Lewis number, so that a better prediction of such behavior can be obtained for all flames of interest.

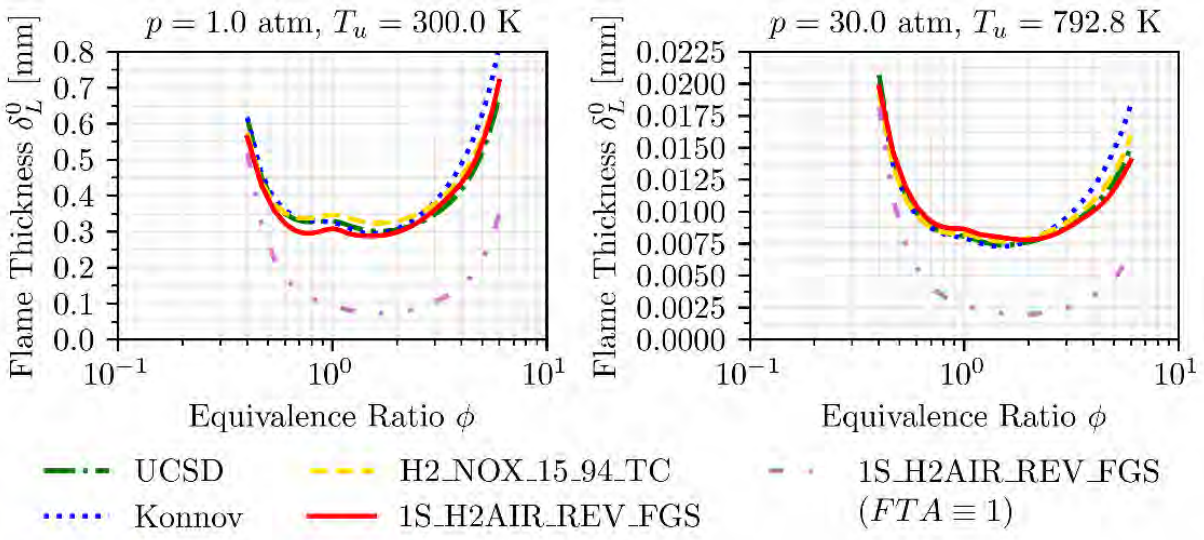

Figure 2. Thermal flame thickness of H_2/air at 1 atm (left) and 30 atm (right) versus equivalence ratio. Comparison between numerical integration with reduced schemes and reference mechanisms.

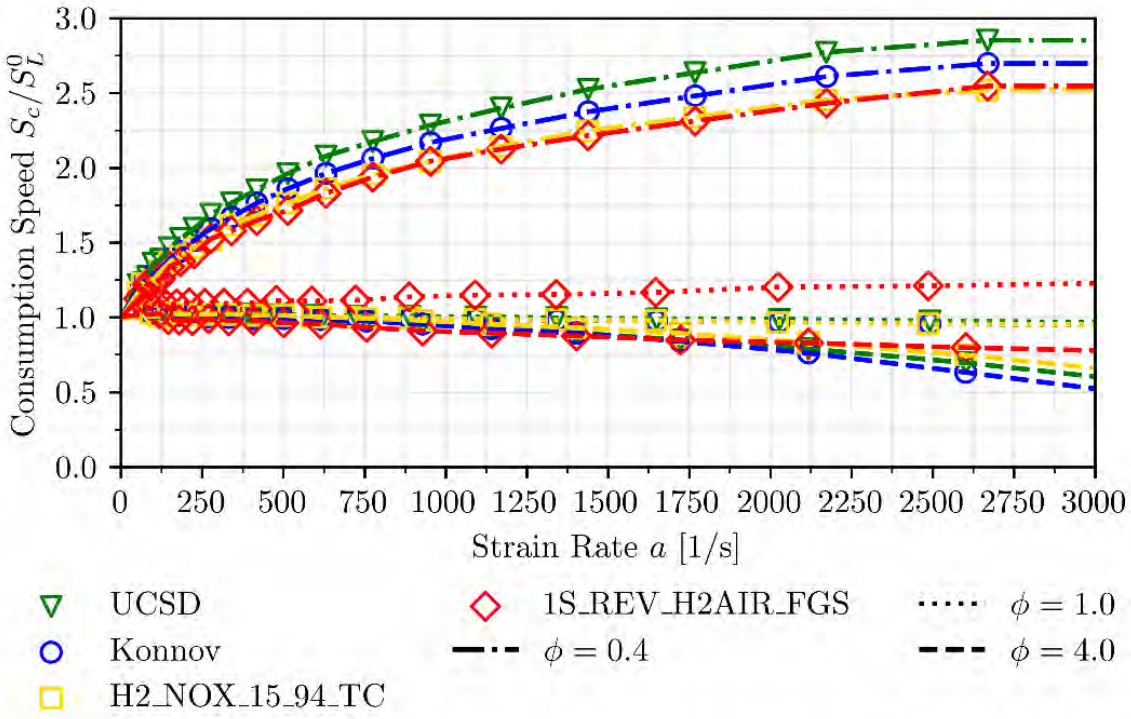

Figure 3. Normalized consumption speed versus global strain rate at different values of equivalence ratio. Comparison between numerical integration with reduced and reference schemes.

Conclusions

In this work, the derivation of a global one-step reduced scheme, based on an Arrhenius formulation, was presented. The mechanism is based on an analytical modelling of hydrogen oxidation to reduce the number of species, hence of transport equations

to solve, in CFD codes, with a significant gain in computational efficiency. The proposed model has been validated by comparison with reference schemes for canonical flamelet configurations, showing an overall good agreement in the prediction of main flame properties. Some limits have been found in the prediction of stretch response for stoichiometric flames, indicating potential for further optimization.

References

[1] Wang, B., Wei, W., Ma, S., Wei, G., "Construction of one-step H2/O2 reaction mechanism for predicting ignition and its application in simulation of supersonic combustion", *International Journal of Hydrogen Energy*, 41(42):19191-19206 (2016).

[2] Aniello, A., Laera, D., Marragou, S., Magnes, H., Selle, L., Schuller, T., Poinsot, T., "Experimental and numerical investigation of two flame stabilization regimes observed in a dual swirl H2-air coaxial injector", *Combustion and Flame*, 249:112595 (2023).

[3] Sánchez, A. L., Williams, F. A., "Recent advances in understanding of flammability characteristics of hydrogen", *Progress in Energy and Combustion Science*, 41:1-55 (2014).

[4] Carpio, J., Li, B., Fernández-Galisteo, D., Sánchez, A. L., Williams, F. A., "Systematically derived one-step kinetics for hydrogen-air gas-turbine combustion", *Combustion and Flame*, 250:112633 (2023).

[5] Coffee, T. P., Kotlar, A. J., Miller, M. S., "The overall reaction concept in premixed, laminar, steady-state flames. I. Stoichiometries", *Combustion and Flame*, 54(1-3):155-169 (1983).

[6] Coffee, T. P., Kotlar, A. J., Miller, M. S., "The overall reaction concept in premixed, laminar, steady-state flames. II. Initial temperatures and pressures", *Combustion and Flame*, 58(1):59-67 (1984).

[7] Egolfopoulos, F. N., Law, C. K., "Chain mechanisms in the overall reaction orders in laminar flame propagation", *Combustion and Flame*, 80(1):7-16 (1990).

[8] Sun, C. J., Sung, C. J., He, L., Law, C. K., "Dynamics of weakly stretched flames: quantitative description and extraction of global flame parameters", *Combustion and Flame*, 118(1-2):108-128 (1999).

[9] Poinsot, T., Veynante, D., *Theoretical and numerical combustion*, RT Edwards, Inc., 2005.

[10] Capurso, T., Laera, D., Riber, E., Cuenot, B., "NOx pathways in lean partially premixed swirling H2-air turbulent flame", *Combustion and Flame*, 248:112581 (2023).

[11] Saxena, P., Williams, F. A., "Testing a small detailed chemical-kinetic mechanism for the combustion of hydrogen and carbon monoxide", *Combustion and Flame*, 145(1-2):316-323 (2006).

[12] Konnov, A. A., "Yet another kinetic mechanism for hydrogen combustion", *Combustion and Flame*, 203:14-22 (2019).

Systematic reaction class-based analysis of PAH formation in benzene flames with automated tools

L. Pratali Maffei*, A. Nobili*, T. Dinelli*, T. Faravelli*
e-mail of corresponding author: luna.pratali@polimi.it
*Department of Chemistry, Materials and Chemical Engineering "Giulio Natta",
Politecnico di Milano, Milan, Italy

Abstract
Automated tools for the analysis of the performance of kinetic mechanisms can greatly aid targeted kinetic model refinement avoiding time consuming user- and experience-dependent manual analyses. This work presents a systematic analysis of the performance of CRECK kinetic mechanism for benzene oxidation and PAHs growth in benzene flames. The reactivity of unsaturated 5- and 6-membered ring moieties is classified. Kinetic simulations of 45 datasets for benzene pyrolysis and oxidation are performed with the recently developed SciExpeM platform and evaluated with a multi-index approach. The analysis of PAH formation in premixed flames (13 datasets) shows good performances but a systematic underestimation of both indene and naphthalene. Reaction class-based model analysis helps identify potential reasons for these shortcomings and guide model improvement.

Introduction
The increasing complexity of kinetic mechanisms for combustion processes and the large amount of data collected and used for their testing call for automated, integrated and standardized procedures for model development, validation, analysis and optimization. Model development is greatly aided by automated kinetic mechanism generation and potential energy surface (PES) exploration tools. However, such tools largely fail for more complex and less known systems such as mono and polycyclic aromatic hydrocarbons (M/PAHs), where even the identification of resonance stabilization by canonical chemical identifiers (e.g., InChIs) fails, and many relevant reaction pathways and reaction types are still unclear. These aspects highlight the need for a broader and less detailed classification of relevant reaction pathways as a starting point for the development of reliable and complete kinetic models. As regards model testing, standardized automated tools for both the storage and the simulation of reactor data are key to highlight systematic trends in the model performance and hence to model improvement.
In this context, this works presents a systematic hierarchical classification of the reactions of CRECK kinetic mechanism involving unsaturated rings with cyclopentadiene-like and aromatic moieties. The kinetic model updated according to this classification is tested against the available data for benzene pyrolysis and oxidation with particular focus on the formation of indene and naphthalene in flames. Model testing and performance evaluation are performed automatically using the

recently developed SciExpeM data ecosystem [1], coupled with a reaction flux-based class analysis implemented in this work.

Reaction class definition

The reaction classification was performed as exemplified in Fig. 1: each reaction class is characterized by a species type, i.e., the group participating in the reaction, which may be a molecule -M, radical -R, or resonance-stabilized radical -RSR; by a class type, i.e., a global reaction pathway generally characterizing the reactants and possibly including different channels. Within each reaction class, the reaction type identifies one (elementary or lumped) specific reaction pathway.

Fig. 1 shows that this classification is hierarchical, in the sense that the species type includes all species with the same reactive moiety: for instance, A1-R indicates the phenyl-like moiety in phenyl, substituted aromatics, as well as PAHs. Hence, the [A1-R][REC_O2_EL_O] reaction will form C_6H_5O + O from phenyl and $C_{10}H_7O$ + O from naphthalene, respectively. Reaction classes involving the X lateral group in substituted aromatics belong to a new A1,X species type; the same logic applies to reactions involving two or more functional groups together, such as the C5,A1-M species type of Fig. 1.

The lumped nature of the PAH growth pathways of CRECK mechanism leads to a less detailed classification for these reactions. Fig. 1 shows that class types are simply defined according to the number of carbon atoms added, while reaction types further specify the type of species being added.

The combination of species, class and reaction type identifies a reaction pathway with assigned rate parameters. Each reaction class and pathway have similar rate parameters, assigned to be the same or scaled by analogy (e.g., number of active sites) or more complex rate rules (e.g., see [2]) with respect to the reference rate constant. Table 1 lists the main species and class types identified in CRECK mechanism in the sub-mechanism of benzene oxidation, involving both decomposition and oxidation pathways and growth to PAHs.

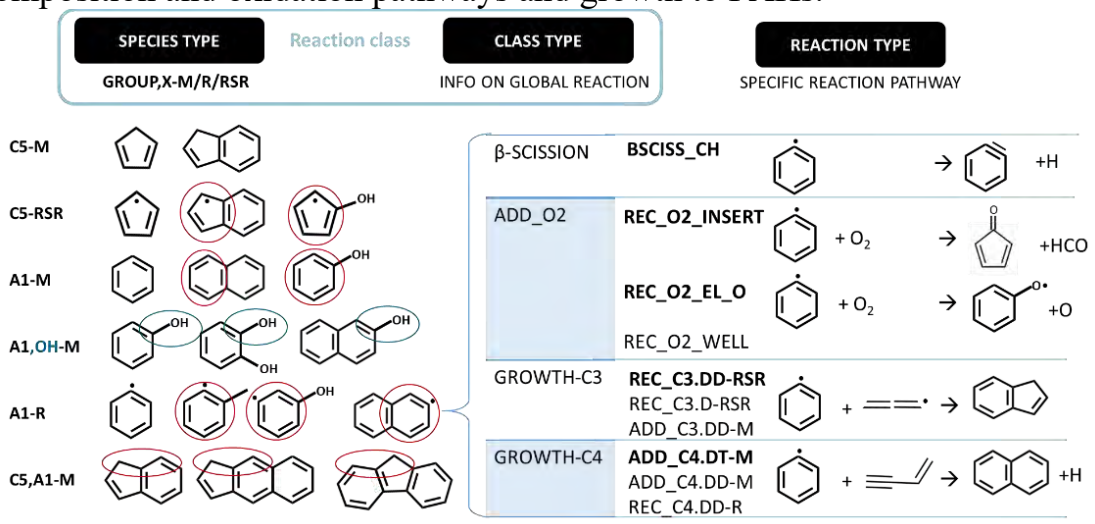

Figure 1. Representation of the hierarchical assignment of classes by species, class and reaction type. Circles highlight the reactive moieties of each species type.

Table 1. Species and classes relevant to benzene pyrolysis and oxidation and corresponding number of reactions in CRECK mechanisms. Colors indicate the source of the rate constant (yellow: theory; green: lumped from theory; blue: analogy/literature; grey: estimate).

	DECO	BONDFISS	βSCISS	ISOM	HABS	IPSO	ADD_H	ADD_OH	ADD_O	ADD_O_2	ADD_HO_2
C5-M	(growth)	(add_h)			286	(bw ipso)	11	12	7	6	2
C5,A1-M									1		
C5,C5-M		1									
C5-RSR	2		(growth)				5	20	7	13	5
C5,A1-RSR	1										
A1-M	(growth)	4			672	8	2	(bw ipso)	6	3	
A1,C2H-M							2	2		1	
A1,OH-M	6	6			349	13					
A2-M							2	11		1	
A1-R	1		2		1		(bondfiss)		1	17	3
A1,OH-R	3		2	3						1	
A2-R										5	
A1O-RSR	9					1	10	4	19	3	7

	C1	C2	C3	C4	C5	C6
C5-M	4	12	4	8	33	
A1-M			12	7	41	
C5-RSR	1	2	20	7	9	
C5,A1-RSR					1	
A1-R		20	25	11	33	89

Kinetic simulations and post-processing using SciExpeM

Kinetic simulations of most of the available literature data for benzene pyrolysis and oxidation (45 datasets) were performed using SciExpeM [1], a data ecosystem integrated with OpenSMOKE++ [3] that allows automated kinetic simulations and data analysis. The evaluation of the performance of the mechanism is evaluated through a multi-index curve matching score (CM), which accounts for the deviation of simulated data from experiments in terms of norm, shape, as well as shift. Fig. 2 shows CM scores obtained for the present model as well as a 3D representation grouped by operating conditions (T, P, Φ). The 3D plots highlight that the data available extensively cover the full range of temperature of interest to combustion conditions, however only fewer sets of data are available above 10 bar. Overall, CM scores are good, however poorer performances correspond to low-pressure shock tube pyrolysis experiments, higher pressure (> 8 bar) shock tube data, and a set of flame data at atmospheric pressure [4]. Overall, the kinetic model performance looks satisfactory.

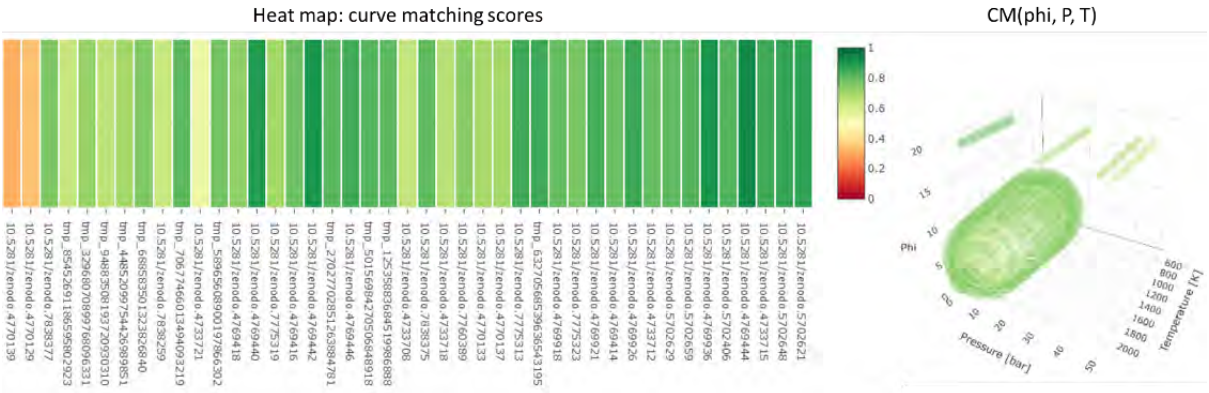

Figure 2. Curve matching scores for the >40 datasets used for the model testing of benzene pyrolysis and oxidation by experiment (left) and operating conditions (right).

Systematic performance analysis: 2-ring PAH growth in flames

Fig. 3 shows CM scores and parity plots for the formation of indene and naphthalene, i.e., the main 2-ring PAHs detected, in benzene flames. It is noted that CM scores are lower only for the set of atmospheric pressure flames of Tregrossi et al. [4], where also global CM indexes are lower than the other low-P flames. In this flame, the residence time and the pressure are higher than in the other cases tested, hence secondary reactivity of growth and oxidation products is expected to be more relevant and is probably represented less accurately in the kinetic mechanism. A worsening of the model performance with increasing pressure is also noted in the simulation of shock tube pyrolysis data, hence these behaviors might be related.

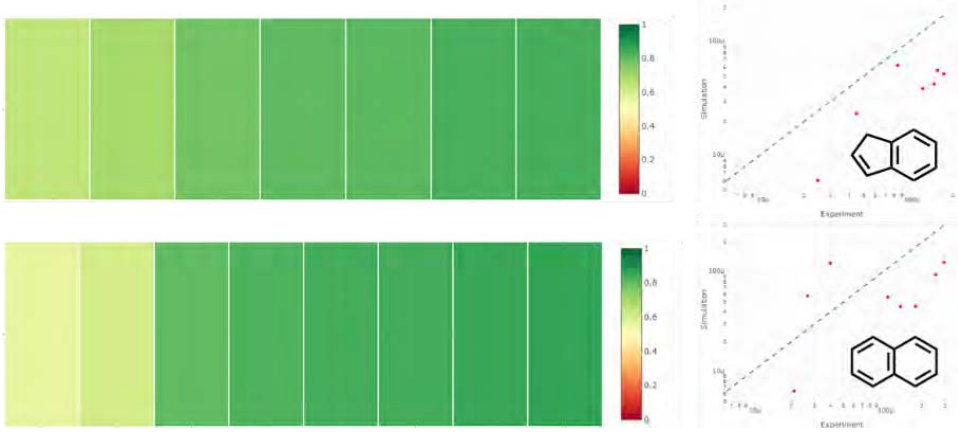

Figure 3. Curve matching scores and parity plots for indene and naphthalene obtained in kinetics simulations of benzene flames with the kinetic mechanism from this work.

Parity plots of Fig. 3 show systematic underestimation of both indene and naphthalene with the exception of the latter in atmospheric pressure flame [4]. Such systematic trends may be related to an overprediction of the oxidation and decomposition of benzene. Fig. 4 shows that this hypothesis is corroborated by 1) the systematic overprediction of phenol and cyclopentadiene, i.e., the main products of benzene oxidation, and 2) the overestimation of relevant products of cyclopentadiene decomposition or oxidation, such as ethylene or butadiene. Better agreement is observed for decomposition products of C_5H_4O (e.g., C_2H_2, CH_4), also derived from phenyl oxidation. Finally, Fig. 4 shows that biphenyl, mostly growing from phenyl recombination, is systematically overestimated. In general, aromatics forming directly from phenyl or C2 species (e.g., biphenyl, styrene, phenylacetylene) are reasonably estimated or overestimated by the model, while indene, naphthalene and larger PAHs the growth of A1 with C3-C5 species are underestimated.

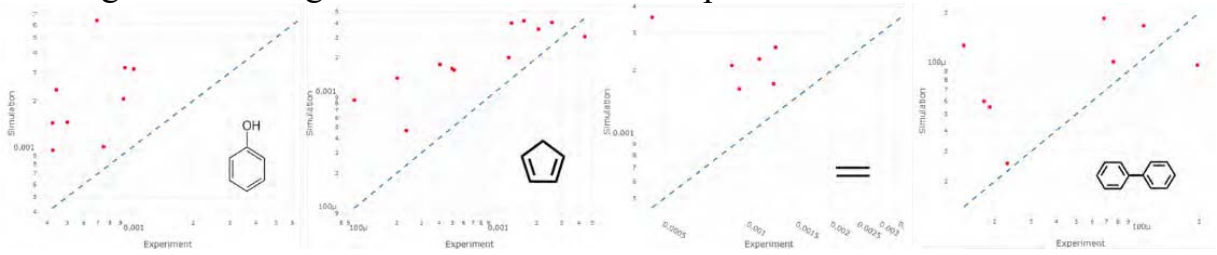

Figure 4. Parity plots for relevant products of benzene oxidation in flames.

Targeted reaction flux analysis by reaction class

The top of Fig. 5 shows the flux analysis for indene, naphthalene and the corresponding radicals in the different kinetic simulations performed for benzene flames, normalized according to the maximum flux associated to each species. Red and blue indicate that the species is produced or consumed according to the identified class, respectively. With few striking discrepancies in the relative importance of the identified classes, all the flames share similar reaction pathways, hence their general features are discussed below.

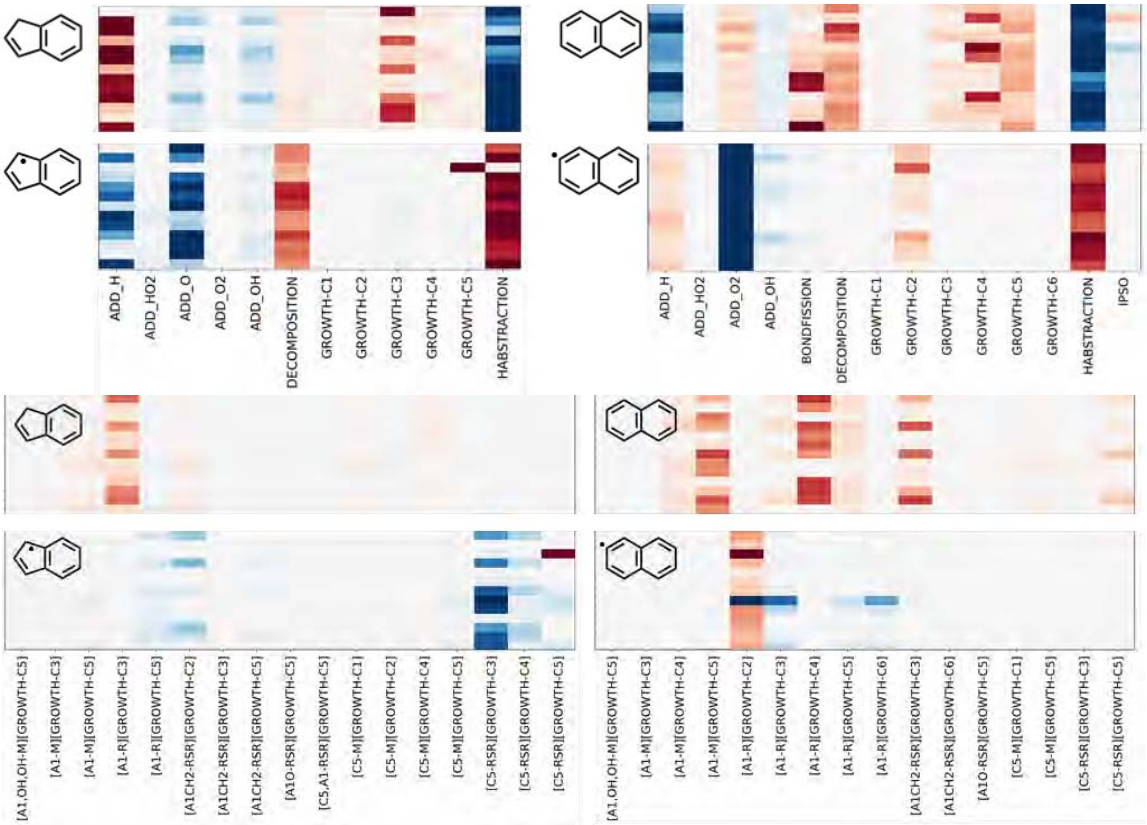

Figure 5. Heat maps of global rate of production analysis of the flame simulations performed in this work (vertical axis) for indene, indenyl (left), naphthalene and naphthyl (right) organized by class (top) and species/class type for growth pathways only (bottom).

Indene and indenyl are closely connected by H recombination on the latter (ADD_H) and by H abstraction reactions from the former. Both species are largely consumed by bimolecular oxidation reactions (ADD_O, O2, OH) derived by analogy with C_5H_6 and C_5H_5. Indene is mostly formed via growth pathways with C3 species (GROWTH-C3). The bottom of Fig. 5 expands the growth pathways according to the species and the class type, highlighting that such growth mostly occurs on phenyl-like radicals (A1-R); the other relevant growth pathways are [A1-M][GROWTH-C5] and [C5-M][GROWTH-C4]. Instead, indenyl grows to larger PAHs via C2-C5 additions, while its main formation pathway is the decomposition of naphthoxy radical (see top of Fig. 5), highlighting a strong interconnection between naphthalene and indene.

Naphthalene and naphthyl share a similar behavior in terms of H abstraction

reactions, while the role of ADD_H class is reversed with respect to indene: in this case, H addition to naphthalene forms both naphthyl and tetralin radical; naphthalene is also closely related to $C_{10}H_{10}$ isomers (and therefore to cyclopentadienyl), which form it via decomposition and bondfission. Formation pathways from the addition of C2-C5 species are expanded in the bottom of Fig. 5: naphthyl mostly grows via acetylene through the HACA pathway, while naphthalene is formed from both benzene and phenyl mostly from the addition of C4/C5. Benzyl (A1CH2-RSR) recombination with propargyl also pays an important contribution.
Finally, the flux analysis for benzene and phenyl (not shown here) supports the hypothesis that growth reactions by C2 and C6 species and decomposition pathways largely prevail over the growth types that lead to indene and naphthalene.
Combining the information of the reaction class-based flux analysis and the trends observed in the parity plots, it can be concluded that phenyl mostly oxidizes or decomposes, while growth reactions with C3-C5 species play a less relevant role, and this is a likely reason for the systematic underestimation of indene and naphthalene. Portions of the kinetic model that should be refined are 1) the mechanism of $C_{10}H_{10}$, important precursor of naphthalene; 2) new potential growth pathways from C_5H_6, C_6H_5OH, C_5H_4O; 3) growth classes of A1 + C3-C5 and their relative importance with respect to A1 + A1 and to benzene decomposition; 4) rate rules for the oxidation of PAHs, which largely consume them.

Conclusions and next steps

This work presented an integrated approach for the systematic classification of reactions and the analysis of the performance of the model through automated tools. The application of this workflow to the analysis of indene and naphthalene formation in benzene premixed flames highlighted the systematic underestimation of 2-ring PAHs, possibly due to the imbalance between benzene and phenyl oxidation, decomposition, and growth through A1 + A1 pathways with respect to growth reactions involving C3-C5 species. These findings, which would have been hardly spotted with an unsystematic approach, are promising to guide model improvement.

References

[1] E. Ramalli, T. Dinelli, A. Nobili, A. Stagni, B. Pernici, T. Faravelli, "Automatic validation and analysis of predictive models by means of big data and data science", *Chem. Eng. J.* 454: 140149 (2023)
[2] L. Pratali Maffei, T. Faravelli, C. Cavallotti, M. Pelucchi, "Electronic structure-based rate rules for : H ipso addition-elimination reactions on mono-aromatic hydrocarbons with single and double $OH/CH_3/OCH_3/CHO/C_2H_5$ substituents: a systematic theoretical investigation", *Phys. Chem. Chem. Phys.* 22:20368–20387 (2020)
[3] A. Cuoci, A. Frassoldati, T. Faravelli, E. Ranzi, "OpenSMOKE++: An object-oriented framework for the numerical modeling of reactive systems with detailed kinetic mechanisms", *Comput. Phys. Commun.* 192:237–264 (2015)
[4] A. Tregrossi, A. Ciajolo, R. Barbella, "The combustion of benzene in rich premixed flames at atmospheric pressure", *Combust. Flame* 117:553–561 (1999)

Model-to-model Bayesian calibration of a Chemical Reactor Network for pollutant emission predictions of an ammonia-fuelled multistage combustor

M. Savarese[1,2,3], L. Giuntini[4], R. Malpica Galassi[5], S. Iavarone[1,3], W. De Paepe[2], C. Galletti[4], A. Parente[1,3]

matteo.savarese@ulb.be

[1]Aero-Thermo-Mechanic Department, École Polytechnique de Bruxelles, Brussels, Belgium
[2]Service de Térmique et Combustion, Université de Mons, Mons, Belgium
[3]Brussels Institute for Thermal-Fluid Systems and Clean Energy (BRITE), Université Libre de Bruxelles and Vrije Universiteit Brussel, 1050 Brussels, Belgium
[4]Department of Civil and Industrial Engineering, Università di Pisa, Pisa, Italy
[5]Department of Mechanical and Aerospace Engineering, University of Rome La Sapienza, Rome, Italy

Abstract
In this work, we propose a Chemical Reactor Network (CRN), composed of only five reactors, to describe the pollutant emissions of a purely NH3-fuelled, micro gas turbine-like, multistage prototype combustor in varying operating conditions. We calibrate the CRN model by treating its most influential model parameters as random variables, and we infer their posterior probability densities in a Bayesian setting using higher-fidelity data from RANS computations and explicitly accounting for model discrepancy. The final goal is to employ the calibrated CRN model with quantified fidelity to determine the combustor performance map and discover a robust optimal operating point that minimizes pollutants emissions.

Introduction
Hydrogen represents undoubtedly a promising alternative to carbonaceous fuels. However, more efficient hydrogen storage means are needed to tackle its energy-intensive handling [1]. This has pushed many research efforts towards investigating alternative and more economically viable hydrogen storage means. Among possible solutions, ammonia (NH_3) shows considerable potential because of its thermophysical properties similar to traditional hydrocarbons, which make it a more efficient H_2 storage mean [2]. However, its direct use as fuel poses technical issues, such as difficulties in achieving stable flames (low reactivity) and increased production of NO_x with respect to hydrocarbons. Therefore, developing ad-hoc combustion technologies suited for NH_3 and its mixtures has been a research challenge within the last few years.
Several experimental and numerical works [3]–[5] highlighted the potential of NH_3 combustion under slightly rich conditions in reducing global NO emissions. Pugh et

al. [6] showed experimentally that a multistage NH_3 combustion process, where rich and lean combustion are performed in sequence, resulted in lower NO emissions. However, the secondary injection of air should be handled carefully. Although practical devices have already been successfully tested [7], [8], the room for improvement is still considerable, and the exploration of new scenarios at a conceptual and design level remains open.
Investigating disparate configurations and operating regimes can be labor-intensive if detailed experiments or numerical simulations such as computational fluid dynamics (CFD) are used. To this end, simplified/reduced-order models can help alleviate the computational cost considerably in the conceptual and preliminary design stages. Chemical Reactor Networks (CRN) models have often been used in ammonia combustion to characterize emissions at a conceptual level [9], [10]. CRNs are particularly useful for performing detailed kinetic simulations of practical combustion devices by schematically representing complex flow fields as a series of interconnected ideal reactor models [11]. CRNs can be designed based on a priori knowledge of the system [12] or by manually observing the main flow field characteristics from CFD or detailed experiments [13]. Due to the low associated computational cost, they enable large design space exploration in a highly reduced amount of time. Therefore, the possibility of employing CRNs for outer-loop applications, such as optimization and Uncertainty Quantification (UQ) tasks, is extremely attractive [14]. As an example, Yousefian et al. coupled a highly schematic CRN model with Non-Intrusive Polynomial Chaos Expansion (NIPCE) [15], [16] and with Bayesian Inference [17] to perform UQ of NO and CO emissions for a practical swirl-stabilized premixed burner. Although the developed tool showed considerable potential, its application has been limited to a simplified test case.
In this work, a joint CRN-UQ approach is pursued for the investigation under uncertainty of multistage ammonia combustion in a practical combustion device, namely a prototype of a micro–Gas Turbine (mGT) combustion chamber. The objective is to calibrate the CRN model parameters in a Bayesian setting using higher-fidelity data from RANS computations, explicitly accounting for model discrepancy. The calibrated model, with quantified uncertainty, can be thereupon employed to investigate a wide spectrum of operating conditions and identify a robust optimal operating point that minimizes pollutant emissions.

Test Case

The test case is a prototype of a mGT combustor consisting of a first, rich, non-premixed combustion stage followed by a secondary lean combustion region, schematically represented in Figure 1. The fuel is injected co-axially to the primary air in the first combustion stage. The hot mixture of reactants proceeds through the sleeve and reaches the secondary lean combustion stage where it reacts with the remaining fraction of air. Globally, the system is designed to operate at large oxygen excess. The air in mGT systems is usually preheated to allow heat recovery from hot gases, thus increasing the thermal efficiency of the cycle. The main operating

parameters influencing the final overall emissions of NO and NH_3, which will be analyzed in this work, are the air inlet temperature and equivalence ratio of the fuel-rich mixture, listed in Table 1 along with their considered ranges. Instead, we fix the outlet temperature at a value close to 1200 K, typically encountered in practical devices installed in gas-turbine devices. Therefore, the lean stream equivalence ratio results from a thermal balance.

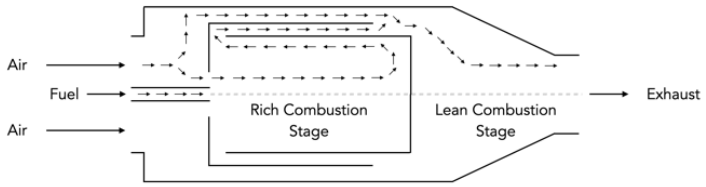

Figure 1: Schematic view of the mGT combustion chamber.

Table 1: Operating parameters and range of conditions considered in this work.

Parameter	Min value	Max value
T_{air}	800 [K]	1000 [K]
ϕ	1.0 [-]	1.6 [-]

CFD Model

We first obtain six Reynolds-Averaged Numerical Simulations (RANS) of the combustion chamber to be later employed as high-fidelity data for the calibration of the CRN's model parameters. The RANS of the system were carried out using an axisymmetric, 2-dimensional grid. The commercial code ANSYS Fluent v19.5 was used to solve the RANS equations on a structured grid of 52k cells. The realizable $k-\varepsilon$ model was used for turbulence, while the Discrete Ordinate model was used to take radiation into account. A finite-rate chemistry approach with the chemical mechanism from Otomo et al. [18] (33 species, 213 reactions) was used to model chemistry, in conjunction with the Eddy Dissipation Concept (EDC) to account for turbulence-chemistry interactions effects. Regarding the boundary conditions, two air mass flow inlets are used so that the amount of air in the two zones can be adjusted by the user. A total of 15 simulations was performed, for five equivalence ratios, namely 1.0, 1.15, 1.3, 1.45 and 1.6, for three different air inlet temperatures, namely 800.0, 900.0 and 1000.0 K.

Chemical Reactor Network model

A Chemical Reactor Network (CRN) model is the simplification of a more complex flow field as a network of interconnected canonical reactor models, such as Perfectly Stirred Reactors (PSR) or Plug Flow Reactors (PFR). The first model is a 0D model, which implies perfectly mixed reactants within the control volume. In contrast, the second is a 1D model with the hypothesis of inviscid flow and perfect mixing along

the radial direction. The model employed in this work to schematically represent the system is displayed in Figure 2.

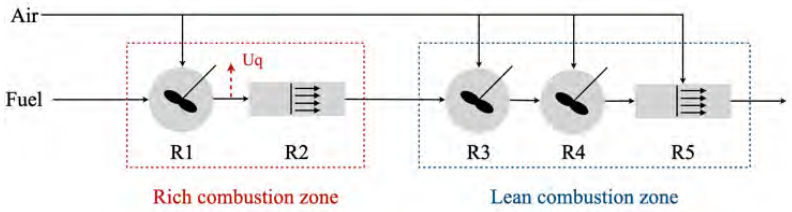

Figure 2: Proposed CRN of the prototype mGT multistage combustor

Model parameters characterize each reactor, such as residence time, volume, or heat transfer coefficient. Those parameters are typically estimated considering the real geometry (e.g., the volumes of the reactors) or by trial-and-error procedures, trying to obtain CRN predictions in agreement with more sophisticated modelling approaches, namely CFD simulations. This procedure is a parameter estimation problem in which prior knowledge and observations are employed to estimate/fit parameter values such that the model response fairly approximates the truth (e.g., measurements or higher-fidelity data).
The main parameters that characterize the proposed CRN are listed in Table 2. The rich combustion zone is modelled as an ignition adiabatic PSR connected with a first post-flame PFR with intermediate quenching. The parameter U_q represents the global heat transfer coefficient of the rich zone. The parameters V_i and F_{ai} are the volumes of the i-th reactor and the fraction of the total air fed to the i-th reactor, respectively. CRN simulations were performed with the solver NetSMOKE++ [19] with the same kinetic mechanism employed in the CFD simulations.

Table 2: List of parameters and their prior distributions

Parameter	Units	Nominal	Range	Distribution
U_q	$W/m^2/K$	10.0	0.0 – 25.0	Uniform
V_1	cm^3	30.0	30.0 – 100.0	Uniform
F_{a1}	n.a.	0.976	0.95 – 1.0	Uniform
F_{a3}	n.a.	0.10	0.05 – 0.15	Uniform
F_{a4}	n.a.	0.15	0.05 – 0.15	Uniform
V_3	cm^3	710.0	600.0 – 1000.0	Uniform
V_4	cm^3	388.0	300.0 – 500.0	Uniform

Global Sensitivity Analysis
To identify the most influential parameters of the CRN and calibrate them in a Bayesian framework, a surrogate model of the CRN was constructed using Polynomial Chaos Expansion:

$$f(y) \simeq f_s(y) = \sum_{j=1}^{P+1} \alpha_j \Psi_j(\boldsymbol{\xi})$$

where α_j are deterministic coefficients, Ψ_j are suitably selected functionals of the random variable $\boldsymbol{\xi}$, while P is the truncation order. Legendre's polynomials were selected in this work, and the coefficient estimation was carried out using the Dakota v6.16 framework using the methodology described here [20]. Sensitivity analysis was conducted by calculating the Sobol's indices for each parameter, which represent their fractional contribution to the total variance of the model's response (NO emissions in this specific case). They can be calculated as:

$$S_i = \frac{V_{\xi_i}(E_{\xi \sim i}(f(\boldsymbol{\xi}|\xi_i))}{V(f(\boldsymbol{\xi}))} = \frac{\sum_{i=1}^{L} \alpha_i^2}{\sum_{j=1}^{P+1} \alpha_j^2}$$

Results are reported in Figure 3. We can observe that only three parameters have a considerable contribution to the overall variance of the model, namely F_{a1}, U_q, and F_{a3}. Therefore, the remaining four parameters can be excluded from the calibration procedure and set to their nominal values.

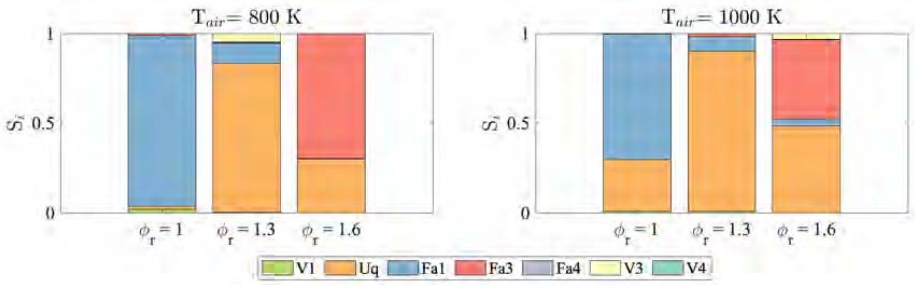

Figure 3: Total Sobol's indices for six selected cases normalized to sum 1

Bayesian Calibration of CRN model parameters on CFD data

Data from CFD simulations, here considered to be high fidelity, can be used in a Bayesian setting to calibrate the CRN parameters, leveraging the Bayes' theorem:

$$\mathcal{P}(\boldsymbol{\theta}|D) = \frac{\mathcal{P}(D|\boldsymbol{\theta})\mathcal{P}(\boldsymbol{\theta})}{\mathcal{P}(D)}$$

Where $\mathcal{P}(\theta|D)$ is the posterior probability of θ given the observed data D, $\mathcal{P}(D|\theta) = \mathcal{L}(\theta)$ is the likelihood density, and $\mathcal{P}(\theta)$ is the posterior probability of the parameters and $\mathcal{P}(D)$ can be seen as a normalizing term. The model error is estimated via the approach developed by Sargsyan et al. [21] by embedding it directly into the model's parameters:

$$y_i \simeq f(x_i, \boldsymbol{\theta} + \boldsymbol{\delta}) + \epsilon_i^d$$

where x_i represent a given operating condition, and the term $\boldsymbol{\delta}$ is the embedded model error, while ϵ_i^d represents the measurements' noise. Calibration was carried out using the UQtk library developed by SANDIA National Laboratories, and results are reported in Figure 4, where a confident agreement can be observed between NO emissions predicted with the calibrated CRN and the emissions predicted by the RANS simulations.

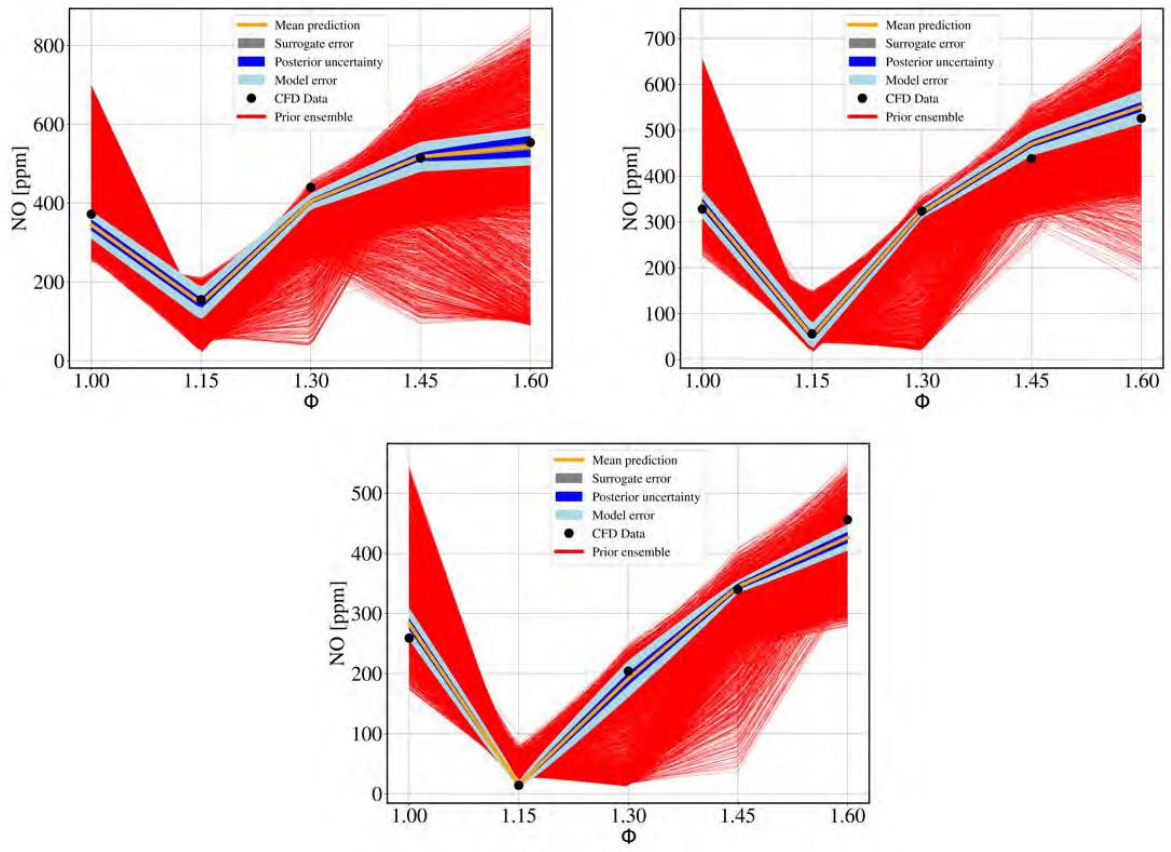

Figure 4: Results of CRN calibration. NO emissions compared with CFD predictions and their confidence bounds.

Conclusions

In this work, model-to-model calibration was used to tune the parameters of a 5-reactor CRN of a multistage, mGT-like prototype combustor fed with pure NH_3. 15 CFD simulations were used as high-fidelity data to update first-guess, a priori distributions of CRN model parameters. The number of parameters to update was chosen by a preliminary sensitivity analysis, where Polynomial Chaos Expansion (PCE) was used to train a surrogate model of the CRN. The Bayesian calibration of the most influential parameters was then performed with model error embedding. Final NO predictions of the calibrated model are in great agreement with the CFD predictions. The advantage of this approach is that the CRN discrepancy is considered, and confidence bounds are also available. This approach is particularly useful when investigation of wide range of operating conditions is necessary.

References

[1] A. Valera-Medina *et al.*, "Review on ammonia as a potential fuel: From synthesis to economics," *Energy and Fuels*, 35:6964–7029 (2021)

[2] H. Kobayashi, A. Hayakawa, K. D. K. A. Somarathne, and E. C. Okafor, "Science and technology of ammonia combustion," *Proceedings of the Combustion Institute*, 37:109–133 (2019)

[3] A. Hayakawa, Y. Arakawa, R. Mimoto, K. D. K. A. Somarathne, T. Kudo, and H. Kobayashi, "Experimental investigation of stabilization and emission characteristics of ammonia/air premixed flames in a swirl combustor," *Int J Hydrogen Energy*, 42:14010–14018 (2017)

[4] K. D. K. A. Somarathne, A. Hayakawa, and H. Kobayashi, "Numerical investigation on the combustion characteristics of turbulent premixed ammonia/air flames stabilized by a swirl burner," *Journal of Fluid Science and Technology*, 11: JFST0026–JFST0026 (2016)

[5] K. D. K. A. Somarathne *et al.*, "Emission characteristics of turbulent non-premixed ammonia/air and methane/air swirl flames through a rich-lean combustor under various wall thermal boundary conditions at high pressure," *Combust Flame*, 210:247–261 (2019)

[6] D. Pugh *et al.*, "Emissions performance of staged premixed and diffusion combustor concepts for an NH3 air flame with and without reactant humidification," *J Eng Gas Turbine Power*, vol. 143, no. 5, pp. 1–8, 2021, doi: 10.1115/1.4049451.

[7] E. C. Okafor *et al.*, "Towards the development of an efficient low-NOx ammonia combustor for a micro gas turbine," *Proceedings of the Combustion Institute*, vol. 37, no. 4, pp. 4597–4606, 2019, doi: 10.1016/j.proci.2018.07.083.

[8] O. Kurata *et al.*, "Development of a wide range-operable, rich-lean low-NOx combustor for NH 3 fuel gas-turbine power generation," *Proceedings of the Combustion Institute*, vol. 37, no. 4, pp. 4587–4595, 2019, doi: 10.1016/j.proci.2018.09.012.

[9] A. Valera-Medina, D. G. Pugh, P. Marsh, G. Bulat, and P. Bowen, "Preliminary study on lean premixed combustion of ammonia-hydrogen for swirling gas turbine combustors," *Int J Hydrogen Energy*, vol. 42, no. 38, pp. 24495–24503, 2017, doi: 10.1016/j.ijhydene.2017.08.028.

[10] R. C. Rocha, M. Costa, and X. S. Bai, "Combustion and Emission Characteristics of Ammonia under Conditions Relevant to Modern Gas Turbines," *Combustion Science and Technology*, vol. 193, no. 14, pp. 2514–2533, 2021, doi: 10.1080/00102202.2020.1748018.

[11] H. Khodayari, F. Ommi, and Z. Saboohi, "A review on the applications of the chemical reactor network approach on the prediction of pollutant emissions," *Aircraft Engineering and Aerospace Technology*, vol. 92, no. 4, pp. 551–570, Jan. 2020, doi: 10.1108/AEAT-08-2019-0178.

[12] S. Mashruk, H. Xiao, and A. Valera-Medina, "Rich-Quench-Lean model comparison for the clean use of humidified ammonia/hydrogen combustion systems," *Int J Hydrogen Energy*, vol. 46, no. 5, pp. 4472–4484, 2021, doi: 10.1016/j.ijhydene.2020.10.204.

[13] M. Zhang, Z. An, X. Wei, J. Wang, Z. Huang, and H. Tan, "Emission analysis of the CH4/NH3/air co-firing fuels in a model combustor," *Fuel*, vol. 291, no. January, p. 120135, 2021, doi: 10.1016/j.fuel.2021.120135.

[14] S. Yousefian, G. Bourque, and R. F. D. Monaghan, "Review of Hybrid Emissions Prediction Tools and Uncertainty Quantification Methods for Gas Turbine Combustion Systems." Jun. 26, 2017. doi: 10.1115/GT2017-64271.

[15] S. Yousefian, G. Bourque, and R. F. D. Monaghan, "Uncertainty Quantification of NOx Emission Due to Operating Conditions and Chemical Kinetic Parameters in a Premixed Burner," *J Eng Gas Turbine Power*, vol. 140, no. 12, 2018, doi: 10.1115/1.4040897.

[16] S. Yousefian, G. Bourque, and R. F. D. Monaghan, "Uncertainty quantification of NOx and CO emissions in a swirl-stabilized burner," *J Eng Gas Turbine Power*, vol. 141, no. 10, pp. 1–13, 2019, doi: 10.1115/1.4044204.

[17] S. Yousefian, G. Bourque, and R. F. D. Monaghan, "Bayesian inference and uncertainty quantification for hydrogen-enriched and lean-premixed combustion systems," *Int J Hydrogen Energy*, vol. 46, no. 46, pp. 23927–23942, 2021, doi: 10.1016/j.ijhydene.2021.04.153.

[18] J. Otomo, M. Koshi, T. Mitsumori, H. Iwasaki, and K. Yamada, "Chemical kinetic modeling of ammonia oxidation with improved reaction mechanism for ammonia/air and ammonia/hydrogen/air combustion," *Int J Hydrogen Energy*, vol. 43, no. 5, pp. 3004–3014, 2018, doi: https://doi.org/10.1016/j.ijhydene.2017.12.066.

[19] M. Savarese, A. Cuoci, W. De Paepe, and A. Parente, "Machine learning clustering algorithms for the automatic generation of chemical reactor networks from CFD simulations," *Fuel*, vol. 343, p. 127945, 2023, doi: https://doi.org/10.1016/j.fuel.2023.127945.

[20] O. P. Le Maitre and O. M. Knio, *Specral Methods for Uncertainty*. 2010.

[21] K. Sargsyan, H. N. Najm, and R. Ghanem, "On the Statistical Calibration of Physical Models," *Int J Chem Kinet*, vol. 47, no. 4, pp. 246–276, Apr. 2015, doi: https://doi.org/10.1002/kin.20906.

DEVELOPING PREDICTIVE TOOLS TO LIMIT THE IMPACT OF WILDFIRES AND URBAN FIRES: A STUDY OF COMBUSTION AND EMISSIONS USING SEMI-DETAILED KINETIC MODELS

M. Mehl[*], C. Saggese[**], A. Cuoci[*], A. Locaspi[*], W. Sun[**]
marco.mehl@polimi.it, saggese1@llnl.gov
*CRECK Modeling Lab, Department of Chemistry, Materials, and Chemical Engineering "G. Natta", Politecnico di Milano (Italy)
**Materials Science Division, Lawrence Livermore National Laboratory, Livermore (USA)

Abstract
Wildfires and fires at the wildland-urban interface are becoming an increasing issue, raising concern about direct infrastructure and property damages and indirect effects related to their emissions. It is crucial for the fire community to comprehend and develop predictive tools to limit the impact of these events and of the resulting emissions. This study employs comprehensive kinetic models and multi-dimensional codes to investigate the combustion and emissions of surrogates of wildland fuels and urban materials, such as biomass and plastics materials. The focus is on identifying the impact of influential parameters, such as flame temperature and atmospheric conditions, on burning rates and emissions, using detailed kinetic mechanisms that capture gas phase chemistry, including the formation and decomposition of partially oxidized by-products. The ultimate aim is to develop simplified models for large-scale fire simulation applications.

Introduction
Wildfires and fires at the wildland-urban interface (WUI) fires cause widespread destruction to infrastructure, resulting in significant economical and society damage [1]. In addition, fires are also a significant source of gases and aerosols that have a detrimental impact on air quality and climate [2]. As a result, the fire community has made it a priority to understand and forecast the spread of these fires and their emissions. However, there are still gaps in predictive fuel consumption models, particularly in relation to fuel moisture for wildland fuels, and simulations currently rely on semi-empirical correlations to estimate critical combustion parameters [3]. Additionally, the development of effective simulation strategies for WUI fire scenarios is hindered by the limited availability of tailored experiments [4].
Detailed kinetics provides an opportunity to examine the fundamental processes governing the pyrolysis of solid materials and the combustion of their volatile components, providing essential information on their thermochemical transformation at a small scale and the yields of specific pollutants. With the increasing availability of precise fundamental models, kinetic studies on idealized

geometries can be used to deduce the combustion behavior of solid fuels and the formation of byproducts, which can provide additional data for the development of the more comprehensive models required for large-scale simulations.
This study employs detailed kinetic models, coupled with 1- and 2-D simulation codes, to investigate the combustion and burning rate of surrogates of wildland fuels (such as biomass) and urban materials (like plastics) in single particle and opposed-flow burner (OFB) configurations. The aim is to evaluate the impact of influential parameters on burning rates and emissions and obtain sub-models for fire modeling.

Biomass pyrolysis and combustion
Natural fuels are represented through their fundamental constituents, such as lignin, cellulose, hemicellulose, water, and extractives, adopting lumped reaction models that reproduce their degradation process [5].

Kinetic model and numerical setup
In this study, the pyrolysis kinetics of biomass are analyzed using a detailed mechanism developed by Debiagi et al. [5]. The kinetic mechanism consists of 32 chemical reactions and accounts for the decomposition of various components of the biomass, such as cellulose, hemicellulose, lignin, and extractives. To predict secondary gas-phase reactions, the mechanism is coupled with homogeneous gas-phase kinetics from the LLNL kinetic model [6]. Char conversion is also considered for smoldering conditions through char combustion and gasification reactions using kinetic parameters from Ranzi et al. [7].
Based on the single-particle model developed by Tufano et al. [8], a 2-D numerical set-up was employed, modelling the particle as a porous medium enclosed by a spherical outer shell that separates it from the exterior gas phase. The physical properties of the biomass were taken from [9].
This study investigates the impact of surrounding gas composition on a particle immersed in a stagnant atmosphere at a temperature of 1000 K. The comparison is made between the products generated from reactions in an inert N_2 atmosphere (pyrolysis conditions) and a gas composition with 90% O_2 and 10% N_2 (combustion conditions). Additionally, the study analyzes the influence of moisture content in the biomass particle and particle size on ignition and primary products under these environments.

Results
Figure 1 displays the comparison of temperature and main products at the particle center for pyrolysis and combustion conditions. In both cases, lignin (LIGC + LIGH + LIGO) decomposition occurs slower than cellulose (CELL) and hemicellulose (XYHW). Fuel components' decomposition is negligibly influenced by the atmosphere, as depletion happens before ignition. Temperature at the particle center rapidly rises to 2000 K upon ignition in the combustion case but slowly increases to 1000 K in equilibrium with the fluid in the pyrolysis case. The temperature rise

accounts for the quick consumption of initial products of lignin and hemicellulose decomposition (LIG, LIGOH and HCE1), and the double peak features in concentrations of many small oxygenated species (CH_2O, CH_3OH) and gas products (H_2, H_2O, CO_2). The significantly accelerated reactions are also reflected in the fast release of CHAR in the solid center, and the oxidation of CHAR lead to an increase in CO concentrations.

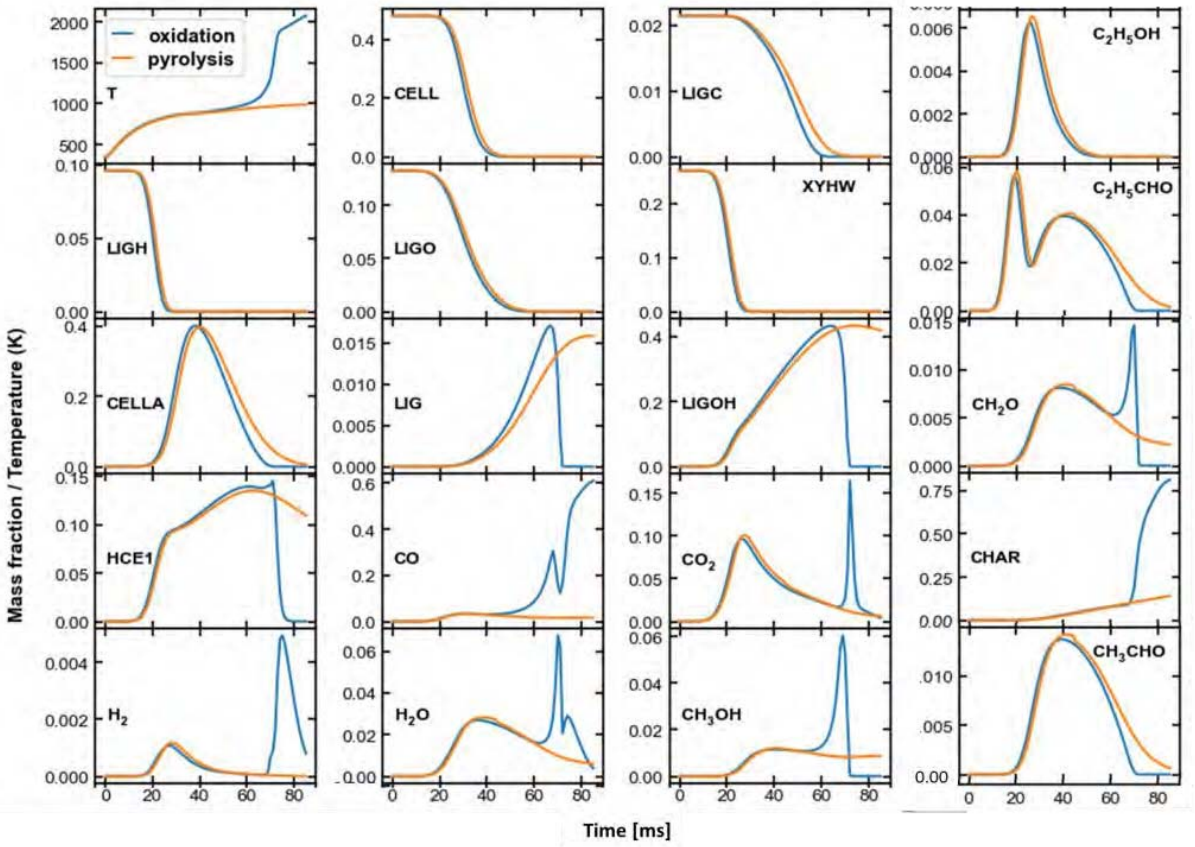

Figure 1. Temperature and concentration time histories for major products at the center of the particle under pyrolysis and oxidation conditions.

Figures 2a elucidates the simulated time histories of temperature and gas-phase species concentrations at the particle center for different moisture contents. Moisture in the fuel slows down the ignition, because of the endothermicity of the evaporation. The effect of the particle size was also considered (Fig. 2b). The ignition of the 2 mm particle occurs at around 180 ms, marked by the stepwise temperature increase at the center of the particle. The species concentration profiles in both cases have similar shapes, but those in the 2 mm particle case cover a much larger temperature window. The products' formation triggered by the ignition shows lower peak concentrations since the temperature increases more gradually for the larger particle.

Plastic materials

Plastic materials are frequently involved in fire incidents in various settings such as urban, industrial, and residential areas. Generally, global pyrolysis models are used

to simulate their behavior in large-scale fire scenarios, assuming a fixed yield of combustion by-products. However, in reality, the chemical composition of the fuel and the products released during the combustion of polymers can strongly impact the fire propagation process and the generation of toxic substances (e.g., PVC can release significant amounts of hydrochloric acid). Once again, simple geometry detailed kinetic simulations can be applied to elucidate the behavior of polymers and provide the foundation for predictive models suitable to large-scale simulations.

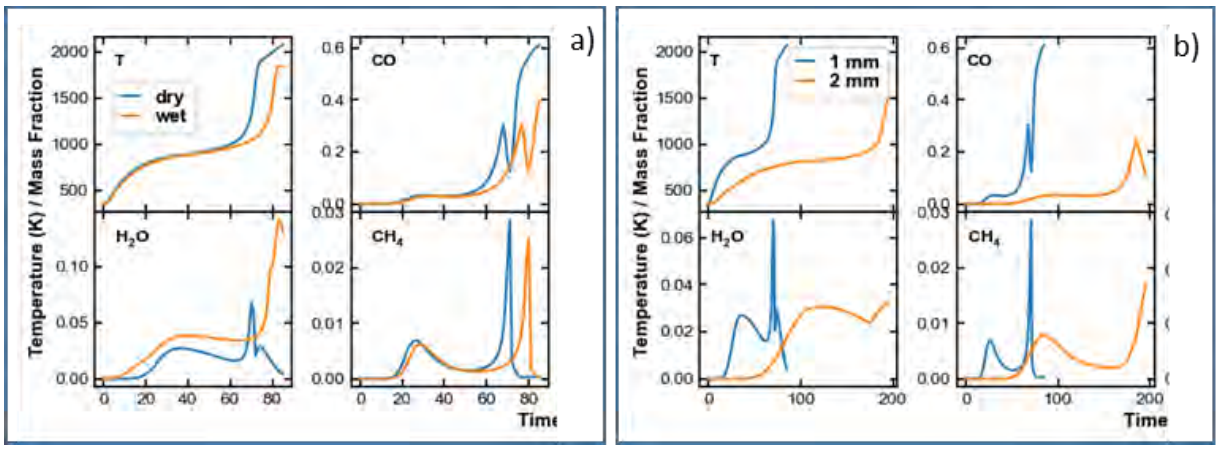

Figure 2. Temperature and mass fraction time histories at the center of the particle during the oxidation: a) dry and wet (10% wt% moisture) biomass; b) particles with different sizes (1 mm and 2 mm in diameter).

Kinetic model and numerical setup

This work proposes some preliminary results on the combustion of polyethylene (PE) in an opposed flame burner. Although semi-detailed kinetic models for PE are available [10-11], this first computational study adopted a single-step chemistry [12]. Figure 3 shows a predicted thermos-gravimetric analysis (TGA) profile obtained using the reduced model in comparison with experimental measures and results from the more detailed versions of the kinetic mechanism reported in [10-11]. The kinetic model used in this study couples the simplified liquid phase model with a detailed kinetic mechanism of the gas phase chemistry, incorporating a soot formation model based on the sectional method approach. The combustion configuration here discussed has been previously employed in experimental studies on non-charring polymers like PE [13-14]. The opposed flame burner system is simulated using a 1-D approach with analogies to the counterflow flame configuration. The numerical simulations were conducted using the OpenSMOKE++ framework [15], which considers both the gaseous and solid phases of the model. The conditions of the oxidizer and the solid/gas interface are modelled as inlet boundaries, with the inlet conditions at the gas end being the experimental ones and the one at the solid surface being dictated by the mass and energy balance at the interface of the pyrolyzing solid. The numerical model was used to simulate the combustion of PE in an opposed flame burner at the conditions tested by Pitz et al. [13]. The simulations (Fig. 4) successfully reproduce the measured profiles of minor species, such as C2 species

and $CO+CH_4$. The calculated phi profile in the flame is well-reproduced, and the soot model indicates low soot yields for the PE flame considered. The surface temperature of the polymer is estimated to be around 740K, consistent with a pyrolyzing pool of molten PE.

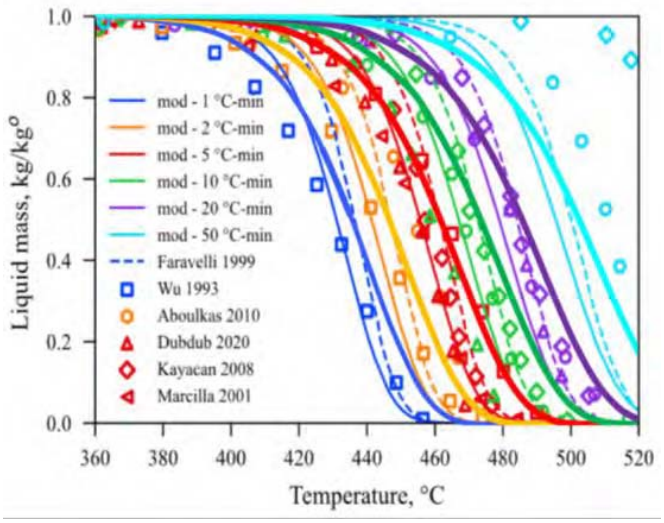

Figure 3. Experimental TGA thermal degradation data from literature of PE vs modeling results obtained using different kinetic models: dashed line: Faravelli et al., 1999 [11]; thin solid line: Locaspi, 2022 [10], solid bold line: 1 step model adopted in this work [12].

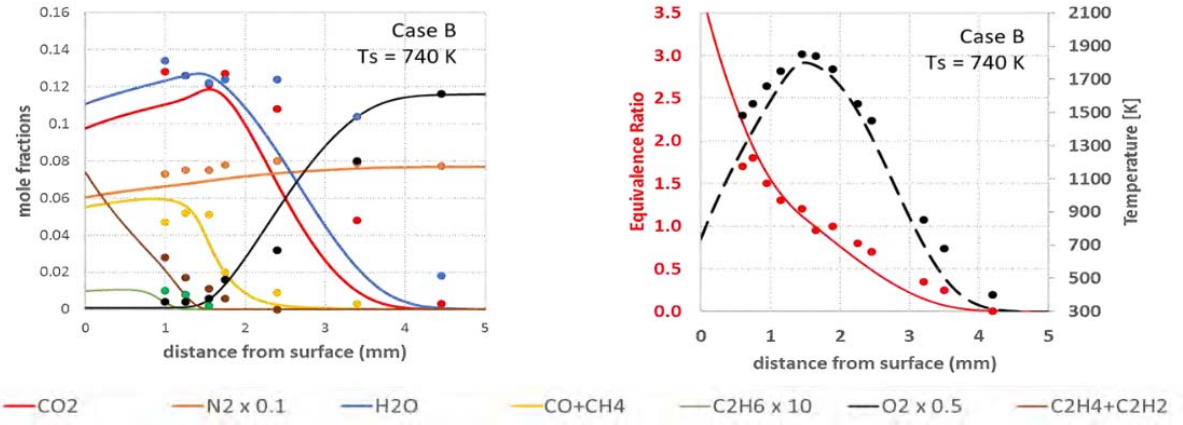

Figure 4. Simulated (lines) vs. experimental [13] (dots) speciation, global equivalence ratio, and temperature profiles in a counterflow PE flame.

Conclusions

This study investigated the use of detailed kinetics to evaluate the effects of surrounding atmosphere, particle size, and moisture content on emissions from biomass combustion. Parallelly, a computational framework for simulating plastic material combustion in the opposed flame burner configuration was developed. These calculations demonstrate how condensed and gas phase mechanisms can be successfully applied to the simulation of burning solids towards the definition of

models useful to large scale calculations. Future work will include more detailed modelling of the solid and liquid phases, as well as the addition of gas-phase reactions for intermediate species formed during biomass pyrolysis. The final goal is the development of fundamentally based multiscale models for wildfires applications.

Acknowledgments
This work was performed under the auspices of the U.S. Department of Energy by Lawrence Livermore National Laboratory under Contract DE-AC52-07NA27344 and was supported by the LLNL-LDRD Program under Project No. 23-LW-007.

References

[1] National Academies of Sciences, Engineering, and Medicine 2022. Washington, DC: The National Academies Press.
[2] Peterson, D.L., McCaffrey, S.M. and Patel-Weynand, T., 2022. Wildland Fire Smoke in the United States: A Scientific Assessment.
[3] Ottmar, R.D., 2014. Forest Ecology and Management, 317, pp.41-50.
[4] Manzello, S.L. and Suzuki, S., 2022. Fuel, 314, p.122805.
[5] Debiagi, P., Gentile, G., Cuoci, A., Frassoldati, A., Ranzi, E. and Faravelli, T., 2018. Journal of analytical and applied pyrolysis, 134, pp.326-335.
[6] Fang, R., Saggese, C., Wagnon, S.W., Sahu, A.B., Curran, H.J., Pitz, W.J. and Sung, C.J., Combustion and Flame, 236, p.111807, 2022.
[7] Ranzi, E., Debiagi, P.E.A. and Frassoldati, A., ACS Sustainable Chemistry & Engineering, 5(4), pp.2882-2896, 2017.
[8] Tufano, G.L., Stein, O.T., Kronenburg, A., Gentile, G., Stagni, A., Frassoldati, A., Faravelli, T., Kempf, A.M., Vascellari, M. and Hasse, C., Fuel, 240, pp.75-83, 2019.
[9] Gentile, G., Debiagi, P.E.A., Cuoci, A., Frassoldati, A., Ranzi, E. and Faravelli, T., 2017. Chemical Engineering Journal, 321, pp.458-473.
[10] Locaspi, A, Pelucchi, M., Mehl, M., Faravelli, T., Waste Management 156 (2023) 107-117
[11] Faravelli,T., Bozzano, G., Scassa, C., Perego, M., Fabini, S. Ranzi, E., Dente, M., J. Anal. Appl. Pyrolysis, 52 (1999) 87-103
[12] Sommariva, S., Frassoldati, A., Derudi, M., Italian Combustion Meeting
[13] Pitz, W.J., Brown, N.J., Sawyer, R.F., Symposium (International) on Combustion, 18 (1981)1871-1879
[14] Korobeinichev O.P., Gonchikzhapov M.B., Paletsky A.A., Tereshchenko A.G., Shundrina I.K., Kuibida L.V., Shmakov A.G., Hu Y. , Combustion and Flame 169 (2016) 261–271
[15] Cuoci, A., Frassoldati, A., Faravelli, T., Ranzi, E., Comput. Phys. Commun., 192 (2015) 237-264

AN AUTOMATIC MERGING PYTHON CODE FOR LARGE MECHANISM: EXAMPLE OF A TRF-IB MECHANISM

T. Fages*, R. Veillet, R. Fournet*, B. Sirjean*, P.-A. Glaude***
timothee.fages@univ-lorraine.fr
* Université de Lorraine, CNRS, LRGP, F-54000 Nancy, France
** Université de Paris Cité and Univ Paris Est Créteil, CNRS, LISA, F-75013 Paris, France

Abstract
TIRAMISU, an automatic merging python code, was developed to generate and compare several kinetic models of combustion of toluene, *n*-heptane, isooctane, blended with isobutanol (toluene reference fuel-isobutanol, TRF-iB), based on detailed mechanisms from the literature. This code consists of a reading and cleaning step, followed by an automatic translation step and a merging and writing final step. Two different fusion tasks are presented: the full fusion of two mechanisms, a TRF and a model for alkyl aromatics (hereafter ALLNL), and the extraction of 3 different isobutanol sub-mechanisms and their integration into ALLNL.

Introduction
Despite the expected increase in the share of electric vehicles in the vehicle fleet over the next few years [1], conventional thermal vehicles, especially gasoline-powered ones, are expected to remain in the majority in 2030 and to become increasingly hybrid. Among gasoline engines, progress in electronic injection control greatly favors direct injection. Nevertheless, these engines suffer from soot emissions especially nano soots, which are going to be regulated in the Euro7 standard.
Biofuels are expected to play an increasing role in decarbonization, growing by about 50% by 2030 [1]. Despite a reduction in soot emissions with the use of alcohols [2], oxygenated fuels raise new problems such as an increase in the production of nitrogen oxides (NO_x), or an increase in aldehydes, which are hazardous to health.
Moreover, ethanol, which is currently used in fuel blends, is one of the lowest energy-density alcohols, supplanting only methanol. The search for new biofuels is shifting to heavier higher carbon content alcohols. Bio isobutanol is one of those that can replace ethanol [3]. Although heavier bio-alcohols are being considered, their production on an industrial scale is non-existent.
To model gasoline combustion with isobutanol addition, a detailed kinetic mechanism based on a gasoline surrogate, such as a toluene reference fuel (TRF) coupled with an isobutanol (iB) sub-mechanism is required. It should also contain a soot precursor and a NO_x sub-mechanism to predict pollutant formation. However, in the literature, such models are quite cumbersome and often lack one of these sub-mechanisms. To complete them, a merging task needs to be done between two or

more mechanisms/sub-mechanisms. In these models, species do not have standardized name (like IUPAC names) due to character limitation used in simulation software such as Chemkin-Pro [4] or Cantera [5]. It is therefore up to the author of the model to establish a convention and to give a name to each species, which makes it difficult and tedious to translate a species from one model to another. According to the author's knowledge, there is currently no software that can automatically perform this translation without the use of a complementary file containing the chemical identifier of the species (such as InChI or SMILES).
The current study introduces TIRAMISU (Thermodynamical Interpretation of Reactions and Automated Merging for Inter-Scheme Union), an automatic merging python code for large mechanisms. It automatically translates most of the species thanks to thermodynamic and reaction data and assists the manual translation for the remaining species. It then merges the two mechanisms.
This code will be illustrated with two different fusion tasks, namely the complete merging of two mechanisms, one devoted to combustion of alkyl aromatics, AlkylaromaticV2.1 (AA) [6] and LLNL [7], in order to complement the aromatic part of LLNL; and the fusion of the newly formed model ALLNL, with 3 isobutanol sub-mechanisms extracted from their models [3,8,9].

Methodology
The goal of the code presented in Figure 1 is to significantly reduce the time required for the merging task, while simultaneously minimizing the potential for human translation error. The TIRAMISU code is divided into three main steps.

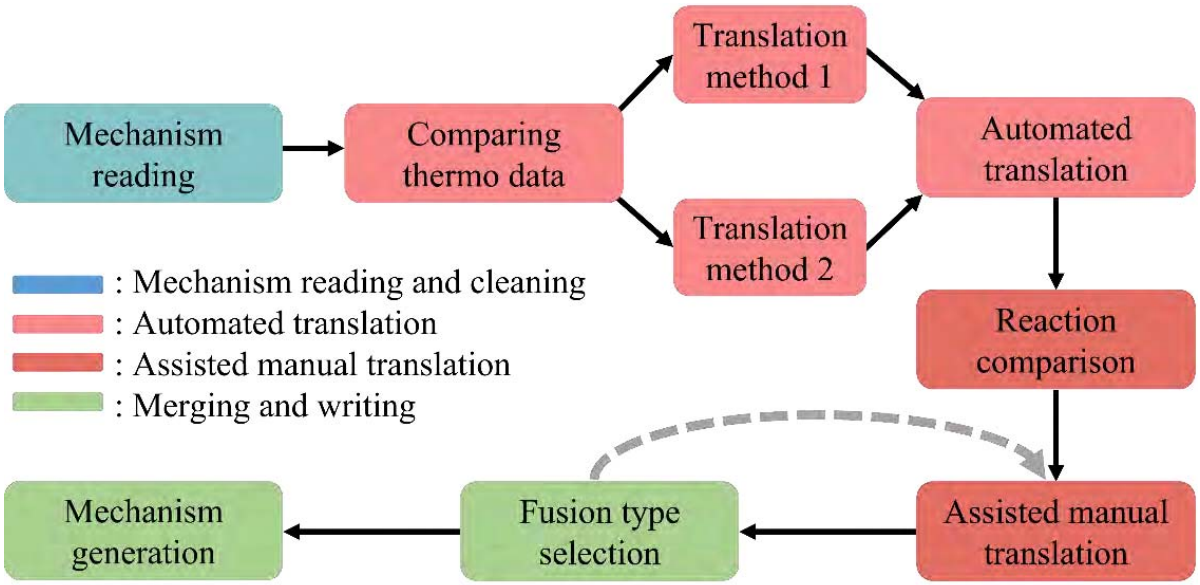

Figure 1. TIRAMISU, an automatic merging python code for large mechanism

Mechanism reading and cleaning: This step reads the mechanism and suppress comments, unnecessary blanks, and empty lines. It also removes duplicate species or species never used in reactions. The entire code relies heavily on this step because

it involves storing the data for each species and modifying each reaction to display the stoichiometric numbers for each species, while accounting for the possibility of reverse reactions. This enables the identification of equivalent reactions such as $CH_3+CH_3=C_2H_6$ and $C_2H_6=2CH_3$.

Automated and assisted translation: To guess the translation differences of the species between two models, species are first separated into isomers group (one isomer group will be called M1 for model 1 and M2 for model 2). The NASA polynomial of each species is then used to compute $h_l^0 - T\,s_l^0$ over the temperature range, following the expression in equations (1) and (2):

$$h_l^0(T) = (a_{1l} + \frac{a_{2l}T}{2} + \frac{a_{3l}T^2}{3} + \frac{a_{4l}T^3}{4} + \frac{a_{5l}T^4}{5} + \frac{a_{6l}}{T})RT \quad (1)$$

$$s_l^0(T) = (a_{1l}\ln T + a_{2l}T + \frac{a_{3l}T^2}{2} + \frac{a_{4l}T^3}{3} + \frac{a_{5l}T^4}{4} + a_{7l})R \quad (2)$$

where a_{il} is the i^{th} coefficient (or the $i+7^{th}$ if T is in the lower bound of the temperature range) of the corresponding NASA polynomial for the species l. The curve H-TS of each species from M1 is then compared to the one of each species from M2 by calculating the normalized mean absolute difference between the two curves. From those results, two different translation methods are used to ensure minimal translation error. The first method consists of computing these values for all translation matches possible between M1 and M2. Then, the pair of names that has the lowest difference is selected. The two species are removed, and this task is repeated until the number of species in M1 or M2 reaches 0. This method is often very effective and scales well with the number of isomers. It also gives the difference between the two species. This difference indicates if the species are well translated or if they are different and have no translation at all. However, in some cases, the thermodynamic data between two isomer groups are slightly shifted; if the difference between species belonging to the same isomers group are of the same order of magnitude, the method could invert species, making a translation error. Indeed, as the method only looks at the lowest difference match at each step, it does not try to achieve the minimal mean difference of all matches. To address this problem, the second method was introduced to help identify and solving those cases. It consists in generating all permutations of combinations between M1 and M2, and choosing the permutation that minimize the global error. It allows finding the best fit of isomer translation in an isomer group, that minimize the error, but also to look at the second-best fit, to see if the difference between the two is relevant. If it is the case, the best fit is probably correct, but should be confirmed with the value given by the first method, to identify species that cannot be translated. Also, this method is very sensitive to the number of species in M1 and M2. The number of permutations is increasing following the equation (3) where $|x|$ is the length of the list x.

$$nb\ permutations = \frac{|M1|!}{|M1|! - |M2|!} \quad (3)$$

When the number of permutations is too high, we cannot use this method for the isomers group.
Overall, the automatic translation of species is restricted to certain requirements that need to be achieved thanks to the two methods. Otherwise, a manual translation needs to be used. It is noteworthy that the number of translation method and requirement that need to be satisfied to make an automatic translation is arbitrary. Too low requirement will translate more species, but at a higher risk of error, while too high requirement will reduce this risk, but increase the number of manual translations.
Those mandatory manual translation are assisted by prediction of method 1 and 2 but also by a comparison between reactions in the two models. An untranslated species from M1 will be translated into a species from M2 and the code will count how many reactions are identical between the two species. As all species have not been translated prior to this task, other species than the one of M1 and M2 will only be represented by their chemical formula. That will therefore produce more matching reactions between models than it should but this step is sufficiently accurate to help the user.
Merging and writing: Two different fusion tasks can be distinguished. The first is the merging of model 1 with a sub-mechanism from model 2 or *vice-versa*. It doesn't require the entire manual translation to be done, as only species encountered in the sub-mechanism need to be translated. To extract this sub-mechanism, the code starts from one or a list of species given by the user. It will then add a list of all reactions containing these species. Then, it will list all new species encountered in those reactions and replace the starting list. Each time the code makes a new loop, it will be called D_n (for "depth" *n*) with *n* being the number of loops, D_1 being the first one. The code will continue until there is no new species encountered or a user provided D_{limit} is reached. The second fusion task is the full merging of model 1 with model 2 and will need all translation to be done. It is based on a "master" mechanism and a "servant" mechanism. Reactions and species in the servant that are not contained in the master will be added to the master model. In this way, the master will have a priority for his own reaction rate constant or NASA polynomials and master and servant can easily be exchanged to compare the impact of these data on the produced mechanism. It is noteworthy that the master for the kinetic does not have to be the master for the thermodynamic.

Merging examples

Full merging: With the aim of improving toluene accuracy on simulations of ignition delay times (IDT) for the LLNL model (1372 species) [7], it was merged with another model from the same team, AA (506 species) [6]. This model is specifically designed for alkyl aromatics compound, and almost the entire model (except species

too big, such as propyl-benzenes or butyl-benzenes) was used as servant or master mechanism. As they come from the same team, their core is quite similar, but their sub-mechanisms follow different conventions. Once automatically translated, only 50 out of the 506 species cannot be translated by method 1 and 2 and were translated manually. Four different mechanisms have been made from this translation, by varying if the LLNL model were master (M) or servant (S) on kinetic or thermodynamic data. This gives the models MM, MS, SM and SS. These models were tested over a large range of TRF IDT, burning velocities and species profiles. Overall, the MM model was better for IDT and SS for burning velocities and species profiles. The two other mechanisms were neither the worse nor the best for any kind of data, but as they have mixed thermodynamic and reaction rate, they are probably less coherent.

Sub-mechanism integration: Following the full merging, the SS and MM model were named ALLNL-1 and ALLNL-2 and merged with 3 isobutanol sub-mechanisms; Sarathy-2012 (279 species, 1892 reactions) [3], Moss-2008 (161 species, 1256 reactions) [9] and Merchant-2016 (376 species, 8324 reactions) [8]. In this example, we will only talk about the merging with ALLNL-1. About the translation, the efficiency depends on the model. For Sarathy-2012, it was very efficient with only 12 species manually translated, but for Moss-2008 and Merchant-2016 there was still 40 % species not translated. For the merging step, different D_{limit} were tested to see its impact on the accuracy on IDT of isobutanol. With the models Sarathy-2012 and Moss-2008, due to the low number of species and reaction added to ALLNL-1 (respectively 26/321 and 13/169 species/reactions), reducing D_{limit} under D_{max} (respectively D_{10} and D_6) has a significant impact on the accuracy of the models, without changing much to his size. However, for the Merchant-2016 model, which has a D_{max} of D_7, a reduction up to D_2 can be made without increasing the relative mean absolute error on IDT by 0.5%. This reduction is highly valuable because it reduces the number of species/reactions added from 191/5857 to 81/1036.

The overall result of this merging can be seen in Table 1. For the Sarathy-2012 merging, the model did not perform as well as the base model. It could be due to lacking reactions with species already present in the ALLNL-1 model or a very different thermodynamic for the core mechanism. For the Moss-2008 and Merchant-2016 merging, the results were equivalent (or better for Merchant-2016) than the base model. That mean that the extraction task was sufficient to extract the most important element of the sub-mechanism.

Table 1. Mean absolute error relative to IDT experimental data [9,10].

Sar.2012	ALLNL-1+ Sar.2012	Moss-2008	ALLNL-1+ Moss-2008	Mer.2016	ALLNL-1+ Mer.2016
66.20%	91.22%	155.46%	156.28%	48.33%	39.52%

Conclusion

The new TIRAMISU automatic merging python code for large models was described and tested over two types of merging: full merging and sub-mechanism integration. This code translates most of the species between two mechanisms thanks to the thermodynamic and reaction data and then merge the first completely with the second, or only one sub-mechanism. The examples show that TIRAMISU could greatly reduce the time needed for translation by automatically making most of them and helping the user for the remaining species. It also shows that the extraction task was sufficiently accurate for at least two of the three models.

References

[1] S. Dale, Energy Outlook, BP, 2022.
[2] M.A. Ghadikolaei, Effect of alcohol blend and fumigation on regulated and unregulated emissions of IC engines—A review, Renewable and Sustainable Energy Reviews. 57 (2016) 1440–1495.
[3] S.M. Sarathy, S. Vranckx, K. Yasunaga, M. Mehl, P. Oßwald, W.K. Metcalfe, C.K. Westbrook, W.J. Pitz, K. Kohse-Höinghaus, R.X. Fernandes, H.J. Curran, A comprehensive chemical kinetic combustion model for the four butanol isomers, Combustion and Flame. 159 (2012) 2028–2055.
[4] J. Schweikart, Reaction Design, Chemical Engineering. 105 (1998) 66.
[5] D.G. Goodwin, H.K. Moffat, I. Schoegl, R.L. Speth, B.W. Weber, Cantera: An Object-oriented Software Toolkit for Chemical Kinetics, Thermodynamics, and Transport Processes, (2022).
[6] M. Mehl, O. Herbinet, P. Dirrenberger, R. Bounaceur, P.-A. Glaude, F. Battin-Leclerc, W.J. Pitz, Experimental and modeling study of burning velocities for alkyl aromatic components relevant to diesel fuels, Proceedings of the Combustion Institute. 35 (2015) 341–348.
[7] M. Mehl, W.J. Pitz, C.K. Westbrook, H.J. Curran, Kinetic modeling of gasoline surrogate components and mixtures under engine conditions, Proceedings of the Combustion Institute. 33 (2011) 193–200.
[8] S.S. Merchant, E.F. Zanoelo, R.L. Speth, M.R. Harper, K.M. Van Geem, W.H. Green, Combustion and pyrolysis of iso-butanol: Experimental and chemical kinetic modeling study, Combustion and Flame. 160 (2013) 1907–1929.
[9] J.T. Moss, A.M. Berkowitz, M.A. Oehlschlaeger, J. Biet, V. Warth, P.-A. Glaude, F. Battin-Leclerc, An Experimental and Kinetic Modeling Study of the Oxidation of the Four Isomers of Butanol, J. Phys. Chem. A. 112 (2008) 10843–10855.
[10] L. Pan, Y. Zhang, Z. Tian, F. Yang, Z. Huang, Experimental and Kinetic Study on Ignition Delay Times of iso-Butanol, Energy Fuels. 28 (2014) 2160–2169.

SESSION IV

BIOMASS AND WASTE THERMOCHEMICAL PROCESSING, RECYCLING, AND VALORIZATION


THE COMBUSTION INSTITUTE
1954

PYROLYSIS OF LARGE WOOD PARTICLES: KINETIC MODELING AND EXPERIMENTAL VALIDATION

Million M. Afessa[1,2], A.Venkata Ramayya[1], Andrea Locaspi[2], Paulo Debiagi[3], Alessio Frassoldati[2], Tiziano Faravelli[2], Anna Szepannek[4,5], Angela Hofmann[4], Christoph Pfeifer[5]

E-mail: millionmerid208@gmail.com /million.merid@ju.edu.et
[1] Faculty of Mechanical Engineering, Jimma Institute of Technology, JiT, Ethiopia
[2] Department of Chemistry, Materials and Chemical Engineering, Politecnico di Milano
[3] Institute for Simulation of Reactive Thermo-Fluid Systems, TU Darmstadt, Germany
[4] Josef Ressel Centre for the Production of Powdered Activated Carbon from Municipal Residues, Innsbruck, Austria
[5] Institute of Chemical and Energy Engineering, Department of Material Sciences and Process Engineering, University of Natural Resources and Life Sciences, Vienna, Austria

Abstract

The pyrolysis of large wood particles, which has a substantial impact in characterizing the pyrolysis process, is the focus of this research. This study provides new experimental data for cubic wood thick particles. The experimental setup was designed mainly to investigate the effect of heat and mass transfer limitations on the decomposition rate of a single biomass particle. Experimental results are compared with 1D modeling results to comprehend the pyrolysis characteristics, aiming at a further validation of a comprehensive mathematical modeling of thermochemical biomass conversion. The results suggest that a 1D model, which assumes an equivalent spherical geometry, can accurately capture the temperature profile at the surface and to an acceptable level at the core of the particle. Likewise, the model results can capture the behavior of exothermic phenomena observed in the experiments. The degree of pyrolysis, i.e. the extent to which the particles pyrolyzed under various scenarios is also correctly predicted. Modest differences in prediction are due to simplifications in particle geometry and chemical composition of biomass samples. These study findings are valuable for understanding pyrolysis of large wood particles and improving the design of efficient conversion technologies.

1. Introduction

Biomass has been widely recognized and exploited as a renewable energy source for decades, and it is now seen as a worthwhile alternative to fossil fuels. Thermochemical processes decompose the complex biomass structure into simpler molecular compounds[1]. Biomass pyrolysis which is a precursor of other thermochemical processes such as gasification, produces solid, gas, and liquid phases[2]. Despite significant progress, this technology has not been commercially effective for large

applications, owing to heat and mass transfer limitations within the pyrolyzing particles [3].

Reducing the sizes of particles to kinetically controlled sizes is one approach to improve heat and mass transfer limitations [4]. However, it increases the processing time and energy demand, and thus it may not be realistic for large-scale applications [5]. Conversely, pyrolysis of relatively large particles using microwave-assisted pyrolysis at lower temperature has been reported to improve heat and mass transfer efficiency [6]. Nevertheless, temperature profiles and reaction extents are highly non-uniform in large particles, rendering pyrolysis a challenging process. In this regard, significant efforts were made to characterize temperature profiles inside large biomass particles [4]. Both endothermic and exothermic phenomena were observed during the pyrolysis of thick particles[7]. It was also revealed experimentally that the endothermicity prevails at low conversion stages [8], whereas exothermic reactions become important at higher conversion rate [9].

Particle model simulations have been also used to study intraparticle transport in larger particles, but the complexity of the simulation varies depending on the kinetic schemes, numerical approaches, and phenomena under consideration. Larger particle sizes, in general, increase modeling complexity[1]. Spherical, cylindrical, and slab-shaped particles have previously been studied through the use of modeling and experimental methods [9]. On thermally thick particles, there are indeed few experimental studies and mathematical modeling in the literature. The new experiment presented in this work represents an effort to provide new data for different kind of wood particles. These experiments constitute a useful dataset to further validate and improve a comprehensive mathematical model of thermochemical biomass conversion. The particle-scale model handles both kinetics and transport phenomena, thus it is able to predict the temporal and spatial evolution of composition and temperature inside the particle.

Accordingly, the objective of this paper is to investigate the pyrolysis characteristics of cubic wood particles in slow pyrolysis conditions, i.e. temperatures of 300, 375, and 450 ºC. This work is also to further evaluate the performances of the 1-D model framework, called BioSMOKE++ developed by the CRECK group at Politecnico di Milano, adopting the recently improved kinetic scheme. The findings contribute to a better understanding on the significance of geometric simplification during 1-D model simulation, as well as implications of transforming a cubic particle (of 3 cm) into an equivalent sphere to predict endothermic and exothermic events in pyrolyzing particles.

2. Experimental Methods

The aim of the present experiment campaign is to determine pyrolysis properties of two types of waste wood and fresh wood from the same species when allothermically pyrolyzed under the defined conditions. The considered materials are spruce (bulk density = 540 kg/m^3) and larch (bulk density = 600 kg/m^3).

2.1. Biomass samples and Characterization

The examined types of wood are commonly used in Austria, and for each one waste wood and the respective fresh wood are considered for comparison. Waste wood is the one exposed to external influences and mechanically and/or biologically weathered over the years. Fresh wood is the one that has already been chopped but has not been exposed to long-term external influences. The ultimate analysis and the established empirical correlations proposed by Debiagi et al. [10] are adopted. Further work will address investigating the real biochemical com position of the biomass samples.

2.2. Experimental setup and procedures

Pyrolysis temperatures (T_{set}) are 300°C, 375°C, 450°C. Thermocouples (Type K, diameter 1mm) are led into the bottom of a pyrolysis box and fixated. Holes (diameter 1,2mm, length 1,5cm) are drilled in the center of the cross section of the cubes, perpendicular to direction of growth. The cubes are then placed directly on the thermocouples. The box is put into a muffel oven (L 15/11/B410, Nabertherm, 3,5 kW max. power) at ambient temperature, where nitrogen is led into (flowrate 1L/min). The oven is heated to T_{set} in 30 min and kept at T_{set} for 90 min. The box then cools down in the oven. T thermocouples are led outside the box and oven, where data is recorded via a thermologger (BTM-420 SC, LT Lutron). For each temperature and wood source four samples are pyrolyzed and results are averaged.
All wood and charcoal samples are ground, using a granulator (Pulverisette 25, Fritsch) and a centrifugal mill (ZM 200, Retsch) to reach particle size <1mm. Degree of pyrolysis and volatile content are determined via thermogravimetric analysis TGA (STA 449 F5 Jupiter, Netsch, Autosampler/ 19 samples per run). 10-20mg of particles are weighed as the initial mass. TGA segments are I (25°C-110°C, 15°C/min, N_2) and II (110°C for 10 min, N_2) to determine moisture content, III 110°C-900°C, 30°C/min, N_2) and IV (900°C for 12 min, N_2) to determine volatile content ($\omega_{\mathrm{vol,c}}$ for charcoal, $\omega_{\mathrm{vol,w}}$ for wood), V (900°C, for 12 min, synthetic air) to determine ash content. Total carbon, hydrogen and nitrogen content is determined via CHN analysis (TruSpec CHN, Leco), with an initial mass of 100-200mg. Samples are analysed twice and the results are averaged. Degree of pyrolysis η is calculated via equation (Eq.1).

$$\eta = 100 \cdot \left(1 - \frac{\omega_{vol,c}}{\omega_{vol,w}}\right) \qquad (1)$$

2.3. Description of the models

The recently revised CRECK-S-B kinetic model proposes a more comprehensive way to describe the kinetics of biomass pyrolysis. In this model, complex structure and composition of biomasses are lumped into a few reference components that

represent the most common components found in biomass feedstock. The detailed multistep pyrolysis scheme going to be applied in this work is based on the one originally developed by [11]and modified in the later stage by [10]. This scheme contains 32 reactions with 58 species (29 volatiles and 29 solid species) and is coupled to a 1-D particle model called the BioSMOKE++_1D. The model solves heat and mass balance equations on a 1D computational grid for both the gas and solid (porous) phase [12].

3. Results and Discussion

Figure 1 shows a comparison between experimental results and predicted temperature profiles at the surface and centre of the particle for three pyrolysis temperatures and for larch wood (old (LA) & fresh (LF)).

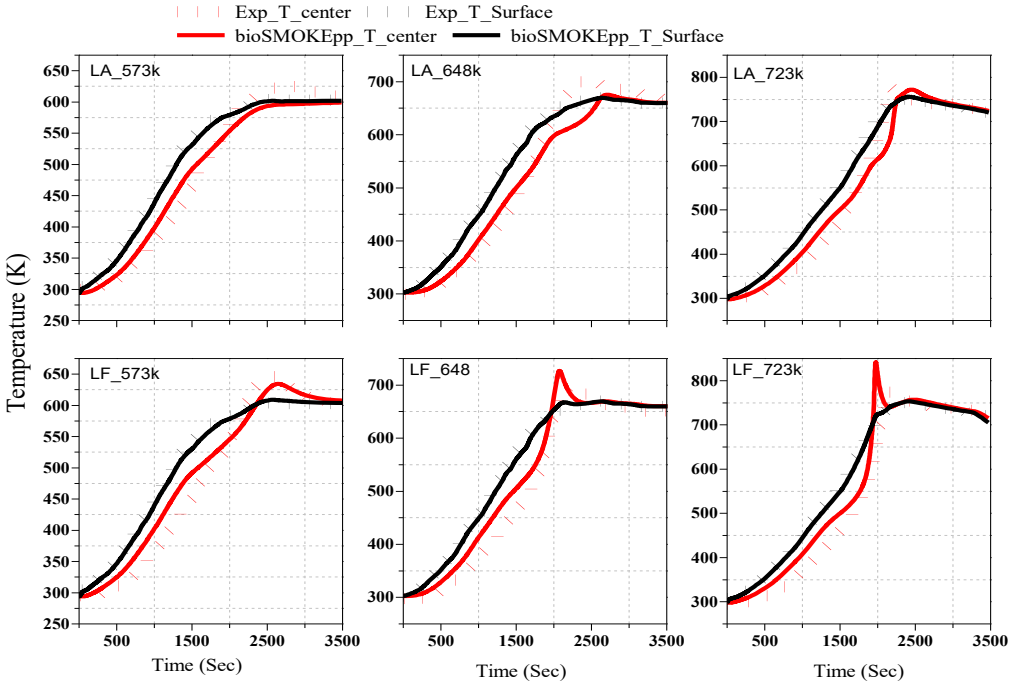

Figure 1. Temperature profiles of the particle compared with simulation for a 3x3x3 cm^3 wood particle modelled as sphere with the same surface area at r = 0 (red) and r = R (black) at three pyrolysis temperatures (300, 375 and 450 °C)

The result shows that temperature in the center can exceed the temperatures measured on the surface of the particles as a result of the exothermic clarification reactions occurring inside the particles. These trends were also encountered in other available studies in literature [13]. The results indicate that a difference in the relative composition of wood in terms of its components (Cellulose, lignin and hemicelluloses) varies widely within species and even within the same tree. Cellulose, lignin and hemicelluloses each have different onset temperatures at which

they degrade. Thus, the biomass composition is a major factor influencing the behaviour of the particle with regard to exothermicity. The anisotropic properties of the particles can influence the pyrolysis behaviour. Therefore, characterization of the chemical composition of the biomass and the adoption of a 3D model, able to account for anisotropic effects would further improve the results. Nevertheless, Figure 1 shows that model predictions agree well with experimental measurements. The model is able to predict the effect of pyrolysis temperature and wood type (LA, LF) on the extent of the exothermic effects.

Model predictions were also compared to the experimentally measured degree of pyrolysis. Figure 2 show that the model can capture the effect of temperature on degree of pyrolysis. On the contrary the model is not able to predict the effect of wood type. This discrepancy is attributed to the assumptions made during numerical simulations, particularly the estimated chemical composition of the biomass and of thermal conductivity of the biomass samples.

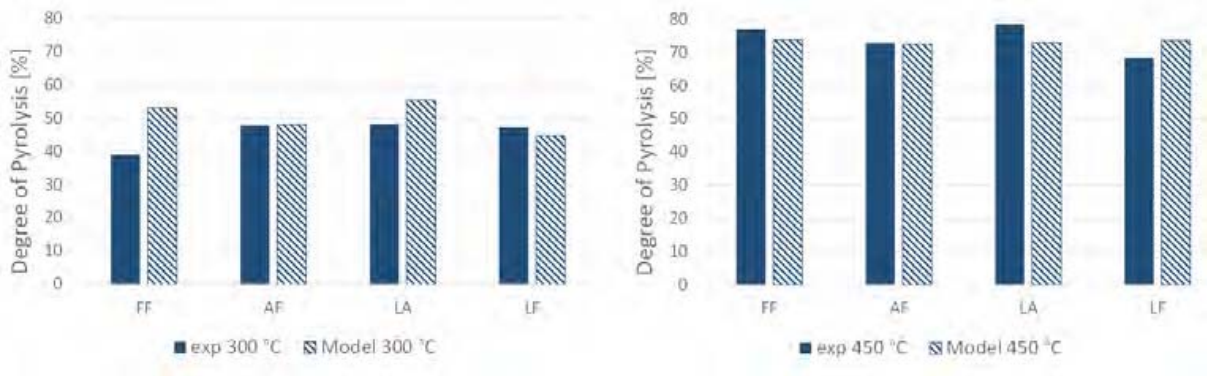

Figure 2. Effect of pyrolysis temperature on degree of pyrolysis for different wood particles. Comparison between experimental measurements and model predictions.

4. Conclusion and Future insights

This work provides new experimental data on the pyrolysis of thick biomass particles of different wood cubes. It also shows that the CRECK kinetic model of biomass pyrolysis, coupled to a simple 1D model for thick particle, is able to replicate the over-shooting of the center temperature of thick particles, while also reasonably predicting the effect of temperature on the degree of pyrolysis for different wood particles. The comparison of experimental and model results has provided insights into the mechanisms and kinetics of biomass pyrolysis, highlighting the importance of parameters such as particle size, geometry, and biomass composition in determining pyrolysis characteristics and biomass pyrolysis product distribution. Further work will be done in the future to extend the experimental dataset, including biomass composition, and to improve the model by including anisotropic effects which cannot be accounted for by the1D model.

Acknowledgements

This study at Politecnico was conducted within the Agritech National Research Center and received funding from the European Union Next-GenerationEU (PNRR) – M4, C2, I1.4, D.D. 1032 17/06/2022, CN00000022). This manuscript reflects only the authors' views and opinions; neither the EU nor the EU Commission can be considered responsible for them.

References

[1] G. Gauthier "Pyrolysis of Thick Biomass Particles: Experimental and Kinetic Modelling," *Chem. Eng. Trans.*, vol. 32, pp. 601–606, Jun. 2013, doi: 10.3303/CET1332101.

[2] A. Garba, *Biomass Conversion Technologies for Bioenergy Generation: An Introduction*. IntechOpen, 2020. doi: 10.5772/intechopen.93669.

[3] M. Van de Velden, J. Baeyens, A. Brems, B. Janssens, and R. Dewil, "Fundamentals, kinetics and endothermicity of the biomass pyrolysis reaction," *Renew. Energy*, vol. 35, no. 1, pp. 232–242, Jan. 2010, doi: 10.1016/j.renene.2009.04.019.

[4] H. Bennadji, K. Smith, M. J. Serapiglia, and E. M. Fisher, "Effect of Particle Size on Low-Temperature Pyrolysis of Woody Biomass," *Energy Fuels*, vol. 28, no. 12, pp. 7527–7537, Dec. 2014, doi: 10.1021/ef501869e.

[5] X. Shi, J. Gao, and X. Lan, "Modeling the Pyrolysis of a Centimeter-Sized Biomass Particle," *Chem. Eng. Technol.*, vol. 42, no. 12, pp. 2574–2579, 2019, doi: 10.1002/ceat.201900085.

[6] M. M. Hasan, X. Hu, R. Gunawan, and C.-Z. Li, "Pyrolysis of large mallee wood particles: Temperature gradients within a pyrolysing particle and effects of moisture content," *Fuel Process. Technol.*, vol. 158, pp. 163–171, Apr. 2017, doi: 10.1016/j.fuproc.2016.12.018.

[7] W. C. Park, A. Atreya, and H. R. Baum, "Experimental and theoretical investigation of heat and mass transfer processes during wood pyrolysis," *Combust. Flame*, vol. 157, no. 3, pp. 481–494, Mar. 2010, doi: 10.1016/j.combustflame.2009.10.006.

[8] C. A. Koufopanos, N. Papayannakos, G. Maschio, and A. Lucchesi, "Modelling of the pyrolysis of biomass particles. Studies on kinetics, thermal and heat transfer effects," *Can. J. Chem. Eng.*, vol. 69, no. 4, pp. 907–915, 1991, doi: 10.1002/cjce.5450690413.

[9] S. Vikram, P. Rosha, and S. Kumar, "Recent Modeling Approaches to Biomass Pyrolysis: A Review," *Energy Fuels*, vol. 35, no. 9, pp. 7406–7433, May 2021, doi: 10.1021/acs.energyfuels.1c00251.

[10] P. Debiagi, G. Gentile, A. Cuoci, A. Frassoldati, E. Ranzi, and T. Faravelli, "A predictive model of biochar formation and characterization," *J. Anal. Appl. Pyrolysis*, vol. 134, pp. 326–335, Sep. 2018, doi: 10.1016/j.jaap.2018.06.022.

[11] E. Ranzi "Chemical Kinetics of Biomass Pyrolysis," *Energy Fuels*, vol. 22, no. 6, pp. 4292–4300, Nov. 2008, doi: 10.1021/ef800551t.

[12] G. Gentile, A. Cuoci, A. Frassoldati, T. Faravelli, and E. Ranzi, "A Comprehensive CFD Model for the Biomass Pyrolysis," *Chem. Eng. Trans.*, vol. 43, pp. 445–450, May 2015, doi: 10.3303/CET1543075.

[13] M. Corbetta "Pyrolysis of Centimeter-Scale Woody Biomass Particles: Kinetic Modeling and Experimental Validation," *Energy Fuels*, vol. 28, no. 6, pp. 3884–3898, Jun. 2014, doi: 10.1021/ef500525v.

THERMOCHEMICAL RECYCLING OF POLYETHYLENE TEREPHTHALATE: EXPERIMENTAL AND KINETIC INVESTIGATION

A. Locaspi*, O. Akin, M. Havaei**, M. Mehl*, M. Pelucchi*, R.J. Varghese**, K.M. Van Geem**, T. Faravelli***

tiziano.faravelli@polimi.it

* CRECK Modeling Lab, Politecnico di Milano, Milano, IT 20133

** Laboratory for Chemical Technology, Ghent University, Zwijnaarde, BE 9000

Abstract

In a circular economy perspective, Plastic Wastes (PW) are a valuable source of chemicals, energy vectors and fuels. Thermochemical recycling technologies as pyrolysis, gasification and partial oxidation are promising processes, which require the definition of suitable condensed phase pyrolysis kinetic models. While mechanical and other chemical recycling technologies are well established for polyethylene terephthalate (PET), thermochemical recycling allows to treat complex and contaminated mixtures. This work proposes a semi-detailed kinetic model for PET pyrolysis based on a consolidated functional group approach and suitable for CFD simulations. The model is validated by a comprehensive set of literature experimental data and new GCxGC speciation data. The present work extends the CRECK kinetic framework for thermochemical recycling of PW mixtures.

Introduction

Waste valorization through chemical recycling is a key step towards circular and sustainable chemical and energy industries. Polyethylene terephthalate (PET) is among the main constituents of Plastic Waste (PW) mixtures due to its widespread use in packaging, fiber production, film applications and in the manufacturing or automotive industry. Several recycling technologies have been developed in the past decades [1], but they involve significant purification and separation costs while, in some cases, also deteriorating the material properties. In this context, thermochemical recycling is a complementary alternative for complex and polluted wastes through waste-to-chemicals processes such as pyrolysis or gasification technologies. To this aim, chemical kinetics and fluid dynamics tool can aid in reactor optimization tailoring the product distribution [2,3].

The kinetics of PET thermal degradation have received less attention compared to other polymers. Several reaction mechanisms have been proposed [4–6], but, to the

authors knowledge, only simple global models have been developed. This work proposes a semi-detailed kinetic model for PET pyrolysis following the functional group approach employed for polyolefins and biomass pyrolysis [7] widening the subset of polymers kinetic models available in the CRECK framework. Model validation, both in terms of mass-loss and product distribution profiles, is performed by comparison with literature experimental data. Additionally, new micro-pyrolysis speciation data by two-dimensional GC are presented.

Methods and Materials

A virgin commercial PET sample is employed for all experimental measurements. The elemental CHNS/O composition of the polymer was analysed with a Thermo Scientific FLASH 2000 analyzer. Five replicates were performed burning 2–3 mg of sample in pure oxygen at 950 °C. An elemental composition of 63.74±1.09%wt C and 4.23±0.03%wt H is measured, where no nitrogen or sulphur is detected.
The pyrolysis experiments are performed in a micro-pyrolysis unit (Rx-3050 TR, Frontier Lab., Japan) coupled with a two-dimensional Gas Chromatography (GCxGC, Thermo Scientific TRACE Ulta) and a separate GC dedicated for analysis of light gases (Thermo Scientific Trace 1310) described in previous works [8,9]. Briefly, experiments are performed at 400, 500, and 600°C dropping 500-800 µg of materials into the preheated pyrolysis furnace. The reactor is operated with a He sweep flowrate of 50 mL/min and a pressure of ~2.7 bar. The released volatiles are collected in a cryo-trap (MJT-1035E) cooled with liquid nitrogen and then simultaneously fed to the two analysis system. The GC columns, an MXT-1 non-polar and a ZB-35HT polar, are operated from 40°C to 350°C with a ramp of 5°C/min. Compound identification is performed with a BenchTOF-Select™ (Markes, United Kingdom) scanning m/z = 50–500 at 70 eV comparing the products spectra with the NIST library database. Compound quantification is performed with an FID calibrated with iso-butane and response factors are calculated via the molecular response factor (MRF) method as reported by De Saint Laumer et al. [10]. Mass closure obtained from the setup increases with temperature, ranging from 30% at 400°C to 70% at 600°C. However, considering ~20 wt% of char formation [11,12], the results are deemed acceptable.

Kinetic Mechanism

According to the functional group approach, the polymer chain distribution is represented through pseudo-species characteristic of the chemical moieties of the polymer, while real species are employed to describe products of interest such as CO, CH_3CO, C_6H_5COOH or the monomers [7]. The starting polymer is characterized only by the terephthalic and ethylene glycol moieties (labelled respectively P-COC_6H_4CO-P and P-OC_2H_4O-P), but, during the degradation process, other groups are formed such as carboxylic acids, alcohols and terminal double bonds, and the corresponding pseudo-species are introduced as well.

The proposed kinetic mechanism stems from literature studies on plausible molecular pathways [4] and analogous radical degradation mechanisms developed for gas-phase oxygenated analogous compounds or lignin [13]. The first involve 6- and 4-member rings degrading in concerted pathways as shown in Figure 1, forming free polymer ends and cyclic oligomers.

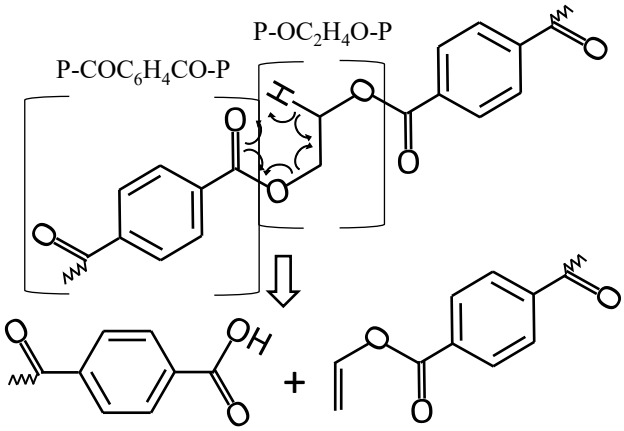

Figure 1. Representation of the pseudo-species describing PET chains and their molecular concerted degradation mechanism

The radical degradation is the main decomposition pathway [5,6], responsible for formation of CO, CH_3CO, and biphenyl structures. Initiation occurs by random scission on the C-C or C-O bonds on the glycol moieties. The produced radicals then undergo propagation reactions such as H-abstractions, β-scissions, and radical additions. Only termination by radical-radical recombination is considered. As with polyvinylchloride and lignin, condensation and radical additions to the aromatic rings result in formation of considerable amounts of carbonaceous residues (char). All proposed reaction classes considerably affect the degradation mechanism. Reaction temperatures are mainly affected by β-scissions, which are the rate determining step, and random scission and recombination reactions, which control the radical pool. H-abstractions and additions affect the product distribution together with β-scissions reactions. The reaction mechanism involves only homogeneous liquid-phase reactions and evaporation is considered separately with appropriate mass-transfer exchange coefficients [3]. The proposed kinetic parameters are obtained from analogy to gas-phase reactions [13] and have similar selectivities to the ones proposed by Huang et al. [5] and Ma et al. [6]. Nevertheless, specific corrections for the transposition from gas to liquid are included [14].

Results

The proposed kinetic model is validated with a comprehensive set of experimental data from literature, both in terms of mass-loss profiles and gas-products distribution, in addition to the new experimental data provided herein. For sake of

brevity, only few comparisons for mass-loss profiles are shown in Figure 2. With respect to dynamic conditions, shown in Figure 2.a, the model proves able to capture correctly both onset temperatures and the differences resulting from different heating rates. Similarly, considering isothermal conditions reported in Figure 2.b, the model correctly describes the temperature effect. Nevertheless, further work is still required to improve predictions of char yields, although, to the authors' knowledge, only few characterization data are reported.

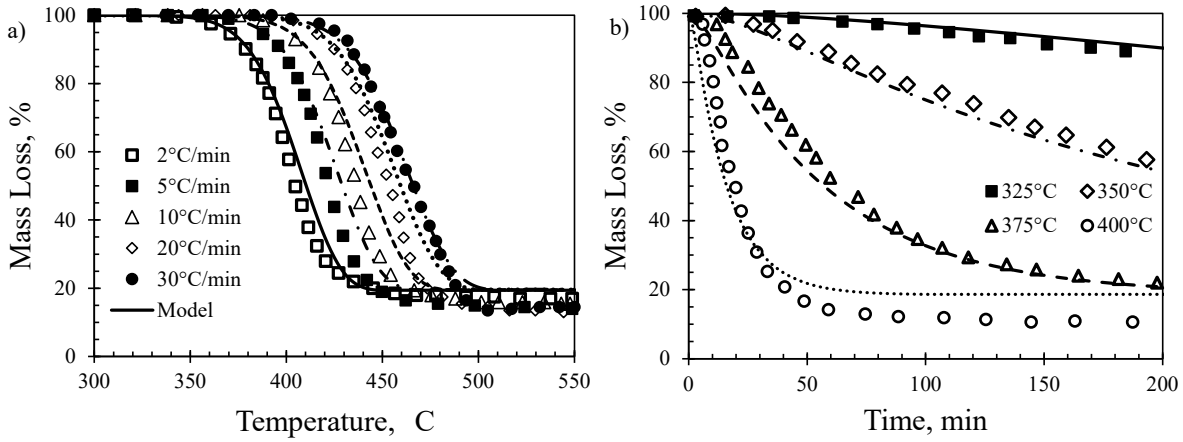

Figure 2. Comparison of predicted (lines) and measured (symbols) mass-loss at: a) constant heating rate [11]; b) isothermal conditions [15]

The main degradation products experimentally measured are shown in Figure 3. The most abundant compound is CO_2, followed by benzoic acid, CO, and CH_3CHO. These results are in line with values reported by Dhahak et al. [4] at low temperatures and Day et al. [12] at higher temperatures. Nevertheless, no CO is detected at 400°C while terephthalic acid is identified at all temperatures. The reduction in its yield at higher temperature is consequent to formation of lower molecular weight compounds such as benzene and acetaldehyde. Similarly, the amounts of vinyl benzoate are comparable to measurements of Dhahak et al. but are lower than those by Day et al. (~30 wt%). Overall, the mass closure is poor at 400°C, although in line with Dhahak et al. [4]. The reason is possibly formation of long-chain products outside the detection range which decompose at higher temperatures [16].

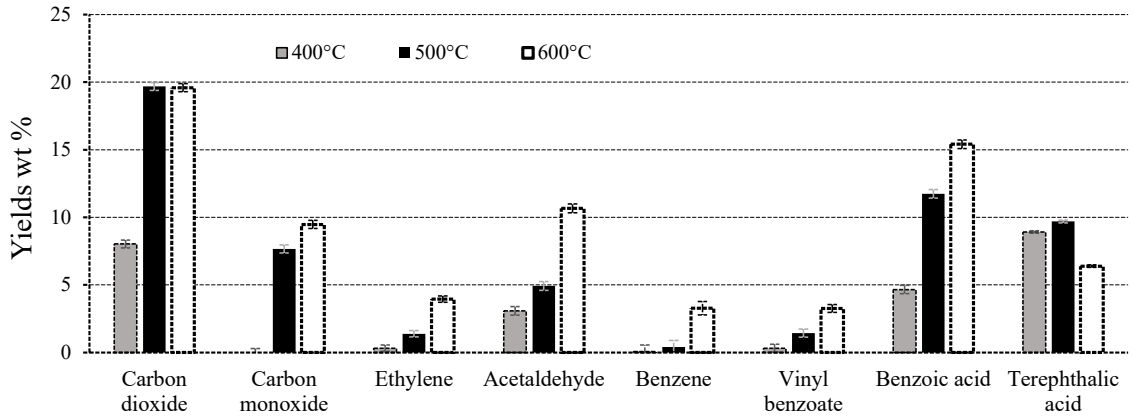

Figure 3. Main volatiles experimentally measured at 400, 500, and 600°C.

Conclusions

The thermal degradation of PET has been investigated experimentally and a kinetic model has been proposed. Speciation data are obtained in a micro-pyrolysis unit coupled to a two-dimensional GC analyser. The model, based on a functional group approach, is validated also with literature experimental data proving able to describe both polymer mass evolution and the release of gas-phase products in a detailed fashion. Further experimental and modelling work are required to investigate char formation and mixture interactions. The present investigation constitutes an important step towards modelling the chemical recycle of plastic waste mixtures.

Acknowledgments

Andrea Locaspi acknowledges Eni S.p.A. for the financial support and all the authors thank the ELECTRO project for the support.

References

[1] L. Brivio, F. Tollini, PET recycling: "Review of the current available technologies and industrial perspectives", *Academic Press*, 2022: pp. 215–267.

[2] O. Dogu, M. Pelucchi, R. Van de Vijver, P.H.M. Van Steenberge, D.R. D'hooge, A. Cuoci, M. Mehl, A. Frassoldati, T. Faravelli, K.M. Van Geem, "The chemistry of chemical recycling of solid plastic waste via pyrolysis and gasification: State-of-the-art, challenges, and future directions", *Prog. Energy Combust. Sci.* 84 (2021) 100901.

[3] S. Madanikashani, L.A. Vandewalle, S. De Meester, J. De Wilde, K.M. Van Geem, "Multi-Scale Modeling of Plastic Waste Gasification: Opportunities and Challenges", *Mater*. 2022, Vol. 15, Page 4215. 15 (2022) 4215.

[4] A. Dhahak, C. Grimmer, A. Neumann, C. Rüger, M. Sklorz, T. Streibel, R. Zimmermann, G. Mauviel, V. Burkle-Vitzthum, "Real time monitoring of

slow pyrolysis of polyethylene terephthalate (PET) by different mass spectrometric techniques", *Waste Manag.* 106 (2020) 226–239.

[5] J. Huang, H. Meng, X. Luo, X. Mu, W. Xu, L. Jin, B. Lai, "Insights into the thermal degradation mechanisms of polyethylene terephthalate dimer using DFT method", *Chemosphere* 291 (2022) 133112.

[6] T. Ma, R. Wang, W. Wang, W. Gu, Y. Yuan, A. Zhang, J. Wei, "Studies on the thermal degradation mechanism of polyethylene terephthalate and its 2-carboxy ethyl (phenyl) phosphinic acid copolymers", *Polym. Degrad. Stab.* 206 (2022) 110185.

[7] A. Locaspi, M. Ferri, F. Serse, M. Maestri, M. Pelucchi, "Chemical kinetics of catalytic/non-catalytic pyrolysis and gasification of solid plastic wastes", *Academic Press*, 2022: pp. 21–76.

[8] Y. Ureel, M.R. Dobbelaere, O. Akin, R.J. Varghese, C.G. Pernalete, J.W. Thybaut, K.M. Van Geem, "Active learning-based exploration of the catalytic pyrolysis of plastic waste", *Fuel*. 328 (2022) 125340.

[9] A. Eschenbacher, R.J. Varghese, E. Delikonstantis, O. Mynko, F. Goodarzi, K. Enemark-Rasmussen, J. Oenema, M.S. Abbas-Abadi, G.D. Stefanidis, K.M. Van Geem, "Highly selective conversion of mixed polyolefins to valuable base chemicals using phosphorus-modified and steam-treated mesoporous HZSM-5 zeolite with minimal carbon footprint", *Appl. Catal. B Environ.* 309 (2022) 121251.

[10] J.Y. De Saint Laumer, E. Cicchetti, P. Merle, J. Egger, A. Chaintreau, "Quantification in gas chromatography: Prediction of flame ionization detector response factors from combustion enthalpies and molecular structures", in: Anal. Chem., *American Chemical Society*, 2010: pp. 6457–6462.

[11] A. Dhahak, G. Hild, M. Rouaud, G. Mauviel, V. Burkle-Vitzthum, "Slow pyrolysis of polyethylene terephthalate: Online monitoring of gas production and quantitative analysis of waxy products", *J. Anal. Appl. Pyrolysis.* 142 (2019) 104664.

[12] M. Day, D.M. Wiles, "Influence of temperature and environment on the thermal decomposition of poly(ethylene terephthalate) fibres with and without the flame retardant tris(2,3-dibromopropyl) phosphate", *J. Anal. Appl. Pyrolysis.* 7 (1984) 65–82.

[13] T. Faravelli, A. Frassoldati, G. Migliavacca, E. Ranzi, "Detailed kinetic modeling of the thermal degradation of lignins", *Biomass and Bioenergy.* 34 (2010) 290–301.

[14] M. Dente, G. Bozzano, T. Faravelli, A. Marongiu, S. Pierucci, E. Ranzi, "Kinetic Modelling of Pyrolysis Processes in Gas and Condensed Phase", *Adv. Chem. Eng.* 32 (2007) 51–166.

[15] P. Das, P. Tiwari, "Thermal degradation study of waste polyethylene terephthalate (PET) under inert and oxidative environments", *Thermochim. Acta*. 679 (2019) 178340.

[16] A. Eschenbacher, R.J. Varghese, M.S. Abbas-Abadi, K.M. Van Geem, "Maximizing light olefins and aromatics as high value base chemicals via single step catalytic conversion of plastic waste", *Chem. Eng. J.* 428 (2022) 132087.

Predicting torrefaction and pyrolysis of biomass using a machine learning approach

P. Brachi*, A. Coppola*, V. Del Duca, P. Salatino*,**, F. Scala*,****
vincenzo.delduca2@unina.it
*STEMS, CNR, P.le Tecchio 80, 80125, Napoli, Italy
**DICMaPI, Università di Napoli Federico II, P.le Tecchio 80, 80125, Napoli, Italy

Abstract
Fast pyrolysis is a technology that shows great potential for converting difficult-to-handle waste and biomass into bio-oil, which is a valuable product. However, optimizing the yield and composition of this bio-oil can be challenging due to the variability in composition and the presence of multiple phases and phenomena in the pyrolysis process. Mathematical modeling of this process is therefore difficult, but machine learning techniques, specifically artificial neural networks (ANNs), can help overcome these limitations by learning complex behaviors from a dataset. This work used artificial neural networks (ANNs) and the Connection Weight Method to quantify variable importance in predicting torrefaction and pyrolysis performance based on biomass characteristics and operating conditions. The goal was to create a forecasting tool with low performance error indicators that predict pyrolysis outputs qualitatively and quantitatively. The database consisted of 274 observations from 29 scientific papers, including chemical-physical characteristics of the raw biomass, operating conditions, and products and by-products of the process.

Introduction
Organic feedstock and plastic waste can be transformed into bio-chemicals, bio-fuels, and bio-energy by means of fast pyrolysis [1]. This process creates a versatile bio-liquid product, bio-oil, which is a complex mixture of organic compounds with high oxygen and water content. Bio-oil from fast pyrolysis is difficult to use directly as a drop-in fuel due to its properties, including poor volatility and ignition, acidic pH, and the tendency to polymerize. Therefore, different reactor configurations and upgrading techniques are under investigation to improve the physical and chemical properties of bio-oil. These techniques include biomass pre-treatments, in situ upgrading, and downstream methods. Among the upgrading techniques, torrefaction and catalytic pyrolysis are promising methods for upgrading bio-oil from various biomasses.
Machine learning (ML) [2,3] techniques are considered a promising tool for optimizing pyrolysis processes in terms of yield and composition of the desired product, depending on the biomass type/characteristics, process operating conditions, and implemented upgrading technique. ML models have been successfully applied in various fields and have shown potential in modelling thermochemical conversion processes, including torrefaction and pyrolysis. ML techniques have been mainly adopted for the prediction of the features of torrefied

biomass, such as the higher heating value, enforcement factor, and solid yield, using proximate analysis of biomass, temperature, and treatment time as inputs.

Methods

Classical chemical-physical models are particularly complex when applied to torrefaction and pyrolysis since hundreds of chemical species and reactions are involved. Artificial intelligence, and in particular machine learning (ML) techniques, have the potential to overcome the limitations of first principles models, as they can learn complex behaviors from dataset with a low-cost model development. Among several ML techniques, artificial neural networks are extensively used in different fields such as machine diagnostics, pattern recognition, quality control as well as fitting experimental data, gaining in the years a relevant role also in chemical engineering. The technique used in this work is the machine learning technique of artificial neural network. The Connection Weight Method is used for quantifying the variable importance in ANN.

Database setup

The database used contains information on torrefaction and pyrolysis processes and includes both qualitative and quantitative information concerning the chemical-physical characteristics of the raw biomass, the different operating conditions investigated, the products and by-products of the process. Altogether 27 different biomasses were considered. More in detail, the database contains a total of 274 observations. The database contains 101 columns which show the different properties of the biomass, the process conditions, and the obtained products. Therefore, the parameters can be divided into 5 macro-categories:1. Raw biomass characteristics; 2. Torrefaction operating conditions; 3. Torrefaction products; 4. Pyrolysis operating conditions; 5. Pyrolysis products.

Of these 101 parameters: 21 are related to the biomass characterization, 13 are related to the torrefaction process conditions, 23 are related to the torrefaction products, 10 are related to the pyrolysis process conditions, and 34 are related to the pyrolysis products. More than half of the variables regarding pyrolysis products, i.e., 26 variables, are related to the characteristics of the produced bio-oil. Of the remaining 8 parameters, 6 are related to the biogas yield and composition and 2 to the biochar. The database was divided into 3 datasets to analyse 3 different situations. The aim was to create a forecasting tool that allows to predict the outputs of the 3 datasets with low performance error indicators (MAE, MSE, SAE, MAPE). The 3 datasets, in terms of macro-characteristics (or macro-categories), are composed as shown in Tables 1, 2, and 3.

Dataset 1 concerns only the torrefaction process: as input we have the raw biomass characteristics (biomass type, proximate and ultimate analysis, HHV, etc.) and the torrefaction operating conditions (reactor type, run time, temperature). As output, we have the biochar yield and the C, H, O content of torrefied biomass. Dataset 2 concerns the pyrolysis process, in which as input we have the torrefied biomass

characteristics (proximate and ultimate analysis, HHV) and the pyrolysis operating conditions (reactor type, run time and temperature); while as output we have the bio-oil yield and the bio-oil HHV. Dataset 3 represents the challenge of this work and concerns the modelling of the pyrolysis process starting from the chemical-physical raw biomass characteristics (biomass type, proximate and ultimate analysis, HHV, etc.), the torrefaction and pyrolysis operating conditions, while as output we have the yields and qualitative characteristics of pyrolysis products.

Table 1. DATASET 1

Input	Output
Raw biomass characteristics Torrefaction operating conditions	Torrefaction products

Table 2. DATASET 2

Input	Output
Torrefaction products Pyrolysis operating conditions	Pyrolysis products

Table 3. DATASET 3

Input	Output
Raw biomass characteristics Torrefaction operating conditions Pyrolysis operating conditions	Pyrolysis products

Artificial Neural Network (ANN)

ANN is typically composed of an input layer which receives input variables, one or more hidden layers that identify nonlinearity to correlate inputs and outputs, and an output layer which represents output variables. Each layer contains neurons or nodes which are interconnected by weighted links to pass input signals from one neuron in input layer to another neuron in hidden layer, and from one neuron in hidden layer to another neuron in the next hidden or output layer [4]. A Matlab code, called *Netoptim*, was developed by the authors to create and train the network. Specifically, the algorithm was conceived within the present research and implemented in Matlab to develop a large number of ANNs, with the goal of evaluating different choices such as: i) the network type (fitnet, feedforwardnet and cascadeforwardnet); ii) the number of neurons in the hidden layer (set, initially, equal to the number of inputs and varied in a range of ± 5); iii) the training function. The transfer function was set

up as the hyperbolic tangent sigmoid, to avoid a further parameter to be investigated. When the ANN is ready to be trained, the dataset samples are automatically divided into training, validation, and testing, with percentages equal to 70%, 15% and 15%, respectively. In this study, the networks developed and explored consisted of one hidden layer to avoid long computational times and a single-output because *Netoptim* is structured in such a way as to optimize performances (find the best network architecture that minimizes the error) for a single output. The performance indicators[1] evaluated in this work were MAE, MSE, SAE, MAPE and R^2. Such indicators were used to compare the performance of the 3 dataset results. For the sake of simplicity, the authors have chosen to report here only the MAPE. The Connection Weight Method was used for quantifying the variable importance in ANNs. The application of the connection weight method permits to evaluate the impact of individual inputs on the machine learning process. Understanding the influence of each input variable on the outputs is useful, as it helps to set optimum values of inputs.

Results

For the sake of brevity and since dataset 3 represents the real challenge of this work, we choose to only show the results for this scenario.

Dataset 3 (Torrefaction + Pyrolysis) results

The output chosen for the simulations of dataset 3 is bio-oil yield (wt, %). The simulation results, in terms of MAPE for ANN technique, are shown in Tables 4.
Test 1, shown in Table 4, is related to the most complete input-set. The start input-set is composed of 14 variables, of which: 1 relates to the type of biomass: material; 8 relate to the characteristics of the raw biomass: moisture content, volatile matter content, fixed carbon, ash from proximate analysis and carbon, hydrogen, nitrogen, oxygen from ultimate analysis; 3 to the torrefaction operating conditions: run time, temperature, apparatus; and 2 to the pyrolysis operating conditions: apparatus, temperature. The start input-variables weights, in terms of variables importance, are obtained applying the connection weight method [5]. The Connection Weight Method results showed that the inputs with a greater weight are the N, O, C contents and the torrefaction apparatus with values of 18.95%, 15.92%, 13,31% and 10.59% respectively; conversely, the inputs with a lower weight are the pyrolysis temperature, the moisture content, the H content and the torrefaction temperature with values of 0.62%, 0.78%, 1.16%, and 1.20% respectively.
We have chosen to proceed with the subsequent simulation tests by eliminating the inputs with a weight less than 2%. Thus, the logic of the subsequent simulations (tests from 2 to 16) was to eliminate, for each test, first individually each input with lower weight (tests 2 to 5); then eliminating a pair of inputs each time (tests 6 to 11);

[1] MAE=mean absolute error; MSE=mean square error; SAE= sum absolute error; MAPE=mean absolute percentage error; R^2=coefficient of determination.

then eliminating inputs in groups of 3 (tests 12 to 15) and finally eliminating all 4 inputs (test 16).
The best ANN result, for the bio-oil yield output, is found in correspondence of test 4 (Table 4) with a MAPE=2.01 (which corresponds to the network architecture: feedforwardnet as network type, 15 neurons in the hidden layer, Bayesian-Regularization algorithm as training function) and nº inputs=13 removing "H" content from the start input-set. It is also noted that by eliminating the "moisture" content (test 3) from the start input-set, we still obtain a low MAPE=2.23, and that in test 9, by eliminating both the "H" and the "moisture", a slightly higher MAPE is obtained, but still low, equal to 2.46. This could be explained by 2 factors: H and moisture contents are respectively the result of the ultimate and proximate analysis, where the sum of the single components is equal to 100 (wt%); the other elements of the ultimate (C, N, O) and proximate (volatiles, fixed carbon, ash) analysis are inputs variables. Therefore, the absence of H and moisture can be considered acceptable to further reduce input set parameters.

Table 4. Dataset 3, bio-oil yield (wt, %), simulations.

# of test	# of input	$MAPE_{ANN}$	R^2
1	14	2.28	0.96
2	13	5.21	0.93
3	13	2.23	0.96
4	13	**2.01**	0.98
5	13	10.42	0.92
6	12	5.52	0.96
7	12	5.06	0.95
8	12	12.00	0.92
9	12	2.46	0.97
10	12	10.81	0.92
11	12	10.42	0.93
12	11	5.23	0.95
13	11	12.12	0.94
14	11	11.96	0.93
15	11	10.60	0.93
16	10	11.9	0.92

For the bio-oil yield, the best result is $MAPE_{ANN}$=2.01 with a R^2=0.98 (test 4). For this case, Figure 1, shows a comparison between the results predicted with the ANN technique and the experimental values.

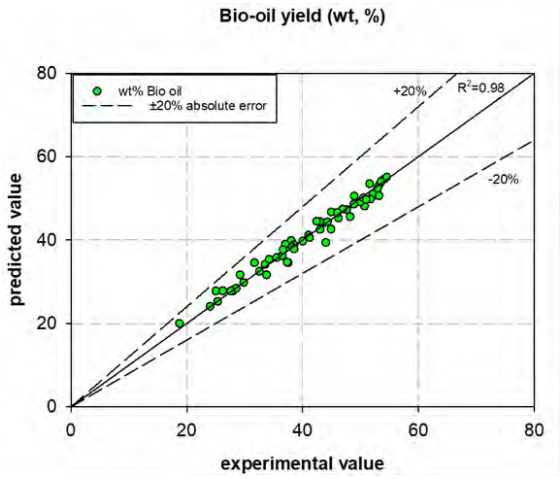

Figure 1. Comparison of the predicted value of the ANN technique with experimental values for bio-oil yield (wt, %).

Conclusions

This study focuses on developing an artificial neural network (ANN) for the prediction of residual biomass valorization processes, specifically for integrated pyrolysis and torrefaction processes. The database used contains qualitative and quantitative information concerning the chemical-physical characteristics of the raw biomass, the operating conditions investigated, and the products and by-products of the process. The ANN was developed using a Matlab code called *Netoptim* and evaluated using performance error indicators (MAE, MSE, SAE, MAPE). The best ANN result was found for bio-oil yield output, with a MAPE of 2.01, using a feedforwardnet network type, 15 neurons in the hidden layer, Bayesian-Regularization algorithm as training function, and 13 inputs. The study suggests that expanding the dataset with additional biomass types undergoing torrefaction and pyrolysis processes could improve the accuracy of the results, while developing further ML techniques would allow for a broader comparison of results.

References

[1] Bridgwater T. Challenges and opportunities in fast pyrolysis of biomass: Part I. Johnson Matthey Technol Rev 2018;62:118–30.
[2] Kartal F, Özveren U. Prediction of torrefied biomass properties from raw biomass. Renew Energy 2022;182:578–91.
[3] Ozonoh M, Oboirien BO, Daramola MO. Optimization of process variables during torrefaction of coal/biomass/waste tyre blends: Application of artificial neural network & response surface methodology. Biomass and Bioenergy 2020;143:105808.
[4] Sun Y, Liu L, Wang Q, Yang X, Tu X. Pyrolysis products from industrial waste biomass based on a neural network model. J Anal Appl Pyrolysis 2016;120:94–102.
[5] García Nieto PJ, García-Gonzalo E, Sánchez Lasheras F, Paredes-Sánchez JP, Riesgo Fernández P. Forecast of the higher heating value in biomass torrefaction by means of machine learning techniques. J Comput Appl Math 2019;357:284–301.

Comparison of bio-crude yield and quality from hydrothermal liquefaction of sewage sludge under different heating rates

F. Di Lauro*, A. Amadei, M. Balsamo***, M. Damizia**, B. De Caprariis**, P. De Filippis**, F. Montagnaro***, P. Salatino*, R. Solimene******

*Dipartimento di Ingegneria Chimica, dei Materiali e della Produzione Industriale, Università degli Studi di Napoli Federico II, Piazzale Vincenzo Tecchio 80, 80125, Napoli, Italy
**Dipartimento di Ingegneria Chimica, Università Sapienza di Roma, Via Eudossiana 18, 00184, Roma, Italy
***Dipartimento di Scienze Chimiche, Università degli Studi di Napoli Federico II, Complesso Universitario di Monte Sant'Angelo, 80126, Napoli, Italy
****Istituto di Scienze e Tecnologie per l'Energia e la Mobilità Sostenibili, Consiglio Nazionale delle Ricerche, Sede Secondaria, Piazzale V. Tecchio 80, 80125, Napoli, Italy

Abstract
Thermochemical valorisation of residual biomasses represents a promising way for reducing the large amount of municipal waste that is annually disposed in landfills (i.e. sewage sludge, food waste, agricultural residues). The high amount of moisture present in the starting sewage sludge makes this biomass less attractive in traditional thermochemical valorization processes due to the high-energy demanding dewatering step commonly associated with processes such as pyrolysis, gasification, torrefaction. In this context, the hydrothermal liquefaction process working in sub-critical water conditions (pressure of 40–200 bar and temperature of 200–375°C) represents a technology capable of valorizing the starting biomass without the expensive pre-drying required in other competitive technologies. This work scrutinises the effect of the heating rate obtained for different reactor volumes on the production of bio-crude during the HTL process. The effect of the reactor scale on the chemical composition of the bio-crude and the solid residue is also evaluated.

Introduction
Technological and economic development, population growth and the progressive urbanization of vast areas of the planet caused an increase in global energy demand. In this context the development of technologies for renewable fuels production from residual biomass represents a promising way to reduce the environmental impact of fossil fuels [1]. In a circular economy perspective, among the different types of biomasses, those defined as "waste" such as agricultural residues, food waste, sewage sludge, are of particular interest since a significant volume of the municipal/industrial waste is discharged into public sewers or landfills at great cost

to the industry and/or the community that accepts these effluents [2]. Among the different thermochemical valorization technologies hydrothermal liquefaction (HTL) process appears of particular interest for higher moisture biomass. In fact, during the HTL process the high pressure of 40–200 bar and the middle temperature of 200–350°C, determine a change of the water physico-chemical properties. In particular, under subcritical conditions water assumes the characteristics of a polar organic solvent capable of solubilising the organic fraction of the starting biomass and converting it into a bio-crude. An aqueous phase and a solid residue and a gas phase are also HTL co-products [3]. HTL process allows, in fact, to exploit the biomass water content for bio-crude production, thus avoiding the high-energy demanding dewatering step commonly associated with other competitive processes of biomass conversion (e.g. oxy-pyrolysis, gasification) [4].
Most literature on the HTL process concerns experimental investigations in batch reactors. Several studies showed that a high heating rate positively affects the bio-crude yield [5–7]. On the other hand, the effect of thermal transients on product yields and quality in lab-scale reactors of larger volumes (order 10^2 mL) is poorly investigated [8–10]. Besides, the separation protocol of the different HTL phases for the bio-crude recovery typically changes in terms of adopted operation units and extraction solvents when the scale of the lab-scale reactor is increased.
In this study, the HTL process applied to a municipal and paper mill sludge, was investigated in two lab-scale plants: i) one consisting in a 500 mL batch autoclave reactor (Hastelloy C-276) with a heating rate up to 330°C of 10°C/min [11], and ii) the other is a 10 mL stainless-steel (AISI 316) tubular microreactor with a mean heating rate of 100°C/min. In particular, the effect of the different reactor scales and the different separation protocols on the bio-crude and solid residue yields and chemical composition were scrutinised.

Materials

Two different sewage sludges were used in this work: i) a municipal sludge and ii) a paper mill sludge. The main properties are reported in the Table 1. For the thermochemical conversion purpose both municipal and paper mill sludges appear an interesting biomass, with a similar composition in terms of carbon, hydrogen, ash, and organic content. The main difference is in the higher N content which is 4% higher in municipal sludge.

Table 1. Main chemical properties of tested sewage sludges (%wt, dry basis).

	C	H	N	O*	Ash	Organic matter
Municipal sludge	33.2	5.4	5.4	28.1	28.1	72.180
Paper mill sludge	31.5	4.9	1.4	29.1	29.1	70.789

*Oxygen calculated by difference (O $\%_{wt}$ = 100 $\%_{wt}$ -ash $\%_{wt}$ -C $\%_{wt}$ -H $\%_{wt}$ -N $\%_{wt}$).

Experimental apparatus and procedure

For the HTL tests two different reactors were used. The first one was a 500 mL batch

autoclave reactor in Hastelloy C-276 equipped with a digital pressure transducer coupled with a needle valve for pressure measurement and control while the main heating system is composed of a tubular electric heater surrounding the reactor external surface, coupled with thermocouples and PID system for temperature setting and measurement. To optimize the thermal transient, the heating stage was carried out also with the support of a band heater (Watlow Series MI band) with a power of 1250 W, coupled with a cylindrical steel block located at the bottom of the vessel, whereas the top of the reactor was insulated with a layer of rock wool. In this configuration the heating rate was 10°C/min. Moreover, the reactor presents a magnetic stirrer with maximum torque of 1.76 Nm and variable speed motor 1/8 hp and an internal single loop coil to ensure the fast cooling of the system. After the HTL test the solid-liquid mixture was filtered on a Büchner under vacuum. Subsequently, the solid phase was subjected to a Soxhlet extraction with dichloromethane (DCM), to recover the bio-crude from the pores of the solid residue and dried in an oven at 105ºC for 24 h to remove DCM and traces of water. The soluble fraction in DCM was, instead, subjected to vacuum distillation at 0.4 bar aimed at evaporating solvent and recovering the bio-crude. On the other hand, the liquid fraction was centrifugated for 10 min at 4000 rpm using a NEYA 8 BASIC ventilated apparatus to optimize the stratification of the bio-crude and the aqueous phase and obtain their separation.
The second experimental apparatus was a 10 mL microtubular reactor, connected to a mechanical stirrer. The reactor was heated in a fluidized sand bath with a heating rate of about 100°C/min at the desired temperature and maintained in isothermal conditions for the selected reaction time. The pressure in the reactor was auto-generated, ranging between 70 and 150 bar. At the end of the tests, the reactor was quenched in a water bath and weighted. Then, the reactor was opened to remove the gaseous products and weighed again to determine the amount of gas phase produced. The water phase was discharged via filtration and the bio-crude was extracted from the solid residue by using 50 mL of dichloromethane as solvent in a Soxhlet extractor. The oil phase was recovered from the extracted solution by evaporating the DCM at 30°C and 556 mbar using a rotary evaporator.
HTL experiments were performed at 330°C and 10 min in the isothermal stage. The main difference between the two reactor is their different heating rate, which results in an order of magnitude higher for the 10 mL reactor (100°C/min and 10°C/min for the 10 mL and 500 mL reactor, respectively).

Results and discussion

Figure 1 shows the bio-crude and solid residue yields derived from HTL of paper mill and municipal sludges in the two different experimental apparatuses. Firstly, it can be observed that both sludges provide very similar values of both bio-crude and solid yield (Y^{db}), as expected from their very similar chemical composition (cf. Table 1). Moreover, for the tested operating conditions the different heating rates during the HTL process do not determine appreciable differences in the products yields. Y^{db}

is 21% and 42% for bio-crude and solid, respectively, regardless of the time required to reach the temperature of 330ºC. These results seem to differ from literature data showing higher yields for high heating rates [5,7]. However, it is important to note that, to reach temperatures of 330ºC in the 500 mL batch reactor, the reaction time in the non-isothermal stage is longer than for the 10 mL microtubular reactor. The contribution at high temperatures in the non-isothermal section could partly compensate the higher bio-crude yield material due to faster hydrothermal liquefaction conditions, especially for short reaction times in the isotherm stage, as in this study (reaction time of 10 min).

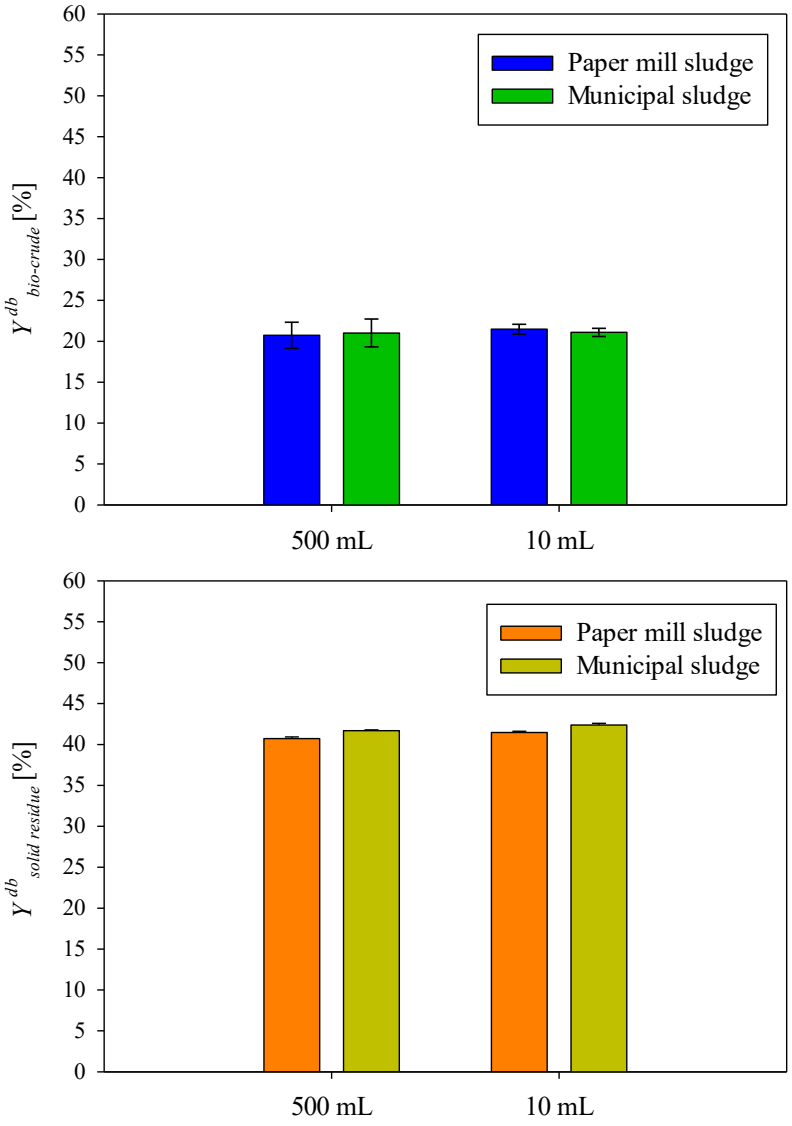

Figure 1. Bio-crude (on the top) and solid residue (on the bottom) yields obtained from HTL of paper mill and municipal sludges under different heating rates (*db* refers to dry-basis).

Table 2 compares the quality of the bio-crude and solid residue in terms of their elemental analysis. It is possible to observe that the different heating rates along HTL

exert a negligible influence on the bio-crude chemical composition, with very similar values for both sludges. In this context, the molar ratio H/C for both bio-crude results equal to about 1.5, while the molar ratio O/C is equal to 0.20. Minor differences can be highlighted in terms of composition of the solid residues.

Table 2. Elemental analysis of bio-crude and solid residue (% wt, dry basis).

	Reactor [mL] (heating rate)	**C [%]**	**H [%]**	**N [%]**	**O* [%]**	**Ash [%]**
Bio-crude (Municipal sludge)	500 (10°C/min)	69.2	8.7	4.3	17.7	-
	10 (100°C/min)	68.7	8.3	4.7	18.2	-
Bio-crude (Paper mill sludge)	500 (10°C/min)	69.1	8.5	4.3	18.1	-
	10 (100°C/min)	68.1	8.3	5.1	18.4	-
Solid residue (Municipal sludge)	500 (10°C/min)	17.1	1.7	1.9	9.3	70.0
	10 (100°C/min)	19.2	2.0	2.2	6.6	70.0
Solid residue (Paper mill sludge)	500 (10°C/min)	14.2	1.5	0.8	16.9	66.6
	10 (100°C/min)	11.2	1.3	1.0	19.78	66.6

*Oxygen calculated by difference (O $\%_{wt}$ = 100 $\%_{wt}$ -ash $\%_{wt}$ -C $\%_{wt}$ -H $\%_{wt}$ -N $\%_{wt}$).

Conclusion

In this study, the energetic valorization of a sewage sludge, in a 500 mL batch reactor and 10 mL microtubular reactor, for bio-crude production via HTL was investigated. In particular, a preliminary analysis of the effect of different heating rates on the yield and quality of bio-crude revealed that for low isothermal reaction times no significant differences were observed. Future experiments in the two reactor scales will be devoted at investigating the role of thermal transients in bio-crude generations.

References

[1] Balsamo, M., Montagnaro, F., Anthony, E.J., 2023, “Socio-economic

parameters affect CO_2 emissions and energy consumptions – An analysis over the United Nations Countries", *Curr. Opin. Green Sustain. Chem.* 40: 100740 (2023).

[2] Barampouti, E.M., Mai, S., Malamis, D., Moustakas, K., Loizidou, M., "Liquid biofuels from the organic fraction of municipal solid waste: a review", *Renew. Sust. Energ. Rev.* 110: 298–314 (2019).

[3] Fan, Y., Hornung, U., Dahmen, N., "Hydrothermal liquefaction of sewage sludge for biofuel application: a review on fundamentals, current challenges and strategies", *Biomass Bioenergy* 165: 106570 (2022).

[4] Gollakota, A.R.K., Kishore, N., Gu, S., "A review on hydrothermal liquefaction of biomass", *Renew. Sust. Energ. Rev.* 81: 1378–1392 (2018).

[5] Ni, J., Qian, L., Wang, Y., Zhang, B., Gu, H., Hu, Y., Wang, Q., "A review on fast hydrothermal liquefaction of biomass" *Fuel* 327: 125135 (2022).

[6] Prestigiacomo, C., Scialdone O., Galia A., "Hydrothermal liquefaction of wet biomass in batch reactors: critical assessment of the role of operating parameters as a function of the nature of the feedstock", *J. Supercrit. Fluids* 189: 105689 (2022).

[7] Qian, L., Wang, S., Savage P.E., "Fast and isothermal hydrothermal liquefaction of sludge at different severities: reaction products, pathways, and kinetics" *Appl. Energy* 260: 114312 (2020).

[8] Prestigiacomo, C., Costa, P., Pinto, F., Schiavo, B., Siragusa, A., Scialdone, O., Galia, A, "Sewage sludge as cheap alternative to microalgae as feedstock of catalytic hydrothermal liquefaction processes" *J. Supercrit. Fluids* 143: 251–258 (2019).

[9] de Caprariis, B., De Filippis, P., Petrullo, A., Scarsella, M., "Hydrothermal liquefaction of biomass: Influence of temperature and biomass composition on the bio-oil production" *Fuel* 208, 618–625 (2017).

[10] Faeth, J.L., Valdez, P.J., Savage, P.E., "Fast hydrothermal liquefaction of Nannochloropsis sp. to produce biocrude" *Energy Fuels* 27: 1391–1398 (2013).

[11] Di Lauro, F., Balsamo, M., Solimene, R., Salatino, P., Montagnaro, F., "Hydrothermal liquefaction process to obtain sludge-derived bio-fuels: setup of the experimental apparatus and preliminary tests" *Chem. Eng. Trans.* 92: 475–480 (2022).

METHANATION OF SYNGAS FROM BIOMASS GASIFICATION: SMALL-SCALE PLANT DESIGN IN ASPEN PLUS™

B. Ciccone[*,*], F. Murena[**], G. Ruoppolo[*], M. Urciuolo[*], P. Brachi[*]**
biagio.ciccone@stems.cnr.it
* Istituto di Scienze e Tecnologie per l'Energia e la Mobilità Sostenibili, Consiglio Nazionale delle Ricerche, P. le V. Tecchio, 80, 80125 Napoli, Italy
**Dipartimento di Ingegneria Chimica, dei Materiali e della Produzione Industriale, Università degli Studi di Napoli "Federico II", P. le V. Tecchio, 80, 80125 Napoli, Italy
*** Dipartimento di Scienza Applicata e Tecnologia (DISAT), Politecnico di Torino, C.so Duca degli Abruzzi 24, 10129, Torino, Italy

Abstract
The goal of this paper is to investigate the upgrading of low-quality syngas from biomass gasification processes into a methane-rich gas stream. The Aspen Plus software package has been used to simulate and compare several plant designs. Reactor sizing and performance are also discussed. Results show that a system with four adiabatic fixed-bed reactors, inter-cooling, and enhanced water removal guarantees an acceptable performance-cost trade-off. An operating pressure of 5 bar has been found to be adequate to reduce the catalyst mass required and to prevent solid carbon deposition. A 99.4% CO conversion, 89.3% CO_2 conversion, and 95.6% CH_4 yield have been achieved, with a final methane molar content of 26.4% and a calorific value of 9.41 MJ/Nm^3.

Introduction
Fossil fuels have been the driving force behind industrial progress due to their cheap costs, high energy-to-volume ratio, and ease of storage and transport. However, they are not sustainable energy sources [1], and their increased exploitation has resulted in a significant rise in CO_2 emissions and negative environmental impacts [2]. To reconcile modern society's expanding energy demands with a sustainable approach to industrial growth, worldwide research on renewable energy utilization drastically increased in the last century. In 2020, renewable energy overtook fossil fuels for the first time, marking a "landmark moment in the history of the EU" [3]. Biomass-derived energy generation has recently gained interest as a promising alternative energy source. Biomass conversion can be achieved through thermochemical, biochemical, and mechanical processes. Gasification is the most intriguing thermochemical pathway for biomass conversion since it produces a versatile syngas, which can be used for the generation of energy (heat/power) as well as for chemical synthesis [4]. Large-scale centralized gasification facilities would not be

ideal for efficient bioenergy generation and waste disposal. Indeed, due to the low bulk densities, most biomass is quite voluminous, resulting in high transportation and storage costs [5]. Thanks to small-scale plants, biomass exploitation might be helpful in improving energy supply in remote places [6]. Catalytic methanation can be used to upgrade syngas produced by biomass gasification. The benefits of synthetic natural gas (SNG) include its high conversion efficiency, interchangeability with natural gas, existing transportation infrastructure (methane pipelines), and proven and efficient end-use technologies.
The aim of this work was to design and simulate a methanation system that employs syngas from a small-scale biomass gasification as raw feedstock using the Aspen Plus software. Different methanation plant schemes were compared, and a sensitivity study was performed to examine the impact of different operating parameters on system performance.

Materials and methods

Aspen Plus™ was used to model the conversion of syngas to bio-methane, with the syngas composition retrieved from an experimental study [7] where biomass gasification with air was performed using a small-scale commercial fixed-bed downdraft gasifier in a micro-CHP plant. Table 1 shows the dry-basis syngas composition adopted in the simulations.

Table 1. Dry-basis syngas composition.

Component	[v/v%] d.b.
CO	15.9
CO_2	9.16
CH_4	1.24
H_2	12.2
N_2	61.5

Thermodynamic analysis. The Aspen Plus RGibbs model was used to perform thermodynamic calculations. In addition to the species reported in Table 1, also water and solid carbon were declared among the simulation compounds. The Peng-Robinson equation of state was chosen as property method because it is suited to describe non-polar or mildly polar gas mixtures under various temperature and pressure conditions. First, a sensitivity study allowed to investigate the trend in the conversion of CO and CO_2, along with the methane and the solid carbon yield, as the reactor temperature and pressure varied (100-1000°C and 1-15-30 atm). Then, leaving the pressure set at 1 bar, the process performance was also evaluated varying the reactor temperature (10-1000°C) and with the amount of added hydrogen as parameter (0 kg/h, stoichiometric conditions, 15% excess).
Kinetic model. The kinetic model by Xu and Froment [8] on a Ni/$MgAl_2O_4$-spinel

catalyst (15.2% Ni) is widely applied in the field of methanation reactor simulation and modeling [9]. The Langmuir-Hinshelwood-Hougen-Watson (LHHW) equations by Xu and Froment consider the CO and CO_2 methanation reactions and the Water-Gas Shift (WGS) reaction. The kinetic of solid carbon formation is not modeled. The kinetic model was validated by comparing simulation results with industrial data reported by Khorsand et al. [10]. Relative errors were always less than 10% suggesting that the model is appropriate.

Reactor sizing & system design. Methanation reactors were simulated using the Aspen RPLUG model, which describes perfect plug-flow reactors in steady-state conditions. Axial mass and heat transfer are assumed to be negligible. The Ergun equation was selected to estimate the pressure drops through the catalytic bed. It was decided to simulate methanation reactors using a single-tube option since the focus is on small-scale applications. The catalyst parameters used in the simulations were taken from Matthischke et al. [11], who refer to a commercial Ni/Al_2O_3 catalyst with sphere-shaped particles. Namely, catalyst particle diameter was 3 mm, bed porosity was 0.39, particle density and bulk density were 1475 kg/m^3 and 900 kg/m^3 respectively.

To set the values of the large number of degrees of freedom of the investigated system, general empirical restrictions gathered by Woods [12] were considered, involving an outlet temperature limit of 550°C to mitigate catalyst sintering and deactivation, a turbulent particle Reynolds number (>100) and an axial Peclet number bigger than 2. Because the purpose of the process is to achieve equilibrium conversion, the length of the reactor was assumed equal to the minimum length needed to achieve thermodynamic equilibrium increased by 20 to 40% as a safety factor. Different plant schemes were considered and simulated, namely:

- a single stage methanation system,
- a single stage recycle reactor,
- a series of FBRs (fixed-bed reactors),
- a system with water condensation.

Sensitivity study & optimization. A sensitivity study was conducted to assess the impact of different parameters (namely, plant pressure, reactor's inlet temperature, condenser location) on plant performance and catalyst mass required.

Results and discussion

Thermodynamic analysis. The thermodynamic analysis allowed to select the proper operating conditions for the process. The main findings can be summarized as follows:

- Low temperature and high pressure favour thermodynamic conversion of the reactants to products, but pressure higher than 8 bar does not give substantial advantage,
- the $H_2/(CO+CO_2)$ ratio should be very close to the stoichiometric. A low hydrogen concentration leads to a low methane production and a significant

amount of solid carbon can deposit on the catalyst surface.

Figure 1 clearly emphasizes how stoichiometric condition are beneficial to obtain high methane yields while mitigating catalyst fouling.

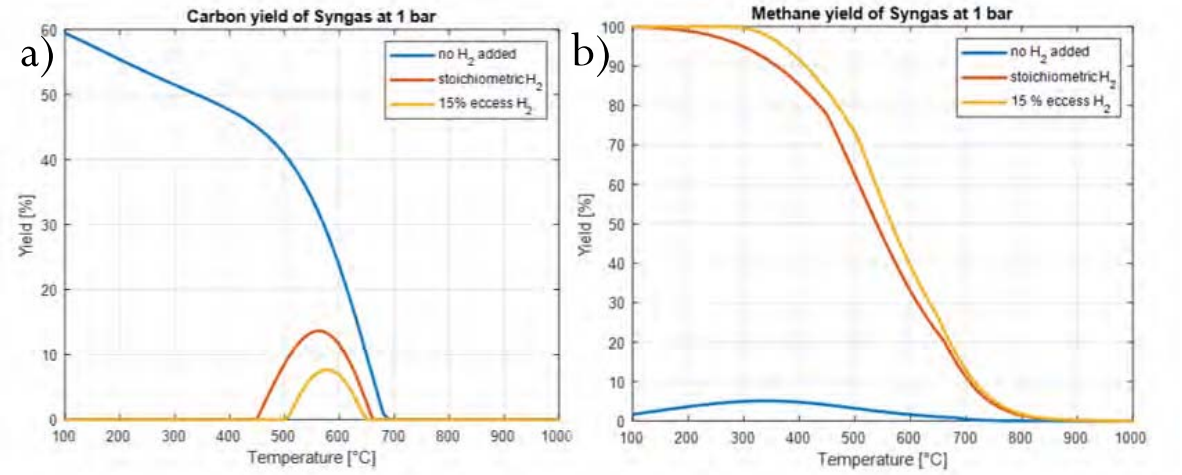

Figure 1. Solid carbon yield (a) and methane yield (b) as functions of reaction temperature and amount of added hydrogen.

Reactor sizing & system design. The multistage adiabatic plant consisting of 5 fixed-bed reactors in series with three condensers- shown in Figure 2- was the end point of the analysis.

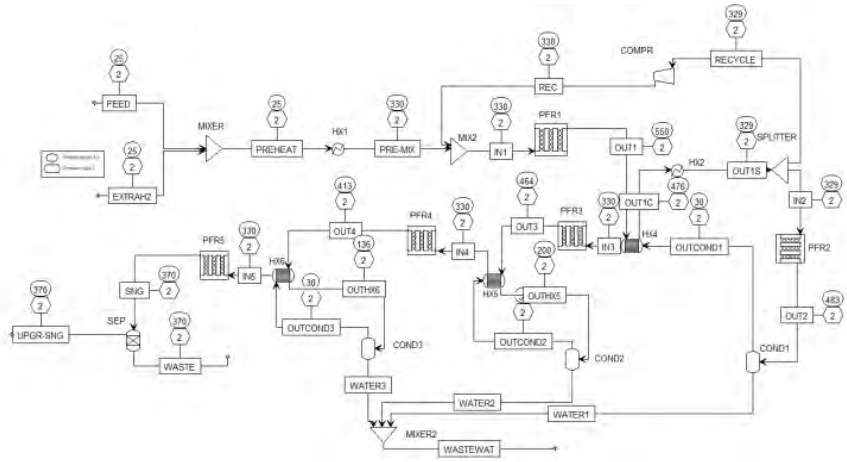

Figure 2. Flowsheet of a multi-stage adiabatic methanation system with inter-condensation.

According to the thermodynamic analysis, water removal can improve the performance of the system by shifting thermodynamic equilibrium toward the products, leading to higher methane generation. The system showed in Figure 2 allowed to achieve a global CO and CO_2 conversion of 99.7% and 90.8% respectively, with an overall methane yield of 96.6%.

Sensitivity study & optimization. The main results of the sensitivity study can be

summarized as follows:

- the 5th reactor in Figure 2 gives little contribution to the overall conversion of carbon oxides while requiring great amount of catalyst; therefore it can be deleted,
- higher pressures mildly favor methane yield but increase catalyst requirements,
- a reactor inlet temperature of 350°C instead of 330°C helps reducing catalyst requirements while having little effect on CO_x conversion,
- a single condenser located after the third reactor is more economically viable compared to the three condensers of Figure 2. Indeed this configuration minimizes catalyst mass while guaranteeing adequately high CO_2 conversions.

Finally, an optimal system characterized by four stages, reactor inlet temperatures of 350°C, an operating pressure of 5 bar, an outlet temperature from the recycle fixed-bed reactor of 550°C, and a single condenser located after the third adiabatic stage was identified. A molar recycle ratio of 2.8 allows having an outlet temperature from the recycle reactor of 550°C. With a total catalyst mass of 20 kg, the optimized system achieves a 99.4% CO conversion, an 89.3% CO_2 conversion and an overall methane yield of 95.9%. Figure 3 illustrates the flowsheet of the optimized plant scheme and Figure 4 shows the CH_4 volume fraction (%) vs. Temperature chart, which summarizes the conversion steps from syngas to SNG.

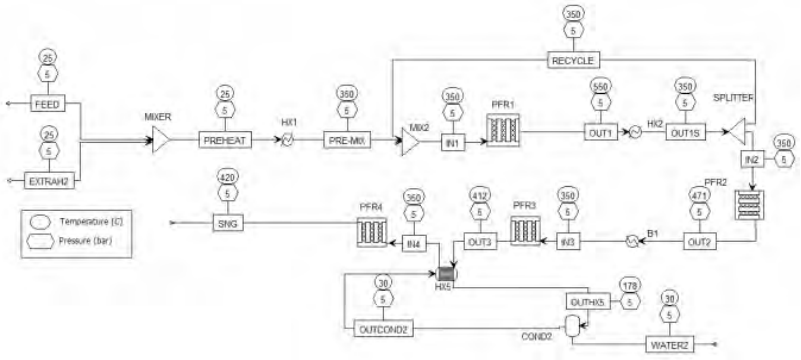

Figure 3. Aspen Plus flowsheet for the optimized system.

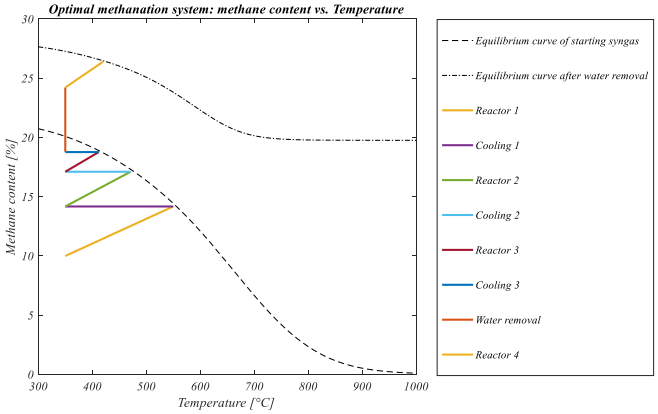

Figure 4. CH_4 content vs Temperature chart for the optimized adiabatic operation.

Conclusion. The research for new clean energy sources is a compulsory necessity worldwide, and biomass can play a key role in the present de-carbonization effort. Methanation is an intriguing method of generating clean energy and storing fluctuating renewable energy as chemical energy. The development of novel catalysts that are more adaptable and resilient against sulfur poisoning and carbon deposition, as well as research into more efficient reactor concepts that can achieve higher performance, are just a few of the issues that come up during the design and construction of biomass-to-SNG plants and to which the future research should devote its attention.

References

[1] Zaman, K., Moemen, M.A., "Energy consumption, carbon dioxide emissions and economic development: evaluating alternative and plausible environmental hypothesis for sustainable growth", *Renew. Sust. Energ. Rev.* 74: 1119-1130 (2017)

[2] Patel, N., "Environmental and economical effects of fossil fuels" *J. Recent Res. Eng. Tech.* 1: 1-12 (2014)

[3] Agora Energiewende & Ember, "The European Power Sector in 2020: Up-to-Date Analysis on the Electricity Transition" (2021)

[4] Jun, K. W., Roh, H. S., Kim, K. S., Ryu, J. S., Lee, K. W., "Catalytic investigation for Fischer–Tropsch synthesis from bio-mass derived syngas", *Appl. Catal. A-GEN* 259.2: 221-226 (2004)

[5] McKendry, P., "Energy production from biomass (part 1): overview of biomass", *Bioresour. Technol.* 83.1: 37-46 (2002)

[6] Ren, J., Liu, Y.L., Zhao, X.Y., Cao, J.P., "Methanation of syngas from biomass gasification: An overview", *Int. J. Hydrog. Energy* 45.7: 4223-4243 (2020)

[7] Cirillo, D., Di Palma, M., La Villetta, M., Macaluso, A., Mauro, A., Vanoli. L., "A novel biomass gasification micro-cogeneration plant: Experimental and numerical analysis", *Energy Convers. Manag.* 243: 114349 (2021)

[8] Xu, J., Froment, G.F., "Methane steam reforming, methanation and water-gas shift: I. Intrinsic kinetics", *AIChE J.* 35.1: 88-96 (1989)

[9] Ronsch, S., Schneider, J., Matthischke, S., Schluter, M., Gotz, M., Lefebvre, J., Prabhakaran, P., Bajohr, S., "Review on methanation- From fundamentals to current projects", *Fuel* 166: 276-296 (2016)

[10] Khorsand, K., Marvast, M.A., Pooladian, N., Kakavand, M., "Modeling and Simulation of methanation catalytic reactor in ammonia unit", *Pet. Coal.* 49.1:46-53 (2007)

[11] Matthischke, S., Roensch, S., Güttel, R., "Start-up time and load range for the methanation of carbon dioxide in a fixed-bed recycle reactor", *Ind. Eng. Chem. Res*. 57.18: 6391-6400 (2018)

[12] Woods, D.R., *Rules of thumb in engineering practice*, John Wiley & Sons, 2007, p. 229-230


THE COMBUSTION INSTITUTE
1954

SESSION V

TURBULENT COMBUSTION


THE COMBUSTION INSTITUTE
1954

DYNAMIC MODELLING OF SUBGRID SCALAR DISSIPATION RATE IN PREMIXED AND PARTIALLY PREMIXED FLAMES WITH DIFFERENTIAL FILTER

G.Ferrante*, I.Langella*
g.ferrante@tudelft,nl
* Faculty of Aerospace Engineering, Delft University of Technology,
Department of Flight Performance and Propulsion
2629 HS Delft, The Netherlands

Abstract
Two test-filtering approaches for LES, based on algebraic and differential equations, are tested for flame configurations at different levels of turbulence. The analysis shows that the differential filter, unlike the algebraic one, is able to mimic also situations of weak turbulence, at the expense of a computational cost up to three times higher.

Introduction
Accurate and cost-effective modelling approaches are required to aid the design of new-generation gas turbines, able to meet the low-emissions targets set by the Paris agreement. Computational fluid dynamics is a powerful tool to predict the complex flow features within this design process. Among various techniques, LES represents a viable compromise between affordable computational cost and accurate prediction of the turbulent flow field. In a LES only large scales are resolved, with models to mimic the effect of the small, subgrid scale (SGS) motions. Since combustion is a small-scale phenomenon [1], the turbulence-combustion interaction must be modelled in a LES. An overview of different modelling approaches for LES of reacting flows can be found elsewhere [1].

The present work focuses on a flamelet-based combustion modelling approach with presumed probability density function (PDF). In this approach, a database of one-dimensional laminar premixed freely-propagating flames (flamelets) is used to describe all possible thermochemical states of the mixture. This database is accessed using a set of controlling variables, namely a Favre-filtered progress variable $\tilde{c}$, mixture fraction $\tilde{\xi}$, and their respective variances $\sigma^2_{c,sgs}$ and $\sigma^2_{\xi,sgs}$, whose Favre-filtered transport equations are directly solved in the LES (e.g. see [2, 3]). In this framework, the progress variable SGS scalar dissipation rate (SDR), $\tilde{\varepsilon}_c$, was shown to be a critical parameter for the correct estimation of $\sigma^2_{c,sgs}$. This term represents the unresolved part of the filtered SDR $\widetilde{N_c}$:

$$\bar{\rho}\widetilde{N_c} = \bar{\rho}\widetilde{D_c}(\nabla\tilde{c}\cdot\nabla\tilde{c}) + \bar{\rho}\widetilde{\varepsilon_c} \quad (1)$$

where $\bar{\rho}$ is the filtered density and $\widetilde{D_c}$ is the filtered diffusion coefficient of c̃. Models for $\widetilde{\varepsilon_c}$ are commonly proportional to the SGS variance and can be written in general form:

$$\widetilde{\varepsilon_c} = \frac{f_1 \sigma_{c,sgs}^2}{\beta_c} \tag{2}$$

where β_c is a modelling constant and f_1 is a function that can be more or less complex, and generally depends on turbulence and combustion parameters. Past works have shown that this function needs to account for the dissipation of both SGS turbulent and reactive processes and therefore simple approaches such as the linear-relaxation model are not suitable for this quantity [4]. In the present study the model originally proposed in [5] and then adapted for LES in [2, 4, 3] is used, and the reader is referred to these works for further details. The model constant β_c depends on flame curvature, diffusion and reaction processes, and is generally scale-dependent. Its choice is of crucial importance to obtain the correct estimation of SGS variance. Note that these considerations are generalizable also for the combustion constants in different modelling approach, although they may signify different processes. Thus, while the use of a static value of the combustion constant may lead to good results, it requires an accurate preliminary tuning. Furthermore, the value might need to change in space and time for cases where the aforementioned processes or the numerical mesh (thus the LES filter) is not homogeneously distributed, and for such case a single constant value might not be suitable.

Relatively recently, scale similarity assumptions for modelling parameters such as flame wrinkling and flame surface density have been proposed and investigated, e.g. see [6, 7, 8, 9]. Dynamic models based on the scalar dissipation rate have been also investigated [10, 2]. Although these models were observed to work on different regimes, the assumption of scale similarity is arguable for reacting quantities, and it is unclear whether the application of dynamic modelling leads to correct estimation of the modelling constant. An example was provided in [11], where it was discussed that on unstructured meshes the classical test-filter approaches based on Gaussian shapes lead to excessive noise and incorrect results due to the pseudo-Fourier condition [12]. Nevertheless, to the best of the authors' knowledge, a thorough investigation of the influence of the test filter in dynamic modelling for combustion LES still does not exist. In the present work we aim to fill this knowledge gap by investigating different techniques for test filtering, and testing the outcomes on two different configurations at different level of turbulence, in or- der evaluate the performance for different turbulent kinetic energy spectra. In particular, classical test-filtering approaches are compared to the so-called differential filters, where the general test filtered quantity $\hat{\tilde{\phi}}$ is obtained through the resolution of a differential equation rather than the direct application of a Gaussian filter. This class of filters has been commonly used for non-reacting flows (e.g. see [13]), but not for reacting cases. In this work we discuss advantages and limitations of these from both

modelling and computational cost sides. The analysis suggests that algebraic formulation only are acceptable at relatively high turbulence levels, while differential formulation provides good estimations for a much wider range of conditions and mesh type at the cost of a relatively marginal increase of computational effort.

Test cases and numerical details

For the analysis in the present work, two test cases are selected. The first, Case A, is the lean premixed, bluff-body stabilized flame studied in [14]. In this set-up, a low bulk velocity stream of (5 m/s) of methane/air mixture with at equivalence ratio 0.75 and inlet temperature of 300K is issued into a cylindrical duct with confinement ratio of $R_{out}/R_{in} = 2$ (see Figure 1a). This configuration leads to moderate levels of turbulence in the bluff body wake, where a recirculation zone is formed, which is ad hoc to compare the ability of the dynamic models for relatively narrow energy spectrum. The second case (Figure 1b), Case B, is the lifted partially premixed case in hot vitiated coflow developed by Dibble et al. [15]. The set up consists of a central nozzle issuing a fuel mixture composed of 25% H_2 and 75% N_2 in volume. The bulk velocity of the fuel stream is 107 m/s. This second case is therefore characterized by higher Re and a relatively wide turbulent kinetic energy.

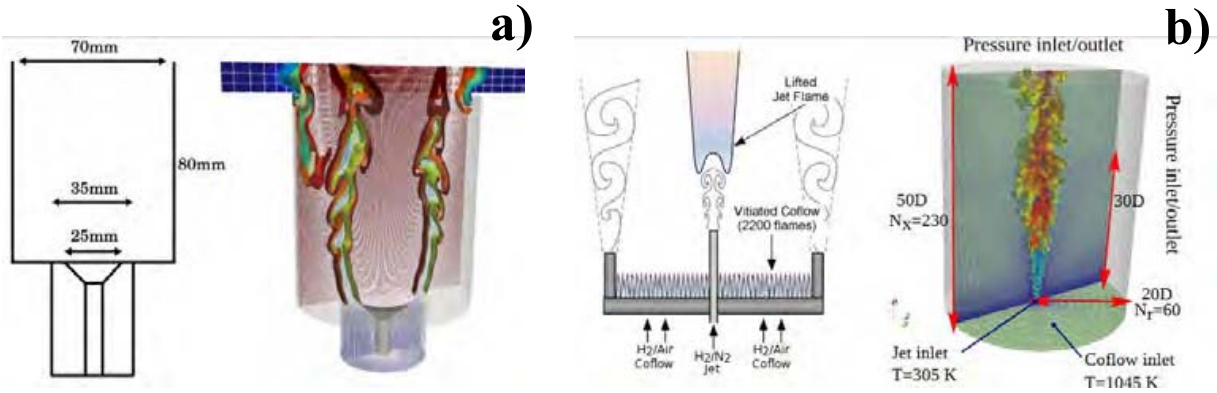

Figure 1. Sketch and numerical domain of the two test cases.

The hot coflow (1045 K) is composed of the products (H_2O, O_2 and N_2) of lean H_2/air flame at an equivalence ratio of $\phi = 0.25$. The two cases are simulated using an in house solver developed in OpenFOAM, which uses a low-Mach approximation and the PISO loop to solve the reacting Navier-Stokes equations along with the four transport equation for the controlling variables discussed in Sec. 1. An implicit Euler scheme is used for time marching along with a time step ensuring that the CFL number is everywhere below 0.3. Second order schemes are used for the spatial gradients, with Gamma limiters in the region of the flame where strong gradients are present. The mesh accounts to 2.5 and 0.9 million cells respectively for cases A and B, and are refined within the flame region to have a ratio between filter size and laminar flame thickness of about 1. Note that these meshes are structured, in order to avoid including additional uncertainty that one would have by the introduction of

unstructured meshes, as discussed in [11]. Unstructured meshes will be explored in a future study.

Test cases and numerical details

Case A (bluff body), which is a weakly turbulent case, is analysed first. By looking at Fig. 2b, when the algebraic filter is used the dynamic procedure is not able to describe the local variations of the combustion model constant β_c across the flame region. The distribution of β_c assumes a bimodal distribution between the imposed boundary values, and $\beta_c \to 0$ in most of the domain (note that β_c in the numerical algorithm is truncated to $\varepsilon > 0$ to avoid a division by zero). This results in erroneous high values of the sub-grid SDR, and consequent low values of subgrid variance, which in turn implies the flame behaves as a laminar flame. This is not the case for this configuration, as could be observed from the OH-LIF images reported in [14]. Previous studies [16] highlighted the importance of the flame turbulence interaction, describing how the flame assumes a laminar-like behaviour close to the base of the bluff body and contributes to turbulence generation further downstream in the shear layer. From the comparison with the calculated non-reacting flow field, the flame appears to damp the weak turbulence generated in the shear layer around the bluff body, as a result of thermal expansion. The flame shape and regime can be qualitatively appreciated from the temperature fields in Fig. 2. On the other hand, the use of the differential filter results in a better calculation of β_c which now assumes a range of different local values across the flame front, and consequently higher values of $\sigma^2_{c,sgs}$ are obtained in the flame region. Note that also in this case the presence of the flame dumps the turbulence at the base of the bluff body, when compared to the non-reacting case (not shown). However, the formation of instabilities sustaining the turbulent structures in the shear layer can be observed further downstream. Test case B (jet flame in hot coflow) is analysed next. In this case the use of an algebraic Gaussian test-filter does not lead to a total failure of the numerical algorithm as for Case A. As can be seen from Fig. 2, the β_c field appears very similar to that predicted by The reason may be traced back to the higher level of turbulence associated with the high bulk velocity of the fuel jet. Overall, the local values of $\sigma^2_{c,sgs}$ are about 40% higher than the maximum values calculated in case A. This result suggests that the dynamic evaluation of β_c is less sensitive on the choice of the test filter at high turbulence. However, the different stabilization mechanism and combustion mode (purely premixed/partially premixed) might also affect the choice of test filter, and this will be investigated in a future study. Next, a scalability test on the 2.5 million cells mesh of case A is carried out to assess the additional computational cost of solving for the differential test filter. The results, reported in Fig. 3, show a 125%-370% computational time increase in seconds per iteration. One can thus conclude that for cases at high level of turbulence, differential filters might not be worth, although one has to be careful of quasi-laminar regions near the anchoring point [16]. Differential filters, however, allow to deal with these

quasi-laminar situations and thus are more versatile. Note also that the present analysis was based on qualitative considerations. Quantitative considerations will be presented in a future study.

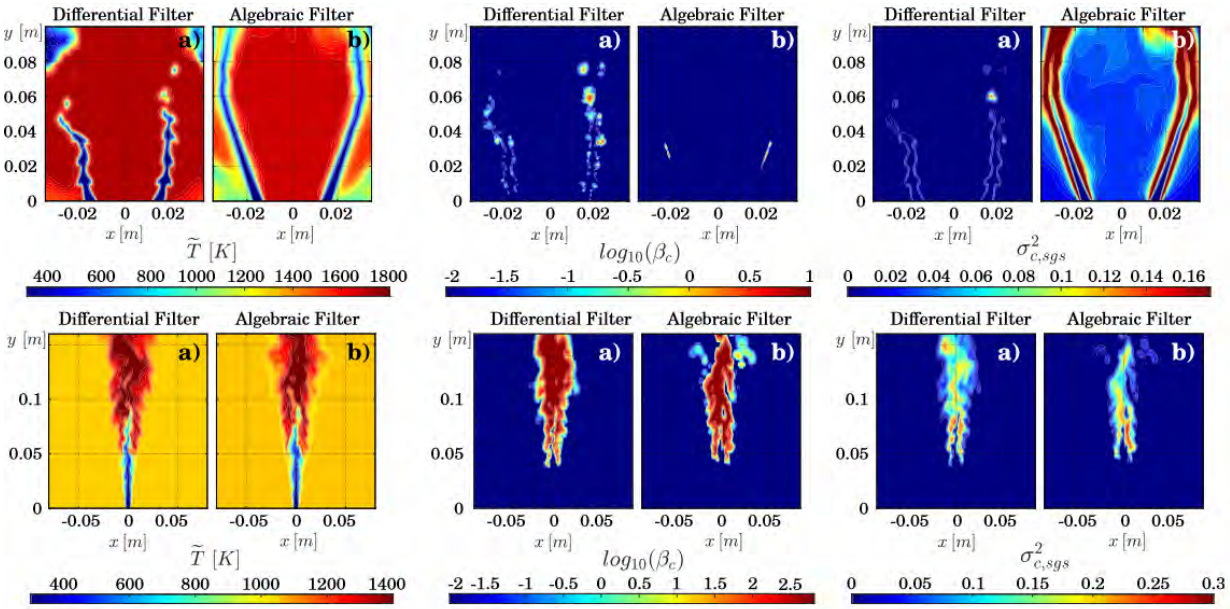

Figure 2. Comparison between instantaneous fields of temperature (left), combustion model constant (centre) and SGS variance of progress variable (right), as predicted using the algebraic and differential filters. Case A is shown on top, Case B on the bottom.

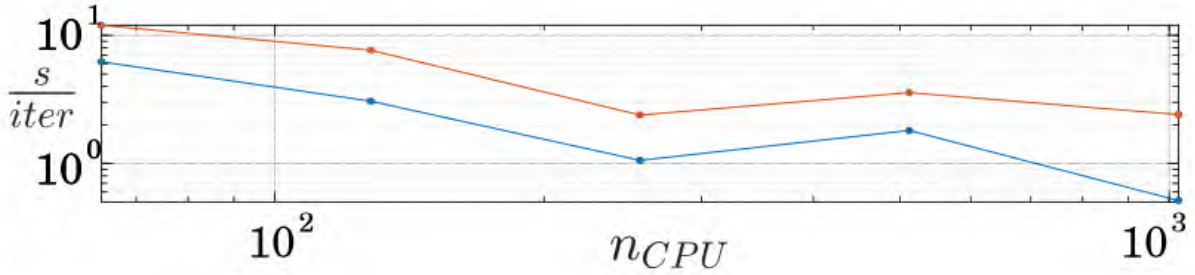

Figure 3. Scalability test: β_c computed via differential (red line) and algebraic (blue line) test filter.

References

[1] T. Poinsot and D. Veynante, Theoretical and Numerical Combustion. T. Poinsot, D.Veynante.

[2] I. Langella, N. Swaminathan, Y. Gao, and N. Chakraborty, “Assessment of dynamic
closure for premixed combustion large eddy simulation,” Combust. Theory Model., vol. 19, no. 5, pp. 628–656, 2015.

[3] I. Langella, Z. X. Chen, N. Swaminathan, and S. K. Sadasivuni, “Large-eddy

simulation of reacting flows in industrial gas turbine combustor," J. Propul. Power, vol. 34, pp. 1269–1284, 2017.

[4] I. Langella and N. Swaminathan, "Unstrained and strained flamelets for LES of premixed combustion," Combust. Theor. Model., vol. 20, pp. 410–440, 2016.

[5] T. Dunstan, Y. Minamoto, N. Chakraborty, and N. Swaminathan, "Scalar dissipation rate modelling for Large Eddy Simulation of turbulent premixed flames," Proc. Combust. Inst., vol. 34, no. 1, pp. 1193–1201, 2013.

[6] F. Charlette, C. Meneveau, and D. Veynante, "A power-law flame wrinkling model for les of premixed turbulent combustion, part ii: dynamic formulation," Combust. Flame, vol. 131, pp. 181–197, 2002.

[7] R. Knikker, D. Veynante, and C. Meneveau, "A dynamic flame surface density model for large eddy simulations of turbulent premixed combustion," Phys. Fluids, vol. 16, p. 91, 2004.

[8] E. Knudsen and H. Pitsch, "A dynamic model for the turbulent burning velocity for large eddy simulation of premixed combustion," Combust. Flame, vol. 154, no. 4, pp. 740–760, 2008.

[9] H. Pitsch, "Large-eddy simulation of turbulent combustion," Annu. Rev. Fluid Mech., vol. 38, pp. 453–482, 2006.

[10] Y. Gao, N. Chakraborty, and N. Swaminathan, "Dynamic closure of scalar dissipation rate for large eddy simulations of turbulent premixed combustion: A direct numerical simulations analysis," Flow Turbul. Combust., vol. 95, pp. 775–802, 2015.

[11] P. Volpiani, T. Schmitt, and D. Veynante, "A posteriori tests of a dynamic thickened flame model for large eddy simulations of turbulent premixed combustion," Combust.Flame, vol. 174, pp. 166–178, 2016.

[12] V. Moureau, P. Domingo, and L. Vervisch, "From large-eddy simulation to direct numerical simulation of a lean premixed swirl flame: Filtered laminar flame-pdf modeling," Combustion and Flame, vol. 158, no. 7, pp. 1340–1357, 2011.

[13] G. I. Park, M. Bassenne, J. Urzay, and P. Moin, "A simple dynamic subgrid-scale model for LES of particle-laden turbulence," Phys. Rev. Fluids, vol. 2, p. 044301, 2017.

[14] J. Dawson, R. Gordon, J. Kariuki, E. Mastorakos, A. Masri, and M. Juddoo, "Visualization of blow-off events in bluff-body stabilized turbulent premixed flames," Proceedings of the Combustion Institute, vol. 33, no. 1, pp. 1559–1566, 2011.

[15] R. Cabra, T. Myhrvold, J. Y. Chen, R. W. Dibble, A. N. Karpetis, and R. S. Barlow, "Simultaneous laser Raman-Rayleigh-LIF measurements and numerical modeling results of a lifted turbulent H2/N2 jet flame in a vitiated coflow," Proc. Combust. Inst., vol. 29, pp. 1881–1888, 2002.

[16] J. C. Massey, I. Langella, and N. Swaminathan, "Large eddy simulation of a bluff body stabilised premixed flame using flamelets," Flow, Turbulence and Combustion, vol. 101, pp. 973–992, 2018.

High-fidelity investigation of FGM and TFM approach on a lean hydrogen flame

M. Amerighi*, P.C. Nassini*, A. Andreini*, C. O. Paschereit**
matteo.amerighi@unifi.it
*Heat Transfer and Combustion Group – University of Florence
**Hermann-Föttinger-Institute – Berlin Institute of Technology

Abstract
Climate change due to carbon emissions is one of the aspects that must be kept under control nowadays. In this fashion, the employment of hydrogen as fuel provides a fundamental solution for both power generation and transportation since lean premixed combustions allow to reset the carbon emissions and limit the NOx ones. The present work aims to study through two different numerical approaches a technically premixed hydrogen flame experimentally investigated at the Berlin Institute of Technology (TUB). The comparison with the experimental data shows the treatment employed drastically influences the obtained outcomes.

Introduction
Hydrogen combustion systems are nowadays studied and developed by many companies and universities since their employment as fuel is considered a valid alternative to reach net-zero CO_2 emission by 2050 [1]. Specifically, lean premixed or technically premixed configurations [2-3] are of great interest because they allow to control the temperature in the primary zone to limit the NOx emissions.
However, lean conditions can drastically increase the flashback and lean blow-off risk. Moreover, hydrogen is characterized by a higher mass diffusivity with respect to the thermal one which can impact both its dynamics and stabilization mechanism since it modifies the flame response to the stretch. This effect is referred in the literature as preferential diffusion [4].
From a numerical point of view, proper modeling is not straightforward since different aspects must be considered.
A strategy can be found in the tabulated chemistry approach in which through a detailed reaction mechanism a look-up table is generated and queried at runtime using the selected control variables and their respective variances. In this way, the reaction occurs as a single-step chemistry, and all the information about the mixing is described with a single variable (e.g., mixture fraction). Without modifications to the original formulation as presented in [5], the preferential diffusion effects are not included.
A second strategy instead can be found in the species transport approach which directly resolves a transport equation for each species involved in the employed reaction mechanism. In this way, each species is characterized by its mass and

thermal diffusivity allowing from a theoretical point of view to include the preferential diffusion effects. Moreover, it is also possible to describe the reactivity of a mixture with different reaction time scales according to the selected reaction mechanism.

The present work aims to assess the results obtained with the aforementioned strategies on a lean, swirl-stabilized, technically premixed hydrogen flame. In the first part of the paper, an explanation of the models employed will be presented. Then, a brief description of the investigated test case will be provided with the numerical strategy used. In the last part of the paper, a detailed comparison of the results obtained and a comparison with the available experimental data will be shown.

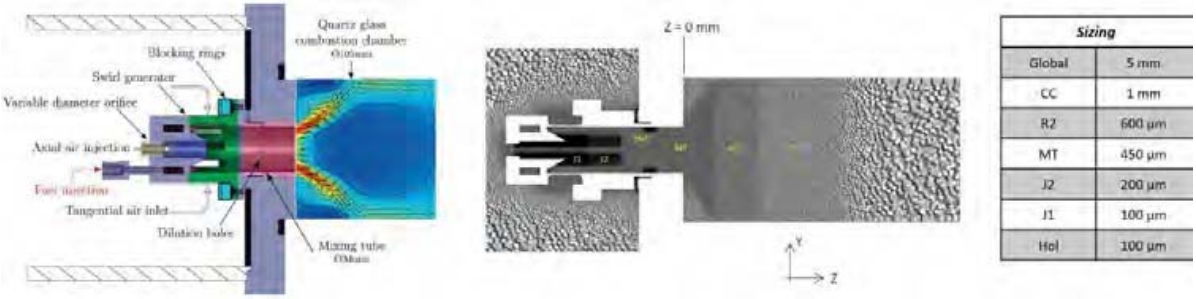

Figure 1. (Left) Experimental test case [3]. (Center-Right) Numerical grid with relative sizing.

Experimental test rig

The rig under investigation is the burner developed during the AHEAD project provided by the Berlin Institute of Technology (TUB) [3] (Fig.1). The quartz combustion chamber has an internal diameter of 104 mm, and it is feds through a mixing tube in which air and fuel mix together reaching technically premixed conditions. The fuel was injected through sixteen holes placed at the bottom of the mixing tube while the air is provided in two different ways. The first one is a pure axial injection characterized by a high momentum aiming to prevent the flashback risk while the second one is a modular swirler which can be adjusted by adding or removing blocking rings. In the present work, the long mixing tube (60 mm) configuration with the maximum axial momentum is analyzed (d_{ax} = 8.8mm and two blocking rings with 7 mm blockage height). The chamber operates under atmospheric conditions with a nominal equivalence ratio of ϕ = 0.6. The air was preheated at 623.15 K and a constant mass flow rate of 130 kg/h feds the plenum while the fuel was provided at 352.15 K. Detailed measurements are available for both non-reactive (PIV) and reactive (PIV and OH-PLIF) conditions. The readers interested in more detailed information about the experimental facilities are referred to [3].

Numerical setup

From a numerical point of view, the commercial pressure-based code ANSYS Fluent 2019R3 is used for all the simulations in the unsteady high-fidelity LES framework. The domain is discretized starting from the air plenum up to the outlet including the swirler, the fuel plenum and the dilution holes located in the middle of the mixing tube. A polyhedral mesh was generated counting roughly 29M elements with ad-hoc refinements at the exit of the axial jet and inside the combustion chamber (Fig.1). For all the simulations, a constant mass flow rate of air and fuel is imposed at the inlet patches, whereas constant pressure is prescribed at the outlet. All the other surfaces are representative of solid walls, so the no-slip conditions are imposed with an adiabatic condition since no information is available for the thermal boundary.
The effect of unresolved eddies is modeled using the Dynamic Smogorinsky-Lilly formulation which dynamically evaluates the Smagorinsky constant. For the tabulated chemistry simulation (named FR in the following), the Flamelet Generated Manifold (FGM) [4] with two control variables (mixture fraction Z and progress variable c) is used to account for the turbulence-chemistry interaction. The un-normalized progress variable is defined as $Y_c = Y_{H_2O} - Y_{H_2}$as deeply explained in [6]. For the laminar look-up table generation, several premixed freely propagating flames were calculated using the detailed ELTE reaction mechanism.
For the species transport simulation instead, the Thickened Flame Model (TFM)[7] is used in which the thermal thickness was described with 5 points. The thickening is dynamically applied only in a narrow band of the flame front thanks to a sensor factor and the sub-scale wrinkling effects were retrieved with the Colin [7] efficiency function. The Boivin mechanism [8] (9S with 12R) is used to describe the reactivity and a mixture-average approach is adopted to evaluate the mass diffusivity according to the kinematic theory. A constant time step of $1.0 \times 10^{-06} s$ is used for both simulations ensuring a convective Courant number below 10 in the zones of interest.

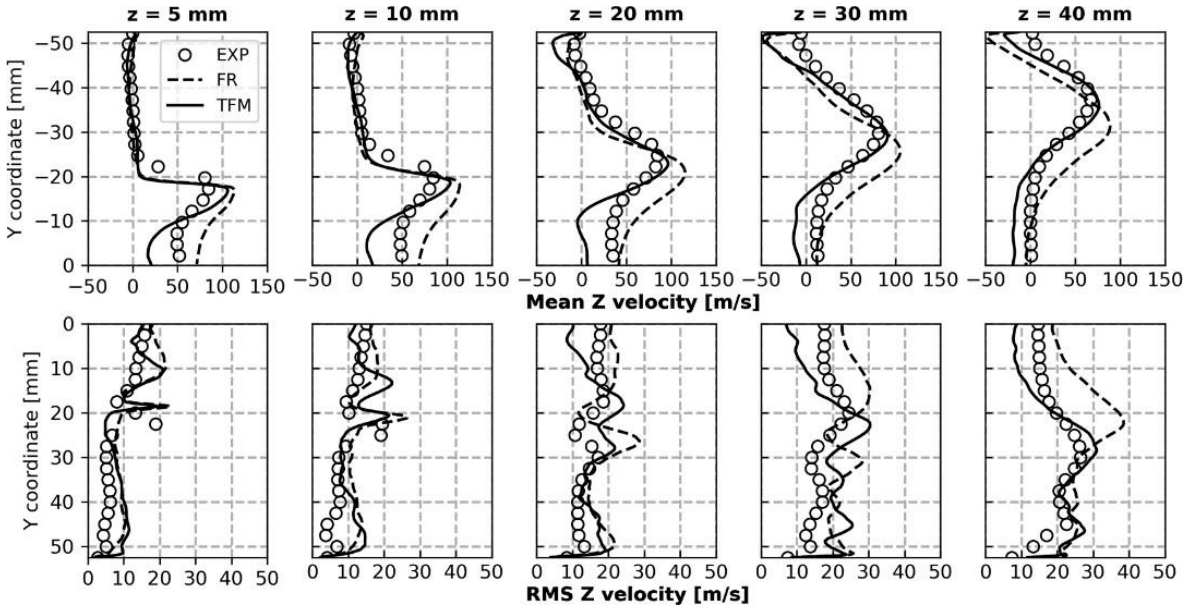

Figure 2. Comparison of mean (top) and rms (bottom) axial velocity profiles.

Results

In this section, a deep analysis of reactive results obtained with the FR and TFM models will be presented. The validation of the non-reactive flow field with a mesh sensitivity is not reported here for the sake of brevity, the reader interested in more details about that is referred to [6]. A comparison in terms of mean and root mean square of axial velocity on five heights inside the combustion chamber is reported in Fig.2. A very good agreement with the experimental data can be pointed out for both simulations at all stages.

It is important to highlight a better prediction of the flow field of the TFM simulation especially at high stages in which the correct opening of the swirling jets is well reconstructed. This is probably caused by the lower velocity at the exit of the mixing tube with respect to the FR case which increases the actual swirl number. Thanks to the local refinements generated in the reaction zone, also the velocity fluctuations in the axial direction are well reconstructed by the simulations even if the FR case slightly overestimates the experimental one.

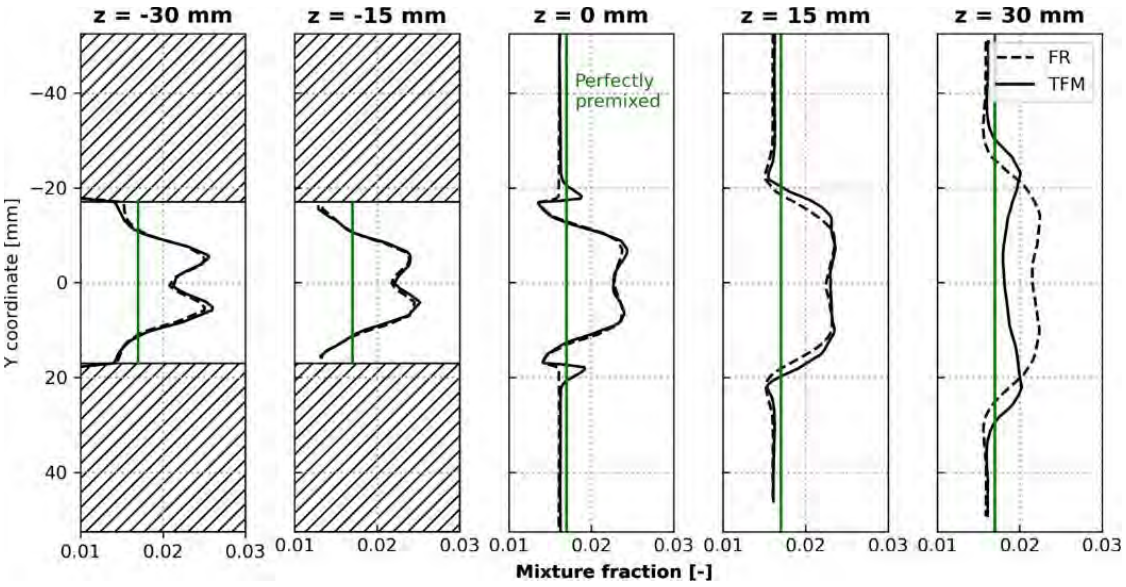

Figure 3. Mean mixture fraction profiles at different heights.

Moving to the mixing process, the mean mixture fraction distribution over five stages across the burner is reported in Fig.3. It is important to highlight that no differences appear between the models inside the mixing tube even if the FR equations are written with the Unity Lewis assumption. This confirms that the preferential diffusion effects affect only the zones in which the reactions take place, as can be observed at the exit of the mixing tube (z = 0 mm, y ≈ ± 20 mm) in which the TFM retrieves a peak of mixture fraction, as will be better explained later. In the plots are also superimposed a green line at the nominal value ($\phi = 0.6$) at which the rig operates. Even in the long mixing tube configuration, only at z > 30 mm the nominal composition is retrieved, showing the technically premixed condition at which the burner operates.

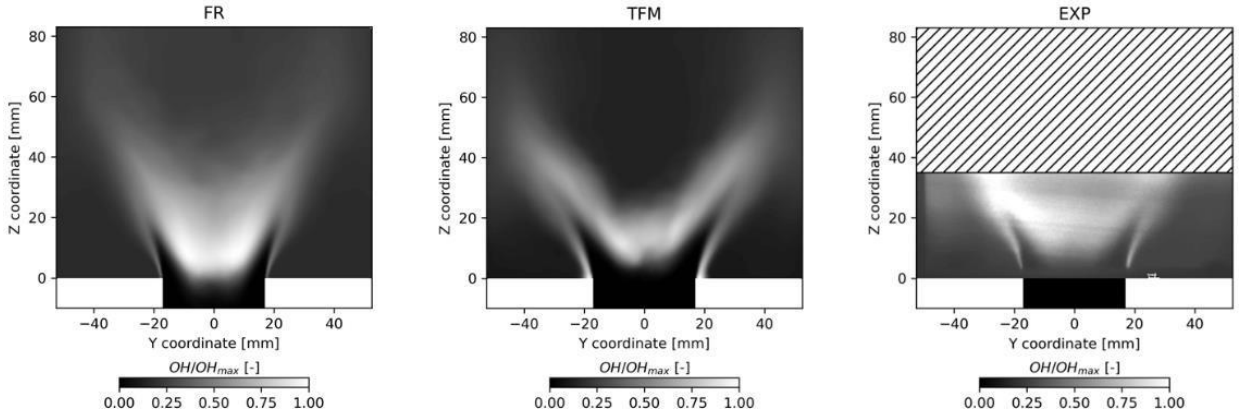

Figure 4. Normalized OH mass fraction distribution.

To validate the flame shape, a comparison in terms of normalized OH mass fraction is performed in Fig.4 in which the numerical maps are compared with the normalized OH-PLIF image (cropped above 35 mm to highlight the stabilization zone). In the FR solution, the flame stabilizes around the exit of the mixing tube due to the higher reactivity of the numerical approach employed. However, from the TFM simulation, the correct flame position and shape are retrieved with respect to what was observed experimentally. In both cases, the flame is attached to the mixing tube exit corner which is probably related to the adiabatic conditions imposed in such walls, as pointed out in [9]. It is also important to highlight the high reactivity observed in such zones from the TFM simulations due to the preferential diffusion effects which locally create a richer mixture (with respect to the FR value, see again Fig.3).
To better investigate this phenomenon, the local temperature probability density functions over the mixture fraction are reported in Fig.5 for the two simulations. A black isoline of the equilibrium temperature computed from its relative reaction mechanism is superimposed in the plots. Histograms of both quantities are also reported dividing the region between the Inner (ISL) and Outer (OSL) Shear Layer. The first observation that can be drawn by analyzing the histogram is the clear presence of a second peak of reactions that occur on the OSL in the TFM results.

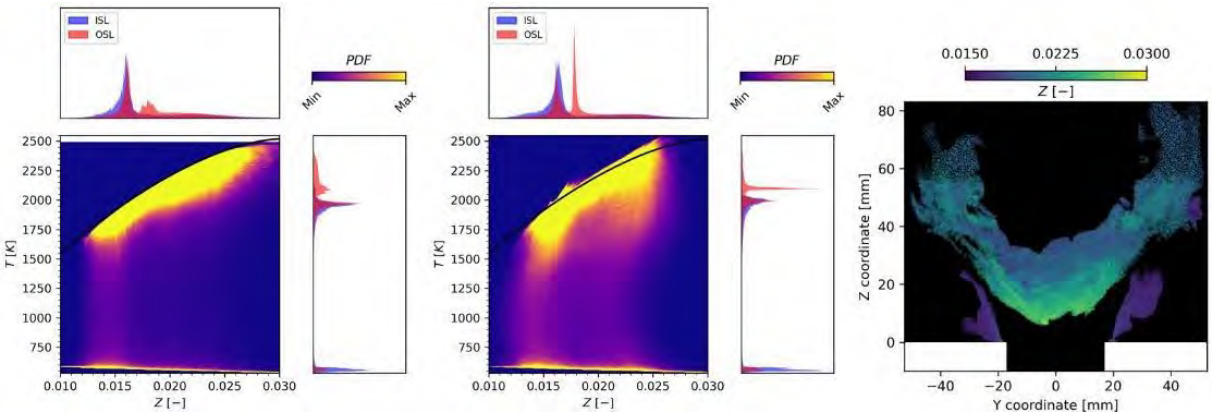

Figure 5. (Left-Center) 2D PDF of temperature and mixture fraction for FR and TFM respectively. (Right) Conditioned scatter plot of mixture fraction for TFM.

Moreover, it is possible to point out how the maximum temperature is always below the equilibrium one in the FR simulation according to the PDF. Instead, in the TFM case, some zones of the domain reach a temperature higher than the one at the equilibrium. This phenomenon is referred in the literature as super-equilibrium and occurs due to the preferential diffusion effects (which act on the high-strain regions [4]). To localize such points, in the last plot of Fig.5 a conditioned scatter plot colored by the local mixture fraction is reported (points with $T > T_{eq}$). In this way is possible to see that the first region (Z ≈0.017) is located on the outer shear layer (where the strain is higher) as previously mentioned while the second one, at a higher mixture fraction (Z>0.02), is located on the stabilization zones in the ISL.

Conclusion

In the present work, a technically premix, swirl-stabilized hydrogen flame is numerically investigated through high-fidelity Large Eddy Simulations. Two turbulence combustion models based on different approaches are tested and the results are compared with the available experimental data provided by the TUB. The TFM model better predicts the flame shape thanks to the inclusion of preferential diffusion effects which locally modify the fuel distribution and flame dynamics.

Nomenclature

c	Progress variable
T	Temperature
Z	Mixture fraction
ϕ	Equivalence ratio

References

[1] Grewe, V., et al., 2021. “Evaluating the climate impact of aviation emission scenarios towards the paris agreement including covid-19 effects”. Nature Communications, 12(1), pp. 1–10.
[2] Pugh, D., Bowen, P., Valera-Medina, A., Giles, A., Runyon, J., and Marsh, R., 2019. “Influence of steam addition and elevated ambient conditions on NO x reduction in a staged premixed swirling NH 3 /H 2 flame”. *Proc. Comb. Inst*, 37(4), pp. 5401–5409.
[3] Reichel, T. G., and Paschereit, C. O., 2017, “Interaction Mechanisms of Fuel Momentum with Flashback Limits in Lean-Premixed Combustion of Hydrogen,” Int. J. Hydrogen Energy, 42(7), pp. 4518–4529.
[4] Van Oijen, J. A., Donini, A., Bastiaans, R. J. M., ten Thije Boonkkamp, J. H. M., and de Goey, L. P. H., 2016, “State-of-the-Art in Premixed Combustion Modeling Using Flamelet Generated Manifolds,” Prog. Energy Combust. Sci., **57**(2016), pp. 30–74.
[5] Mukundakumar, N., Efimov, D., Beishuizen, N., and van Oijen, J., 2021, “A New Preferential Diffusion Model Applied to FGM Simulations of Hydrogen Flames,” Combust. Theory Model., **25**(7), pp. 1245–1267.
[6] Amerighi, M., Nassini, P. C., Andreini, A., Orsino, S., Verma, I., Yadav, R., and Patil, S., 2023. “Assessment of Flamelet Generated Manifold Approach with Inclusion of Stretch effects of Pure Hydrogen Flames”. Proceedings of the ASME Turbo Expo 2023.
[7] Colin, O., Ducros, F., Veynante, D., and Poinsot, T., 2000, “A Thickened Flame Model for Large Eddy Simulations of Turbulent Premixed Combustion,” Phys. Fluids, **12**(7), pp. 1843–1863.
[8] Boivin, P., Sánchez, A. L., and Williams, F. A., 2013, “Four-Step and Three-Step Systematically Reduced Chemistry for Wide-Range H2–Air Combustion Problems,” Combust. Flame, **160**(1), pp. 76–82.
[9] Capurso, T., Laera, D., Riber, E., and Cuenot, B., 2023, “NOx Pathways in Lean Partially Premixed Swirling H2-Air Turbulent Flame,” Combust. Flame, **248**(x), p. 112581.

COMPUTED TOMOGRAPHY OF CHEMILUMINESCENCE USING A SPARSE SENSING FRAMEWORK

A. Procacci*,, R. Amaduzzi*,**, A. Coussement*,**, A. Parente*,****
alberto.procacci@ulb.be
*Aero-Thermo-Mechanics Department, Université Libre de Bruxelles, Av. Franklin Roosevelt 50, Bruxelles, 1050, Belgium
**Brussels Institute for Thermal-Fluid Systems and Clean Energy (BRITE), Université Libre de Bruxelles and Vrije Universiteit Brussel, Pleinlaan 2, Bruxelles, 1050, Belgium

Abstract
The aim of this work is to demonstrate the use of sparse sensing for the prediction of the 3D chemiluminescence field of a flame from the line-of-sight integrated chemiluminescence signal. Sparse sensing is a machine-learning technique that leverages the intrinsic low-dimensionality of physical phenomena to predict the state of the system given few measurements. This makes it a good candidate to be employed in Computed Tomography of Chemiluminescence (CTC), an imaging technique used to reconstruct the 3D chemiluminescence field from chemiluminescence images. The methodology is demonstrated on a virtual experiment based on the data coming from the Large Eddy Simulation of a jet flame in a vitiated coflow, where OH is employed as a surrogate of OH*.

Introduction
Combustion technologies will have to drastically reduce their carbon emissions by adopting zero-carbon fuels to meet the objective set by the European Commission [1]. The introduction of these fuels involves a radical change in the design and operation of combustion system, and the short timeline for the development of these new technologies does not allow a traditional trial-and-error approach.
Luckily, the advancement in combustion modelling [2,3], as well as the development of new diagnostic techniques [4], have produced a set of tools that can be used for the rapid design and validation of new combustion systems. However, these cannot always be transferred from lab-scale to industrial applications.
A simpler diagnostic tool that is extensively used in industrial applications is chemiluminescence [5]. Chemiluminescence is a phenomenon in which light is emitted from excited species produced by chemical reactions. In the context of combustion, chemiluminescence is often associated with the excited species OH* and CH* [6]. The advantage of chemiluminescence over laser diagnostics is that it does not require an external light source, and thus can be employed also when the optical access is limited. The downside lies in the fact that the signal is line-of-sight integrated, resulting in incomplete information about the 3D distribution of the

chemiluminescent sources. To reconstruct the 3D chemiluminescence field, the Computed Tomography of Chemiluminescence (CTC) is generally employed [7]. CTC generally involves the acquisition of multiple 2D chemiluminescence images at different viewing angles, which are combined using tomographic reconstruction algorithms to generate a 3D representation of the chemiluminescence field.
The goal of this paper is to first develop such an algorithm based on sparse sensing, and then to demonstrate its capability by reconstructing the 3D OH field from 2D OH images. Sparse sensing is a machine-learning technique that exploits the intrinsic low-dimensional representation of physical, to predict the state of the system using few measurements. The mathematical framework of sparse sensing was developed by Candes and Tao [8], and techniques for the selection of the optimal sensors' placement were developed by Manohar et al. [9]. Recently, we have successfully applied sparse sensing to the prediction of the 3D temperature field of the ULB furnace given few temperature measurements [10].

Computed tomography of chemiluminescence

The CTC problem is essentially an inversion problem in which the objective is to reconstruct the 3D field $\boldsymbol{f}(x_f, y_f, z_f)$, given its projection on the camera sensor $\boldsymbol{p}(x_p, y_p)$ and the point spread function $\boldsymbol{C}(x_f, y_f, z_f, x_p, y_p)$ that relates the amount of light produced by a point source onto the sensor's plane:

$$\boldsymbol{p} = \boldsymbol{C}\boldsymbol{f} \tag{1}$$

Figure 1 shows a schematic representation of the CTC mathematical framework. In computed tomography, $\boldsymbol{f}$ is usually discretized into n voxels and the light emitted from each voxel is focused by the camera system onto the sensor's plane.
The size s of $\boldsymbol{p}$ depends on the number of pixels in the x_p and y_p directions, as well as on the number of images such that $s = n_{x_p} \times n_{y_p} \times n_i$.
The point spread function depends only on the position and characteristics of the camera system. The computation of $\boldsymbol{C}$ is essentially a ray-tracing problem, where the objective is to compute the path of the light from the source to the observer.
The size of $\boldsymbol{C}$ can quickly become computationally challenging. For example, if the system is discretized using $n = 64 \times 64 \times 64$ and the resolution of the sensor is 512×512 with 5 cameras installed, the size of $C = s \times n = 389120 \times 262144$.

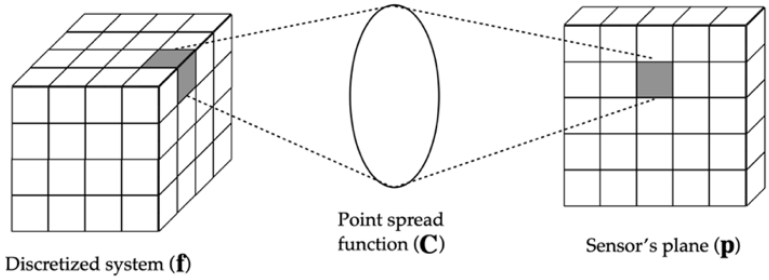

Figure 1. Schematic representation of the CTC mathematical framework.

Sparse sensing

Sparse sensing assumes that physical phenomena admit a low-dimensional representation in a transforming basis. This fact can be leveraged to achieve the prediction of the system's state using a small set of sensors.

The first step in the sparse sensing algorithm is to reduce the dimensionality of the system's state $\boldsymbol{f}$ by finding a transforming basis $\boldsymbol{\Phi}$, such that:

$$\boldsymbol{f} = \boldsymbol{\Phi}\boldsymbol{\psi} \tag{2}$$

where the size r of the low-dimensional vector $\boldsymbol{\psi}$ is much smaller than n.

An obvious choice for computing the transforming basis is to use the Proper Orthogonal Decomposition (POD) [11], because it ensures that the r-order truncation minimizes the l_2 norm reconstruction error.

To compute the POD basis, we can employ the Singular Value Decomposition (SVD):

$$\boldsymbol{F}(r,t) = \boldsymbol{U}(r)\boldsymbol{\Sigma}\boldsymbol{V}^T(t) \tag{3}$$

The matrix $\boldsymbol{F}$ contains m system's states $\boldsymbol{f}$ arranged as column vectors. In our case, $\boldsymbol{F}$ includes multiple timesteps of the 3D chemiluminescence field. The matrix $\boldsymbol{U}$ contains the spatial modes, while the matrix $\boldsymbol{V}$ contains the POD temporal coefficients. The matrix $\boldsymbol{\Sigma}$ is a diagonal matrix containing the singular values, which are a measure of the amount of information captured by each mode.

The linear system in Eq. 1 can be then rewritten as:

$$\boldsymbol{p} = \boldsymbol{C}\boldsymbol{f} = \boldsymbol{C}\boldsymbol{U}\boldsymbol{a} = \boldsymbol{\Theta}\boldsymbol{a} \tag{4}$$

where $\boldsymbol{a}$ is the low-dimensional POD projection of $\boldsymbol{f}$. The matrix $\boldsymbol{\Theta}$ has dimensions $s \times r$, and the conditioning number of this matrix is much lower than the conditioning number of the matrix $\boldsymbol{C}$, provided that some conditions between the placement of sensors with respect to the POD modes are met [12]. This means that the new linear system can be solved by inverting the matrix $\boldsymbol{\Theta}$, using conventional approaches such as least-squares regression.

To improve the prediction accuracy of the low-dimensional projection, physical constraints such as positivity can be introduced, so that the constrained objective function becomes:

$$\begin{aligned} \boldsymbol{a}* = \ & \underset{\boldsymbol{a}}{\operatorname{argmin}} \, || \, \boldsymbol{y} - \boldsymbol{\Theta}\boldsymbol{a} ||_2^2 \\ & \boldsymbol{s.t.} \quad \mathbf{U}_r\boldsymbol{a} > 0 \end{aligned} \tag{5}$$

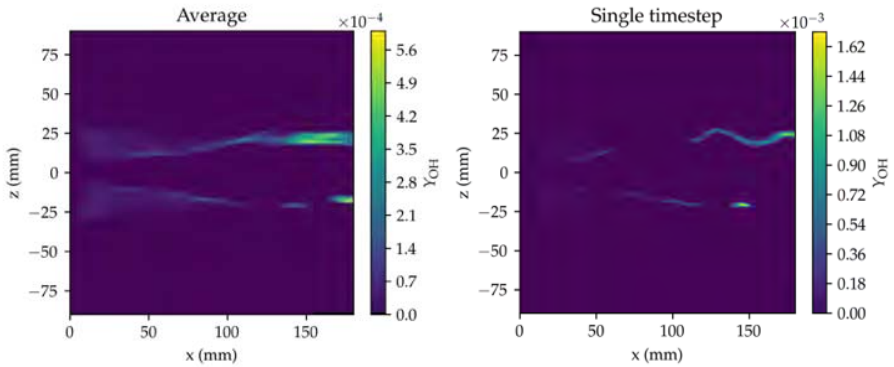

Figure 2. Average and instantaneous OH mass fraction distribution.

Numerical dataset

The numerical dataset comes from the 3D Large Eddy Simulation (LES) of the Jet in Hot Coflow (JHC). The OpenFOAM based, finite-rate solver FiReSMOKE is employed for the simulation. The code solves Favre-filtered mass, momentum and energy conservation equations along with the filtered transport equations for the species. The filtered species source terms are determined from the Partially-Stirred Reactor (PaSR) turbulence-chemistry interaction model [3]. The PaSR model separates each computational cell into a reactive structure where combustion takes place and a surrounding fluid where only mixing occurs.

The simulation domain includes the first 180 mm downstream of the fuel jet exit in the axial direction and 90 mm in the radial direction from the centerline. The domain is discretized as a 3D cylinder structured mesh made of approximately 1.5M cells. We generate inlet turbulence for all three streams using the LEMOS inflow generation method [13]. The inlet profiles for temperature and H_2O, CO_2 and O_2 mass fractions are taken from the experimental measurements in Dally et al. [14].

The kinetic mechanism employed for the detailed reference simulation is the GRI3.0 without the NOx sub-mechanism. It consists of 36 species and 219 reactions. The minimum turbulent kinetic energy resolved in the grid is 80% in every cell and above 90% in most locations of interest.

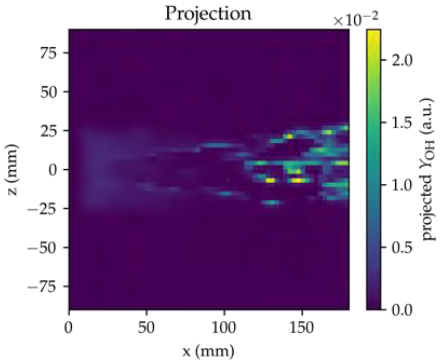

Figure 3. Projection of the instantaneous OH mass fraction distribution on the sensor's plane (p).

Results

The dataset contains 61 timesteps, of which the first 60 were employed as training data to build the POD modes matrix $\boldsymbol{U}$, while the last timestep was used to test the sparse sensing model.

Figure 2 shows the average and instantaneous (last timestep) OH mass fraction distribution. Before computing the SVD, the dataset has been downscaled and interpolated on a $64 \times 64 \times 64$ regular grid, where each voxel has a volume equal to around $22\ \mathrm{mm}^3$.

Figure 3 shows the projection p on the sensor's plane for the last timestep, which is used as input to the sparse sensing model in Equation 4. The obtained prediction is

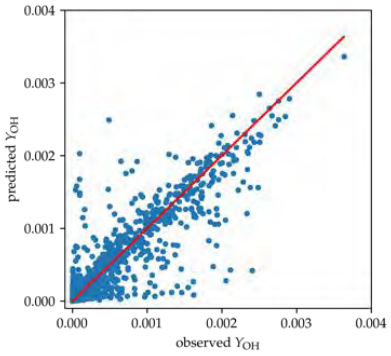

Figure 4. Parity plot of the observed and predicted OH mass fraction distribution. The red line indicates the perfect correlation.

compared to the observed OH mass distribution in the parity plot shown in Figure 4. The prediction is overall accurate with a coefficient of determination $R^2 \approx 0.9$. The comparison between the observed and predicted OH mass distribution for different slices is shown in Figure 5. The model sometimes underpredict or overpredict the pixel values, but the overall distribution is remarkably close to the original one.

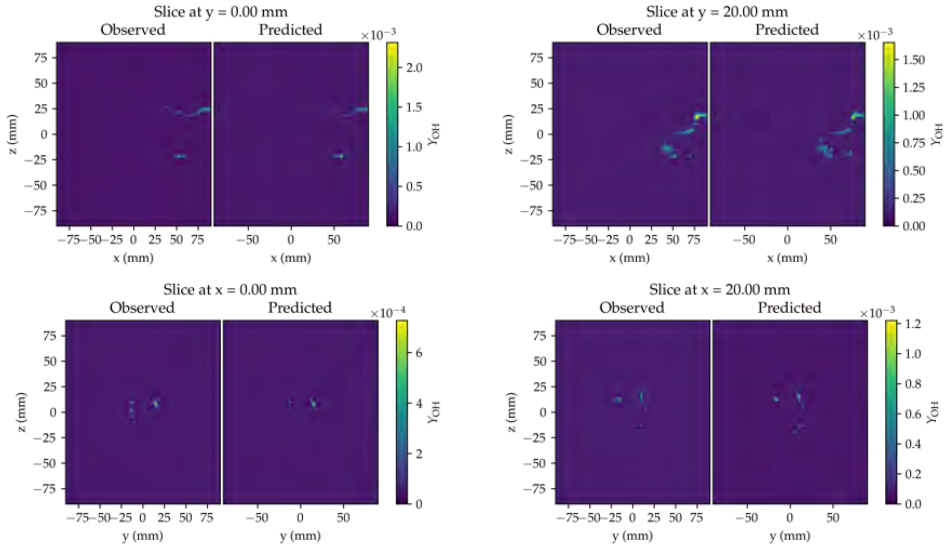

Figure 5. Comparison between the observed and predicted OH mass fraction for different slices.

Conclusions

This work demonstrates how to employ a sparse sensing framework to solve the CTC problem. A 3D LES of the JHC has been used as a synthetic dataset, and the OH mass fraction distribution has been employed as a surrogate for the OH* chemiluminescence signal. The results show that the model can predict the 3D OH field with good accuracy using a single projection, which is much less than what is

generally needed for conventional CTC techniques. This indicates that the proposed technique could be also applied on industrial experiments with very limited optical access. The next step will be to validate this technique on experimentally measured chemiluminescence emissions.

References

[1] European Commission, "A Hydrogen Strategy for a climate neutral Europe" July, 2020.

[2] A. Giusti and E. Mastorakos, "Turbulent Combustion Modelling and Experiments" Flow, Turbul. Combust., vol. 103, no. 4, pp. 847–869, 2019.

[3] A. Péquin, S. Iavarone, R. Malpica Galassi, and A. Parente, "The partially stirred reactor model for combustion closure in large eddy simulations: Physical principles, sub-models for the cell reacting fraction, and open challenges," Phys. Fluids, vol. 34, no. 5, 2022.

[4] K. Kohse-Höinghaus, R. S. Barlow, M. Aldén, and J. Wolfrum, "Combustion at the focus: Laser diagnostics and control," Proc. Combust. Inst., vol. 30, no. 1, pp. 89–123, 2005.

[5] M. J. Bedard, T. L. Fuller, S. Sardeshmukh, and W. E. Anderson, "Chemiluminescence as a diagnostic in studying combustion instability in a practical combustor," Combust. Flame, vol. 213, pp. 211–225, 2020.

[6] A. Procacci, M. Cafiero, S. Sharma, M. M. Kamal, A. Coussement, and A. Parente, "Digital Twin for Experimental Data Fusion Applied to a Semi-Industrial Furnace Fed with H2-Rich Fuel Mixtures," Energies, vol. 16, no. 2, pp. 1–14, 2023.

[7] X. Li and L. Ma, "Capabilities and limitations of 3D flame measurements based on computed tomography of chemiluminescence," Combust. Flame, vol. 162, no. 3, pp. 642–651, 2015.

[8] E. J. Candes and T. Tao, "Near-optimal signal recovery from random projections: Universal encoding strategies?," IEEE Trans. Inf. Theory, vol. 52, no. 12, pp. 5406–5425, 2006.

[9] K. Manohar, B. W. Brunton, J. N. Kutz, and S. L. Brunton, "Data-Driven Sparse Sensor Placement for Reconstruction," 2017.

[10] A. Procacci, R. Amaduzzi, A. Coussement, and A. Parente, "Adaptive digital twins of combustion systems using sparse sensing strategies," Proc. Combust. Inst., 2022.

[11] G. Berkooz, P. Holmes, and J. L. Lumley, "The proper orthogonal decomposition in the analysis of turbulent flows," Annu. Rev. Fluid Mech., vol. 25, no. 1, pp. 539–575, 1993.

[12] S. L. Brunton and J. N. Kutz, Data-Driven Science and Engineering: Machine Learning, Dynamical Systems, and Control. Cambridge University Press, 2019.

[13] N. Kornev, H. Kröger, and E. Hassel, "Synthesis of homogeneous anisotropic turbulent fields with prescribed second-order statistics by the random spots method," Commun. Numer. Methods Eng., vol. 24, no. 10, pp. 875–877, 2008.

[14] B. B. Dally, A. N. Karpetis, and R. S. Barlow, "Structure of turbulent non-premixed jet flames in a diluted hot coflow," Proc. Combust. Inst., vol. 29, no. 1, pp. 1147–1154, 2002.

FLASHBACK IN HYDROGEN-FUELED PERFORATED BURNERS: QUANTIFICATION OF UNCERTAINTIES AND SENSITIVITY TO PARAMETERS

F. Fruzza*, R. Lamioni*, A. Mariotti*, M.V. Salvetti*, and C. Galletti*
filippo.fruzza@phd.unipi.it
*Dipartimento di Ingegneria Civile e Industriale, University of Pisa, Pisa 56126, Italy

Abstract
We use generalized Polynomial Chaos expansion to build a complete map of flashback velocities for CH_4/H_2 mixtures in the space of the relevant variables involved, i.e., hydrogen content, equivalence ratio, and geometry parameters, with a limited number of CFD simulations. Furthermore, we use Stochastic Sensitivity Analysis techniques to provide a quantitative understanding of the influence of the different parameters, and of the interactions between them, on the flashback propensity. The 2D numerical model used for the estimation of flashback velocities mimics a single slit of a real perforated burner typically found in domestic condensing boilers.

Introduction
With a growing interest in hydrogen as a clean fuel for providing heat in residential and commercial sectors, the development of new designs for end-user devices is becoming increasingly necessary to ensure efficiency and safety. These devices are typically equipped with cylindrical or flat perforated burners, working in premixed conditions. Due to the significant differences in the physical properties of natural gas and hydrogen, the design of these burners needs to be revised to avoid excessive burner temperatures and flashback phenomena when burning H_2-enriched mixtures, up to 100% H_2. Despite some experimental data exist on the flashback limits of H_2-enriched mixtures [1,2], and some correlations based on numerical models have been proposed to estimate the flashback velocities of hydrogen in practical configurations [3], a complete understanding of the flashback mechanism in real burners is still lacking. The present work intends to identify and quantify the effects of the various parameters involved in the flashback propensity, to provide useful information for the burner design.

Numerical model
We focus on a multi-slit configuration representing a portion of a real burner typically used in domestic condensing boilers. The computational domain consists of a 2D slit as shown in Fig. 1, where the solid zone corresponding to the burner is in black. The domain extends enough both downstream (*10 mm*) and upstream (*6 mm*) of the solid to be able to enclose the flame even in flashback conditions and

hence avoid the influence of boundary conditions. The slit width is denoted by W, while the distance between two adjacent slits is denoted by D.

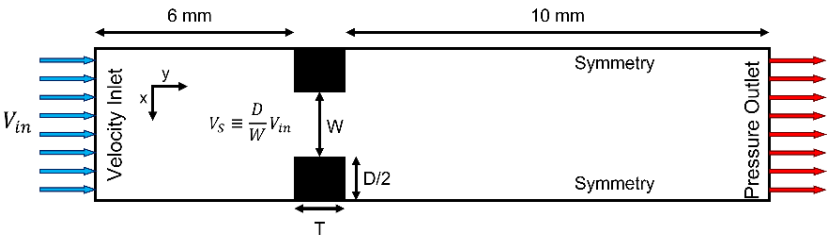

Figure 1: *Computational domain.*

For any variation of W, the distance between the slits D has been varied to keep fixed the porosity of the burner at $W/D = 0.5$. The burner thickness is $T = 0.6\,mm$ for all cases.

The problem may be described by conservation equations for mass, momentum, energy, and transport/reaction equations for the chemical species. Inside the solid domain, we solve the energy equation. The equations are solved on a structured grid, with characteristic cell size in the reaction front region of $25\ \mu m$. We use detailed chemistry, employing the Kee-58 mechanism with 17 chemical species and 58 reversible reactions. Full multicomponent diffusion, Soret diffusion and radiation (Discrete Ordinates (DO) method with weighted-sum-of-gray-gases model) are included. The burner is modeled as a solid with the properties of the stainless steel typically used for this kind of burner. The conjugate heat transfer (CHT) between the fluid and the solid zones is modeled to take account of the interaction between the flame and the burner plate. Uniform velocity and uniform temperature of $T_u = 300\ K$ are set at the gas inlet, while a pressure outlet with $p = 1\ atm$ is imposed at the exit of the domain. The external edges of the domain are modeled as symmetry boundaries to take account of the interaction with the flames from the nearby slits.

Estimation of flashback velocity

To evaluate flashback, we set steady-state simulations using a pressure-based coupled algorithm. Starting from a stable flame with a high inlet velocity, the inlet speed is gradually decreased until a critical velocity is reached for which a stable configuration of the flame is not found: here, we assume that flashback has occurred. The inlet velocity steps used in this procedure are $\Delta V_{in} = 0.1 m/s$, with an additional refinement of $\Delta V_{in} = 0.01 m/s$ when approaching the flashback limit. This method allows us to estimate the flashback velocity for each mixture. We define the *cold-flow* bulk velocity at the slit entry as $V_S \equiv \frac{D+W}{W} V_{in}$, where V_{in} is the uniform inlet velocity, which is the velocity we would have for a cold flow, i.e., neglecting the density variations of the

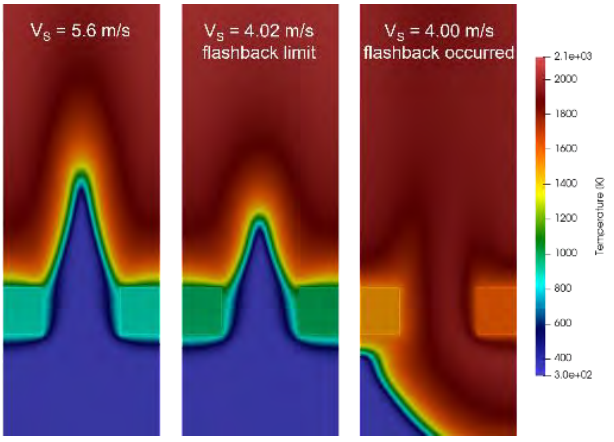

Figure 2: *Temperature profiles for decreasing inlet velocity.*
H_2 content = 95%, ϕ = 0.835, W = 1 mm.

mixture due to the high burner temperatures. We define the flashback velocity V_{FB} as the *cold-flow* bulk velocity at the slit entry, defined in Eq. 1, just before flashback occurs. We show an example of this procedure in Fig. 2. By decreasing the inlet velocity, the flame approaches the hole entry, increasing the burner temperature, until a stable configuration is not found with the flame flashing back into the hole.

Stochastic Sensitivity Analysis

In this work, a Stochastic Sensitivity Analysis is carried out, using the generalized Polynomial Chaos (gPC) method, to investigate quantitatively how the burner temperature at the flashback limit T_B and the flashback velocity V_{FB} are related to the hydrogen content, the equivalence ratio ϕ, and the slit width W. This is done to obtain continuous response surfaces in the parameter space obtained for each couple of parameters, limiting the number of deterministic simulations and, at the same time, preserving a good level of accuracy of the results. Since the input random variables are characterized by a uniform PDF, Legendre polynomials are selected for the gPC. The following ranges of variation are identified for the three parameters: $H_2 \in [80\%, 100\%]$, $\phi \in [0.5,1.0]$, and $W \in [0.5\ mm, 1.2\ mm]$. These intervals were chosen to obtain the largest possible volume in parameter space where the flashback occurs. The polynomial expansion is truncated to the 3rd order in each dimension. Thus, 4 quadrature points are necessary for each variable (Gauss-Legendre points). Analyzing the impact of the parameters two by two and following then a tensor product expansion, 16 simulations are carried out for each analysis to evaluate the stochastic response surfaces for the quantities of interest. The sensitivity of the quantities of interest to a single input parameter or to a combination of them is computed using the variance decomposition method proposed by Sobol [4].

Results: effect of H_2 content and ϕ

The sensitivity analysis of the burner plate temperature at the flashback limit T_B and the flashback velocity V_{FB} is performed as the H_2 content and the equivalence ratio vary in the ranges $H_2 \in [85\%, 100\%]$ and $\phi \in [0.5,1.0]$. The slit width is fixed, being $W = 1\ mm$. We point out again that, lowering ϕ while keeping fixed the H_2 content at 85% or lowering the H_2 content while keeping fixed $\phi = 0.5$, we observe the flame quenching for low inlet velocity, and a flashback velocity cannot be defined. Fig. 3 shows the burner plate temperature map in the parameter space mentioned above and the relative Sobol

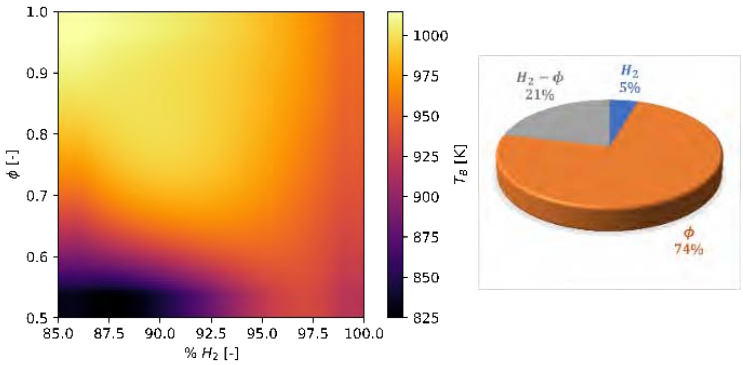

Figure 3: *(a) Stochastic response surface for the burner plate temperature in the parameter space of H2 content and ϕ. (b) Partial sensitivities.*

indices given as percentages. We observe a large variability of the burner plate temperature in the investigated region, with a minimum of $T_B \simeq 825\ K$ for low H_2 content and low ϕ and a maximum of $T_B \simeq 1010\ K$ for low H_2 content and high ϕ. Over most of the domain, the T_B variability is mainly due to the variation of ϕ. This is confirmed by the Sobol indices, with I_ϕ indicating a dependence of 74% on ϕ and I_{H2} indicating a dependence of 5% on the H_2 content. However, approaching 100% H_2, T_B becomes almost independent on ϕ, being $T_B \simeq 950\ K$ for all equivalence ratios. This difference in the sensitivity of T_B to ϕ in different zones of the parameter space is quantified by the interaction Sobol index $I_{H2,\phi} = 21\%$.

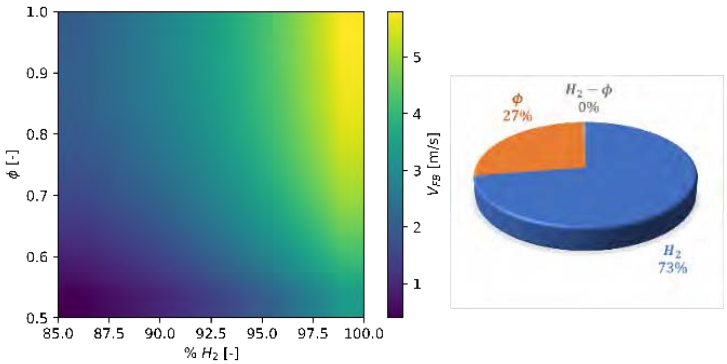

Figure 4: *(a) Stochastic response surface for the flashback velocity in the parameter space of H2 content and ϕ. (b) Partial sensitivities.*

Fig. 4 shows the flashback velocity VFB as a colored map in the H2 content - ϕ space, with the relative Sobol indices. We observe $V_{FB} \in [0.4\ m/s, 2\ m/s]$ for 85% H2 and $V_{FB} \in [3.3\ m/s, 5.8\ m/s]$ for 100% H2. V_{FB} is mainly dependent on the H_2 content, being $I_{H2} = 73\%$, with a weaker but not negligible dependence on ϕ, with $I_{H2} = 27\%$. Moreover, the sensitivity of V_{FB} to the two parameters is uniform all over the domain, as shown by the interaction Sobol index $I_{H2,\phi}$ that is almost zero.

Results: effect of H_2 content and W

A similar analysis is performed by varying the content of H_2 in the range $H_2 \in [80\%, 100\%]$ and the slit width W in the range $W \in [0.5\ mm, 1.2\ mm]$, while keeping a constant equivalence ratio of $\phi = 0.7$. Fig. 5 shows the burner plate temperature map in the parameter space and the relative Sobol indices. We note that T_B is highly dependent on the size of the slit, with higher burner plate temperatures for wider slits, as indicated by the Sobol index $I_W = 72\%$. The maximum burner temperature, which is around 1000 K, is located in the region with $W = 1.2\ mm$ and $H_2 \in [85\%, 90\%]$, while

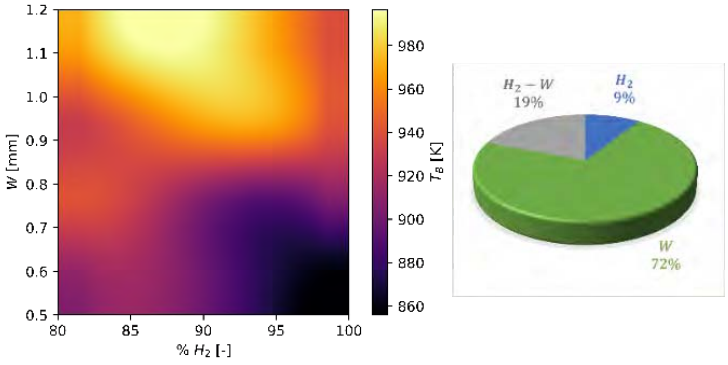

Figure 5: *(a) Stochastic response surface for the burner plate temperature in the parameter space of H_2 content and W. (b) Partial sensitivities.*

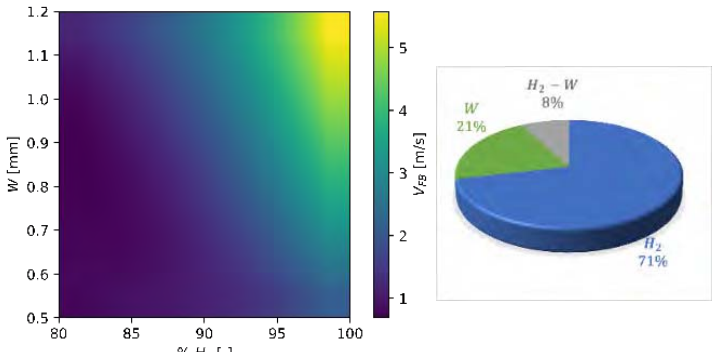

Figure 6: *(a) Stochastic response surface for the flashback velocity in the parameter space of H_2 content and W. (b) Partial sensitivities.*

the minimum burner temperature, $T_B \simeq 860\,K$, is located in the region around $H_2 = 100\%$ and $W = 0.5\,mm$. However, as demonstrated by the interaction Sobol index $I_{H_2,W} = 21\%$, the variation of T_B over the region of interest is not uniform.Fig. 6 shows the flashback velocity V_{FB} as a function of the two input parameters and the relative Sobol indices. As expected, the variation of the flashback velocity depends mainly on the H_2 content, being $I_{H2} = 71\%$. However, the slit width W also affects V_{FB} in a non-negligible way, especially for high H_2 contents, where we observe the flashback velocity varying from $V_{FB} \simeq 2.5\,m/s$ to $V_{FB} \simeq 5.5\,m/s$. We point out that the flashback velocity shows a large variability over the entire domain, with the maximum value, $V_{FB,max} \simeq 5.5\,m/s$, being almost ten times larger than the minimum, $V_{FB,min} \simeq 0.7\,m/s$.

Results: effect of ϕ and W

Finally, the stochastic sensitivity analysis is performed on the last couple of parameters, i.e., the equivalence ratio ϕ and the slit width W, in the ranges $\phi \in [0.5,1.0]$ and $W \in [0.5\,mm, 1.2\,mm]$, with fixed H_2 content $H_2 = 100\%$. The variation of the burner plate temperature T_B in the domain of interest is shown in Figure 7 with the relative Sobol indices. We observe the burner temperature varying uniformly over the parameter space, with T_B increasing when increasing both ϕ and W. The Sobol indices indicate a stronger dependence on W, being $I_W = 66\%$ and $I_\phi = 34\%$. We note that the burner plate temperature varies considerably on the domain, with an increase of ≈ 20% going from the lower-left corner ($T_B \simeq 760\,K$) to the upper-right corner ($T_B \simeq 940\,K$) in Figure 7.

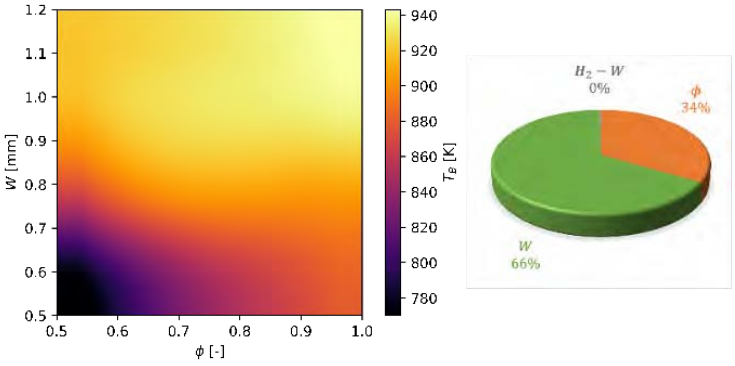

Figure 7: *(a) Stochastic response surface for the burner plate temperature in the parameter space of ϕ and W. (b) Partial sensitivities.*

In Figure 8, we show the flashback velocity V_{FB} as a function of the two input parameters. Even without changing the H_2 content, we observe a considerable variability of the flashback velocity over the conditions analyzed. V_{FB} depends mainly on the slit width W, being $I_W = 75\%$. In particular, we note that V_{FB} doubles as W changes for certain values of ϕ. We also observe a weak dependence of the flashback velocity on the equivalence ratio, indicated by $I_\phi = 16\%$.

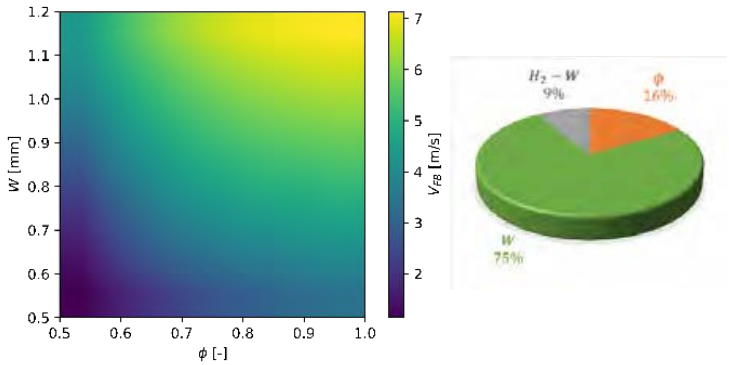

Figure 8: *(a) Stochastic response surface for the flashback velocity in the parameter space of ϕ and W. (b) Partial sensitivities.*

Conclusions

In this work, we used Stochastic Sensitivity Analysis to characterize the dependence of the flashback velocity and the burner temperature at the flashback limit on some relevant mixture and geometry parameters, i.e., H_2 content, equivalence ratio, and slit width. A 2D numerical model encompassing conjugate heat transfer was employed to estimate the flashback velocities and the burner plate temperatures at the flashback limits. By means of gPC, we reconstructed response surfaces of the quantities of interest over domains defined by the three couples of parameters varying in ranges of practical interest. Using a stochastic sensitivity analysis, we obtained the Sobol indices, which quantify the dependence of the quantity of interest on the two parameters and on the interaction of the two. We think the results of this paper can represent a good starting point for the design of new burners, which will have to be able to work in different conditions and with different CH_4/H_2 blends.

References

[1] H. de Vries, A. V. Mokhov, and H. B. Levinsky, The impact of natural gas/hydrogen mixtures on the performance of end-use equipment: Interchangeability analysis for domestic appliances, *Applied Energy 208*, 1007 (2017).

[2] A. Aniello, T. Poinsot, L. Selle, and T. Schuller, Hydrogen substitution of natural-gas in premixed burners and implications for blow-off and flashback limits, *International Journal of Hydrogen Energy* (2022).

[3] F. Vance, L. de Goey, and J. van Oijen, Development of a flashback correlation for burnerstabilized hydrogen-air premixed flames, *Combustion and Flame* 112045 (2022).

[4] I. Sobol', Global sensitivity indices for nonlinear mathematical models and their monte carlo estimates, *Mathematics and Computers in Simulation* 55, 271 (2001).

LES MODELS FOR TURBULENT HYDROGEN FLAMES WITH CONVOLUTIONAL NEURAL NETWORKS

A. Attili*, M.G. D Jansen*, N. Sorace*, M. Bruce*, T. Grenga, L. Nista***, L. Berger***, H. Pitsch*****

antonio.attili@ed.ac.uk

* School of Engineering, Institute for Multiscale Thermofluids, University of Edinburgh, Edinburgh, EH9 3FD, United Kingdom

** Faculty of Engineering and Physical Sciences, Department of Aeronautics and Astronautics, University of Southampton, Southampton SO16 7PX, United Kingdom

*** Institute for Combustion Technology, RWTH Aachen University, 52056 Aachen, Germany

Abstract

Lean hydrogen flames are prone to thermodiffusive instabilities, which have a strong effect on the structure and dynamics of the flame and can enhance flame speed by several times. Conventional combustion models perform poorly for unstable hydrogen flames and often fail in capturing the effects of thermodiffusive instabilities. In this work, the capability of Convolutional Neural Networks (CNN) to model the unclosed reaction rate term in Large Eddy Simulations (LES) of turbulent hydrogen premixed flames is investigated using high-fidelity data from a large-scale Direct Numerical Simulation (DNS). It is shown that the CNN model can accurately reproduce the filtered reaction rate over a large range of filter sizes. Traditional models usually require at least two scalars, e.g., two progress variables or a progress variable and a mixture fraction, to capture the local fluctuations of equivalence ratio caused by thermodiffusive effects; remarkably, the CNN-based model requires only a single progress variable, due to its ability to consider the topology of the three-dimensional progress variable field, which embeds the information regarding the fluctuations of equivalence ratio. Finally, the capability of the CNN to generalize to different filter sizes and filter kernels is investigated.

Introduction

Recent developments in Machine Learning (ML) have granted remarkable success in several challenging tasks and sparked interest into the possibility to use ML in turbulence and combustion modelling. ML models are often based on the idea of training a Neural Network (NN) using high-fidelity data of turbulent (reactive) flows, which result from Direct Numerical Simulations (DNS) or sophisticated experiments. In Large Eddy Simulation (LES) of turbulent premixed flames, the filtered non-linear reaction rate needs to be modelled in terms of the resolved fields. Convolutional Neural Networks (CNN) have been shown to perform remarkably well in approximating the filtered reaction rate [1] and the subgrid flame wrinkling

[2,3]. However, it has been observed in many applications, ranging from speech recognition to medical diagnosis, that ML-based approaches might perform poorly when applied to data that are different from those employed for training. In this work, we investigate the application of CNN-based models for the computation of the filtered reaction rate in hydrogen flames. In addition, we perform a systematic analysis of the effect of the filter size used to filter the data for the training of the Neural Network. This is important in applications, since the filter size in an actual LES is typically strongly inhomogeneous due for example to grid refinement and most likely unknown a-priori since it results from a complex interaction of grid spacing, numerical accuracy, and modelling assumptions.

DNS database

A large-scale DNS of a lean hydrogen flame of Berger *et al.* [4] is used to train the CNN-based models and to verify their performance. The DNS features a jet Reynolds number of Re = 11000 and a Karlovitz number of Ka ≈ 15. The simulation is performed using detailed finite-rate chemistry, non-unity Lewis numbers, and including the Soret effect. A slot turbulent premixed jet flame with equivalence ratio φ=0.4, a temperature of T_u = 298 K and a pressure of 1 bar, surrounded by a coflow of burnt gases, is considered.

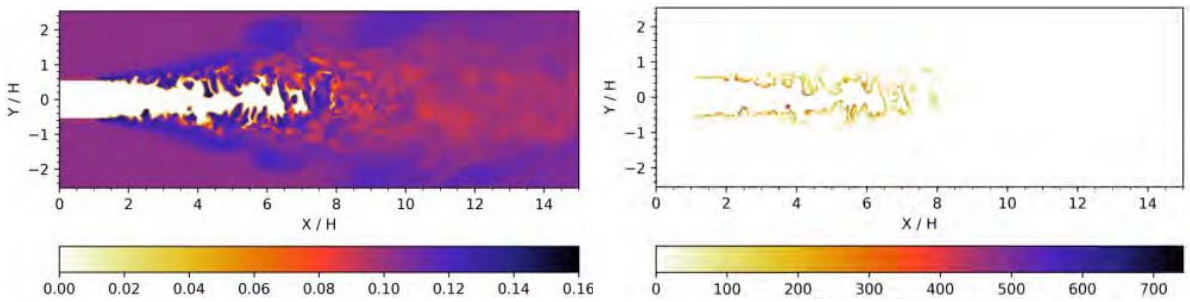

Figure 1. H_2O mass fraction (left) and H_2O reaction rate (right) in the DNS of Berger *et al.* [4] for a turbulent hydrogen flame in a two-dimensional cut of the three-dimensional simulation domain.

Impact of thermodiffusive instabilities and related modelling challenges

Figure [1] shows the mass fraction of water and its reaction rate. The flame is strongly affected by the thermodiffusive instability [4], which causes the typical overshoots of product mass fraction visible in the H_2O mass fraction plot. The thermodiffusive instability is even more evident in the reaction rate, which is very large in regions where the flame surface has positive curvature (convex towards the unburned gas), while the reaction rate is smaller, or even zero, where the curvature is negative. Because of differential diffusion, hydrogen tends to diffuse preferentially towards positive-curvature regions, increasing the local equivalence ratio, which enhances the local reactivity and flame speed for a globally lean flame. A remarkable fact, observed by Aspden *et al.* [5,6] and Berger *et al.* [4], is that turbulence does not cancel-out the impact of thermodiffusive effects, except for the case of very large

Karlovitz numbers [5,6], but turbulence and instability interact synergistically with thermodiffusive effects being even stronger in the turbulent regime than in laminar flames [4]. As shown in Fig. 2, for a methane at similar conditions, [7] the reaction rate is always very close to the one dimensional unstretched laminar flame (flamelet), while there is very large scatter in the hydrogen case.

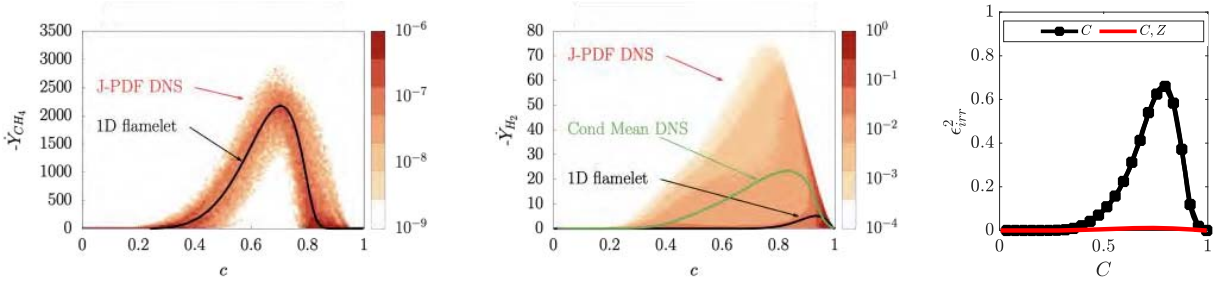

Figure 2. Statistics of the fuel reaction rate for a methane [7] (left) and a hydrogen [4] (center) turbulent flame DNS, compared with a flamelet (one dimensional unstretched laminar flame). Irreducible error for two different parametrizations of the reaction rate in a turbulent hydrogen flame [8].

A direct consequence is that reaction rates in hydrogen flames cannot be parametrized by the progress variable only [8] as usually more than adequate for methane flames [7]. A second variable, such an additional progress variable, a mixture fraction, or curvature, is therefore required to parametrize the local reaction rate. This is quantitatively assessed in Fig. 2, where the irreducible error for the parametrization with only the progress variable C and with the progress variable and mixture fraction Z is also shown.

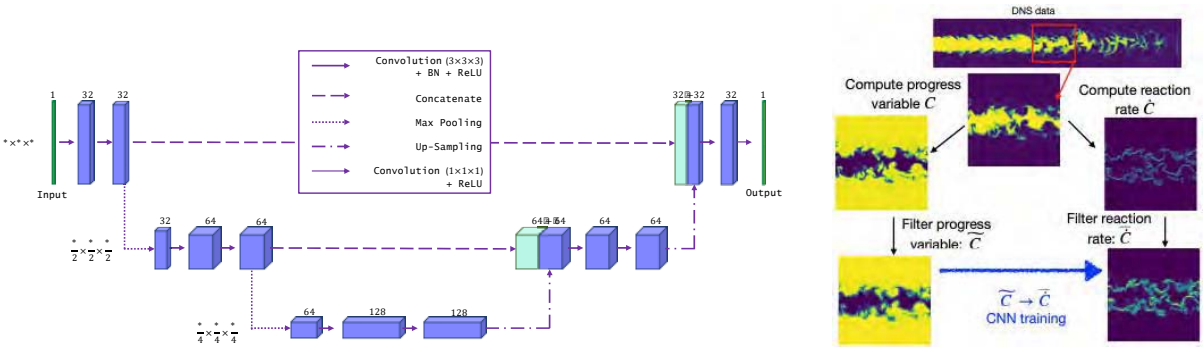

Figure 3. Architecture of the UNET CNN (left) and pipeline to extract and process DNS data and CNN training (right).

CNN-based models

An alternative approach to traditional closures of the filtered reaction rate in LES, is the use of neural networks (NNs). Specifically relevant in the present context are the Convolutional Neural Networks (CNN) employed in approximating the filtered reaction rate by Seltz *et al*. [1] and the subgrid flame wrinkling by Lapeyre *et al*. [2] and Attili *et al.* [3]. A neural network is trained to learn the relation between an input field, in this case the filtered progress variable, and the desired output, the reaction

rate. The data for the NN training need to be obtained from high-fidelity databases, which in the present case are the DNS of the turbulent hydrogen flame. The CNN architecture employed here is shown in Fig 3. A Convolutional Neural Network (CNN) derived from a U-net architecture has been designed to consider (multiple) three- dimensional (3D) input fields, e.g., $\bar{C}$ and $\tilde{Z}$, and provide 3D fields as output, i.e., the filtered reaction rate.

Results

Traditional models for hydrogen flames require to account for the fluctuations of local equivalence ratio. It has been shown that the fluctuations of equivalence ratio correlate with the topology of the progress variable field [4], opening to the possibility to parametrize the reaction rate by adding non-local information of the progress variable field. Being able to learn the relation between 3D fields (filtered or not), CNN-based models could be employed for that. A comparison of two CNN models which employ as input *i)* only the progress variable and *ii)* progress variable plus mixture fraction is shown in Fig. 4. The performance is extremely good in both cases. It is worth noting that the results for the joint probability density function J-PDF are shown in log scale to highlight the very small difference. The accuracy for both models in Fig. 4 are comparable to those shown in Fig. 2 when progress variable and mixture fractions are used and both are largely superior to a local parametrization with only the progress variable. We conclude that a CNN with only the progress variable can be used for the reaction rate in lean hydrogen flames.

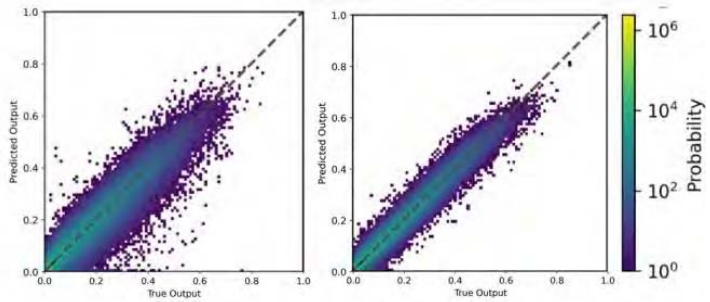

Figure 4. J-PDF of true filtered reaction rate from DNS and predicted values by the CNN models using only the progress variable (left) and the progress variable and mixture fraction (right) as inputs of the CNN. The result is shown for a filter size of $\Delta_{train} = \Delta_{test} = 8\,\Delta$, where Δ is the DNS grid cell size.

When employing ML models for subgrid closure, a critical factor to consider is their ability to extrapolate and generalize. ML models should be able to perform well when the fields used for training are different from the fields on which the model is applied. A requirement is the capability to extrapolate at higher Reynolds number since DNS data used for training cannot be generated at the high Reynolds number that is typical of applications. This aspect is discussed by Attili *et al.* [3] and it is shown that CNN models are capable to extrapolate at higher Reynolds numbers if the Reynolds number of the training data is high enough and the ratio between the

filter size and the Kolmogorov scale of turbulence is properly considered. In this work, we investigate an important aspect related to the size of the filter size. In Fig. 4, the filter size used for training is the same as that used in the model test. In actual LES applications, the filter size can change significantly in the simulation domain, for example due to local grid refinement. Even more importantly, the actual filter size in LES is not known, since it results from a complex combination of grid size, numerical accuracy, and the formulation of the LES model itself. Therefore, it is important to assess how the CNN model performs when the filter size used in training Δ_{train} is not the same as that used when the model is tested Δ_{test}. A summary of this systematic analysis is shown in Fig 5. The model performs extremely well when the training and test filters are the same $\Delta_{train} = \Delta_{test}$, while a large bias is observed otherwise. This challenge is expected, and it must be addressed; otherwise, the model would have limited use in a practical LES setting.

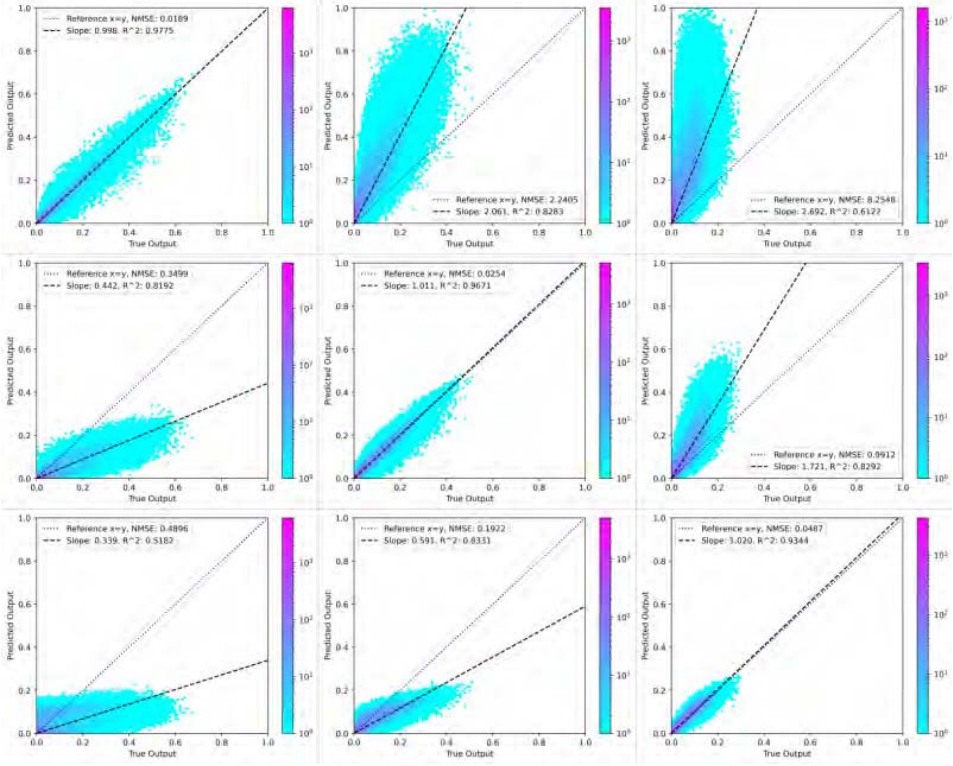

Figure 5. J-PDF of true and predicted values for different combinations of the raining and testing filter sizes. Top to bottom: $\Delta_{train} = 4$, $\Delta_{train} = 8$, $\Delta_{train} = 16$; left to right: $\Delta_{test} = 4$, $\Delta_{test} = 8$, $\Delta_{test} = 16$.

The idea considered here is to train with a collection of fields obtained by filtering DNS data with multiple filter sizes, up to the limit of including data obtained with all possible filter sizes in a certain range. An assessment of this approach is summarized in Fig. 6, where the error for several different models (each line represents a CNN model), obtained by training with different set of data, is shown. When all the possible filter sizes are used for training (blue line in the right graph) the model performs extremely well for all sizes of the filter used in the testing data. As certain filter sizes are progressively removed from the training set, the

performance degrades in the range of Δ_{test} that have not been covered by the training. We conclude that, using multiple filter sizes in training is a viable option to build a model that works for a wide range of filter sizes, and that the model obtained in this way is as good as the model trained with a single filter size and applied to test data with the same filter used for training.

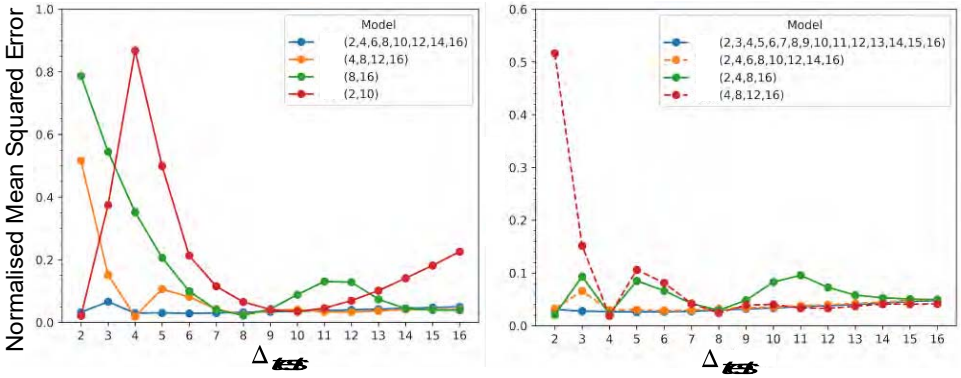

Figure 6. Error for models trained with different combinations of filter sizes and tested for filter sizes ranging from $\Delta_{test} = 2$ to 16. Each line represents a model trained with a collection of data obtained with the set of filters shown in the legend.

References

[1] A. Seltz, P. Domingo, L. Vervisch, Z. M. Nikolaou, "Direct mapping from LES resolved scales to filtered-flame generated manifolds using convolutional neural networks", *Combust. Flame* 210: 71–82 (2019).

[2] C. J. Lapeyre, A. Misdariis, N. Cazard, D. Veynante, T. Poinsot, "Training convolutional neural networks to estimate turbulent subgrid scale reaction rates", *Combust. Flame* 203:255–264 (2019).

[3] A. Attili, et al, "Investigation of the Extrapolation Performance of Machine Learning Models for LES of Turbulent Premixed Combustion", *10th European combustion meeting*. Naples (2021).

[4] L. Berger, A. Attili, H. Pitsch., "Synergistic interactions of thermodiffusive instabilities and turbulence in lean hydrogen flames", *Combust. Flame* 224: 112254 (2022).

[5] A.J. Aspden, M.S. Day, J.B. Bell., "Turbulence–flame interactions in lean premixed hydrogen: transition to the distributed burning regime", *Journal of Fluid Mechanics* 680, 287-320 (2011)

[6] A.J. Aspden, M.S. Day, J.B. Bell., "Towards the distributed burning regime in turbulent premixed flames", *Journal of Fluid Mechanics* 871, 1-21 (2019).

[7] S. Luca, A. Attili, E. Lo Schiavo, F. Creta, F. Bisetti, "On the statistics of flame stretch in turbulent premixed jet flames in the thin reaction zone regime at varying Reynolds number", *Proc. Combust. Inst.* 37 (2019).

[8] L. Berger, A. Attili, J. Wang, K. Maeda, H. Pitsch "Development of Large-Eddy Simulation Combustion Models for Thermodiffusive Instabilities in Turbulent Hydrogen Flames" *Proceeding of the Summer Program, Center for Turbulence Research, Stanford University* pp. 247 (2022).

INVESTIGATIONS ON LEAN TURBULENT PREMIXED HYDROGENATED FLAMES

D. Güleryüz*, C. Allouis, İ. Gökalp*****
dilay.guleryuz@metu.edu.tr
*Middle East Technical University, Ankara; TÜBİTAK Marmara Research Ctr., Türkiye
**STEMS-CNR, Naples, Italy; TÜBİTAK Marmara Research Ctr., Türkiye
***ICARE-CNRS, Orléans, France; TÜBİTAK Marmara Research Ctr., Türkiye

Abstract
Hydrogen's ability to enhance carbon neutrality in combustion processes puts forward the use of hydrogenated fuels. However, hydrogen alters the flame structure by reducing flame thicknesses and heights while raising the flame temperature. Optimizing lean premixed flames is also an approach for achieving efficient and cleaner combustion. Yet, lean premixed flames are prone to instabilities, hence when combined with hydrogen addition, determining the instability limits is crucial. These factors all indicate that hydrogenated fuels should be researched as potential fuels for lean premixed combustion in the future.
In this study, lean premixed turbulent flames of hydrogenated conical methane-air mixtures are investigated experimentally in a high-pressure combustion chamber, Lean methane-air premixed flames with varying hydrogen addition rates up to 20% are investigated with chemiluminescence measurements of OH and CH radicals and Mie scattering. The data is used for investigating the characteristics of the turbulent flame front dynamics.

Introduction
The reduction in carbon emissions forces the research towards low carbon fuels such as hydrogenated fuels in leaner conditions to decrease the emissions in industrial applications; therefore, it is crucial to study the effect of hydrogen addition rates to fossil fuels in high-pressure environments for turbulent premixed flames [1,2]. Non-intrusive techniques such as chemiluminescence measurements and Mie scattering are useful for lean-premixed flames since the chemiluminescence emissions of OH* and CH* radicals are established to be correct representatives of the lean-premixed flames [3] and Mie scattering can be used to track the flame front and measure turbulence characteristics.
In this study, we present the first experiments of the newly installed high-pressure chamber and the turbulent Bunsen burner, working with natural gas-hydrogen mixtures in lean conditions. The details of the experimental setup and the chemiluminescence data from the experiment are discussed. The chemiluminescence data is used for calculating the effect of hydrogen in terms of flame height and turbulent flame speed and the Mie scattering data is used to measure the turbulent flame front characteristics.

Experimental Set-up

The high-pressure combustion chamber is made up of two separate parts, including three windows mounted for optical measurements of the turbulent Bunsen flame generated by the Bunsen burner. The chamber operates between 1 and 9MPa of pressure. At the bottom module, a Bunsen burner with a perforated plate as a turbulence generator is placed. In the bottom chamber module, three quartz windows allow optical measurements of the flame from various angles.

The Bunsen burner presented in this study works with premixed fuels, therefore the gas mixing line is modified accordingly. In the gas supply system, three mass flow controllers control the gas inlet flow rates of air, methane, and hydrogen in the inlet. Through the line, the gas pressure is monitored continuously with pressure transducers in each gas line. The fuel and oxidizer (air)are mixed inside a gas mixer, which is a stainless-steel pipe of 1-inch diameter and 25-inch length filled with glass beads. The static inline mixer has 5 inlets to allow mixtures of air, CH_4, H_2, C_2H_4, and N_2.

The burner is ignited with the help of a continuous pilot flame. The pilot flame is a stoichiometric methane-air mixture for each test case, and the flow rate supplied to the pilot flame is always 13% of the total premixture flow rate in the main inlet. The pilot flame is controlled with another gas line, having two mass flow controllers for air and methane, and has a separate inline static mixer. The pilot flame is always on during the experiments.

Burner and Operating Conditions

A typical image of the investigated flames and the Bunsen burner are shown on Fig.1. The burner allows for measurements of various fuel mixtures. The pilot flame accounts for the stabilization of the lean premixed flame. The diameter of the burner is 25 mm, at the exit. The titanium perforated plate used in this study has 2.5mm holes with a 42% blockage ratio inside the burner.

Figure 1. a. The turbulent premixed flame of 0.8 equivalence ratio with no hydrogen addition. **b.** The burner.

In the experiments, a series of equivalence ratios of 0.6, 0.7, and 0.8 are investigated for molar hydrogen addition rates of 0%, 10%, and 20% to the main which is natural gas in this study. The Reynolds number is kept constant in all experiments, by keeping the inlet premixture velocity at 1.90 m/s.

Chemiluminescence Imaging for Turbulent Flames

Chemiluminescence images are captured using an intensified Dantec HiSense Zyla camera. The line-of-sight images are collected using two filters, namely OH* with a bandpass of 300-325nm and CH* with 420 to 440 nm. The camera exposure time is set as 250ns, while the intensifier gain is 50. In each experiment, 1000 images are collected within 1s. Therefore, the images are collected at 1 ms time intervals. Image processing is performed using MATLAB.

Flame height and the turbulent flame speed are calculated using the chemiluminescence images. The effect of hydrogen addition and equivalence ratio changes are then investigated.

Since chemiluminescence measurements provide line-of-sight measurements, the inverse Abel transform is performed to find the 2D images from 3D images, using the Fourier-based Abel inversion technique, which is previously done for projecting radial 2D distribution to a 1D measurement [5]. The postprocessing method applied to the chemiluminescence images are summarized in Fig. 3.

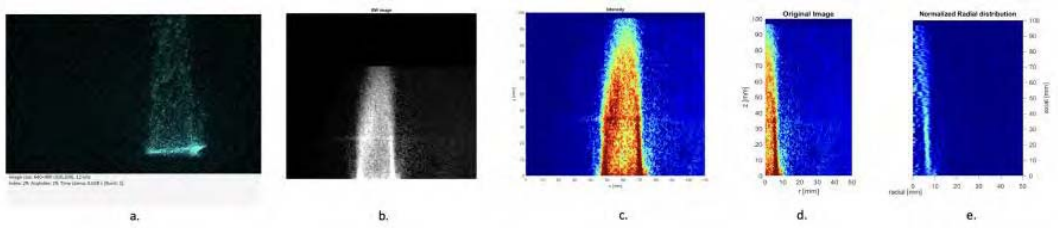

Figure 3. a. The raw image from the CCD camera. **b.** Scaled and binarized image. **c.** The chemiluminescence intensity. **d.** Radially averaged and axially symmetric flame image. **e.** Inverse Abel transformed flame.

Both OH* and CH* radicals can be used to indicate the flame front, but in this study, the CH* signals are used as an indicator of the heat release rate, and therefore to estimate the progress variable. The inverse Abel-transformed flames are normalized according to the maximum light intensity values of CH* and presented in Figs. 4-6.

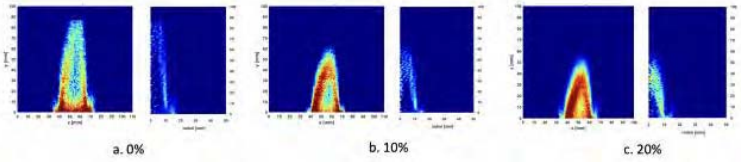

Figure 4. Normalized radial intensity (top) and intensity (bottom) values for 0.6 equivalence ratio for a. 0%, b. 10% and c. 20% of H2 addition.

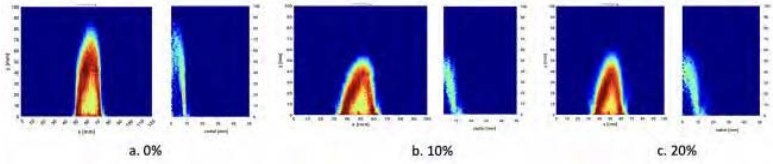

Figure 5. Normalized radial intensity (top) and intensity (bottom) values for 0.7 equivalence ratio for a. 0%, b. 10% and c. 20% of H2 addition.

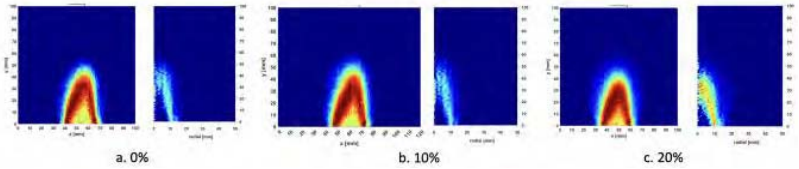

Figure 6. Normalized radial intensity (top) and intensity (bottom) values for 0.8 equivalence ratio for a. 0%, b. 10% and c. 20% of H2 addition.

The OH* and CH* radicals' comparison is shown in Fig. 7. As the hydrogen addition rate increases, the light intensity of OH* radicals change significantly, while CH* intensity is not significantly changing with the overall flame structure changes. This is another reason why we chose CH* radicals for indicating the flame structure.

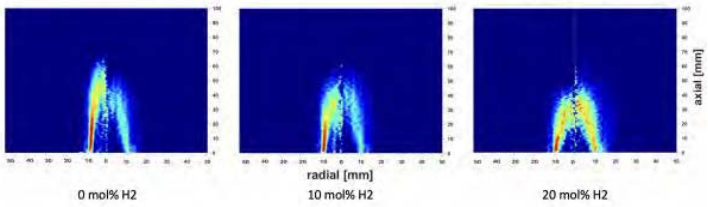

Figure 7. Normalized radial intensity for OH* (right) and CH* (left) values for 0.8 equivalence ratio for various H2 addition rates.

Turbulent Flame Speed

Chemiluminescence measurements were used to calculate the turbulent flame speed using the cone approach for Bunsen burners [6,7,8]. Here, the CH* images were used to represent the progress variable. The CH* images were normalized between 0 and 1, creating a progress variable (c) contour. The cone reference surface is selected as c=0.5. The turbulent flame speed is calculated using the equation below,

$$S_T = \sqrt{U^2/(1+(H/R)^2)} \quad (1)$$

where R is the burner radius, U is the mean inlet velocity and H is the reference surface height constructing the cone.

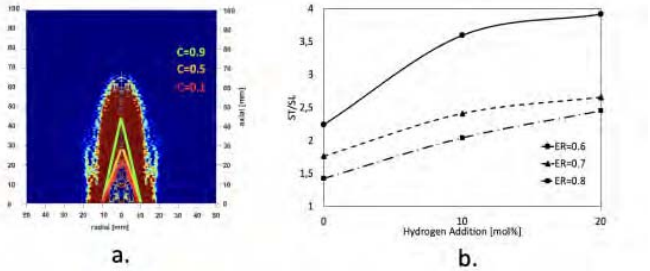

Figure 8. a. The cones for turbulent flame speed calculations. **b.** Normalized turbulent flame speed.

The turbulent flame speed normalized by the laminar flame speed for various hydrogen addition rates and equivalence ratio is shown in Fig. 8.b. The increase in

turbulent flame speed with hydrogen addition for all equivalence ratios is higher than the laminar flame speed, which agrees with previous literature results [6]. The calculated turbulent flame speeds are lower than Halter's results [6], which may be explained by the choice of cone reference point.

Mie Scattering for Turbulent Flames

Mie scattering experiments are performed using a continuous, 532 nm solid-state laser of 4kW power. The premixture is seeded using olive oil droplets. The images are collected at 240 fps using a 532nm bandpass filter, with 3840x2160 pixels. 500 frames are used for each case.

Flame front tracking is performed with MATLAB. The snapshots are averaged for 500 images for each case, binarized, and dilated for creating a clean binarized image of the flame. After, the flame front is filtered with Gaussian and Wiener filters. The image is finally segmented.

The flame front is tracked using the exterior boundaries of the binarized image as shown in Fig. 10. The flame front is also recorded by fitting a B-Spline curve to the boundary; therefore, the flame front location could be stored inside an x-y matrix.

The stored B-Spline curve is divided into equal distance points, such that the linear distance between consecutive points is equal to 5 mm. After that, for every 3 points, a circle is fitted, and the radius values of the circles are collected. The cross product of the vectors formed by the 3-points is used to decide if the curvature is convex or concave to decide the sign of the curvature. The curvature is found using $K = 1/r$, where r is the radius of the fitted circle and K is the curvature.

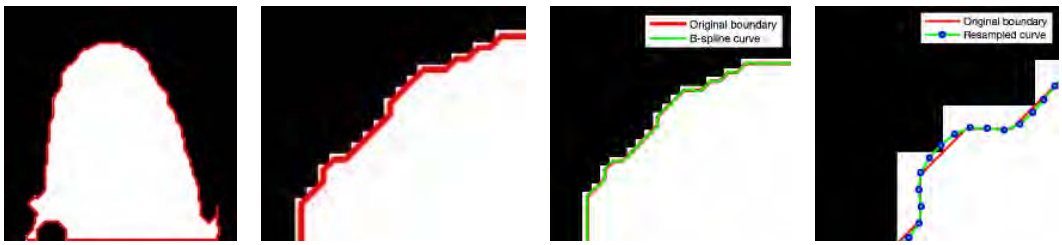

Figure 10. a. The boundary tracking. **b.** B-Spline Curve **c.** Divided curve.

The probability density function is calculated for each case using MATLAB's default pdf function. The range is decided to cover the maximum and minimum values of all cases, and the number of points is decided to be the square root of the curvature datapoint number, as 100. The probability density function graphs for all cases are provided in Fig. 11. All the PDFs are balanced around their mean and follow the normal distribution.

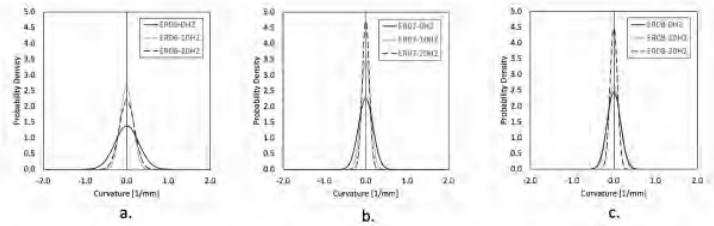

Figure 11. PDF of equivalence ratios, **a.** 0.6, **b.** 0.7 and **c.** 0.8.

Conclusions

In this work, the effect of hydrogen addition and equivalence ratio in lean premixed methane-hydrogen-air flames is studied experimentally. The chemiluminescence imaging technique is used for the measurements. The results are processed using inverse Abel transformation to convert the line-of-sight images.
The light intensity of the chemiluminescence of radicals increases with the hydrogen addition rate. With increasing hydrogen addition rate, the flame height is found to be decreasing while the normalized turbulent flame speed increases. The equivalence ratio significantly contributes to flame speed and height, which is the opposite of the hydrogen addition rate effect.

Acknowledgements

This work was supported b the International Fellowship for Outstanding Researchers Program of TÜBİTAK (Projects Nos: 118C287 &118C233)

References

[1] Lachaux, T. “Etude des effets de la haute pression sur la structure et la dynamique des flammes turbulentes de prémélange pauvre de méthane-air.” https://tel.archives-ouvertes.fr/tel-00010401
[2] Halter, F. “Caractérisation des effets de l’ajout d’hydrogène et de la haute pression dans les flammes turbulentes de prémélange méthane/air.” https://tel.archives-ouvertes.fr/tel-00591421
[3] Souflas, K. (2022). Experimental investigation of OH*/C* ratio variations in turbulent, disk stabilized, lean propane-air flames with inlet mixture preheat and stratification. Exp. Ther. Fluid Sci. https://doi.org/10.1016/j.expthermflusci.2022.110670
[4] Pretzier, G. (1991) “A new method for numerical abel-inversion,” Zeitschrift für Natur- forschung A, vol. 46, no. 7, pp. 639–641.
[5] Killer, C. (2023). Abel Inversion Algorithm https://www.mathworks.com/matlabcentral/fileexchange/43639-abel-inversion-algorithm. MATLAB Central File Exchange.
[6] Halter, F., Chauveau, C., & Gökalp, I. (2007). Characterization of the effects of hydrogen addition in premixed methane/Air Flames. Int. J. Hdrogen Energy, 32(13), 2585–2592. https://doi.org/10.1016/j.ijhydene.2006.11.033
[7] Ranganathan, S., Petrow, D., Rockwell, S. R., & Rangwala, A. S. (2018). Turbulent burning velocity of methane–air–dust premixed flames. Combustion and Flame, 188, 367–375. https://doi.org/10.1016/j.combustflame.2017.10.015
[8] Kobayashi H, Tamura T, Maruta K, Niioka T (1996). Burning velocity of turbulent premixed flames in a high-pressure environment. Proc. Comb. Inst. 26:389
[9] Vargas, A. C., García, A. M., Arrieta, C. E., Sierra del Rio, J., & Amell, A. (2020). Burning velocity of turbulent methane/air premixed flames in subatmospheric environments. ACS Omega, 5(39), 25095–25103. https://doi.org/10.1021/acsomega.0c02670.

A DATA-DRIVEN APPROACH FOR HYDROGEN PREMIXED COMBUSTION MODELING

A. Remiddi*, G. Indelicato*,, D. Cavalieri*, P.E. Lapenna*, A. Attili***, L. Berger****, H. Pitsch****, F. Creta***

arianna.remiddi@uniroma1.it

*Dept. of Mechanical and Aerospace Engineering, La Sapienza University of Rome, Italy

**CASE Dept., Barcelona Supercomputing Center (BSC), Spain

***School of Engineering, University of Edinburgh, UK

**** Institute for Combustion Technology, RWTH Aachen University, Germany

Abstract

Lean premixed hydrogen flames are characterized by the high mobility of the hydrogen molecule that yields mixtures with an effective sub-unity Lewis number. This causes formation of intrinsic instabilities as a consequence of the hydrodynamic and thermo-diffusive mechanisms. The interaction of these instabilities leads to complex and non-linear corrugations of the flame front, even in laminar fla-mes, with characteristic length-scales falling under the subgrid level, requiring therefore dedicated modeling when approaching the flame to LES. In this contribution, a data-driven model for lean premixed hydrogen combustion is presented. It consists in a two-scalars manifold representation, obtained by the spatial filtering of a two-dimensional, fully resolved, unstable, self-wrinkling DNS hydrogen/air dataset. The method is validated a-priori and a-posteriori against a two-dimensional DNS.

Introduction

Hydrogen combustion is a promising alternative to fossil fuels due to its sustainability characteristics [1]. Due to the higher adiabatic flame temperatures of hydrogen, leaner mixtures are employed compared to conventional fuels. Hydrogen combustion is characterized by the high mobility of the hydrogen molecule that causes the mixture Lewis number to decrease under sub-unity values. Under such condition, particularly crucial for lean mixtures, the flame is prone to develop combustion instabilities [2] since small-scale perturbations are amplified leading to the formation on self-wrinkled unstable cellular structures [3]. These are caused by the local perturbations of the flame speed as a consequence to the local imbalance between the thermal conductivity of the mixture and the molecular diffusivity of the controlling reactant, with a mechanism known as thermo-diffusive instability [4]. In addition, these can be enhanced by the interaction with the large-scale hydrodynamic (or Darrieus-Landau) instabilities, which cause the further corrugation of the flame front as a consequence of the thermal expansion [5]. The flame propagation is significantly affected by the interaction of such instability mechanisms, resulting in the formation of non-linear multi-scale self-wrinkling structures that are largely different from the laminar one-dimensional flame structure. The smallest flame front

corrugations are of the order of the flame thickness, and require therefore dedicated modeling when resorting to the LES framework, with the twofold aim of reproducing the flame structure and accounting for the cellular wrinkling falling at the LES subgrid level even in a laminar setting [6,7]. Models for the turbulence-chemistry inter-action are usually sought, in this context, to reduce the computational cost associ-ated to the solution of the reactive chemistry. Among these, tabulated chemistry approaches are used to represent the thermo-chemical properties on lower-dimen-sional manifolds defined by a few conserved scalars, whose transport equations are solved at run time. For what concerns hydrogen premixed combustion, it has been shown that at least two scalars are needed to have a sufficiently accurate representation of the complex multi-scale, unsteady, stretched character of thermo-diffusively unstable flames, with a significant accuracy improvement with respect to the one-dimensional manifolds found in literature [7,8,9]. In the work by Lapenna et al. [7], the manifold parameterization is given as a function of the non-dimensional temperature Θ and the deficient reactant mass fraction Y_{H2}. Regele et al., instead, presented a manifold parameterized as a function of the progress variable C, based on the water mass fraction, and of the mixture fraction Z [8].

Theoretical formulation

The model presented in this work targets the modeling of unstable self-wrinkling lean hydrogen premixed flames, in a laminar setting, through a manifold representation using as defining scalars two species mass fractions, namely Y_{H2} and $Y_{H2O.}$ The model is based on the F-TACLES method, which is one of the original implementations of the tabulated approaches [10]. Both the models are based on the spatial filtering of a detailed flame solution, in order to recover all the filtered quantities as functions of the filtered progress variable, with the advantage of retaining by construction the original stretched laminar flame speed also in absence of the turbulence leading to subgrid wrinkling [10]. While the F-TACLES approach uses a 1D flame solution as source for the filtering procedure, the approach proposed in the present work employs instead a fully resolved, 2D, unstable, self-wrinkling flame [7]. Such flames are chosen since it has been demonstrated that 2D flames subject to hydrodynamic instabilities present most of the morphological features of the corresponding 3D large-scale flames [11]. The model aims in particular at using the smallest scale DNS which presents the formation of at least one of the characteristic structures of the large-scale target flame. The DNS used in this work belong to the multi-step chemistry hydrogen/air dataset by Berger et al. [4], consisting of statistically planar premixed flames, two realizations are shown in Fig. 1. In particular, a large-scale DNS with a cross-wise dimension $L_x = 800\ \ell_T$, will be considered as target flame in the following, while a small-scale flame with $L_x = 50\ell_T$, will be used as source for the filtering procedure. In both cases, the stream-wise dimension is $L_y = 200\ell_{T,}$ where $\ell_{T\ is}$ the laminar thermal flame thickness of a 1D unstretched flame. The unburned mixture features

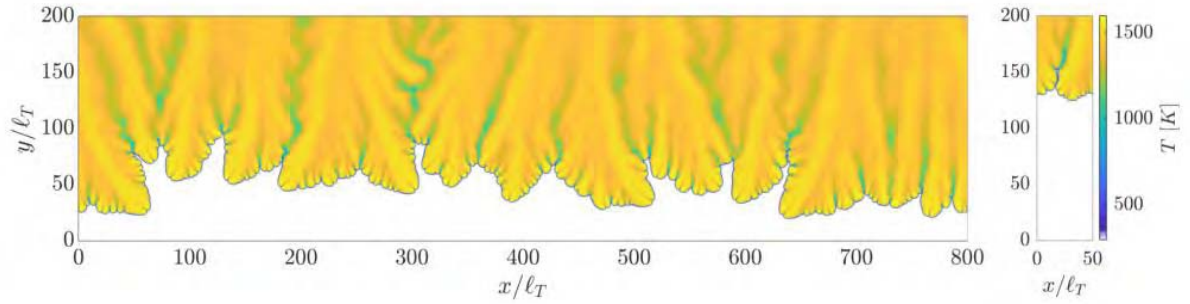

Figure 1. Temperature field in the DNS dataset [4].

an equivalence ratio of φ = 0.4, an unburned temperature of T_u = 298 K and a pressure of p = 1 bar.
The chosen scalars are normalized in order to retrieve two progress variables as shown in Eq. (1), where the subscripts *min* and *max* refer respectively to the minimum and maximum values of the corresponding mass fraction found in the employed dataset.

$$C_1 = 1 - \frac{Y_{H2} - Y_{H2,min}}{Y_{H2,max} - Y_{H2,min}} \quad C_2 = \frac{Y_{H2O} - Y_{H2O,min}}{Y_{H2O,max} - Y_{H2O,min}} \tag{1}$$

The transport equations for the two chosen manifold parameters read:

$$\frac{\partial}{\partial t}\left(\rho C_{1,2}\right) + \nabla \cdot \left(\rho u C_{1,2}\right) = \nabla \cdot \left(\rho D_{1,2} \nabla C_{1,2}\right) + \dot{\omega}_{C_{1,2}} \tag{2}$$

Where ρ is the density, D the diffusivity and $\dot{\omega}$ the scalar source term. The LES equations are obtained from Eq. (2) by means of filtering:

$$\frac{\partial}{\partial t}\left(\bar{\rho}\tilde{C}_{1,2}\right) + \nabla \cdot \left(\bar{\rho}\tilde{u}\tilde{C}_{1,2}\right) = \nabla \cdot \left(\overline{\rho D_{1,2} \nabla C_{1,2}}\right) - \nabla \cdot \left(\bar{\rho} u \tilde{C}_{1,2} - \bar{\rho}\tilde{u}\tilde{C}_{1,2}\right) + \overline{\dot{\omega}}_{C_{1,2}} \tag{3}$$

where – operator and ~ operator respectively represent the spatial filtering and the density-weighted filtering operation. The *unfiltered* tabulated manifold is obtained by calculating for each thermochemical quantity in Eq. (2) the conditional average with respect to the two unfiltered parameters from the small-scale DNS shown in Fig. 1, which, for a generic quantity ψ is $\psi = \langle \psi | C_1, C_2 \rangle$. In order to obtain the *filtered* tabulated manifold, the source DNS must be filtered with a Gaussian filter whose size is representative of a LES grid size, as shown in Fig. 2. The thermochemical properties and unclosed terms of Eq. (3) will be therefore calculated as $\tilde{\psi} = \langle \tilde{\psi} | \tilde{C}_1, \tilde{C}_2 \rangle$. Figure 3 reports two examples of the obtained tables.

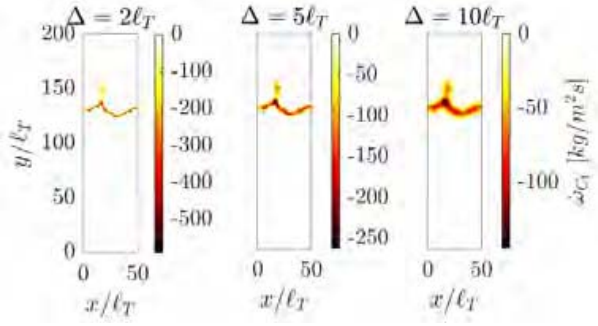

Figure 2. C_1 source term in the filtered small-scale DNS at several filter sizes.

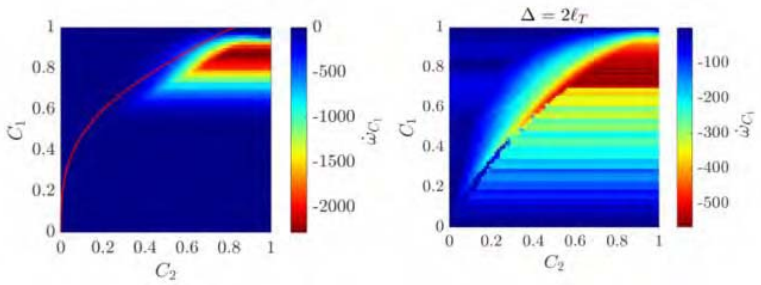

Figure 3. Unfiltered (left) and filtered (right) tables for the C_1 source term.

Results

The model is first validated *a-priori* comparing the unfiltered/filtered target DNS field with the field built accessing the unfiltered/filtered manifold with the state of the target flame. The analysis has been conducted for both the unfiltered and filtered manifolds, Fig. 4 shows a qualitative comparison performed on the first scalar source term $\dot{\omega}_{C_1}$ for the filtered case employing several filter sizes shown before. For the sake of conciseness only portions of the large-scale filtered fields have been reported. It is found that the model reproduces satisfactorily the filtered large-scale DNS for all the filter sizes, with some minor differences in the peak values reconstruction for the largest filter size. Figure 5 reports a quantitative comparison in terms of normalized consumption speed $S_C = \frac{-1}{L_y \rho_u} \int \dot{\omega}_{C_1} dxdy$ between the filtered large-scale target DNS and the fields obtained from the manifolds. It is observed that the error on the prediction increases with the filter size, with a maximum error lower than ~13%.

The unfiltered manifold is then tested *a-posteriori* performing the numerical simulation of the small-scale DNS retrieving all the thermochemical quantities needed in Eq. (2) from the unfiltered manifold. The numerical domain employed is equivalent to the DNS one. The simulation is started with a uniform unstretched solution, to which is added an initial sinusoidal disturbance in order to trigger instability formation. The flame propagation responds to the initial perturbation with a corrugation of the flame front characterized by a wavelength of ~6 ℓ_T in agreement with the linear stability analysis performed in [4]. The initial corrugation is then enhanced up to the formation of the large-scale unstable structure reported

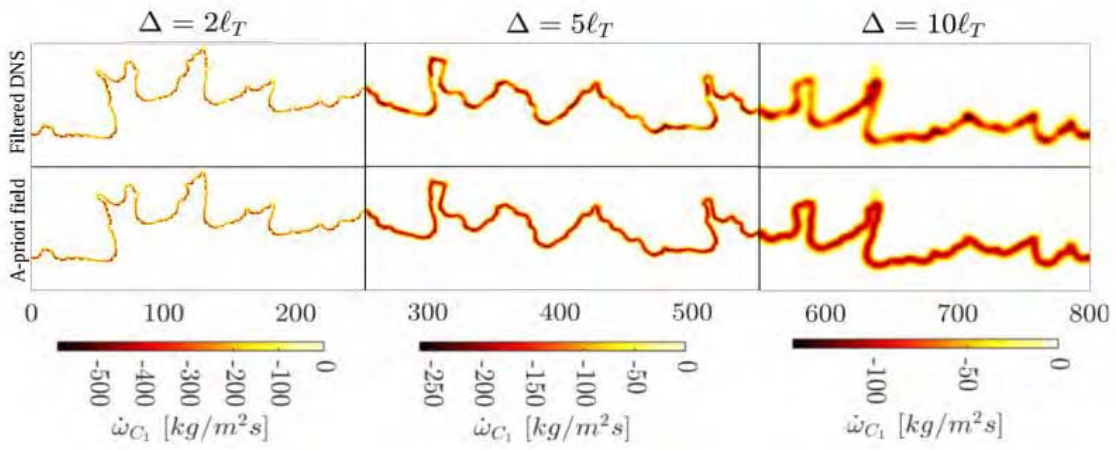

Figure 4. Comparison between the filtered DNS (top) and the a-priori field built from the filtered manifolds (bottom) for different filter sizes.

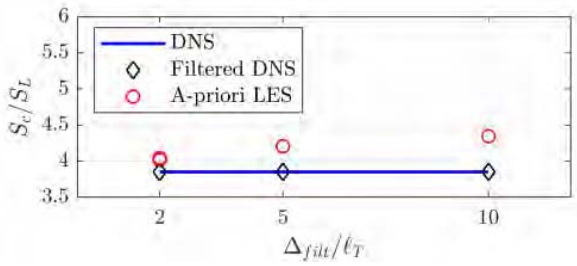

Figure 5. Consumption speeds from the a-priori analysis of the filtered manifold.

in Fig. 6, showing that the model is capable of qualitatively predicting the self-wrinkling of a thermo-diffusively unstable flame. The quantitative comparison in terms of consumption speeds results for the unfiltered setting in an error of ~2.4%.

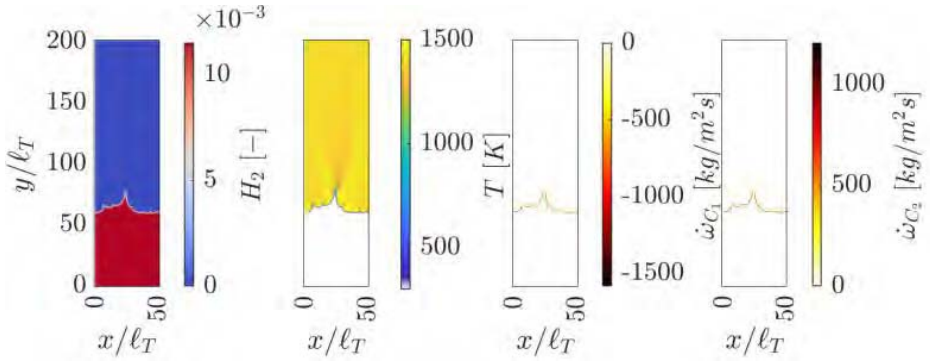

Figure 6. *A-posteriori* unfiltered simulation.

Conclusions

This work proposes a data-driven approach for lean premixed hydrogen combustion. The model is based on a two-scalars manifold representation obtained through the spatial filtering of a fully-resolved, two-dimensional, thermo-diffusively unsta-

ble flame. A set of two-dimensional tables has been developed both in an unfilte-red and filtered setting, using for the latter three different filter sizes representative of as many LES grid sizes. The *a-priori* validation of the model has shown that it correctly reproduces the morphological features of the large-scale target field and satisfactorily retains the consumption speed value with a small error for the largest filter size. The *a-posteriori* validation of the unfiltered tabulation has shown promising results in terms of prediction of the self-wrinkling nature of the thermo-diffusive flames and the formation of its characteristic instabilities.

Acknowledgments

This work is partially supported by the Italian Ministry of University and Research (MUR) and by Lazio-Innova. The support of Sapienza University by means of the early stage researchers funding is also gratefully acknowledged. H.P. and L.B. acknowledge funding by the European Union (ERC, HYDROGENATE, 101054894)

References

[1] Dreizler, A. et al., "The role of combustion science and technology in low and zero impact energy transformation processes", *Appl. Energy Combust. Science* 7,100040 (2021).
[2] Matalon, M., "Flame dynamics", *Proc. Comb. Inst.,* 32(1):57–82, 2009.
[3] Matalon, M., "Intrinsic flame instabilities in premixed and nonpremixed combustion", *Ann. Rev. Fluid Mech.*, 39(1):163–191, (2007)
[4] Berger, L. et al., "Characteristic patterns of thermodiffusively unstable premixed lean hydrogen flames", *Proc. Comb. Inst.* 37, 1879–1886 (2019).
[5] Creta, F. et al., "Propagation of premixed flames in the presence of Darrieus–Landau and thermal diffusive instabilities", *Combust. Flame* 216, 256 (2020)
[6] Lapenna, P.E. et al., "Subgrid modeling of intrinsic instabilities in premixed flame propagation", *Proc. Comb. Inst.,* 38, (2021).
[7] Lapenna, P.E. et al., "Data-driven subfilter modelling of thermo-diffusively unstable hydrogen–air premixed flames", *Combust. Theory Model.,* 25, 1064 (2021)
[8] Regele, J.D. et al., "A two-equation model for non-unity Lewis number differential diffusion in lean premixed laminar flames", *Combust. Flame*, 160(2):240–250, (2013)
[9] Pope, S.B., "Small scales, many species and the manifold challenges of turbulent combustion", *Proc. Comb. Inst.,* 34(1):1–31, (2013)
[10] Fiorina, B. et al., "A filtered tabulated chemistry model for LES of premixed combustion", *Combust. Flame* 157, 465 (2010)
[11] Lapenna, P.E. et al., "Large scale effects in weakly turbulent premixed flames", *Proc. Comb. Inst.,* 37, 1945 (2019)

ON THE EFFECT OF MANIFOLD TOPOLOGY IN REDUCED-ORDER MODELING OF TURBULENT COMBUSTION

K. Zdybał*, J. C. Sutherland, A. Parente***

kamilazdybal@gmail.com

* Université Libre de Bruxelles, École polytechnique de Bruxelles, Aero-Thermo-Mechanics Laboratory, Brussels, Belgium

* BRITE: BRussels Institute for Thermal-fluid systems and clean Energy, Brussels, Belgium

** Department of Chemical Engineering, University of Utah, Salt Lake City, Utah, USA

Abstract

It has been recognized that, under some conditions, reduced-order models (ROMs) of turbulent combustion work very well, but in other can fail dramatically. At the same time, many aspects of data-driven ROMs have not yet been understood. In particular, undesired topological behaviors can be introduced on a data projection through dimensionality reduction. This can hinder the performance of a ROM. The most problematic behavior is an overlap on a projection that leads to non-uniqueness in representing quantities of interest (QoIs). Here, we investigate the effect that low-dimensional manifold (LDM) topologies have on data-driven ROMs. We particularly focus on assessing the effects of steep gradients and non-uniqueness in representing various projection-independent and projection-dependent QoIs. We show how the recently proposed cost function for manifold quality assessment can be used in reduced-order modeling workflows to distinguish between promising and poor manifold topologies. We discuss the effect of severe and subtle differences in manifold topologies. We link those differences with the behavior of a ROM at model runtime and with the mispredictions of the thermo-chemical state variables from the evolved LDM parameters.

Introduction

While many reduced-order models (ROMs) of turbulent combustion have been developed in the past literature, there remain some unanswered questions. For example, in [1], a data-driven ROM was built for a zero-dimensional reactor case. The principal component analysis (PCA) and Gaussian process regression (GPR) based model was shown to lead to generally good reconstruction of the thermo-chemical variables, but some mispredictions of the composition in the reactor were observed. In another study done in [2] the authors have observed high errors in predicting minor chemical species and the projected source terms in the context of a PCA and artificial neural network (ANN) based ROM. In addition, modeling low-temperature combustion was more challenging compared to modeling high-

temperature combustion in the context of diesel fuel. The works done in [1] and [2], and also in other studies [3], do not investigate the cause of such poor ROM behaviors injected in certain regions of the low-dimensional manifold (LDM).

In order to address the current gaps in the literature, one of the yet unanswered questions that we tackle in this work is: How does manifold topology affect the ROM? Specifically, our goal is to relate various topological behaviors in LDMs, such as overlaps or steep gradients, with the predictions done by closure models, and with the reconstruction of the thermo-chemical state-space from the transported manifold parameters. Tackling this question allows us to shed more light on the benefits that improved manifold topologies bring in reduced-order modeling of reacting flows. A more in-depth discussion on the inner working of ROMs is only beginning to make its way into the combustion literature [4, 5].

We find that well-behaved manifolds can bring significant benefits in accuracy of ROMs. We advocate that quantitative assessments of manifold quality be incorporated into the reduced-order modeling workflows. We demonstrate the effects that poor manifold topologies have on closure models and on predictions of the thermo-chemistry from the transported ROM solution. Specifically, non-uniqueness on a manifold can cause significant departures from the training manifold. We also show the effects of steep gradients near the initial condition where the ROM simulation originates from. We find that the recently proposed cost function [6] can be a good tool to guide the *a priori* selection of manifolds, able to detect subtle differences in LDMs that can have large importance in ROMs.

Formulating the reduced-order model

In this work, we consider a simple canonical system of an adiabatic, incompressible, zero-dimensional reactor. We can write the governing equations for the zero-dimensional reactor in the matrix form:

$$d\boldsymbol{X}^T / dt = \boldsymbol{S}^T, \tag{1}$$

where $\boldsymbol{X}$ is the thermo-chemical state-space and $\boldsymbol{S}$ are the thermo-chemical source terms. Given a low-dimensional basis matrix, $\mathbf{A}$, that is constant in time, we can project Eq. (1) onto that basis:

$$d\boldsymbol{A}\boldsymbol{X}^T / dt = \boldsymbol{A}\boldsymbol{S}^T. \tag{2}$$

By keeping only q basis vectors, the projection from Eq. (2) yields

$$d\boldsymbol{\eta}^T / dt = \boldsymbol{S}_{\boldsymbol{\eta}}{}^T, \tag{3}$$

where $\boldsymbol{\eta} = [\eta_1, \eta_2, \ldots, \eta_q]$ are the q LDM parameters, and $\boldsymbol{S_\eta} = [S_{\eta,1}, S_{\eta,2}, \ldots, S_{\eta,q}]$ are the q projected thermo-chemical source terms. We formulate a nonlinear regression model, F, in order to predict $\boldsymbol{S_\eta}$ from the LDM parameters at the current time step, such that the equation solved by the numerical solver is

$$d\boldsymbol{\eta}^T / dt = F(\boldsymbol{\eta}^T). \quad (4)$$

The ROM for a q-dimensional LDM is thus described by a set of q coupled ODEs.

Computing the low-dimensional manifold parameters

In parameterizing reacting flows, we want to avoid folded, multi-valued, discontinuous manifolds, or manifolds that are not smooth [7]. Fig. 1 presents in an illustrative way various manifold challenges and undesired topological behaviors on manifolds. These are selected from the most common behaviors that we have encountered throughout our research, whether from PCA or from other dimensionality reduction strategies. Overcoming some of the challenges such as overlaps, twists, sharp turns, or steep gradients in dependent variables is possible with various novel approaches proposed by the authors [5, 8]. Other challenges, such as data sparsity in certain regions on a manifold, approaching manifold edge, or tackling uneven data density, are much more challenging to tackle simply by altering manifold topologies. These challenges manifest themselves when building regression models and can be addressed through skillful modification of a regression model. Fig. 1 can be viewed as guidance of what types of problems we might be facing when building data-driven ROMs of reacting flows. The future research on

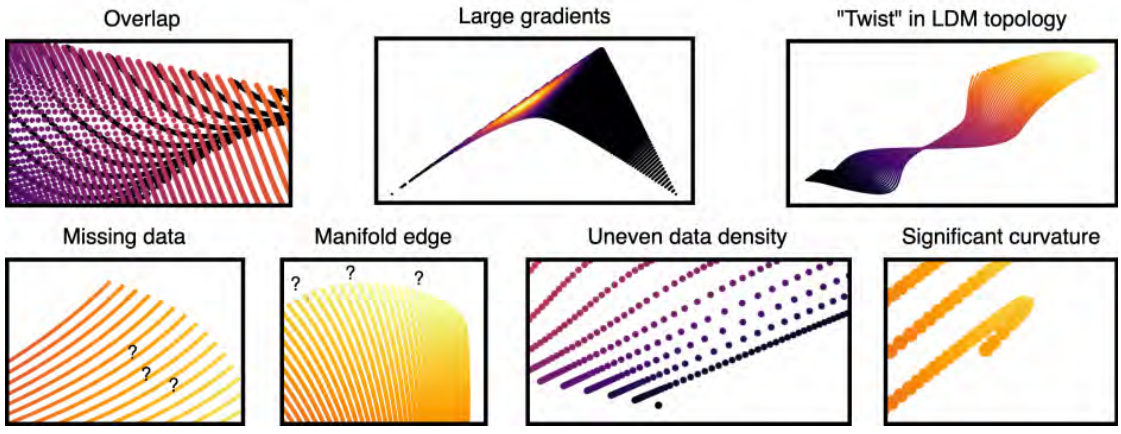

improving ROMs should aim at addressing each of these challenges.

Figure 1. Illustrative demonstration of various manifold challenges commonly encountered when building data-driven ROMs from combustion datasets.

Fig. 2 shows the cost function [6] assessments of various PCA projections of the same zero-dimensional reactor data for combustion of syngas in air, but across

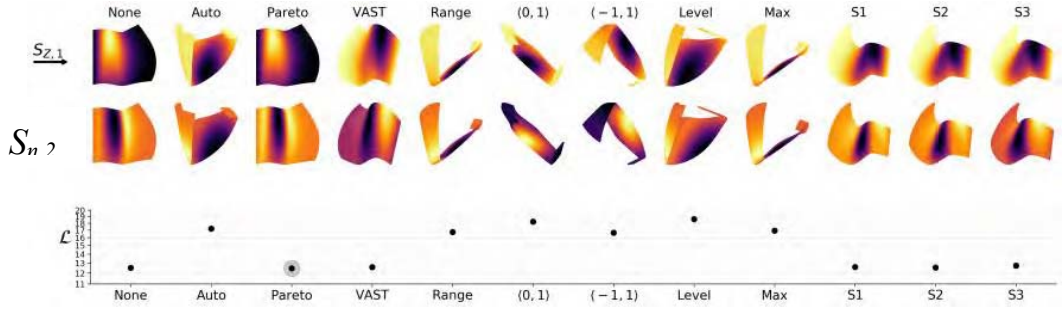

$S_{\eta,1}$ different data scaling criteria (noted along the x-axis). A smaller cost value indicates a better manifold topology. The visualized projections are colored by the first (top row) and the second (bottom row) projected source terms, $S_{\eta,1}$ and $S_{\eta,2}$. We note that projections that exhibit overlaps are associated with higher costs. The best projection of that dataset happened for Pareto scaling and it can be further used as the best candidate for building a ROM.

Figure 2. Ranking of various PCA-based LDMs using the cost function, L.

Low-dimensional manifold with a severe overlap

Fig. 3 shows the path taken by the transported test trajectory during ROM simulation (blue solid line) using the PCA-Auto manifold (see Fig. 2). We show the location of the true test trajectory (black dashed line). We observe that the transported test trajectory deviates significantly from the true test trajectory due to topological issues occurring at the training manifold. Near the initial condition (IC), the trajectory first departs in a wrong direction. It snaps onto one of the training trajectories that overlaps the observations corresponding to initial conditions. The solution continues across the unique interior part of the manifold undisturbed, towards the region corresponding to the steady-states (SS). Once the transported trajectory reaches the second region of overlap on a manifold, it is deflected, as it sees the presence of the overlapping trajectories for which $S_{\eta,1}$ and $S_{\eta,2}$ approach zero. It is then attracted to one of the SS. Note, that the transported test trajectory eventually leaves the training manifold. This is likely the effect of the ANN closure model not being able to predict the zeroing projected source terms exactly at the SS. If the ROM simulation is allowed to continue in time, the transported test trajectory continues to move away from the training manifold.

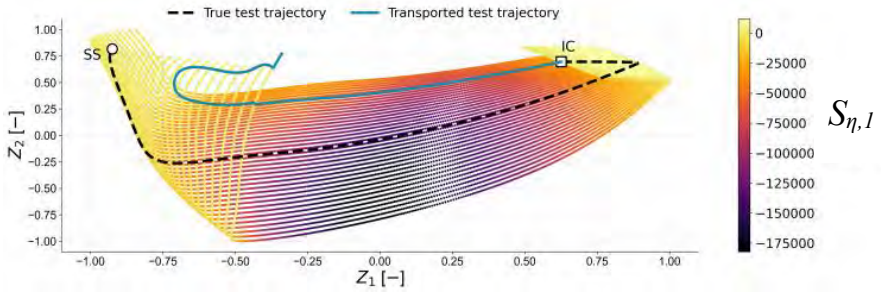

Figure 3. True and transported test trajectory corresponding to the PCA-Auto manifold (see Fig. 2). ANN is used as a closure model for the projected source terms. IC denotes the initial condition and SS denotes the steady-state condition.

Low-dimensional manifold with a subtle overlap

We show another demonstration of forcing the ROM simulation to pass through a region of non-uniqueness on a manifold. We select a case where the overlap is limited to a small region on a manifold. As a result, the transported test trajectory stays reasonably close to the true test trajectory. We use the same PCA-Auto manifold as in the previous section but we limit the training manifold to the close neighborhood of the true test trajectory. Not taking all of the original training data observations allows us to limit the significance of the two overlaps to just a small portion of the training manifold. In particular, the folded region on the manifold near the IC does not contain observations laying directly below them anymore, since we

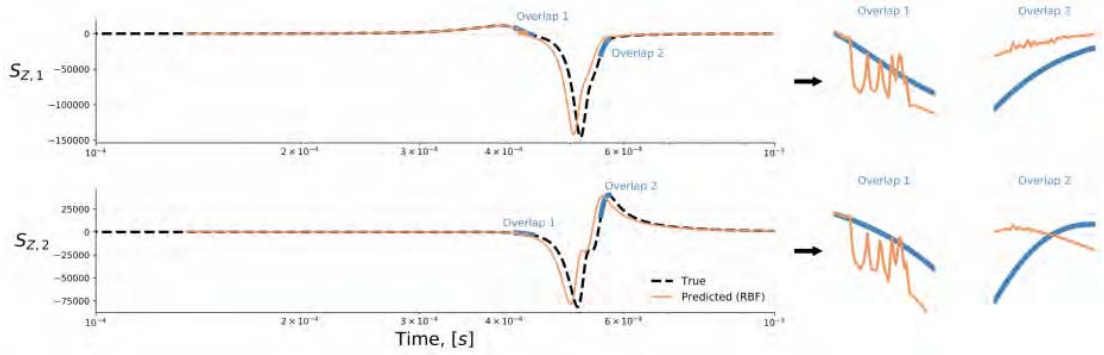

do not include the corresponding trajectories into the training data.

Figure 4. Prediction of the two projected source terms, $S_{\eta,1}$ and $S_{\eta,2}$, at ROM simulation runtime using a nonlinear regression closure model. We annotate the two regions of subtle overlap that happen on the training manifold.

$S_{\eta,1}$

$S_{\eta,2}$

Fig. 4 shows the *a posteriori* predictions of the two projected source terms, $S_{\eta,1}$ and $S_{\eta,2}$, using the nonlinear regression closure model. In blue, we mark

the time stamp where the two overlaps happen on a test trajectory. We note that in both regions of overlap, the closure model introduces wiggles in predicting $S_{\eta,1}$ and $S_{\eta,2}$. These wiggles are further visualized in the four close-ups. Despite those poorer predictions of $S_{\eta,1}$ and $S_{\eta,2}$ at model runtime across the two regions of non-uniqueness, the test trajectory transported using the ROM stays close to the true test trajectory. This allows us to predict the thermo-chemistry reasonably well from the transported manifold parameters. We do however observe poorer predictions within the highlighted time stamps that correspond to the solution passing through an overlap on a training manifold. Overlap on a manifold can thus cause sudden mispredictions in the species profiles at certain times in a ROM simulation. These results can help understand the possible reasons for mispredictions in the reconstructed thermo-chemistry reported in the past research. We highlight, however, that this case is carefully selected, and not every manifold with even subtle overlap is guaranteed to give reasonable results within certain error bounds.

Conclusions

This work collects many individual insights about data-driven approaches developed by the authors into a reduced-order modeling workflow. Our main goal here is to provide insights into how various aspects of the LDM topology affect the closure models for the projected source terms, the ROM simulations, and the *a posteriori* predictions of the thermo-chemistry. We focus our demonstrations on a simple system of a zero-dimensional reactor. Although the ODE corresponding to this system incorporates a significant level of simplifying assumptions, we show that it can in fact be a challenging test case. The challenge stems from the fact that the temporal evolution in this system is entirely dependent on the the closure model used for the projected source terms. These closure models are built on top of a LDM, and various topological issues on manifolds immediately propagate as errors in evolving ROMs in time.

We investigate the effects of steep gradients, or large compression of data observations on a training manifold. We show how manifold edge effects, especially in the presence of large gradient near the manifold edge, can affect the entire solution trajectory. For example, in the context of a zero-dimensional reactor system, large compression of observations corresponding to pre-ignition can cause mispredictions of the ignition time in the reactor, thereby shifting the entire solution in time. We also discuss the effect of overlap generating non-uniqueness on a manifold. We split this discussion into two qualitatively different types of assessment: (1) the effect of severe overlap, and (2) the effect of subtle overlap. We highlight the fact that the most severe effect of overlap on a manifold, generating non-uniqueness in the projected source terms, can cause the ROM simulation to diverge entirely from the training manifold, resulting in no usable results. The more subtle effects of overlap on a manifold can cause mispredictions located at or near the region of overlap. More

subtle effects can also derail the transported solution after passing through the region of overlap, thus leading to significant mispredictions of the thermo-chemistry.

References

[1] Malik, M.R., Isaac, B.J., Coussement, A., Smith, P.J. and Parente, A., "Principal component analysis coupled with nonlinear regression for chemistry reduction", *Combust. Flame*. 187:30-41 (2018)

[2] Dalakoti, D.K., Wehrfritz, A., Savard, B., Day, M.S., Bell, J.B. and Hawkes, E.R., "An a priori evaluation of a principal component and artificial neural network based combustion model in diesel engine conditions", *Proc. Combust. Inst.* 38(2):2701-2709 (2021)

[3] Zhang, Y., Xu, S., Zhong, S., Bai, X.S., Wang, H. and Yao, M., "Large eddy simulation of spray combustion using flamelet generated manifolds combined with artificial neural networks", *Energy and AI*. 2:100021 (2020)

[4] Malik, M.R., Coussement, A., Echekki, T. and Parente, A., "Principal component analysis based combustion model in the context of a lifted methane/air flame: Sensitivity to the manifold parameters and subgrid closure", *Combust. Flame.* 244:112134 (2022)

[5] Zdybał, K., Sutherland, J.C. and Parente, A., "Manifold-informed state vector subset for reduced-order modeling", *Proc. Combust. Inst.* 39:1–10 (2022)

[6] Zdybał, K., Armstrong, E., Sutherland, J.C. and Parente, A., "Cost function for low-dimensional manifold topology assessment", *Sci. Rep.* 12(1):14496 (2022)

[7] Pope, S.B., "Small scales, many species and the manifold challenges of turbulent combustion", *Proc. Combust. Inst.* 34(1):1-31 (2013)

[8] Zdybał, K., Parente, A., Sutherland, J.C., "Improving reduced-order models through nonlinear decoding of projection-dependent model outputs", *In preparation for PNAS*. (2023)

Experimental Investigation of Flame Dynamics of Swirled Methane-Air Flame with H_2 addition

S. Bonuso*, P. Di Gloria*, G. Mehdi*, M.G. De Giorgi*
sara.bonuso@unisalento.it
*University of Salento, Lecce, Italy

Abstract
This study investigates the impact of hydrogen enrichment on flame structures while maintaining a constant thermal output of 5.06 kW. High speed chemiluminescence images were captured for two fueling conditions: pure methane/air and methane with hydrogen addition. The results show that hydrogen enrichment leads to a slightly shorter flame length and a wider flame angle due to increased expansion in the Combustion Recirculation Zone. UV emissions are significantly affected, with a shifted luminosity zone and reduced variance. Proper Orthogonal Decomposition (POD) and Singular Proper Orthogonal Decomposition (SPOD) analyses reveal coherent structures and energetic modes. Hydrogen enrichment results in smaller structures near the nozzle exit, longitudinal oscillations, and vortex shedding. The findings enhance our understanding of hydrogen's impact on flame characteristics and contribute to improving flame stability.

Introduction
The gas turbine industry is exploring lean premixed combustion of hydrogen-enriched fuel blends as a promising solution for reducing greenhouse gas emissions and NOx emissions [1]. Many gas turbines currently have the capability to burn mixtures of hydrocarbons and hydrogen in varying proportions [2, 3]. However, efficiently mixing hydrogen and air prior to combustion is challenging, and micromixing technologies have been developed to prevent high-temperature stoichiometric reaction layers at the hydrogen injector outlet, which can lead to high NOx emission levels and thermal stress [4-6]. This study proposes an alternative approach of injecting hydrogen into a conventional swirl burner, enabling partial premixing with methane before combustion to avoid the formation of diffusion reaction layers, without requiring significant combustor redesign [7]. The study then analyzes the effects of H2-enrichment on flame shape and dynamics using modal decomposition techniques. To properly identify, separate, and temporally resolve dynamic components, the study employs spectral proper orthogonal decomposition (SPOD), a modified version of the traditional POD technique that incorporates spectral analysis [8, 9].

Experimental Characterization
In this experimental study, a burner with a square section area of 105 mm width and

360 mm height was used to investigate the swirl flames. The atmospheric nozzle, consisting of two co-rotating swirlers, was used to generate swirl flames inside the burner. More details on the experimental apparatus can be found in Figure 1.
The flowrate of pure methane in the first case and hydrogen and fuel in the second one were calculated to assure that the thermal power remained constant at 5.06 kW. In particular, in the first case, the CH_4 flowrate is equal to 9.33 l/min while in the second one the H_2 flowrate is 3.33 l/min (i.e. the 5% by mass and about the 30% by volume of the total flow rate of mixture) and CH_4 flowrate is 8.32 l/min. The starting equivalence ratio (ϕ value) for ignition was fixed at 0.748, and in the case of the mixture, it slightly decreased to 0.734. The experiments were conducted under constant inlet air flow rate conditions, with a value of 113.3 l/min.
In the present study, high-speed imaging of reaction zone chemiluminescence was utilized to investigate the spatio-temporal distribution of the flame front and primary combustion zone. The emissions were acquired using a Phantom M320S camera equipped with a Lambert image intensifier, as shown in Figure 1. No spectral filtering was applied during imaging. The grayscale images were captured at a framerate of 1000 Hz, with each pixel point being discretized using 8 bits ranging from 0 to 255. Proper Orthogonal Decomposition (POD) and Spectral Proper Orthogonal Decomposition (SPOD) were used in this study to perform modal spatio-temporal characterization of the flame using high-speed acquisitions. [8,9]

Results

High-speed chemiluminescence imaging of reaction zones.

Chemiluminescence images were recorded (without any spectral filtering) for both cases, without and with H_2-enrichment of methane fuel at high-speed (1000 frames/sec framing rate). Such imaging was performed to compare the appearance of reaction zones at the presence of H_2 percentage addition to methane fuel.
The broadband chemiluminescence techniques are utilized to qualitatively examine the impact of hydrogen addition on flame structure. The captured images utilize the same ICCD settings for both the conditions with and without hydrogen at a constant thermal power, facilitating a comparison of the relevant differences.
In Figure 2a, the image in the first column was acquired with pure methane/air, and in the second one with the presence of hydrogen.
Figure 2 provides an analysis of the average flame structures, offering an overall insight into the impact of hydrogen addition on the flame structure. When the fuel mixture is enriched with hydrogen, the mean flame length is slightly shorter compared to case of pure methane, and the flame angle is wider. This phenomenon is attributed to the increased expansion of the burnt gases within the Combustion Recirculation Zone (CRZ) due to the higher rate of heat release. The flame root position however does not differ significantly from the two cases even if the position of the maximum of heat release rate is located closest to the burner exit in the case of H_2 addition. It was noticed that the effects of hydrogen presence on the UV

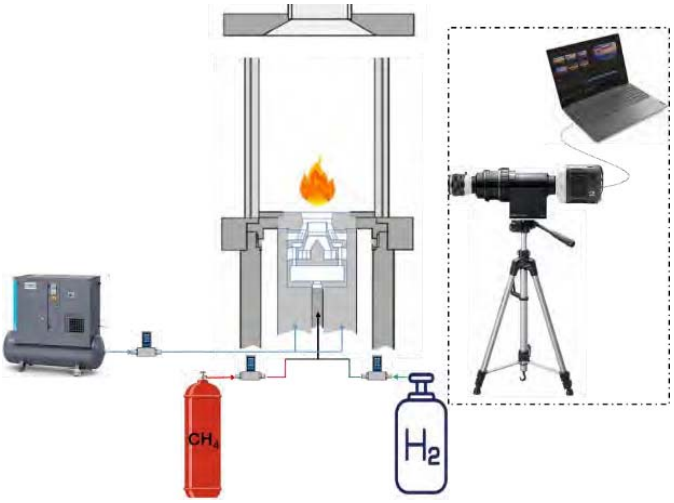

Figure 1 Experimental setup.

emissions were more significant and it was noted that the luminosity zone was shifted to the nozzle exit. The UV variance was greatly reduced with the use of hydrogen. The reductions of fluctuations lead to improved flame stability. To better understand how hydrogen enhances combustion, the Proper Orthogonal Decomposition (POD) method is employed to identify the coherent structures and energetic modes of the flame.

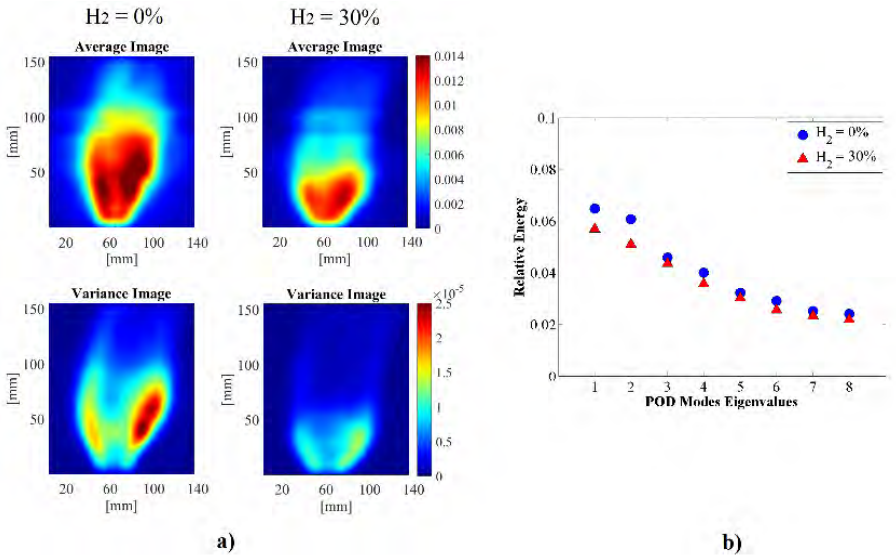

Figure 2. a)Time-averaged and variance of the broadband chemiluminescence signal (line-of-sight) without and with H_2 addition; b) Relative Energy of the details of POD of chemiluminescence images

The POD technique separates dynamic data into orthogonal modes that are arranged by decreasing energy, with the lowest order mode having the most energy. The energy contribution of each mode to the flow field reconstruction is described by their energy. Figure 2b illustrates the relative energy contributions of the 1-8 eigenmodes (fluctuations) with and without the hydrogen addition. It was observed that the first 8 modes generally account for the majority of the relative energy. Additionally, it was noted that the energy content of the first mode in the hydrogen/methane flame was lower than that of the pure methane flame. It is evident that with the use of hydrogen, the heat fluctuations of modes 1-8 were decreased in the first few modes. This decrease in energy content for the mixture flame can be attributed to the stabilizing effect of the hydrogen, which results in lower heat release fluctuations that are represented by the energy content in the highest modes.

In Figure 3, a comparison is presented between the first four POD modes for UV chemiluminescence images in two cases: one without hydrogen addition and another with hydrogen addition. The contour plots illustrating the mode shapes are arbitrary in terms of scale and sign, as they are scaled by their respective time coefficients, the colour red and blue are used to highlight zones with the highest intensity of fluctuations. However, these colours represent opposite changing directions, indicating a phase difference π between different zones. It is important to note that these modes represent the fluctuations in heat, ordered from the most energetic mode (1st mode).

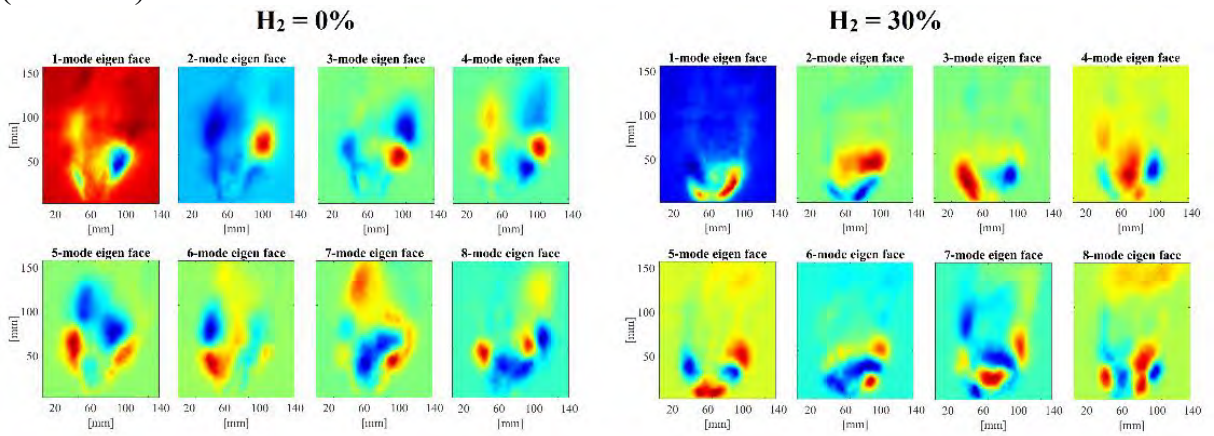

Figure 3. Proper Orthogonal Decomposition of chemiluminescence images.

Higher modes show coherent structures that can be correlated with flow features. As the mode number increases, the wavenumber of this motion increases.
In the methane flame, larger-scale coherent structures that start from the exit of the burner and then develop downstream are evident. In particular, the first two modes display rotating fluctuations, while the third and fourth modes exhibit vortex shedding along the shear layers near the burner exit. Additionally, the fourth mode demonstrates an alternate ring vortex propagation in the swirl combustion mode. The enrichment with H_2 leads to smallest structures closest to the nozzle exit, with an longitudinal oscillation in the second mode, while vortex shedding can be clearly observed in modes 3 and 4.

Frequency analysis of heat and acoustic signals.

In order to gain a better understanding of flame fluctuations, a simultaneous evaluation of the power spectral density (PSD) has been conducted from both microphone signals and the Proper Orthogonal Decomposition (POD) eigenmodes for different cases (Figure 4). The addition of hydrogen to methane had a notable influence on the frequency of fluctuations observed in both the acoustic signal and POD modes, which can be qualitatively linked to heat transfer. Clearly, distinct frequencies emerge as dominant within the combustor when comparing fuels with and without hydrogen. Microphone measurements revealed broadband sound spectra with minor peaks around 124 Hz, 209 Hz, 417 Hz, and 536 Hz for the methane case. These frequencies align with the findings of previous studies [10], particularly the peak at 530 Hz, which was associated with the Precessing Vortex Core (PVC).

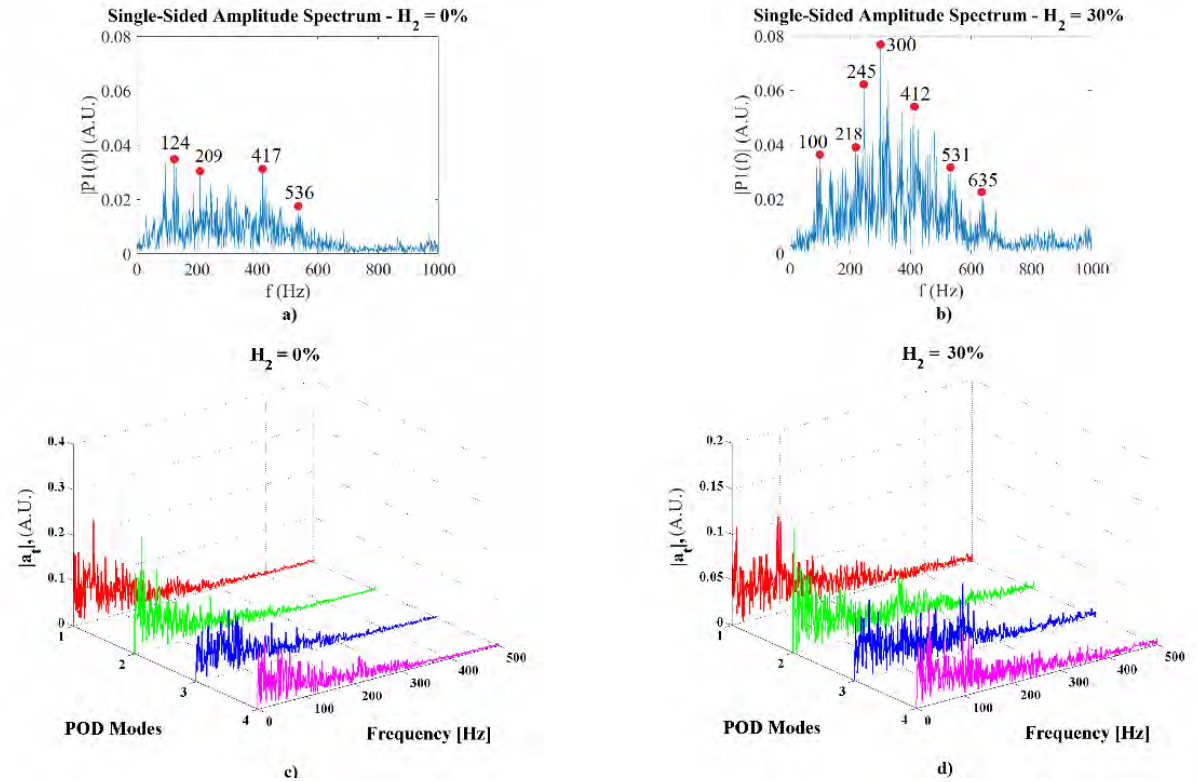

Figure 4. Power spectral density of microphone signal with pure methane (a) and with hydrogen enrichment (b); POD eigenmodes.

In [10], the acoustic peaks observed at higher frequency ranges (greater than 530 Hz) were found to be correlated with the acoustic modes of the combustor. The amplitude of these acoustic mode peaks increased with a higher percentage of hydrogen in the fuel, which was also evident from the audible signature of the reaction zones during experiments. Additionally, in our present study, a certain level of sound power was concentrated in the frequency band close to 635 Hz when hydrogen was added. The introduction of hydrogen resulted in frequencies falling within the same bands (100 Hz, 245 Hz, 412 Hz, and 531 Hz) and other peaks at 300 Hz and 635 Hz, with a significant portion of the sound power concentrated near 300 Hz. Importantly, higher values of peak sound intensity indicate combustion-induced instabilities that could potentially cause damage to the system. However, the high frequencies near 635 Hz were not observed in the PSD of the POD eigenmodes. Combustion-induced instabilities, which can generate large pressure oscillations or sound levels, have the potential to harm the system and should be avoided. Therefore, the benefits of hydrogen addition in terms of emissions must be carefully considered in relation to the requirement of ensuring the structural integrity of the combustor.

Regarding the POD eigenmodes, the peaks are within the frequency range of 0-220 Hz. Specifically, for pure methane flames, high peaks were observed in the range of 0-100 Hz for the first two modes, which are characterized by rotating and transversal oscillations. In modes 3 and 4, there was evident content around 200 Hz, indicating

longitudinal oscillations. In the case of hydrogen addition, longitudinal oscillations were present from the second mode onwards, leading to an increase in content around 218 Hz. This frequency was also noticeable in the microphone signal. The first mode exhibited a peak at 93 Hz, close to the 100 Hz peak detected in the microphone measurements.

Spectral Proper Orthogonal Decomposition.

The SPOD analysis of the methane flame, depicted in Figure 5a, highlights a significant energy concentration in the low-frequency range, prominently peaking at approximately 15 Hz. Moreover, a distinct peak is observed around 210 Hz in the high-frequency range. Upon enriching the methane fuel with H_2, there is a reduction in energy intensity within the low-frequency range. Interestingly, a novel peak emerges at approximately 90 Hz. It is noteworthy that despite the H_2 enrichment, the original peaks at 15 Hz and 210 Hz persist. The first SPOD mode at the frequency of about 15 Hz exhibits rotating structures, corresponds to one of the dominant modes that was less clear by the POD analysis. The rotating structures captured in this mode signify the presence of transversal flame oscillation, indicating the whirling nature of the reaction zone. These rotating structures are larger in the case of methane flame. The first mode at a high frequency, approximately 210 Hz, reveals distinct longitudinal oscillations in both fueling conditions. In the case of H_2 enrichment, at a frequency of 93.75 Hz, the first mode exhibits an approximately axisymmetric fluctuation. In this mode, the strong response area alternates between upward and downward directions, indicating vigorous axial movement of the flame within the spatial domain. These characteristics signify an axial oscillation mode, where the flame moves forcefully along the axial direction.

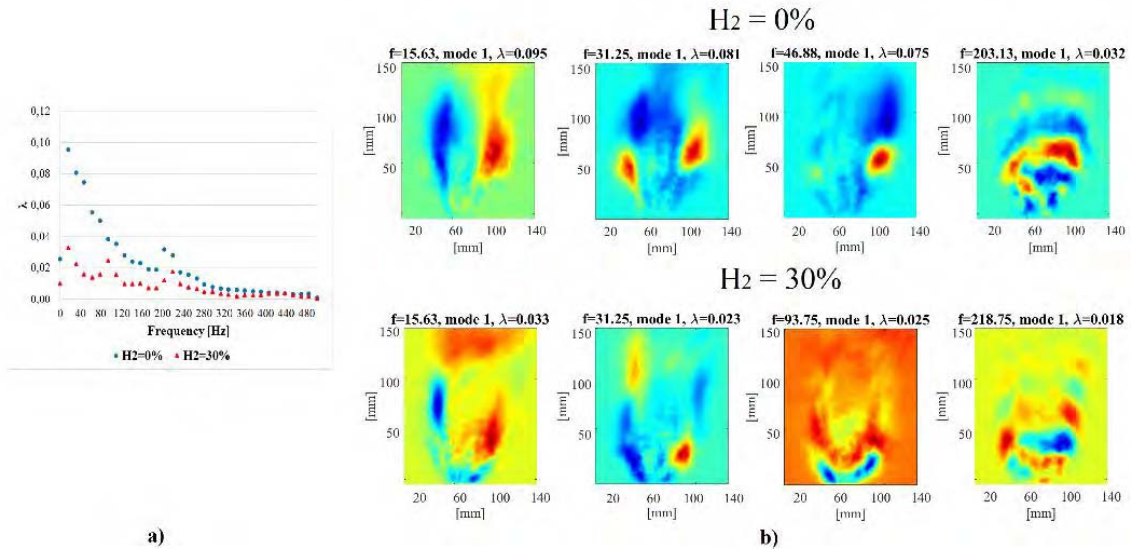

Figure 5. SPOD of chemiluminescence images: a) SPOD energy content; b) Mode 1 at selected frequency values.

Conclusions

This study compared chemiluminescence images of flame structures in two fueling conditions: pure methane/air and methane with hydrogen enrichment. The addition

of hydrogen resulted in a slightly shorter flame length and wider flame angle due to increased expansion in the Combustion Recirculation Zone. UV emissions were significantly affected, with a shift in the luminosity zone and reduced variance. Proper Orthogonal Decomposition (POD) and Singular Proper Orthogonal Decomposition (SPOD) analyses revealed coherent structures and energetic modes. Hydrogen enrichment led to smaller structures near the nozzle exit, longitudinal oscillations, and vortex shedding. Overall, hydrogen influenced flame characteristics and improved stability. The addition of hydrogen to methane fuel significantly also influenced the frequency of flame fluctuations, both in the acoustic signal and the POD modes.

Reference

[1] Chiesa P, Lozza G, Mazzocchi L. Using hydrogen as gas turbine fuel. J Eng Gas Turbines Power 2005;127(1):73e80. https://doi.org/10.1115/1.1787513.

[2] Lam K-K, Geipel P, Larfeldt J. Hydrogen enriched combustion testing of Siemens industrial SGT-400 at atmospheric conditions. J Eng Gas Turbines Power 2015; 137 (2):21502. https://doi.org/10.1115/1.4028209

[3] Bothien MR, Ciani A, Wood JP, Fruechtel G. Toward decarbonized power generation with gas turbines by using sequential combustion for burning hydrogen. J Eng Gas Turbines Power 2019; 141(12):121013. https://doi.org/10.1115/1.4045256

[4] Dahl G, Suttrop F. Engine control and low-NOx combustion for hydrogen fuelled aircraft gas turbines. Int J Hydrogen Energy 1998;23(8):695e704. https://doi.org/10.1016/S0360-3199(97)00115-8.

[5] Cozzi F, Coghe A. Behavior of hydrogen-enriched nonpremixed swirled natural gas flames. Int J Hydrogen Energy 2006;31(6):669e77. https://doi.org/10.1016/j.ijhydene.2005.05.013.

[6] Oh J, Hwang J, Yoon Y. EINOx scaling in a non-premixed turbulent hydrogen jet with swirled coaxial air. Int J Hydrogen Energy 2010;35(16):8715e22. https://doi.org/10.1016/j.ijhydene.2010.04.159.

[7] Funke HH-W, Beckman N, Keinz J, Horikawa A. 30 years of dry-low-NOx Micromix combustor research for hydrogenrich fuels: an overview of past and present activities. J Eng Gas Turbines Power 2021;143(7):71002. https://doi.org/ 10.1115/1.4049764.

[8] Lumley, J. L. 1967. The structure of inhomogeneous turbulence. Atmospheric Turbulence and Wave Propagation. AM Yaglom, VI Tatarski, 166-178.

[9] Sirovich, l. 1987. Turbulence and the dynamics of coherent structures part iii: dynamics and scaling. Quarterly of Applied Mathematics, 45(3): 583-590.

[10] Rishi Roy, Ashwani K. Gupta, Performance enhancement of swirl-assisted distributed combustion with hydrogen-enriched methane, Applied Energy, Volume 338, 2023, 120919, ISSN 0306-2619, https://doi.org/10.1016/j.apenergy.2023.120919.

ANALYSIS OF A PARTIALLY PREMIXED H2-NATURAL GAS-AIR FLAMES STABILIZED BY A SWIRL BURNER USING EXPERIMENTAL AND NUMERICAL METHODS

Emre Böncü[1], Dilay Güleryüz[1], Mehmet Karaca[1], Christophe Allouis[1,2], İskender Gökalp[1,3]

[1] Middle East Technical University, Ankara, Türkiye
[2] STEMS-CNR, Napoli, Italy
[3] ICARE-CNRS, Orléans, France; TÜBİTAK Marmara Research Centre, Türkiye

Abstract

A partially premixed swirl stabilized burner is analyzed using experimental and numerical studies. The fuel composition is changed throughout the experiments and numerical simulations. In the experiments, fuel composition is started from pure natural gas, and gradually hydrogen is added to the fuel mixture. The effect of hydrogen addition is analyzed using chemiluminescence imaging. The total volumetric fuel flow rate is kept constant throughout the experiments. The experiments are conducted up to a hydrogen ratio that causes the flame to change stabilization mode from a lifted-off flame to a flame attached to the central fuel pipe below the injection holes. Both lifted-off flame dimensions and stability mode change is analyzed using numerical simulations. StarCCM+ software is used with Large Eddy Simulation (LES) turbulence model, Flamelet Generated Manifold (FGM) combustion model, and Thickened Flame Model (TFM) turbulence-chemistry interaction model.

Introduction

One approach to combatting CO2 emissions from the combustion of fossil fuels is the introduction of low or zero-carbon fuels. Hydrogen is a promising candidate for this, but its unique properties compared to other fuels make it challenging to optimize combustion while maintaining safety. Adopting a premixed combustion approach for pure hydrogen or hydrogen blends can be risky due to the potential for unwanted combustion initiations and flame flashback. On the other hand, a non-premixed or diffusion flame approach can lead to high-temperature hydrogen flames that can damage the burner elements, as well as increase nitric oxide emissions. The optimal solution appears to be a non-premixed reactant feeding to the burner or combustion chamber, followed by rapid and efficient mixing at the exit of the burner to stabilize a well-mixed flame structure. In this study, both experimental and computational fluid dynamics approaches are applied to achieve this objective.

Experimental Setup

An experimental setup has been installed within the facility of Tubitak-SAGE to analyze a swirl-stabilized partially-premixed combustor. A swirl burner has been designed and produced for the experiments. The burner design has been inspired by the experiments conducted by Prof. Boushaki and Prof. Gokalp in ICARE laboratories [1]. The designed burner consists of an annular air duct with swirler blades. In the middle of the air duct sits a central fuel pipe. The central fuel pipe discharges fuel to the surrounding swirled air flow through eight radial holes. The burner geometry is illustrated in Fig. 1.

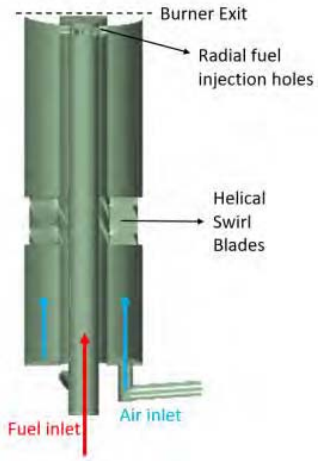

Figure 1. Swirl burner geometry

Air is fed into the burner from a compressor, and the flow is regulated using a mass flow controller. Natural gas and hydrogen are fed to the burner from fuel bottles and controlled by mass flow controllers as well. Before entering the central fuel pipe, natural gas and hydrogen are mixed in an in-line static gas mixer. Experiments start with purely natural gas fuel and gradually go up to a 70% volumetric hydrogen ratio in fuel. Throughout the experiments, the total volumetric flow rate of fuel and air is kept constant. The air flow rate is kept constant at 259.1 SLPM and the total fuel volumetric flow rate is kept constant at 21.8 SLPM. Thus, for example for a pure natural gas fuel mixture, the natural gas flow rate is kept at 21.8 SLPM while the hydrogen flow rate is kept at zero. On the other hand, for a 60% hydrogen ratio natural gas flow rate is kept at 8.7 SLPM, and the hydrogen flow rate is kept at 13.1 SLPM. Since hydrogen is less dense than natural gas and has less heating value per volume, the total mass flow rate of fuel and the power of the burner goes down as hydrogen is added to the mixture.

The changing global equivalence ratio and the power output of the burner for these fuel mixture cases are plotted in Fig. 2.

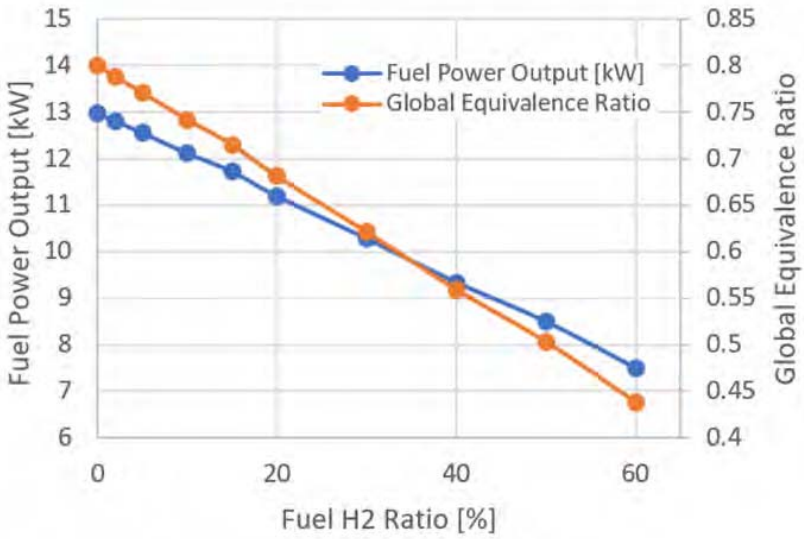

Figure 2. Fuel power output (calculated using LHV) and global equivalence ratio plotted against fuel hydrogen ratio

The resulting flames are imaged using a Dantec HiSense Zyla camera with an image intensifier and filters for OH* and CH*. Results are gathered for both CH* and OH* filters, and without a filter. Every image series are taken within a one-second span using 250 µs exposure time. Within a one-second span, one thousand images are taken for post-processing.

Numerical Setup

For the numerical simulations, StarCCM+ software is used. Simulations are conducted for pure natural gas, 30%, 60%, and 70% hydrogen cases. Simulations used Large Eddy Simulation (LES) turbulence model with Flamelet Generated Manifold (FGM) combustion model and Thickened Flame Model (TFM) turbulence-chemistry interaction model. The numerical mesh consists of ~35 M polyhedral cells and simulations are conducted with a 1e-5 second time step. The FGM table is generated using GRI 3.0 chemical kinetics mechanism and a 1-d freely propagating laminar flame reactor. The numerical mesh is illustrated in Fig. 4.

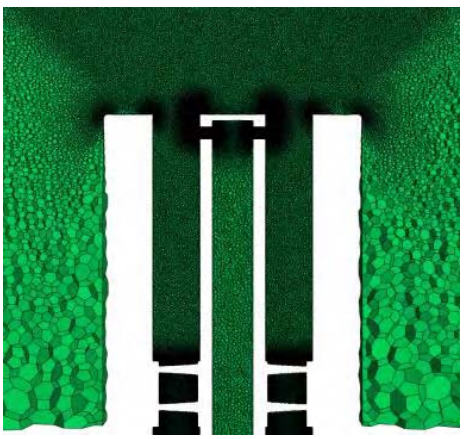

Figure 3. Axial slice of the polyhedral mesh

The numerical mesh quality is validated by using the criteria introduced in the book "Turbulent Flows" by S. B. Pope [2]. Within the relevant part of the numerical domain, it has been confirmed that no cells remain with a sub-grid scale turbulence energy ratio higher than 20% of the total turbulence energy. The resolved turbulence energy was determined using the variances of the velocity vector components.

Experimental Results

In the experiments, a total of 10,000 images were captured over a recording duration of one second for the eleven different cases, using an OH* chemiluminescence filter. For cases with up to 60% hydrogen in fuel, a lifted-off flame has been stabilized. However, for the 70% case, the flame became attached to the central fuel pipe. The images for each case were then averaged to create an average OH* field image. A picture of the burner was taken with a millimeter-paper for reference. In this picture, the average images for different fuel cases (for lift-off flames) have been superimposed to determine the flame dimensions. The results for pure natural gas fuel and 60% hydrogen fuel cases are illustrated in Figs. 5a,5b.

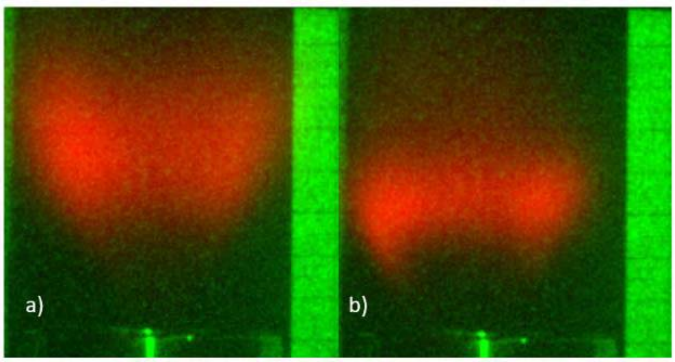

Figure 4 Experimental chemiluminescence OH* concentration results from a) for 0% hydrogen and b) for 60% hydrogen

As seen from the figures, for the lifted flames it is clear that the addition of hydrogen to the fuel mixture has a shrinking and lowering effect on the flame structure. As hydrogen is added to the fuel mixture, the flame lowers down to the burner exit so the lift-off height gets smaller. Also, the flame gets narrower and shorter. For the attached flame, no OH* results were gathered due to safety concerns regarding the operation of the burner with an attached flame. To analyze the lift-off height, width, and length of the flame, average images are processed as follows. The superimposed average images are analyzed by identifying the pixels with an intensity value equal to 0.5 times the maximum intensity value in the picture with a relative tolerance of 0.005. From the uppermost, lowermost, leftmost, and rightmost pixels within this group of pixels, the flame height, width, and lift-off height are determined. The results are plotted in Fig. 6.

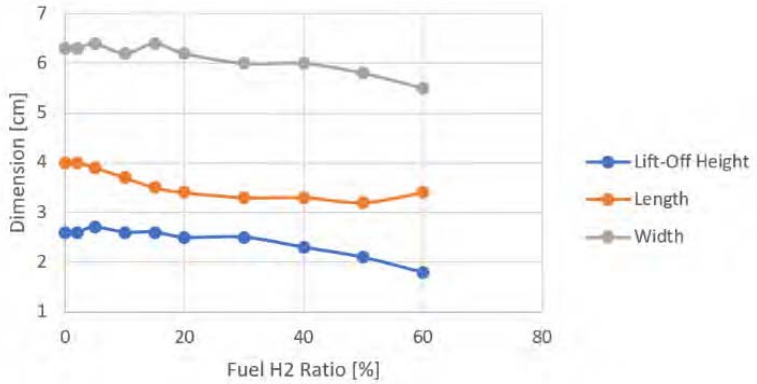

Figure 5 Flame dimensions plotted against the hydrogen ratio in the fuel

Numerical Results

Numerical simulations were started with a pure natural gas fuel mixture. Following simulations were started from the last time step of the previous one. For every fuel mixture case, a new FGM table was created. This also reflects the strategy used in the experiments. For the pure natural gas case, after ignition 0.4 seconds have been simulated without starting to take the mean of values, to achieve quasi-stability. After achieving quasi-stability, the simulation has been conducted for a further 0.4 seconds to take the mean of the resulting values. The following cases were given 0.1 seconds to reach quasi-stability and the mean of values were taken for 0.4 seconds after that. From pure natural gas to a 60% hydrogen ratio fuel mixture a lifted-off flame has been predicted, and with the 70% hydrogen mixture fuel an attached flame to the central fuel pipe has been predicted. This obviously parallels the flame stabilization mode results gathered from the experiments. In Figs. 7a,7b, the numerical results are compared side-by-side to the experimental results. The experimental line-of-sight OH* concentration results are compared with the numerical volume rendered line-of-sight chemical heat release rate contours since these values are shown to correspond well to each other in literature [3]. In Fig. 7c, the attached flame numerical result is displayed.

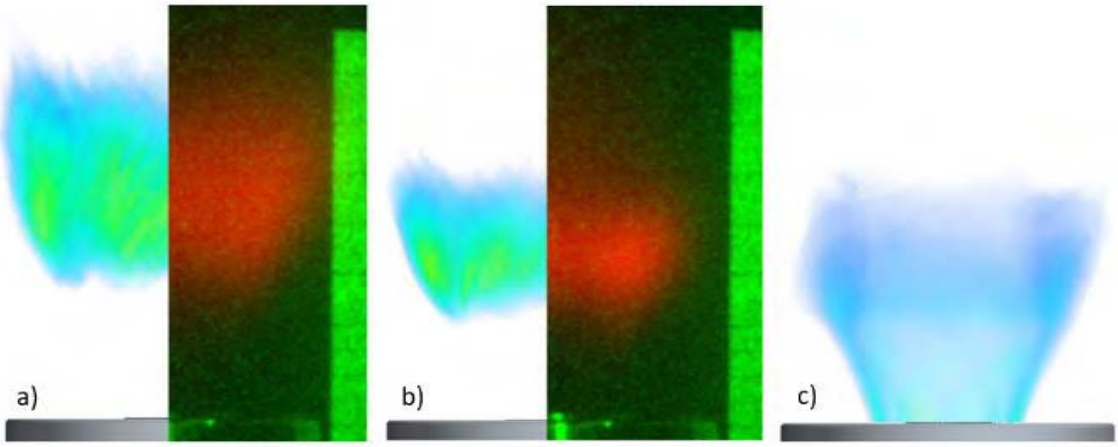

Figure 6 Numerical mean chemistry heat release rate results are compared to the experimental OH* concentration images for a) 0% hydrogen and b) 60% hydrogen

The numerical flame lift-off, width, and height dimensions were determined similarly to the experimental procedure. The cells having a larger chemistry heat release rate value than the 50% of the maximum heat release rate value have been grouped. And in this group, values of the highest and lowest axial and radial coordinates were gathered. Using these values, flame dimensions have been determined. In Fig. 8, for the lifted-off flames, the numerical flame dimension results were compared with the experimental ones.

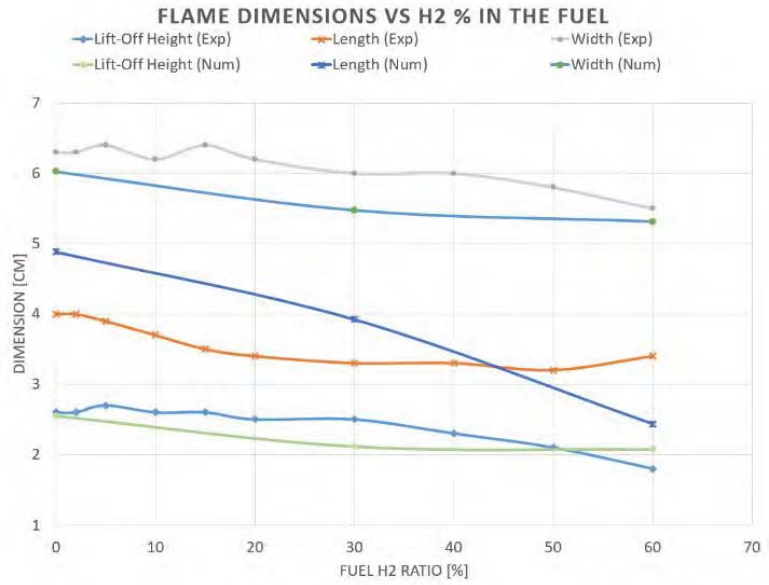

Conclusions

The study investigates the impact of hydrogen addition to natural gas in swirl-stabilized flames with partial premixing, along with numerical analysis of pure methane cases. Experimental results show that the addition of hydrogen to methane results in a more compact flame closer to the combustor exit, which could be due to increased flame speed resulting from hydrogen addition. Similarly, pure methane fuel cases analyzed through LES simulations show comparable results.

References

[1] Boushaki, T., Merlo, N., De Persis, S., Chauveau, C., & Gökalp, I. (2019) Experimental investigation of CH4-air-O2 turbulent swirling flames by Stereo-PIV. Experimental Thermal and Fluid Science, 106, 87-99.

[2] Pope, S. B. (2000). Turbulent flows. Cambridge university press.

[3] Liu, Y., Tan, J., Wang, H., & Lv, L. (2019) Characterization of heat release rate by OH* and CH* chemiluminescence. Acta Astronautica, 154, 44-51.

SESSION VI

FUEL SYNTHESIS, UPGRADING, AND CCUS PROCESSES


THE COMBUSTION INSTITUTE
1954

DEVELOPMENT OF A SECOND-GENERATION NAPHTHENIC DROP-IN FUEL FOR SPARK IGNITION APPLICATIONS

T. Robeyn*, T. Larsson*, S. Verhelst*
tom.robeyn@ugent.be
*Ghent University
Research Group STFES (Sustainable Thermo-Fluid Energy Systems)
Sint-Pietersnieuwstraat 41
B-9000 Gent, Belgium

Abstract
Second-generation (2G) biofuels are one of the pathways to sustainable mobility. Not relying on feedstock or land use for food production, these types of biofuels offer advantages over their first-generation (1G) counterparts. However, the production techniques involved present considerable challenges on a technical and an economical level. A novel 2G biofuel production technique has been designed in an effort to overcome these challenges. Based on a catalytic process that operates at low temperature, it converts woody biomass feedstock into a stable light naphtha. The process development is integrated in the Belgian federal government funded Ad-Libio project (short for "Advanced Liquid Biofuels"). The process outcome mainly consists of hydrocarbons containing five to six carbon atoms. The ultimate goal is to produce a drop-in fuel that can be fully interchanged with the gasoline fuels in use today. Since the Ad-Libio fuel components differ significantly from gasoline fuel components, the suitability of several blends of these components needs to be investigated. To that end, a fuel blend calculator with integrated fuel database has been developed. Enabling fast SI fuel property calculations, the tool is used to make quick decisions on the fuel production process outcome. This allows modification of the production process so that only promising fuel blends are generated. Verification of the fuel blend calculations were then performed in the lab by means of a simplified octane verification method. Finally, the most promising fuel blend was sent to an ASTM-compliant laboratory for Research Octane Number (RON), Motor Octane Number (MON) and Reid Vapor Pressure (RvP) evaluation, confirming the promising results from the fuel blend calculator. This article describes the calculation and verification methodology of the blends that are generated by the novel production process, ultimately aiming for a sustainable second-generation drop-in gasoline fuel replacement.

The importance of biofuels

Germany's FVV's Future Fuels Study IV [1] states that, when assuming that a fully defossilized energy/fuel supply is achieved by 2050, cumulative greenhouse gas (GHG) emissions are dominated by the world's remaining gasoline/diesel vehicle fleet, with a total GHG contribution of 66-74%. A quick ramp-down of fossil fuel usage in transport applications is therefore a crucial factor to minimize cumulative GHG emissions. Sustainable drop-in fuels are one option to eliminate net GHG emissions of existing internal combustion engine (ICE)-powered vehicles. The use of first-generation (1G) biofuels like ethanol is common today, but when the volume ratio exceeds 10% in the fuel blend, flex-fuel engine technology is required. For compression ignition (CI) or diesel engines, Fatty Acid Methyl Esters (FAMEs, also known as biodiesel) are widely used as a partial replacement for fossil diesel. The use of FAME as a low-blend component in transport fuel (up to 7 % in Europe, compliant to EN590) does not require any changes in the distribution system or the engine, but modifications to the distribution as well as the engine infrastructure (e.g. seals, piping) are required for use of 10% FAME/diesel blends up to 100 % pure FAME fuel. So neither ethanol nor FAME can be considered as drop-in fuels. For CI engines, a second-generation alternative is available in the form of HVO (Hydrotreated Vegetable Oil). HVO claims to be a true drop-in fuel that can be used in legacy CI-powered vehicles. It is produced from waste, residues and dedicated crops not in competition with food crops and makes up for an estimated 7% of biofuels consumed in 2020, according to the International Energy Agency's Transport Biofuel report of that year. The production of sustainable drop-in fuels for legacy spark ignition (SI) engines is less established. Sustainable synthetic EN-228 compliant gasoline, made out of ethanol is already available today, though in very limited quantities [2]. Production capacity for green methanol-based synthetic gasoline is expected to increase considerably in the coming years [3]. Complementary to these production efforts, a novel biorefinery process designed by researchers at KU Leuven generates naphthenic biofuel components that might be used as drop-in fuels for SI engines. Although the production cost of naphthenic biofuels with the Ad-Libio process is currently unknown, an economic study is foreseen within the project and will be completed at the end of 2023. However, some major potential advantages of Ad-Libio over fermentation processes can already be identified. The process efficiency is situated between 70 to 80%, which is an improvement compared to the 50% that are associated with fermentation processes. Ad-Libio omits the use of woody biomass-compatible yeasts that are complex to synthetize, costly to produce and hard to recycle. Also, Ad-Libio does not suffer from carbon loss in the form of CO_2-emissions like fermentation processes do. Contrary to fermentation processes, Ad-Libio does not have alcohols as main output stream, but C5-C6 hydrocarbons that will likely not require flex-fuel technology for them to be used as combustion engine fuel.

The initial Ad-Libio production process

In the Ad-Libio process [4], debarked and milled wood particles undergo basic extraction of the non-structural compounds such as fats, oils, proteins and terpenes. Then, lignin (step 1, Figure 1) is extracted from the lignocellulosic network in the presence of an alcohol solvent and subsequently stabilized by catalytically depolymerizing it in stable fragments. Next to the lignin oil, cellulose pulp is retained, which predominantly consists of C6 and C5 sugars. This fibrous sugar pulp is then further treated with hydrogen molecules, resulting in a hydrocarbon mixture in the naphtha-range (C5-C6 molecules)

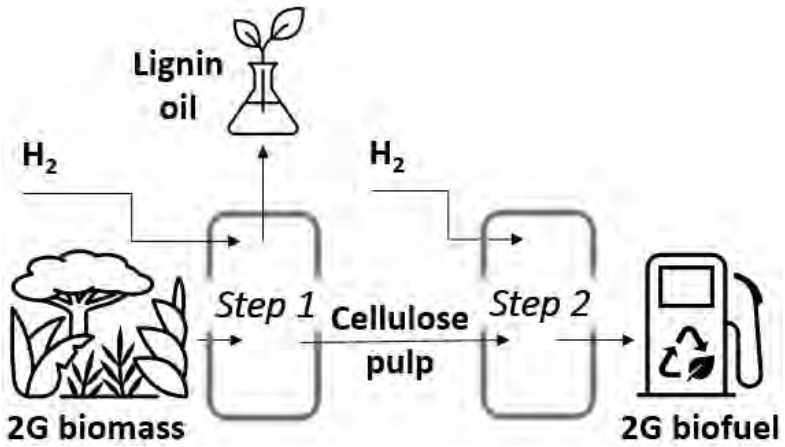

Figure 1. The Ad-Libio production process.

The initial composition of the process outcome was theoretically defined by the chemists at KU Leuven and were listed. The data mentioned in table 1 were extracted from a SI fuel database from RWTH Aachen university [7]. This database contains more than 600 fuel components and lists, for each component, the physical and chemical properties including research and motor octane numbers, octane sensitivity, cetane number, heat of vaporization, liquid density, surface tension, viscosity, boiling point, melting point, vapor pressure, lower heating value, H/C ratio, oxygen content, molecular weight, and water solubility. Most of the listed values are experimentally determined but in the case of missing experimental evidence, values are estimated by using an artificial neutral network-based octane number model or other established quantitative structure-property relationship models.

Table 1. Initial Ad-Libio fuel composition.

Ad-libio fuel component	**Vol %**	**RON**
n-hexane	70	24.8
n-pentane	13	61.7
Methyl cyclopentane	9	91.3
2-methylpentane	1	73.4
cyclopentane	1	101.3
3-methylpentane, methyl/ethyl/propyl- cyclohexane, et al.	5	45-103
tetrahydrofuan, (di)methyl tetrahydrofuran	1	73-101
Result of the fuel blend (linear molar calculation)		**41.2**

The listed components were investigated for usability as a drop-in replacement for gasoline, starting with the fuel's research octane number (RON). To predict the octane number of the blend, a fuel blend calculator from Bath University was modified, to enable blend calculations of up to 20 blend components. For simplicity, a linear molar relationship was used to calculate the RON of the blend, as shown in equation (1)

$$RON_{blend}=\Sigma x_i.RON_i \quad (1)$$

The result of the blend calculator, mentioned in table 1, was a RON of 41,2 for the blended components. The calculated result was experimentally verified by means of a CFR engine with variable compression ratio (CR), using a simplified approach. A fuel's octane rating was estimated by generating a fixed average peak pressure pulsation (APPP) value from 200 knocking cycles, expressed in kPa, by reading the corresponding CR. Comparing this CR with the one at which a primary reference fuel mixture (PRF) knocks with the same APPP then yields an estimation of the fuel's octane number [7]. Although this experimental method is not ASTM D2699-compliant [6], it was sufficient to confirm the previously made calculations. A measured octane number (ON) value of 37.9 compared to a calculated ON of 41.2 indicated a difference of slightly more than 10%, but this can be subscribed to the fact that at low octane numbers, the experimental method becomes less accurate.
Compared to a minimum RON of 95 according to the European norm EN228 for gasoline, it is clear that the initial process output of the Ad-Libio was not suitable as a drop-in replacement for gasoline.

Revised production process outcome

After feedback with KU Leuven, the production process parameters were altered in an attempt to increase the RON of the end product. By varying different process parameters, isomerization of the initial molecules could be obtained and different alternative process outcomes could be calculated. Table 2 lists ten different

theoretical fuel blends, with each "x" indicating the presence of a fuel component in the blend. For simplicity, the exact volume fractions of the components are not listed.

Table 2. Initial Ad-Libio fuel composition.

Blend #	**1**	**2**	**3**	**4**	**5**	**6**	**7**	**8**	**9**	**10**
Pentane	x	x		x	x	x	x	x	x	x
Methylbutane		x	x	x	x	x	x	x	x	x
Hexane	x	x		x	x	x	x	x	x	x
2-methylpentane		x	x	x	x	x	x	x	x	x
3-metylpentane		x	x	x	x	x	x	x	x	x
2,2-dimethylbutane		x	x	x	x	x	x	x	x	x
2,3-dimethylbutane		x	x	x	x	x	x	x	x	x
Ethanol					x	x	x	x	x	x
Pentanol				x						
Hexanol				x						
Methylfuran						x				
Dimethylfuran						x				
Methylbenzene							x	x	x	x
Ethylbenzene							x	x	x	x
Propylbenzene							x	x	x	x
1- & 2-pentene								x		x
1-, 2- & 3-hexene									x	x
Calculated RON	**38**	**76**	**84**	**71**	**82**	**91**	**94**	**95**	**92**	**94**

The fuel blend calculator proved to be helpful by providing fast estimated RON calculations of every blend. It is clear that the isomerization of the original molecules leads to a significant increase in knock-resistive properties of the Ad-Libio fuel, with blend #8 being the most promising. It was decided to synthesize this specific blend in the lab and have it tested for research octane number (RON), motor octane number (MON) and Reid vapor pressure according to ASTM. The results confirmed the initial calculations with a RON of 96.2, a MON of 86.5 and a RvP at 37,8°C of 47.3 kPa.

Conclusions

A new 2G drop-in biofuel serving SI engine applications is under development. Thanks to a fuel blend property calculator, quick decisions could be made to tune the production process, turning its outcome into a promising fuel that may possibly be used as a drop-in replacement for gasoline. Further investigation with regards to performance and emissions with real-life engines is necessary and is planned for the forthcoming year.

References

[1] Research Association for Combustion Engines, "*FVV Future Fuels Study IV: Final report"* (2021)

[2] Esarte, C. "Development of 100% Renewable EN228 Gasoline Formulation and its Compatibility with Different Elastomeric Materials", *Proc 10th International Conference Fuel Science – From Production to Propulsion.* Aachen, Germany, 2022.

[3] Hannibal, W., *E-fuels and Hydrogen in Mobility Conserve the Earth's Resources,* MTZ worldwide, 2022. p. 66.

[4] Op de Beeck, B., et al., "Direct catalytic conversion of cellulose to liquid straight-chain alkanes", *Energy & Environmental Science.* 8(1): 230-240 (2004)

[5] vom Lehn, F., et al., "A property database of fuel compounds with emphasis on spark-ignition engine applications", *Applications in Energy and Combustion Science*. 5: p. 100018 (2021)

[6] ASTM D2699-15a., *Standard Test Method for Research Octane Number of Spark-Ignition Engine Fuel,* ASTM International, 2015

[7] Robeyn, T., Larsson, T., Verhelst, S., et al., "Development of a Novel Drop-in Naphthenic Spark Ignition Biofuel by Means of a Fuel Blend Calculator and a Simplified Octane Number Verification Method", *SAE Technical Paper* 2023-01-0317 (2023)

SULFUR TOLERANT DUAL FUNCTION MATERIALS FOR THE INTEGRATED CO_2 CAPTURE AND METHANATION

S. Cimino, E.M. Cepollaro, L.Lisi
stefano.cimino@cnr.it
* STEMS- CNR, Napoli, Italy

Abstract
The combined CO_2 capture and methanation with Dual Function Materials (DFM) is emerging as a vibrant field of research for its potential to increase the efficiency and reduce the cost of current multistage CCU processes. In this work, we set out to investigate for the first time the impact of sulfur poisoning over a Na-Ru/Al_2O_3 DFM operated in a fixed bed reactor with alternate feeds under realistic conditions including the presence of SO_2, H_2O and O_2 in the process gas stream. The results of the extensive characterization of the fresh and sulfated (reaction-aged) DFM evidenced a remarkable intrinsic tolerance of the combined CO_2 capture and methanation process to high concentrations of SO_2 in the feed due to a self-regeneration mechanism of the Ru catalytic sites.

Introduction
Converting CO_2 captured from flue/process gases or even from air using green hydrogen made from renewable energy is a way to contribute to reaching the ambitious decarbonization goals set for 2050 and also a valuable solution to store excess electrical energy in fuels/chemicals solving the intrinsic variability of renewable sources. The integrated CO_2 capture and methanation with Dual Function Materials (DFM) is emerging as a vibrant field of research for its potential to increase the efficiency and reduce the cost of current multistage CCU processes [1-2]. DFMs contain both a CO_2 adsorbent and a hydrogenation catalyst, which are intimately coupled and generally nanodispersed on a high surface area oxide support [1-2]. Therefore, the DFM can work as the chemical looping mediator, being exposed to alternate steps of CO_2 capture and reduction with H_2 (regeneration) in cyclic operations. Previous works focusing on the screening of several DFM formulations for methane production at intermediate temperatures (200–400 °C) treated simplified flue gas compositions containing various concentrations of CO_2 in N_2: best performances were reported with DFMs containing Li, Na, or Ca (hydro)oxides/carbonates (5-15 %wt.) as the regenerable sorbent phase, and Ru (0.5-5 %wt.) or Ni (5-15 %wt.) as the active phase both dispersed on γ-Al_2O_3 [1-4]. However, when capturing CO_2 from either flue gas or air, the DFM has to be exposed to O_2, H_2O, and other common impurities such as NO_x and SO_x, which cause

pronounced effects on the catalyst and challenge the stability of performance over multiple cycles. In particular, sulfur species can induce strong adverse effects by completely and irreversibly deactivating both the sorption and the catalytic sites in the DFM [5]. This is a common issue affecting other CO_2 capture techniques [1], and catalyst poisoning by sulfur compounds is one of the main factors to be considered when designing and operating methanation plants [5], which must be equipped with an appropriate sulfur removal system. Therefore, testing the S-tolerance and durability of DFMs during prolonged cyclic operation with feeds containing sulfur impurities is an area requiring detailed investigation before the integrated process is to be scaled up to applications [1]. In this work, we set out to investigate for the first time the effect of sulfur poisoning during the cyclic CO_2 capture and methanation performed over a Na-Ru on γ-Al_2O_3 DFM, which is reported among the best performing formulations at mid-low temperatures [1-4].

Experimental

Ru and Na were dispersed sequentially inside 1mm Al_2O_3 spheres by impregnation with water solutions of nitrate precursors. Their loadings in the final DFM were deliberately kept low (ca. 1 % and 2.8 % wt., respectively) to better highlight the possible sulfur-poisoning effects on both the sorption and catalytic functionalities.
Combined CO_2 capture and methanation tests were performed in a fixed bed quartz reactor with an annular section (d_{in}=4mm, d_{out} =10 mm) that was loaded with ca 2.3 cm^3 (packed-volume) of Na-Ru/A DFM. The reactor was operated at atmospheric pressure and at a fixed temperature of 300 °C and total inlet flowrate (20 Sl/h) by switching alternatively the feed between the CO_2 capture and methanation phases. During the first step a feed gas stream containing 5% vol. CO_2 in N_2 with the possible additional presence of 0.25% O_2 and/or 1% H_2O as well as 10-100 ppmv SO_2 was stepwise admitted to the reactor and flowed over the DFM. After an intermediate purge (2 min, pure N_2), the methanation phase was started by switching the feed to 15% vol. H_2 in N_2. Continuous gas analyzers (ABB Optima Advance) were used to measure the molar fractions of CO_2, CH_4, CO, and SO_2, H_2S.

Results and Discussion

Temporal profiles of (CO_2, CH_4, and CO) concentrations and temperatures measured at the exit of the DFM fixed bed during representative tests of integrated CO2 capture and methanation are shown in Figure 1. Average results relevant to four sequential runs for each one of the four different feed compositions are presented in Figure 2, showing highly repeatable performances across cycles. In particular, the Na-Ru/A DFM was able to capture ca 300 μmol/g_{DFM} of CO_2 from a dry N_2 stream at 300 °C, producing 207 μmol/g_{DFM} of CH_4: those values fall within the range of data obtained in the literature with other Na-Ru/Al_2O_3 DFMs (CH_4 prod from 47 to 614 μmol/g [4]). Roughly, 20% of the CO_2 uptake was released during the purge of the reactor by N_2; thereafter, upon feeding H_2, methane was quickly formed with negligible CO production (CH_4 selectivity above 99.6%) and ca 90% CO_2

conversion. Due to the exothermal nature of both the CO_2 adsorption and methanation processes, a transient temperature increase was measured in the DFM bed at the beginning of each phase (Figure 1d): the maximum temperature gradients during each step were similar (5.3 and 6.0 °C, respectively).

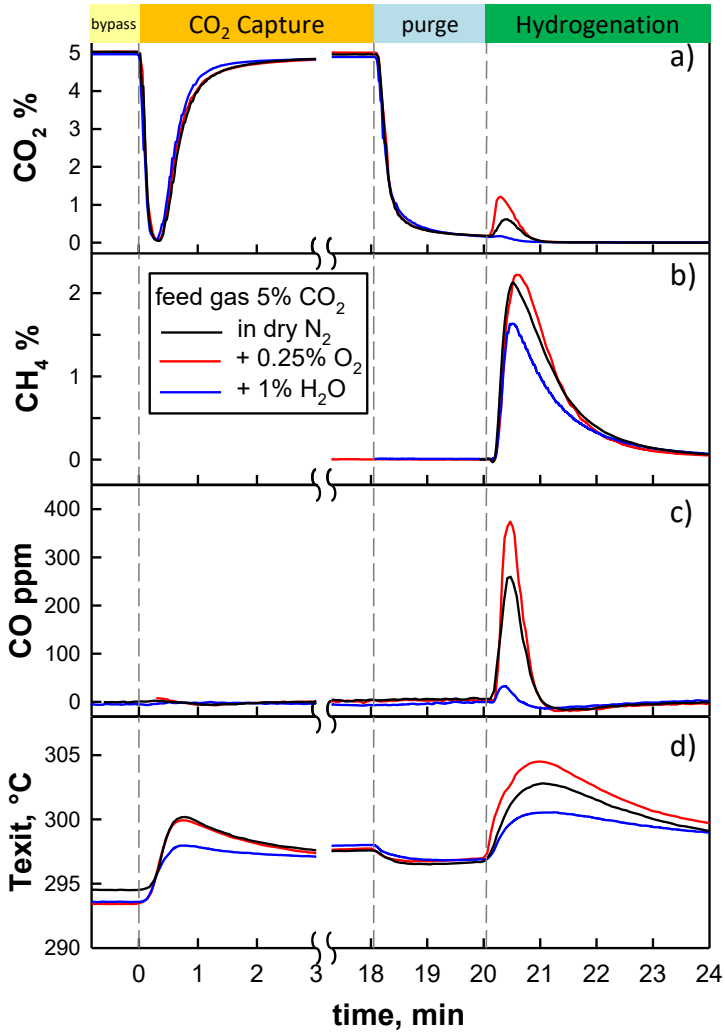

Figure 1. Integrated CO_2 capture and methanation cycles on Na-Ru/A DFM at 300 °C with 3 different feed gas compositions: 5% CO_2 in N_2, with the addition of +0.25% O_2 or +1% H_2O. Temporal profiles of CO_2 (a) CH_4 (b) and CO (c), and corresponding temperature at the exit of the catalytic bed (d). Step duration: 18 min CO_2 capture, 2 min N_2 purge, 14 min hydrogenation (15% H_2 in N_2).

Steam addition caused a 20% reduction of the CO_2 capture capacity of the DFM, possibly due to the competition of water for the same CO_2 adsorption sites. Moreover, the presence of H_2O mitigated the temperature rise during both the adsorption and methanation phases (Figure 1d): As a consequence, the CO_2 conversion increased up to ca. 94% and almost no CO was detected resulting in a process selectivity to CH_4 above 99.9%. At variance, the presence of O_2 during adsorption showed a marginal positive effect on the CO_2 uptake of the DFM. After purging (not affected), the DFM was able to produce roughly the same amount of

methane as in the reference ideal case, but with a slightly lower selectivity and conversion, due to a corresponding increase in the amount of thermally desorbed CO_2 and a marginally higher CO formation (Figure 1 a,c). This is consistent with the higher temperature increase observed in the DFM bed when O_2 was co-fed with CO_2.

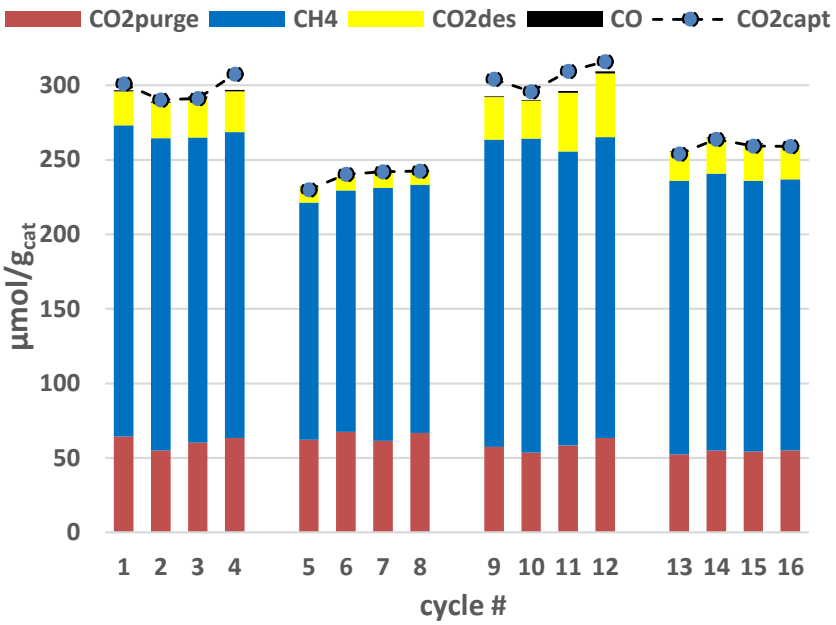

Figure 2. CO_2 adsorption (dots), CH_4 and CO production, and CO_2 desorption (bars) during 4 sets of 4 repeated cycles of CO_2 capture and methanation on Na-Ru/A DFM with variable feed gas compositions. All cycles were performed at 300 °C and 1 atm; adsorption conditions 5% CO_2 in N_2 (cycles # 1-4), +1% H_2O (# 5-8), +0.25% O_2 (# 9-12), +1% H_2O +0.25% O2 (# 9-12).

Reaction tests performed with the simultaneous presence of H_2O and O_2 with CO_2 in the feed gas showed the superimposition of the contrasting effects individually induced by single species. Specifically, the addition of O_2 partially mitigated the negative impact of H_2O on the CO_2 capture capacity of the DFM, which turned out to be only 13% lower than in the reference case (CO_2 in dry N_2). This circumstance directly translated into a similar recovery of methane production (up to 183 $\mu mol/g_{DFM}$), since CO_2 conversion was almost identical to the reference case, and the selectivity to CH_4 was even improved due to the effect of water.

The impact of the addition of 10 ppmv SO_2 to the inlet feed gas containing CO_2 and O_2 was investigated either under dry or humid conditions. Not surprisingly, during the capture step, the exit gas concentration of SO_2 quickly dropped to zero and the DFM retained all of the sulfur fed to the reactor due to the formation of stable sodium and/or aluminum sulfite/sulfates.

Therefore, the results are presented in Figure 3 in terms of SO_2 and CO_2 capture, CH_4 and H_2S production, CO_2 conversion during each cycle of CCM as a function of the cumulative amount of SO_2 retained by the DFM across cycles. It appears that the addition of SO_2 caused no adverse effect on the performance of the Na-Ru/A

DFM since all process outcomes obtained under either dry or humid conditions fell within the corresponding range of data previously measured with the S-free feeds.

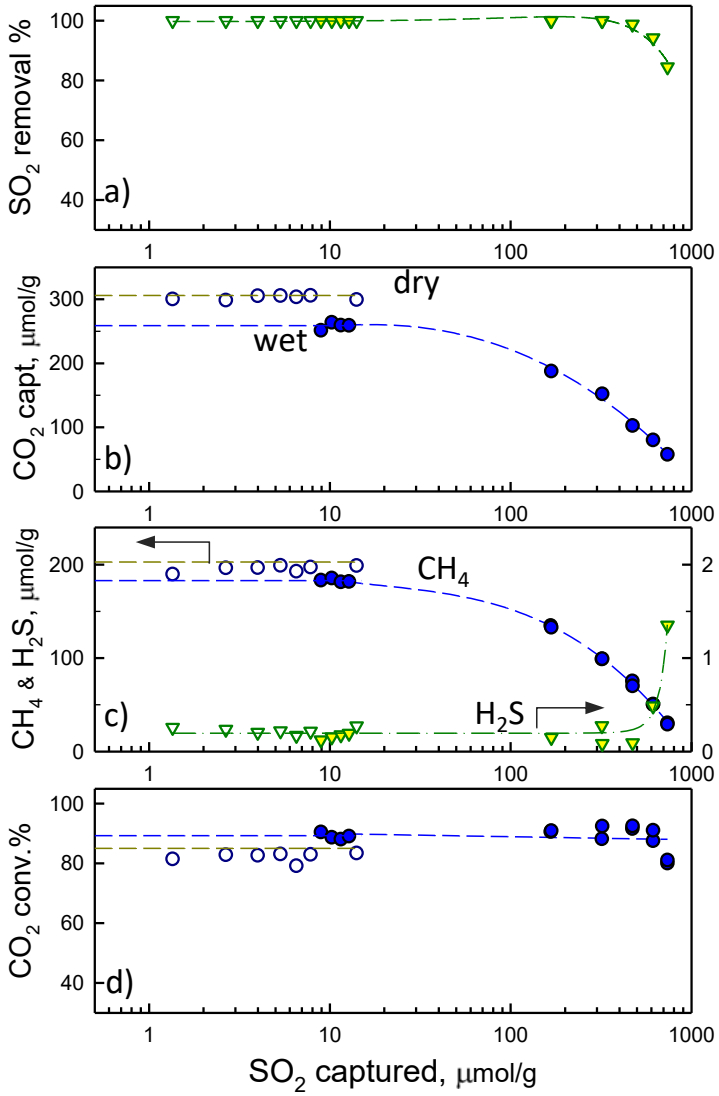

Figure 3 CO_2 capture and methanation cycles on Na-Ru/A DFM operating at 300 °C with a simulated flue gas containing 5% CO_2, 0.25% O_2, and 10ppmv SO_2 in dry N_2 (open symbols) or with the addition of 1% H_2O (closed symbols). SO_2 and CO_2 adsorption (a, b), CH_4 and H_2S production (c), CO_2 conversion (d) as a function of the cumulative amount of SO_2 retained on the DFM across cycles.

A close inspection of the temporal gas-phase concentration profiles at low sulfation levels of the DFM indicated a barely detectable emission of H_2S during methanation ($\leq$ 1 ppmv), confirming that the stored sulfur species were rather refractory to react with hydrogen at 300 °C: H_2S production remained low across cycles (Figure 3c) corresponding to less than 10 % conversion of the previously captured SO_2. Generally, H_2S is a strong poison for supported Ru methanation catalysts, even at low concentrations, due to the rapid formation of inactive and stable superficial RuS_x

species [5]. Nevertheless, the Na-Ru/A DFM showed an uncommon/unexpected tolerance to S-poisoning, apparently preserving its catalytic activity unaltered under those conditions. The accumulation of sulfur on the DFM above ca 100 μmol/g_{DFM} caused a slow and progressive decrease in the CO_2 capture capacity (Figure 3b), due to the corresponding saturation of the basic adsorption sites. However, the SO_2 removal efficiency of the DFM remained at 100 % up to roughly 600 μmol/g_{DFM} (corresponding to S : Na atomic ratio close to 1 : 2) and the amount of H_2S formed during the methanation steps was constantly low (Figure 3a,c). The CH_4 production decreased following the same trend of the CO_2 uptake (Figure 3c) since the efficiency of the catalytic process was not altered even at the highest sulfation levels. In particular, the formation of methane was not delayed by the increasing sulfur content on the DFM, while the conversion of CO_2 was steady (around 90 %, Figure 3d) and the selectivity to CH_4 even increased approaching 100 %.

Those results demonstrate for the first time the high sulfur tolerance of Na-Ru DFM, and suggest the existence of a peculiar and favorable self-regeneration mechanism for the catalytic Ru sites, preserving them from any significant sulfur poisoning effect. Specifically, it can be argued that Ru nanoparticles, which are partially covered by inactive RuS_x species at the end of the CO_2 hydrogenation step, can be periodically restored by the oxidation/reduction cycle naturally occurring during operation in the combined CO_2 capture and methanation process with alternate feeds.

References

[1] Merkouri, L.-P., Reina, T.R., Duyar, M.S. “Closing the Carbon Cycle with Dual Function Materials”, *Energy & Fuels* (2021).

[2] S. Sun, H. Sun, P.T. Williams, C. Wu, “Recent advances in integrated CO_2 capture and utilization: a review”, *Sustain. Energy Fuels* 5: 4546–4559 (2021)

[4] Cimino, S., Boccia, F., Lisi, L., “Effect of alkali promoters (Li, Na, K) on the performance of Ru/Al_2O_3 catalysts for CO_2 capture and hydrogenation to methane”, *J. CO_2 Util.* 37: 195–203 (2020).

[4] Porta, A., Matarrese, R., Visconti, C.G., Castoldi, L., Lietti, L., “Storage Material Effects on the Performance of Ru-Based CO_2 Capture and Methanation Dual Functioning Materials”, *Ind. Eng. Chem. Res.* 60: 6706–6718 (2021)

[5] Kuzmenko, D., Nachtegaal, M., Copéret, C., Schildhauer, T.J., “Molecular-level understanding of support effects on the regenerability of Ru-based catalysts in the sulfur-poisoned methanation reaction”, *J. Catal.* 375: 74–80 (2019)

Steam-assisted MILD-POX: a flexible process for the production of hydrogen

M. Lubrano Lavadera*, A. Coussement*, A. Parente*
marco.lubrano.lavadera@ulb.be
*Aero-Thermo-Mechanics Department, Université Libre de Bruxelles, 1050 Bruxelles, Belgium.

Abstract
The aim of the present work is to propose an alternative hydrogen production process using water and sustainable feedstocks to promote the utilisation of cheap and renewable raw materials on a large scale by increasing flexibility, efficiency, and eco-compatibility of existing technologies, without sacrificing their reliability and affordability. The idea to accomplish this aim is to combine non-catalytic Partial Oxidation and MILD combustion technologies by adding water. Thermodynamic equilibrium calculations, accompanied by kinetic modelling, were used to assess and interpret the general behaviour of a potential unit that uses the interaction of these two technologies and to compare the performances over a range of operating conditions of interest. The presented results have shown that thermochemical production of H_2 using the proposed process is theoretically feasible and has the potential to offer many advantages over standard processes.

Introduction
The overall purpose of the present work is to propose and assess an alternative prospective process to produce H_2 based on the combination of conventional non-catalytic partial oxidation (POX) and innovative Moderate or Intense Low-oxygen Dilution (MILD) technologies by adding H_2O.
Although considerable work has been carried out in the separate fields of MILD combustion and POX, the information on the hybrid process is limited. In particular, the establishment of steam-assisted MILD-POX has never been previously investigated. Therefore, the specific objective of the present study is to present a computational investigation of thermodynamic and kinetic features for assessing the influence of the governing parameters, i.e., operating temperature, pressure, carbon/oxygen ratio, H_2O concentration, and residence time on fuel conversion, H_2 yield, and product distribution. The analysis focuses on low/intermediate temperature conditions of practical interest to MILD combustion applications and fuel-rich conditions of interest to POX. Since very little is currently known about this chemical process regarding the impact of the different constituents forming a reactant mixture, the process is characterized using methane (CH_4) as a fuel. Its chemical kinetics is crucial since it constitutes the base of hierarchical chemistry for oxidation processes of bio-derived feedstocks and is sufficiently simple. Methane is among the main components of gaseous biofuels such as biogas, landfill and

pyrolysis gas. Therefore, a good understanding of the behaviour of CH_4 with high concentrations of H_2O is central to optimising the design of the proposed technology for any more complex feedstock. In addition, the use of CH_4 provides a way of comparing the proposed process to conventional steam reforming (SR) and POX, where CH_4 is widely used due to its high hydrogen-to-carbon ratio and, thus, the lowest level of generated by-products.

Thermodynamic and kinetic analysis

The CRECK reaction scheme provides an excellent prediction of the reactions of CH_4 under the conditions of interest [1]. This section aims to use it to theoretically assess and interpret the general behavior of a potential unit that uses the steam-assisted MILD-POX route of CH_4 for syngas production and to compare the performances over a range of different operating conditions. The H_2O/CH_4 feeding ratio is selected as the primary variable for the parametric study as dilution variation through internal or external recirculation is the most suitable way to achieve MILD conditions and thus for controlling the process. The H_2O/CH_4 ratio is also essential in industrial SR and POX to prevent carbon deposits. However, while traditional SR and POX generally employ ratios of 3-5 and 0-3, respectively, MILD-POX conditions require this ratio to be from ~5 up to 500, which makes the proposed process significantly different from the conventional ones. The H_2O/CH_4 ratio is restricted at its lower end by the MILD combustion definition; namely, the adiabatic temperature increase must be lower than the autoignition temperature. The upper limit of H_2O admixing employed here has been set to have a minimum temperature increase of 10 K, the criterion commonly used for defining the ignition delay time in MILD combustion.

First, a thermodynamic analysis employing Gibbs free energy minimisation has been performed with mixtures of CH_4 and O_2, highly diluted in H_2O, at atmospheric pressure and T_{in}=900 K, to examine the equilibrium conversion limits and product gas yield and composition as a function of process parameters.

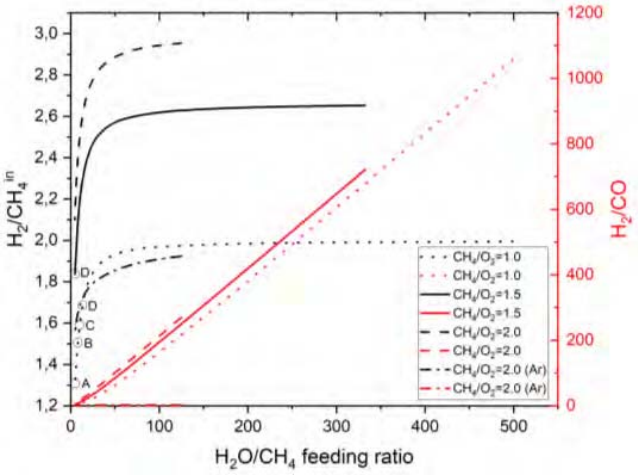

Figure 1. Effect of H_2O/CH_4 feeding ratio on the H_2/CH_4^{input} ratio (black lines, left axis) and H_2/CO ratio (red lines, right axis) for $CH_4/O_2/H_2O$ mixtures at equilibrium, T_{in}=900 K, and p=1.0 atm for three CH_4/O_2 feeding ratios. Dotted

lines: CH_4/O_2=1.0. Solid lines: CH_4/O_2=1.5. Dashed lines: CH_4/O_2=2.0. Dash-dotted lines: CH_4/O_2=2.0 with H_2O replaced by Ar. Open circles: A-B: τ^{90}<10 s; B-C: 10<τ^{90}<100 s; C-D: 100<τ^{90}<1000 s. Where no circles are reported τ^{90}>1000 s.

Figure 1 shows the effect of the H_2O/CH_4 inlet mole ratio on the reformed gas's equilibrium composition at the adiabatic temperature for three defined CH_4/O_2 inlet mole ratios under MILD-POX conditions, thus T_{in}>autoignition temperature, fuel-rich and highly diluted mixtures. The selected CH_4/O_2 ratios (1.0, 1.5, and 2.0) correspond to Φ=2.0, 3.0, and 4.0, where the latter is the one usually employed in conventional POX.

The first interesting result, not displayed in Fig. 1, is that the conversion is always complete for the explored H_2O/CH_4 and CH_4/O_2 ratios. In addition, no free carbon is present, and the expected products are, independent of the operating conditions, only H_2, carbon oxides, and residual H_2O. Therefore, for all the equilibrium results, the product composition is unambiguously presented in terms of H_2/CH_4^{input} and H_2/CO since the main interest is the efficient conversion of CH_4 to H_2. Calculations show that the main trends strongly depend on H_2O addition; in particular, it can be seen that the H_2/CH_4^{input} yield (left axis) first significantly grows with increasing H_2O/CH_4 ratio and then reaches a plateau for values higher than ~50, independent on the CH_4/O_2 ratio. At the same time, the quantitative values of H_2/CH_4^{input} strongly grow with CH_4/O_2 ratio starting from about 1.3-2.0 at CH_4/O_2=1.0 to 2.1-2.95 at CH_4/O_2=2.0. Note that for CH_4/O_2 ratios of 1.5 and 2.0, the H_2/CH_4^{input} ranges from the one typical of POX (~2.0) to the one of SR (~3.0). On the other hand, the H_2/CO ratio (right axis) increases quasi-linearly with the addition of H_2O, and the improvement may be considerable. In this case, increasing the CH_4/O_2 ratio does not have a significant influence for a fixed H_2O/CH_4 ratio, but lower CH_4/O_2 ratios can be beneficial because they would allow extending the H_2O/CH_4 range. Surprisingly, the synthesis gas composition in terms of H_2/CO ratio, ranging from 3.0 to 1060, is always significantly higher than that obtainable with conventional processes (1-2 for POX and ~3.0 for SR), which is beneficial for H_2 production. Low temperatures favour the H_2 yield and selectivity; thus, from the analysis, it needs to be clarified if the changes in process performances with the addition of H_2O are influenced by a decrease in the adiabatic temperature or by the presence of steam itself. Therefore, an additional case has been investigated at CH_4/O_2=2.0 with argon dilution instead of H_2O (dash-dotted lines). Thermodynamic calculations suggest that the nonlinear increasing trend of H_2/CH_4^{input} is very similar in the case of dilution by an inert gas, which is therefore explained by the fact that the diluent addition to the mixture shifts the adiabatic temperature to lower values. However, the H_2/CH_4^{input} yield drops by a factor of 1.36-1.54, and the conversion is never complete, but ranges from 95 to 97%. On the other hand, increasing the Ar/CH_4 ratio does not influence the H_2/CO ratio, which is ~2.0 in the entire explored range. It confirms that the steam-assisted MILD-POX process extracts H_2 from the hydrocarbon feedstock and H_2O. Indeed, 27-35% of the H_2 produced comes from the steam when CH_4 is used as a feedstock. This

contrasts with some numerical studies [2-4] in which no significant effect of H_2O/CH_4 ratio on H_2 yield was observed. In addition, steam is the only cause for the enhanced H_2/CO ratio. This result justifies using surplus H_2O that increases the syngas yield, the H_2/CO ratio, and the CH_4 conversion.
The description based on thermodynamic analysis is approximate because it can only suggest the potential product composition. However, it does not provide any information on reactor residence times required to achieve proper CH_4 conversion in real systems; thus, calculations must include reaction kinetics. Therefore, zero-dimensional, adiabatic simulations have been carried out over the entire range of conditions reported in Fig. 1 employing the PSR code of the ANSYS Chemkin-Pro 2021® software, implementing the CRECK reaction mechanism and setting the residence time to 10, 100, and 1000 s. In Fig. 1, the conditions that allow a CH_4 conversion of more than 90% (τ^{90}) at the reactor outlet are shown with open circles. For CH_4/O_2 ratios higher than 1.0, reactions need more than 1000 s to reach equilibrium in the whole H_2O/CH_4 range, which is not practical. A conversion higher than 90% is attained for $\tau<1000$ s only at $CH_4/O_2=1.0$ and $H_2O/CH_4<16$ where the adiabatic temperature ranges from 1300 to 1750 K. These very long residence times are not related to the use of H_2O, because also in the case of dilution with Argon the results are similar. At $CH_4/O_2=2.0$, $\tau^{90}<10$ s only if $H_2O/$ or $Ar/CH_4=0$ (not shown in Fig. 1). As a matter of fact, the non-catalytic POX of hydrocarbons is controlled by reaction kinetics, which, despite being faster than SR, is intrinsically much slower than conventional flame burners, and even an approximation to equilibrium can only be achieved by accepting very high temperatures ($1500<T<3000$ K), where chemical reactions are sufficiently rapid. Below 1500 K, catalysts are typically added to the POX system to enhance reaction kinetics and approach an acceptable conversion. However, the objective of the present work is to propose a process that can be realised within residence times typical of non-catalytic POX, i.e., $\tau<\sim50$ s, and adiabatic temperatures typical of MILD combustion, i.e., 1000-1500 K. These factors have given preference to optimal values for the present analysis, namely $T_{in}=1300$ K, p=50 atm, $CH_4/O_2=1.5$, $H_2O/CH_4=21.56$, and $\tau=20$ s that allow matching appropriate conditions relevant for a practical application. Before starting the analysis, an array of preliminary computations has been performed using adiabatic and isothermal PSR and PFR to choose the best reactor configuration. An adiabatic PFR approach has been selected to model the system because it maximises the CH_4 conversion. The analysis presented in Fig. 1 shows that H_2O is not only the diluent but may also chemically interact with the oxidation kinetics releasing H_2. Therefore, a fictitious species (H_2O_v) with identical molecular structure and thermodynamic properties to H_2O has been defined in the simulations. This virtual species does, however, not appear in the elementary reactions of the kinetic mechanism. Simulations have been performed diluting the fuel mixtures with H_2O and H_2O_v to understand the chemical contribution of H_2O. In addition, it is known that H_2O may indirectly participate in oxidation chemistry as a third body in termolecular reactions with chaperon efficiencies that are significantly higher than

other collision partners. To isolate this contribution, calculations have been carried out by defining a second fictitious species (H_2O_v*) with identical molecular structure, thermodynamic properties, and third body efficiencies to H_2O. This virtual species does, however, not appear as a reactant or product in the elementary reactions of the kinetic mechanism. Differences between simulations performed diluting the fuel mixtures with H_2O_v and H_2O_v* isolate the chemical contribution of H_2O as a collider in termolecular reactions, while differences between simulations with H_2O and H_2O_v* isolate the direct chemical effect of H_2O in bimolecular reactions. A summary of the results is provided in Table 1, which compares exhaust products for the three simulations under the same conditions. H_2O brings the system to nearly complete conversion and reduces the production of undesirable intermediate compounds, which is essential for the process to be economical. Indeed, for the other two cases, CH_4 conversion is only around 82% at 20 s, and the selectivity to form H_2 and CO_2 is much lower. The fact that dilution by H_2O_v and H_2O_v* brings the same results means that there is no third-body effect of H_2O.

Table 1. Chemical and third body contributions of H_2O on global outputs in an adiabatic PFR at T_{in}=1300 K, p=50 atm, CH_4/O_2=1.5, H_2O/CH_4=21.56, and τ=20 s.

	H_2O dilution	H_2O_v dilution	H_2O_v* dilution
CH_4 conversion (%)	98.15	81.65	81.55
H_2/CO	11.90	1.71	1.71
H_2/CH_4^{input}	2.26	1.14	1.13
Dry composition of the product gas	% H_2 70.48 CO 5.92 CO_2 23.02 CH_4 0.58 ppm C_2H_4 1.20 C_6H_6 11.15	% H_2 54.32 CO 31.77 CO_2 4.91 CH_4 8.78 C_2H_4 0.11 ppm C_2H_6 36.53 C_2H_2 824.44 C_3H_6 3.61 C_3H_4 (Propyne) 8.06 C_3H_4 (Allene) 2.87 C_6H_6 210.10	% H_2 54.25 CO 31.75 CO_2 4.94 CH_4 8.84 C_2H_4 0.11 ppm C_2H_6 37.42 C_2H_2 854.58 C_3H_6 3.75 C_3H_4 (Propyne) 8.43 C_3H_4 (Allene) 3.00 C_6H_6 234.60

Conclusions

The goal of the present work was to propose the combination of non-catalytic POX and MILD combustion technologies with the addition of H_2O and assess its potential for the efficient generation of H_2 from any sustainable gaseous or liquid feedstock, leaving a minimal environmental footprint. The CRECK chemical kinetic

mechanism was used in the theoretical analysis based on the models' predictive performances. Thermodynamic equilibrium calculations, accompanied by kinetic modeling, were used to interpret and assess the general behavior of a potential unit that uses the steam-assisted MILD-POX route of CH_4 for syngas production and to compare the performances over a range of operating conditions of interest. In particular, the effects of H_2O/CH_4 and CH_4/O_2 ratios, inlet temperature, and pressure on CH_4 conversion, H_2 yield, and product gas composition were computationally investigated. Particular emphasis was devoted to the effect of H_2O on gas-phase chemistry. The presented results demonstrate that thermo-chemical production of H_2 using the proposed process is theoretically feasible and can be accomplished without a catalyst, making the process highly feedstock-flexible and impurity-tolerant. The achieved performances can be even better than those of the existing technologies over a wide range of process parameters, subject to the constraints of characteristic times. In particular, equilibrium favours the formation of H_2 and CO_2 at low adiabatic temperatures and high H_2O/CH_4 and CH_4/O_2 ratios in the input gas. At the same time, reaction kinetics are faster at elevated temperatures and pressures and low H_2O/CH_4 and CH_4/O_2 ratios. Therefore, a compromise must be made among these parameters to maximize performance. The immediate advantage of such an approach is that a very high H_2/CO ratio can be obtained that could eliminate the water gas shift conversion stages, making the reactor more compact and simple than conventional reformers. Moreover, water vapor addition limits the formation of soot precursors due to a "leaning" effect from the release of OH radicals.

Although the present analysis shows that H_2 production via this hybrid system is possible, more experimental and modelling research is required to transform a promising idea into an industrially viable reality. The potential benefits of steam-assisted MILD-POX justify spending effort in developing and optimizing this process. In this regard, this study is expected to act as a basis for future investigations.

References

[1] Bagheri, G., Ranzi, E., Pelucchi, M., Parente, A., Frassoldati, A., Faravelli, T., "Comprehensive kinetic study of combustion technologies for low environmental impact: MILD and OXY-fuel combustion of methane", *Combust. Flame* 212: 142-155 (2020).

[2] Benilov, M.S., Naidis, G.V., "Modeling of hydrogen-rich gas production by plasma reforming of hydrocarbon fuels", *Int. J. Hydrogen Energy* 31: 769-774 (2006).

[3] Dobrego, K.V., Gnezdilov, N.N., Lee, S.H., Choi, H.K., "Partial oxidation of methane in a reverse flow porous media reactor. Water admixing optimization", *Int. J. Hydrogen Energy* 33: 5535-5544 (2008).

[4] Kumar, S., Kumar, S., Prajapati, J.K., "Hydrogen production by partial oxidation of methane: Modeling and simulation", *Int. J. Hydrogen Energy* 34: 6655-6668 (2009).

METHANE PRODUCTION FROM BIOMASS-DERIVED SYNGAS: ISSUES AND BENEFITS

A. Coppola*, R. Ruggiero, F.Scala*,**, M.Urciuolo***
roberto.ruggiero4@unina.it
*STEMS, CNR, P.le Tecchio 80, 80125, Napoli, Italy
**DICMaPI, Univeristà di Napoli Federico II, P.le Tecchio 80, 80125, Napoli, Italy

Abstract
The use of biomass is considered to be interesting for the production of biofuels such as bio-methane or bio-methanol in order to limit the use of fossil fuels. The first step to obtain these substances by thermal processes is typically the gasification of biomass for syngas production, which can be then used as the feedstock for catalytic hydrogenation processes. Different oxidizing agents and can be used, as air, steam, a blend of air and steam, oxygen etc. Methane has the advantage to be easily stored and transported using the existing infrastructure.
The main problems related to syngas catalytic methanation are: i) the requirement to remove pollutants contained in the syngas, such as tar, to prevent catalyst deactivation; ii) the adjustment of the syngas H/C ratio which is typically too low with respect to the stoichiometric requirement for methanation. Pollutant abatement and improvement of the H/C ratio are identified as cleaning and conditioning processes of the syngas, respectively.
In this paper, the principles and effect of syngas methanation are discussed. In addition, an overview about the contaminants and the operations of gas cleaning and gas conditioning is given.

Introduction
The effects of global warming and climate change continue to be evident due to the use of fossil fuels [1]. Events such as the rise of the earth's temperature, and the occurrence of the melting of glaciers are becoming more and more common. So it is necessary to develop new ways to sustain the energy demand that our society needs, and renewable energies are recognized as the most promising choice thanks to the low emissions involved in their exploitation. The use of biomass looks promising, thanks to the capacity of being carbon neutral.
Numerous thermochemical or biochemical processes exist to convert biomass in chemical products or energy, such as combustion, pyrolysis, gasification, anaerobic digestion etc. In particular, methanation is a catalytic process that is used to convert the syngas obtained from gasification into Synthetic Natural Gas (SNG), which desired reactions are the following:

$$CO + 3H_2 \leftrightarrow CH_4 + H_2O \qquad \Delta H = -\frac{206KJ}{mol}\ at\ 298\ K \qquad (1)$$

$$CO_2 + 4H_2 \leftrightarrow CH_4 + H_2O \qquad \Delta H = -\frac{164KJ}{mol} at\ 298\ K \qquad (2)$$

Since the main product of gasification is syngas, a mixture of CO and H_2, reaction (1) has been studied in more detail, but for both reactions it is possible to note that they are extremely exothermic and involve a reduction of volume. So higher conversions can be reached at high pressures and at low temperatures. In addition, the occurrence of other reactions, such as water-gas-shift, Boudouard reaction, dry-reforming, etc. [2] should be considered.
Obviously, the catalyst plays a key role in the success of a methanation process ensuring high chemical activity and selectivity towards the desired product. It should possess elevated thermal and chemical stability, and, if possible, be relatively cheap. Numerous studies have been conducted on different catalysts, and the best one for commercial applications has been found to be a Ni-based catalyst, possibly enhanced by promoters, MgO, La_2O_3, CeO_2 and supported by alumina [3–7]. The heterogeneous gas-solid reaction kinetic models are built on Langmuir - Hinshelwood or Eley-Rideal mechanisms [3,6].

Effects of methanation and applications
Syngas-obtained from biomass gasification can be used for multiple purposes such as thermal and electrical energy generation (cogeneration [8]), fuel synthesis, or production of H_2 used in fuel-cells [9]. Depending on the final use of the syngas different characteristics are required [10]. What we can see from [9] is that syngas characteristics such as toxicity, lower and upper explosion limits, are highly influenced by gasification conditions such as the choice of the oxidation agent. In fact, not all of the gasification techniques look promising to generate high methane concentrations. For example, syngas produced from steam-gasification appears to be more promising than the others thanks to its high content of hydrogen and for the absence of inert gases like nitrogen. Some of the advantages related to the methanation of the raw syngas are the improved effect on flammability interval (Figure 1), which is now smaller and safer compared to the original syngas, the improved value for high calorific value, smaller concentration of carbon monoxide, and presence of a safer and more manageable substance as methane.
In order to perform methanation and avoid Ni catalyst deactivation, with phenomena such as fouling or poisoning of the active phase, it is necessary to remove undesired substances from the raw syngas and to improve its H/C ratio.

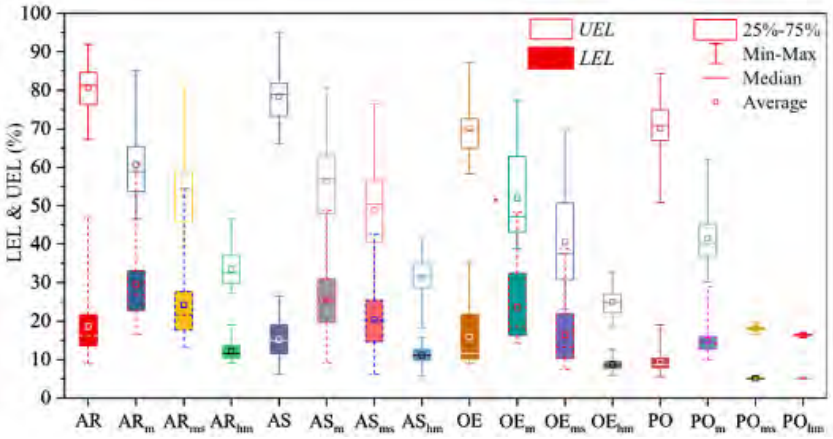

Figure 1.Effect of methanation on flammability limit [9]

Contaminants and operations of cleaning and conditioning

Typical contaminants contained in syngas are reported below:

- Particulate matter: residual solid-carbon, inorganic matter, catalyst, and bed material from the gasification reactor.
- Tars: derived from the pyrolysis of the biomass, and not converted into incondensable gases. They are formed by different compounds like oxygenated products, heavier deoxygenated hydrocarbons and polycyclic aromatic hydrocarbons (PAHs) [11].
- Sulphur: these compounds are mainly present as hydrogen sulphide H_2S and carbonyl sulfide COS.
- NH_3 and HCN: their concentration typically depends on the biomass composition and nature. Ammonia is the most common form.
- Alkali compounds: alkali and alkali earth metals are often contained in biomass feedstock, and their concentration is often higher than in coal.
- Chlorine: chlorides are the predominant halide in syngas, usually in the form of hydrochloric acid (HCl), which is formed by the reaction that occurs from chlorine in biomass as alkali metal salts react with water vapour to form HCl.

In the last years, numerous techniques have been proposed to remove these contaminants. Such techniques can be described using the following classification taken from [10], based on the working temperature:

-*Hot gas clean-up* (HGC): Including all the operations that are usually conducted in the temperature range [350-1000 °C], has historically focused on removal of particulate matter and tar, with the goal of minimizing maintenance of syngas combustion equipment, and to remove these contaminants with a higher energy efficiency. In literature it has been found that this kind of approach is suitable for the removal of almost all the contaminants:

- Particulate removal can be conducted with filters, cyclones, and electrostatic separators [12].

- Tars can be removed through catalytic cracking, thermal cracking and physical separation using sorbents. In particular, the catalyst (Ni-based, zeolites, or minerals such as dolomite and olivine) used for the catalytic cracking shows also a good activity in NH_3 reduction, allowing a simultaneous removal of contaminants [10].
- Sulphur compounds, alkali compounds and chlorine are removed using sorbents that can work at high temperature such as ZnO [13], Al_2O_3 , CaO [14].
- *Cold gas clean-up* (CGC): These operations are often conducted at temperatures below 100 ºC and, unlike the Hot Gas Clean-up, a liquid sorbent is used. The separation of the contaminants can be conducted in wet scrubbers. The efficiency can be improved using devices that enhance the turbulence and hence the contact between the gas and the liquid phases, such as in spray scrubbers, impactor scrubbers, venturi scrubbers. These operations are the most used in the last years, considering that they can carry out a simultaneous removal of different contaminants [10]. In fact, for example using a proper device working with water is possible to remove particulate matters, tars, and NH_3. Also, the choice of the proper liquid in the scrubber is crucial to increase the gas cleaning [15]. However, cleaning operation at low temperature is not the optimal choice if the goal is to obtain a high energy efficiency [10].
-*Warm gas clean-up (WGC)*: These operations are conducted in an intermediate range of temperature with respect to the previously described processes, typically [100-350 ºC]. Researchers have found that working in this temperature range could mitigate the drawbacks of both the hot gas clean-up and cold clean-up technologies since high-cost materials are no more required and low temperature is not necessary [10]. However, not all the contaminants can be removed in this way, but there are some examples of combined removal, such as the Olga process [16], which allow the simultaneous removal of tars and particulate matter. Chlorine can also be successfully removed in this range using lime-based slurry systems [17].

Gas conditioning: in this classification we have all the operations whose objective is to improve the H_2/CO stoichiometric ratio to obtain a more suitable composition for processes such as methanation. Operations such as thermal cracking or catalytic cracking of tars can reduce the level of these contaminants and simultaneously enhance this ratio [15]. Another operation that is usually conducted before or during the methanation step is the water-gas-shift reaction (with the addition of external steam) which can form more hydrogen and decrease the level of CO. For example, in the Comflux process [6] WGS is conducted in the same reactor by adding steam, to progressively enhance the formation of hydrogen that will be used for the methanation reaction. Enhancing the simultaneous methanation and WGS reactions looks like an interesting idea to limit the flow rate of hydrogen-make-up, and also to promote the gasification of coke (due to the addition of steam), that can cover the active phase of the catalyst [18,19].

Conclusions

The next steps in this research program will be a deeper research in literature to find more information about the processes that will be more effective for the production of methane, using a syngas obtained from air gasification, or air and steam gasification. Also, the correct design of cleaning and conditioning operations to improve the syngas quality, will be studied in detail. Furthermore, before the start of an experimental campaign, an initial simulative approach (using Aspen plus) will be conducted, for the optimization, from a technical and economic point of view, of the cleaning and conditioning operating parameters and of the methanation operating parameters. The experimental campaign will be aimed at confirming the results obtained from the simulation activity, and to be able to carry out an effective syngas methanation preventing the deactivation of the catalyst.

Acknowledgments

We wish to acknowledge CMD S.P.A. for financing the PhD fellowship of Roberto Ruggiero.

References

[1] Crownley.J.T. Causes of climate change over the past 1000 years 2000. Science 2000; Vol 289, Issue 5477 pp. 270-277.

[2] Gao J, Wang Y, Ping Y, Hu D, Xu G, Gu F, et al. A thermodynamic analysis of methanation reactions of carbon oxides for the production of synthetic natural gas. RSC Adv 2012;2:2358–68.

[3] Sehested J, Dahl S, Jacobsen J, Rostrup-Nielsen JR. Methanation of CO over nickel: Mechanism and kinetics at high H2/CO ratios. Journal of Physical Chemistry B 2005;109:2432–8.

[4] Kopyscinski J Schildhauer TJ, Biollaz SMA. Production of synthetic natural gas (SNG) from coal and dry biomass - A technology review from 1950 to 2009. Fuel 2010;89:1763–83.

[5] Bolt A, Dincer I, Agelin-Chaab M. A critical review of synthetic natural gas production techniques and technologies. J Nat Gas Sci Eng 2020;84.

[6] Rönsch S, Schneider J, Matthischke S, Schlüter M, Götz M, Lefebvre J, et al. Review on methanation - From fundamentals to current projects. Fuel 2016;166:276–96

[7] Schildhauer TJ, Biollaz SM. Synthetic natural gas from coal, dry biomass, and power-to-gas applications, Wiley, U.S.A., 2016.

[8] Tuccillo R. Performance and Transient Behaviour of MGT Based Energy Systems. Micro Gas Turbines Educational Notes, RTO-EN-AVT-131, Paper 6 2005

[9] Song G, Xiao J, Yan C, Gu H, Zhao H. Quality of gaseous biofuels: Statistical assessment and guidance on production technologies. Renewable and Sustainable Energy Reviews 2022;16

[10] Woolcock PJ, Brown RC. A review of cleaning technologies for biomass-derived syngas. Biomass Bioenergy 2013;52:54–84.

[11] Stevens, D J. Hot Gas Conditioning: Recent Progress with Larger-Scale Biomass Gasification Systems; Update and Summary of Recent Progress. United States: N. p., 2001

[12] Hoffmann AC, Stein LE. Gas Cyclones and Swirl Tubes: Principles, Design and Operation, Springer Nature, U.S.A.,2007
[13] S. S. Tamhankar, M. Bagajewicz, G. R. Gavalas, P. K. Sharma, and M. Flytzani-Stephanopoulos. Mixed-oxide sorbents for high-temperature removal of hydrogen sulfide. Industrial & Engineering Chemistry Process Design and Development 1986 25, 429-437
[14] Zhao Y, Liu G, Huang J, Veksha A, Wu X, Giannis A, et al. Sorbents for high-temperature removal of alkali metals and HCl from municipal solid waste derived syngas. Fuel 2022;321
[15] Andersson KJ, Skov-Skjøth Rasmussen M, Højlund Nielsen PE. Industrial-scale gas conditioning including Topsoe tar reforming and purification downstream biomass gasifiers: An overview and recent examples. Fuel 2017;203:1026–30
[16] Rabou LPLM, Zwart RWR, Vreugdenhil BJ, Bos L. Tar in biomass producer gas, the Energy research Centre of the Netherlands (ECN) experience: An enduring challenge. Energy and Fuels 2009;23:6189– 98.
[17] Spooren T, Raveel A, Adams B, du Toit G, Waller P. Semiwet scrubbing: Design and operational experience of a state-of-the-art unit. Environmental Progress 2006;25:201–7.
[18] Calvin, H., Bartholomew. (2001). Mechanisms of catalyst deactivation. Applied Catalysis A-general, 212(12):17-60
[19] Wang Y, Liu J, Li Q, Yu J, Su F, Xu G. Performance comparison of syngas methanation on fluidized and fixed bed reactors, *13th International conference on Fluidization Engineering* (2010), paper 12-2.

Design and modeling of an autothermal co-flow reactor for turquoise hydrogen production

Francesco Cenvinzo*, Emanuele Alberto Scelzo*, Giancarlo Sorrentino, Mario Commodo**, Andrea D'Anna***
f.cenvinzo@studenti.unina.it

* Dipartimento di Ingegneria Chimica, dei Materiali e della Produzione Industriale - Università degli Studi di Napoli Federico II, P.le Tecchio 80, 80125 Napoli, Italy
**Istituto di Scienze e Tecnologie per l'Energia e la Mobilità Sostenibili (STEMS), Consiglio Nazionale delle Ricerche (CNR), V.le Marconi 4, 80125 Napoli, Italy

Abstract
Within the current framework of the industrial processes it is noticeable a shift towards alternative and more green sources of energy: great attention has been focused on hydrogen utilization as energy carrier due to the major advantages brought by its combustion, thus receiving the attention of policy makers. Warming impact of continuous fossil fuels utilization could be mitigated introducing in the current energy mix environmentally friendly sources. Henceforth the motivation of this work, in which it is looked at a possible design for producing the so-called "turquoise hydrogen". The advantage of this design lies in the way heat is provided to the system – paired with the simple geometry of the reactor system. Analysis of performances, costs and environmental impact is provided in detail as well to highlight the large flexibility of the proposed design (according to different optimization criteria).

Introduction
Taking advantage of the large natural gas (NG) availability, one possible solution to produce clean hydrogen is represented by methane pyrolysis, giving rise to the "turquoise" hydrogen: thermal conversion of natural gas (96% methane content) in O_2-free environment, may aid the synthesis of such with the only by-product being solid carbon. Thus, giving the possibility of including a climate-friendly process chain that does not require any further downstream processing addressing CO_2 [1-3]. Relative to the solid carbon formation, different forms may be produced, each one of them having in common the same precursor being soot. Previous studies have helped in understanding how soot forms in relation to processing conditions [4]; yet some questions remain. Generally soot is said to be formed because of polycyclic aromatic hydrocarbons (PAHs) presence, and proper insights can be given if it is considered to combine a detailed gas-phase kinetic model, fluid dynamics and transport processes to the model for soot formation. Thus, in this work, a CFD model has been developed to quantify both the hydrogen and solid carbon production through a methane pyrolysis process. Such model has been adapted to design a simple reactor configuration, for understanding whether it is possible to achieve competitiveness with respect to the currently available technologies used for hydrogen production, being the aim of this study.

Methodology

In order to simulate the methane pyrolysis, the gas-phase reaction mechanism introduced is based upon a combustion model known as GRI-Mech [5]. The actual model used is truncated of the oxidation part to set up a model made of 104 reactions and 22 species – yet capable of closely reproducing combustion characteristics – named DRM 22. Deviation from the former mechanism is in the order of 2-4% [6].

For investigation of soot particle formation, it is introduced a computational model where a two-step procedure is followed according to Leung & Lindstedt [7]: a first phase of incipient particle formation is followed by surface growth through acetylene addition. Predicting its formation is deemed fundamental since good predictive model helps in regulating the formation of such as well as its removal. In the framework of the reactor in exam, within the simulation environment it was used a model named Moss-Brookes [8]. The soot fields described by that same model are soot particle number (N) and soot mass concentration (M) seen in *eq. 2-3*:

$$\frac{dN}{dt} = aN_A \left(X_{C_2H_2} \frac{P}{RT}\right)^l e^{-\frac{21100}{T}} - \left(\frac{24RT}{\rho_{soot} N_A}\right)^{\frac{1}{2}} d_p^{\frac{1}{2}} N^2 \quad (2)$$

$$\frac{dM}{dt} = aM_p \left(X_{C_2H_2} \frac{P}{RT}\right)^l e^{-\frac{21100}{T}} + b\left(X_{C_2H_2} \frac{P}{RT}\right)^m e^{-\frac{12100}{T}} \left[(\pi N)^{\frac{1}{3}} \left(\frac{6M}{\rho_{soot}}\right)^{\frac{2}{3}}\right]^n \quad (3)$$

a, l, b, m and n are model constant; P is the total pressure, N_A is the Avogadro number, d_p is the particle diameter, and X_i represents a mole fraction. Radiative interaction of soot is then addressed introducing the Weighted-Sum-of-Grey-Gases (WSGG) model, for definition of absorption coefficient.

In order to validate the model, results from the experimental investigation of Deutshcmann *et al.* [9] have been considered. Simulations are performed to match the experimentally recorded temperature profile as shown in *fig. 1* (for more detail please refer to [9]).

Table 1. Comparison between experimental and simulation data recorded at the tail end of the reactor (exp and sim respectively). Data source: [10]

T (K)	H_2 exp	H_2 sim	CH_4 exp	CH_4 sim	C_2H_2 exp	C_2H_2 sim
1473	0,862	0,765	0,111	0,171	0	0,051
1673	0,945	0,846	0,035	0,0458	0	0,103
1873	0,906	0,869	0,068	0,085	0	0,12

It can be noted that the accuracy of the prediction can be improved moving towards larger values of the temperature, maintaining the error within the 10% margin in the case of 1473K. Reasons of discrepancies in the carbonaceous compounds prediction are comprehensively explained in [10].

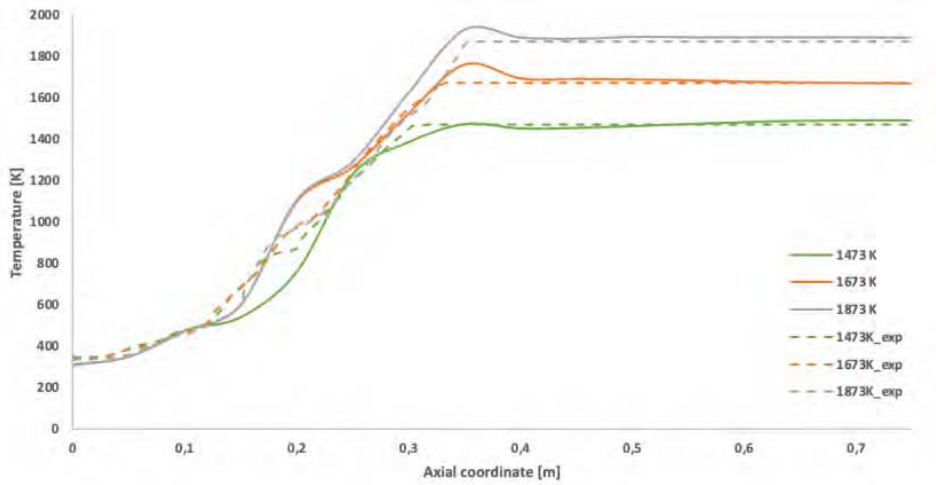

Figure 1. Numerically predicted temperature profile according to the chosen setup parameters.

Reactor design

Simulations have been performed adopting a design where a pyrolysis tube is enveloped in between exhausts of a methane/air stoichiometric flame produced upstream to the reactor itself (determining the possibility of having the so-called autothermal reactor): hence the presence of three streams – "M1" made solely of methane that undergoes pyrolysis, "FG1" and "FG2" which are composed of typical gaseous components of a flame with equivalence ratio 1.01 – arranged according to the scheme shown in *fig. 2*.
M1 is fed at ambient condition pressure and pre-heated to a temperature of 1000K, in a reactor which is made of three co-axial tubes having diameter of *2.6*, *5.0* and *8.0 cm* respectively, and a length of *60 cm* – co-axial laminar flows establishes in the latter. Streams have been introduced to have M1 in the middle tube and FG1-2 in the outwards ones. Setup parameter of interest is the flow rate with which FG1-2 are introduced – varying their velocity – allowing to regulate the temperature field developed in the tube.

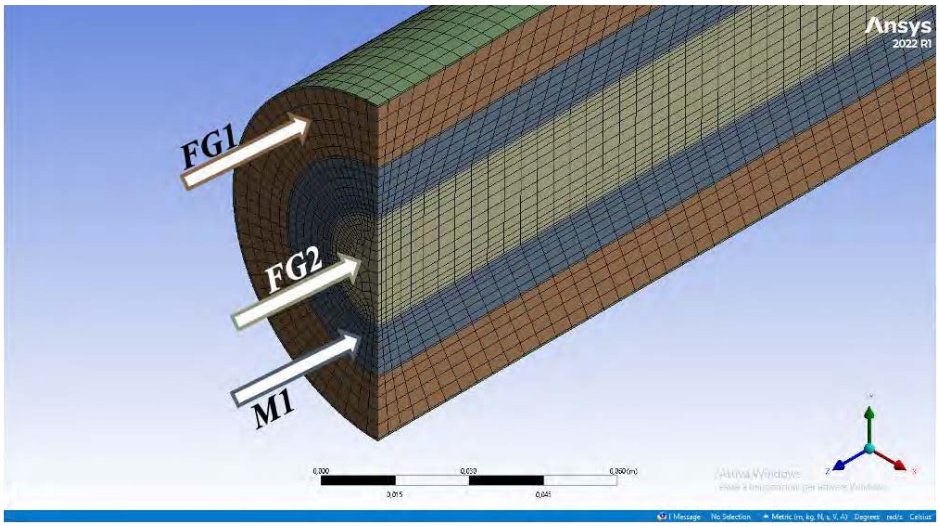

Figure 2. Streams arrangement on a half-section view of the reactor design in exam.

Results

Results from numerical predictions are obtained adopting the model and geometry reported in the previous section. The interest of this work lies in the performance parameters as well as the environmental and economic ones.

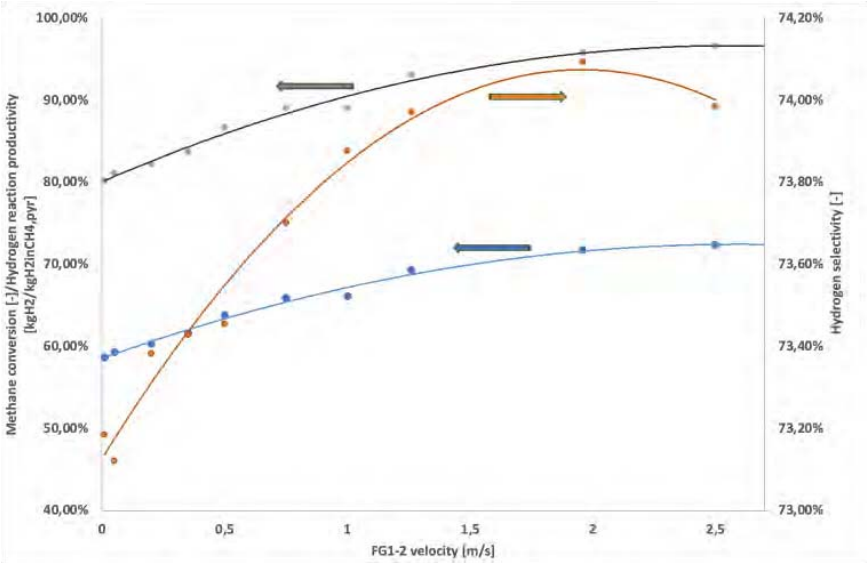

Figure 3. Methane conversion, H_2 reaction productivity and selectivity for different premix velocity cases (grey line is methane conversion, orange line is hydrogen selectivity, and blue line is hydrogen reaction productivity).

Reducing FG1-2 velocity, hydrogen purity is expected to be reduced because of the carbon residues and similarly does methane conversion: for sake of being coherent with the proposed idea, methane is intended to be exploited at best to avoid excess waste. Looking at hydrogen selectivity, it is looked to maintain the largest possible values because of the various carbonaceous gaseous products; the same goes for productivity.

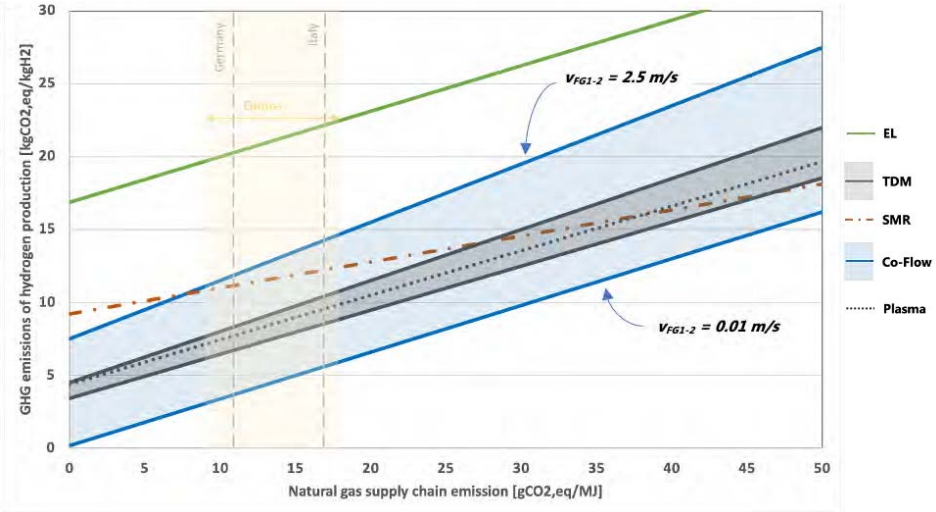

Figure 4. H_2 production GWI according to the natural gas supply chain GWI. Data for

methane pyrolysis are theoretical. Data source: Timmerberg *et al.* (2020) [11].
Moving to the Global Warming Impact (GWI, CO_2 emitted per unit of hydrogen produced) (*fig. 4*), it is noticeable the least amount of carbon emissions for low velocity systems – reasoning to be made is that approximatively it will be used a reduced amount of the required methane, thus producing less emissions. Reducing velocity to 1.96 m/s for FG1-2 already show to have fulfilled the desired task of having GWI smaller than that of steam methane reforming (SMR), representing the benchmark process to compare with (SMR is currently the most used technology for satisfying the hydrogen global demand [12]).
Finally, it can also be reported an economic analysis based on data reported in literature through the work of *Keipi et al.* (2018) [13].

Table 2. Comparison of main voices of costs between major hydrogen manufacturing technologies and the analyzed cases, expressed in k€/year for **OPEX** and k€ for *CAPEX* (Equipment cost is assessed via Peter, Timmerhaus & West (2003) [14]).

Technology /Cases	**CH_4 supply chain**	**CO_2 emission allowances**	**Electricity**	**O&M**	*Equipment*
TDM-SS	780	8	-	27	3233
TDMG-SS	547	42	6	24	2361
SMR-SS	618	61	11	87	10705
2.5 m/s	1135	33.7	-	111.8	5589
1.96 m/s	1064	26.65	-	104.8	5239.4
1.26 m/s	991	17.72	-	97.6	4880.6
1 m/s	996	14.74	-	98	4903.6
0.5 m/s	946.57	7.63	-	93.2	4661.02
0.05 m/s	936.10	0.82	-	92.2	4609.5
0.01 m/s	956.21	1.66	-	94.17	4708.47

Conclusion

Through the set of numerical data obtained it is possible to enable a comparison with respect to other hydrogen technologies, highlighting the real strength of such innovative design. At first, if it is looked at how those compare on an economic scale: the co-flow design looks to have the upper hand if it is possible to still have economically sustainable values of NG supply chain costs – second largest voice of cost to address (it is implicitly said that going on way large NG cost makes all the related technology not feasible on any scale).
Then, looking to the environmental scale, competitiveness with SMR can be achieved under current European NG supply chain condition: there will be region where it can be produced similar or even lower emission values – in favour of the autothermal technology.
It is important to clarify that ahead of the numerical solutions here presented, a more detailed analysis must be introduced. The information retrieved from the different simulations may serve as a tool for having a first optimization of the design to be built.

This analysis also highlights the main upside of the co-flow design, being its simple approach to the pyrolysis mechanism: it does not require downstream processing other than that related to heterogenous phases separation and does not ask for upstream treatment of natural gas. Finally, it can be concluded that overall, the selected design has behaved well in a wide range of operating conditions involving different temperature and species residence times.

Reference

[1] Sánchez-Bastardo, N., Schlögl, R., & Ruland, H. (2020). Methane Pyrolysis for CO2-Free H2 Production: A Green Process to Overcome Renewable Energies Unsteadiness. Chemie Ingenieur Technik, 92(10), 1596-1609.
[2] Ehrhardt, K.; Scheiff, F.; Flick, D.; Lott, P.; Mokashi, M.; Heitlinger, H.; Pashminehazar, R.; et al. Pyrolysis of methane: interplay between industrial design considerations and detailed chemistry evaluation. 13th European Congress of Chemical Engineering; ECCE-ECAB, 2021.
[3] Lott, P., & Deutschmann, O. (2022). Heterogeneous chemical reactions—A cornerstone in emission reduction of local pollutants and greenhouse gases. Proceedings of the Combustion Institute.
[4] Tesner, P. A.; Shurupov, S. V. Some Physico-Chemical Parameters of Soot Formation During Pyrolysis of Hydrocarbons. Combust. Sci. Technol. 1995, 105, 147−161.
[5] Smith, G.P., Golden, D.M., Frenklac, M., Moriarty, N.W., Eiteneer, B., Goldenberg, M., et al. (1999).
[6] Kazakov A., Frenklach M. Reduced reaction sets based on GRI-mech 1.2. 1994.
[7] Leung, K. M., Lindstedt, R. P., & Jones, W. P. (1991). A simplified reaction mechanism for soot formation in nonpremixed flames. Combustion and flame, 87(3-4), 289-305.
[8] Brookes, S. J., & Moss, J. B. (1999). Predictions of soot and thermal radiation properties in confined turbulent jet diffusion flames. Combustion and Flame, 116(4), 486-503.
[9] Shirsath, A. B., Mokashi, M., Lott, P., Müller, H., Pashminehazar, R., Sheppard, T., & Deutschmann, O. (2023). Soot Formation in Methane Pyrolysis Reactor: Modeling Soot Growth and Particle Characterization. The Journal of Physical Chemistry A, 127(9), 2136-2147.
[10] Frenklach, M. (1996). On surface growth mechanism of soot particles. Symposium (International) on Combustion, 26, 2285−2293.
[11] Timmerberg, S., Kaltschmitt, M., & Finkbeiner, M. (2020). Hydrogen and hydrogen-derived fuels through methane decomposition of natural gas–GHG emissions and costs. Energy conversion and management: X, 7, 100043.
[12] IMIA (2022), Insuring hydrogen infrastructure. Zurich, Germany (Switzerland).
[13] Keipi, T., Tolvanen, H., & Konttinen, J. (2018). Economic analysis of hydrogen production by methane thermal decomposition: Comparison to competing technologies. Energy Conversion and Management, 159, 264-273.
[14] Peters, M. S., Timmerhaus, K. D., & West, R. E. (2003). Plant design and economics for chemical engineers (Vol. 4). New York: McGraw-hill.

SESSION VII

NUMERICAL COMBUSTION


THE COMBUSTION INSTITUTE
1954

ON THE USE OF PROJECTION TO LATENT STRUCTURES AND GAUSSIAN PROCESS REGRESSION FOR CHEMISTRY REDUCTION

Himanshu Dave*, Mohammad Rafi Malik, Kamila Zdybał*, Hong G. Im**, Alessandro Parente***

himanshu.dave@ulb.be

*Aéro-Thermo-Mécanique (ATM) Department, Ecolé Polytechnique de Bruxelles, Université Libre de Bruxelles (ULB), Brussels, 1050, Belgium

**King Abdullah University of Science and Technology (KAUST), Thuwal, Saudi Arabia

Abstract

Combustion chemistry is nonlinear and multiscale. These aspects increase dimensionality of chemical space and computational cost of simulations. In this study, we propose a new, supervised dimensionality reduction technique, called Projection to Latent Structures (PLS), to project chemical species to a reduced space with fewer variables (or scores). In this reduced space, we solve score transport equations, analogous to species transport equations in chemical space. We trained a linear map and a Gaussian Process Regression (GPR) based nonlinear map to predict source terms of the scores. We found that both linear and nonlinear regression maps allow a significant reduction in the number of transported scores. Secondly, we compared the PLS-score and PLS-GPR modeling techniques with previously investigated Principal Component Analysis (PCA) based PC-score and PC-GPR techniques. We observed that PLS-based techniques allow an improved modeling of chemical species than PCA-based techniques, while maintaining comparable training and simulation time. We demonstrated our proposed techniques on methane-oxygen and propane-air datasets from canonical, well-stirred reactor simulations.

Introduction

Combustion is expected to play a significant and synergistic role in meeting our future energy demands across several sectors [1]. Existing combustion devices thus need to be improved and new combustion modes, like Moderate and Intense Low-oxygen Dilution (MILD) [2, 3], need to be investigated. Numerical simulations play a key role in realizing those improvements and novel technologies [4]. It is well known that combustion chemistry takes a significant fraction of the simulation time. Large computational costs are attributable to aspects of combustion chemistry, such as nonlinear Arrhenius-based source terms in species transport equations, stiffness of governing equations, large spatio-temporal dimensionality, etc. Several species and small time-steps are required to capture complex combustion dynamics. For engineering purposes, the transport equations must be accurately solved on large meshes with time-step size $\left(\Delta t \sim \mathcal{O}(10^{-7} - 10^{-9}\mathrm{s})\right)$. To contribute to the

overarching goal of a better integration of numerical simulations in the design process, accelerating combustion chemistry is, therefore, extremely important.
To accelerate chemistry computations, two broad frameworks are possible – hardware-oriented and modeling-oriented. In [5], the former framework was investigated by taking logarithm of the Arrhenius kinetic models to enable matrix-based formulations and leverage the use of Graphical Processing Units (GPUs). The number of species transport equations is not reduced, rather models are re-formulated to take advantage of better computing architectures. In the latter framework, chemistry computation time is reduced by alternative modeling strategies. Data-driven techniques [6-9] are being increasingly employed for this purpose. Among them, reducing number of transport equations with the help of Principal Component Analysis (PCA) is widely used and established [3, 8, 9].
In this study, we take inspiration from [9] and extend the investigation to the use of Projection to Latent Structures (PLS) [10] for dimensionality reduction. We purport that as PLS focuses on maximizing covariance between chemical variables and their source terms, it extracts a manifold, in a supervised fashion, that is better-informed about the chemical kinetics. Unsupervised PCA extracts a manifold that maximizes explained variance in the chemical space. The species transport equations are then projected onto the manifolds to analogously obtain score transport equations. Given that we require very few scores to be transported, combustion chemistry is reduced in complexity paving way for faster computations.

Various Machine Learning (ML) techniques

Principal Component Analysis (PCA)

PCA is a widely used unsupervised statistical technique [11] that extracts a set of hierarchical principal directions in a dataset by maximizing the variance explained along those directions. The dataset is arranged in a data matrix, $\boldsymbol{X} \in \mathbb{R}^{n_o \times n_c}$, of n_o observations and n_c variables. A covariance matrix, $\boldsymbol{S} = \boldsymbol{X}^{\mathrm{T}}\boldsymbol{X}/(n_o - 1)$, is built and eigen-decomposed as $\boldsymbol{S} = \boldsymbol{A}\boldsymbol{L}\boldsymbol{A}^{\mathrm{T}}$, to extract the principal directions. These directions are columns in $\boldsymbol{A}$. Using only the first few (q) directions, we perform dimensionality reduction and project $\boldsymbol{X}$ onto another, reduced manifold, $\boldsymbol{A}_q$, and get the Principal Component (PC) scores, $\boldsymbol{Z}_q \in \mathbb{R}^{n_o \times q}$, where $\boldsymbol{Z}_q = \boldsymbol{X}\boldsymbol{A}_q$. Transport equations for $\boldsymbol{Z}_q$ are derived from species transport equations and $\boldsymbol{A}_q$, as shown in Ref. [8].

Projection to Latent Structures (PLS)

PLS is a supervised dimensionality reduction technique. It operates on two data matrices $\boldsymbol{X}$ and $\boldsymbol{Y}$ simultaneously and extracts reduced variables that maximize covariance between them. We performed PLS with chemical species in $\boldsymbol{X}$ and their source terms in $\boldsymbol{Y}$ and used the Nonlinear Iterative Partial Least Squares (NIPALS) algorithm [10] to obtain PLS scores $\boldsymbol{T}_q = \boldsymbol{X}_q\boldsymbol{R}_q$. The manifold is stored in $\boldsymbol{R}_q = \boldsymbol{W}_q\left(\boldsymbol{P}_q^{\mathrm{T}}\boldsymbol{W}_q\right)^{-1}$, where $\boldsymbol{W}_q$ and $\boldsymbol{P}_q$ are the weight and loading matrices of $\boldsymbol{X}$. Due to space limitations, we cannot provide complete details here. For details, refer to [10].

Gaussian Process Regression (GPR)

GPR does not assume a specific model form and the dependent variables, such as source terms in this study, can be described by a Gaussian distribution with mean function, m, and kernel, K, as: $\phi \approx GP(m(x), K(x, x'))$.

Results and Discussion

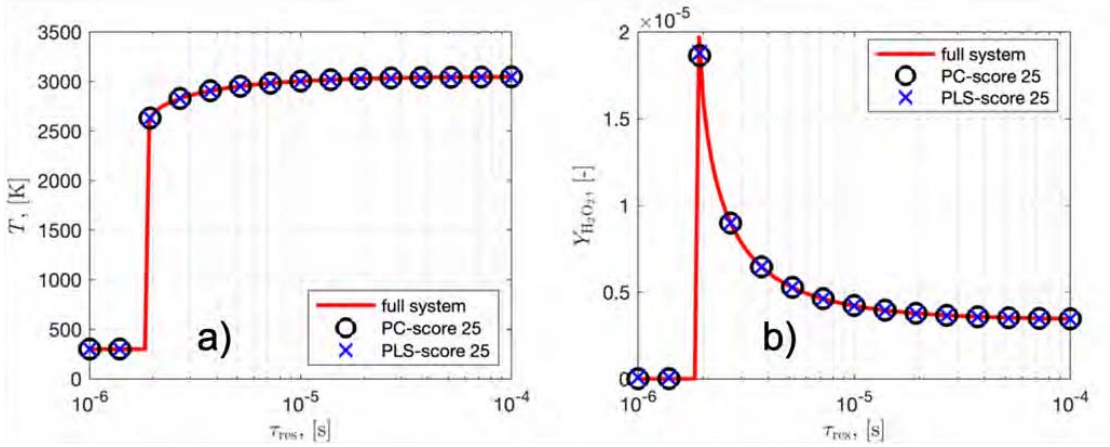

Figure 1. a) Temperature, T, and b) mass fraction of H_2O_2, $Y_{H_2O_2}$, as function of residence time, τ_{res}. PC-score and PLS-score approaches with 25 scores are compared with the detailed solution from Cantera.

Variable	NRMSE PC-score	NRMSE PLS-score	% Improvement
T	1.78×10^{-3}	1.73×10^{-3}	2.8
CH_4	1.26×10^{-3}	9.41×10^{-4}	25.3
OH	5.32×10^{-3}	3.68×10^{-3}	30.8

Table 1. Normalized root mean squared error, NRMSE, for different variables with respect to detailed solution. Last column shows improvement in accuracy on using PLS-score instead of PC-score.

Figure 1a shows temperature, T, as a function of the residence time, τ_{res}, of the well-stirred reactor. Profile of T from proposed PLS-score technique (blue crosses) is compared with PC-score (black circles) technique used in [9] and the detailed solution (or full-order solution) from Cantera for CH_4-O_2 mixture at equivalence ratio, $\phi = 1.0$. Figure 1b shows a similar plot, but for the mass-fraction of H_2O_2. In PC-score and PLS-score techniques, the functional relationship between source terms of scores and their corresponding scores ($\boldsymbol{Z}_q$ or $\boldsymbol{T}_q$) is linear. It can be readily inferred that both linear reduced-manifold modeling techniques allow at least 26% reduction (from original 34 chemical species to 25 scores) in chemistry while maintaining proximity to the detailed solutions. While visually, the techniques are comparable to each other, the normalized root mean squared error, NRMSE, between the full-order and reduced-order solutions are lower for PLS-score than PC-score. Last column in Table-1 shows significant improvements of at least 20% over PC-score with the proposed PLS-score technique.

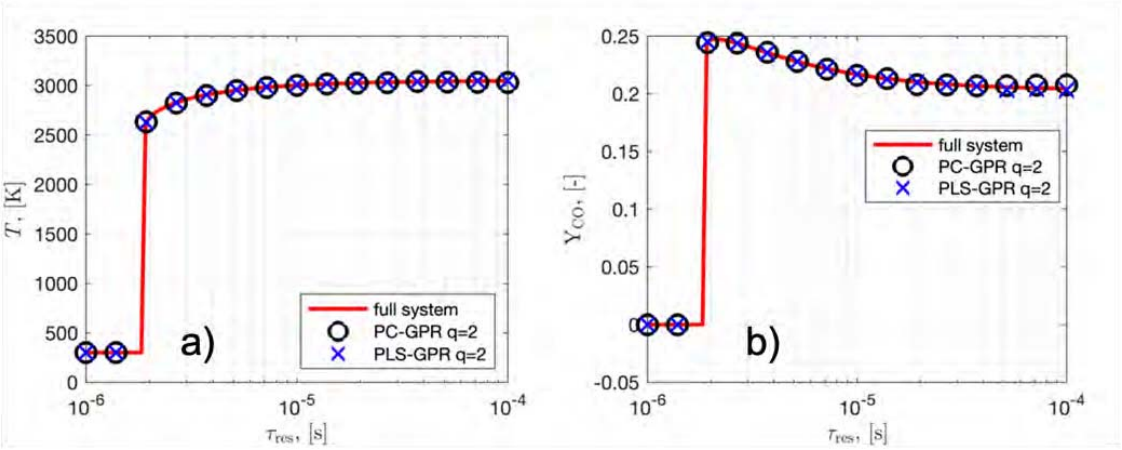

Figure 2. Comparison of a) T and b) Y_{CO} profiles with respect to τ_{res} from proposed PLS-GPR with existing PC-GPR [see Ref. 9] and detailed solution.

Variable	NRMSE PC-GPR	NRMSE PLS-GPR	% Improvement
T	6.96×10^{-3}	3.34×10^{-3}	52
CH_4	2.06×10^{-3}	1.39×10^{-3}	32.5
OH	1.10×10^{-2}	8.55×10^{-3}	22.3

Table 2. NRMSE for variables with respect to detailed solution. Last column shows improvement in accuracy with respect to PC-GPR on using PLS-GPR.

Figure 2 and Table 2 show results as shown previously, however, now instead of using linear PCA or linear PLS based relationship between scores and their source terms, we use trained GPR-based regression functions. These regression functions nonlinearly map the scores ($\boldsymbol{Z}_q$ or $\boldsymbol{T}_q$) to their corresponding source terms and closes the set of equations in reduced space. First, it can be readily inferred that with nonlinear, GPR-based functions we see a drastic reduction of number of transported scores from 34 chemical species to just 2 scores. Also, compared to 25 scores with linear approach only 2 scores are transported to obtain NRMSE of same order as PC-score or PLS-score. Secondly, we see a significant improvement in accuracy of 20% and more with respect to PC-GPR as we use PLS-GPR.

To demonstrate the generality of our technique, we used PLS-GPR to reduce combustion chemistry for C_3H_8-Air mixture at $\phi = 1.0$. Figure 3 shows the variation of T with respect to τ_{res}. We used San-Diego reaction mechanism (50 species) in Cantera to model chemistry and obtain detailed solutions. Unlike previous figures, a significant improvement in the accuracy of predicted T profile is visually evident with PLS-GPR. The PLS-GPR predictions (blue crosses) lie closer to the detailed solution (solid red curve) than PC-GPR solution (black circles), and we see a quantitative improvement of nearly 70% over PC-GPR solution.

Thus, we can infer that both supervised PLS and its unsupervised counterpart PCA can reduce number of transport equations to be solved by nearly 90%. However, PLS coupled with nonlinear regression with GPR is shown to significantly improve predictions by at least 20% over PC-GPR technique. The improvements being more

apparent with complex fuels like propane. PLS is therefore a valuable supervised dimensionality reduction technique useful for reducing combustion chemistry. The predicted thermo-chemical variables obtained from score transport equations (on PLS basis) and subsequent reconstruction are closer to the detailed solution.

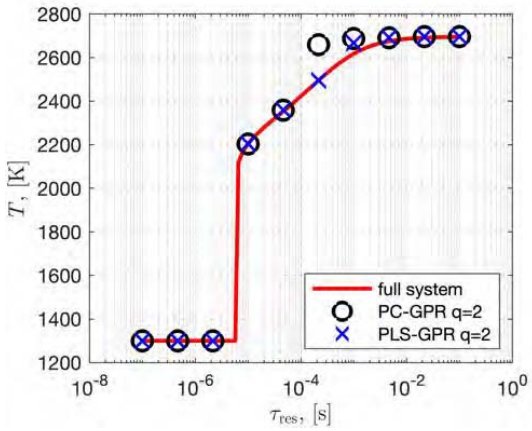

Figure 3. Comparison of T with respect to τ_{res} profiles for existing PC-GPR [see Ref.10], proposed PLS-GPR, and detailed solution from Cantera. The chemical mixture is propane-air at $\phi = 1.0$.

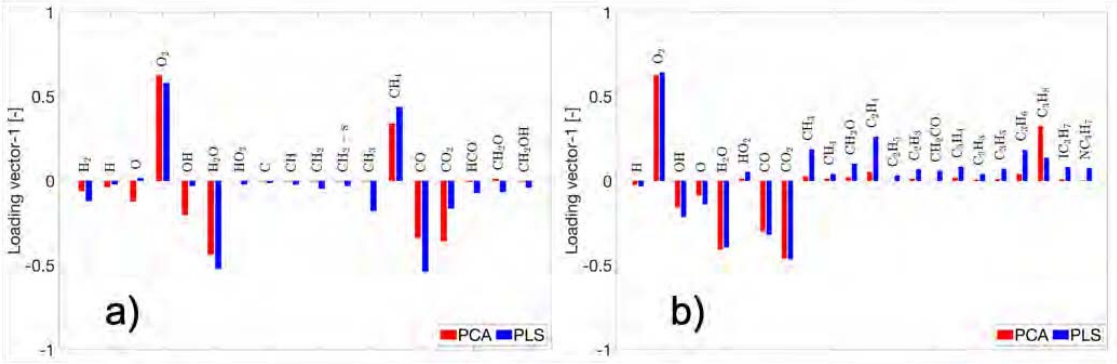

Figure 4. Comparison of PCA and PLS loadings on 1st loading vector for a) methane-oxygen and b) propane-air datasets.

To understand possible reasons for observed improvements with PLS, we now investigate the loadings on the direction of reduced manifolds. The first direction (or loading vector) of the manifold identifies dominant structures and consequently most relevant variables. Figure 4 shows bar plots representing the loadings on 1st loading vectors of PCA and PLS-manifolds. PCA identifies species such as fuel (CH_4 or C_3H_8), O_2, CO, CO_2, H_2O, etc. as important, indicated by greater heights of the red bars. However, PLS vector also have significant loadings on reaction intermediates that appear on fuel break-up, such as CH_3, C_3H_6, C_2H_4, along with species that appear on their eventual oxidation, such as CO and CH_2O. This is evident from the heights of the blue bars. It is remarkable that PLS identifies additional species that appear in reaction pathways of methane and propane oxidation without significant intervention from user. We attribute this property of PLS as a reason behind the improvements in prediction accuracy discussed previously.

Conclusions

In this study, we used a new supervised dimensionality reduction technique, abbreviated as PLS for reducing combustion chemistry. Unlike unsupervised PCA, PLS extracts a manifold that is informed about chemical kinetics. We used methane-oxygen and propane-air mixtures for our investigations. We found that PLS-GPR like PC-GPR can reduce transport equations by nearly 90%. However, PLS-GPR is found to be more accurate (at least 20%) than PC-GPR technique for assessed thermo-chemical variables. The accuracy being more pronounced for propane-air mixture encourages utility for complex fuels. Thus, the newly proposed PLS-GPR, a reduced manifold modeling technique, is favorable for simplifying combustion chemistry and accelerating it. This is attributed to its ability to identify important species and radicals that appear in reaction pathways. The training time for PLS-GPR and PC-GPR were found to be comparable.

References

[1] Swaminathan, N., "Physical insights on MILD combustion from DNS", *Front. Mech. Eng. 5,* 59 (2019)
[2] Cavaliere, A., & De Joannon, M., "MILD Combustion", *Prog. Energy Combust. Sci. 30*(4) 329-366 (2004)
[3] Parente, A., Sutherland, J. C., Dally, B. B., Tognotti, L., & Smith, P. J., "Investigation of the MILD combustion regime via Principal Component Analysis", *Proc. Combust. Inst. 33*(2) 3333-3341 (2011)
[4] Bilger, R. W., "Future progress in turbulent combustion research", *Prog. Energy Combust. Sci. 26*(4-6) 367-380 (2000)
[5] Barwey, S., & Raman, V., "A neural network-inspired matrix formulation of chemical kinetics for acceleration on GPUs", *Energies 14*(9) 2710 (2021)
[6] Owoyele, O., Kundu, P., Ameen, M. M., Echekki, T., & Som, S., "Application of deep artificial neural networks to multi-dimensional flamelet libraries and spray flames", *International Journal of Engine Research 21*(1) 151-168 (2020)
[7] Parente, A., Sutherland, J. C., Tognotti, L., & Smith, P. J., "Identification of low-dimensional manifolds in turbulent flames", *Proc. Comb. Inst. 32*(1) 1579-1586 (2009)
[8] Sutherland, J. C., & Parente, A., "Combustion modeling using Principal Component Analysis", *Proc. Comb. Inst. 32*(1) 1563-1570 (2009)
[9] Malik, M. R., Isaac, B. J., Coussement, A., Smith, P. J., & Parente, A., "Principal Component Analysis coupled with nonlinear regression for chemistry reduction", *Combust. Flame 187* 30-41 (2018)
[10] Wold, S., Johansson, E., & Cocchi, M, "PLS: partial least squares projections to latent structures", In *3D QSAR in Drug Design: Theory, Methods and Applications* (pp. 523-550) Kluwer ESCOM Science Publisher (1993)
[11] Jolliffe, I. T., & Cadima, J., "Principal Component Analysis: a review and recent developments", *Philos. Trans. Royal Soc. A 374*(2065) 20150202 (2016)

TABULATION-BASED SAMPLE-PARTITIONING ADAPTIVE REDUCED CHEMISTRY AND CELL AGGLOMERATION

A. Cuoci*, A. Nobili*, A. Parente, T. Grenga*****
alberto.cuoci@polimi.it
*CRECK Modeling Lab, Department of Chemistry, Materials, and Chemical Engineering "G. Natta", Politecnico di Milano (Italy)
**Université Libre de Bruxelles, Ecole Polytechnique de Bruxelles, Aero-Thermo-Mechanics Laboratory, Bruxelles (Belgium)
***Faculty of Engineering and Physical Science, University of Southampton (UK)

Abstract
In this study, we combine the SPARC (Sample-Partitioning Adaptive Reduced Chemistry) and the Cell Agglomeration (CA) techniques, to accelerate the simulation of laminar and turbulent reactive flows with detailed kinetics.
More specifically, the reduced mechanisms adopted by SPARC are generated on the basis of representative thermochemical states corresponding to laminar, steady-state flamelets parametrized by the mixture fraction and a progress variable, similar to the TRAC (Tabulated Reactions for Adaptive Chemistry) method, recently proposed by Surapaneni and Mira (*Comb. & Flame* 251, 2023). To further speed-up the calculation, CA (consisting in grouping the computational cells having similar thermochemical states during the chemical step) is carried out before identifying the local reduced mechanism by SPARC.
To demonstrate the effectiveness of the approach, we considered two benchmark cases: i) a laminar, pulsating laminar coflow diffusion flame fueled by a mixture of C_2H_4 and N_2 burning in air; ii) a 2D, turbulent, non-premixed flame burning n-C_7H_{16} in air subject to decaying isotropic turbulence. In both cases, a detailed kinetic mechanism accounting for the formation of PAHs and soot particles and aggregates was considered. Preliminary numerical tests were conducted to investigate the feasibility of the proposed tabulation-based SPARC-CA methodology. The results are promising, showing both accuracy and computational efficiency, demonstrating the potential of the proposed methodology for advancing multi-dimensional CFD simulations of reactive flows with complex chemistry.

Introduction
In the pursuit of more effective design of combustion devices, such as industrial/domestic burners and gas turbines, detailed kinetics has emerged as a crucial factor for predictive simulations of laminar and turbulent flames. However, the computational coupling of Computational Fluid Dynamics (CFD) and detailed chemistry poses significant challenges, primarily due to the number of species

involved and the wide range of chemical timescales associated with complex chemistry [1]. While various acceleration techniques have been proposed during the years, the computational cost of CFD including detailed chemistry remains a concern, particularly for complex fuels.

CFD solvers based on the operator-splitting strategy are especially suitable for simulation of reactive flows with detailed kinetic mechanisms. In operator-splitting methods most of the computational time is spent to solve the chemical step, which consists in solving a number of independent, stiff, nonlinear systems of ordinary differential equations (ODEs), one per computational cell [2]. The independent nature of these ODE systems makes the application of adaptive chemistry techniques straightforward and highly effective. The core idea behind adaptive chemistry revolves around the observation that within small temperature and composition ranges, numerous species have negligible concentrations, and only a limited number of species remain chemically active. Consequently, the kinetic mechanism required to describe the chemical evolution within a specific thermo-chemical space may demand fewer species and reactions than the complete mechanism applicable to the entire thermo-chemical space. At the highest level of adaptivity and reduction, the local thermo-chemical state is evaluated *on-the-fly*, and a reduced kinetic mechanism is specifically generated in each computational cell (Dynamic Adaptive Chemistry) [3]. However, the computational cost associated to the reduction operations is substantial, especially for higher levels of reduction and complex mechanisms.

To alleviate the additional cost of adaptive reduction, the Sample-Partitioning Adaptive Chemistry (SPARC) approach was recently proposed and applied [4]. In SPARC, the *on-the-fly* mechanism reduction overhead is avoided, by building in a preprocessing phase a library of reduced mechanisms to be used in different regions of the domain during the CFD simulation. In SPARC, the challenge lies in effectively partitioning the composition space into clusters, ensuring that each cluster exhibits sufficient homogeneity from a kinetic point of view. Several approaches have been considered, from combination of Self Organizing Maps (SOM) with k-means to Principal Component Analysis (PCA).

In the present work we explore the possibility to use low-dimensional manifolds to identify regions with different chemical activities, in line with the TRAC (Tabulated reactions for adaptive chemistry) method, recently proposed in [5]. More specifically, we applied the pre-partitioning operations on representative thermochemical states corresponding to laminar, steady-state flamelets parametrized by the mixture fraction ξ and a normalized progress variable Y_c^n. The advantage over SOM or PCA is that the multi-dimensional data generated in the preprocessing phase are now linked to two control variables (ξ and Y_c^n) having a clear physical interpretation and direct connection with chemical kinetics.

To further speed-up the calculation, Cell Agglomeration (CA) was combined with SPARC. In CA, at each reaction step, the computational cells with similar properties, also called *features*, are grouped together in a single zone with averaged values. Chemistry calculations are carried out per zone (instead of computational cells) and

the results are mapped back to the original, individual cells. Since the number of zones is usually much smaller than the total number of cells, CA is expected to result in significant computational saving. Instead of using the temperature and selected key-species, the idea in this work is adopt ξ and Y_c^n as *features* in the agglomeration process, consistently with the SPARC algorithm.
In the next Section, the SPARC and CA techniques based on tabulated chemistry will be described with more details. Then, two examples of application of the proposed methodology will be presented and briefly discussed.

Methodology

The general idea behind the adaptive chemistry approach here proposed is the assumption that not all the species contained in a detailed kinetic mechanism are (locally) equally necessary. Depending on the physics of the reacting flow, a reduced set of species and reactions can be identified in each cell at each time step.
The proposed procedure consists of 2 phases. The first phase is carried out as a preprocessing step and consists of the following operations:

1. Dataset generation: the training dataset is constructed from the solutions of steady and unsteady adiabatic diffusion flamelets. The steady flamelets are simulated by varying the applied strain rate until an extinction limit. The composition space between the most strained flamelet and mixing limit is covered by using an unsteady formulation of flamelets.
2. Dataset parameterization: the generated database is remapped over two control variables, the mixture fraction ξ and the normalized progress variable Y_c^n, using a 401×401 grid with uniform spacing.
3. Partitioning of the thermochemical space: a clustering algorithm is adopted to identify in the $\xi - Y_c^n$ space continuous regions (i.e., clusters) having similar kinetic behavior. In the present work, for simplicity, the $\xi - Y_c^n$ space is decomposed in 40×40 clusters by means of a regular 2D grid. Thus, each cluster is uniquely identified by the ξ and Y_c^n values at its center.
4. Generation of reduced mechanisms: for each cluster of the dataset, a reduced mechanism is generated via the Directed Relation Graph (DRG) method [6]. The total number of reduced mechanisms is 1,600.

The second phase corresponds to the chemical step of the CFD simulation and consists of the three following operations:

1. Cell agglomeration: cells having similar thermochemical state (identified by ξ and Y_c^n variables only) are grouped together and their average mixture fraction $\bar{\xi}$ and progress variable $\bar{Y}_c^n$ are estimated. The Dynamic Multi-Zone (DMZ) algorithm [7], which is based on an unsupervised evolutionary clustering algorithm which automatically determines the optimal number of clusters for a user-defined level of accuracy, is here adopted.
2. Identification of reduced kinetic mechanism and chemical integration: based on averaged $\bar{\xi}$ and $\bar{Y}_c^n$, the reduced kinetic mechanism in each cluster is identified from the library built in the preprocessing step. The conservation equations of

species and energy are then solved according to the reduced kinetic mechanism.

3. Back-mapping: the calculated thermo-physical state at the cluster level is mapped back to the original cells, using the backward remapping procedure proposed by Liang et al. [3], which ensures the conservation of mass.

Results and discussion

The first configuration chosen to test the proposed methodology is an axisymmetric, time-varying, non-premixed laminar coflow flame. The fuel is a mixture of 60% C_2H_4 and 40% N_2 (molar basis), while the oxidizer stream is regular air. Both streams are fed at ambient temperature and atmospheric pressure. A transient behavior was induced by a sinusoidal perturbation in the velocity profile of the fuel stream with frequency $f = 10$ *Hz* and amplitude $A = 0.90$. Additional details can be found in [8].

The second configuration here adopted is the two-dimensional, turbulent, non-premixed flame burning a mixture of n-C_7H_{16} and N_2 (0.844/0.156 by volume) in air subject to decaying isotropic turbulence, proposed by Bisetti et al. [9].

In both cases, the simulations have been carried out using a detailed kinetic mechanism developed by the CRECK Modeling Lab including the chemistry of PAHs (Polycyclic Aromatic Hydrocarbons) and accounting for the formation of soot particles and aggregates via a Discrete Sectional Method (DSM) [10], with a total number of species and reactions equal to 185 and ~8,000, respectively.

As mentioned in the previous section, the training dataset was built from the solutions of steady and unsteady adiabatic laminar flamelets, from a strain rate of $a = 0.01$ *1/s* (close to thermodynamic equilibrium), to the extinction, corresponding to $a_q = 250$ *1/s* (laminar coflow flame fed with C_2H_4) and $a_q = 90$ *1/s* (turbulent diffusion flame fed with n-C_7H_{16}). The dataset was parameterized through the mixture fraction ξ and a progress variable Y_c^n defined as suggested in [5]. Figure 1 presents the maps of temperature and mass fractions of soot particles and aggregates stored in the training dataset as a function of ξ and Y_c.

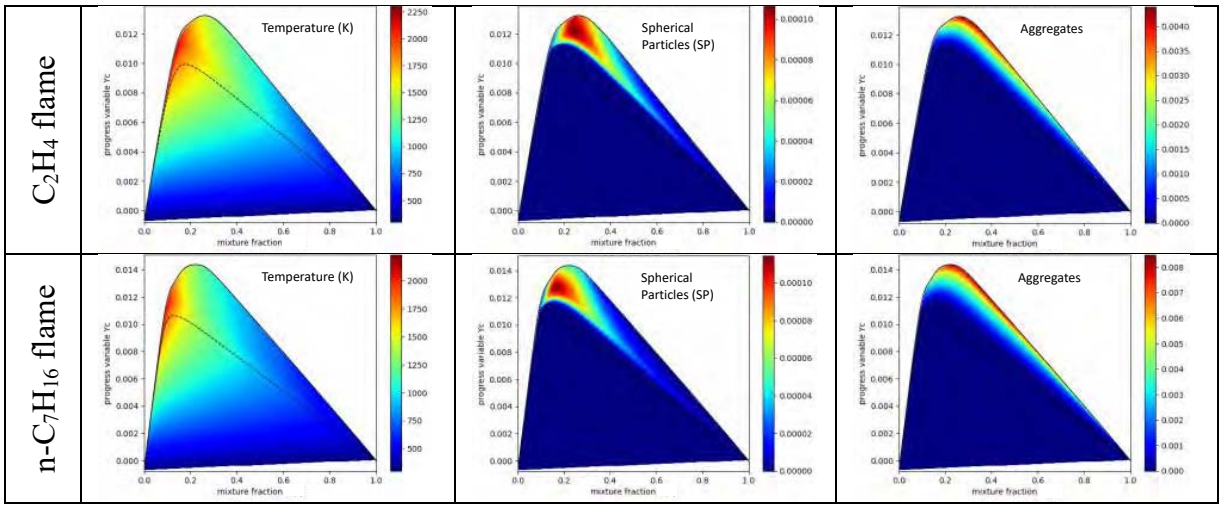

Figure 1. Temperature and soot mass fraction fields (spherical particles and aggregates) as a function of mixture fraction ξ and progress variable Y_c.

The chemical reduction was carried out as a preprocessing step using the DRG technique. In particular, for both the datasets, six key-species (fuel, O_2, N_2, OH, BIN5AJ and BIN13AJ) were selected and a tolerance $\varepsilon_{DRG} = 0.05$ was adopted. BIN5AJ and BIN13AJ are the discrete sections corresponding to the smallest soot spherical particle and the smallest soot aggregate. They were included in the set of key-species since to properly capture the soot kinetics during the reduction phase. Figure 2 presents the number of active species and reactions in the ξ-Y_c^n space and the regions were BIN5AJ is retained in the reduction process. A region of reduced mechanisms with high number of species and reactions is evident in the rich side, where the formation of soot is expected to be relevant (see Figure 1).

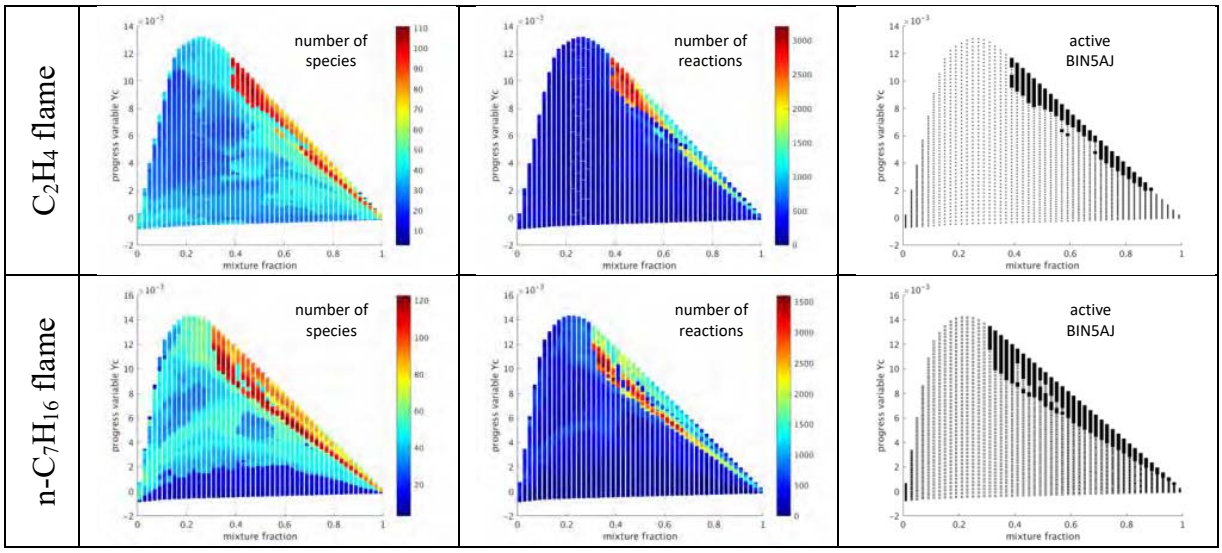

Figure 2. a, b) Maps of active species and reactions after the reduction process via DRG; c) regions (in black) where the pseudo-species BIN5AJ is retained.

The CFD simulations were carried out using the laminarSMOKE++ code [2]. The solutions calculated with the complete detailed kinetic mechanism are compared with those obtained from the application of the proposed methodology, which combines tabulated-based SPARC and CA (in which ξ and Y_c^n are assumed as features, with a tolerance $\varepsilon_{CA} = 0.01$). Figures 3 and 4 show the calculated fields of temperature and selected mass fractions at different times for the two benchmark cases. The agreement is quite good in both cases: the dynamics is well captured, and no significant deviations of the SPARC-CA results are evident, for temperature and soot.

In both cases here investigated, ~95% of total CPU time is spent for performing the chemical step when the complete kinetic mechanism is adopted. Thus, since the SPARC-CA method is able to accelerate the chemical step only, the maximum theoretical speed-up which can be achieved is ~20. For the unsteady laminar coflow flame fed with C_2H_4 the measured average (over a single cycle of oscillation) speedup was ~16 (i.e., about 80% of theoretical maximum). Similarly, for the turbulent n-C_7H_{16} flame, the average (in the 0-30 ms interval) speedup was ~15 (i.e.,

~75% of theoretical maximum). As demonstrated in [7], the additional computational cost of CA is negligible with respect to the time for carrying out the chemical step (of the order of ~1%). Since the partitioning is available as a 2D regular grid in the $\xi - Y_c^n$ space, the additional cost to identify the reduced kinetic mechanism is negligible, requiring only the local values of ξ and Y_c^n.

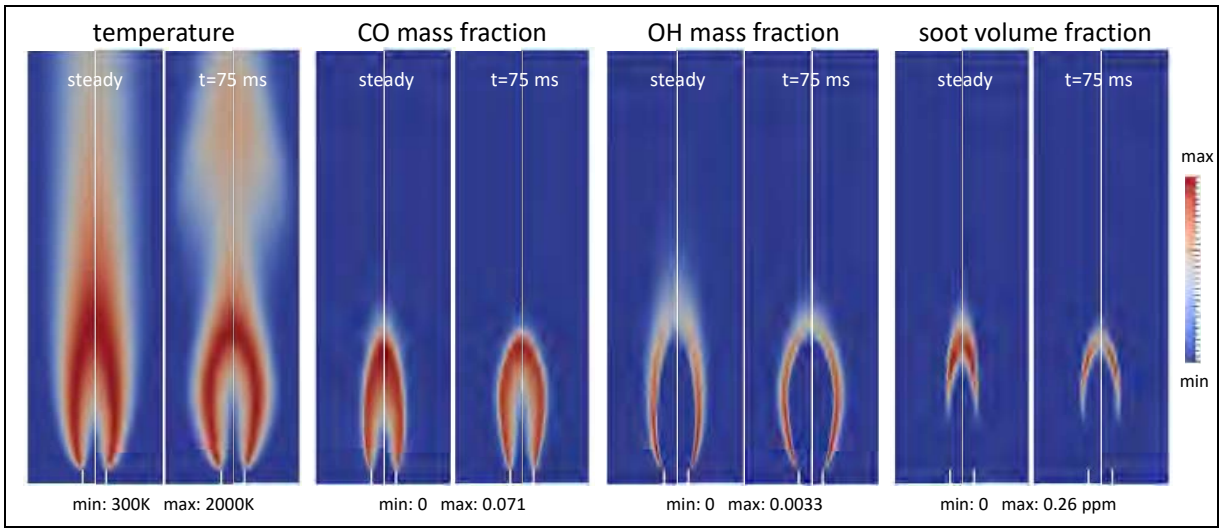

Figure 3. Calculated maps of T, mass fractions of CO and OH and soot volume fraction. Left sides: fully resolved solution; right sides: SPARC-CA solution.

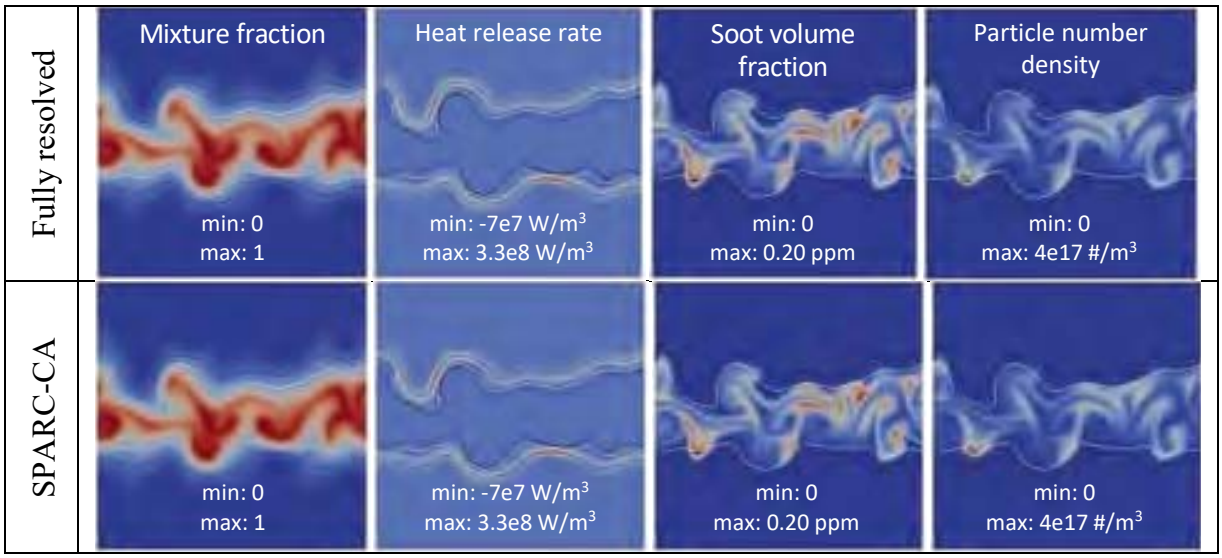

Figure 4. Maps of selected variables in the turbulent non-premixed flame fed with n-C_7H_{16} at *t=10 ms*. The black and white lines identify the isolines $\xi = 0.143$ and $\xi = 0.3$, respectively.

Conclusions

In this work, we combined the SPARC (Sample-Partitioning Adaptive Reduced Chemistry) and the Cell Agglomeration (CA) techniques with tabulation of

chemistry in a 2D space, to accelerate the simulation of laminar and turbulent reactive flows with detailed kinetics. The proposed approach was applied to laminar and turbulent flames. The results, even if preliminary, are satisfactory: the accuracy is good in both the benchmark cases with good levels of acceleration, close to ~80% of theoretical maximum speed up. More systematic and complete analyses are required to better asses the performances and the limitations of the methodology. To conclude, the tabulation-based SPARC-CA method is a promising technique to accelerate simulations of reactive flows, especially considering that its implementation in operator-splitting-based CFD codes is very straightforward.

References

[1] Lu T., Law C., *Prog. Energy Comb. Sci.* 35: 192-195 (2009)
[2] Cuoci A., Frassoldati A., Faravelli T., Ranzi E., *Energy & Fuels* 27:7730-7753 (2013)
[3] Liang L., Stevens J., Farrell J., *Proc. Comb. Inst.* 32:527–534 (2009)
[4] D'Alessio G., Parente A., Stagni A., Cuoci A., *Comb. & Flame* 211:68-82 (2020)
[5] Surapaneni A., Mira D., *Comb. & Flame* 251:112715 (2023)
[6] Lu T., Law C., *Proc. Comb. Inst.* 30:1333–1341 (2005)
[7] Liang L., Stevens J., Farrell J., *Comb. Sci. Tech.* 181(11):1345-1371 (2009)
[8] McEnally C., Schaffer A., Long M., Pfefferle L., Smooke M., Colket M., Hall R., *Proc. Comb. Inst.* 27: pp. 1497–1505 (1998)
[9] Bisetti F., Blanquart G., Mueller, M.E., Pitsch H., *Comb. & Flame* 159(1):317-335 (2012)
[10] Nobili A., Pejpichestakul W., Pelucchi M., Cuoci A., Cavallotti C., Faravelli T., *Comb. & Flame* 243:112073 (2022)

TIME-LAG AUTO-ENCODERS FOR CHEMISTRY DIMENSIONALITY REDUCTION

L. Castellanos*, R. S. M. Freitas, A. Parente**, F. Contino***
luisa.castellanos@uclouvain.be
*IMMC-TFL, Universite Catholique de Louvain, Louvain La Neuve, Belgium
**Aerothermo-mechanics Department, Universite Libre de Bruxelles, Brussels, Belgium

Abstract.
Chemical kinetics modeling is a challenge. One of the challenges is related to the curse of dimensionality. Many reduction techniques have been applied, searching for alternatives to accelerate reacting flow simulations. Lately, Machine Learning techniques have been applied to this task. The present study assesses the applicability of Time-lag Auto-Encoders for chemistry reduction.

1 Introduction

Many industrial applications include reacting flows as a key issue to model and foresee. This means that efficient modeling techniques are a must; nowadays, the most common tools are Computational Fluid Dynamics (CFD) simulations, which unfortunately, hold a high computational overhead in proportion to the chemical mechanism considered and the number of physical phenomena to be modeled [9]. Since the principal issue regarding chemical kinetics is the curse of dimensionality, many dimensionality reduction techniques have been applied. For this study, there is a particular interest in Machine Learning (ML) techniques, from which, the application of PCA [6], and auto-encoders (AE) [12] are worth noticing. However, both come with advantages and disadvantages; in the case of PCA, even if it is an easy-to-apply technique, it just allows the representation of linear phenomena, failing to capture many of the chemistry kinetics non-linearities. On the other hand, AE offers a better representation of these non-linearities, however, as in the case of PCA, the reduced components are not directly related to chemical variables, making it difficult to develop closure models. In the present work, a time shift will be added to an AE network architecture, which gives place to a time-lag auto-encoder (TAE) [11]. The application of such a network adds a temporal characterization to the reduced components, which becomes a dynamical characterization of the chemistry. The aim of the present study is to assess the feasibility of such an approach for chemistry reduction.

2 Theoretical Background

A TAE follows the same concept and architecture as an Auto-encoders (AE), which is a type of neural network that is used for finding reduced representations of a given input vector [5]. The main difference is that a time shift is applied between the network's inputs and outputs, which means modeling a dynamical system as a time series starting from a thermochemical initial state. Moreover, the final goal of TAE

is to find an encoding and decoding which minimizes the time-lagged reconstruction loss (L_{TAE}); for having a physically constrained model, a physically aware loss function is proposed, which reflects the mass conservation principle:

$$L_{TAE} = \frac{1}{M}\sum_{t=0}^{t=t_{nt}} |X_{t+\Delta t} - \tilde{X}_{t+\Delta t}|^2 + \frac{\beta}{M}\sum_{t=0}^{t=t_{nt}} |Y_{t+\Delta t} - \tilde{Y}_{t+\Delta t}|^2 \quad (1)$$

In which variables with (˜) refer to the TAE's output, while X stands for the correct output state vector, and Y stands for the species mass fractions, which should sum up to a constant value. β is the regularization constant and M stands for the number of time samples in all the ignition cases. However, a reduction technique is evaluated in accordance with their respective reconstruction error, therefore, it is important to understand the reconstruction benefits of TAE regarding typical reconstruction techniques, such as PCA. Therefore, the question to answer is how much the reconstruction inaccuracies are altered by the application of a TAE while keeping a constant number of features for both methods. Additionally, it should be emphasized that TAE gives direct information about the thermochemical state evolution, while PCA techniques just provide information about a present state. Thus, it is intended to analyze both techniques under equality of conditions, a one-layer auto-encoder is proposed to mimic the PCA technique, called a PCA-like auto-encoder.

3 Experimental Layout

In the present work, we test the capability of TAE as a feature extraction technique for hydrogen combustion. The dataset for training the machine learning models is obtained with isobaric batch reactors simulations, developed with the Cantera software [4]. The reduced version of the University of San Diego chemistry mechanism for hydrogen combustion is used [8], which consists of 9 species and 21 reactions. For the different ignition conditions, different values of equivalence ratio (ϕ) and initial temperature are considered. A Latin Hypercube Sampling was implemented [1] with a uniform distribution; 100 samples are obtained in a region delimited by $\phi \in [0.9, 1.2]$ and $T \in [1100, 1200]$ Kelvin. The thermochemical state vectors are defined using mass fractions values and temperature values, the dataset normalization is done with a general maximum value per quantity, meaning that each quantity is divided by its maximum occurrence among all the ignition points. This allows all the datasets to lie in the same manifold. The applied time shift equals a single time step. At the same time, different sizes of bottleneck layers were explored; the latent spaces range is described by $Z \in [1, 4]$, therefore, four different networks are meant to be studied, so it is possible to discuss the number of components for accurate reconstruction. For the chemical carrier's identification, a correlation analysis is performed using Kendall's Tau B correlation index, due to its boundedness and resistance to outliers [2].

4 Results

The first item to assess is the quality of reconstruction achieved by the TAE networks while feeding with the training data. Random ignition cases are used, and the quality of reconstruction is assessed via R^2 scores [3] which evaluates the quality of the model's output, scoring it within a constrained range of [0, 1], where 0 is given to a poorly performing model, and 1 to a perfect prediction. The ignition cases ($\phi = 0.92$, $T_0 = 1140.35$K), and ($\phi = 1.09$, $T_0 = 1120$K) were sampled; both cases proportion a minimum R^2 score of 0.95, result compatible with a satisfactory quality of reconstruction. Once the quality of reconstruction is assessed in training data, it is possible to extrapolate to unseen conditions, which means ignition points that were not used during training. Three interpolation ignition cases will be studied; interpolation means an ignition point not considered in the training data but contained inside the LHS sampling limits. These ignition points are available in Table 1.

Table 1. Interpolation ignition cases

Case	T[K]	ϕ
1	1160	0.93
2	1200	1.0
3	1130	1.10

4.1 TAE Reduced Manifolds

For obtaining these manifolds, the TAE network is fed with K time series that describe the hydrogen-air homogeneous autoignition problem in different ignition scenarios at the time interval $[t_0, t_{nt-1}]$, where nt stands for the number of time steps. The expected output is the future values of the time series, it is to say, the state vectors for the time interval $[t_{0+\Delta t}, t_{nt}]$. The R^2 score will be used again to assess the quality of reconstruction of the interpolation cases described in Table 1. The R^2 score values are available in Figure 1.

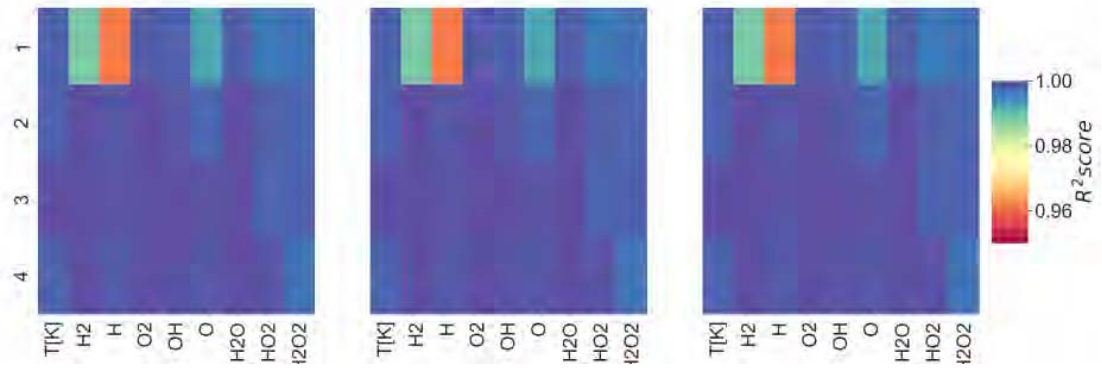

Figure 1. R^2 scores for interpolation cases, y-axe describes the number of latent variables considered by the model, at left: ignition case ($\phi = 0.93$, $T_0 = 1160$K), center: ignition case ($\phi = 1.0$, $T_0 = 1200$K), right: ignition case ($\phi = 1.10$, $T_0 =$

1130K). The numbers in the y-axis refer to the latent space dimension.

After observation, it is visible that the models retain a good representation of the dynamic behavior, returning R^2 scores larger than 0.96, while the lower scores belong to the latent space z = 1. Such output could be associated with combustion's high non-linearities, meaning that larger representations are required for an accurate description of the thermochemical states. In the previous section, the application of different bottleneck sizes is mentioned, which will be used to observe the chemical carriers that might appear in each case, such association is obtained using Kendall Tau B correlation index. The resulting associated species are available in Table 2.

Table 2. Chemical carriers' identification

Manifold Size (Z)	Chemical Carriers
1	T
2	T, O
3	H2O2, T, OH
4	O2, O, T, T

It is important to mention that the same chemical carriers repeat for all the ignition cases, accordingly to the bottleneck size. The temperature can be considered a key variable since it appears in all the models. The temperature repetitiveness in the manifold z = 4 suggests that four variables lead to overparametrization of the states. Figure 2 shows the latent space behaviour of z = 2 for the three ignition cases under study. It is to notice the same behaviour of the curves in all cases, with magnitudes differences associated to the ignition case, further, the time shift from the Ignition Delay Time is observed. The chemical carrier's repetitiveness suggests that a chemical mechanism variance can be described by key thermochemical variables.

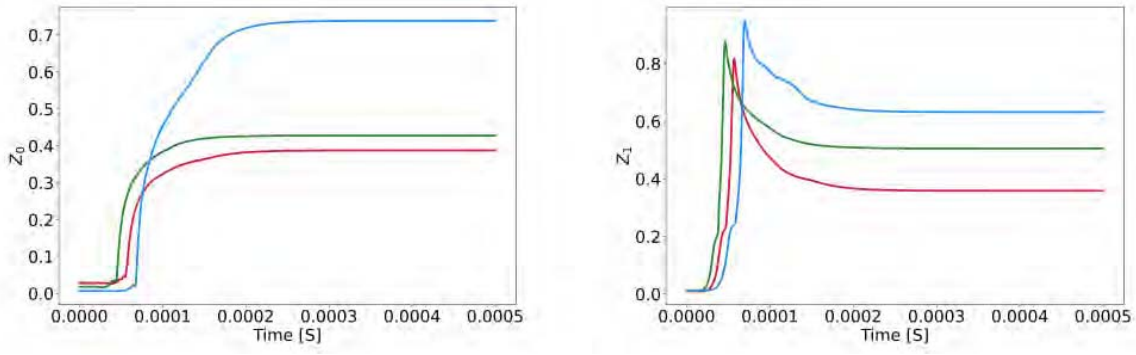

(a) (b)

Figure 2. Latent space visualization for manifold size z = 2, (a) shows the first latent variable, and (b) the second latent variable. The red curve stands for the ignition case (ϕ = 0.93, T_0 = 1160K), green curve for ignition case (ϕ = 1.0, T_0 =

1200K), and blue curve for ignition case (ϕ = 1.10, T_0 = 1130K)

4.2 PCA comparison

Here, the comparison will be performed based on the reconstruction error. For avoiding circumstances that could benefit one model over another, the PCA Autoencoder is trained with the same normalization and datasets used for the TAE training, and evaluations consider the same ignition cases. The scoring technique will be changed by the Mean Absolute Error (MAE) [7], so it is possible to estimate the average deviation between the predicted values and the real ones. The comparison highlights a significant difference between the numerical inaccuracies since the PCA reconstruction error (range [0, 0.04]) is easily four times higher than the one presented in TAE reconstruction (range [0, 0.01]). This suggests that TAE presents better reconstruction capabilities. However, the representation of fast phenomena must be assessed too. However, PCA does not manage to reproduce such events, issue that does not happen with TAE. The normalized reconstruction curves for T, OH, and HO2 are presented in Figure 3 for a latent space z = 2. Such selection of species searches to portray the behaviour in major, intermediate, and minor thermochemical variables.

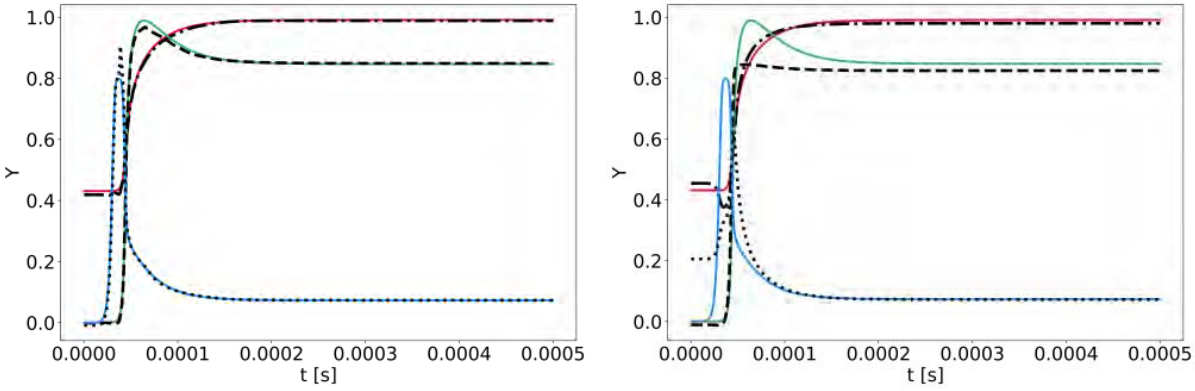

(a) (b)

Figure 3. Normalized chemical species reconstruction for a latent space size z = 2, the red curve shows the simulated behavior or temperatures, the green curve shows OH behavior, and the blue curve shows the behavior of HO2 for an ignition case ϕ = 1.0, T0 = 1200K (a) shows the TAE reconstruction (b) shows the PCA reconstruction.

5 Conclusion

In this study, an exploration of TAE capabilities for chemistry reduction was presented. It is assessed how the resultant latent variables are a more efficient representation of the thermochemical variables, allowing at the same time, a temporal characterization. It is also important to remark that TAE's manifolds and

their associated species (chemical carriers) could be used for the development of surrogate models that promise greater interpolation and extrapolation characteristics in the low data limit. Future work should be aimed at the development of better strategies for the description of manifold dynamics, as well as testing possible applications for the identified chemical carriers.

References

[1] Cavazzuti, M., *Design of Experiments*, Springer Berlin Heidelberg, Berlin, Heidelberg, 2013, pp. 13-42.

[2] Croux, C., Dehon, C., "Influence functions of the spearman and kendall correlation measures", Statistical Methods & Applications 19:497-515 (2010).

[3] Darlington, R.B., Hayes, A.F., *Regression analysis and linear models*, New York,NY: Guilford, 2017, pp. 603–611.

[4] Goodwin, D.G., Speth, R.L., Moffat, H.K., Weber, B.W., "Cantera: An Object-oriented Software Toolkit for Chemical Kinetics, Thermodynamics, and Transport Processes" (2021).

[5] Hinton, G., Salakhutdinov, R., "Reducing the dimensionality of data with neural networks", *Science* (New York, N.Y.) **313**:504–507 (2006).

[6] Parente, A., Sutherland, J., Tognotti, L., Smith, P., "Identification of low-dimensional manifolds in turbulent flames", *Proceedings of the Combustion Institute* **32**:1579–1586 (2009).

[7] Sammut, C., Webb, G.I. (eds.), *Mean Absolute Error*, Springer US, Boston, MA, 2010, pp. 652–652.

[8] Saxena, P., Williams, F.A., "Testing a small detailed chemical-kinetic mechanism for the combustion of hydrogen and carbon monoxide", *Combustion and Flame* **145**:316–323 (2006).

[9] Veynante, D., Vervisch, L., "Turbulent combustion modelling", *Progress in Energy and Combustion Science* **28**:193–266 (03 2002).

[10] Wartha, E.M., Bosenhofer, M., Harasek, M., "Characteristic chemical time scales for reactive flow modeling", *Combustion Science and Technology* **193**(16), 2807– 2832 (2021).

[11] Wehmeyer, C., NoéF., "Time-lagged autoencoders: Deep learning of slow collective variables for molecular kinetics", *The Journal of Chemical Physics* **148** (Oct 2017).

[12] Zhang, P., Sankaran, R., "Autoencoder neural network for chemically reacting systems", *Journal of Machine Learning for Modeling and Computing* **3**:1–28 (2022).

Effect of Selection Procedures of High-Fidelity Data in Multi-Fidelity Surrogate Modeling

A. Özden*, A. Procacci*, R. Malpica Galassi*, F. Contino, A. Parente***

aysu.ozden@ulb.be

*Aero-Thermo-Mechanics Lab., Université Libre de Bruxelles, Avenue F. D. Roosevelt, 1050, Brussels, Belgium

** UC Louvain, Institute of Mechanics, Materials, and Civil Engineering, Louvain-la-Neuve, Belgium

Abstract

This study introduces a multi-fidelity digital twin for a combustion furnace that operates under MILD conditions. The digital twin aims to accurately predict the 3-dimensional reacting flow field at different operating conditions while keeping computational costs low. The training data comprises RANS simulations with detailed chemistry that cover the design space, which includes the H2 mole fraction (0-100%), equivalence ratio (0.7-1), and injector diameter (16, 20, and 25 mm). To reduce the costs of the training, lower fidelity 2-dimensional simulations replace some of the 3-dimensional simulations. The multi-fidelity model development strategy involves data compression using Principal Component Analysis, data fusion of the different fidelity inputs using Manifold Alignment, and interpolation of the latent variables with CoKriging. The trained model exhibits predictions that depend on the number of high-fidelity data replaced by lower-fidelity data. Therefore, an incremental sampling strategy is proposed to determine the minimal amount and location in design space of the high-fidelity data to fulfill accuracy requirements within a computational budget. Specific subsets of design conditions are found to be a better fit than others, and promising results are obtained in terms of temperature and species accuracy.

Introduction

Despite the increase in energy-related CO2 emissions due to persistent demand for fossil fuels, the combustion industry is exploring solutions like Moderate and Intense Low-oxygen Dilution (MILD) [1] combustion to meet emission targets. However, designing and understanding these systems require accurate and affordable tools to predict system response across a broad range of operating conditions. Reduced Order Models (ROMs) [2] have emerged as an effective tool, but for complex systems like combustion, a single fidelity ROM may not be practical. To address this, the Multi-fidelity Reduced Order Model (MF-ROM) combines sparse high-fidelity data with dense low-fidelity data to achieve acceptable accuracy within a fixed computational budget. This approach has been applied successfully in various areas over the past decade, such as in modeling an RAE 2822 airfoil [3]. This paper aims to develop a

multi-fidelity surrogate model of a combustion furnace in the MILD combustion regime that can predict its performance with acceptable accuracy using H_2 mole fraction, equivalence ratio, and injector diameter as design parameters. The developed surrogate model shows promising results, and further work is needed to fine-tune the model and improve its accuracy.

Methodology

Principal Component Analysis

The Principal Component Analysis (PCA) is a method of reducing the dimensionality of a dataset $\boldsymbol{X} \in \mathbb{R}^{\boldsymbol{nxp}}$, which contains n observations of p features, assuming that there are a large number of interrelated variables in the dataset [4]. In this study, CFD simulation results are used to construct the datasets. In this dataset, n observations are the number of numerical simulations while p represents the number of the number of grid points times the number of features, such as temperature and select chemical species mass fractions. In combustion problems, p is typically much larger than n. To perform PCA, $\mathbf{Z}$ of size ($n \times k$) and a matrix $\mathbf{\Phi}$ of size ($p \times k$) are computed, where $k \ll p$, by solving for the eigenvectors of the covariance matrix $\boldsymbol{C} = \frac{\mathbf{1}}{\boldsymbol{n}}\boldsymbol{X}^{\boldsymbol{T}}\boldsymbol{X}$. The columns of $\mathbf{\Phi}$ are known as the PCA modes, or eigenflames [5], and the matrix $\mathbf{Z}$ is called the PCA coefficients matrix. The lower dimension k is determined by the Relative Information content (RIC) value [6], which is interpreted as the total variance captured by the PCA. A threshold value of 99.9% or higher is commonly chosen. Since the eigenvectors are orthogonal and the principal components are linear combinations of the original variables, the high-fidelity response ($\mathbf{X}_{\mathbf{rec}}$) of an undiscovered point ($\mathbf{z}_{\mathbf{j}}$) in design space can be calculated as $\boldsymbol{X_{rec}} = \mathbf{\Phi} \boldsymbol{z_j}$.

Manifold Alignment

A multi-fidelity surrogate model combines information from datasets with different dimensions and topology to solve the same physical problem. To transfer information between these datasets, manifold alignment with the assumption of these datasets shares a common low-dimensional subspace is used [7]. Procrustes manifold alignment is a specific method that utilizes PCA to align the low-dimensional representations of these datasets, allowing for optimal alignment between them. This technique has been successfully applied in various fields, such as protein alignment [8] and image matching [9]. In this study, the Procrustes manifold alignment technique is used, which involves using PCA as the first step. Procrustes analysis is employed to remove translational, rotational, and scaling components from one manifold to achieve an optimal alignment with the other [10]. The high-dimensional and low-dimensional datasets are identified as $\boldsymbol{X} \in \mathbb{R}^{\boldsymbol{nxp}}$ and $\boldsymbol{Y} \in \mathbb{R}^{\boldsymbol{mxq}}$, respectively. In this case $n < m$ and the low-fidelity dataset involves a linked subset $\boldsymbol{Y_L} \in \mathbb{R}^{\boldsymbol{nxq}}$, which shares the same input design parameters as the high-fidelity dataset. As the first step of the method, both outputs are subjected to PCA

for dimensionality reduction, and PCA modes $\mathbf{\Phi} \in \mathbb{R}^{pxk}$ and $\mathbf{\Psi} \in \mathbb{R}^{qxk}$, with PCA coefficients $\boldsymbol{Z} \in \mathbb{R}^{nxk}$ and $\boldsymbol{W} \in \mathbb{R}^{mxk}$, are obtained for high- and low-fidelity inputs, respectively. The objective of this transformation is to find the transformed manifold $\mathbf{T}$ that minimizes $\|\mathbf{Z}-\mathbf{T_L}\|$, and this orthogonal Procrustes manifold is solved using the procedure of Wang and Mahadevan [8]. The first step is to ensure that the linked datasets $\mathbf{Z}$ and $\mathbf{W_L}$ both have their centroids at the origin. Then, the scaling factor (s) and rotation matrix ($\mathbf{Q}$) can be obtained by computing the Singular Value Decomposition (SVD) $\boldsymbol{U\Sigma V^T = W_L Z^T}$, where $U \in \mathbb{R}^{kxk}$, $V \in \mathbb{R}^{kxk}$, and $\Sigma \in \mathbb{R}^{kxk}$ are the left and right singular vectors and the diagonal matrix containing the singular values, respectively. Finally, after computing the scaling factor $s = \frac{tr(\Sigma)}{tr(W_L W_L^T)}$ and rotating matrix $Q = VU^T$, the transformed matrix, which is the low-fidelity approximation of $\mathbf{Z}$, can be obtained as $\boldsymbol{T = sQW}$.

Regression Model: CoKriging

The Gaussian Process Regression (GPR) [11] is commonly used as an interpolation model in statistics and machine learning to predict output for undiscovered design points. When combining high- and low-fidelity data, a multi-fidelity regression model like CoKriging is necessary [12]. The CoKriging regression model used in this study follows the auto-regressive model of Kennedy and O'Hagan [12], which assumes that low-fidelity data cannot provide any additional insights if a high-fidelity counterpart is available [13]. The process of generating a CoKriging model involves constructing two Kriging models in sequence. First, a Kriging model based on low-fidelity data is constructed. Then, a second Kriging model is created to capture the discrepancies between the high-fidelity and low-fidelity data, expressed as $\hat{Y}_H = \rho Y_L + \delta$, where $\hat{Y}_H$ represents the high-fidelity approximation, ρ is a constant scaling factor, and δ is the difference between the high- and low-fidelity models.

Dataset

This study uses 3D and 2D computational fluid dynamics (CFD) simulations of a semi-industrial MILD combustion furnace with a nominal power of 20 kW. The simulations are conducted using ANSYS Fluent 19.1 software [14]. The standard k-ε turbulence model is used in combination with the PaSR [15] model for turbulence-chemistry interactions, and the kinetic scheme employed is the Kee mechanism with 17 species and 58 reactions. Radiation is modeled using the discrete ordinate (DO) method with the weighted-sum-of-gray-gases (WSGG) model. The high- and low-fidelity simulations have grid sizes of 216360 and 28683, respectively. The fuel composition, equivalence ratio, and injector diameter collectively define the design space with the ranges of 0-100% for H2 mole fraction, 0.7-1 for equivalence ratio (φ), and 16-20-25mm for the air injector diameter. The design of experiments (DoE) is generated using latin hypercube sampling (LHS) method, as previously performed by Aversano et al. [16], with a total of 45 simulations performed and 4 test cases

excluded for testing purposes. The simulations are used to train the regression model, with the features of interest being temperature and major (CH_4, H_2, O_2, H_2O, OH) /minor species (CO and OH). The design parameters for the test simulations are listed in Table 1.

Table 1. Design conditions for test cases from Aversano et al. [16]

Simulation No	Air Inj. Dia. (mm)	H_2 (%)	ER (-)
1	16	60	0.93
2	20	50	0.83
3	20	90	0.74
4	25	65	0.91

The crucial decision is to determine the selection and quantity of simulations for constructing the high-fidelity dataset. For an initial comparison, 10 high-fidelity simulations are utilized, chosen based on the leave-one-out analysis conducted by Aversano et al. [22]. As previously stated, the low-fidelity dataset is separated into 10 connected data points with identical design parameters to the 10 high-fidelity solutions, which are required for the manifold alignment process, as well as 31 additional unconnected data points.

Results

The Normalized Root Mean Square Error (NRMSE) is a frequently used metric for assessing the accuracy of predictions compared to the results of CFD simulations for the test cases. NRMSE is calculated by dividing the Root Mean Square Error (RMSE) by the mean of the observations:

$$NRMSE = \frac{1}{\overline{X_{obs}}}\sqrt{\frac{\sum_{i=1}^{N}\left(X_{obs,i}-X_{pred,i}\right)^2}{n}} \quad (1)$$

Figure 1 displays a comparison of the temperature and OH fields, respectively, for test simulation #4 between the CFD and multi-fidelity ROM. The temperature field prediction demonstrates that the MF-ROM can accurately predict the temperature distribution, closely resembling the original data. In terms of the OH field, although there is room for improvement of low-fidelity, the overall species distribution appears satisfactory.

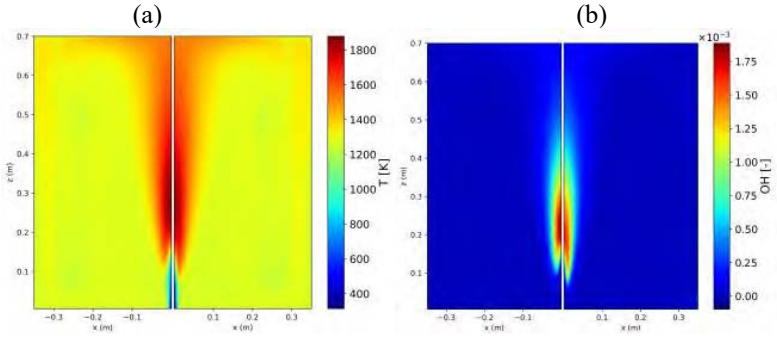

Figure 1. Temperature (a) and OH (b) field comparison between the CFD simulation *(left)*, and the multi-fidelity ROM prediction *(right)*, case #4.

The current study has highlighted the sensitivity of the prediction accuracy to the number and distribution of high-fidelity simulations in the design space. To understand the selection of simulations, an incremental sampling decision-making strategy was developed, which involves adding high-fidelity samples where the trained model exhibits the largest uncertainty. The effect of additional samples is evaluated using 10-fold cross-validation on the train/test data split, and the results are presented in Figure 2, showing that error metrics decrease almost monotonically with increasing high-fidelity samples, confirming that the incremental sampling strategy is well-posed. A saturation point is also observed after the addition of ~20 high-fidelity samples. Additionally, when certain cases are selected as test cases, NRMSE values can be amplified by up to 200%, suggesting that these cases should be included in the training dataset.

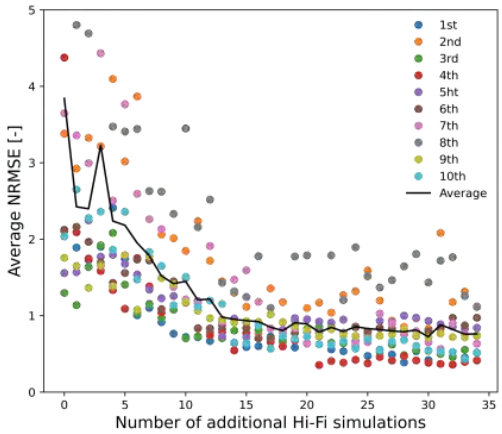

Figure 2. Impact of additional high-fidelity samples for 10-fold cross validation

Conclusion

This study aimed to develop a multi-fidelity surrogate model for predicting the three-dimensional spatial fields of a MILD combustion furnace based on the design parameters of air injector diameter, H_2 mole fraction, and equivalence ratio. The approach exploits Principal Component Analysis, Procrustes Manifold Alignment, and CoKriging to project data in a shared latent space and interpolate the latent variables over the whole design space. 45 high-fidelity and low-fidelity simulations are used to build the model. A model trained with 10 high-fidelity and 41 low-fidelity simulations exhibited prediction errors below 10% for temperature and H_2O, but errors were higher for other species, especially CH_4, H_2, OH, and CO. However, temperature and OH reconstructed fields showed good qualitative agreement with the CFD counterpart. Incremental sampling was found to be crucial in determining the optimal number of simulations and design locations in the DoE of high-fidelity simulations to meet the accuracy requirement for a given computational budget. An uncertainty-based selection method indicated that specific subsets of design conditions are a better fit than others for the high-fidelity dataset to improve prediction accuracy. Promising results were obtained for the determination of an optimal number of simulations, but further investigation is needed to fine-tune CoKriging hyper-parameters and formalize the results of the sampling strategy.

References

[1] Cavaliere, A., De Joannon, M., "Mild combustion", *Progress in Energy and Combustion Science,* 30 (4):329-366 (2004)

[2] Lucia, D.J., Beran, P.S., Silva, W.A., "Reduced order modeling: new approaches for computational physics", *Progress in Aerospace Sciences*, 40 (1-2):51-117 (2004)

[3] Han, Z.H., Zimmermann, Görtz, S., "Alternative cokriging method for variable-fidelity surrogate modeling", *AIAA journal*, 50 (5):1205:1210 (2012)

[4] Jolliffe, T.J., *Principal component analysis for special types of data*, Springer, 2002.

[5] Aversano, G., Bellemans, A., Li, Z., Coussement, A., Gicquel, O, Parente, A., "Application of reduced-order models based on pca & kriging for the development of digital twins of reacting flow applications", *Computers & chemical engineering* 121:422-441 (2019).

[6] Pinnau, R., *Model order reduction: theory, research aspects and applications*, Springer, 2008, pp. 95–109.

[7] Wang, C., Mahadevan, S., "A general framework for manifold alignment", *2009 AAAI Fall Symposium Series* (2009)

[8] Wang, C., Mahadevan, S., "Manifold alignment using procrustes analysis" *Proceedings of the 25th international conference on Machine learning*, pp. 1120-1127 (2008)

[9] Ham, J., Lee, D., Saul, L., "Semisupervised alignment of manifolds" *International Workshop on Artificial Intelligence and Statistics*, pp. 120-127. (2005)

[10] Luo, B., Hancock, E.R., "Feature matching with Procrustes alignment and graph editing", pp. 72-76, (1999)

[11] Williams CK, Rasmussen CE., "Gaussian processes for machine learning", *MA: MIT press Cambridge*, vol:2 (2006)

[12] Kennedy, M.C., O'Hagan, A., "Predicting the output from a complex computer code when fast approximations are available", *Biometrika*, 87(1):1-13 (2000)

[13] Forrester, A.I., Sóbester, A., Keane, A.J., "Multi-fidelity optimization via surrogate modelling", *Proceedings of the Royal Society A: Mathematical, Physical and Engineering Sciences*, 463(2088): 3251-3269 (2007)

[14] M. Ferrarotti, M. FÅNurst, E. Cresci, W. De Paepe, and A. Parente, "Key modeling aspects in the simulation of a quasi-industrial 20 kw moderate or intense low-oxygen dilution combustion chamber", *Energy & fuels*, 32(10): 10228-10241 (2018)

[15] Chomiak, J., "Combustion a study in theory, fact and application", (1990)

[16] Aversano, G., Ferrarotti, M., Parente, A., "Digital twin of a combustion furnace operating in flameless conditions: reduced-order model development from CFD simulations", *Proceedings of the Combustion Institute*, *38*(4):5373-5381 (2021)

Self-learning Digital Twin of a combustion furnace through the Kalman Filter method

L. Donato[1,2,3], A. Procacci[1,2], C. Galletti[3], A. Coussement[1,2] and A. Parente[1,2]
laura.donato@ulb.be
[1]Aero-Thermo-Mechanics Lab., Université Libre de Bruxelles, Avenue F. D. Roosevelt, 1050, Brussels, Belgium
[2]BRITE - Brussels Institute for Thermal-fluid systems and clean Energy, Brussels, Belgium
[3]Department of Civil and Industrial Engineering, University of Pisa, Largo L. Lazzarino 2, 56122, Pisa, Italy

Abstract
This study aims to develop a self-learning Digital Twin (DT) model using a data assimilation approach, i.e., the Kalman Filter, which can adjust a numerical model with the sparse sensing (SpS) model. The numerical model, i.e., the DT, is obtained by coupling a dimensionality-reduction method, the Proper Orthogonal Decomposition (POD), and the Gaussian Process Regression (GPR) model for several Reynolds-averaged Navier-Stokes (RANS) simulations of a semi-industrial combustion furnace. The SpS technique leverages dimensionality reduction to predict the state of the system using experimental measurements as input. Finally, the DA framework has been used to provide a solution with lower uncertainty bounds. The results show that this framework can be used to upgrade the DT by considering a SpS model built from experimental values.

Introduction
Meeting society's energy needs is challenging due to intermittent renewable sources and the requirement for long-term storage and high-density energy for transportation and manufacturing. One solution is storing excess renewable energy as synthetic fuels, integrated with combustion systems. Novel combustion technologies such as Moderate and Intense Low-oxygen Dilution (MILD) combustion offer high efficiency and fuel flexibility with low emissions [1]. While CFD tools have advanced significantly, the use of physics-based reduced-order models (ROMs) is becoming increasingly attractive for real-time simulations. These models can simplify the relationship between inputs and outputs, allowing for faster simulations of complex combustion regimes like MILD combustion. Additionally, the development of digital twins (DTs), for industrial systems presents numerous opportunities, including using data to anticipate system response and using simulations to develop new technologies through virtual prototyping [2]. Accurately assessing the reliability of numerical models is a crucial and challenging task, given a lot of uncertainties that are not yet fully understood or quantified. To improve design models, a blend of experimental data and numerical models is necessary. Data

assimilation (DA) offers this type of solution by combining both experimental and numerical models to enhance accuracy in numerical forecasts and minimize errors related to both sources [3]. This work introduces a novel framework for DA that efficiently integrates experimental data with a digital twin (DT) developed for a combustion furnace. The proposed DA scheme combines results collected from experiments with DT predictions to enhance the DT's accuracy. This goal is achieved by developing the DT as a ROM using Gaussian Process Regression (GPR) and Proper Orthogonal Decomposition (POD) and comparing it to the results obtained using a Sparse Sensing (SpS) method. This GPR-based ROM methodology, demonstrated by Aversano et al. [4] to develop ROMs of turbulent reacting flow applications, was applied to build the DT of a MILD combustion furnace. The SpS method [5] is used to construct a hybrid experimental-numerical DT for MILD combustion by coupling POD modes, recovered from numerical simulations, with experimental measurements [6].

Numerical and Experimental set-up

The test case used for this study is the ULB semi-industrial combustion furnace, with a nominal power of 20 kW. The furnace is composed of a cubic combustion chamber insulated with a thick high-temperature ceramic foam layer. The furnace incorporates a burner with a heat exchanger to recover heat from the exhaust gases and preheat the combustion air. Fuel injection occurs through a central nozzle, surrounded by a coaxial air jet. The unit is equipped with four air cooling tubes located inside the furnace. An opening is available for measurements on each vertical wall of the chamber. Fig. 1 reports the schematic representation of the furnace. In-flame temperature profiles are sampled at different axial and radial locations of the furnace, with a suction pyrometer equipped with N-type thermocouples. Electrochemical sensors with nominal accuracy for different species are used to measure the exhaust gas composition. All the experiments are performed at steady-state operating conditions. More details can be found in [7].

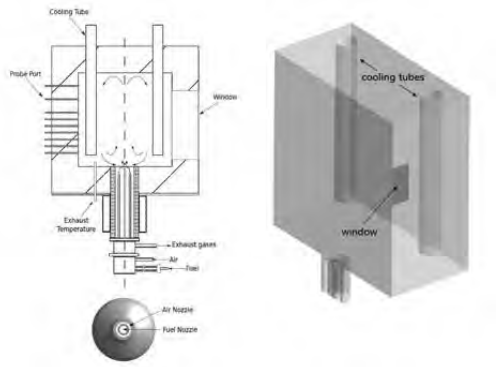

Figure 1. Vertical cross-section (top left), burner nozzle (bottom left), and 3D half geometric representation (right) of the ULB MILD combustion furnace.

41 RANS simulations were generated to obtain the necessary samples for developing

the ROM of the furnace. Three input parameters were considered to produce the simulation samples: the content of hydrogen, 0-100%, the equivalence ratio ($\emptyset = 0.7 - 1$) and air nozzle diameter (ID = 16, 20 and 25 mm). Regarding the setup of the numerical simulations, we consider the standard $k - \varepsilon$ turbulence model with the Partially Stirred Reactor (PaSR) model for the turbulence-chemistry interactions with a C_{mix} of 0.5 and the KEE (17 species and 58 reactions) for the kinetic mechanism. The computational domain is a 45° angular sector of the 3D geometry of the chamber, given the symmetry of its domain. The selected grid contains about 200k cells. More detailed information on the simulation can be found in [4, 7].

Methodology

The goal of the ROM is to predict the complete thermo-chemical state of the furnace at unexplored operating conditions. This outcome can be accomplished by combining dimensionality reduction through POD with regression conducted via GPR. The POD (also known as Principal Component Analysis [8]) is a data compression method where the data matrix $\boldsymbol{X} \subset \mathbb{R}^{n,p}$ is decomposed into:

$$\boldsymbol{X} = \boldsymbol{U}\boldsymbol{A}^T$$

with $\boldsymbol{U} \subset \mathbb{R}^{n,p}$ and $\boldsymbol{A} \subset \mathbb{R}^{p,p}$, which are orthogonal matrices that constitute a basis for the columns and rows of $\boldsymbol{X}$, respectively. POD is used to reduce dimensionality since the truncation of the new basis to the q-order minimizes the reconstruction error in the l_2 norm. This implies that the matrix $\boldsymbol{X}$ can be approximately estimated as:

$$\boldsymbol{X} \approx \boldsymbol{U}_q \boldsymbol{A}_q^T$$

where $\boldsymbol{U}_q \subset \mathbb{R}^{n,p}$ and $\boldsymbol{A}_q \subset \mathbb{R}^{p,p}$ are the q-order truncation of $\boldsymbol{U}$ and $\boldsymbol{A}$. The matrix $\boldsymbol{X}$ is constructed by gathering the outcomes of the numerical simulations, by varying the three parameters explained in the previous section: each column of $\boldsymbol{X}$ contains the results of a simulation, and the number of rows is the number of computational cells times the number of variables. The variables considered are the temperature inside the furnace and the species mass fraction. To predict the solution in the unexplored region of the design space, a GPR model is employed. This regression problem is expressed as $y = f(x) + \varepsilon$, where y is the observed value, f(x) is the underlying function we are modeling (a sample from a Gaussian Process (GP)), x is the independent variable and is the noise ε formulated as an independent, identically distributed (i.i.d.) random variable. More details about GPR method can be found in [9]. After training the model, the ROM can map each simulation made of a specific set of parameters to the low-dimensional representation a_{GPR}. The solution is produced by projecting a_{GPR} in the original higher dimensional space:

$$x_{GPR} = \boldsymbol{U}_q \, a_{q,GPR}$$

Regarding the experimental point of view, the SpS model is a powerful framework that leverages the concept of sparsity to efficiently capture and reconstruct signals or data. By exploiting the inherent sparsity in a signal, which refers to the fact that only

a small number of elements contribute significantly to its representation, sparse sensing techniques enable the reconstruction of high-quality signals using a reduced number of measurements. The mathematical formulation of SpS is described in detail in [6]. To summarize, the goal of SpS is to solve this linear system $\mathrm{y} = \mathbf{C}\mathrm{x}$, with $y \subset R^s$ contains the measured values, $\boldsymbol{C} \subset R^{s,n}$ represents the measurement matrix and $x \subset R^n$ is the state of the system. Assuming a sparse representation of the system in a different basis, we can approximate the variable $x \approx \boldsymbol{\Phi}_q a_q$, where $\boldsymbol{\Phi}_q \subset R^{n,q}$ represents the q-order truncation of the transforming basis, and a_q is the projection of x onto this truncated basis. The transforming basis is determined by applying the Proper Orthogonal Decomposition (POD) to the dataset. Consequently, we can rephrase the original linear system as:

$$y = \boldsymbol{\Theta} a_{q,SpS}$$

with $\boldsymbol{\Theta} = \boldsymbol{C}\boldsymbol{U}_q$, where $\boldsymbol{U}_q$ is computed through Singular Value Decomposition (SVD) applied to the data matrix.

Data Assimilation

Data assimilation aims to merge observations with model predictions in a way that optimally integrates the available information by considering the uncertainties in both the model and the observations. By doing so, DA methods can provide improved estimates of the current state of a system and even make better predictions about its future behaviour. The assimilation between the GPR model and the SpS model is done by applying the Kalman filter [10]. The Kalman filter can produce the optimal estimate of the system's true state given the model's prediction and the experimental observations.

$$a_{q,adj} = a_{q,GPR} + \boldsymbol{K}\left(a_{q,SpS} - a_{q,GPR}\right)$$
$$\boldsymbol{C}_{adj} = \boldsymbol{C}_{GPR} - \boldsymbol{K}\boldsymbol{C}_{GPR}$$
$$\boldsymbol{K} = \frac{\boldsymbol{C}_{GPR}}{\boldsymbol{C}_{GPR} + \boldsymbol{C}_{SpS}}$$

where $a_{q,adj}$ is a linear combination through the so-called Kalman gain, **K**, between $a_{q,GPR}$ and $a_{q,SpS}$, which represent low-dimensional representation of the GPR and the SpS model respectively. In addition, $\boldsymbol{C}_{GPR}$ and $\boldsymbol{C}_{SpS}$ are diagonal matrices containing the GPR and SpS model uncertainty, respectively.

Results

As mentioned before, the DT model has been applied to the matrix containing 41 simulations obtained with different combinations of the three parameters: $\emptyset, ID_{air}, \%H_2$. The feature included in the data matrix is the temperature field inside the furnace. Fig. 2a shows the temperature given by CFD simulation and the one predicted by the DT for the case: $\emptyset = 0.93, ID_{air} = 16mm\,, \%H_2 = 60$.

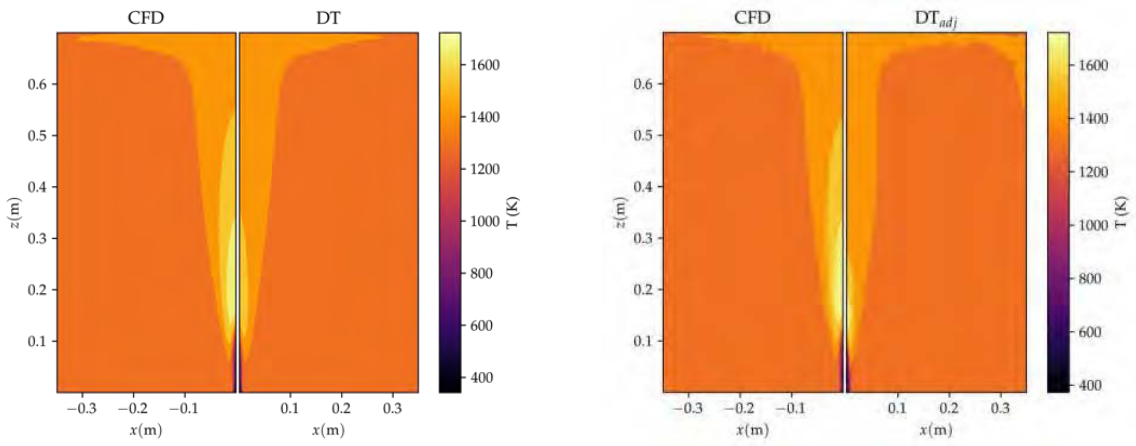

Figure 2. a) Comparison between the original temperature field (on the left) and the temperature field predicted by the GPR ROM (on the right); b) Comparison between the original temperature field (on the left) and the temperature field predicted by the GPR ROM (on the right), after data assimilation.

By assimilating the GPR-POD solution with the one derived from SpS, an adjusted solution can be obtained through the KF algorithm. The adjusted solution is therefore visualized in Fig. 2b. Through assimilation, the model's uncertainty is reduced by comparing the uncertainties associated with the GPR and SpS models. This expression can be illustrated in Fig. 3 for several radial profiles of temperature at different axial positions. The GPR model's prediction is characterized by a significantly higher uncertainty level than the SpS model. Consequently, the adjusted solution experiences a minor reduction in uncertainty.

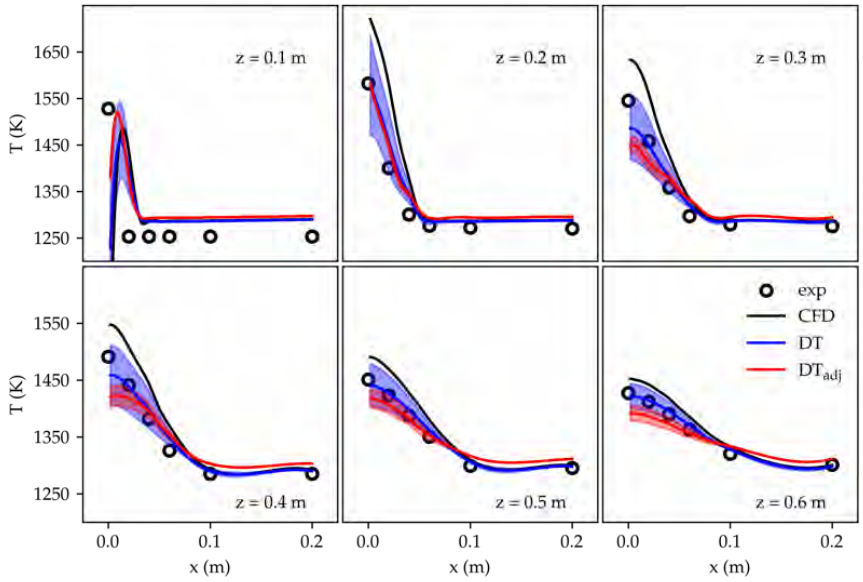

Figure 3. Several radial profiles of measured temperature along with the adjusted value obtained by assimilating the GPR and SpS models.

Conclusions

The aim of this study is to create a DA framework that combines a DT, which is a ROM obtained by coupling GPR and POD, with SpS to obtain an improved DT, with lower uncertainty. To achieve this, a dataset consisting of 41 RANS simulations of a semi-industrial combustion furnace has been used as the training data, each simulation performed with different combinations of a set of three parameters ($\emptyset, \boldsymbol{ID_{air}}, \%\boldsymbol{H_2}$). First, POD has been applied to the dataset, and the GPR method has been trained on the set of POD coefficients, enabling the construction of a model capable of predicting the POD coefficients for unexplored combinations of the parameters. Then, to include experimental information, a SpS model has been constructed. This approach is aimed at finding the set of POD coefficients that minimizes the l_2 distance with the experimental measurements. Finally, DA is employed to blend the DT model with the SpS one to have an adjusted DT with lower uncertainty than both the initial sources.

References

[1] Cavaliere A., De Joannon M. Mild combustion. Progress in Energy and Combustion science. (2004).
[2] E. Glaessgen, D. Stargel, The Digital Twin Paradigm for Future NASA and U.S. Air Force Vehicles.
[3] M. Asch, M. Bocquet, M. Nodet, Data Assimilation: Methods, Algorithms, and Applications. (2016)
[4] Aversano G, Ferrarotti M, Parente A. Digital twin of a combustion furnace operating in flameless conditions: reduced-order model development from cfd simulations. Proceedings of the Combustion Institute (2021)
[5] Manohar K, Brunton BW, Kutz JN, et al. Data-driven sparse sensor placement for reconstruction: Demonstrating the benefits of exploiting known patterns. IEEE Control Systems Magazine (2018)
[6] Procacci A, Amaduzzi R, Coussement A, et al. Adaptive digital twins of combustion systems using sparse sensing strategies. Proceedings of the Combustion Institute (2022)
[7] M. Ferrarotti, M. F¨urst, E. Cresci, W. de Paepe, A. Parente, Key modeling aspects in the simulation of a quasi-industrial 20 kw moderate or intense low-oxygen dilution combustion chamber, Energy & Fuels. (2018)
[8] Parente A, Sutherland JC. Principal component analysis of turbulent combustion data: Data pre-processing and manifold sensitivity. Combustion and Flame 160(2):340–350. (2013)
[9] Rasmussen CE, Williams CKI. Gaussian Processes for Machine Learning (Adaptive Computation and Machine Learning). The MIT Press. (2005)
[10] Kalman RE. A New Approach to Linear Filtering and Prediction Problems. Journal of Basic Engineering. (1960).


THE COMBUSTION INSTITUTE
1954

SESSION VIII

POLLUTANTS FORMATION, MONITORING AND CONTROL INCLUDING NANOMATERIALS AND LARGE MOLECULES


THE COMBUSTION INSTITUTE
1954

SOOTING TENDENCY OF OIL EXTRACTED FROM SPENT COFFEE GROUNDS

V. Esposito*, Rosa Colucci Cante, Alessandro Nigro***, Isidoro Garella***, Stefano Cimino****, Christophe Allouis****, M.M. Oliano****, B. Apicella****, C. Russo****, R. Nigro*, M. Sirignano***

vincenzo.esposito9@unina.it

* Università di Napoli Federico II, Piazzale Tecchio 80, 80125 Napoli, Italy

**UNICUSANO Via Don Carlo Gnocchi, 3, 00166 Roma RM

***ITP Srl, Viale dei Campi Flegrei 34,80078 Pozzuoli, Italy

****STEMS – CNR, Piazzale Tecchio 80, 80125 Napoli – Italy

Abstract

The control and reduction of particulate matter from fossil fuel combustion pose significant challenges for combustion devices due to increasingly strict emission regulations. Alternative fuels have been explored as potential substitutes or additives for diesel and gasoline. Spent coffee grounds (SCG), a notable waste product of the coffee industry, contain approximately 15 wt% coffee oil. This study focuses on the impact of coffee oil on carbon particulate formation in burner-stabilized premixed flames with different equivalence ratios when blended with ethylene. Laser-Induced Fluorescence (LIF) and Incandescence (LII) techniques were employed to examine particle formation and growth in flames of pure ethylene and ethylene/coffee oil blends. The results reveal a decrease in the total number and size of soot particles, as indicated by the soot volume fraction, across all equivalence ratios. However, the number of small nanoparticles remains relatively unchanged.

Introduction

Biodiesel, a ecofriendly and portable liquid fuel, has gained attention as a viable alternative to fossil fuels [1]. However, its higher cost compared to traditional fuels limits its applications [2, 3]. The primary production cost of biodiesel lies in its feedstock [4[. Currently, the biodiesel industry faces the challenge of acquiring affordable and high-quality feedstock [5]. To address this, industries are utilizing waste vegetable oil, grease, and animal fats, particularly from poultry, to produce cost-effective biodiesel [5, 6]. Additionally, researchers are actively developing high-oil-content crops exclusively for biodiesel production [7-10].

Coffee, a major agricultural product primarily used for beverages, has a global production of 16.34 billion pounds per year [11] and it is now the second largest traded commodity worldwide, following petroleum. As a result, the coffee industry generates substantial waste. Approximately 50% of globally produced coffee is processed for soluble coffee preparation, resulting in solid residues known as spent coffee grounds (SCG). On average, the production of one ton of green coffee yields around 650 kg of SCG. Oil can be extracted from spent coffee grounds. The oil content in coffee varies between 11 and 20 wt % depending on the type [12, 13]. Spent coffee grounds, on average, contain around 15% oil, which can be converted into an equivalent amount of biodiesel through transesterification methods. This is significant compared to other biodiesel feedstocks like rapeseed oil (37-50%), palm oil (20%), and soybean oil (20%) [14]. It could contribute approximately 340 million gallons of biodiesel to the global fuel supply. Biodiesel derived from coffee exhibits improved stability

due to its high antioxidant content, which inhibits the rancimat process [15, 16]. The remaining solid waste can be utilized as compost or as a feedstock for ethanol production [17], as well as fuel pellets.
In this work we tested the sooting tendency of oil extracted from spent coffee grounds in a lab scale combustion system by means of optical measurements

Methods

The experimental setup proposed in this work has been used to study other alternative fuels such as butanols [18], furans [19], ethanol [20], dimethyl ether [21], and most recently OMEn [22]. Details of the experimental setup can be found in previous papers and are reported briefly here. Atmospheric pressure, premixed ethylene/air flames with equivalence ratios, φ, equal to 2.01, 2.16, 2.31, and 2.46, which represent lightly to heavily sooting conditions, are stabilized on a capillary burner [22]. These flames are the reference cases for studying the effect of coffee oil blending on soot particle formation and growth. Coffee oil, extracted by an innovative subcritical fluid technique [23], was added by replacing some of the ethylene (20 % of the total carbon) fed to the reference ethylene/air flames. The combustion conditions investigated in this work are reported in Table 1.
Laser-Induced Emission (LIE) measurements in the 200 nm to 550 nm range are applied to detect particles in the flame, using the fourth harmonic of an Nd:YAG laser at 266 nm as the excitation source. The emitted spectra are collected with an ICCD camera with a gate of 100 ns, allowing to distinguish between the broad Laser-Induced Fluorescence (LIF) signal, ranging between 300 nm and 400 nm, and the Laser-Induced Incandescence (LII) following a blackbody curve and evaluated at 550 nm

Table 1. Fuel composition in terms of carbon provided by each fuel.

φ	Species	100 % C2H4	20 % OIL + 80 % C2H4
2.01	C2H4	0.1234	0.0987
	O2	0.1841	0.178
	N2	0.6925	0.711
	OIL	0	0.0123
2.16	C2H4	0.1313	0.1051
	O2	0.1824	0.1763
	N2	0.6862	0.7055
	OIL	0	0.0131
2.31	C2H4	0.1392	0.1114
	O2	0.1808	0.1747
	N2	0.68	0.7
	OIL	0	0.0139
2.46	C2H4	0.1469	0.1175
	O2	0.1792	0.1732
	N2	0.6739	0.6949

OIL	0	0.0147

Results and Discussion

Nanoparticles and soot particles have been measured for the investigated equivalence ratios and different coffee oil-blended mixtures. As done in previous works, here LIF signal is associated with aromatic hydrocarbons in the condensed-phase, i.e., nanoparticles [22], whereas the LII signal arises from the larger, solid soot particles and aggregates. Coffee oil reduces the formation of large soot aggregates significantly, while the formation of smaller nanoparticles is less affected. LII measurements show the onset of soot formation at an equivalence ratio of $\phi = 2.16$ for oil/C2H4mixture, while no soot is measured for $\phi = 2.01$.
The effects of coffee oil shown so far have been similarly observed in ethylene flames doped with other oxygenated compounds such as ethanol [20], dimethyl ether [21], butanols [18] and furans [19]. This suggests, as for the other fuels, that the particle reduction must mainly be attributed to the modification of gas-phase precursors when coffee oil is added.

Conclusions

In this study, the effects of coffee oil addition on soot particle formation in burner-stabilized premixed ethylene flames have been investigated with optical techniques. 20% of the total carbon was replaced with coffee oil for four equivalence ratios – 2.01, 2.16, 2.31 and 2.46 – while the cold gas velocity was kept constant. The experiments indicate that there is a reduction in the total number and the size of soot particles in the coffee oil-blended flame. An almost negligible effect was observed on the small condensed-phase nanostructures tracked by the LIF signal.

References

[1] Marchetti, J. M.; Miguel, V. U.; Errazu, A. F. Renewable Sustainable Energy ReV. 2007, 11, 1300–1311.
[2] Balat, M. Energy Sources, Part A 2007, 29, 895–913.
[3] Beer, T.; Grant, T.; Williams, D.; Watson, H. Atmos. EnViron. 2002, 36, 753–763.
[4] Nelson, R. G.; Hower, S. A. Bioenergy'94, Proceedings of the Sixth National Bioenergy Conference, Reno/Sparks, NV, 1994.
[5] Nebel, B. A.; Mittelbach, M. Eur. J. Lipid Sci. Technol. 2006, 108, 398–403.
[6] Lebedevas, S.; Vaicekauskas, A.; Lebedeva, G.; Makareviciene, V.; Janulis, P.; Kazancev, K. Energy Fuels 2006, 20, 2274–2280.
[7] Encinar, J. M.; Gonzalez, J. F.; Rodriguez, J. J.; Tejedor, A. Energy Fuels 2002, 16, 443–450.
[8] Cardone, M.; Mazzoncini, M.; Menini, S.; Rocco, V.; Senatore, A.; Seggiani, M.; Vitolo, S. Biomass Bioenergy 2003, 25, 623– 636.

[9] Azam, M. M.; Waris, A.; Nahar, N. M. Biomass Bioenergy 2005, 29, 293–302. (10) Gressel, J. Plant Sci. 2008, 174, 246–263.
[11] Pumphrey, D. Tropical product: World market and trade. U.S. Department of Agriculture, December 2007; Accessed March 6, 2008; http://www.fas.usda.gov/htp/tropical/2006/12-06/ tropical1206.pdf.
[12] Daglia, M.; Racchi, M.; Papetti, A.; Lanni, C.; Govoni, S.; Gazzani, G. J. Agric. Food Chem. 2004, 52, 1700–1704.
[13] Barkenbus, C.; Zimmerman, A. J. J. Am. Chem. Soc. 1927, 49, 2061–2064.
[14] Gui, M. M.; Lee, K. T.; Bhatia, S. Energy 2008, 33, 1646–1653.
[15] Yanagimoto, K.; Ochi, H.; Lee, K. G.; Shibamoto, T. J. Agric. Food Chem. 2004, 52, 592–596.
[16] Campo, P.; Zhao, Y.; Suidan, M. T.; Venosa, A. D.; Sorial, G. A. Chemosphere 2007, 68, 2054–2062.
[17] Sendzikiene, E.; Makareviciene, V.; Janulis, P.; Kitrys, S. Eur. J. Lipid Sci. Technol. 2004, 106, 831–836.
[18] Russo, C., D'Anna, A., Ciajolo, A., & Sirignano, M. 2019). The effect of butanol isomers on the formation of carbon particulate matter in fuel-rich premixed ethylene flames. Combustion and Flame, 199, 122-130.
[19] Conturso, M., Sirignano, M., & D'Anna, A. (2017). Effect of 2, 5-dimethylfuran doping on particle size distributions measured in premixed ethylene/air flames. Proceedings of the Combustion Institute, 36(1), 985-992.
[20] Salamanca, M., Sirignano, M., Commodo, M., Minutolo, P., & D'anna, A. (2012). The effect of ethanol on the particle size distributions in ethylene premixed flames. Experimental Thermal and Fluid Science, 43, 71-75.
[21] Sirignano, M., Salamanca, M., & D'Anna, A. (2014). The role of dimethyl ether as substituent to ethylene on particulate formation in premixed and counter-flow diffusion flames. Fuel, 126, 256-262.
[22] Schmitz, R., Russo, C., Ferraro, F., Apicella, B., Hasse, C., & Sirignano, M. (2022). Effect of oxymethylene ether-2-3-4 (OME2-4) on soot particle formation and chemical features. Fuel, 324, 124617.
[23] R. Colucci Cante, C. Allouis, S. Cimino, F. Stanzione, I. Garella & R. Nigro. Feasibility as liquid fuel of lipid fractions from spent coffee for spray combustion. MCS11, Tenerife, Spain, 16-20 June 2019.

FLAME SYNTHESIS AND CHARACTERIZATION OF SELF-ASSEMBLED NANOSTRUCTURED FILMS OF TIO_2-CARBON NANOPARTICLES

G. De Falco*, M. Commodo, P. Minutolo**, A. D'Anna***
gianluigi.defalco@unina.it
*Dipartimento di Ingegneria Chimica, dei Materiali e della Produzione Industriale, Università degli Studi di Napoli "Federico II", Napoli, Italy
**Istituto di Scienze e Tecnologie per l'Energia e la Mobilità Sostenibili, STEMS-CNR, Napoli, Italy

Abstract
In this work, nanostructured films of flame-formed carbon (CNPs) and TiO_2 (TNPs) nanoparticles are produced through a simple procedure based on the flame synthesis of nanoparticles and their deposition by thermophoresis into films. A two-step procedure is used to produce composite TNP-CNP films. First, carbonaceous granular film is produced by thermophoresis-driven self-assembling of CNPs with diameters of about 20 nm. The flame reactor used for the synthesis of CNPs is a laminar premixed flame of ethylene and air operated in fuel-rich conditions. Then, the composite film is produced by the subsequent thermophoretic deposition of anatase TNPs with a mean diameter of 3.5 nm produced in a flame-synthesis system. The electronic properties of TNP-CNP films are characterized by measuring the electronic band gap using the scanning tunneling spectroscopy (STS) technique and comparing these results to UV-vis absorption optical band gaps. Composite of TNPs with CNPs resulted in a decrease of measured band gap of the film (both optical and electronic) and so in an improvement of the electrical conductivity with respect to pure TNPs films. The STS measurements allow also to quantify the band edge energy distribution of the nanomaterials from the distribution of the positions of conduction band and valence band edges.

Introduction
Nowadays, it is widely accepted that climate change and air pollution derived from massive consumption of fossil fuel are increasingly affecting our energy-demanding society [1]. Development of electric energy and electrification of fossil fuel-dependent transportation have been regarded as efficient strategies to face these serious problems. Thus, there is the need of efficient energy storage systems (EES), due to their important role to balance electric energy supply and demand. Various rechargeable ion batteries, especially lithium-ion batteries (LIBs) and sodium-ion batteries (SIBs), are the best candidates for these devices thanks to the high specific energy and energy density.
TiO_2 has been regarded as one of the most important inorganic compounds in present

world due to its unique physical and chemical properties. Particularly, it attracts attention as a promising alternative material for rechargeable ion battery electrodes [2]. Due to excellent operation safety and good reversible capacity, TiO_2 exhibits more advantages than other materials for large-scale EES applications. Among the different crystalline phases of TiO_2, anatase presents huge potential and it has been widely applied as electrode material in energy storage devices including LIBs, SIBs and other rechargeable ion batteries, thanks to its ability to accommodate Li ions through an electrochemical process. Although anatase TiO_2 has exhibited great applicable potential in both LIBs and SIBs, it still has some shortcomings that need to be overcome, such as the slow ion diffusion and the low electric conductivity. To enhance the electrochemical performance of anatase TiO_2 anodes two main strategies can be adopted. The first one is decreasing the material size to the nanoscale, which can effectively reduce the diffusion pathways of charge carriers. Moreover, the reduction of size can also result in an increase in the surface area of the electrode material, leading to improved interfacial lithium storage performance. The second strategy is compositing anatase TiO_2 with other high-conductivity materials to improve the electric conductivity and the structural stability of the entire electrode. Carbonaceous materials are one of the most used materials to produce composites with anatase TiO_2.

Compared to other methodologies, flame aerosol synthesis provides a direct and continuous one-step process, with a high production rate, fast processing time, high scalability, simple manufacturing and collection with few wastes, and by-product generation. In addition, flame aerosol synthesis offers the possibility to obtain nanostructured films and coatings by placing a substrate downstream of the flame synthesis burner, on which nanoparticles are then deposited by thermophoresis [3].

Considering the above, the present work's purpose is the production of nanocomposite films of flame-synthesized anatase TiO_2 nanoparticles and graphitic-like carbon nanoparticles and the application of the Scanning Tunneling Spectroscopy technique for the first time to investigate the electronic properties of such nanostructured films.

Experimental

The composite films were obtained by a two-step process consisting in producing a porous nanostructured carbon film through the thermophoretic deposition of carbon nanoparticles (CNPs) on selected substrates and then by the subsequent thermophoretic deposition of smaller TiO_2 nanoparticles (TNPs) on the surface of the carbon film. The flame reactors used to produce CNPs and TNPs consist of two laminar premixed flames. A sketch of the experimental production system is reported in Figure 1.

CNPs flame reactor was an ethylene/air laminar premixed flame stabilized on a water-cooled McKenna burner, where CNPs can be synthesized and collected at different heights above the burner surface (HAB), which correspond to changes in the residence time of the CNPs and so resulting in different particle sizes [4].

Recently, we demonstrated that flame-formed CNPs exhibit apparent quantum confinement and that the particle size is the single most important factor that governs the band gap of flame-formed CNPs [4]. We selected HAB = 20 mm to produce particles in the order of 20 nm, characterized by a low band gap (< 0.5 eV) and so high electrical conductivity. For both AFM and STS measurements, CNPs were deposited on mica substrates coated with a submicron gold layer deposited by vapor deposition. The collection time was 0.1 s during each insertion. CNP films were produced with a total sampling time of 10 s. TiO_2 particles were then produced in a custom-made flame reactor composed of a honeycomb burner [5] and deposited by thermophoresis on the surface of CNP films, where they intercalate between the carbon grains and diffuse within the pores. CNPs-TNPs films were obtained by inserting the CNP films into the TiO_2 flame reactor for a total sampling time of 40 s.

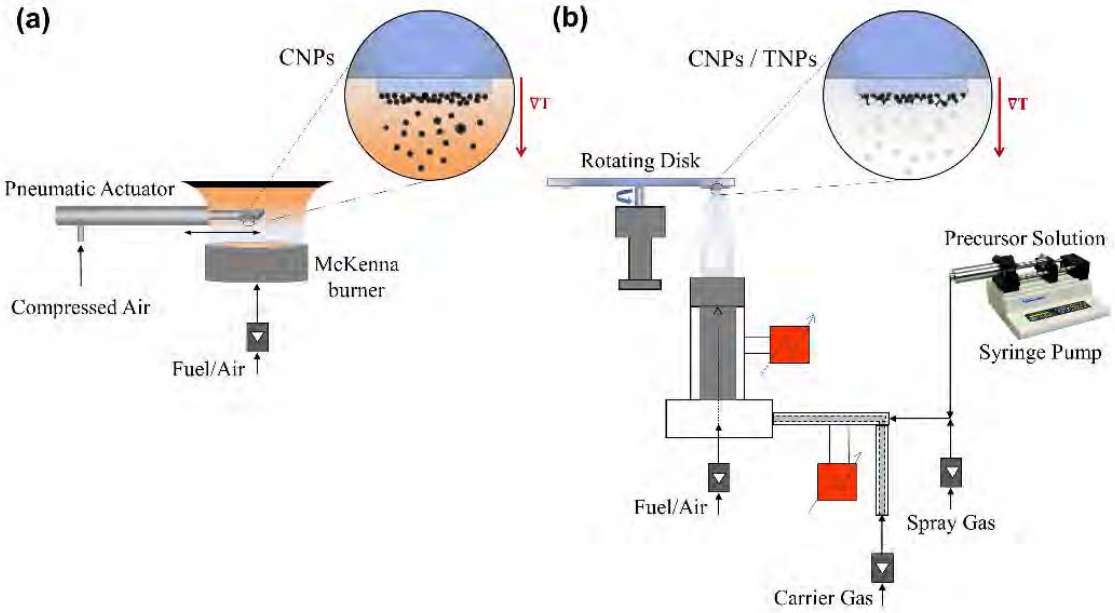

Figure 1. Schematic of the experimental set-up for the synthesis and deposition of CNPs (a) and TNPs (b).

An NT-MDT NTEGRA scanning probe microscope was used to perform STS measurements. STS measurements were performed in room air at 30% relative humidity. The tip for the microscope was obtained by mechanically cutting a Pt/Ir (80:20% by mass) wire (diameter = 0.25 mm). For each sample, an STM topographic image was first acquired in a constant- current operation mode. Based on the scanned image, several locations on the sample surface were selected to perform punctual measurements in the STS mode, obtaining the differential conductance dI/dV spectra at many different points on each nanostructured film.

Results and discussion

Figure 2 reports a typical Raman spectrum measured on CNP/TNP nanostructured film. The four main Raman bands assigned to the anatase phase of TiO_2 are present,

together with the typical features of disordered graphitic-like carbon compounds, i.e., the G peak and the D peaks.
The optical characterization of CNP and TNP films was performed by depositing the films on quartz slides and measuring UV-Vis absorption spectra, reported in Figure 3 (left side). Both TiO_2 and CNPs contribute to the absorption spectrum of the CNP-TNP composite film in the UV region. The slow decrease in the visible range is entirely due to light absorption from CNPs. Indeed, the CNP spectrum presents a maximum at 230 nm and then slowly decreases when wavelength increases.

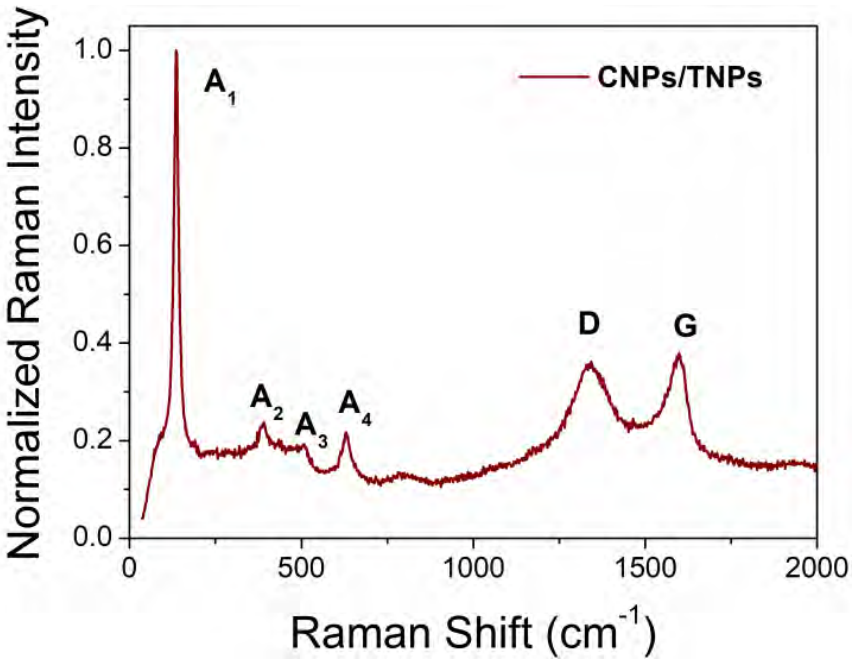

Figure 2. Raman spectrum of composite CNP/TNP film.

From UV-Vis spectra the Tauc plots for the absorbance spectra of the three samples were obtained. The optical band gap $E_{g,opt}$ for CNP sample was measured to be 0.29, which is characteristic of a carbon semiconductor material with a high degree of graphitization. The optical band gap $E_{g,opt}$ for TNP sample is equal to 3.05 eV and it is slightly lower than the bulk anatase material (3.2 eV). Compositing TNPs with CNPs has led to a reduction of the band gap of TiO2 down to 2.7 eV and so to an improvement of the electrical conductivity with respect to the pure TNP films.
Typical STS differential conductance spectra of the three samples are reported in Figure 3 (right side). The differential conductance spectra are related to the Fermi level of the material tested and yield approximately the local density of states, LDOS. The positions of the valence band (VB) and the conduction band (CB) are thus determined from the positions of the abrupt changes in dI/dV that correspond to the edges of CB and VB. Because bias voltage was applied to the tip in the experimental set-up used in this work, the first peak in the positive voltage of a dI/dV spectrum represents the withdrawal of electrons from the material and hence the VB-edge of the semiconductor. Similarly, the first peak in the negative voltage represents electron injection and therefore the CB-edge.

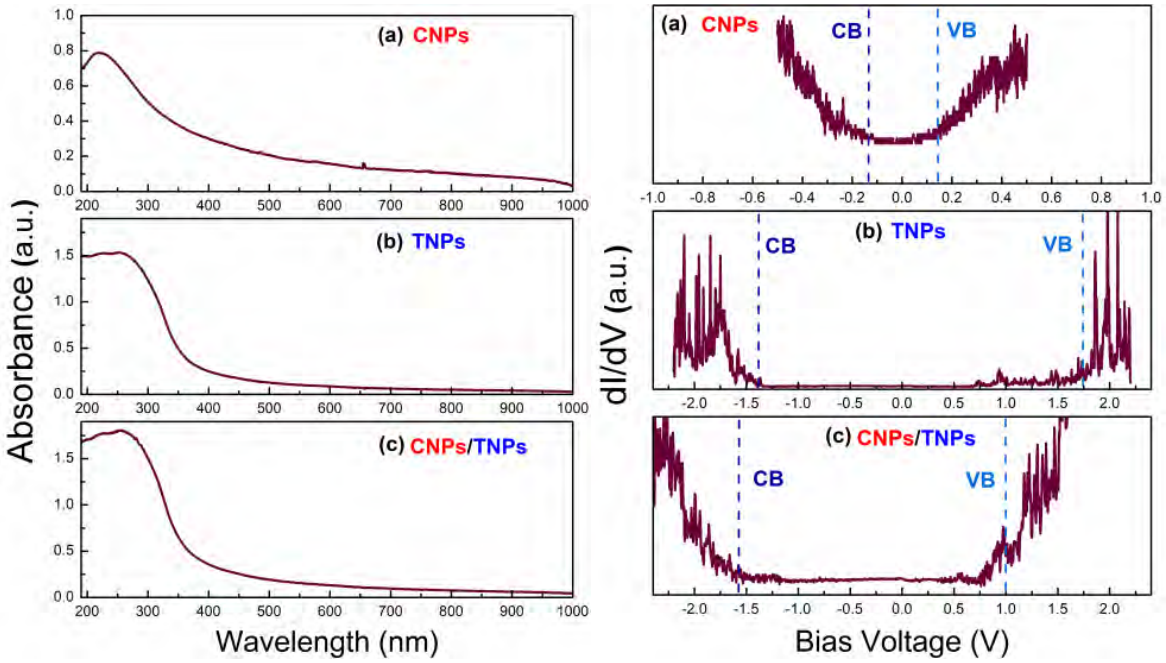

Figure 3. UV-visible absorption spectra (left) and STS differential conductance spectra (right) of CNP films (a), TNP films (b) and composite CNP/TNP films (c).

The STS electronic band gap values $E_{g,ele}$ are summarized in Table 1. For all three samples $E_{g,ele}$ are similar to optical values. However, optical absorption spectroscopy provides information on films on a macroscopic scale and $E_{g,opt}$ is a bulk property of the films. On the other hand, STS probes local band-edges separately on a microscopic scale and so furnishes a more accurate evaluation of the band gap through $E_{g,ele}$. Also, the electronic band gap of the material can be slightly different from the band gap optically measured since they share the same physical origin but are also different in some respect.

Moreover, STS measures not only $E_{g,ele}$, but also the position of the edges of CB and VB. The mean values of CB- and VB-edge positions, which are reported in Table 1, provide additional information. It is possible to observe that for CNP/TNP films the position of VB-edge is shifted with respect to the VB-edge of pure TNP films, while CB-edge is substantially unchanged. Also, VB-edge is significantly closer to the EF (zero), as compared to the CB, suggesting a p-type electronic conductivity behavior. This evidence cannot be ascribed to oxygen vacancies states, whose energy level position is supposed to be from 0.75 to 1.18 eV below CB of TiO_2 [6]. Because STS is an extremely localized mode of measurement, this spectroscopy provides band-edges at the microscopic scale of the material, that is, at the exact point of electron tunneling. Hence, when measurements were carried out at many different points of a thin film, the standard deviation of average band positions can be obtained from the width of band-edge histograms, which would provide a measure of the localized topological or structural inhomogeneity. In flame-formed carbon nanoparticles, local differences in band edges are expected since a large complexity/variety of the aromatic compounds and thus a distribution of benzenoid rings has been recently visualized by HR-AFM [7]. Structural effects are also due to the fact that nonplanar

molecular components have been also observed and more distorted bond angles will lead to smaller E_g values. Since STS probes local band-edges on a microscopic scale, this technique is very powerful in monitoring local inhomogeneities and deriving the width of band-edges distributions [8].

Table 1. Summary of optical and electronic band gap and position and width of band edges with respect to the Fermi level of the gold substrate (Φ=5.5 eV).

Sample	$E_{g,opt}$ (eV)	$E_{g,ele}$ (eV)	VB (eV)	CB (eV)
CNPs	0.29	0.25 ± 0.1	0.12 ± 0.05	-0.12 ± 0.05
TNPs	3.05	3.10 ± 0.20	1.55 ± 0.20	-1.60 ± 0.15
CNP/TNPs	2.70	2.65 ± 0.20	1.10 ± 0.25	-1.55 ± 0.30

Conclusions

In this work, composite films made of TNPs and graphitic-like CNPs were produced by flame synthesis and direct termophoretic deposition. A two-steps procedure was developed, consisting of the self-assembling of flame-synthesized 20 nm CNPs into a nanostructured porous film and the subsequent deposition and self-assembling of flame-synthesized 3 nm TNPs on the CNP film. Scanning Tunneling Spectroscopy was successfully applied for the first time to measure the electronic band gaps of nanocomposite films and to compare these results to UV-Vis absorption optical band gaps. Compositing TNPs with CNPs resulted in a decrease of band gap of the film (both optical and electronic) and so an improvement of the electrical conductivity with respect to pure TNPs films is expected. The STS technique provided a measure of the edges of CB and VB individually, allowing to quantify the local inhomogeneity through the width of CB and VB edge distributions. Future work will be devoted to performing a more complete electrical characterization of the films, as well as to apply the STS technique to films produced with different amount and relative ratio of CNPs and TNPs and to improve the production procedure (from two-steps to one-step).

References

[1] von Schneidemesser, E., et al., *Chem. Rev.* 115: 3856–3897 (2015)
[2] Liang, S., et al., *Energy Storage Mater.* 45: 201–264(2022)
[3] Li, S., et al., *Prog. Energy Combust. Sci.* 55: 1-59 (2016)
[4] De Falco, G., et al., *Proc. Comb. Inst.* 38 1805-1812 (2021)
[5] Commodo, et al., *Materials* 14: 4672 (2021)
[6] Cronemeyer, D.; Gilleo, M., *Phys. Rev* 82: 975 (1951)
[7] Commodo, M., et al., *Combust. Flame* 205: 154–164 (2019)
[8] Dan, S., et al., A.J., *J. Phys. Chem. Lett.* 13: 1660−1667 (2022).

SECONDARY AEROSOL FORMATION IN AN OXIDATION FLOW REACTOR – MASS SPECTROMETRY AND PARTICLE SIZE MEASUREMENTS

F. Sasso*, F. Picca, A. Pignatelli†, M. Commodo‡, P. Minutolo ‡, A. D'Anna***

fabio.sasso@unina.it

* Dipartimento di Ingegneria Chimica, dei Materiali e della Produzione Industriale, Università degli Studi di Napoli Federico II, Napoli, 80125, Italy

** Centro Servizi Metrologici e Tecnologici Avanzati, Università degli Studi di Napoli Federico II, Napoli, 80146, Italy

†Dipartimento di Fisica, Università degli Studi di Napoli Federico II, Napoli, 80125, Italy

‡ Istituto di Scienze e Tecnologie per l'Energia e la Mobilità Sostenibili, CNR, Napoli, 80125, Italy

Abstract

Secondary organic aerosol is formed from the atmospheric oxidation of gas-phase organic compounds and primary aerosol. Despite the danger that this class of particles constitutes for human health and climate, secondary aerosol studies are limited; how the principal emissions' sources contribute to the secondary organic aerosol formation is still unknown. This work analyses the formation of secondary organic aerosol from the oxidation of soot precursor nanoparticles generated by a premixed laminar ethylene-rich flame. Flame exhausted gases and particles are sent to an oxidation flow reactor to replicate the atmospheric conditions through which the secondary aerosol formation reactions occur. As an on-line measurement, the oxidized aerosol is sent to a scanning mobility particle sizer system to evaluate the particles' size distributions; as off-line measurement, the collected aerosol is analysed by the High Resolution - Time of Flight - Aerosol Mass Spectrometer for a chemical characterization. The secondary aerosol formed displays an increase in mean diameter at different oxidation conditions and reveals an enhancement factor with respect to primary aerosol.

Introduction

Atmospheric aerosols have important implications for global warming and human health. Aerosols can influence the Earth's climate by reflecting incoming sunlight to outer space, thus having a cooling effect on the climate; absorbing aerosols can trap energy within the atmosphere, thus warming. Light absorbing aerosols can also potentially modify cloud properties either directly, acting as cloud condensation nuclei (CCN) and incipient nuclei (IN), or indirectly by stabilizing the atmosphere and diminishing the convection and thus the potential for cloud formation [1, 2]. In this way the atmospheric temperature is increased reducing the relative humidity,

inhibiting cloud formation, and enhancing the evaporation of existing clouds. In addition, black carbon and other light absorbing aerosols deposited on snow or ice surfaces may reduce the surface albedo, leading to reduced reflectance of solar radiation and a heating effect [2].

Organic aerosols (OA) constitute a substantial fraction of submicron aerosols worldwide; it is operationally separated into hydrocarbon-like OA (HOA) and oxygenated-like OA (OOA), and sometimes other primary components. HOA and OOA are good surrogates for primary OA (POA) and secondary OA (SOA) under most conditions [3]. SOA produced in the environment comprises a significant and variable fraction (20−90%) of $PM_{2.5}$, the Particulate Matter with sizes below 2.5 μm, and it is believed to be formed via the atmospheric oxidation of both biogenic and anthropogenic gas-phase organic compounds, e.g., volatile organic compounds, VOCs, [4]. Despite the danger that this class of particles constitutes, our understanding of SOA formation processes and their chemical and physical properties is limited [5–7]. Several approaches have been used to estimate and constrain the quantity of SOA that can form from a mixture of organic compounds emitted from fuel combustion. Estimation methods include top-down approaches based primarily on ambient air quality measurements and bottom-up processes focusing on the in-depth characterization of fuel emissions [8]. The bottom-up approach consists of the oxidation of fresh exhaust from the combustion system in environmental chambers or oxidation reactors to simulate potential SOA formation in the ambient atmosphere [9].

In this work, the formation of SOA from the oxidation of the products of incomplete combustion of ethylene in a premixed laminar ethylene-air-rich flame is studied. The products of incomplete combustion include NOx, VOC, mono- and polycyclic aromatic compounds, and soot nanoparticles collected at different residence times in the flame and convoyed to an oxidation flow reactor which simulates the conditions that combustion exhausts find in the atmosphere. The evolution of the particles' size distributions (PSD) was measured by a scanning mobility particle sizer (SMPS) system using high dilution sampling system to reduce the temperature and particle concentration in order to avoid further reactions and coagulation in the sampling line. The nucleation of new particles and change of the chemical composition of the incomplete combustion products in an environment which mimic the atmospheric transformation are analysed by an High Resolution – Time of Flight – Aerosol Mass Spectrometer (HR-ToF-AMS).

Experiment

An atmospheric pressure laminar premixed ethylene-air flame, operated under fuel-rich, lightly sooting conditions, was used to produce incomplete combustion products; the flame was stabilized on a water-cooled sintered bronze McKenna burner having a diameter of 6 cm. The cold gas velocity was set at 9.8 cm/s, and the carbon to oxygen (C/O) atomic ratio was maintained constant at 0.67 (equivalence ratio $\phi = 2.01$).

For all the investigations, the combustion products were extracted from the flame centreline through a tubular dilution probe, as described in previous studies [10–12] s. In this work, the Height Above the Burner (HAB) was fixed at 8, 10, and 14 mm, representing three different times/regimes of the soot formation process, particle nucleation (8 mm), particle growth (10 mm), and particle coagulation (14 mm).
The sampled unburned gases and particles were convoyed to an Oxidation Flow Reactor developed by Dekati® (DOFR^{TM}). This reactor is an OFR254-type oxidation flow reactor [13]: OH radicals are produced from the photolysis of the ozone with 254 nm UV radiation. An ozone flux is generated by an external ozone generator (model 1000 Jelight Company Inc.), which produces O_3 from oxygen photolysis by 185 nm UV radiation (Ozone concentration is monitored by Model 205 Dual Beam Ozone Monitor - 2B Technologies). A detailed description is reported by Simonen et al. [9]. Different amounts of ozone and water molecules allow mimicking different residence times in the atmosphere, thus following the aerosol aging time from a few hours up to a few days. The detailed experimental setup is represented in Figure 1.

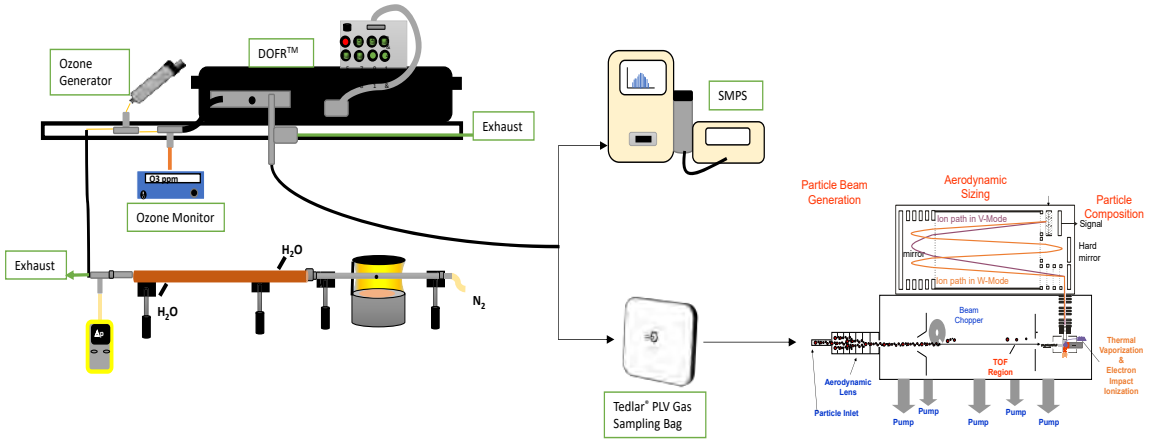

Figure 1: Experimental set-up

Particle size distributions, PSDs, were measured online by a scanning mobility particle sizer (SMPS) system. Unburned gases were collected in 5L Tedlar® PLV Gas Sampling bags and analysed by an HR-ToF-AMS enabling fully molecular-resolved online quantification of organic aerosol [14]. Aerosol particles are sampled through the $PM_{2.5}$. aerodynamic lenses and focused into a narrow beam that impacts a resistively heated (ca. 600°C) capture vaporizer where the non-refractory particle species are vaporised. The vapours are subsequently ionised with a 70-eV electron beam, and the ions are extracted into a mass spectrometer to be analysed.

Results and Discussion

The PSDs measured at the three sampling locations are related to four different ozone concentrations, mimicking about 2 days of aging time (5ppm O_3), 3 days of aging time (10ppm O_3), 15 days of aging time (55ppm O_3), and 20 days of aging time (75ppm O_3), respectively.

At 8mm, the activation of photo-oxidation reactions induces the formation of new and larger particles; their concentration increases as ozone concentration, i.e., the aging time, increases. The same behavior is observed at 10mm, whereas at 14mm, another effect is highlighted: particles with sizes intermediate between those collected in the flame are observed. The effect is clearly shown in Figure 2 where the PSDs of the particle after 3 days of aging (10ppm O_3) produced by the photo-oxidation of incomplete combustion products at different residence times are reported.

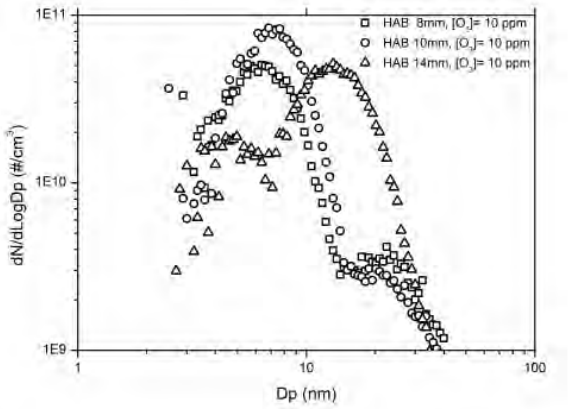

Figure 2: PSD measured at the exhaust of the DOFR with an [O_3] equal to 10ppm.

This new particle mode is observed particularly at 14mm and could be attributed to soot particle oxidation fragmentation or the formation of inorganic particles in a flame region where NOx are more abundant. The chemical characterization of this particle mode could help in understanding their origin. Figure 3 reports the mass spectra of 0 and 5 ppm of ozone concentration for the three HABs, in the 100-1100 m/z range. The upper diagrams report the oxidized conditions (5 ppm), the lower plots describe the no-oxidized conditions (0 ppm).

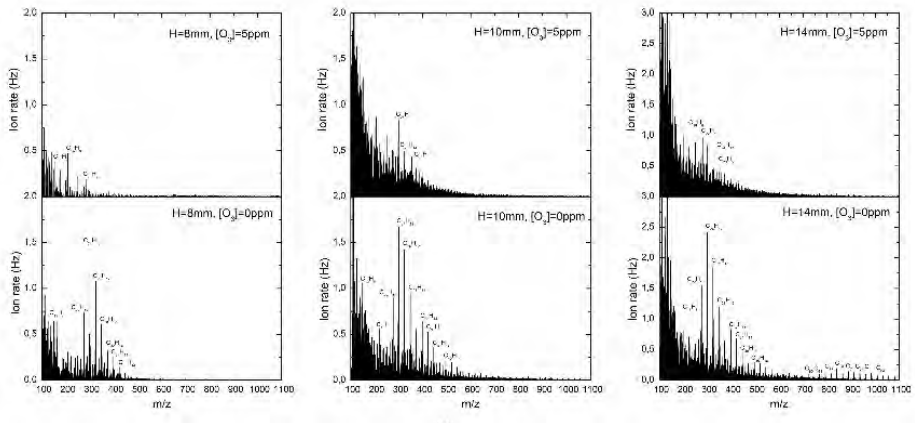

Figure 3: Mass spectra of unburned gas. From left to right, HAB = 8 mm, 10 mm, 14 mm. Upper side: ozone concentration of 5ppm Lower side: without oxidation

The mass spectra of the incomplete combustion products collected at 8, 10 and 14 mm above the flame have been analyzed by HR-ToF-AMS. Several PAHs of moderate size (about the size of coronene to ovalene) are present and even a series of peaks attributed to pure carbon species (Cx) in 14 mm spectrum are noticed.
A preliminary analysis of the spectra highlights that by photo-oxidation of the samples, most of the PAH peaks disappear and new particles are nucleated. Indeed, the peaks observed in the m/z range from 300 to 500 for HAB equal to 8 and 10mm, and those registered in the m/z range 700-1000 for HAB equal to 14mm, seem to participate to oxidative processes.

Conclusion

In this work a bottom-up approach was carried out to study the secondary organic aerosol formation by the oxidation of unburned gases. The use of an oxidation flow reactor allows to replicate the atmospheric conditions ranging from 1 to 20 days of equivalent aging time. Photo-oxidation induces the nucleation of new particles in the 5-20 nm range. The mass spectra analysis highlights that these particles mainly comprise PAHs. The mass concentration of the new particles is about 2-4 times greater than the emitted primary particles. Higher ozone concentrations induce the formation of intermediate size particles whose origin needs to be investigated.

References

[1] Gentner, D.R. et al: Elucidating secondary organic aerosol from diesel and gasoline vehicles through detailed characterization of organic carbon emissions. Proc. Natl. Acad. Sci. U. S. A. 109, 19318–18323 (2012)

[2] Chirico et al: Impact of aftertreatment devices on primary emissions and secondary organic aerosol formation potential from in-use diesel vehicles: results from smog chamber experiments. Atmos. Chem. Phys. 10, 11545–11563 (2010)

[3] Jimenez, J.L.; C.M.R.; D.N.M.; P.A.S.H.; Z.Q.; K.J.H.; D.P.F.; A.J.D.; C.H.; N.N.L.; et al.: Evolution of organic aerosols in the atmosphere. Science (1979). 326, 1525–1529 (2009)

[4] Gentner, D.R., Jathar, S.H., Gordon, T.D., Bahreini, R., Day, D.A., el Haddad, I., Hayes, P.L., Pieber, S.M., Platt, S.M., de Gouw, J., Goldstein, A.H., Harley, R.A., Jimenez, J.L., Prévôt, A.S.H., Robinson, A.L.: Review of Urban Secondary Organic Aerosol Formation from Gasoline and Diesel Motor Vehicle Emissions, (2017)

[5] Suarez et al: Primary emissions and secondary organic aerosol formation from the exhaust of a flex-fuel (ethanol) vehicle. Atmos. Environ. 117, 200–211 (2015)

[6] Tkacik et Al: Secondary organic aerosol formation from in-use motor vehicle emissions using a potential aerosol mass reactor. Environ, Sci, Technol. 48, 11235–11242 (2014)

[7] Bahreini, R., Middlebrook, A.M., de Gouw, J.A., Warneke, C., Trainer, M., Brock, C.A., Stark, H., Brown, S.S., Dube, W.P., Gilman, J.B., Hall, K., Holloway, J.S., Kuster, W.C., Perring, A.E., Prevot, A.S.H., Schwarz, J.P., Spackman, J.R., Szidat, S., Wagner, N.L., Weber, R.J., Zotter, P., Parrish, D.D.: Gasoline emissions dominate over diesel in formation of secondary organic aerosol mass. Geophys Res Lett. 39, (2012). https://doi.org/10.1029/2011GL050718

[8] Abulude, F.O., Bahloul, M., Olubayode, S., Adeoya, E.A.: A review on top-down and bottom-up approach for air pollution studies. World Journal of Environmental Research. 7, 52–60 (2018). https://doi.org/10.18844/wjer.v7i2.3427

[9] Simonen, P., Saukko, E., Karjalainen, P., Timonen, H., Bloss, M., Aakko-Saksa, P., Rönkkö, T., Keskinen, J., Dal Maso, M.: A new oxidation flow reactor for measuring secondary aerosol formation of rapidly changing emission sources. Atmos Meas Tech. 10, 1519–1537 (2017). https://doi.org/10.5194/amt-10-1519-2017

[10] Zhao, B., Yang, Z., Wang, J., Johnston, M. v., Wang, H.: Analysis of soot nanoparticles in a laminar premixed ethylene flame by scanning mobility particle sizer. Aerosol Science and Technology. 37, 611–620 (2003). https://doi.org/10.1080/02786820300908

[11] Zhao, B., Yang, Z., Johnston, M. v., Wang, H., Wexler, A.S., Balthasar, M., Kraft, M.: Measurement and numerical simulation of soot particle size distribution functions in a laminar premixed ethylene-oxygen-argon flame. Combust Flame. 133, 173–188 (2003). https://doi.org/10.1016/S0010-2180(02)00574-6

[12] Sgro, L.A., Basile, G., Barone, A.C., D'Anna, A., Minutolo, P., Borghese, A., D'Alessio, A.: Detection of combustion formed nanoparticles. In: Chemosphere. pp. 1079–1090. Elsevier Ltd (2003)

[13] Li, R., Palm, B.B., Ortega, A.M., Hlywiak, J., Hu, W., Peng, Z., Day, D.A., Knote, C., Brune, W.H., de Gouw, J.A., Jimenez, J.L.: Modeling the radical chemistry in an oxidation flow reactor: Radical formation and recycling, sensitivities, and the OH exposure estimation equation. Journal of Physical Chemistry A. 119, 4418–4432 (2015). https://doi.org/10.1021/jp509534k

[14] Canagaratna, M.R., Jayne, J.T., Jimenez, J.L., Allan, J.D., Alfarra, M.R., Zhang, Q., Onasch, T.B., Drewnick, F., Coe, H., Middlebrook, A., Delia, A., Williams, L.R., Trimborn, A.M., Northway, M.J., DeCarlo, P.F., Kolb, C.E., Davidovits, P., Worsnop, D.R.: Chemical and microphysical characterization of ambient aerosols with the aerodyne aerosol mass spectrometer, (2007)

Effect Of Ethanol Addition On Ethylene-Air Flame On The Primary And Secondary Particle Size Distribution

A. Pignatelli *, F. Picca, F. Sasso †, M. Commodo‡, P. Minutolo ‡, A. D'Anna †**

alessia.pignatelli@unina.it

* Dipartimento di Fisica, Università degli Studi di Napoli Federico II, Napoli, 80125, Italy

** Centro Servizi Metrologici e Tecnologici Avanzati, Università degli Studi di Napoli Federico II, Napoli, 80146, Italy

†Dipartimento di Ingegneria Chimica, dei Materiali e della Produzione Industriale, Università degli Studi di Napoli Federico II, Napoli, 80125, Italy

‡ Istituto di Scienze e Tecnologie per l'Energia e la Mobilità Sostenibili, CNR, Napoli, 80125, Italy

Abstract

The aim of this study is to investigate the effects of the introduction of different ethanol concentrations in a premixed ethylene/air flame. The impact of the ethanol addition is studied in terms of primary (PA) and secondary aerosol (SA) formation through the analysis of particle size distribution functions (PSDs). The PSDs of doped and undoped flames are collected through a scanning mobility particle size (SMSP) system at different heights above the burner (HAB), i.e. different residence times. Different ethanol concentrations, equal to 10% and 20%, were used to dope the flame in order to replicate commercial mixtures available on the national market. The secondary aerosol formation process is replicated through the use of an Oxidation Flow Reactor developed by Dekaty® (DOFR™) and an ozone flux, applied to the main stream, in order to simulate an atmospheric aging time of two days. The comparison among the pre-mentioned conditions is performed so to highlight the presence of trends in PSDs functions and to crosscheck if the ethanol addition decreases the emissions in terms of both PA and SA.

Introduction

Over the last decades, the use of biofuel has drastically risen [1] due to the necessity of reducing fossil fuel dependence. Among the available alternatives to petroleum-derived fuels, bioethanol represents a valid solution as it can be obtained from biomass at reasonable costs [2].

In addition to the economic reasons, the understanding of the impact of ethanol from the environmental point of view has revealed to be crucial. In this research, an analysis on the effects of the addition of ethanol on a premixed ethylene-air flame is proposed. According to previous studies [3–5] a decrease in the formation of soot, polycyclic aromatic hydrocarbon (PAH) precursors and other health-damaging

compounds should be observed in an ethanol-doped flame. It has to be mentioned that these effects are detected only for specific experimental conditions: in particular, for certain type of flames [6], equivalence ratios and ethanol concentrations. Hence, the identification of the variables acting on the formation of the main hazardous compounds is decisive to reduce the risks associated to these anthropogenic emissions. Moreover, it has been demonstrated that particles' size and number have a stronger correlation with toxicity than mass concentration [7]. In this context, an accurate analysis of the PSDs functions is essential in order to perform further investigation.
Several studies have been realized in engines about the emissions of an ethanol-doped system; mainly investigating nitrogen oxide, particulate matter, carbon monoxide and total hydrocarbons. Usually, a reduction in the particulate matter formation is observed. For instance, Lapuerta and coworkers [8] proposed a study about the emissions from a diesel–bioethanol blend in an automotive diesel engine, for which a particulate matter reduction is observed for the doped flame..
In this analysis, a flame with an equivalence ratio of 2.01 is chosen, in order to investigate an intermediate sooting condition. Two ethanol volume concentrations were adopted, specifically 10% and 20%, in the ethylene/air flame system. Timonen at al. demonstrated that the PAH and soot reductions expected for an ethanol-doped flame are observed only for specific concentrations of the alcohol. Too high values do not show advantages in terms of both primary and secondary aerosol formation, hence a tradeoff has to be found in order to optimize and reduce as much as possible the presence of polluting compounds in the atmosphere [9].
The PSDs were collected with a Scanning Mobility Particle Sizer equipped with a Differential Mobility Analyzer (DMA)-model TSI3085, and a Condensation Particles Counter (CPC)-model TSI3776. The PSDs functions were collected at different points of the experimental circuit in order to estimate separately the contributions of primary and secondary aerosols. Primary aerosol consists in organic and inorganic compounds directly emitted from the combustion system; secondary aerosol is produced in the atmosphere from gaseous precursors by condensation of vapours on pre-existing particles or by nucleation of new particles [10]. Another factor affecting the formation of SA is oxidation: oxidative conditions observed in the atmosphere are mainly due to the presence of OH radicals, NO_3 and O_3. The use of a DOFR^{TM} reactor combined with an ozone flow allows to replicate these atmospheric conditions.
The DOFR^{TM} was used with an ozone concentration of 5ppm in order to simulate an aging time of the particles equal to two days.

Experimental Setup

An atmospheric pressure laminar premixed ethylene-air flame was used to produce incomplete combustion products; the flame was stabilized on a water-cooled sintered bronze McKenna burner having a diameter of 6 cm. The cold gas velocity was set at 9.8 cm/s, with an equivalence ratio of 2.01, kept constant. The ethanol introduction

was performed through a Controlled Evaporeted Mixer (CEM)- model W202-A Bronkhorst. A turbulent flow dilution probe (N_2 as carrier gas) with a 1 cm outer diameter shape with a 0.2mm orifice was used to extract the combustion products at the centerline of the burner; the exhausts were collected at different heights above the burner in a range between 8mm and 14mm.
The analysed conditions can be schematized as follows:
- PSDs of exhausts of doped and undoped flame collected immediately after the dilution probe, in order to characterize primary aerosol.
- PSDs of exhausts of doped and undoped flame collected after the DOFR™ reactor, with an ozone concentration of 5ppm, simulating secondary aerosol composition.

The main variables of each collecting condition are reported in Table 1:

Table 1. Example of a table.

Phi	Air [L/min]	Ethylene [L/min]	Ethanol [L/min]	Ethanol Percentage	Ozone Concentration
2.010	14.570	2.051	-	-	0ppm and 5ppm
2.010	14.570	1.846	0.205	10%	0ppm and 5ppm
2.010	14.570	1.641	0.41	20%	0ppm and 5ppm

The oxidation flow reactor is an OFR254-type oxidation flow reactor [11]. The reactor is a 3.3L (52 cm x 9 cm inner diameter) quartz glass cylinder surrounded by two constant power ozone-free low-pressure mercury lamps which emit 254 nm UV light. The lamps are placed outside the reactor to ensure laminar flow and to decrease the surface-to-volume ratio. An external ozone generator (model 1000 Jelight Company Inc.) produces O_3 from oxygen photolysis by 185 nm UV radiation (Ozone concentration is monitored by Model 205 Dual Beam Ozone Monitor - 2B Technologies). The photolysis of the ozone in the reactor due to 254nm UV radiations generates OH radicals that acts as oxidizing agent.

Results

As previously mentioned, according to literature-reported experience[3, 4], the ethanol introduction in a premixed flame at 10% and 20% concentrations reduces soot formation, inhibiting the precursors responsible of toxic and hazardous compounds. The aim of this study is to investigate the effects of different ethanol concentrations in a premixed ethylene/air flame on the primary and secondary aerosol formation. A preliminary analysis of the PSDs functions confirms the results reported in the previous studies about PA, showing a change in the modal distribution as ethanol concentration increases. Ethylene-air flame PSDs exhibit the following general picture: particle size distribution functions appear unimodal at low

heights while the trend becomes bimodal increasing residence times in the flame. The PSDs shape of the doped flame ,instead, reveals a clear change. Indeed, the bimodality of the functions appears less marked as ethanol concentration increases. For the same residence time in the ethanol doped flames, the mean size of particles results smaller and also the particle size distribution function is deeply different as shown in Figure 1. These results confirm the role of ethanol, as soot and soot precursors inhibitor showing a reduction of the coagulation efficiency which forces particles to remain smaller.

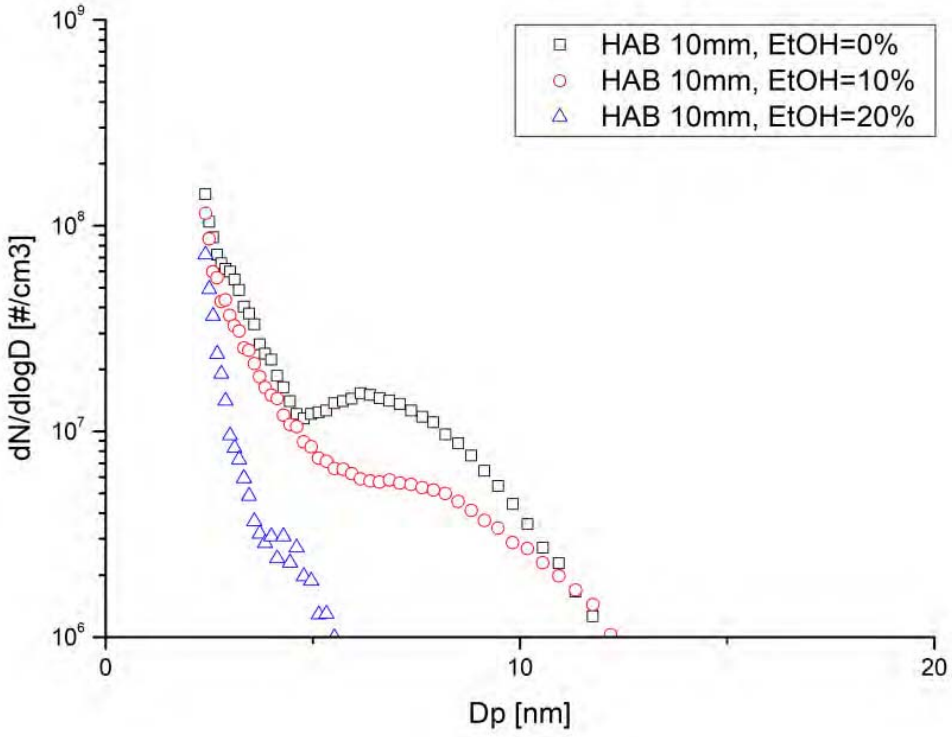

Figure 1. Particle Size Distribution at HAB=10mm and different Ethanol (EtOH) Concentrations for Primary Aerosol.

A similar trend is observed also for PSDs reporting SA formation. A preliminary investigation for the un-doped ethylene-air flame highlights the effect of photooxidation reactions. At 8mm, the activation of photo-oxidation processes induces the formation of new and larger particles. The PSDs show a unimodal trend with a mean particle diameter that shifts to higher values as HAB increases. At 14 mm another effect is visible. A new particle mode is observed which could be attributed to soot particle oxidation-fragmentation or to the formation of inorganic particles in the flame region where NOx are more abundant.
Ethanol addition shows similar and stronger results on PSDs of SA as observed in the functions collected for PA characterization. To explain these results a ripple effect is supposed. The inhibition of ethanol on soot and soot precursors formation is correlated to the reduction of the signals registered in the SA-PSDs . It suggests

that the particles on which ethanol acts could potentially represent precursors of secondary aerosol. Figure 2 shows clearly the effect of ethanol addition on SA PSDs.

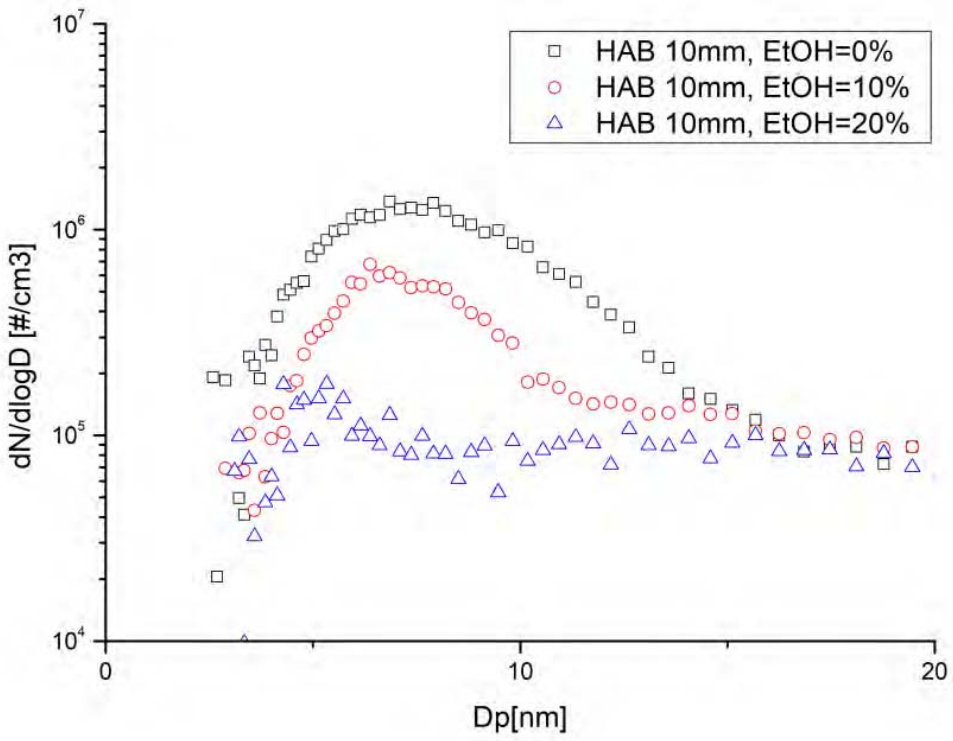

Figure 2. Particle Size Distribution at HAB=10mm and different Ethanol (EtOH) Concentrations for Secondary Aerosol.

Conclusions

A reduction of the particles number as function of the amount of ethanol added to a laminar premixed ethylene flame was found. The ethanol acts as an inhibitor for soot and soot precursors, having an impact on both primary and secondary aerosol formation due to a probable ripple effect. The compared analysis of the PSDs functions collected at different experimental conditions, confirms the role of ethanol in slowing the reaction rate of processes that bring to the formation of several health-damaging compounds. Further investigation will be done in order to chemically characterize the collected samples.

References

[1] Energy Information Administration, U.: Monthly Energy Review - April, 2023. (2023)

[2] Huang, Y., Chen, C.W., Fan, Y.: Multistage optimization of the supply chains of biofuels. Transp Res E Logist Transp Rev. 46, 820–830 (2010). https://doi.org/10.1016/j.tre.2010.03.002

[3] Salamanca, M., Sirignano, M., Commodo, M., Minutolo, P., D'Anna, A.: The effect of ethanol on the particle size distributions in ethylene premixed flames. Exp Therm Fluid Sci. 43, 71–75 (2012). https://doi.org/10.1016/j.expthermflusci.2012.04.006

[4] Salamanca, M., Sirignano, M., Danna, A.: Particulate formation in premixed and counter-flow diffusion ethylene/ethanol flames. Energy and Fuels. 26, 6144–6152 (2012). https://doi.org/10.1021/ef301081q

[5] Wu, J., Song, K.H., Litzinger, T., Lee, S.Y., Santoro, R., Linevsky, M., Colket, M., Liscinsky, D.: Reduction of PAH and soot in premixed ethylene-air flames by addition of ethanol. Combust Flame. 144, 675–687 (2006). https://doi.org/10.1016/j.combustflame.2005.08.036

[6] Yakimov, S.A., Knyazkov, D.A., Bolshova, T.A., Shmakov, A.G., Korobeinichev, O.P., Yang, J., Qi, F.: Study of stoichiometric ethylene and ethylene/ethanol low pressure premixed flames using mass-spectrometry with synchrotron photoionization and modeling. (2011).

[7] Alföldy, B., Giechaskiel, B., Hofmann, W., Drossinos, Y.: Size-distribution dependent lung deposition of diesel exhaust particles. J Aerosol Sci. 40, 652–663 (2009). https://doi.org/10.1016/j.jaerosci.2009.04.009

[8] Lapuerta, M., Armas, O., Ballesteros, R., Fernández, J.: Diesel emissions from biofuels derived from Spanish potential vegetable oils. Fuel. 84, 773–780 (2005). https://doi.org/10.1016/j.fuel.2004.11.010

[9] Timonen et al: . Influence of fuel ethanol content on primary emissions and secondary aerosol formation potential for a modern flex-fuel gasoline vehicle. . Atmos. Chem. Phys. 17, 5311–5329 (2017)

[10] Jimenez, J.L.; C.M.R.; D.N.M.; P.A.S.H.; Z.Q.; K.J.H.; D.P.F.; A.J.D.; C.H.; N.N.L.; et al.: Evolution of organic aerosols in the atmosphere. Science (1979). 326, 1525–1529 (2009)

[11] Li, R., Palm, B.B., Ortega, A.M., Hlywiak, J., Hu, W., Peng, Z., Day, D.A., Knote, C., Brune, W.H., De Gouw, J.A., Jimenez, J.L.: Modeling the radical chemistry in an oxidation flow reactor: Radical formation and recycling, sensitivities, and the OH exposure estimation equation. Journal of Physical Chemistry A. 119, 4418–4432 (2015). https://doi.org/10.1021/jp509534k

A theoretical investigation of acetylene addition on graphene armchair and zigzag edges

C. Giudici*, M. Ferri, G. Contaldo**, M. Maestri**, M. Pelucchi***
matteo.pelucchi@polimi.it
* Department of Chemistry, Materials and Chemical Engineering, Piazza L. Da Vinci, 32
** Department of Energy, Via Lambruschini, 4
Politecnico di Milano, Milano, Italy

Abstract
Density functional theory methods can be applied to gain insights into the microkinetic phenomena of the pyrocarbon "growth/deposition mechanism" that occur in chemical vapor infiltration processes. This work investigates the addition of acetylene at the active sites edges of a graphene sheet and the following reactions leading to the formation of a new carbon ring. The CI-NEB methodology is used to find the transition states, and the vibrational modes are calculated from a finite difference approximation of the Hessian. The growth chemistry of both armchair and zigzag edge configurations is studied, providing insights into the formation of structural defects during pyrocarbon growth. The results are compared with analogous gas-phase reactions governing the growth of polyaromatic hydrocarbon, ultimately allowing to investigate the effect of the solid surface in the acetylene addition mechanism. The kinetic constants of the investigated reactions are derived through classical transition state theory and can be implemented in existing detailed kinetic models for CVD/CVI processes.

Introduction
Pyrocarbons are a family of solid carbon materials with exceptional properties and several fields of application. The main process used to produce pyrolytic carbon (PyC) is chemical vapor infiltration (CVI) where a hydrocarbon feedstock is pyrolyzed at high temperatures (800-2000 °C), causing the deposition of carbon atoms on a substrate and the release of hydrogen (H_2) molecules in the gas phase. The resulting material appears as a hard, shiny surface deposit where carbon atoms are organized in a lamellar structure close to that of graphite but differ from it because of disorganizations within the sheets and sheet stacking defects [1]. This is due to the presence of carbon rings with 5/7/8 atoms or non-SP2 carbons that lead to sheet curvatures lowering the properties of the final material. In CVI reactors, carbon deposition occurs according to the H-Abstraction-Carbon-Addition (HACA) mechanism also involved in the growth of polycyclic aromatic hydrocarbons (PAHs) and particulate matter formation. According to this "growth mechanism" [2], active sites are firstly generated at the edge of graphene sheets by H-abstraction reactions from gas-phase radicals. Then, hydrocarbons are deposited on these sites and new carbon rings are formed through surface reactions (i.e., isomerization, internal

addition, β-scission). Repetition of this HACA process allows continuous growth of graphene sheets contributing to preform densification in CVI processes. Knowledge of these elemental steps has enabled the development of heterogeneous kinetic mechanisms that allow simulating the process of preform densification that occurs during CVI [3]. However, a total understanding of the deposition mechanisms is still not achieved because of the complexity of the phenomena involved in the process which also depends on the effect of several operating variables often scarcely explored in the literature. Considering also the difficulties in characterizing the final material, deriving a correlation between the operating conditions and the microstructure of the obtained material is still a critical challenge. To address these gaps, further investigations into the gas/solid interactions and the growth mechanisms involved in PyC infiltration are needed. Z.-B. Ding et al., [4] used density functional theory (DFT) methods to estimate the kinetic rates of the abstraction reactions of H by the major alkyl and alkenyl radicals at the edges of graphene. This approach is adopted here to study the subsequent elemental reactions involved in the HACA mechanism of pyrolytic carbon growth. DFT method is employed to first investigated the deposition reactions of C_2H_2 on the radical site of the armchair and zigzag edges, and then the subsequent surface reactions leading to a new carbon ring. Differences and similarities between the heterogeneous growth of PyC and the homogeneous growth of PAHs are discussed by comparing the potential energy surfaces of the investigated systems with those from similar gas-phase systems. In addition, the formation of pentagonal carbon ring during the zigzag edge growth provides valuable insights into the formation of microstructural defects.

Theoretical method and graphene modeling

Growth of the graphene sheet by addition of acetylene to the active sites at the edge is studied through DFT calculations for both armchair and zigzag configurations. All the calculations are performed using the Quantum-Espresso package implementing the generalized gradient approximation proposed by Perdew-Burke-Ernzerhof (PBE) [5] with periodic plane waves and ultrasoft pseudo-potentials waves. This method has been parameterized to describe the properties of carbon-based materials and has been often used in graphene-related studies [2]. A kinetic energy cutoff of 544 eV is used to converge the total energy per atom within 0.01 eV. The Grimme-D3 scattering correction is adopted to consider the contribution of long-range van der Walls interactions. The transition state structures (TS) of the studied reactions are identified using the Climbing-Image nudged elastic band (CI-NEB) methodology [10] using a convergence threshold of 0.05 eV $Å^{-1}$. Vibrational frequency analysis is performed with the finite difference approximation of the Hessian matrix as implemented in Atomic Simulation Environment (ASE) [11]. Each TS structure is confirmed by the presence of one single imaginary frequency along the reaction coordinate and then all the reaction barriers are calculated as the difference between the TS energy and the energy of the closest local minima on the initial state side.
The unit cell selected for the armchair and zigzag configurations are reported in

Figure 1. In the armchair edge model, the graphene repeats along the armchair direction three times and five times along the zigzag direction while in the zigzag configurations the width is equivalent to four and three benzene rings along the zigzag and armchair direction, respectively. The missing hydrogen at each of the two edges corresponds to the active site where acetylene addition occurs. This molecule is placed at 4.2 A° from the radical site to avoid any interactions with the graphene sheet at this initial stage. Thus, the resulting unit cells account for 50 carbon atoms and 9 hydrogens. To avoid the interactions among the periodic replicated images, the vacuum is set equal to 8.5 and 9.8 Å along the direction perpendicular to the armchair and zigzag graphene plane, respectively. The first Brillouin zone for the primitive cell of the graphene is described using a 5x1x1 Monkhorst-Pack k-points and is then adjusted according to the size of the supercell. The zigzag edge model is treated as anti-ferromagnetic in accordance with previous studies [2].

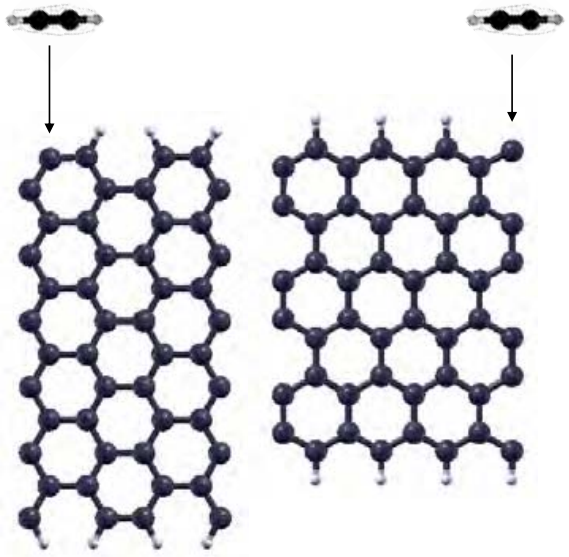

Figure 1. Selected unit cells for the armchair (left side) and zigzag (right side) site configurations.

Results and discussions

Acetylene deposition on an active site at the graphene edge can lead to the formation of a new aromatic ring at either 6 or 5 carbon atoms depending on whether the growth is on armchair (**Figure 2**a) or zigzag edge (**Figure 2**b).

Figure 3 shows the potential energy surfaces (PES) for each of the investigated configurations, i.e., red for armchair edge and blue for zigzag edge. The energies of the intermediates and TSTs are given in kcal/mol with respect to the reactants (A0 and Z0 for armchair and zigzag, respectively). Energy values of the '4-phenanthrenyl+ C2H2' system from [13] and the '1-naphthalenyl + C2H2' system from [14] are given in brackets as analogous gas-phase pathways to be used for comparison with the growth chemistry on armchair and zigzag edges, respectively.

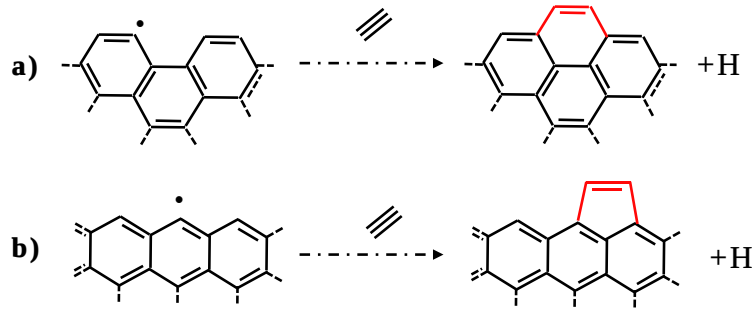

Figure 2. C_2H_2 deposition on armchair (a) and zigzag (b) edge leading to a new aromatic carbon ring (in red).

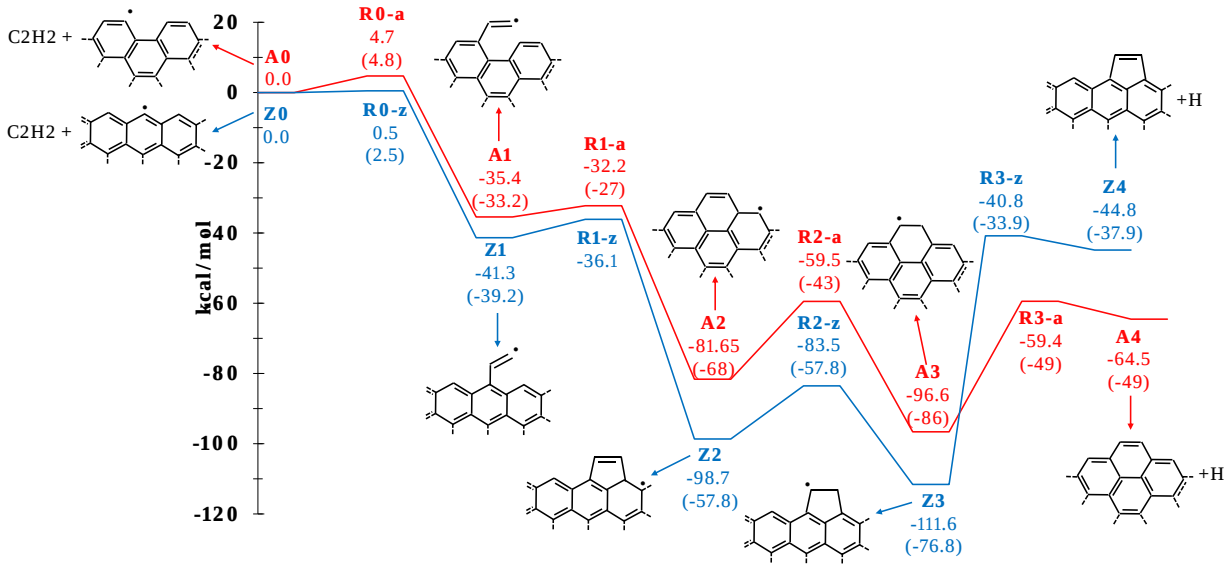

Figure 3. PES of the growth pathways of armchair (red) and zigzag (blue) edge investigated using the CI-NEB method. Values in the brackets referred to analogous gas-phase systems as specified in the main text.

The first reactive step involves the deposition of C_2H_2 on the active site at the armchair(/zigzag) edge with formation of the intermediate A1(/Z1) through a small energy barrier of 4.7(/0.5) kcal/mol. Next, a ring closure reaction, R1-a(/R1-z), with an energy barrier of ~7(/~5) kcal/mol gives rise to a new hexagonal(/pentagonal) ring at the edge, named A2(/Z2). A2 then undergoes an isomerization reaction in which a hydrogen atom is transferred between two vicinal carbons. This leads to the A3(/Z3) species through the reaction R2-a(/R2-z) with an activation energy of bout 22(/15) kcal/mol. The last reaction involved is a beta-scission, R3-a(/R3-z) where the radicality of the system is lost because of the release of a hydrogen atom (H) in the gas phase. This reaction, R3-a(/R3-z), has an endothermicity of 32(/65) kcal/mol, in contrast to all the other exothermic reactions, and an activation energy of 30(/70). The relative energies of the intermediates and TS are in good agreement with the values of the similar gas-phase systems reported for comparison. Greater discrepancies are observed for the values of the intermediate structures, A2/Z2 and A3/Z3. In fact, while the energy barriers of the R2-a and R2-z reactions are very

close to that of the gas systems, the presence of many resonance sites makes these structures (especially Z2 and Z3) significantly more stable than the gas-phase analogous.

Kinetic rates of the investigated reactions are calculated according to the transition state theory (TST) as reported in (1):

$$k = \frac{k_b T}{h} e^{\left(-\frac{\Delta G}{RT}\right)} \quad \left[\frac{1}{s}\right] \tag{1}$$

Where k_b is Boltzmann's constant, h is Plank's constant, R is the universal gas constant and ΔG is the Gibbs free energy calculated with the quasi-harmonic approximation. These rates were then fitted according to the modified Arrhenius equation (2) considering a range of temperatures of interest for CVI processes [i.e., 900-1800 K].

$$k = AT^n e^{\left(-\frac{Ea}{RT}\right)} \quad \left[\frac{1}{s}\right] \tag{2}$$

Thus, the three kinetic parameters, A (pre-exponential factor), n (temperature dependence factor) and Ea (activation energy), were derived for each of the investigated reactions.

Conclusions

This work presents a systematic investigation of the gas-solid interactions that occur during PyC growth in CVI reactors. The chemical pathways involved in the formation of a new carbon ring on both zigzag and armchair edges following acetylene deposition were studied to further investigate the microkinetic of the "growth mechanism." The kinetic constants of the elementary steps involved were estimated through TST. These constants will allow further upgrading of an existing semi-detailed kinetic mechanism [3] to describe pyrocarbon deposition from hydrocarbons cracking in CVI reactors, ultimately extending it to also include the formation of structural defects. In fact, the formation of 5-carbon ring, as observed in C_2H_2 deposition on zigzag edge, could have a strong impact on the quality of the final material (e.g., through curvature). Overall, this work constitutes a further step forward in the development of predictive kinetic models in the context of turquoise hydrogen and value-added carbon materials production.

References

[1] X. Bourrat, J. Lavenac, F. Langlais, R. Naslain, The role of pentagons in the growth of laminar pyrocarbon, Carbon. 39 (2001) 2376–2380.
[2] M. Guellali, R. Oberacker, M.J. Hoffmann, W.G. Zhang, K.J. Hüttinger, Textures of pyrolytic carbon formed in the chemical vapor infiltration of capillaries, Carbon. 41 (2003) 97–104.
[3] F. Serse, Z. Ding, M. Bracconi, M. Maestri, A. Nobili, C. Giudici, A. Frassoldati, T. Faravelli, A. Cuoci, M. Pelucchi, A comprehensive kinetic framework for solid carbon deposition and hydrogen production from the pyrolysis of light hydrocarbons streams, Carbon Trends. 11 (2023) 100263.

[4] Z.-B. Ding, E.D. Marco, M. Pelucchi, T. Faravelli, M. Maestri, First-principles assessment of the analogy between gas-phase and gas-solid H-abstraction reactions at graphene edges, Chemical Engineering Journal. 377 (2019) 119691.
[5] J.P. Perdew, K. Burke, M. Ernzerhof, Generalized Gradient Approximation Made Simple, Phys. Rev. Lett. 77 (1996) 3865–3868.
[6] H. Shu, X. Chen, X. Tao, F. Ding, Edge Structural Stability and Kinetics of Graphene Chemical Vapor Deposition Growth, ACS Nano. 6 (2012) 3243–3250.
[7] T. Ma, W. Ren, X. Zhang, Z. Liu, Y. Gao, L.-C. Yin, X.-L. Ma, F. Ding, H.-M. Cheng, Edge-controlled growth and kinetics of single-crystal graphene domains by chemical vapor deposition, Proceedings of the National Academy of Sciences. 110 (2013) 20386–20391.
[8] W. Zhang, X. Yu, E. Cahyadi, Y.-H. Xie, C. Ratsch, On the kinetic barriers of graphene homo-epitaxy, Applied Physics Letters. 105 (2014) 221607.
[9] X. Zhang, L. Wang, J. Xin, B.I. Yakobson, F. Ding, Role of Hydrogen in Graphene Chemical Vapor Deposition Growth on a Copper Surface, Journal of the American Chemical Society. 136 (2014) 3040–3047.
[10] G. Henkelman, B.P. Uberuaga, H. Jónsson, A climbing image nudged elastic band method for finding saddle points and minimum energy paths, The Journal of Chemical Physics. 113 (2000) 9901–9904.
[11] A.H. Larsen, J.J. Mortensen, J. Blomqvist, I.E. Castelli, R. Christensen, M. Dułak, J. Friis, M.N. Groves, B. Hammer, C. Hargus, E.D. Hermes, P.C. Jennings, P.B. Jensen, J. Kermode, J.R. Kitchin, E.L. Kolsbjerg, J. Kubal, K. Kaasbjerg, S. Lysgaard, J.B. Maronsson, T. Maxson, T. Olsen, L. Pastewka, A. Peterson, C. Rostgaard, J. Schiøtz, O. Schütt, M. Strange, K.S. Thygesen, T. Vegge, L. Vilhelmsen, M. Walter, Z. Zeng, K.W. Jacobsen, The atomic simulation environment—a Python library for working with atoms, Journal of Physics: Condensed Matter. 29 (2017) 273002.
[12] L. Pisani, J.A. Chan, B. Montanari, N.M. Harrison, Electronic structure and magnetic properties of graphitic ribbons, Phys. Rev. B. 75 (2007) 064418.
[13] L. Zhao, R.I. Kaiser, B. Xu, U. Ablikim, M. Ahmed, D. Joshi, G. Veber, F.R. Fischer, A.M. Mebel, Pyrene synthesis in circumstellar envelopes and its role in the formation of 2D nanostructures, Nature Astronomy. 2 (2018) 413–419.
[14] T.-C. Chu, M.C. Smith, J. Yang, M. Liu, W.H. Green, Theoretical study on the HACA chemistry of naphthalenyl radicals and acetylene: The formation of C12H8, C14H8, and C14H10 species, International Journal of Chemical Kinetics. 52 (2020) 752–768.

SESSION IX

LOW-CARBON FUELS AND LOW-EMISSION STATIONARY COMBUSTION CONCEPTS


THE COMBUSTION INSTITUTE
1954

Direct numerical simulation of thermodiffusively unstable lean NH3/H2-air flame

F. D'Alessio*, P.E. Lapenna*, F. Creta*
francesco.dalessio@uniroma1.it
*Department of Mechanical and Aerospace Engineering, Sapienza University of Rome, Via Eudossiana 18, Rome, 00186, Italy

Abstract
Carbon-neutral fuels and energy carriers are crucial for decarbonization, and ammonia has recently gained attention as a promising candidate due to its potential as a hydrogen carrier and carbon-free fuel. However, ammonia combustion poses challenges due to its low reactivity and high nitrogen oxide emissions, which require additional research efforts. In this contribution, we use a high-order, low-Mach number reactive flow solver to perform a direct numerical simulation of ammonia premixed combustion and shed light on intrinsic instabilities of the ensuing flame. The thermodiffusive stability limits of mixtures of technical interest are investigated and a numerical reconstruction of the dispersion relation of a target mixture is carried out. Then a direct simulation is performed on a medium-scale domain in order to investigate the impact of intrinsic instability on flame propagation and pollutants formation. The onset of cellular structures typical of intrinsically unstable flames is observed resulting in regions of super-adiabatic temperatures leading to enhanced pollutant formation.

Introduction
Ammonia has gained attention as a potential carbon-neutral fuel source due to its versatility and possible direct use in combustion-based processes [1,2]. However, direct combustion of ammonia poses significant challenges, including high NOx emissions and poor reactivity. While reactivity issues can be addressed by hydrogen-enrichment or cracking the ammonia molecule [3], the high NOx emissions are still a problem that can only be addressed through efficient and innovative combustion strategies [4]. A strategy to reduce NOx emission is to consider lean Ammonia-Hydrogen mixtures, containing high hydrogen percentages. These mixtures are prone to the thermodiffusive instability generated by the unbalance in thermal and molecular diffusion and the Darreius-Landau instability. Lean hydrogen mixtures have a low Lewis number due to the high mass diffusivity of hydrogen relative to the thermal diffusivity, which can activate the thermodiffusive instability mechanism and lead to severely corrugated flame fronts and increased fuel conversion rates [5,6,7]. Extensive asymptotic studies have been conducted on the stability of planar flames, although none of the theoretical models are able to completely describe flame development in the presence of thermo-diffusive instabilities [8,9]. Direct numerical simulations with detailed chemistry, which can resolve all spatiotemporal scales, are

necessary to eliminate any simplifying assumptions [10,11]. Analytical methods are used to identify the thermodynamic conditions that favour the occurrence of thermodiffusive instabilities in an ammonia-hydrogen mixture. A stability analysis, which monitors the growth rate of a planar flame subjected to initial weak harmonic disturbances, is used to fully characterize the stability properties of these mixtures. Direct numerical simulations are used to establish the flame's dispersion relation and associated cut-off wavelength for the typical conditions of a gas turbine burner. Finally, a medium size 2D DNS simulation allows for extensive local analysis of NOx formation downstream of the convective structures typical of thermodiffusively unstable flames.

Numerical setup and methodology

A preliminary study on conditions of presumed thermodiffusive instability for NH3/H2/air flames was conducted using an approach recently proposed by [9,12,13]. Different blends, equivalence ratios and pressures were considered at this stage. Linear stability analysis on a premixed flame front yields Eq.1 expressing the growth rate $\tilde{\omega}$ of a perturbed flame front with perturbation of wavenumber $\tilde{\kappa}$:

$$\tilde{\omega} = \omega_{DL}\tilde{\kappa} + \omega_2 \tilde{\kappa}^2 \quad (1)$$

where $\tilde{\omega}=\omega\tau_f$, with $\tau_f=l_t/S_L^0$ the characteristic flame time computed through the thermal flame thickness l_t . The Darrieus-Landau coefficient ω_{DL} takes the form:

$$\omega_{DL} = \frac{1}{\sigma+1}\sqrt{\sigma^3+\sigma^2}-\sigma-\sigma \quad (2)$$

where $\sigma=\rho_b/\rho_u$ is the expansion ratio due to thermal gradient. The ω_2 coefficient introduced by Matalon [14] takes the form:

$$\omega_2 = B_1 + \beta\left(Le_{eff}-1\right)B_2 + PrB_3 \quad (3)$$

where Pr is the Prandtl number, β is the Zel'dovich number, Le_{eff} is the effective Lewis number [15,16,17]. Parameters B_1,B_2,B_3 are all functions of the expansion coefficient once the dependence of the transport coefficients on temperature is specified [9]. The sign of ω_2 ,the coefficient of the second-order term, characterizes the thermo-diffusive stability of premixed flames. The region where instabilities are expected to develop corresponds to $\omega_2 > 0$ as this translates into thermodiffusive effects becoming destabilizing, i.e., contributing to an increase in the growth rate in addition to the hydrodynamic effect, as can be seen in Eq. 1. Figure 1(left) shows a map of ω_2 as a function of equivalence ratio and hydrogen content in ammonia mixtures. Such a map was obtained through unstretched laminar flame simulations performed in Cantera [18] using the kinetic mechanism proposed by Stagni et al. [19] which involves *31* species and *203* reactions.

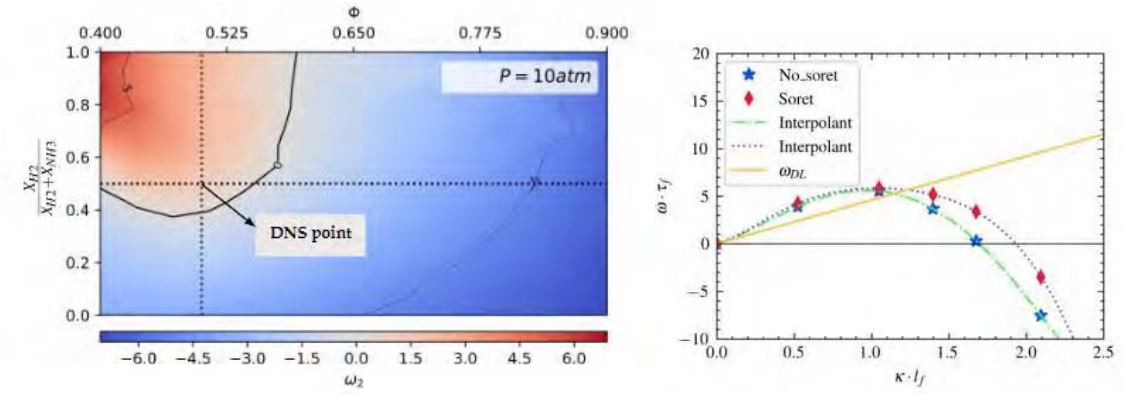

Figure 1. (Left) ω2 field as a function of equivalence ratio, and hydrogen volumetric percentage in the mixture at 10 atm. **(Right)** Numerical dispersion relation for a flame with without The Soret effect. DNS data are marked with stars (without Soret) and diamonds (with Soret).

The unstable region widens with increasing pressure and hydrogen content. Upon examination of such maps, the point chosen for further DNS investigation is well into the instability region and is indicative of a small-size gas turbine burner pressure of *10atm*, a mixture temperature of *500K* and a fuel composition of *50%NH3/50%H2* (% in vol). Direct numerical simulations are performed under the low-Mach assumption using the spectral element code Nek5000, which was heavily modified to accomodate a detailed chemistry formulation. Chemical kinetic and transport properties were tabulated as a function of temperature. Species diffusion is modeled via the Hirschfelder-Curtiss approximation with a correction velocity, while the Soret effect is considered only for lighter species (*H, H*2) following the work from Schlup and Blanquart [20]. The Kinetic model used is a skeletal mechanism proposed by Gotama et al. [21] involving *25* species and *110* reactions. This mechanism was preferred to that proposed by Stagni et al. [19] due to the smaller size. As mentioned, the dispersion relation is the function $\omega(k)$ linking the growth rate to the initial perturbation wavenumber $\kappa=2\pi/\lambda$, while the value of the wavelength corresponding to the transition from negative to positive growth-rates determines the cut-off scale λ_c. The cut-off wavelength λ_c represents a thermochemical length scale dependent on the mixture properties alone. If the flame is constrained laterally by the hydrodynamic length L, then it is unstable to perturbations of wavelengths $\lambda_c<\lambda<L$ [22].

Results and discussion

To compute the cut-off length scale through DNS, a planar flame was selectively perturbed by a harmonic perturbation of variable wavelength and the growth rate monitored. The wavelength is set to the same spanwise length as domain D_y and is varied by changing the domain size in that direction. The ensuing numerical dispersion relation is shown in Figure 1 (right panel) for the DNS point depicted on the ω_2 map in Figure 1 with two distinct transport models with and without the Soret

effect, respectively. Results are shown in non-dimensional units. The Soret effect marginally modifies the cut-off wavelength; in dimensional units, $\lambda_{Coff}^{NS}=1.2mm$ without the Soret effect and drops to $\lambda_{Coff}^{S}=1.0mm$ with the Soret effect. The Soret effect seems to impact the cut-off wavelength alone, while the maximum growth rate is unaltered: $\omega_{Max}=0.926\ s^{-1}$, which corresponds to a $\lambda_{\omega_{Max}}=2.09mm$. The nonlinear evolution of the flame is studied by letting the flame evolve in a domain measuring $D_x=60l_t$ in the streamwise direction and $D_y=10\lambda_c \approx 37l_t$ in the spanwise direction. A spatial resolution of *50* points in flame thickness was chosen for perturbed flames while *20* points in flame thickness was chosen for the medium-scale simulation. The nonlinear evolution produces unstable chaotic cell structures along the flame front, which annihilate and continuously regenerate. Because of their tendency to form wrinkles, such flames are characterized by higher reactivity in the regions that are positively curved and stretched. In fact, the Markstein length of a thermodiffusively unstable mixture is negative, therefore a positive stretch results in a higher local flame speed [23]. The consumption speed S_c provides an integral measure of flame speed and is defined as:

$$S_c = -\frac{1}{\rho Y_{r,u} D_y}\int \dot{\omega}_r\, dxdy = I_0 \frac{\Sigma}{A_0} S_L^0 \tag{4}$$

where ρ_u is the mixture density in the unburnt side, $Y_{r,u}$ is the mass fraction of a reactive that is fully depleted across the flame front (in this paper we choose NH_3), D_y is the y-domain length, and $\dot{\omega}_r$ is the net specie's production rate. To better understand the reasons for the flamespeed increase, the consumption speed may be represented as a function of the area growth ratio Σ/A_0 caused by flame surface wrinkling and I_0 which accounts for changes in reactivity caused by a flame stretch where Σ is defined as the area of an iso-surface of progress variable [24], while A_0 is the laminar flame's hydrodynamic length, in our case $A_0=D_y$. The average consumption rate starts at *15* flame times after reaching a fully non-linear regime $\langle S_C \rangle \approx 2.93 S_L^0$. The average contribution of area growth factor $\langle \Sigma/A_0 \rangle \approx 2.26$ while the contribution due to changes stretched flame reactivity $\langle I_0 \rangle \approx 1.35$. While the significant increase in the flame surface area contributes the most to the rise in flame speed, even little changes in flame reactivity can result in major changes in *NOx* generation. Because of the difference between thermal and mass diffusion, lighter species such as *H* and *H2* concentrate in the positively curved regions of the flame, affecting the nominal equivalence ratio [20,25]. Figure 2 shows the local equivalence ratio adimensionalized with respect to nominal equivalence ratio. Figure 3 shows the joint PDF of the mass fraction of *NO* and NO_2 with respect to the progress variable. The conditional mean $\langle Y_k | C_{NH_3} \rangle$ and the unstretched flamelet are shown too. On the side, the PDFs of the *NO* and NO_2 mass fraction are shown for clarity for all data with $C_{NH3} > 0.05$ so as not to bias the PDF with the portion of the domain corresponding to the fresh mixture. Again, the values

corresponding to $C_{NH3} = 1$ of the unstretched flamelet and the conditional mean are shown on this graph. There is a significant spread of Y_{NO} and Y_{NO2} with respect to C_{NH3} and significant differences with respect to the unstretched flamelet. Two branches of pollutant concentration can be distinguished, one with high production and the other with significantly reduced or absent production compared to the unstretched flame.

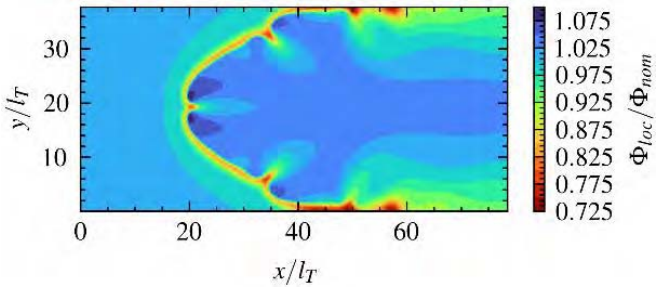

Figure 2. Local equivalence ratio field adimensionalized w.r.t. nominal equivalence ratio ϕ=0.5

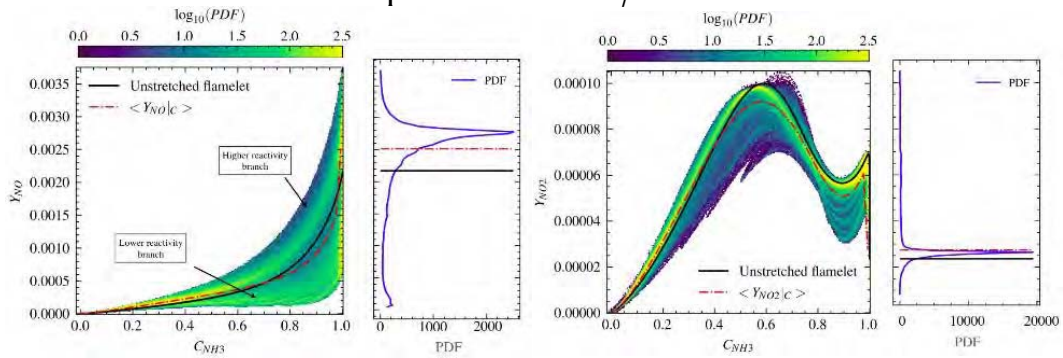

Figure 3. Joint PDF of the mass fraction of *NO* and NO_2 with respect to the progress variable

Overall, however, *NO* and NO_2 production in the corrugated flames is higher than in the unstretched one-dimensional flames. This result is striking as the natural morphology of the flame seems to be responsible for an increased global production of *NOx* with respect to the nominal unstretched 1D flame.

Conclusion

In this study, a mixture of 50%NH_3-50%H_2 was analysed under conditions typical of a small gas turbine. Under these conditions, the occurrence of thermodiffusive instabilities was predicted by analytical methods and subsequently numerically quantified. These instabilities profoundly change the structure of the flame front by creating wrinkles that increase the area and stretch the flame front, impacting on the consumption speed and on the production of *NOx*, which, immediately downstream of the flame is 23% higher in the wrinkled flame than in the unstretched 1D flamelet.

References

[1] H. Kobayashi, A. Hayakawa, K. D. A. Somarathne, E. C. Okafor, Proceedings of the Combustion Institute 37 (2019) 109–13.

[2] C. Tornatore, L. Marchitto, P. Sabia, M. D.Joannon, Frontiers in Mechanical Engineering 8 (2022).
[3] B. Mei, J. Zhang, X. Shi, Z. Xi, Y. Li, Combustion and Flame 231 (2021).
[4] MG Božo, S Mashruk, S Zitouni, A Valera-Medina Energy Conversion and Management 227, 113625.
[5] M. Baum, T. J. Poinsot, D. C. Haworth, N. Darabiha, Journal of Fluid Mechanics 281 (1994) 1–32.
[6] E. G. Groff, Combustion and Flame 48 (1982) 51–62.
[7] L. Berger, A. Attili, H. Pitsch, Combustion and Flame 240 (2022).
[8] F. Creta, P. E. Lapenna, R. Lamioni, N. Fogla, M. Matalon, Combustion and Flame 216 (2020) 256–270.
[9] M. Matalon, Fluid Dynamics Research 50 (2018).
[10] C. E. Frouzakis, N. Fogla, A. G. Tomboulides, C. Altantzis, M. Matalon, Proceedings of the Combustion Institute 35 (2015) 1087–1095.
[11] C. Altantzis, C. E. Frouzakis, A. G. Tomboulides, K. Boulouchos, Combustion and Flame 162 (2015) 331–344.
[12] T. L. Howarth, A. J. Aspden, Combustion and Flame 237 (2022).
[13] A. Attili, R. Lamioni, L. Berger, K. Kleinheinz, P. E. Lapenna, H. Pitsch, F.Creta, Proceedings of the Combustion Institute 38 (2021) 1973–1981.
[14] M. Matalon, Annual Review of Fluid Mechanics 39 (2007) 163–191.
[15] M. Matalon, C. Cui, J. K. Bechtold, Journal of Fluid Mechanics 487 (2003) 179–210.
[16] Lapalme D., Lemaire R., Seers P, International Journal of Hydrogen Energy, (2017), 8314-8328, 42(12).
[17] P. Clavin, P. Garcia-Ybarra, Journal de Physique Theorique et Appliquee 2 (1983) 245–263.
[18] D. G. Goodwin, H. K. Moffat, I. Schoegl, R. L. Speth, B. W. Weber, Cantera, https://www.cantera.org, 2022. Version 2.6.0
[19] A. Stagni, C. Cavallotti, S. Arunthanayothin, Y. Song, O. Herbinet, F. Battin-Leclerc, T. Faravelli, Reaction Chemistry and Engineering 5(2020) 696–711.
[20] J. Schlup, G. Blanquart, Combustion and Flame 191 (2018) 1–8
[21] G. J. Gotama, A. Hayakawa, E. C. Okafor, R. Kanoshima, M. Hayashi, T. Kudo, H. Kobayashi, Combustion and Flame 236 (2022).
[22] P. E. Lapenna, R. Lamioni, G. Troiani, F. Creta, Proceedings of the Combustion Institute 37 (2019)
[23] G. K. Giannakopoulos, A. Gatzoulis, C. E. Frouzakis, M. Matalon, A. G. Tomboulides, Combustion and Flame 162 (2015) 1249–1264
[24] L. Vervisch, E. Bidaux, K. N. C. Bray, W. Kollmann, Physics of Fluids 7 (1995) 2496–2503.
[25] C. Netzer, A. Ahmed, A. Gruber, T. Løv˚as, Combustion and Flame 232 (2021)

The Decarbonization of Steel Heating Processes – Tenova Simulation/Experimentation Model for the Net-Zero Challenge

A. Della Rocca*, A. Astesiano**
alessandro.dellarocca@tenova.com
*, ** Tenova S.p.A., Via Albareto, 31 - 16153 Genova, Italy

Abstract
An integrated approach combining simulation and experimentation has traditionally been used in Tenova to guide the development of novel combustion technologies. This approach is here reviewed and updated towards the new challenges posed by the net-zero goal for the world steel industry. In particular, the in-house modeling experience is substituted with a collaborative approach bringing together academia and industry expertise for ad hoc development of scalable modeling approaches. In parallel, the new T-Lab is designed as a resource that can be shared in combustion research as well as in industrial development applications through different funding vehicles (public or private). This open development strategy is well suited to the technology agnostic approach that steel industry is facing in order to meet its 2050 objectives.

The net-zero challenge of the steel industry

Hard-to-abate sectors are facing increasing pressure from the global community to steer their production technologies towards Paris compliant solutions. The steel industry is part of this effort, since it is already aligning its investment strategy in directions that will tackle the decarbonization challenge. It is estimated that 8% of world greenhouse gas emissions come from iron and steel industry, totaling about 2.6 Gt_{CO2e} per year and giving a carbon emission intensity of 1.38 t_{CO2e} per ton of crude steel. Therefore, the most advanced steelmakers are already taking into account several energy transition strategies to hit the carbon neutrality by 2050.
Originally, the decarbonization efforts on the steel production processes were concentrated on the upstream portion (i.e., the liquid steel production either from iron ores or from scrap recycling). Since it is well know that steel scrap recycling is very efficient in terms of input energy and is characterized by low direct emissions, much of technological developments were concentrated on the integral route (Figure 1). Direct reduction technologies, either based on natural gas or involving green hydrogen as reducing agent, are the emerging production routes to substitute traditional blast furnaces while more than halving standard emission intensity.

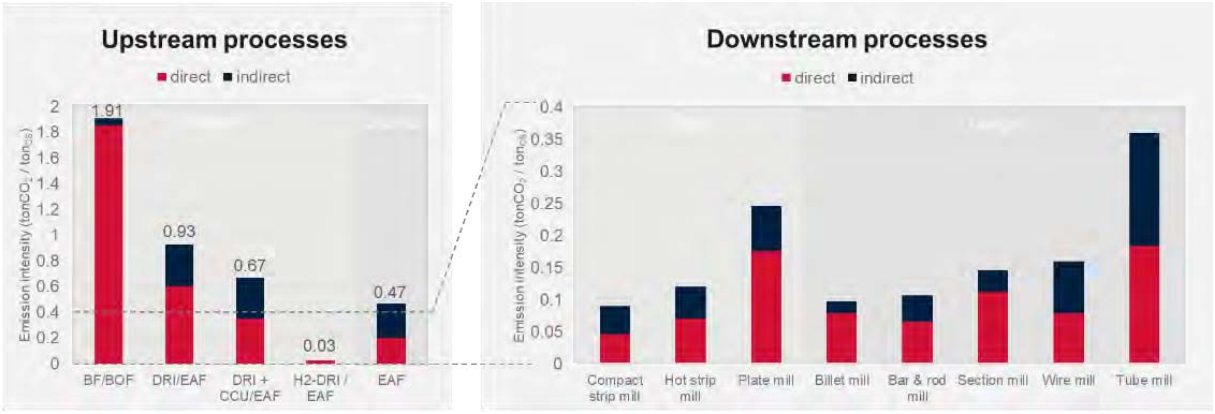

Figure 1. Carbon emission intensity of different steel production technologies. Upstream processes: blast furnace route (BF/BOF), direct reduction with electric melting without (DRI/EAF) and with CCU (DRI+CCU/EAF), hydrogen-based direct reduction with electric melting (H2-DRI/EAF). Downstream processes: divided by hot rolling mill type for flat and long products.

Relevantly, also downstream processes have an impact when compared against steel recycling or direct reduction processes. Generally, the more the transformation steps required form the final products, the higher the CO2 emission intensity. This exemplifies the need for decarbonization of heating furnaces, which are the main carbon emitters in downstream processes.
For these reasons, steel industry required the implementation of low-carbon heating technologies in alternative to traditional fossil fuel firing of industrial burners. Direct use of electrical energy, either by resistive, inductive or plasma solutions, is not sufficient in substituting existing combustion systems due to intrinsic process constraints (i.e., high process temperature, thermal power density, steel product dimensions, surface oxidation). Combustion technologies with low carbon footprint are thus required for industrial heating furnaces: either by the carbon direct avoidance route, making use of low-carbon energy carriers such as hydrogen, ammonia or methanol, or by smart carbon usage, such as CCUS and high efficiency solutions.

Updating Tenova's simulation/experimentation model to the net-zero challenge
During the previous three decades, Tenova developed its own approach for the development of industrial combustion systems. In particular, the R&D approach began integrating computational fluid dynamics (CFD) modeling since the very early days of this technique in 1908s. Originally devoted to very special projects, it was not until 2000s that Tenova integrated CFD simulations into its standard burner development workflow [1].
During these early applications, it became clear that simulation activity could not exist without a parallel experimentation work. These lab tests were carried out at full industrial scale, but limiting the burner thermal power to the lower end of the typical range in real furnace installations.

This iterative approach between CFD simulations and corresponding laboratory tests of the same CFD model was the basis of all the burner development activities that were carried out from 2005 until now [1], leading to the development of large flameless (MILD) burners (1-5 MW), regenerative, self-regenerative, self-recuperative and radiant tube burners.
This same successful approach must be properly adapted to tackle the challenges of steel industry decarbonization [2]. From Tenova's perspective of equipment & technology provider to steel producers, there is no win-it-all solution to reduce the carbon intensity of heating furnaces in the downstream applications. Instead, a combination of heating and emission reduction technologies must be in place in order to reach the techno-economic balance. Above these solutions, heating process efficiency plays a fundamental role in this framework, since nowadays any low-carbon technology is likely to increase transformation cost. Being able to control combustion process conditions accurately or even predicting the most likely evolution of its state variables on a short time range brings a new challenge to statistical process model (e.g., machine learning models). To this end, digitalization and pervasive sensorization applied to industrial burners [2, 3] are able to produce a huge amount of process data at relatively limited cost.
For these reasons, the simulation/experimentation model of Tenova burner development must be properly updated by integrating industrial data analysis from the burner installations sites, as well as adding a new layer of advanced combustion diagnostics and measurements during the burner characterization tests (Figure 2).

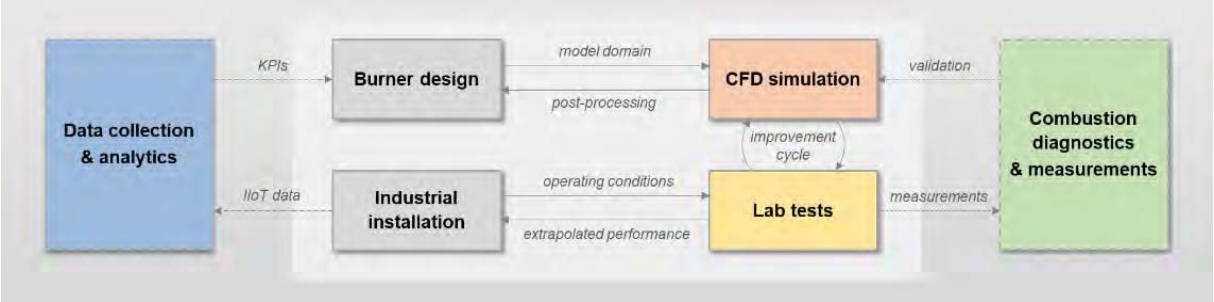

Figure 2. Tenova simulation/experimentation model for burner development. The standard model at the core is expanded with digitalization activities performed at industrial installation sites (left) and combustion diagnostics activities performed during laboratory characterization tests (right).

The combustion diagnostics and measurements stage is added in parallel to standard measurements (i.e., temperature, pressure and chemical species in fumes) carried out during lab tests of industrial prototypes with the aim to gather insight about the development of the combustion process. This proves to be a challenging step for laboratory measurement techniques, because the prototypes are realized in full industrial scale (1-5 MW for free flame burners, 50-300 kW for radiant tube burners). Advancements and proper adjustments in measurements techniques, on example by using spontaneous chemioluminescence rather than standard laser induced flame

spectroscopy, are required to cover the dimensional gap. The measured quantities (radicals concentration, flame velocity, radiative flux, etc) would provide valuable information to the verification of CFD modeling activities (turbulence model, turbulence/chemistry closure, skeletal kinetic scheme, radiation model, etc) and the continuous improvement of the simulation approach. These topics are essential additions to the standard simulation/experimentation model in the current energy transition scenario that is considering use of mixtures between fossil fuels and green fuels (e.g. green hydrogen or methanol) or use of other energy carriers (e.g., green ammonia). Furthermore, all these activities require a heterogeneous team mixing the industrial expertise from Tenova with more specialist knowledge from academia and research organizations.

On the application side, data collection and analytics are made possible with Industrial Internet of Things (IIoT) approaches, which rely on a large amount of low cost sensors integrated into specific burner components [2]. If on one side a large data collection is required from real industrial installations in order to extract robust statistics and relevant Key Performance Indicators (KPIs), on the other side the large amount of sensors required must result from a dedicated development approach. Accurate and expensive industrial sensors are not an affordable solution in IIOt applications, thus soft sensing techniques and use of mass-produced sensors (e.g, from automotive industry) appear as the most promising routes to arrive at sustainable solutions. Once again, these activities require a close cooperation between burner designers or installation technicians and experts in advanced measurements models and techniques. No standard workflow is thus applicable to tackle the energy transition challenge for the steel industry and a proper integration between different backgrounds appears to be necessary to quickly develop novel combustion technologies.

T-Lab as a demonstrator for low-carbon combustion technologies

Recognizing the change of perspective required to attain the decarbonization goals of the steel industry, Tenova dedicated a relevant effort in developing the proper R&D organization to navigate this challenge. During 2020 Tenova started construction and installation works for T-Lab, a large industrial scale combustion laboratory equipped with state-of-the-art combustion technologies and laboratory equipment (Figure 3). The goal of this infrastructure was far from being limited to burner characterization tests, since it was aimed at creating the proper playground for the newly mixed project teams required in developing low-carbon combustion technologies. In particular, T-Lab was designed by having in mind the need to directly integrate combustion tests with Tenova Digital Platform extending from novel proprietary sensors and measurement equipment (e.g., Tenova EFSOP® off-gas analyzer) up to IIoT devices (e.g., Tenova AlphaEdge units). Additional layout space was left around the building to allow installations of low-carbon pilots, such as containerized electrolyzers for green hydrogen production. While the essential infrastructure with standard natural gas piping and combustion air fan is currently

fully operative, T-Lab buildings are still at an expansion stage, with a new bunker for e-fuels and syngas truck storage and an oxygen storage unit still at design stage. All these efforts are also complemented by actively participating in the European Seventh Framework Programmes, such as the European Steel Technology Platform (ESTEP), involving customers and partners in public research funds in Research Fund for Coal and Steel (RFCS) and HorizonEU programs and supporting academic & research organizations in COST Actions, Marie Skłodowska-Curie Actions and other research programmes with the goal to build a network of expertise about combustion science & technology.

Figure 3. Tenova T-Lab panoramic picture showing the control room for enhanced automation and digital applications (left), the waste gases and heat recovery system (middle) and one of the test furnaces (right).

References

[1] Ageno, M., Della Rocca, A., Fantuzzi, M., Battaglia, V., Malfa, E., Zanusso, U., "Tenova FlexyTech® TRGX burner modelling and testing", *Proc. AISTech Conf.*, Pittsburgh, PA, May 3-6, 2010.

[2] Della Rocca, A., Astesiano, D., Malfa, E., "Rolling mill decarbonization: Tenova SmartBurners with 100% hydrogen", *Mat. & Tech.*, 109:309, 2021.

[3] Astesiano, D., Bissoli, M., Della Rocca, A., Malfa, E., "Tenova SmartBurners: full hydrogen flexibility to reduce furnaces CO_2 footprint", *Proc. INFUB 13*, Algarve, Portugal, April 19-22, 2022.

LES study of a H2/Air cyclonic combustor operating in MILD regime

S. Carpenella*, D. Cecere*, I. Quaranta*, E. Giacomazzi*, G. Sorrentino, P. Sabia** and G. Battista Ariemma****

simone.carpenella@enea.it

*TERIN-PSU-IPSE, ENEA, Rome, Italy

**CNR-STEMS, Naples, Italy

Abstract

MILD combustion is one of the promising techniques to reduce pollutant emissions, such as NO_x, in combustion processes. It is also a promising technique to burn hydrogen: the highly diluted conditions mitigate its reactivity and its calorific power. The cyclonic flow configuration adopted in this work may represent a proper way to enhance the mixing process while allowing for residence times long enough to achieve complete oxidation of diluted and preheated mixtures. In this work, Large Eddy Simulation (LES) of a Hydrogen/Air cyclonic burner operating in the MILD combustion regime at atmospheric pressure is performed using ENEA's in-house code, HeaRT. Accurate molecular transport properties and a reduced chemical mechanism are considered. Radiative and wall heat exchange effects are also modelled. Results show that temperature is quite uniform along the whole burner, with an average value of 1350 K, lower than that typically measured in standard hydrogen combustion. This condition leads to very low NO_x emissions, the thermal path being the main NO formation mechanism. The NO_x values obtained at the burner outlet are lower than 30 ppm, confirming the possibility of burning hydrogen under MILD combustion conditions.

Introduction

The scientific community interest is focused on the identification of new technologies that would allow more efficient energy production systems, in terms of energy production and of pollutants abatement. As a matter of fact, despite some innovative combustion technologies [1], the simultaneous attainment of a high combustion efficiency and of an acceptably low pollutant emission is very difficult due to increasingly more stringent regulations on pollutant emission limits. Among them, Mild combustion is based on the concept of hot exhaust gas recirculation, and consequently preheating and dilution of reactants. In fact, while the heat from the exhaust gases causes an increase in the reactants' temperature, the exhaust gases dilute the mixture, reducing the oxygen concentration and maintaining a low temperature in the combustion region [2]. In this combustion process, the inlet temperature of the reactant mixture is higher than the mixture self-ignition temperature whereas the maximum allowable temperature increase with respect to inlet temperature during combustion is lower than the self-ignition temperature [3]. Because of these conditions and of the presence of inert species concentration in the

comburent flow, which is much larger than in the air condition, the characteristic times of chemical kinetics and turbulent mixing are comparable and the process is characterized by: a distributed reaction zone, relatively uniform temperatures, high radiative heat transfer, no visible flame, low noise, tendency to dampen fluctuations and instabilities, negligible soot formation, very low NO_x and CO emissions and flexibility with respect to fuel. A particular application of Mild combustion is in processes that employ hydrogen as fuel. In fact, Mild operative conditions allow mitigating the hydrogen characteristics such as its high laminar flame speed, high adiabatic flame temperature, and heating value, high reactivity, which make conventional burners unsuited [4]. To realize Mild combustion operating conditions, configurations with high momentum injection of the reactants are adopted: the flue gas recirculation reduces the oxygen concentration in the flame zone, due to a fast mixing between the oxidizer and the combustion products flows, and increases the temperature of the fresh reactants realizing mixtures under ignition conditions distributed throughout the burner volume. An effective method to create the recirculation zone involves the use of a cyclonic configuration which allows long residence time inside the combustor, large and multi-reaction zones, high turbulence levels generated from the high shear between oxidant and fuel streams, as well as large toroidal recirculation zone. In this work a Large Eddy Simulation (LES) of a cyclonic burner operating in the Mild combustion regime at atmospheric pressure is performed. Accurate molecular transport properties were taken into account and a detailed kinetic mechanism [5] for hydrogen-air combustion, consisting of 18 transported species and 77 elementary reactions and radiative and wall heat exchange effects are also modeled.

Test case definition and methodology

The test case defined for this study consists of a prismatic 20×5×20 cm burner (in the x-y-z direction respectively) at atmospheric pressure. The geometry is the same as that of the experimental device already analyzed in [6]. Two anti-symmetric couple of jets and the gas exit positioned at the central part of the burner top induce the cyclonic flow-field within the combustor chamber. Each couple of jets is composed of two cylindrical ducts, the oxidizer with an internal diameter of 0.8 cm, the fuel with 0.15 cm. The oxidizer flows are preheated to the inlet temperature of 550 K and injected at 28.9 m/s, while the fuel is 300 K with a velocity of 207 m/s. The nominal equivalence ratio is set to the stoichiometric value. The walls are set at 1253 K as in the experimental test. The oxidant injectors are located at 2 cm from the lateral walls, whereas the fuel injectors are at 4.5 cm. The domain is discretized through 330×111×250 points in the x,y and z directions respectively. Appropriate refinement of the grid is performed in the regions with higher gradients: the minimum grid width is located near the injection zones with $\Delta x = 85\mu m$, $\Delta y = 130\mu m$ and $\Delta z = 350\mu m$. The temperature and NO concentration are sampled with a frequency of 50 kHz on the yz-plane at x = 8 cm. Their average values are computed with 1000 samples at the moment, but new and more accurate statistics will be added.

The simulation was performed on the Linux cluster CRESCO (Computational Center for Complex Systems) at ENEA requiring ~ 3000 CPU hours on 3900 processors. The solution was advanced at a constant time step of 5.9 ns, with a CFL (Courant–Friedrichs–Lewy) set to 0.11, in order to ensure the stability of the numerical methods.

The simulation was performed using the "HeaRT" code, which solves the fully compressible reactive Navier-Stokes equations in their conservative formulation (the unfiltered Eqs. 1-4 in [7]) with the fully explicit third-order time accurate TVD Runge-Kutta scheme of Shu and Osher and a third order hybrid WENO spatial scheme for non-uniform grid. The ideal gas equation of state was assumed. In the HeaRT code, the Hirschfelder and Curtiss approximate formula is adopted to model molecular transport in a multicomponent mixture. Soret thermo-diffusive effect was considered. Binary diffusion coefficients and the n-th species thermo-diffusion coefficient were calculated through kinetic theory. All molecular properties for individual chemical species, except their binary mass diffusivities, are calculated a priori by using the software library provided by A. Ern (EGlib) [8]. In particular, kinetic theory is used for dynamic viscosity. The calculated values are stored in a look-up table from 200 to 5000 K with a delta of 100 K. Values for intermediate temperatures are calculated at run-time by linear interpolation. Binary mass diffusion coefficients are calculated by means of kinetic theory expressions at run-time. The mixture average properties are estimated by means of Wilke's formula with Bird's correction for viscosity, and Mathur's expression for thermal conductivity. Preferential diffusion is modeled according to the Hirschfelder and Curtiss law. Radiation M1 model is taken into account while turbulent viscosity is calculated by means of dynamic Smagorinsky model and the LTSM model for turbulent combustion closure [9].

Results

The main operational characteristics of cyclonic combustion burner were investigated through temperature and exhaust gas emission numerical predictions. MILD Combustion regime was achieved with reduced combustion peak temperatures due to the H_2O recirculation. Figure 1a reports the predicted average temperature and the average NO concentration profiles along the air jet axis. The temperature profile is quite uniform from 10 cm downstream of the air injector, with an average value of 1250 K, lower than that typically measured in standard hydrogen combustion. This condition leads to very low NO emissions, the thermal path being the main NO formation mechanism. The maximum dry basis NO concentration is lower than 9 ppm and it's located 15 cm downstream of the inlet holes, but better statistics are necessary for a more accurate prediction. Fig.1b shows the instantaneous temperature field on a slice at y = 0.025m. While the walls are set at the experimental temperature of 1253 K, it has a quite uniform field inside the volume, with an average value of about 1350 K. In addition, the isosurface at 1800

K shows how higher temperature values are confined in small regions of the combustion chamber, whereas the isosurface at 550 K highlights the air jet expansion and where the reactions begin to take place.
The injection system coupled with the position of the exit and due to its lower pressure allows for the establishment of a toroidal flow field (cyclonic motion) within the chamber. MILD combustion is therefore attained in the combustor due to the strong recirculation process of burned gases toward fresh reactants induced by this toroidal flow field. Figure 2 shows the average momentum field and the streamlines on a slice at y=0.025m. A trapped vortex takes place in the burner as well as two eddies near the corners in front of the jets, due to the presence of the walls. The high hydrogen momentum leads to a sharp change in the flow direction and because of its cross-flow injection, the H_2 jet is curved towards the near air jet; the longer potential core and suction effect of the air jet enhances the hydrogen jet bending. Moreover, where the two jets meet, a reacting shear layer develops exhibiting a non-premixed combustion with high-temperature hot pockets.

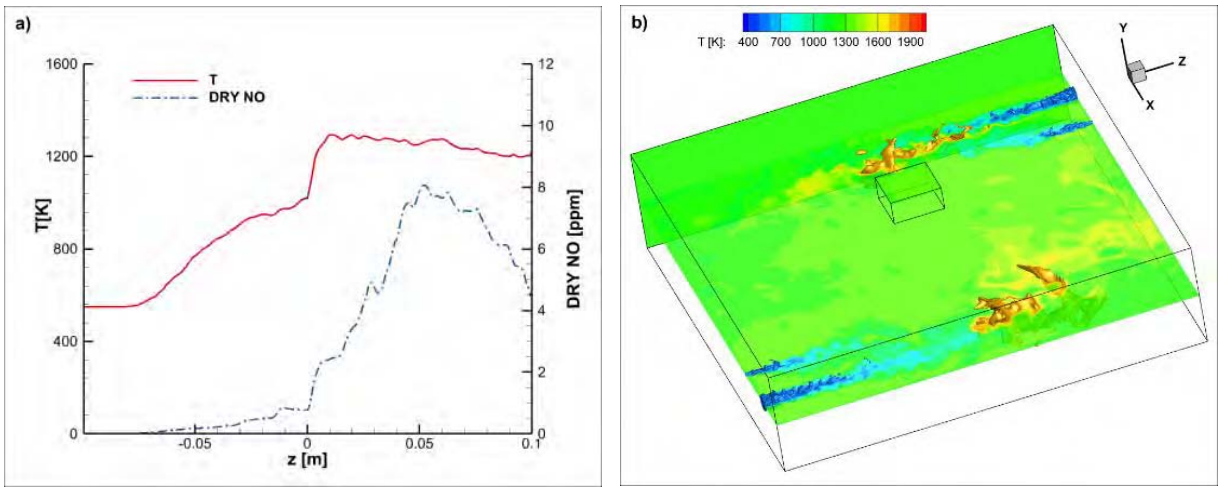

Figure 1. a) Predicted average temperature (solid line) and average dry basis NO concentration (dashed line) along the air jet. b) Temperature instantaneous contour on a slice at y = 0.025 m and temperature isosurface at T = 1800K.

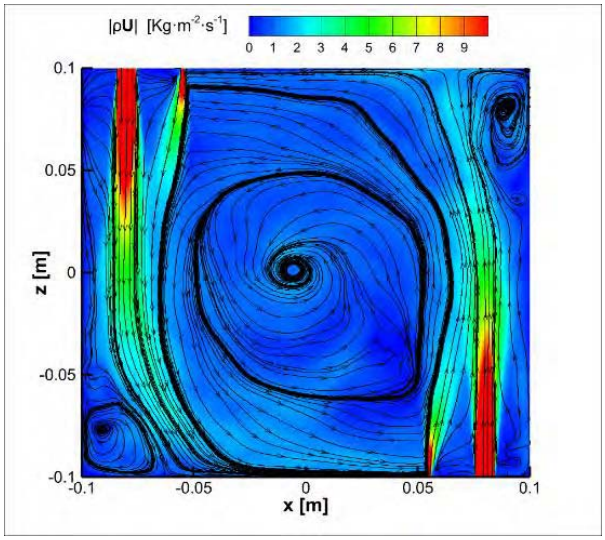

Figure 2. 2D average momentum field and streamtraces on a slice at y=2.5cm.

References

[1] G. Sorrentino, P. Sabia, P. Bozza, R. Ragucci and M. de Joannon, "Impact of external operating parameters on the performance of a cyclonic burner with high level of internal recirculation under MILD combustion conditions", *Energy*, 137: 1167-1174 (2017)

[2] Cecere D., Giacomazzi E., Picchia F. R., Arcidiacono N., "LES of H_2\Air MILD Combustion", *In Proceedings of the 31st Meeting of the Italian Section of the Combustion Institute*, 2008.

[3] Cavaliere A., de Joannon M., "Mild Combustion", *Progress in Energy and Combustion Science*, 30: 329-366 (2004).

[4] Galletti C., Parente A., Derudi M., Rota R., Tognotti L., "Numerical and experimental analysis of NO emissions from a lab-scale burner fed with hydrogen-enriched fuels and operating in MILD combustion", *International Journal of Hydrogen Energy,* 34: 8339–8351 (2009).

[5] Bowman C.T., Hanson R.K., Davidson D.F., Gardiner W.C., Lissianski Jr., V., Smith G.P., Golden D.M., Frenklach M., Goldenberg M., http://www.me.berkeley.edu/gri mech/.

[6] Ceriello G., Sorrentino G., Cavaliere A., Sabia P., de Joannon M., Ragucci R., "The role of dilution level and canonical configuration in the modeling of MILD combustion systems with internal recirculation", *Fuel*, 264: 116840 (2020).

[7] Cecere D., Giacomazzi E., "An immersed boundary method for Large Eddy Simulation of compressible flows using a staggered-grid approach.", *Comput. Methods Appl. Mech. Engrg*, 280: 1-27 (2014).

[8] Ern A., Giovangigli V., "Multicomponent Transport Algorithms", *Lecture Notes in Physics, M24*, Springer-Verlag, Heidelberg, 1994.

[9] Giacomazzi E., Cecere D., “A Combustion Regime-Based Model for Large Eddy Simulation”, *Energies*, 14(16): 4934 (2021).

MILD Combustion of Ammonia/Hydrogen mixtures

G.B. Ariemma*, G. Sorrentino*, P.Sabia*, R. Ragucci*, M. de Joannon*

corresponding author: giovannibattista.ariemma@stems.cnr.it

* Institute of Sciences and Technologies for Sustainable Energy and Mobility (STEMS-CNR), Naples, Italy

Abstract

In the present scenario related to the energy transition, fuel-flexible technologies for clean power generation and propulsion are of paramount importance. In this context, ammonia is considered as a key decarbonized energy carrier, due to its very high hydrogen-density and well-established production processes. MILD combustion already proved to be a very effective technology in burning ammonia in terms of stability and emissions performance. Despite that, the utilization of fuel enhancers in MILD combustion conditions can be useful to further improve the process characteristics. In this respect, the present work focuses on the combustion performance of ammonia/hydrogen blends. Experimental investigations were performed in a cyclonic-flow chamber operating under MILD Combustion conditions. NH_3/H_2/air mixtures oxidation was characterized in terms of process stability, operational temperatures and NO_x emissions, as a function of the equivalence ratio and $\%H_2$ in the fuel mixture. Results confirmed the MILD Combustion effectiveness for NH_3/H_2 blends conversion, with reasonable NO_x emissions. H_2 widens the stable operational region for NH_3 oxidation, because of the boosted OH production, that also increases the NH_3 yield to NO, thus entailing higher NO_x emission than the pure NH_3.

Introduction

The world energy scenario is currently faced with several economic and geopolitical constraints that are rapidly and continuously changing the possible scenarios of the near future energy market panorama. One of the hot topics that is currently on the table is the integration of several energy carriers capable of both supporting the "energy shift" and satisfying the energy demand [1]. In this framework, there is broad agreement that energy storage is a cornerstone of future renewable energy systems, for overcoming the limitations that hinder RES integration. In particular, chemicals-based storage [2] offers the advantage of storing large amounts of energy for long periods and at any location [3]. In this respect, renewable energy can be stored as synthetic chemical energy carriers, to produce fuels. In particular, electrical energy can be converted into hydrogen by electrolysis, that can be stored directly or converted into liquid or gaseous synthetic fuels like ammonia [3]. In this respect, using carbon-free chemical energy carriers such as hydrogen (H_2), ammonia (NH_3) [4] and metals [5] avoids any CO_2 release in the atmosphere. However, although hydrogen is globally recognized as an effective candidate to meet the requirements

of zero CO_2 emissions, the long-term nature of this scenario hinders its wide use on large scale. Therefore, several advantages make ammonia a key species as hydrogen carrier and energy vector. Similarly to hydrogen, ammonia can be used as a clean energy carrier because it can potentially be oxidized exhausting only water and nitrogen. In addition, ammonia cost per stored energy volume is three times less expensive than hydrogen [6]. However, with respect to its use for the power generation, ammonia is still under evaluation, especially because of several issues related to its corrosive nature and scarce combustion properties. A feasible way to overcome these issues could be blending ammonia with more reactive fuels, such as hydrogen, alcohols, methane, gasoline or diesel. In particular, the use of ammonia blends shows by promising results in terms of combustion stability, even though high NO_x emission levels still represent an open issue[7]. On the other hand, the use of ammonia-hydrogen blends represents the most attractive possibility, since hydrogen can be directly obtained from ammonia partial cracking [8]. Given this background, the utilization of ammonia as a fuel still needs huge efforts, especially with respect to its stable and efficient conversion. In particular, conventional systems based on traditional flame stabilization mechanisms are not able to meet the requirements of high stability and low NO_x emissions for ammonia combustion. In this respect, promising technologies are the so-called non-conventional or diluted combustion. In particular, MILD Combustion [9] is able to inherently satisfy the general criteria of sustainability, fuel flexibility and readiness level required to promptly support the energy transition. Pure ammonia and blends with methane or alcohols were already identified as target non-conventional fuels and investigated with respect their combustion performances under MILD conditions [7,10]. In this respect, NH_3/H_2 blends were studied in this work in order to shed light on the influence of blending ammonia with more reactive fuels of different type. Experimental campaigns were carried out at atmospheric pressure, using a cyclonic flow reactor in which local highly diluted and preheated conditions allow to attain MILD conditions. The quantification of all major/minor species concentrations, main pollutant emissions, as well as the oxidation process stability, were systematically explored.

Experimental Setup

To achieve an efficient MILD Combustion process, the establishment of an effective mixing process between recirculating burned gases and fresh reactant jets cover a key role. These requirements can be achieved through a proper design of the combustion chamber. In this respect, one of the most effective methods to create and stabilize a recirculation zone inside a confinement involves the use of a cyclone-like configuration [11]. In these arrangements, the recirculation of hot active species is achieved through two key features, i.e. the main jet entrainment and the flow development imposed by the geometry of the reactor. These features characterize the test case considered in this study, the Laboratory Unit CYclonic (LUCY) burner

shown in Figure 1, extensively described in previous works [7,12].

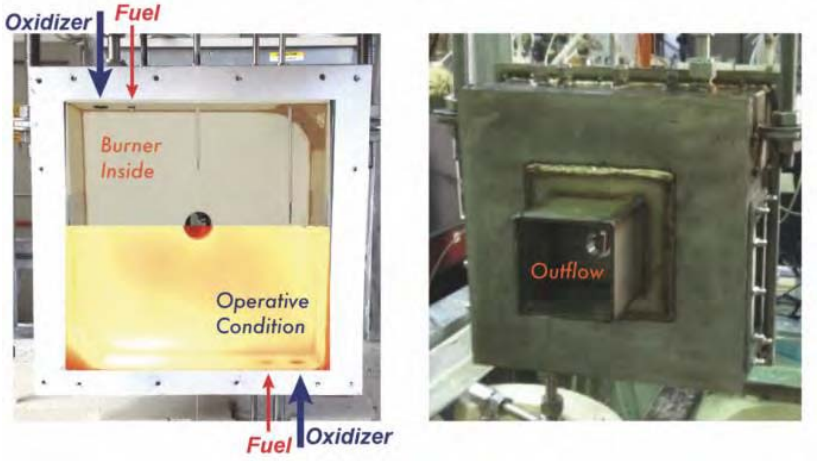

Figure 1. Sketch of the cyclonic chamber.

The experimental setup allows for the characterization of the thermochemical process as a function of several system parameters. The establishment of a cyclonic flow field promotes a large toroidal recirculation zone. This ensures a strong internal recirculation of mass and sensible enthalpy, that in turn entails the dilution of fresh reactants and their temperature increase above the autoignition one, thus attaining MILD conditions. The MILD combustion process was monitored by means of several movable N-type thermocouples, located at the mid-plane of the chamber and at the center of the outflow section of the reactor, to detect the characteristic temperature of the flue gases. As a result of the uniform temperature distribution and the reduced temperature gradients within the combustion chamber, the temperature measured at the outflow section is reported as a reference parameter to compare experimental outcomes. Gas sampling was realized through a water-cooled probe installed at the chamber outlet. The sampled gases were then analyzed by means of several online and offline gas analyzers, i.e. Sick GME700, an Agilent micro-GC analyzer and a TESTO 350, to detect NH_3, H_2, O_2, N_2, NO and NO_2 emissions. All the concentrations of detected species were then normalized to 15% vol O_2. The experimental campaign was carried out by highlighting the effects of progressively adding H_2 to NH_3/air mixtures. Process stability, operative temperatures and emissions were analyzed as a function of the inlet equivalence ratio (ϕ) and volumetric H_2/NH_3 ratio ($\%H_2$). This latter was varied from pure NH_3 to pure H_2, by keeping constant the thermal power at 7 kW. Both the oxidizer and fuel flows were fed to the combustion chamber at environmental conditions (T_{in}=300 K, P=1 Atm).

Results

In Figure 2, operational temperatures (T) and NO_x emissions for pure NH_3, pure H_2 and NH_3/H_2 blends as a function of ϕ are reported. The investigated volumetric fraction of hydrogen ($\%H_2$) in the fuel mixture was varied from 5% up to 100%.

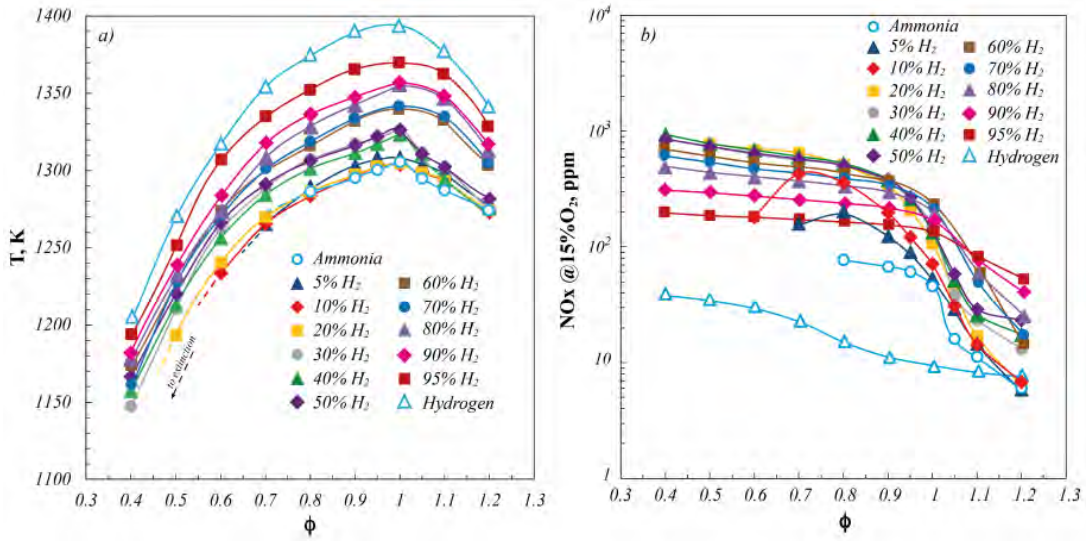

Figure 2. Operational temperatures (a) and NO_x emissions (b) for pure NH_3, pure H_2 and NH_3/H_2 blends as a function of ϕ. P=7 kW.

With reference to the operative temperatures (Figure 2a), for all the reported cases operational temperatures show a non-monotonic trend as a function of ϕ, as expected, with the maximum located at the stoichiometric condition (ϕ=1) and decreasing trends towards both fuel-lean and fuel-rich conditions. For pure NH_3, T increases from 1290 K at ϕ=0.8 to the maximum value of 1310 K at the stoichiometric condition. Afterwards, T decreases down to 1270 K at ϕ=1.2. Similarly, for pure H_2, T increases from 1210 K at ϕ=0.4 to the maximum value of 1395 K (ϕ=1) and then decreases down to 1340 K at ϕ=1.2. Results also highlight the effectiveness of H_2 as ammonia fuel enhancer in widening the operational stable window in which the oxidation process stabilization is achieved, with respect to both ϕ and minimum operative temperature levels. In particular, within the investigated ϕ range, sudden extinction behaviors occur for pure ammonia and ammonia/hydrogen blends up to $\%H_2$=20 for fuel-lean conditions. For the case of pure NH_3, extinction phenomena occur at ϕ<0.8 and ϕ>1.2, while the H_2 presence in the fuel blend extends the process stability towards fuel-leaner conditions. Such extinction phenomena are driven by the recirculated sensible enthalpy required to promote auto-ignition and sustain the oxidation process. For the fuel-lean extinction limits, the lower temperatures and mixture averaged residence times, that became comparable with characteristic chemical ones, defining a condition in which the reactant mixture struggles to attain the ignition conditions, entailing the oxidation process is prone to extinguish. On the other hand, NO_x emissions (Figure 2b) for pure ammonia show a monotonic decreasing trend, from about 80 ppm at ϕ=0.8 to 5 ppm at ϕ=1.2. On the other hand, ammonia blends at $5\%H_2$ and $10\%H_2$ show a non-monotonic trend as a function of ϕ. In fact, for these cases NO_x emissions increase from ϕ=0.6 ($5\%H_2$) and ϕ=0.5 ($10\%H_2$) up to ϕ=0.8 ($5\%H_2$) and ϕ=0.7 ($10\%H_2$), where the maximum is detected for both the cases. Then, for higher ϕ, NO_x emissions decrease. As previously analyzed in Figure 2a, such a behavior can be ascribed to the different extinction

conditions that characterize the investigated fuel blends. In fact, for mixtures not achieving extinction conditions in the investigated ϕ range (%H_2>10), a monotonic decreasing trend is detected for NO_x emissions, in accordance with findings related to NH_3/alcohols mixture [10]. Remarkably, ammonia/hydrogen blends exhibit the highest NO_x emission levels, in agreement to results reported for ammonia/methane and ammonia/alcohol blends in previous works [7,10]. Specifically, the NO_x increase with respect to the pure ammonia case is more marked for ammonia blends with 5-10%H_2, especially in fuel-lean conditions. Moreover, for %H_2>10 and up to 50% NO_x profiles almost overlap, whereas they keep the same trend and lower NO_x levels for higher %H_2. In particular, the marked NO_x emissions increase detected by blending ammonia with hydrogen can be ascribed to the boosted OH radical production resulting from the rapid H_2 oxidation chemistry, that increase the NH_2 selectivity towards NO_x production [7]. Finally, the lowest NO_x emissions were detected for 100%H_2, in the whole investigated ϕ range. In this respect, NO_x levels always keep lower than 40 ppm, reaching 10 ppm around the stoichiometric point.
The analysis of experimental results confirmed the effectiveness of hydrogen in increasing the reactivity of ammonia and thus enlarging the stable operational window of the oxidation process. The only non-linear significant interaction between the two fuels is related to NO_x emissions, higher when NH_3 and H_2 are blended.
To better highlighting this aspect, Figure 3 reports NO_x emission levels in linear scale as a function of the volumetric H_2 and NH_3 inlet concentration, for several fuel-lean conditions and the stoichiometric one.

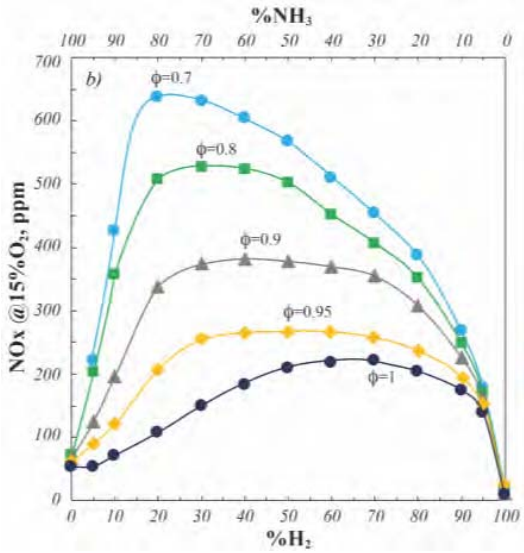

Figure 3. NO_x emissions as a function of %H_2-%NH_3 for 0.7<ϕ<1.

Firstly, NH_3/H_2 blends NO_x emission are higher than both the pure fuels, in the whole range of blending ratios, with non-monotonic trends as a function of the blending ratio itself. In particular, when H_2 is added to NH_3, NO_x distribution depends on the considered ϕ. Specifically, the NO_x maximum concentration decreases and shifts toward higher %H_2 in the fuel blend by increasing ϕ, moving from about 650 ppm and 20%H_2 at ϕ=0.7 up to 220 ppm and 70%H_2 at ϕ=1.

Conclusion

Pure NH_3, H_2 and their blends combustion characteristics were experimentally analyzed under MILD Combustion conditions. Process stability, speciation and pollutant emissions were analyzed as a function of ϕ and NH_3/H_2 ratio. Results showed the effectiveness of H_2 in increasing the reactivity of ammonia and thus enlarging the stable operational window of the oxidation process. In particular, H_2 addition results in an even more marked enlargement of the oxidation stability range than that due to methane or alcohols addition. In agreement with previous outcomes, NO_x emission levels strongly depend on the fuel blend composition, with always higher NO_x emissions for ammonia blends. In particular, a sudden NO_x increase was detected even at 10%H_2 in the fuel blend. In fact, H_2 fast chemistry directly affects the radical production by increasing the H, OH and HO_2 concentration. Finally, the cyclonic configuration allowed to achieve MILD conditions also for 100%H_2, with operative temperature not exceeding 1400 K and NO_x emissions lower than 40 ppm.

References

[1] Dietzenbacher E, Kulionis V, Capurro F. Measuring the effects of energy transition: A structural decomposition analysis of the change in renewable energy use between 2000 and 2014. Appl Energy 2020;258:114040.
[2] Barton JP, Infield DG. Energy storage and its use with intermittent renewable energy. IEEE Transactions on Energy Conversion 2004;19:441–8.
[3] Valera-Medina A, Xiao H, Owen-Jones M, David WIF, Bowen PJ. Ammonia for power. Prog Energy Combust Sci 2018;69:63–102.
[4] Kobayashi H, Hayakawa A, Somarathne KDKA, Okafor EC. Science and technology of ammonia combustion. Proc Combust Inst 2019;37:109–33.
[5] Bergthorson JM. Recyclable metal fuels for clean and compact zero-carbon power. Prog Energy Combust Sci 2018;68:169–96.
[6] Zamfirescu C, Dincer I. Using ammonia as a sustainable fuel. J Power Sources 2008;185:459–65.
[7] Ariemma GB, Sorrentino G, Ragucci R, de Joannon M, Sabia P. Ammonia/Methane combustion: Stability and NOx emissions. Combust Flame 2022;241:112071.
[8] Lamb KE, Dolan MD, Kennedy DF. Ammonia for hydrogen storage; A review of catalytic ammonia decomposition and hydrogen separation and purification. Int J Hydrogen Energy 2019;44:3580–93.
[9] Sabia P, Sorrentino G, Ariemma GB, Manna M V., Ragucci R, de Joannon M. MILD Combustion and Biofuels: A Minireview. Energy and Fuels 2021;35:19901–19.
[10] Ariemma GB, Sorrentino G, Sabia P, Ragucci R, de Joannon M. MILD Combustion of Methanol, Ethanol and 1-Butanol binary blends with Ammonia. ProcCombust Inst 2022.
[11] Alekseenko S V., Kuibin PA, Okulov VL, Shtork SI. Helical vortices in swirl flow. J Fluid Mech 1999;382:195–243.
[12] Sabia P, Sorrentino G, Bozza P, Ceriello G, Ragucci R, De Joannon M. Fuel and thermal load flexibility of a MILD burner. Proc Combust Inst 2019;37:4547–54.

Numerical design of a rich-lean micro-Gas Turbine combustor for ammonia fueling

L. Giuntini[*], **C. Galletti**[*], **A. Parente**[**,***]

lorenzo.giuntini@phd.unipi.it

[*] Department of Civil and Industrial Engineering, University of Pisa, Largo L. Lazzarino 2, 56122, Pisa, Italy
[**] Aero-Thermo-Mechanics Lab., Université Libre de Bruxelles, Avenue F.D. Roosevelt, 1050, Brussels, Belgium
[***] BRITE - Brussels Institute for Thermal-fluid systems and clean Energy, Brussels, Belgium

Abstract
The use of ammonia in micro-Gas Turbines (mGTs) is a promising solution in the energy transition scenario. However, burning ammonia poses challenges due to its low reactivity and high emissions of NO_x. To address this, we aim to develop a multi-stage combustor for mGTs using virtual prototyping with Computational Fluid Dynamics. Results show that this technology has the potential to significantly reduce pollutant emissions and achieve efficient oxidation of ammonia with low-NO_x.

Introduction
The shift towards renewable energy sources in recent years has prompted the need for combustion technologies capable of ensuring an efficient and flexible use of different fuels under varying load conditions. In this regard, micro-Gas Turbines (mGTs) have become increasingly popular due to their low cost and flexibility. The goal of this study is to redesign a natural gas-fired mGT combustor to allow 100% ammonia feeding. Ammonia is a promising fuel due to its carbon-free nature, high energy density, and ease of liquefaction for storage and transportation. However, burning ammonia presents challenges, including low reactivity, narrow flammability range, and a tendency to produce high nitrogen oxide (NO_x) emissions, which can limit its widespread application. Blending ammonia with hydrogen can improve reactivity, while operating at equivalence ratios (φ) greater than 1 can reduce NO_x emissions. However, operating at $\varphi>1$ leads to fuel slips, negatively impacting the environment and system efficiency. Multi-stage combustion can enhance the use of ammonia by performing its oxidation at different equivalence ratios, typically from fuel-rich to fuel-lean conditions, enabling complete conversion of the fuel with low levels of NO_x. Additionally, multi-stage combustion benefits from increased flame stability due to the large amount of hydrogen released by the thermal decomposition of ammonia. However, there are few studies on this topic [1], and most models employed are based on Chemical Reactor Networks (CRNs) and, hence, have low-fidelity [2-4]. To address these gaps, this study uses Computational Fluid Dynamics

(CFD) simulations to provide detailed information on the thermo-chemical processes in a system operating under multi-stage combustion conditions. The study focuses on an mGT burner originally designed for natural gas but converted for rich-lean combustion of ammonia. Various geometric adjustments are tested, and the influence of different factors on pollutant formation and consumption is demonstrated. The proposed modifications lead to significant reductions in NO_x emissions, showing that low-NO_x combustion of ammonia is feasible.

Micro-Gas Turbine burner

The combustor being studied is part of a micro-Gas Turbine (mGT) system that produces combined heat and power with a thermal input of 48kW_{th}. Originally designed for natural gas and LPG, it is being converted to burn ammonia in a multi-stage configuration. In this system, ambient air (N_2/O_2=79/21mol%) is compressed to 2.5 bar, pre-heated to 953 K, and split into primary and secondary streams. The fuel and the primary air are supplied to the internal combustion chamber in a non-premixed configuration and, here, ammonia oxidation occurs under fuel-rich conditions, as shown in Figure 1. The secondary air serves to complete ammonia oxidation and reduce exhaust temperature down to 1223 K. To do so, a global fuel-to-air equivalence ratio, φ_{tot}, of 0.12 is set. The amount of air issued to the first stage is varied to analyze the effect of different equivalence ratios, i.e., φ_1=1.15 and φ_1=1.30 on NO_x emissions. The flow rate of air in the second stage is derived accordingly. Geometric modifications made to the burner, presented in Figure 1, are further discussed in the following sections.

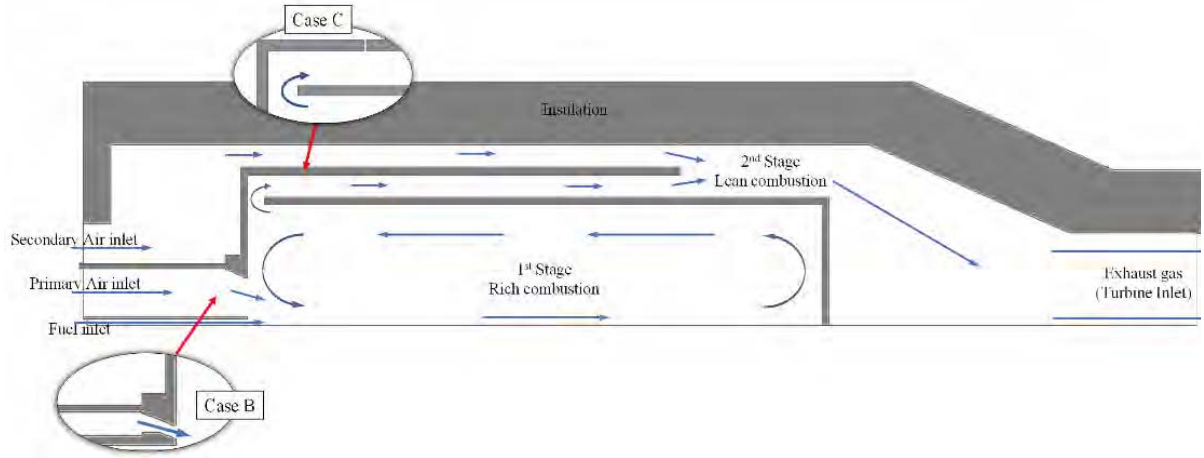

Figure 1. 2D axisymmetric representation of the mGT combustor with indications of the flow direction. The modifications made to the base geometry are highlighted as Case B and Case C, respectively.

CFD model

Steady-state Favre-Averaged Navier-Stokes (FANS) simulations were performed

with Fluent 19.3 by ANSYS Inc. The Realizable k-ε model was employed to treat the turbulence, while the Eddy Dissipation Concept for the turbulence-chemistry interactions, and the Otomo mechanism [5] (consisting of 33 chemical species and 213 reactions) for the NH_3 oxidation kinetics. The combustor geometry presents a cylindrical symmetry, hence, a 2D axisymmetric mesh was built, consisting of 53,000 quadrilateral/triangular elements. Uniform boundary conditions were set at the inlets, according to the details provided in the previous section; internal walls were treated as non-adiabatic, while the external ones were considered adiabatic. Second order upwind interpolation schemes were employed. At convergence normalized residuals did not change with iterations and were all well below 10^{-6}.

Methodology

CFD simulations were carried out with two different equivalence ratios in the first stage, specifically φ_1=1.15 and φ_1=1.30. Initially, the base geometry of the burner (Case A) was tested to determine its suitability for double-stage combustion of ammonia, considering that the original design was intended for natural gas fueling. Subsequently, geometric modifications to optimize the burner operation and reduce NO_x emissions were proposed, resulting in two new cases, B and C, shown in Figure 1. In Case B, the external diameter of the primary air nozzle was reduced to achieve an inlet velocity of approximately 90 m/s. This modification improved mixing within the first stage of the combustor and enabled the gas to fully utilize the available volume, thus increasing the residence time. In Case C, we implemented four evenly spaced holes on the baffle which separates the secondary air from the products of the first stage, while also retaining the modification proposed in Case B. These holes enabled a more gradual entrainment of secondary air in the lean combustion stage, essentially allowing the system to operate in a multi-stage configuration.

Results

At first, 2-dimensional CFD simulations were performed on the base geometry (Case A) at φ_1=1.15 and φ_1=1.30. Results are shown in Figure 2 (left) in terms of distributions of velocity magnitude (v_M), temperature (T), and molar fractions of NO and NH_2. Looking at the velocity field, the fuel enters the chamber at high speed, i.e. about 100 m/s, while the primary air is fed more slowly, i.e. approximately 20 m/s, leading to inadequate mixing, with little differences between the two equivalence ratios. This is due to the fact that this geometry was originally designed for hydrocarbons and operated at $\varphi_1 \approx 0.5$, while now $\varphi_1 > 1$. Analyzing the temperature field, we can observe that within the primary chamber the temperature is not uniform, presenting peaks and a flame not fully developed due to the slow air jet. In the second stage, the temperature rises further as the ammonia slipped from the first stage reacts; then, the gases proceed reacting and mixing to the outlet. Examining the NO and NH_2 fields, it can be noticed that the highest concentrations of NO are located where temperature peaks occur, i.e., where both thermal-NO and fuel-NO formation rates are high. However, due to the fuel-rich combustion conditions, a

significant amount of NH_2 is also produced, triggering De-NO_x reactions which consume the NO as the gas proceeds along the reactor, with almost zero ppm of NO and NH_2 before reaching the second stage. In the second stage, ammonia reacts in large excess of oxygen generating a considerable amount of NO, especially in the A30 scenario. Table 1 reports the predicted emissions of key species, such as NH_3, H_2, NO, NO_2, and N_2O. Although both A15 and A30 scenarios achieve complete conversion of the fuel, they also generate unacceptably high concentrations of NO_x and N_2O. This means that the original geometry is not optimal for double-stage combustion of ammonia and needs modification.

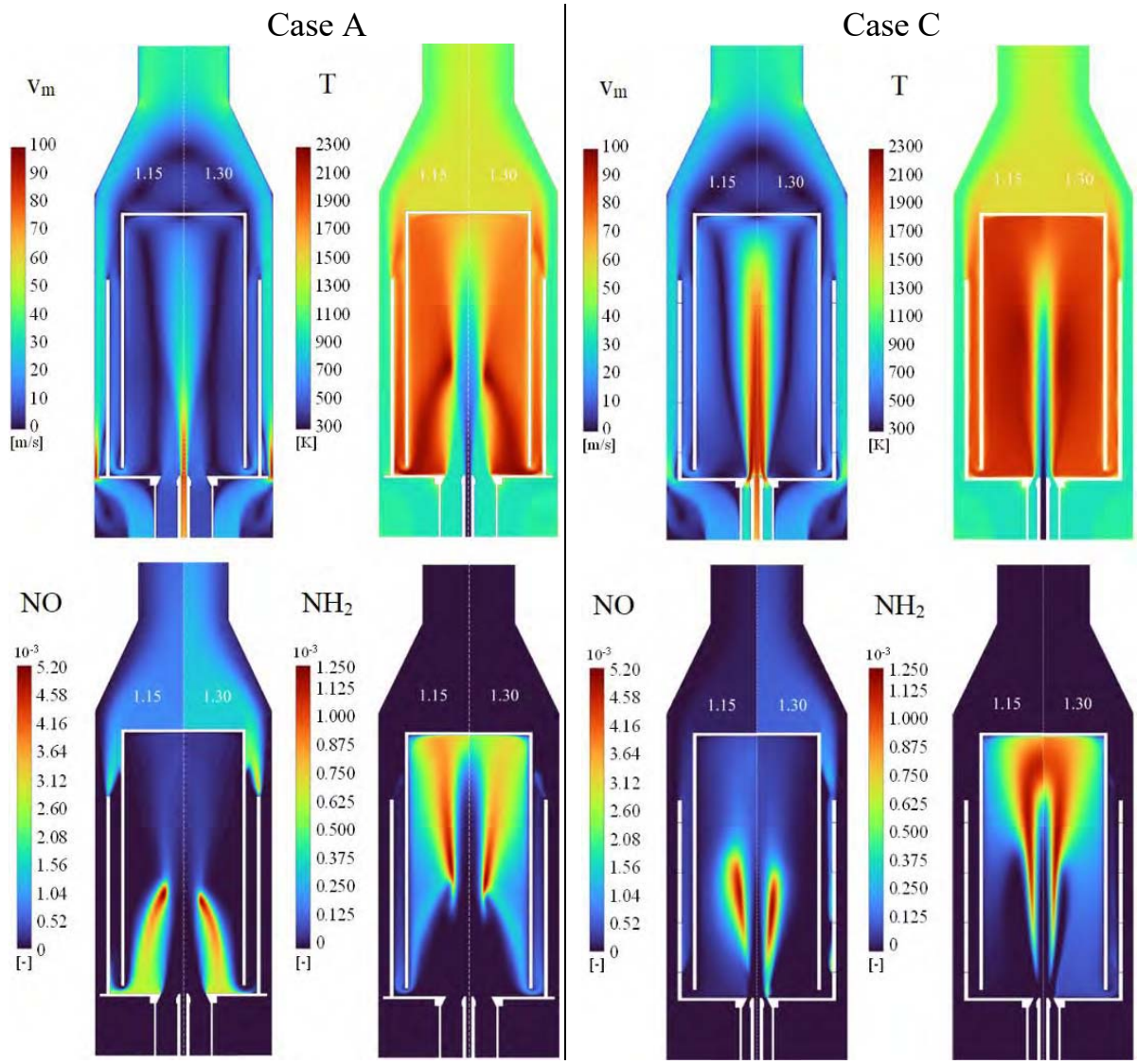

Figure 2. Distributions of velocity magnitude (v_M), temperature (T), and molar fractions of NO and NH_2 predicted at $\varphi_1 = 1.15$ and $\varphi_1 = 1.30$ for the Case A (left) and the Case C (right).

Based on such results, two alternative cases, namely Case B and Case C, were devised as shown in the Methodology section. Case B focuses on reducing the

diameter of the primary air nozzle to enhance mixing in the main chamber, whereas Case C introduces a further modification involving the incorporation of four rows of holes on the baffle wall.

Figure 2 (right) shows the distributions of velocity magnitude (v_M), temperature (T), and molar fraction of NO and NH_2 inside the reactor for Case C. However, we must say that, in the first stage, Case B and Case C are identical and hence the same considerations are valid there. Analyzing the flow field, we can notice that the primary air is fed at about 90 m/s, which makes the mixing much more intense and the temperature field more uniform with respect to the base geometry, both for φ_1=1.15 and φ_1=1.30. Additionally, the flame fully develops within the main chamber and its residence time increases, leading to two important consequences: the NO is consumed by NH_2 much earlier in the reactor's length, as demonstrated by the NO and NH_2 distributions of Figure 2; more ammonia is thermally decomposed in the first chamber, and hence fewer ammonia reacts in the subsequent lean stage, leading to lower fuel-NO_x production. This latter effect is confirmed by the fact that pollutant emissions for cases B15 and B30 show an important reduction with respect to the A15 and A30 cases, as reported in Table 1. More precisely, at φ_1=1.15 all pollutants are reduced by about 70% with respect to the A15 case, while at φ_1=1.30 the reduction is less important, i.e., by about 12% with respect to the A30 case.

Besides, pollutant emissions can be further reduced in Case C, as reported in Table 1, where C15 and C30 cases permit a NO_x emission reduction by about 86% and 60% with respect to the A15 and A30 cases, respectively. Such important reductions are due to the holes implemented in Case C, which substantially enables a multi-stage combustion of ammonia permitting a better control of the pollutant formation, as also shown in the NO distribution of Figure 2 (right) both for φ_1=1.15 and φ_1=1.30.

Table 1. Emissions predicted at the outlet for the cases investigated.

Case	φ_1	X_{NH3} [ppm]	X_{H2} [ppm]	X_{NO} [ppm]	X_{NO2} [ppm]	X_{N2O} [ppm]
A15	1.15	0	1	336	15	4
A30	1.30	0	2	590	26	13
B15	1.15	0	1	94	5	0
B30	1.30	0	2	498	23	7
C15	1.15	0	0	48	2	0
C30	1.30	0	0	221	9	2

Conclusions

Numerical simulations were carried out to investigate whether it is possible to burn ammonia with high efficiency and low pollutant emissions in a mGT combustor originally designed for natural gas fueling. More specifically, the CFD analysis provided detailed information on staged combustion of ammonia, thanks to the visualization of flow and temperature fields as well as the production/consumption of key species, such as NO and NH_2.

We found that the original geometry is not able to operate properly when fuelled with ammonia resulting in high emission of pollutants. The reasons are the presence of a not fully developed flame, a low residence time, and a poor mixing within the main chamber, leading to much ammonia reaching and reacting in the lean stage with considerable amounts of fuel-NO_x produced. Therefore, it is important to provide NH_3 enough time to thermally decompose in the rich stage, so that only a few of that reacts in lean conditions. The modifications proposed in Case B were intended to increase the residence time within the main chamber, so that fewer quantities of fuel-NO_x were produced in the lean stage, resulting in a great reduction of pollutant emissions, i.e., of about 70% for φ_1=1.15 and of about 12% for φ_1=1.30. Case C further improved the combustor performance by introducing four holes on the baffle wall. This modification allowed a more gradual entrainment of secondary air in the second stage, substantially enabling a multi-stage configuration in which ammonia is consumed at about stoichiometric conditions, instead of burning in large excess of oxygen. With this improvement pollutant emissions were reduced more than 85% at φ_1=1.15 and more than 60% at φ_1=1.30, with respect to Case A.
Based on such analysis and results, we believe that the present work may contribute to the understanding of the thermo-chemical processes taking place in staged combustion of ammonia, and, in particular we demonstrated, for the first time and with a real application, that the efficient and low-NO_x combustion of ammonia is feasible.

References

[1] Kurata, N. Iki, T. Inoue, T. Matsunuma, T. Tsujimura, H. Furutani, M. Kawano, K. Arai, E. C. Okafor, A. Hayakawa, et al., “Development of a wide range-operable, rich-lean low-nox combustor for nh3 fuel gas-turbine power generation”, *Proc. of the Comb. Inst.*, 37, 4587 (2019)

[2] Z. Li and S. Li, “Effects of inter-stage mixing on the nox emission of staged ammonia combustion”, *Int. J. of Hydrogen En*., 47, 9791 (2022)

[3] S. Mashruk, H. Xiao, and A. Valera-Medina, “Rich-Quench-Lean model comparison for the clean use of humidified ammonia/hydrogen combustion systems”, *Int. J. of Hydrogen En*, 46, 4472 (2021)

[4] M. Gutesa Bozo, S. Mashruk, S. Zitouni, and A. Valera-Medina, “Humidified ammonia/hydrogen RQL combustion in a trigeneration gas turbine cycle”, *Energy Conversion and Management*, 227, 113625 (2021)

[5] J. Otomo, M. Koshi, T. Mitsumori, H. Iwasaki, and K. Yamada, “Chemical kinetic modeling of ammonia oxidation with improved reaction mechanism for ammonia/air and ammonia/hydrogen/air combustion, Int. J. of Hydrogen En., 43, 3004 (2018).

Tenova Ultra Low NOx Regenerative Burners Working with Hydrogen and Oxygen Enrichment

D. Astesiano[1], A. Della Rocca[1], C. Leoncini[1]

[1]Tenova
Via Albareto 31, Genova (GE), Italy, 16153
Phone: +39 010 6054046
Email: davide.astesiano@tenova.com

Keywords: decarbonization, hot rolling, heating furnace, hydrogen, oxygen, combustion, burner, regenerative

THE CHALLENGE FOR THE DECARBONIZATION OF THE STEEL INDUSTRY

In downstream hot rolling processes, fossil feedstocks are used as a fuel and it is responsible of carbon footprint of final steel products from about 100 kg CO2/tCS in the case of billets to more than 250 CO2/tCS in the case of flat products. Therefore, the contribution of downstream processes to Scope 1 emissions is already comparable or higher respect to that originated from the production of liquid steel in the scrap based EAF route and it has a relevant influence on the final CO2 reduction scenario (2050 and beyond) also for the steel production route from iron ores (Figure 1).

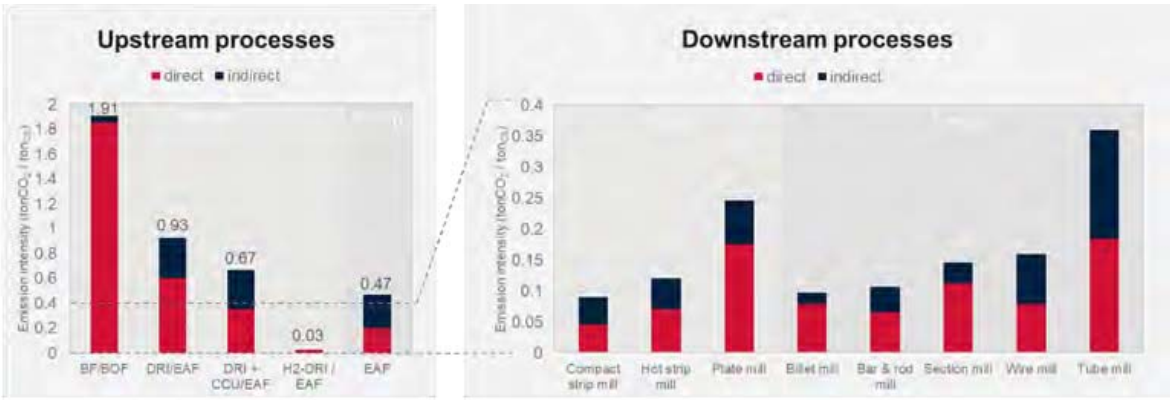

Figure 1: carbon emission intensity divided into direct and indirect (electricity) emissions for the different liquid steel production routes (BF/BOF: blast furnace/basic oxygen furnace, EAF: electric arc furnace, NG-DRI: natural gas based direct reduction) and hot rolling mill process.

This is in line with the holistic approach proposed by the Clean Steel Partnership that indicates the integration of different technology building blocks to the complete transformation of steel production process from liquid steel production (upstream) up to the rolling and finishing lines (downstream).

HYDROGEN COMBUSTION IN STEELMAKING

Hydrogen is not new as fuel in steelmaking sector: coke oven gas (COG) is already used in reheating and treatment furnaces, containing hydrogen up to 60% in volume in some cases. Experience in using such gases in industrial combustion systems shows that the NOx emissions increase as the % of hydrogen, especially in highly efficient furnace where high temperature combustion air or oxygen is used. This is the main effect of the fast hydrogen kinetics, that enhances the reactivity of the system and increases NOx emissions via thermal route (Figure 2).

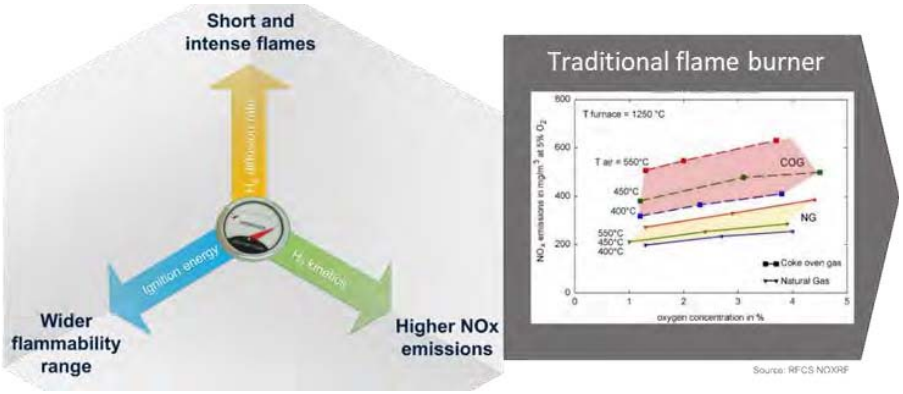

Figure 2: the technology challenges of hydrogen reach gaseous combustion.

Non-conventional combustion technologies, such as flameless combustion, represented an effective solution to overcome this issue. The key aspect is the dilution of fuel and oxidizer streams with the gases resulting from the combustion process: the result is a reaction structure characterized by non-visible flame and more uniform temperatures, leading to a strong NOx reduction.

Background experience in firing hydrogen-rich fuels is therefore present in the steel sector, both for reheating and treatment furnaces. Nevertheless, the possibility to keep NOx emissions very low when the hydrogen content is higher than 60% (vol) was not yet proven, requiring further investigations.

H2/NG REGENERATIVE BURNERS

Development of regenerative burners H2/NG

The latest evolution of hydrogen ready burners concerns compact and high efficiency regenerative burners able to work with any type of mixture of natural gas and hydrogen. For Tenova, the hydrogen ready burner concept is not limited to the ability of the burner to operate with hydrogen, but it is based on the fact that the performance of the combustion system are maintained at maximum level as the mixture varies. Performance refers to the reliability of the burner and its components and furthermore, to the efficiency of air pre-heating (regeneration) and NOx emissions which must be guaranteed at minimum levels and comparable to natural gas one.

It is known that the higher flame temperature linked to the higher air preheating temperature produces a potentially higher quantity of NOx; this phenomenon is increased by working with hydrogen, which produces a higher flame temperature than the natural gas one. The challenge is therefore to keep NOx emissions to a minimum level without reducing the preheating efficiency and as already mentioned, the solution consists in the use of flameless combustion. For this reason, the burner couple is equipped with double gas inlet: the first working in flame mode at low temperature and the second in flameless above the self-ignition temperature of the furnace.

Considering the following definition of global efficiency of the burner η_g it is possible to underline that it is at 86% with all the type of NG/H2 mixtures:

$$\eta_g = 1 - (Q_{wg1} * H_{wg1} + Q_{wg2} * H_{wg2}) / (Q_{fuel} * LCV) , \quad (1)$$

where Q_{wg1} is the flow of flue gases exiting through the burners, H_{wg1} the respective enthalpy referred to the temperature at the exit of regenerator, Q_{wg2} is the flow of flue gases exiting trough the main furnace exit and H_{wg2} is the respective enthalpy, Q_{fuel} is the flow of fuel gas and LCV is its low calorific value.

The couple of burners (Figure 6) is designed for a thermal power of 1 MW but the burners will be able to work up to 5 MW with different sizes.

Oxygen enrichment

If the use of regenerative burners allows maximizing efficiency, it is known that also the enrichment of the combustion air with oxygen has an important impact on the reduction of gas consumption. Oxyfuel burners are in fact used to increase the productivity of a plant or to reduce the specific consumption of a plant fed with combustion air. Although the two technologies are usually in opposition, the burner is fed with air enriched with oxygen. The use of oxygen is very interesting when it is produced by electrolysis and in combination with the production of hydrogen; in this case, in fact, the cost of oxygen production is minimal considering the fact that the primary objective of an electrolyser is related to the production of hydrogen. For these reasons, it is therefore decided to test the regenerative burner with oxygen enrichment in the combustion air. Oxygen is therefore injected into the combustion air upstream of the regenerator and the amount of oxygen used is limited to obtain an air-oxygen mixture of 29% oxygen.

CFD analysis of the burner prototype

Following the consolidated Tenova approach, the burner design was refined by means of the CFD tools before testing it on the test facility. This step allows to optimize the burner and to align its performances in term of flame length, NOx emission, temperature uniformity, air preheating efficiency to the desired characteristics and project goals. All the simulations were carried with EDC turbulence-chemistry coupling approach, DO radiation model and detailed kinetic mechanisms able to capture the effect of NG/H2 combustion process.

After an initial review phase, an optimal burner geometry able to maintain a constant temperature peak at any percentage of hydrogen content within the NG/H2 fuel mixture was identified.

Experimental tests of regenerative H2/NG burner

The test furnace having an internal section of 2 x 2 m and an available length (wall-to-wall) of about 5 m is made of a steel casing with internal refractory and ceramic fiber linings. The burners are placed on the two frontal walls of the furnace, as shown in Figure 8, while the waste gases outlet is placed at the middle of the furnace. The furnace is water-cooled by means of several movable water lances and it features 10 thermocouples placed at different axial positions and several optical inspection ports in order to monitor the flame appearance. The hydrogen was supplied from a truck trailer with eleven hydrogen bottles, while the natural gas was coming from the standard pipeline.
In addition, a bottle pack is used to supply oxygen to combustion air for enriching it up to 29%, limit for which it is not necessary to provide special piping suitable for combustion with pure oxygen.

During the tests, the burner behavior was changed according to different control parameters in order to map their effect on burner operation and performance. The tests were carried out over several test days during which the burner was cold ignited with natural gas and then fed with any type of H2/NG mixture once the flame was ignited. When the furnace temperature reached 850°C the burner was also operated in flameless mode in order to measure the NOx emissions.

Figure 3 represents the trend of the burner and regenerator temperatures during the working conditions with the furnace at 1250°C and an air excess of 10%: the graph on the left side shows the temperature of the 2 burners working in natural gas and on the right side the temperatures of the system working with hydrogen:

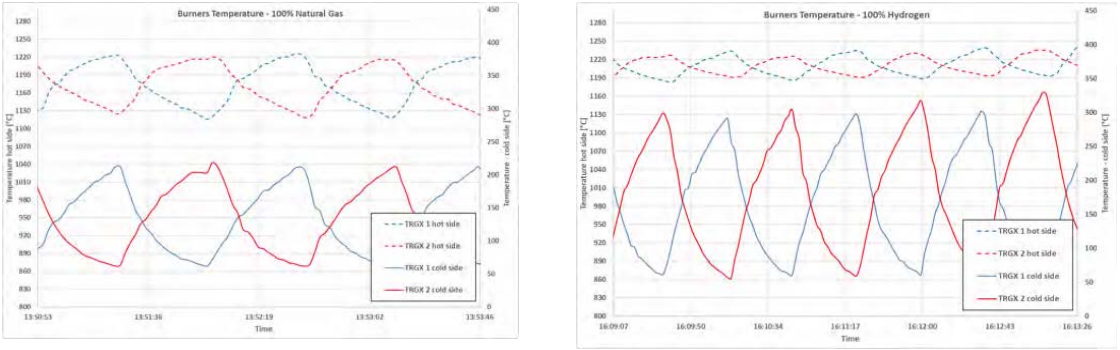

Figure 3: temperatures of the burners during regenerative cycles

The operating cycle of the burners working with hydrogen is characterized by a smaller amplitude of temperatures on the hot side and greater amplitude on the cold side. This tendency derives from the fact that, despite having the same percentage of sucked waste gases in both cases (about 80% of the total), the ratio between the air and the aspirated flue gases in hydrogen operation is lower than that of natural gas. This means that by feeding the burners

with hydrogen, the flue gases outlet temperature is higher and the average temperature of the regenerator is higher but the global efficiency (1) is constant.

In terms of NOx emissions, the following Figure 4 and 5 shows the trend of NOx and oxygen during tests with furnace at 1250°C and 10% of air excess: in the left graph, burners are working in flameless combustion with natural gas while in the right with hydrogen:

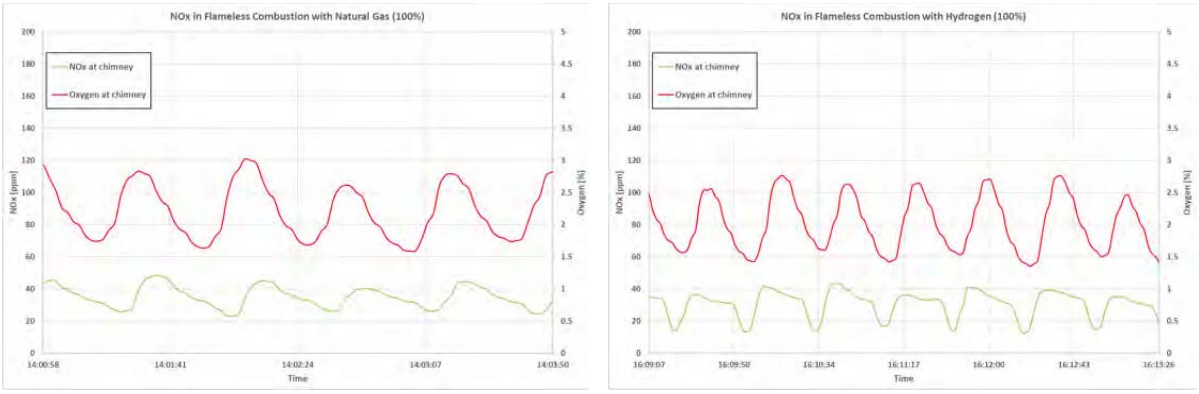

Figure 4: emissions of the burners during regenerative cycles

As shown in the Figure 4 and 5, the trend of NOx emissions in flameless combustion is almost flat, remaining constant for any percentage of hydrogen enrichment; the burners are able to produce very low level of nitrogen oxide - 70 mg/Nm3 @ 3% oxygen at 1250°C (as NO_2) and 55 mg/Nm3 with furnace at 1150°C.

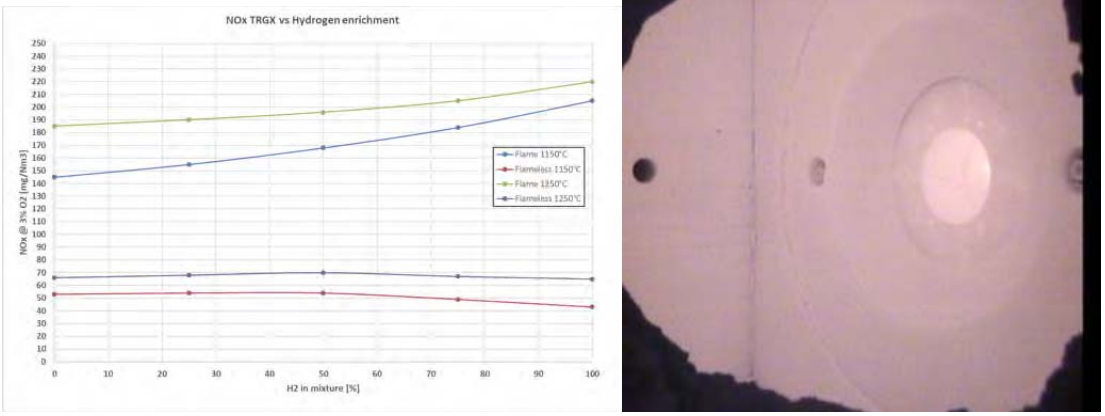

Figure 5: on the left: trend of the emissions of the burners during regenerative cycles at different percentage of hydrogen in the mixture and on the right an internal view of the test furnace where the burner is running with hydrogen in flameless mode

In flame mode, the higher flame temperature of the hydrogen combustion is traduced in a higher production of NOx emissions: increasing H2 %, the nitrogen oxides pass from 145 and 185 mg/Nm3 @ 3% of O2 with 0% H2 to 205 and 220 mg/Nm3 with 100% H2, respectively with furnace temperature of 1150°C and 1250°C.

During the experimental session, the burners were also fed with enriched combustion air: in this case, a flow of oxygen is injected in the combustion air for reaching an amount of oxygen at 29%. The higher value of oxygen in the air permits to reduce the percentage of nitrogen and consequentially to increase both the flame temperature and the heat exchange thanks to the higher presence of water vapor and CO2 (in case of natural gas presence). This means lower gas consumption but high flame temperatures produce high NOx emissions and, as shown by the following graphs of Figure 6, the trend is confirmed by experimental results where the burners reach more than 800 mg/Nm3 of NOx in flame combustion with hydrogen. The burners working in flameless mode are able to drastically reduce the NOx emissions bringing the values back to levels very similar to those of combustion with air at 21% oxygen. In fact, in Figure 13, the graph shows the NOx emission curves produced by the flameless burners fed with air and with air enriched at 29%: the maximum value is about 85 mg/Nm3 @ 3% of O2.

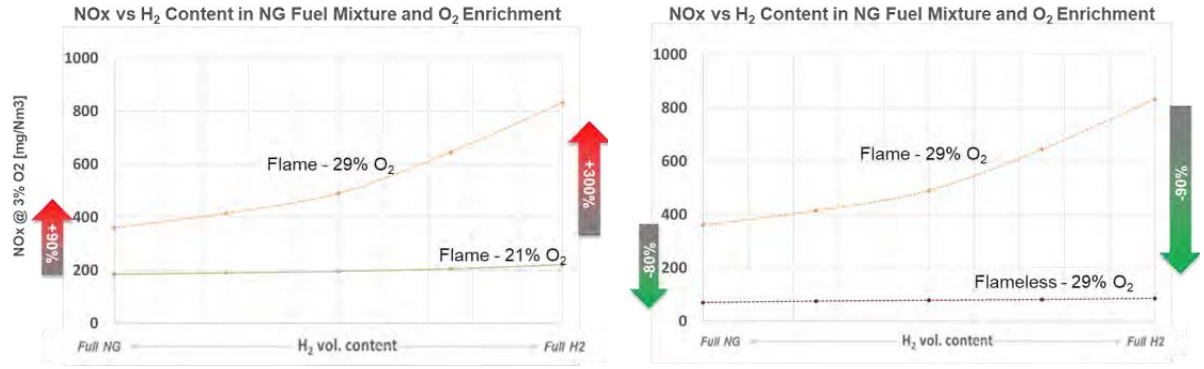

Figure 6: NOx emissions of the burners working with 21 and 29% of oxygen in the combustion air with furnace at 1250°C

CONCLUSIONS

The race for the decarbonization of the steel industry has already started. For the steel production from the electric arc furnace route, the energy transition scenario mainly entails to cut down carbon dioxide emissions from reheating and heat treatment furnaces of the hot rolling shops. This is particularly true for plate mills and tube mills for which the direct and indirect carbon intensity exceeds the carbon intensity for the electric arc furnace route by a large amount.

In order to foster the decarbonization of industrial furnaces Tenova has started a transition process of its combustion system portfolio towards a 'hydrogen-ready' SmartBurner platform, where full hydrogen flexibility (from 0% up to 100% enrichment of traditional fossil fuels) is combined with advanced IIoT solutions for simplifying maintenance, tuning and commissioning of future-proof combustion systems.

The development of the regenerative burner powered by hydrogen can be defined as the state of the art of low environmental impact burners thanks to the high efficiency which reduces gas consumption, OPerational EXpenditure and CO_2 production, the optimization of flameless combustion which minimizes NOx emissions and for the use of hydrogen which potentially eliminates CO_2.

The introduction of the theme relating to the enrichment of the air with oxygen is a further step towards increasing the efficiency of the combustion system, allowing it to obtain particularly advantageous results in terms of gas consumption, whether fossil or hydrogen. In fact, compared to a standard regenerative burner, the presence of enriched air at 29% O2 reduces consumption by about 7%, while compared to a burner with preheated air at 400°C the reduction is about 20%.

The adoption of hydrogen as a fuel in hot rolling processes is already an industrial reality, and Tenova is able to offer the combustion system with the best efficiency.

A (preliminary) ANALYSIS OF THE AMMONIA COMBUSTION RESEARCH FEVER

I. Gökalp
iskender.gokalp@tubitak.gov.tr*
iskender.gokalp@cnrs-orleans.fr**
TÜBİTAK MARMARA RESEARCH CENTER, Gebze. Türkiye
ICARE-CNRS, Orléans, France

Abstract
The paper presents and discusses some bibliometric data on the quantitative evolution of hydrogen and ammonia combustion research based on the number of publications indexed in the Web of Science data bases and, in addition, constructed using the presented papers in the last three International Symposium on Combustion. The comparison between the dynamics of hydrogen combustion and ammonia combustion is highlighted. Some inferences are made concerning the rapid development of ammonia combustion research.

The combustion problem

Combustion is a mature science and technology area developed since more than 200 years by combining several knowledge bodies such as chemical kinetics, fluid mechanics, turbulence, aerodynamics, multi-phase flows, atomization, heat transfer, thermodynamics, physics, optics, applied mathematics, numerical simulation.
Based on this huge accumulation of theoretical, technological, and practical knowledge, many sophisticated technologies were developed and optimized such as burners / boilers / furnaces, internal combustion engines, gas turbines, aerospace propulsion engines, reactors, gasifier, mainly. These developments helped to contribute to many aspects of human activities such as heating & cooking, various industrial processes (from cement to iron & steel, glass making, gasification, incineration, etc.), electricity and heat generation (stationary gas turbines, gas engines), mobility and transport (car and heavy-duty engines, sea/water platforms), aerospace propulsion, defense technologies. These activities constitute a very important part of the world energy system.
The main energy system related problem is, we are told today, the chemical conversion of energy (CCE) of carbon containing fuels as they generate the greenhouse gas CO2 during their combustion. There are also other pollutants, such as nitric oxides and particulate matter, but CO2 emissions are declared as the main enemy to combat. We may recall that until recently the main indicator of a "good combustion" was considered as the full conversion of the fuel into CO2.
Based on these developments, it is allowed to think that the problem is not the CCE processes, especially combustion, but the carbon containing fuels. So, following the adage "don't throw out the baby with the bathwater", the combustion community concentrated on the fuel and obviously on non-carbon containing fuels, such as

hydrogen and metal fuels, mainly. In parallel, other energy conversion technologies such as electro-chemical ones (fuel cells) and carbon mitigation approaches such as carbon capture are also developed.
Hydrogen is considered today as the main solution, both as a fuel and an energy carrier, to decarbonize the economy. Given the technological problems posed by the transport of hydrogen, ammonia appeared as an alternative solution albeit its production also needs hydrogen. Therefore, “green” hydrogen, meaning generated without CO2 emissions, is the common ground to introduce these two “new” energy carriers. In fact, they are not new in the sense of newly discovered; they are new in the sense they are called to intervene in new large-scale applications. This development triggered some important changes in the interest areas of the combustion science and technology communities. This work is a preliminary attempt to document these changes and discuss them.

Dynamics of Research Areas

Academic research is a very dynamic environment. Research areas can change rapidly, especially if the field of research concerns topics that are highly competitive or those with a strong application or social challenge dimension. Researchers may start their careers in one discipline or in a sub-area of that discipline, especially during their doctoral studies, and evolve differently during their mature or autonomous research periods over time.
Schematically, there may be two main regimes or modes of this evolution. The mature researcher may remain in his or her main discipline but may move to a different subfield. This is a kind of weak transfer of skills. For example, a researcher may have pursued an early career in the field of general aerodynamics and may shift to a more restricted field in the same discipline, such as supersonic aerodynamics.
In the other research area evolution mode, the mature researcher can leave his/her first discipline and move to a subfield of another discipline. This is a kind of strong transfer of competence. Examples are numerous; for example, a researcher who specializes in turbulence in fluid mechanics in his first career period may move on to the application of statistical mathematics in international finance. Such competence transfer mechanisms have also triggered the initiation of new interdisciplinary fields, such as bioinformatics, for example.
The observation of a kind of mass movement in the same sub-area of a particular discipline or from one discipline to another within a relatively short period of time may indicate some profound changes in the concerned community and the related area of research. The recent strong interest in ammonia combustion research within the general combustion community seems related to the above-mentioned first regime of mass movement in the changes of research subjects, i.e., observed in the same sub-area of a discipline, therefore characterized by short cognitive distances between the original or initial research field and the new research domain. Such dynamics may be traced quantitatively by collecting bibliometric data on the concerned research areas.

Bibliometric data on hydrogen and ammonia combustion research and their discussion

The paper presents and discusses some bibliometric data on the quantitative evolution of hydrogen and ammonia combustion research based on the number of publications indexed in the Web of Science data bases and, in addition, constructed using the presented papers in the last three International Symposium on Combustion. The comparison between the dynamics of hydrogen combustion and ammonia combustion is highlighted. Some inferences are made concerning the rapid development of ammonia combustion research.


THE COMBUSTION INSTITUTE
1954

SESSION X

GAS TURBINE COMBUSTION


THE COMBUSTION INSTITUTE
1954

OPTIMIZATION OF INTERCOOLED REGENERATIVE REHEAT GAS TURBINE SYSTEM FOR MULTI-FUEL COMBUSTION

G.B. Ariemma*, G. Langella, G. Sorrentino*, R. Ragucci*, P. Sabia***
corresponding author: giuseppe.langella@unina.it
*STEMS - CNR
**University of Naples "Federico II"

Abstract
The simultaneous adoption of intercooling, regeneration and reheating allows to obtain very good results in increasing the efficiency of a gas turbine cycle. In particular, the reheating technique requires correct design to ensure efficient combustion conditions. The paper reports an analysis of reheating process for a small power gas turbine aimed at optimizing the combustion conditions in the reheater. Different configurations with different degrees of bypass were analyzed, by focusing the attention on the chemical kinetics. The aim was to optimize temperatures and oxygen concentrations at the reheater according to the specific fuel to be used.
The analysis was conducted with reference to methane, which is currently the most used fuel in land-based applications. In a broader vision and in the perspective of using alternative fuels, the adopted methodology is particularly useful for fuels which require particular conditions to stabilize the combustion process, such as ammonia.

Introduction
One of the most important challenges of this century for humanity is undoubtedly that of satisfying a growing energy demand. However, this will have to be done by simultaneously reducing the use of fossil fuels and therefore the production of CO2, to mitigate climate change [1]. Along this road, the technological perspective focuses on increasing the use of renewable sources and alternative fuels on the one hand, and on the other that of increasing the efficiency of energy production systems [2].
Regarding to gas turbines, the increase in efficiency can be achieved using one or suitable combination of some technological solutions as intercooling, reheating and regeneration. Unlike large-scale plants, usually combined with steam plants, in medium and small power gas turbines, all three of these techniques may coexist [3].
The technological evolution of plants with gas turbines has primarily concerned the increase in efficiency thanks to the increase in the maximum temperature TIT (turbine inlet temperature); all this has required the development of increasingly sophisticated refrigeration techniques for the blades and combustion techniques to mitigate the production of thermal NOx [4]. The coexistence of the three techniques already mentioned, allows for significant increases in efficiency without the need for too high TIT values. Among the applications that have recently seen the greatest development of these techniques there is certainly the automotive sector, using micro

gas turbines coupled to electric generators for recharging the batteries [5]. That's the case of range extender applications (RE) and several studies are in progress on the optimization of the Brayton cycle of such turbo gensets [6].
The proposed study concerns a similar application, a plant with a low-power, intercooled, reheated and regenerative gas turbine. In this specific case the attention was paid to the reheating section, analyzing different configurations with different degrees of by-pass of the gases coming from the first expander. The study of the chemical kinetics of the combustion process in the second combustor was carried out for methane, in the first analysis; however, the methodology adopted can also be applied to the study of alternative fuels. Ammonia, for example, which presents significant combustion problems due to its low reactivity, could be burnt in the reheater, by creating the right condition in terms of reactant temperature and oxygen concentration and eventually methane blending [7].

Methodology

The reported study aims at identifying the suitable solutions to optimize a Brayton external combustion gas-turbine system for extended range electric vehicles. In particular, an intercooled-reheat Brayton cycle, equipped with a regenerator recovering heat on the outlet of the second turbine to preheat the incoming air stream fed to the first combustion system (reported in Figure 1 along with the respective operative characteristics) was considered, with specific focus on the combustion system optimization.

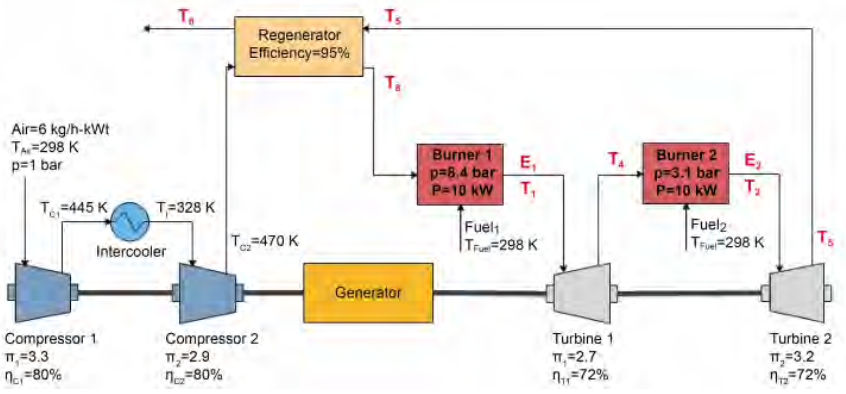

Figure 1. *Brayton system configuration considered in the analysis.*

In this respect, a parametric numerical analysis was carried out in order to identify the most effective configuration and the optimal operative conditions ensuring stable combustion, acceptable pollutant emissions (namely CO and NO_x) and suitable operational temperatures (red in Figure 1), while meeting the operative requirements reported in Table 1. Specifically, fundamental prerequisites driving the performed optimization analysis were the turbine inlet temperature limit, fixed at 1373 K to be compatible with specific alloys of turbine elements for medium temperature applications, and the air mass flow rate (6 kg/h-kWt), essential to ensure a global efficiency about 43%.

Table 1. *Operative requirements and burner specifics.*

Turbine inlet temperature limit, K	*1373*
Air mass flow rate, kg/h-kWt	*6*
Efficiency	*> 43%*
Maximum cycle pressure, bar	*8.76*
T_{in} Air Burner 1 (T_8), K	*1023*
Fuel	*CH_4*
Total thermal power, kW	*20*
T_{in} Fuel (T_0), K	*298*
Burners Volume, cm^3	*2000*
Heat Transfer Coefficient, cal/cm^2-K-s	*$1.8 \cdot 10^{-3}$*

To meet the identified requirements, a cyclonic-flow combustion chamber, extensively described in literature [7–9] and operating under MILD combustion conditions [10], was considered as combustion unit. In this respect, the intense internal recirculation of combustion products due to the burner design and feeding mode was already demonstrated to ensure a wide range of combustion stability, flexibility to the fuel type, reduced pollutants formation and moderate operative temperatures (<1500 K) [7,9]. Both the burners reported in Figure 1 were modelled as a Perfectly Stirred Reactors (PSR), provided by CHEMKIN PRO [11] package, with a volume of 2000 cm^3 and a nominal thermal power P=10 kW each, using methane as fuel.
Simulations were carried out in non-adiabatic conditions, by fixing the heat transfer coefficient equal to $1.8 \cdot 10^{-3}$ cal/cm^2-K-s, as estimated in a previous work [12], and an exchange area of 1200 cm^2. Combustion stability and pollutant formation were investigated by the C_1-C_3 detailed kinetic mechanism [13].

Results

Preliminary analyses were performed in order to evaluate the characteristic ignition delay times τ_{ig} (ΔT=10 K with respect to the non-reactive conditions) and oxidation times τ_{ox} (time to achieve the final system temperature) of a reactant mixture evolving under the conditions reported in Table 1. Specifically, the air mass flow rate was set equal to 120 kg/h, as required for a thermal power equal to 20 kW, at 1023 K, while the operative pressure was systematically varied in the range 2 bar<p<10 bar. Obtained result, not reported for the sake of brevity, highlighted 0.1s<τ_{ig}<0.17s and 0.3s<τ_{ox}<1s for all the investigated pressures levels, while the nominal residence time always keeps lower than 0.3 seconds. In this respect, to ensure the reactants ignition and their complete and stable oxidation, it is essential to investigate suitable configurations able to achieve longer residence times. Among the possible effective solutions (i.e. larger reactor volumes, reduced thermal power etc.) the partition of the total air flow rate fed to the first reactor was investigated, following the flowsheet reported in Figure 2. The influence of the air bypass ratio (R_1=Air_2/Air) was systematically investigated, in terms of combustion stability, pollutants emissions and operative temperature levels of the Bryton system. In particular, the air bypass stream is supposed to be fed around the burner case, to

continuously heat exchange, and then mixed with the combustion product exit from the burner. The investigated bypass ratio levels were fixed to entail equivalence ratio values of the Burner 1 between 0.1-1.

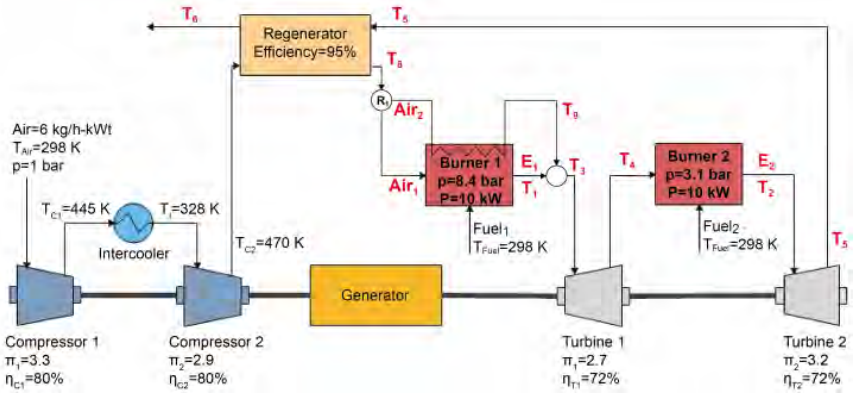

Figure 2. *Scheme1: System configuration with Air bypass to Burner 1.*

Main results are reported in Figure 3, in terms of operative temperatures and pollutant emissions. With reference to Figure 3a, by increasing R_1 the burner operative temperature increases, as expected, due to the resulting equivalence ratio increase with R_1, that in turn ensures the oxidation process stabilization. On the other hand, inlet turbine temperatures smoothly increase by increasing R_1. They always keep lower than the allowable limit, not exceeding 1260 K and 1150 K, respectively.

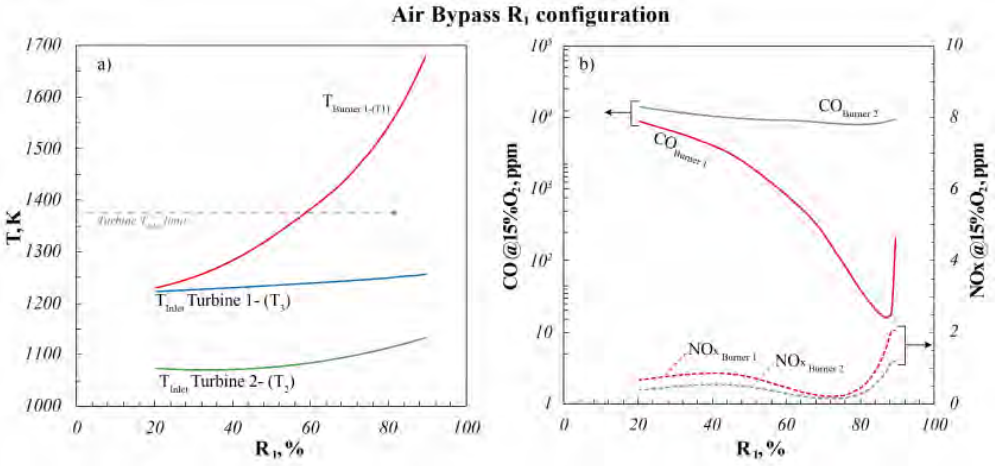

Figure 3. *Scheme 1: Operative T (a), CO and NO_x emissions (b) vs %R_1.*

In Figure 3b NO_x and CO emissions, normalized at 15% of O_2, and characterizing both the burners are reported as a function of R_1. Specifically, NO_x emissions always stay below 3 ppm. Instead, CO emissions show different behavior depending on the considered burner. In particular, a non-monotonic trend characterizes CO levels of Burner 1, with a minimum of about 16 ppm located around R_1=87% and increasing CO emissions for both higher and lower R_1. For R_1<87% the decreasing residence times within the reactor do not allow the complete conversion of the fuel mixture, while for R_1>87% the lower oxygen availability entails increasing CO emissions, as

reported in previous works [7]. Instead, CO emissions of the Burner 2 are always about 10^4 ppm, independently of the investigated bypass ratio of the Burner 1. In this respect, too short residence times characterize Burner 2, thus entailing incomplete fuel oxidation. Therefore, in order to obtain a complete combustion and reduce the CO emissions for Burner 2, a further system configuration with Burner 2 inlet flow bypass, as though for Burner 1, was investigated (Figure 4).

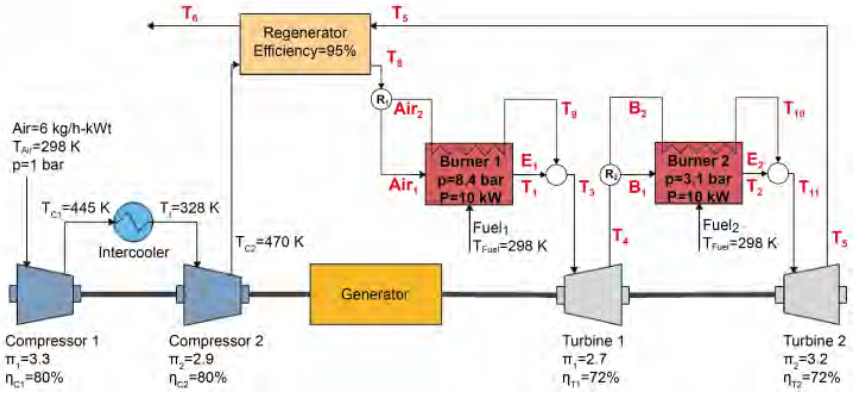

Figure 4. *Scheme2: System configuration with Air bypass for both the burners.*

In this respect, the bypass ratio R_1 was set equal to 87%, identified as optimal operative condition for Burner 1. In particular, results reported in Figure 5 highlight operative temperatures and emission levels for Burner 2 as a function of the bypass ratio (R_2) coherent to the ones obtained for Burner 1.

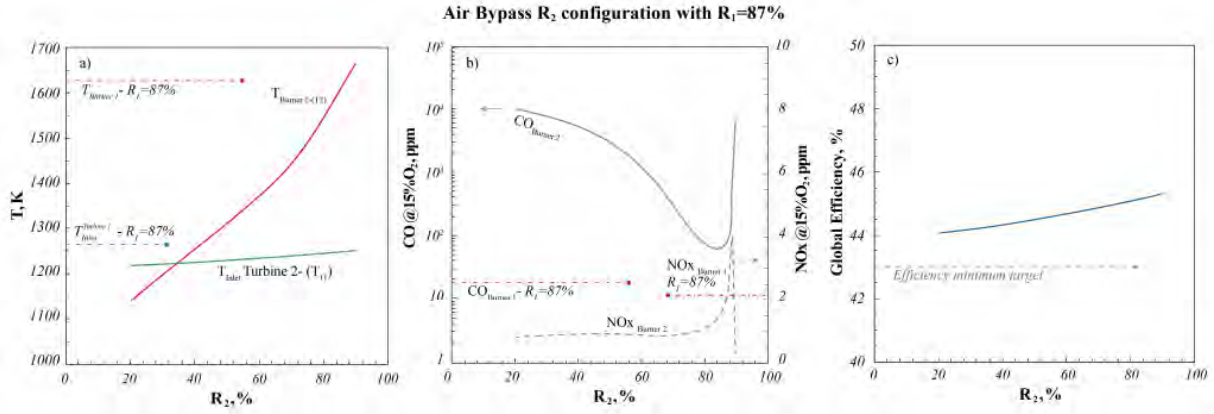

Figure 5. *Scheme 2: Operative T (a), CO-NO_x emissions (b), global efficiency (c) vs %R_2. R_1=87%.*

In particular, by providing a bypass ratio for Burner 2 equal to R_2=85% stable and complete combustion is achieved, with inlet temperature for turbine 2 of about 1240 K, while CO and NO_x emissions keep lower than 60 ppm and 2 ppm, respectively. Furthermore, the Bryton system configuration with bypass for both the burners and bypass ratios R_1=87% and R_2=85% allows to achieve a global efficiency equal to 45% (Figure 5c), thus meeting the minimum required target (>43%). Therefore, such a configuration is identified as the optimal one to ensure stable combustion and suitable operational temperatures, while minimizing both CO and NO_x emissions

and meeting the intercooled-reheat-regenerative Bryton system operative requirements.

Conclusion

In the proposed work the reheating process in a low-power, intercooled, regenerative and reheated gas turbine plant was analyzed. By the analysis of different configurations, the best operating conditions for methane combustion have been outlined. In particular, the plant configuration with bypass systems for both the burners and bypass ratios R_1=87% and R_2=85% ensures stable combustion and minimized pollutant emissions, with a global efficiency of about 45%. The methodology developed has led to interesting results especially for the use of alternative energy carriers such as ammonia or low-grade fuels, thus leading to the optimization of operative conditions with respect to the combustion process.

References

[1] Newell R, Raimi D, Villanueva S, Prest B. Global Energy Outlook 2021: Pathways from Paris 2021.
[2] IEA, Energy Technology Perspectives 2020. Rep., Int. Energy Agency Paris. n.d.
[3] Global E. Micro Gas Turbine Technology: Research and Development European Collaboration 2017.
[4] Liu Y, Sun X, Sethi V, Nalianda D, Li YG, Wang L. Review of modern low emissions combustion technologies for aero gas turbine engines. Progress in Aerospace Sciences 2017;94:12–45.
[5] Kim H, Nutakor C, Singh S, Jaatinen-Värri A, Nerg J, Pyrhönen J, et al. Design process and simulations for the rotor system of a high-efficiency 22 kW micro-gas-turbine range extender for electric vehicles. Mech Mach Theory 2023;183:105230.
[6] Bou Nader WS, Mansour CJ, Nemer MG. Optimization of a Brayton external combustion gas-turbine system for extended range electric vehicles. Energy 2018;150:745–58.
[7] Ariemma GB, Sorrentino G, Ragucci R, de Joannon M, Sabia P. Ammonia/Methane combustion: Stability and NOx emissions. Combust Flame 2022;241:112071.
[8] Ariemma GB, Sorrentino G, Sabia P, Ragucci R, de Joannon M. MILD Combustion of Methanol, Ethanol and 1-Butanol binary blends with Ammonia. Proceedings of the Combustion Institute 2022.
[9] Ariemma GB, Bozza P, De Joannon M, Sabia P, Sorrentino G, Ragucci R. Alcohols as energy carriers in MILD Combustion. Energy and Fuels 2021;35:7253–64.
[10] Sabia P, Sorrentino G, Ariemma GB, Manna M V., Ragucci R, de Joannon M. MILD Combustion and Biofuels: A Minireview. Energy and Fuels 2021;35:19901–19.
[11] ANSYS. CHEMKIN-PRO 15131 2013.
[12] Sorrentino G, Sabia P, De Joannon M, Cavaliere A, Ragucci R. The Effect of Diluent on the Sustainability of MILD Combustion in a Cyclonic Burner. Flow Turbul Combust 2016;96:449–68.
[13] CRECK Modeling. C1-C3 HT+NOx mechanism.

Numerical Modelling of Swirl Stabilised Lean-Premixed H_2-CH_4 Flames with the Artificially Thickened Flame Model

S. Castellani*, P.C. Nassini*, A. Andreini*, R. Meloni, E. Pucci**, A. Valera Medina***, S. Morris***, B. Goktepe***, S. Mashruk*****

simone.castellani@unifi.it

*Department of Industrial Engineering, University of Florence, Italy

**Baker Hughes, Via F. Matteucci 2, 50127, Florence, Italy

***Cardiff University School of Engineering, Cardiff, Wales, UK, CF24 3AA

Abstract

In this work, high-fidelity simulations of perfectly premixed swirl stabilized flames have been performed varying the H2 content in the fuel from 0 to 100% to investigate the effect of the hydrogen addition on a natural gas fired combustor. The artificially thickened flame model (ATFM) has been used to treat the turbulent chemistry interaction. The numerical results have been compared with the detailed experimental data performed at Cardiff University's Gas Turbine Research Centre showing a very good prediction accuracy.

Introduction

Hydrogen integration into the gas turbine combustion systems requires significant changes in the combustor architecture. Nevertheless, dealing with hydrogen, one of the most attractive solutions is still the lean premixed technology, representing nowadays the state of the art for low carbon fuel combustion in land-based gas turbines. The enabling of Dry-Low NOx (DLN) technology to high H2 content allows the exploitation of part of the industry's know-how acquired over years for Natural Gas (NG) combustion. Moreover, starting the redesign process from configurations already capable to manage the NG combustion, would help to preserve a certain degree of retrofitting and fuel flexibility. In the transitional phase toward using carbon-free fuels, the new combustion systems need to ensure fuel flexibility overcoming the discontinuous hydrogen supply.

The lean premixed burner design could face several difficulties related to the different thermodynamic and chemical properties of H2 with respect to conventional fuels. Due to the higher adiabatic flame temperature of H2 with respect to CH4, H2-fueled systems must be operated in leaner conditions to contain NOx emissions. Moreover, the high H2 reactivity rises the flashback risk altering the stability margin of the combustor and worsening its operability under low loads.

All these arguments rise the need to experimentally investigate the effect of H2 addition in lean-premixed conditions, likewise, validating the numerical model prediction capacity.

The combustion modelling of high hydrogen-containing mixtures must be able to account for the differential diffusion to correctly characterize the flame propagation characteristics. The species transport models are intrinsically capable to account for all these aspects on the solved flame front. In this work, the Artificially Thickened Flame Model (ATFM) [1] has been adopted to model the turbulence chemistry interaction.
The CH4-H2 lean premixed flames have been heavily studied in the literature with both experimental and numerical work. Agostinelli et al. [2] have recently investigated the PRECCINSTA burner operated up to 50%vol of H2 with CH4 under pressure, highlighting how the computational cost rises sharply with the pressure increase with H2. Nevertheless, the prediction capability of the ATFM in these conditions is excellent as it also shows an accurate reconstruction of the thermoacoustic behaviour. To the authors' knowledge, no single study in the literature considers H2 contents from 0% up to 100% on lean premixed swirl stabilized flames. This work aims to investigate the effect of hydrogen addition from 0% to 100% on the flame morphology experimentally and numerically. Moreover, the measured OH* chemiluminescence allows the validation of the ATFM prediction capacity when preferential diffusion effects are expected to be essential for flame propagation.

Experimental Facility

The test case studied in this work has been investigated during the experimental campaign conducted in the GTRC laboratory at Cardiff university research centre. The facility (described in detail in [3]) consists of a high-pressure rig with optical accesses. The air supply line includes an electric heater that allows the mixture to reach a temperature of up to 573 K with a flow capacity of 0.25 kg/s. The facility is equipped with a radial-tangential swirler (having geometric swirl number 0.8) based on industrial lean premixed design. In the context of this study, the burner has been operated in fully premixed conditions and the whole rig is at atmospheric pressure.
The high-speed OH*chemiluminescence image capture system utilizes a combination of a high-speed camera, relay lens, high-speed image intensifier, UV lens (RicohFL-GC7838-VGUV, f/8) with a 310nm narrow bandpass filter.

Computational domain and numerical setup

The test case just introduced has been numerically investigated with high-fidelity LES simulations. The spatially filtered Navier Stokes equations have been solved with the pressure-based solver ANSYS Fluent 2022R2. The turbulent combustion has been modelled with the ATFM with constant thickening since all the investigated cases are perfectly premixed. Nevertheless, the thickening is only applied on the flame front using a dynamic thickening factor. Sub-scale wrinkling effects have been taken into account through the efficiency function formulation proposed by Colin et al. [1]. Most of the efficiency function formulations require the estimation of the dilatation-free velocity fluctuation at the test filter. Colin et al. [1], have proposed a

formulation that requires the third-order derivative of the filtered velocity, a non-trivial task on an unstructured mesh. Instead, the approach proposed by Durand et al. [4] is adopted here.
A 26 species and 119 reactions skeletal mechanism derived from the UCSD mechanism is employed; the chemistry set was retrieved leveraging the commercial code CHEMKIN-Pro and a detailed description of the reduction procedure can be found in the work of Meloni et al [5]. The chemical source terms are computed using a stiff chemistry solver, that allows the decoupling of the chemical timestep with the simulation timestep.

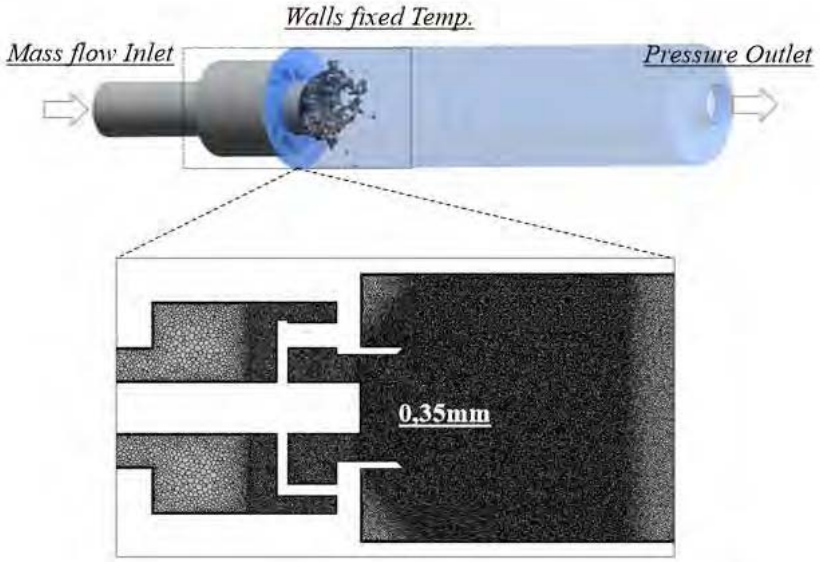

Figure 1 Schematic visualization of the computational domain, and mesh with the refinement zone

The computational domain is shown in Figure 1. All the walls are treated with a wall function approach and a fixed temperature is imposed on the different quartz tube regions according to the measurements.
The mesh for all the investigated conditions counts 16 million polyhedral elements. The refinement zone is shown in Figure 1, and includes the swirler and all the expected flame regions with an average size of the elements of 0.35mm. Three prismatic layers have been placed on the walls in order to improve the discretization of the boundary layer. Some information about the test points investigated are reported in Table 1.

Table 1 Summary of test points investigated

	0H2	**60H2L**	**100H2L**
%H2 by vol. [-]	0%	60%	100%
Φ [-]	0.6	0.465	0.265
F_{max}	5.4	5.2	3.3
LFS	0.38	0.36	0.2
$T_{ad}[K]$	1822	1608	1277

u_{bulk}[m/s]	21.1	26.5	41.4

Results

The OH* radical is solved to be directly compared with the experimental OH* chemiluminescence signal. In Figure 2 the time-average Line Of Sight (LOS) of the Y_{OH}^{*} has been compared with the experimental OH* chemiluminescence for all the investigated test points. In all the conditions the model prediction shows an overall good agreement with the experimental measurements. Experimentally, the flame is V-shaped and its length is very sensitive to the change in the inlet mass flow and %H2. The flame morphology is well reconstructed by the model that successfully captures the flame extinction on the external shear layer. Moreover, also the flame length variation with H2 addition is well predicted. The simulations underestimate slightly the flame length decreasing the H2 content. This discrepancy may be ascribable to the near-wall flame heat loss characterization since, for the 0% H2 case, the flame interacts with the wall making the uniform wall temperature boundary a less realistic assumption. It can be easily seen that the increase in the H2 content of the mixture finally results in a more compact flame. This suggests that the turbulent flame speed increases with the increase in the H2 content allowing a higher fuel consumption rate.

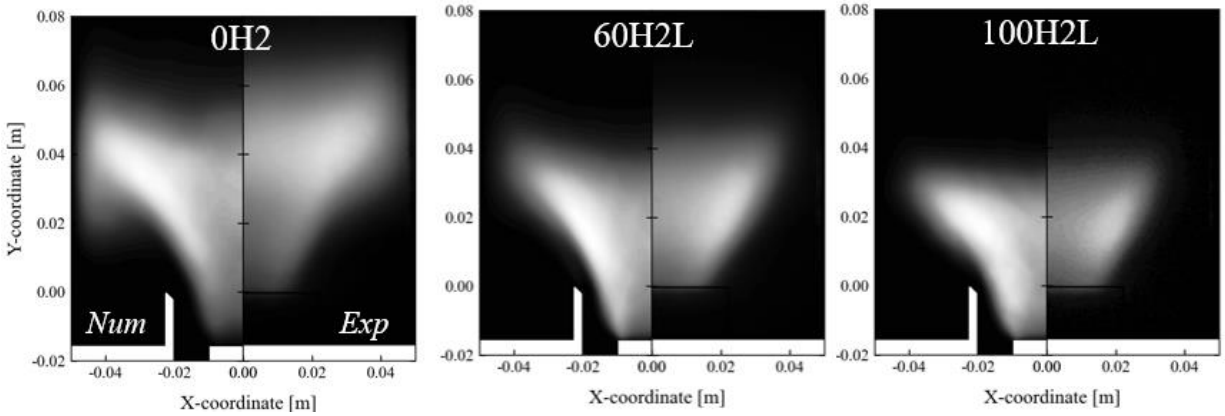

Figure 2 Comparison between the numerical time-averaged OH* LOS (left) and the experimental time-averaged OH* signal (right) for all the test points (Table 1).

This global increase in the flame reactivity moving toward higher H2 content is not explainable by the unstretched LFS of the mixture shown in Table 1. Indeed, increasing the H2 content, the LFS decreases due to the lower equivalence ratio of the mixture, but the overall turbulent flame speed S_T is found to increase leading to a shorter flame even considering the higher bulk velocity.

The dashed line in Figure represents the heat released (HR) from the reference 1D unstretched laminar flame. The scatterplot shows that the turbulent solution overestimate heavily the unstretched 1D HR increasing the H2 content. Such higher HR levels are explainable including the effect of the strain in the laminar flamelet. With this purpose, a series of laminar flamelet solutions have been reported in Figure increasing the strain rate level for each %H2 (continuous lines). The effect of the

strain combined with the H2 differential diffusion makes the unstretched solution to be not representative of the strained tri-dimensional flame front. For this reason, the flame reactivity is found to deviate from the unstretched estimation as much as the H2 content increases, thus contributing to explain the flame shortening with the H2 increase. The colour of the scatterplot in Figure represents the local level of enthalpy loss with respect to the adiabatic unburnt conditions and is evaluated as:

$$H_{rel} = \left(h_s + \sum_{k=1}^{N} Y_k \, \Delta h_{f,k}^0\right) - \left(h_s + \sum_{k=1}^{N} Y_k \, \Delta h_{f,k}^0\right)_{unburnt} \quad \textbf{Equation 1}$$

In which h_s is the sensible enthalpy, and $\Delta h_{f,k}^0$ is the formation enthalpy of the species k. Another contribution to the flame shortening is the decreasing level of H_{rel} (Figure) at which the flame is subjected, which is mainly due to the decrease of the flame temperature with the increase of the H2 content.

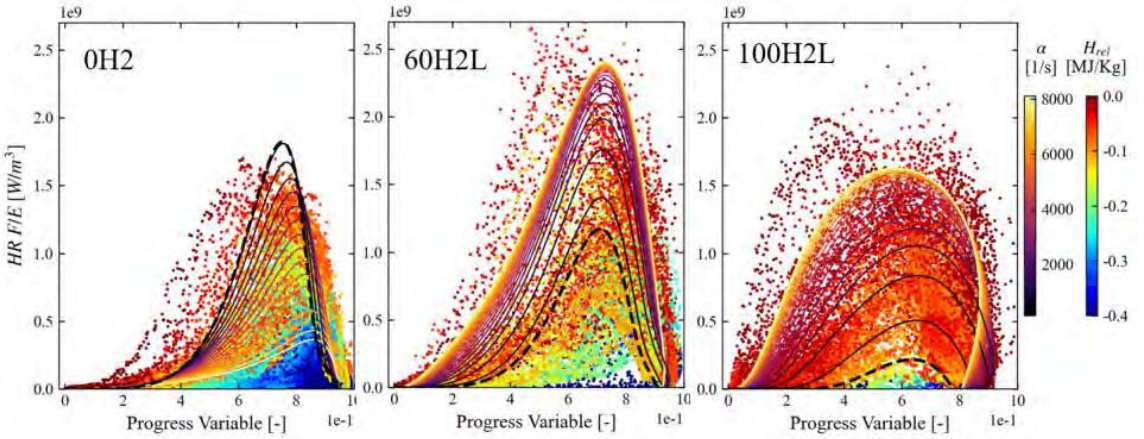

Figure 3. Scatter plot showing scaled HR respect to the normalised PV ($Y_{PV} = -Y_{H2} + Y_{H2O} + Y_{CO2} + Y_{CO}$) sampled from an instantaneous solution on the xy-plane. Colours represent the local level of H_{rel}. (Continuous lines) HR of laminar counterflow flamelet increasing α; (Dashed lines) laminar unstretched flamelet solution.

Nomenclature

F_{max}	Maximum Thickening Factor [-]
H_{rel}	Relative sensible and chemical enthalpy [MJ/kg]
Y	Species Mass Fraction [-]
S_T	Turbulent flame speed [m/s]
T_{ad}	Adiabatic burnt temperature [K]
u_{bulk}	Swirler exit bulk velocity [m/s]
α	Strain Rate [1/s]
Φ	Equivalence Ratio [-]

Acronyms

ATFM	*Artificially Thickened Flame Model*
DLN	*Dry-Low NOx*
HR	*Heat Released*
LES	*Large Eddy Simulation*
LFS	*Laminar Flame Speed [m/s]*

LOS *Line Of Sight*

Conclusion

A perfectly premixed swirled stabilized flame has been investigated both experimentally and numerically considering an increasing level of H2 in the H2-CH4 fuel mixture (from 0% to 100%). The accordance between the experimental OH* measurements and the numerical results proves the effectiveness of the ATFM to be predictive in the whole range of conditions.

Contrary to what may be expected, the measured and predicted flame extensions are against the mixture laminar flame speed trend. Thus, increasing the H2 content the mass flow, the flame gets shorter despite the mixture LFS estimation decreases. The comparison between the heat released of the numerical simulation with some laminar flamelet shows that the heat loss and presence of stretch on a flame front having Le<1 are two contributions that lead the reactivity to heavily differs from the unstretched adiabatic laminar condition.

References

[1] O. Colin, F. Ducros, D. Veynante, T. Poinsot, A thickened flame model for large eddy simulations of turbulent premixed combustion, Phys. Fluids. 12 (2000) 1843–1863. https://doi.org/10.1063/1.870436.

[2] P.W. Agostinelli, D. Laera, I. Chterev, I. Boxx, L. Gicquel, T. Poinsot, On the impact of H2-enrichment on flame structure and combustion dynamics of a lean partially-premixed turbulent swirling flame, Combust. Flame. 241 (2022) 112120. https://doi.org/10.1016/j.combustflame.2022.112120.

[3] D.G. Pugh, P.J. Bowen, R. Marsh, A.P. Crayford, J. Runyon, S. Morris, A. Valera-Medina, A. Giles, Dissociative influence of H2O vapour/spray on lean blowoff and NOx reduction for heavily carbonaceous syngas swirling flames, Combust. Flame. 177 (2017) 37–48. https://doi.org/10.1016/j.combustflame.2016.11.010.

[4] L. Durand, W. Polifke, Implementation of the thickened flame model for large Eddy simulation of turbulent premixed combustion in a commercial solver, Proc. ASME Turbo Expo. 2 (2007) 869–878. https://doi.org/10.1115/GT2007-28188.

[5] R. Meloni, S. Orsino, R. Yadav, N. Ansari, D. Bessette, S. Castellani, A. Andreini, P.C. Nassini, I. Boxx, Partially Premixed Hydrogen-Methane Flame Simulations at Relevant Gas Turbine Conditions with a Thickened Flame Model Enhancement, Proc. ASME Turbo Expo 2023 Turbomach. Tech. Conf. Expo. Tech. Conf. Expo. (2023) 1–12.

FGM vs ATFM: a comparative analysis in predicting the flame characteristics of an industrial swirler

G. Lemmi*, P.C. Nassini*, S. Castellani*, A. Picchi*, S. Galeotti*, R. Becchi*, A. Andreini*, G. Babazzi, R. Meloni****

gianmarco.lemmi@unifi.it

*Department of Industrial Engineering, University of Florence, Italy

**Baker Hughes, Via F. Matteucci 2, 50127, Florence, Italy

Abstract

The present work focuses on the comparison between two of the most used combustion models, the Flamelet Generated Manifold (FGM) and the Artificially Thickened Flame Model (ATFM), when applied to an industrial lean premixed burner operated with methane at atmospheric pressure. Both the models represent extended versions specifically intended to overcome their respective limitations. Detailed chemiluminescence images revealing the flame shape and position will represent the main benchmark for the numerical validation. Furthermore, the differences in terms of flow field and fuel concentration at the burner exit will be shown as well as the overall CO prediction.

Introduction

Reactive Computational Fluid Dynamics (CFD) codes rely on just few models whose performance can be design-dependent and/or extremely sensible to the fuel composition as well. Detailed experimental measurements of the flame are extremely useful for the validation of such models allowing the designers to know *when-and-how* a combustion model can be preferred to another one and at which computational cost. Nowadays the literature is dominated by two families of combustion models: the tabulated-chemistry approach, where the FGM [1] is the most widespread, and the ATFM [2]. The FGM is known for its computational efficiency related to the decoupling of the reaction time scale from the convection/diffusion ones, allowing the pre-tabulation of the chemistry. Despite that, important physical aspects having an impact on the flame brush (like stretch and heat loss) are not directly embedded into commercial codes and have to be introduced as customization [3]. On the other hand, the ATFM can naturally consider all these aspects and, more importantly, take care of preferential diffusion aspects, crucial for hydrogen combustion. The limitation of the latter model lies in its correct application only to perfectly premixed mixtures even if, recently, some dedicated variants have been proposed to overcome this issue [4]. From the computational cost perspective, surely the TFM implies higher costs, especially when detailed or skeletal mechanisms are considered.

In this work, detailed experimental measures related to an industrial burner are leveraged to compare the results provided by an enhanced version of both the FGM

and the ATFM. The mathematical formulation of the two approaches will be presented in the next paragraph which will be followed by a brief summary of the investigated test conditions. The Results and Discussion section will provide a detailed comparison among the models in terms of flame morphology, thermal, mixing, and velocity fields.

Test Rig Conditions

Tests are performed in an optically accessible rig with an industrial burner fed through two fuel lines [5]. The main premixer injects the fuel through the counter-rotating swirler to deliver a uniform mixture into the combustor. Conversely, the pilot line is responsible for the flame stabilization delivering the gas directly into the primary zone. Figure 1 sketches the assembly of the main components of the dome as well as the computational grid in a longitudinal plane where the different sizing in the different regions of the model can be appreciated. The mesh is the same for all the investigated combustion models.

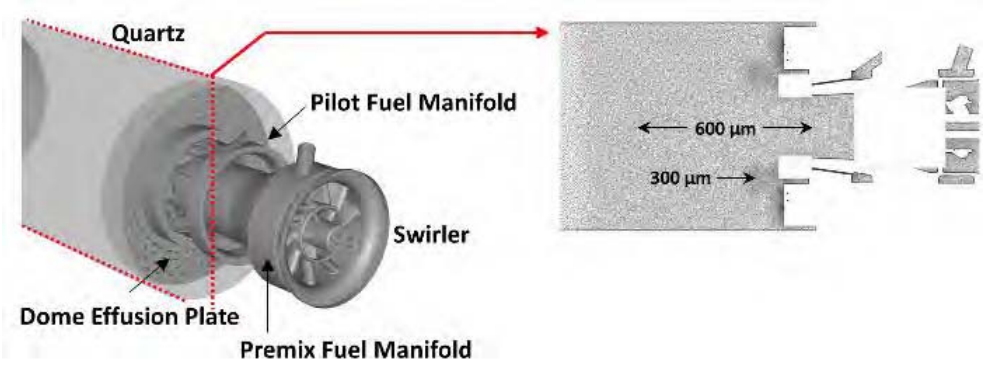

Figure 1. Detailed view of the burner-dome assembly and view of the grid in a longitudinal plane.

The rig is operated at atmospheric pressure, with the air temperature set to 300 °C and pure methane as fuel. A Horiba is used to analyze the flue gas, sampled after about 9 ms of residence time, and to retrieve the main pollutant emissions like CO and NO_x. The chemiluminescence is executed through a Phantom MIRO M340 camera and an intensifier equipped with a filter at 310 nm. Images are collected at 1000 Hz, with the gain and the gate set to 5 and 0.5 ms, respectively.

Mathematical Formulations of the Tested Combustion Models

Extended-ATFM

The approach presented in [4] is applied in the present study. A flame index is employed to identify the cell-based combustion regime: for positive values, the original formulation is applied [2] with the flame thickness discretized through 9 mesh points. Instead, the flame front is not thickened (consequently a finite-rate closure is adopted) when the diffusive regime is detected. A 19 species – 62 reactions skeletal mechanism derived ad-hoc for this investigation is used for the methane-air oxidation.

Extended-FGM-FR

This study exploits an enhanced version of the conventional FGM approach that incorporates the effects of flame stretch and heat loss in a pre-calculated table (Γ-table), thus directly impacting the combustion process reactivity. For this purpose, a new parameter (Γ) is defined and tabulated as a function of the strain rate k and heat loss ψ in order to correct the turbulent progress variable source term:

$$\widetilde{\dot{\omega}_c}\left(\tilde{Z},\tilde{c}\right) = \Gamma(\psi,k)\iint \widetilde{\dot{\omega}_c}\,(Z,c)P(Z)P(c)dZdc \qquad (1)$$

with $\Gamma(\psi,k)$ multiplying the standard Finite Rate (FR) turbulent source term extracted from the look-up table. $\Gamma(\psi,k)$ is defined as the ratio between the maximum values of the strained, non-adiabatic progress variable source term and the adiabatic, unstrained one in a 1D laminar flame:

$$\Gamma(\psi,k) = \frac{\max \dot{\omega}_c(Z,c,\psi,k)}{\max \dot{\omega}_c^0(Z,c)} \qquad (2)$$

with ψ identifying the heat loss parameter, defined as the ratio between the burnt gas temperature and the corresponding equilibrium value, and k representing the strain, evaluated from the velocity flow field according to [6]. Cantera libraries are used to solve several freely propagating flames ($k = 0$) and premixed counterflow flames ($k > 0$) in order to generate the $\Gamma(\psi,k)$ table. More details are available in [7].

Results and Discussion

Flame Morphology and thermal field

The prediction of the flame shape and position of the two numerical models against the measurements is reported in Figure 2.

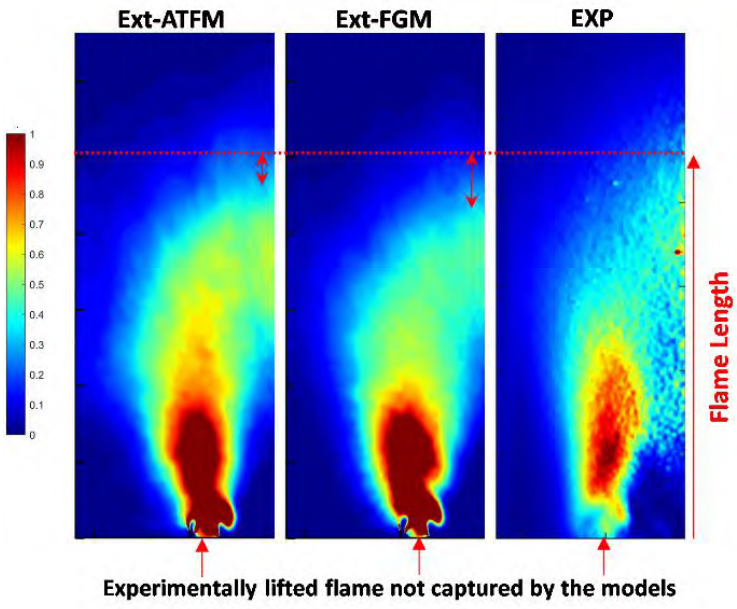

Figure 2. Normalized time-averaged heat release rate from the ATFM (left) and the Ext-FGM (center) compared with the Abel-deconvoluted OH* from the test (right).

The experimental map is the Abel-deconvoluted OH* signal acquired with the camera placed orthogonally to the combustor axis. This map is compared with the time-averaged contour plots of the heat release on the midplane, shown in Fig. 1. To enable effective visual comparison between computed and experimental results, only half of the domain is reported. Both the combustion models predict the flame length reasonably well: the Ext-FGM has a higher underprediction of such quantity with respect to the ATFM, meaning that the former approach is affected by a higher reactivity. More importantly, despite both models can identify the main flame stabilization around the pilot jets, the experiments reveal that the corresponding heat release is more lifted. Numerically, the heat release reaches the peak value right downstream of the pilot fuel injection. Surely, such a finding is influenced by the adiabatic thermal boundary condition imposed on the burner wall of both models, adopted since no direct measure of the wall temperature is available in that position. The enhanced reactivity of the FGM has a direct impact on the thermal field. Figure 3 reports the contour plot of the time-average temperature in a longitudinal and in a cross-section inside the primary zone of the flame tube. Both these locations highlight that the peak temperature is higher for the FGM model compared with the ATFM all around the pilot-stabilized region. This behavior can potentially have an impact on the prediction of pollutant emissions, especially for NO_x.

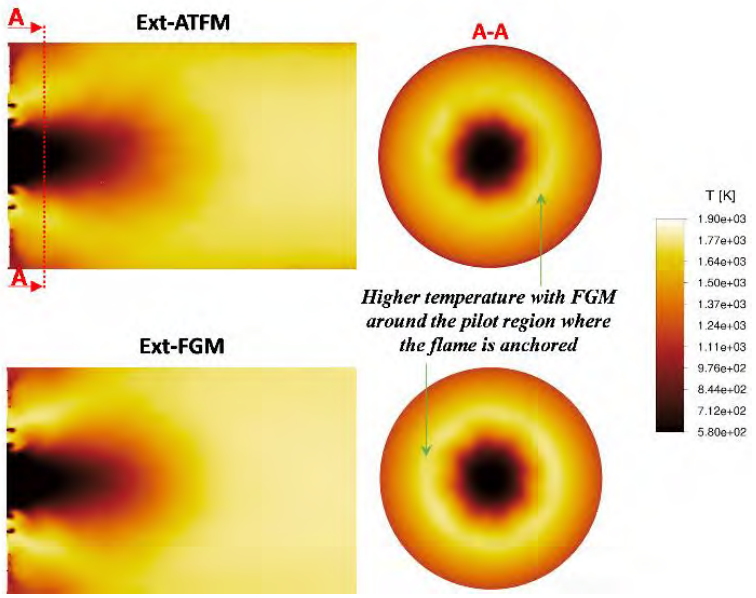

Figure 3. Time-averaged temperature field in a longitudinal and a transversal plane within the primary zone for both the numerical models.

Mixing and Velocity Field

The minor differences in the flame shape prediction between the two models do not appear to significantly affect the flow field in the burner exit region. Moreover, the flow fields within the combustion chamber exhibit strong agreement between the two numerical approaches, with only a few small discrepancies. Along the centerline ($Z = 0$), corresponding to the main region, the ATFM model exhibits a more axially

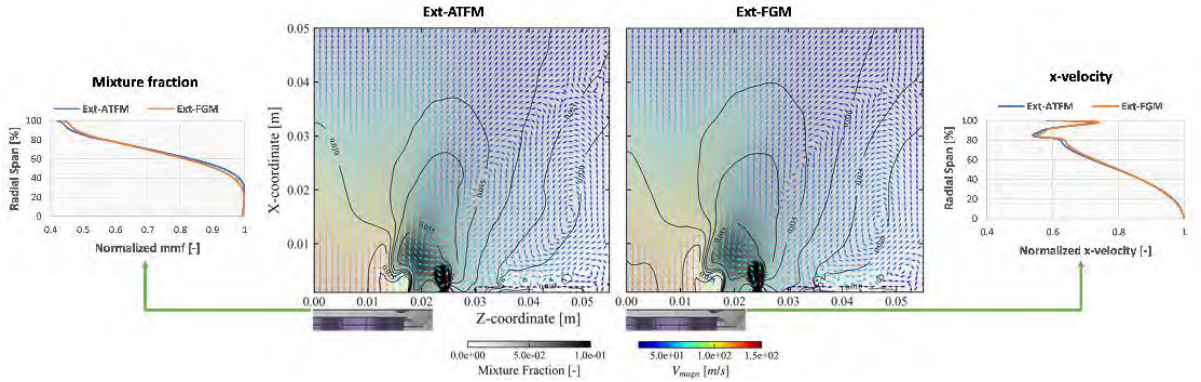

Figure 4. Time-averaged mixture fraction field and planar velocity vector-plot in a longitudinal plane within the primary zone for both the numerical models. Normalized mean values are plotted along the radius in a transversal section located at the main burner exit.

developed fluid region outside the main burner characterized by higher values of mixture fraction compared to the FGM model. Conversely, in the pilot region, the zone with higher mixture fraction values appears to be shorter for the ATFM model. These observations suggest that in the ATFM model, the pilot flame mainly enriches the main region rather than the recirculation zone.

Conclusion

In this work, an assessment of the flame shape prediction of two enhanced versions of the FGM and ATFM combustion models is performed through a direct comparison between the computed results and experimental data obtained from an in-house test rig.

Both models are capable of accurately predicting the flame topology, with ATFM showing slightly higher accordance with the experimental measurements compared to the FGM, the latter marginally underestimating the flame length, thus indicating a higher reactivity affecting the approach. The small discrepancies observed in predicting the flame shape between the two models do not seem to have a substantial impact on the flow field in the burner exit region.

It is important to note that the exclusion of wall heat losses from the analysis may impact the flame shape, and further investigations for both models will be carried out to estimate this effect.

Nevertheless, the FGM has shown its suitability for design-phase simulations by reasonably replicating the results from more computationally intensive models, such as the ATFM.

Nomenclature

ATFM Artificially Thickened Flame Model
CFD Computational Fluid Dynamics
FGM Flamelet Generated Manifold

FR Finite Rate
LES Large Eddy Simulation
P Probability Density Function
Z Mixture Fraction
ω Source Term

Subscripts
c Progress variable

Superscripts
o Adiabatic unstrained
~ Mean value

References

[1] J. A. V. Oijen and L. P. H. D. Goey, "Modelling of Premixed Laminar Flames using Flamelet-Generated Manifolds," *Combustion Science and Technology,* vol. 161, no. 1, pp. 113-137, 2000

[2] O. Colin, F. Ducros, D. Veynante and T. Poinsot, "A thickened flame model for large eddy simulations of turbulent premixed combustion," *Physics of Fluids,* vol. 12, no. 7, pp. 1843-1863, 2000

[3] N. Klarmann, B. T. Zoller and T. Sattelmayer, "Numerical modeling of CO-emissions for gas turbine combustors operating at part-load conditions," *Journal of the Global Power and Propulsion Society,* vol. 2, pp. 376-387, 2018

[4] A. Aniello, D. Laera, S. Marragou, H. Magnes, L. Selle, T. Schuller and T. Poinsot, "Experimental and numerical investigation of two flame stabilization regimes observed in a dual swirl H2-air coaxial injector," *Combustion and Flame,* vol. 249, 2023

[5] S. Romano, R. Meloni, G. Riccio, P. C. Nassini and A. Andreini, "Modeling of Natural Gas Composition Effect on Low NOx Burners Operation in Heavy Duty Gas Turbine," *Journal of Engineering for Gas Turbines and Power,* vol. 143, no. 3, 2021

[6] P. C. Nassini, D. Pampaloni, R. Meloni and A. Andreini, "Lean blow-out prediction in an industrial gas turbine combustor through a LES-based CFD analysis," *Combustion and Flame,* vol. 229, no. 111391, 2021.

[7] M. Amerighi, P. C. Nassini, A. Andreini, S. Orsino, I. Verma, R. Yadav and S. Patil, "Assessment of Flamelet Generated Manifold approach with inclusion of stretch effects of pure hydrogen flames," in *ASME Turbo Expo 2023 Turbomachinery Technical Conference and Exposition (GT2023)*, Boston, MA, 2023

IMPACT OF HYDROGEN ADDITION ON THE THERMO-ACOUSTIC STABILITY OF A METHANE FUELLED MICRO GAS TURBINE

V. Ceglie*[, a], J. Bompas[c], M. Stefanizzi[a], F. Fornarelli[b], W. De Paepe[c], S. M. Camporeale[a], D. Laera[a],

*vito.ceglie@poliba.it
[a] Polytechnic University of Bari, Department of Mechanics, Mathematics & Management, via Orabona 4, 70125, Bari, Italy
[b] University of Foggia, Department of Sciences of Agriculture, Food, Natural Resources and Engineering, via Napoli, 25, 71121, Foggia, Italy
[c] University of Mons (UMONS), Thermal Engineering and Combustion Unit, Faculty of Engineering, Place du Parc 20, 7000, Mons Belgium

Abstract
In recent years great efforts have been made on the use of hydrogen (pure or mixed with standard hydrocarbons) as a fuel in combustion systems, in order to enable a greater penetration of renewable energy sources in the actual energy mix. In this context, micro gas turbines (mGT) are an emerging technology for achieving an efficient cogeneration of heat and power (CHT) considering their higher efficiency, flexibility and environment friendliness. Unfortunately, although these systems can be designed to operate with different fuels (natural gas, syngas, biogas, etc.), the substitution in fuel composition may lead to the onset of unwanted phenomena such as thermo-acoustic instabilities which limit system stable operation and raise safety problems. To prevent these damaging events, it is essential to be able to predict the onset of such instabilities at the design stage. In the present study, the impact of hydrogen addition on the stability map of a typical mGT, i.e., the AE (ex Turbec) T100, is numerically investigated. The results show that the introduction of hydrogen in the mixture leads to an increase in instabilities in the combustion chamber.

Introduction
The production of CO_2 is strongly related to combustion processes involved in transportation, industry, heating applications, and power generation sectors. The current energy generation and supply system must support the growing demand for a drastic reduction of CO_2 emissions. In the future power generation market, the trend is shifting toward decentralized power generation technology. Micro gas turbines currently represent the most promising technology in order to decentralize power generation. Integration of green hydrogen in micro gas turbines (mGT) will encourage the upcoming energy transition. However, the hydrogen enrichment in gas turbine burners might cause the displacement of combustion instabilities. Combustion instability is a physical phenomenon that happens during the combustion process due to the interaction between acoustic waves propagating

inside the combustion chamber and thermal release fluctuations. Even if there is an increasing number of experimental and numerical studies on gas turbine burners fueled by pure hydrogen and methane-hydrogen blends, the investigations on the thermoacoustic behavior of these mixtures are very few. On the numerical level, a linear analysis of the flame acoustic perturbation and a detailed modeling of the acoustic damping of the system is required in order to predict correctly the thermoacoustic behavior of burner designed for methane-air mixture in case that hydrogen is used as fuel. Three basic methods, low-order numerical models, CFD (Computational Fluid Dynamics) models, and Helmholtz solver models, are used to examine thermoacoustic instability. Low-order models divide the thermoacoustic system into a network of basic acoustic domains (such as pipes, burners, flames, etc.), where the acoustic field is modeled as a Helmholtz equation solution [1] [2]. CFD methods (for example, soling RANS, URANS, and LES techniques) allow for a more realistic characterization of the thermo-fluid dynamic flow fields inside the combustor; nevertheless, this comes at a significant computational cost [3] [4]. By using the Fourier transform, Helmholtz solvers are used to translate time domain-based differential equation problems into eigenvalue issues in the frequency domain [5] [6]. Simulations based on Helmholtz solvers offer the possibility to account for the real geometry of the burner with the fluid-dynamic properties obtained by CFD simulation. Indeed, this approach requires information on the heat release, time delay, flow field, pressure, and temperature distribution, in order to correctly model instabilities during the combustion process. This method has not been frequently utilized to calculate instabilities within mGT burners.
In the present study the thermoacoustic influence of hydrogen as a component of a mixture with hydrocarbons, in micro gas turbine burners has been presented. Specifically, the AE T100 combustor has been used as a case study. Indeed, this mGT was designed to work with only methane. With the aim to adapt these machines to work with methane/hydrogen blends for the energy transition phase, it is important to understand their thermoacoustic behavior caused by hydrogen enrichment. In this framework, this study presents a thermo-acoustic stability analysis of the AE T100 combustor. In details, RANS simulations have been carried out on the combustor fueled both by methane and methane enriched with hydrogen at 30%v (on volume basis). The results from CFD simulations have been used in a Helmholtz solver in order to understand the influence of hydrogen addition on the thermoacoustic stability map of the combustor.

Geometry AE-T100

The geometry of combustion chamber of the AE-T100 [7] [8] [9] investigated in this study is shown in Fig. 1. Combustion air enters in counter-current in the gap between the outer casing and inner walls. A portion of air reaches the pilot injector through the 12 jet holes of swirler 1 consumed in diffusion mode. The 15 radial vanes of swirler 2 and 30 jet holes of swirler 2', allow residual air to mix with the main fuel resulting in a premix flame. At the exit of the combustor, burned gasses are diluted

with fresh air coming through dilution holes to reach the desired turbine inlet temperature (TIT) of 950°C.

CFD simulations of AE-T100

In the RANS study on the burner of AE-T100, the aim is to develop the field of fluid-dynamic quantities in order to use it in the thermoacoustic simulations, as well as studying the impact of increase of hydrogen in the fuel blend. Starting with a constant air flow rate of $\dot{m}_{air} = 690\ g/s$ and a constant thermal power of $P_{th} = 333\ kW$, the fluid-dynamic parameters of RANS simulations for the two mixtures are set. The parameters of the analyzed cases are summarized in Table 1.

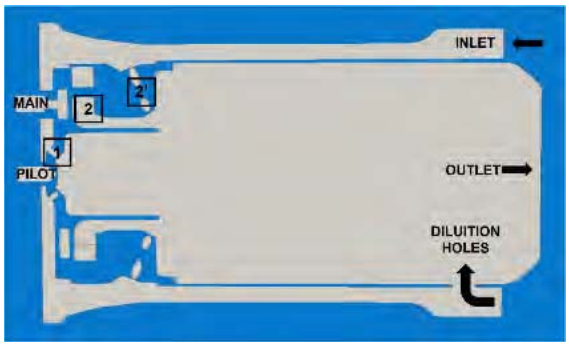

Figure 1. Burner geometry of AE-T100: (a) Fuel injection system main and pilot through plane highlighting the counter-flow air inlet, the pilot (1) and main (2,2') swirlers, and the dilution holes.

Table 1. Parameters of CFD simulations of AE-T100.

Parameters	100 % CH_4	70 % CH_4 + 30% H_2	Units
T_{air} = air inlet temperature	300	300	K
Ø = equivalence ratio	0.38	0.31	-
$\dot{m}_{fuel}$= mass flow	6.65	6.20	g/s
p = pressure	4 x 10^{-5}	4 x 10^{-5}	Pa
LHV=lower heating value	50.1	53.7	kJ/g

The 3D RANS CFD simulations on the burner of AE-T100 have been carried out by means open source code OpenFOAM. The reactingFoam solver has been used to perform reacting flow simulations. The turbulence model employed was the k-ε model. For all mixtures, the simulation of the AE-T100 burner has been performed by using the GRI-mech 3.0 chemical mechanism that consists of 53 chemical species and 325 reactions. Fig. 2 shows the results of this analysis in terms of contours of heat release rate (Fig. 2(a)) and temperature (Fig. 2(b)) in the combustion chamber of AE-T100 fueled by pure methane and 70%$_v$ CH_4-30%$_v$ H_2 mixtures. The hydrogen-enriched flame is shorter with respect to pure methane flame of burner fueled by pure methane, due to the higher burning velocity of the hydrogen. The

temperature distribution is clearly influenced by the addition of hydrogen in the mixture: particularly, a higher temperature peak is observed close to the pilot flame whereas the temperature slightly drops further inside the combustor as shown in Fig. 2(b). This may be explained by the fact that in the two cases the air mass flow rate and thermal power are kept constant resulting in a leaner mixture characterized by a lower adiabatic flame temperature.

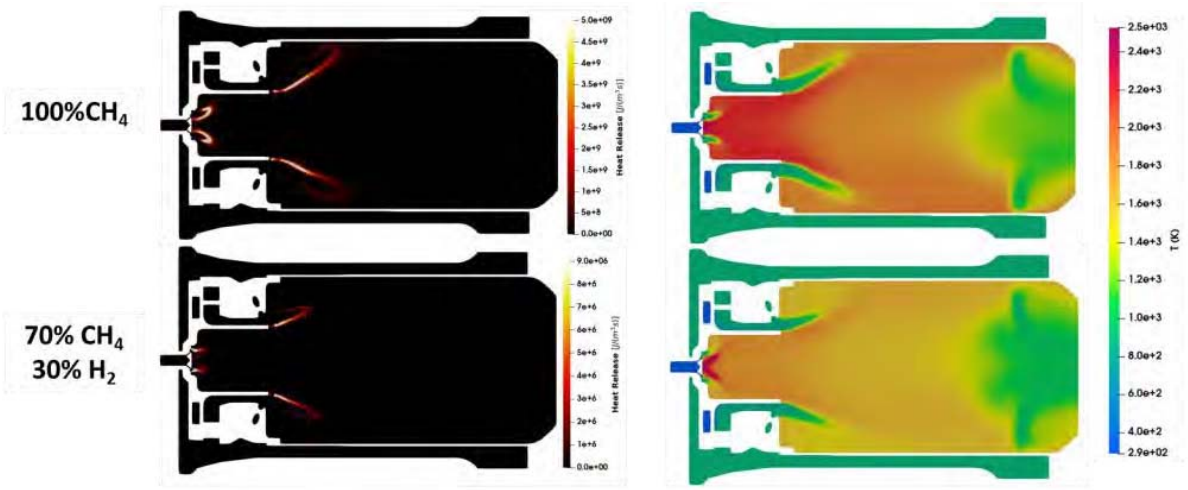

(a) (b)

Figure 2. Contour on Longitudinal Plane for two mixture (100% CH_4 and 70%$_v$ CH_4 -10%$_v$ H_2): (a) Heat release, (b) temperature.

The thermo-acoustic model

For the thermo-acoustic analysis, only the combustion chamber and pilot duct were considered, as the area variation between the swirlers/injectors and dilution holes was deemed sufficient to achieve acoustic decoupling. The inlet sections are considered to behave like a hard-acoustic walls (u'=0), while a pressure node (p'=0) is imposed at the outlet section of the combustion chamber.

The thermo-acoustic stability study was performed using the Acoustic Pressure and Frequency Domain model in COMSOL Multiphysics. This solves the acoustic differential equations problem converting it into a eigenvalues problem in the frequency domain. Three-dimensional mean fields of speed of sound and density are taken from CFD simulations. In the frequency domain, in the case of small perturbations, the local flame response to an acoustic perturbation can be represented by the Flame Transfer Function (FTF). This is a complex function that depends only on the excitation or angular frequency $\omega = 2\pi f$, where f is the frequency. This function is defined as the ratio of the heat release rate fluctuation $\hat{\dot{Q}}(\boldsymbol{x})/\bar{\dot{Q}}(\boldsymbol{x})$ to the velocity fluctuation $\hat{u}(\boldsymbol{x})/\bar{u}(\boldsymbol{x})$ taken at a reference position i:

$$\frac{\hat{\dot{Q}}(\boldsymbol{x})}{\bar{\dot{Q}}(\boldsymbol{x})} = FTF\,\frac{\hat{u}_i(\boldsymbol{x})}{\bar{u}_i(\boldsymbol{x})} = n\exp(-i\omega\tau)\,\frac{\hat{u}_i(\boldsymbol{x})}{\bar{u}_i(\boldsymbol{x})}$$

where n is the gain factor and τ the time delay between the two fluctuations, and **x** is the spatial coordinate. In the present work, only dynamics of the main flame is considered. The time delay was computed using a particle tracking technique: released at the exit of main swirler (reference location i), particles are tracked and a mean convective time computed until the flame front is reached. The value of this time was set equal to 7 ms and 2 ms in the pure methane and methane/hydrogen case, respectively.

Results

Results from the linear stability analysis show that when adding hydrogen, the system becomes more instable (see Fig. 3 and Table 2).

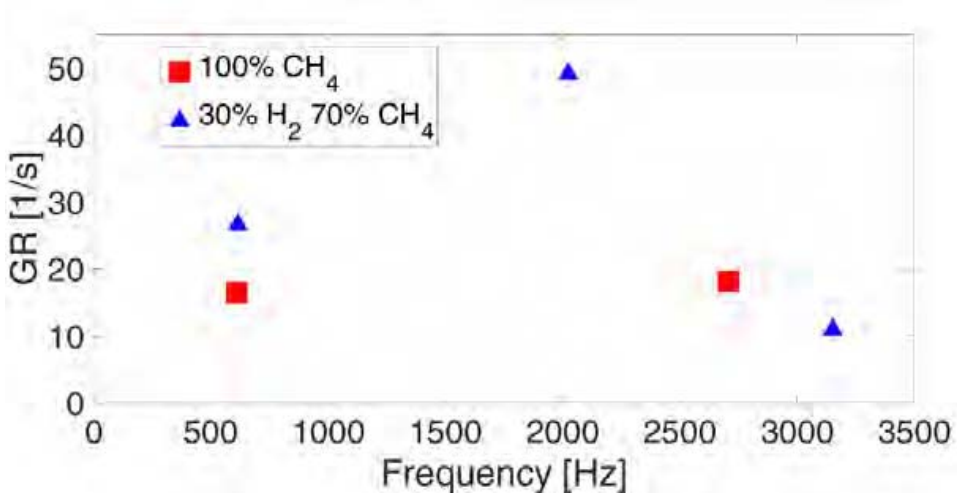

Figure 3. Frequencies and Growth Rate for the AE-T100 burner fueled by three different mixtures.

The first mode at 600 Hz is more unstable observed when hydrogen is injected. The modes of the burner, in each case, are longitudinal. In particular in the burner fueled by pure methane the first mode is a mode of the combustion chamber and the second is related to the pilot chamber. When hydrogen is injected, the second mode of the methane case is split into two modes for the combustion chamber. These differences are due to the different flame shape of the two mixtures, which result in a difference in the convection times of the burner operating with the two different mixtures. This causes a different iteration between velocity and heat fluctuations within the burner. In the future, the development of the Flame Transfer Function, in order to forecast in a more precise way the thermoacoustic response of these burners, may be appointed.

Table 2. Acoustic pressure between the burner fueled by two mixtures for first longitudinal e fourth azimuthal mode. In particular, an increase of the growth rate of

100% CH_4	70% CH_4+30% H_2	
611.18+16.45 [Hz] 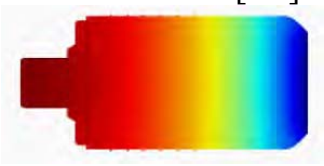	615.22+26.63 [Hz] 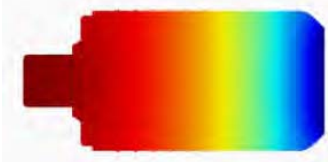	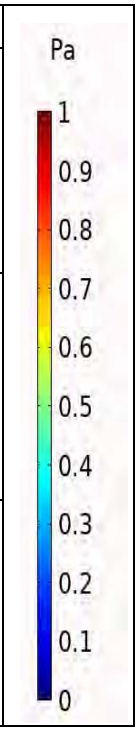
	2024.35+49.13 [Hz] 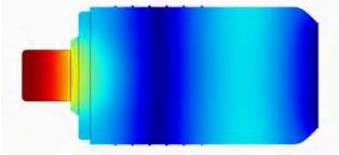	
2705.92+18.63 [Hz] 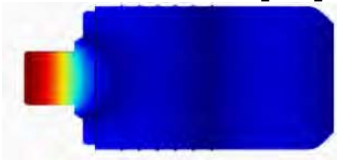	2781.18+10.96 [Hz] 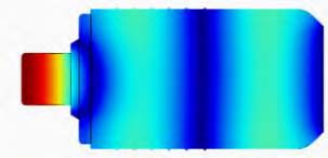	

References

[1] Stow, Simon R and A. P. Dowling , "Low-order modelling of thermoacoustic limit cycles," *Turbo Expo: Power for Land, Sea, and Air,* pp. 775-786, 2004.

[2] S. P. Evesque and W. Polifke, "Low-order acoustic modelling for annular combustors: Validation and inclusion of modal coupling.," Amsterdam, The Netherlands, 3–6 June 2002.

[3] G. Boudier, L. Gicquel, T. Poinsot, D. Bissieres and C. Bèrat, "Comparison of LES, RANS and experiments in an aeronautical gas," in *Proc. Combust. Inst.* , 2007, 31, 3075–3082.

[4] G. Staffelbach, L. Gicquel, G. Boudier and T. Poinsot, "Large Eddy Simulation of self excited azimuthal modes in annular combustors.," in *Proc. Combust. Inst.* , 2009, 32, 2909–2916.

[5] S. Camporeale, B. Fortunato and G. Campa, "A finite element method for three-dimensional analysis of thermo-acoustic combustion instability.," *J. Eng. Gas Turbines Power,* vol. 133, p. 011506, 2011.

[6] D. Laera and S. Camporeale, "A weakly nonlinear approach based on a distributed flame describing function to study the combustion dynamics of a full-scale lean-premixed swirled burner.," *J. Eng. Gas Turbines Power* , vol. 139, p. 091501, 2017.

[7] "AE-T100NG: Technical description," http://ariatermo.com/wp-content/uploads/2016/06/Ansaldo-Energia.pdf.

[8] J. Bompas, A. Pappa and W. De Paepe, "Analysis of Combustion Performance of Non-Conventional Syngas in mGT Combustor: Assessment of the Impact of the Quality of Synthesis Gas Towards Flame Stability and Emissions," in *Turbo Expo: Power for Land, Sea, and Air, Vol. 86052, American Society of Mechanical Engineers*, Rotterdam, 2022.

[9] A. Pappa, L. Bricteux, P. Bérnard and W. De Paepe, "Can water dilution avoid flashback on a hydrogen-enriched micro-gas turbine combustion?—a large eddy simulations study," *Journal of Engineering for Gas Turbines and Power,* p. 143, 2021.

Experimental characterization of an industrial burner operated with simulated EGR

S. Galeotti*, A. Picchi*, R. Becchi*, R. Meloni, G. Babazzi**, C. Romano**, A. Andreini***
sofia.galeotti@unifi.it
*Department of Industrial Engineering, University of Florence, Italy
**Baker Hughes, Via F. Matteucci 2, 50127, Florence, Italy

Abstract
This work presents the results of an experimental campaign investigating the behavior of an industrial burner operated with simulated Exhaust Gas Recirculation (EGR). EGR is recreated by diluting standard air with CO2, and tests are performed at ambient pressure using natural gas as fuel.
Burner characterization has been performed in terms of emission measurements both in standard conditions and with CO_2 vitiated air. Flame topology has been studied with OH* chemiluminescence, evaluating the effect of fuel split and CO_2 addition.
CO_2 addition has been found to trigger thermoacoustic instabilities up to a certain threshold, therefore limiting the EGR operability window.

Introduction
While the employment of Exhaust Gas Recirculation (EGR) is a well-established technique in Internal Combustion Engines to limit NOx emissions, its adoption in Gas Turbine engines hasn't yet found a practical application due to its expensive and complex installation that doesn't justify the emissions reduction when compared to already established DLN combustion technologies. EGR becomes an interesting option in GT engines considering the possibility of increasing the CO_2 content of the exhaust gases to improve the efficiency of Carbon Capture and Storage (CCS) units. However, the decrease in oxygen content of the combustion air is extremely challenging in terms of combustion stability. CO and UHC emission increase therefore limits the achievable EGR level [1-2]. Different strategies can be explored in order to extend the combustor operability window. The optimization of the burner design can benefit from less stringent limitations for NOx emissions, which are already lowered by EGR. Therefore, pilot flames can be exploited to help the flame stabilization, even with local injections of hydrogen.
European project TRANSITION (fuTure hydRogen Assisted gas turbiNeS for effective carbon capTure IntegratiON) fits in this context with the purpose of developing advanced combustion technologies for natural gas fired Gas Turbines to permit engine operations with high EGR rates leading to an increase of the CO_2 content in the exhaust gases and a drastic reduction of the CCS costs and units' size

[3]. The present work describes the results of the first experimental campaign within the project, performed on the baseline burner at ambient pressure. Experimental data will be used to calibrate CFD models employed to optimize the burner design, in order to enlarge the operability window with EGR by improving the flame stability.

Test Rig and burner

The burner was investigated in the reactive test cell of the THT Lab of the University of Florence, whose schematic layout is outlined in Figure 1a. The same test cell has been exploited in the past for investigations on novel low NOx burners for heavy duty gas turbines [4].

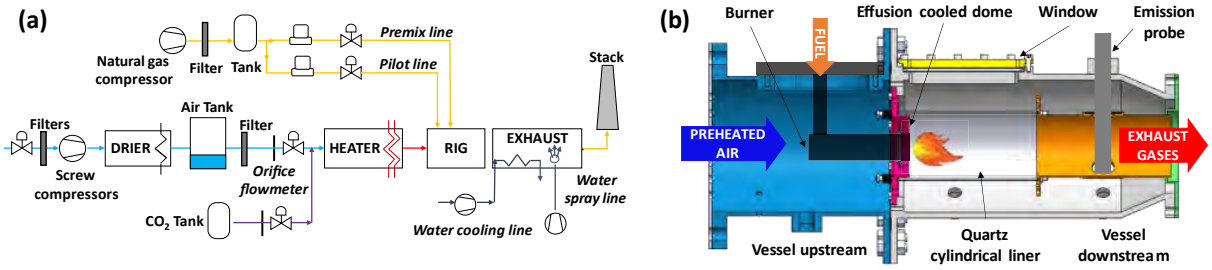

Figure 1. Combustion test rig (a) and close-up of the combustor set-up (b).

Two screw compressors supply the filtered and dried airflow to the test rig, and an electric heater is used to regulate the inlet flow temperature. A water jacket exhaust duct is placed right after the rig. It is equipped with water sprayers used to quench the hot gases and control the flow exit temperature.

Recreating real EGR conditions in lab scale is quite challenging because of the associated costs and plant complications. CO_2 addition in the airflow feeding the burner has been chosen to reproduce EGR condition, because it offers the opportunity to manage storage better than mixtures with nitrogen, while preserving the purpose of the investigation. CO_2 is stored in a pressurized tank and injected in the main air flow line upstream the electric heater, in order to deliver to the test section a homogeneous mixture, both in terms of temperature and composition.

The test cell is equipped with two fuel lines that deliver natural gas taken from the domestic line. The fuel composition is analyzed after each test.

The test rig is designed to allow optical measurements on the flame region.

A cross-section of the test article is shown in Figure 1b. The external casing consists of an upstream vessel, through which the burner enters the test article, and a downstream vessel, equipped with two perpendicular optical windows for the flame visualization. The combustor is made of a 2.5 mm thick cylindrical quartz liner, held in place thanks to a blocking system made of four tie rods and four springs that connect the dome to the following duct, used to convey the exhaust gases towards the test rig exhaust system. The quartz cylinder is approximately 2.5 diameters long, to ensure a complete flame development for a proper flame visualization. The flame tube is cooled by forced convection of a fraction of the incoming air that flows in the annulus between the liner and the confining vessel, not used in the combustion process. The dome plate is cooled through a series of inclined effusion holes.

The investigated burner is a lean premixed burner developed by Baker Hughes for industrial gas turbine applications. A thorough description of the burner geometry and its design can be found in [5]. It is composed by two counter-rotating swirlers and a center body with an air purge. Two independent fuel lines are present: the pilot line injects the fuel directly in the combustor chamber through circumferentially equally spaced holes, helping the flame stabilization. The premixed line delivers the fuel at the tip of the inner swirler, so that it mixes with the airflow thanks to the strong turbulence created by the shear layer generated between the two swirlers.

Operating conditions and measurement techniques

The experimental campaign has been performed at ambient pressure with natural gas as fuel. As anticipated EGR-like conditions have been reproduced by diluting the airflow entering the test rig with CO_2. The lower oxygen content in the oxidizer due to EGR strongly affects the combustion process. EGR condition is here defined by the inlet oxygen molar fraction x_{O2}, which is a key similarity parameter between real EGR and simulated conditions. All the presented results have been obtained at the same adiabatic flame temperature. The inlet oxygen content has been varied to simulate different EGR levels. The inlet temperature of the oxidizer has been kept constant at 300°C and the burner pressure drop is 4.2%. The ratio of the fuel flow injected with the pilot line and the total fuel flow rate is denoted as PLT. It has been scaled with a reference value for proprietary reason. PLT/PLT_{ref} covers a range from 0 to 1, going from a premixed flame towards a more diffusive flame. The fuel split has been varied in order to study the combined effect of this parameter with the oxygen depletion due to EGR.

Concerning the rig instrumentation, the test article is equipped with various thermocouples and static pressure ports to monitor the flow conditions. An emission probe is employed to analyze the exhaust composition through a HORIBA PG350. The probe is made of several radially spaced holes, and it is plunged into the flame tube to extract the exhaust gases. After being extracted, the gases flow through a thermally insulated pipeline kept at 150°C, are dried by a HORIBA PSS-5H refrigerator and finally reach the gas analyzer. The gas analyzer is properly calibrated right before each test employing a rack of calibrated gas mixture tanks.

Chemiluminescence of the OH* radical was employed to detect the reaction zone and its position in various operating conditions. For OH* chemiluminescence measurements a high-speed camera (Phantom M340) was coupled with the Hamamatsu image intensifier through a relay lens. In addition, a UV lens and bandpass filter (CWL=310 +/- 5nm) were mounted on the image intensifier to be able to capture the OH* transition, which has its peak emission intensity in the UV spectrum at around 310 nm. Images were acquired at 1000 Hz with a 0.5 ms intensifier gate.

A dynamic pressure sensor (PCB) is also installed on the test rig to monitor pressure oscillations, with an acquisition frequency of 12.8 kHz.

Results and discussion

The burner flame structure and position have been investigated through OH* chemiluminescence measurements at different operating conditions in terms of fuel split and inlet oxygen content, keeping the flame temperature (Tflame) constant. Figure 2 presents the time averaged maps of OH* intensity.

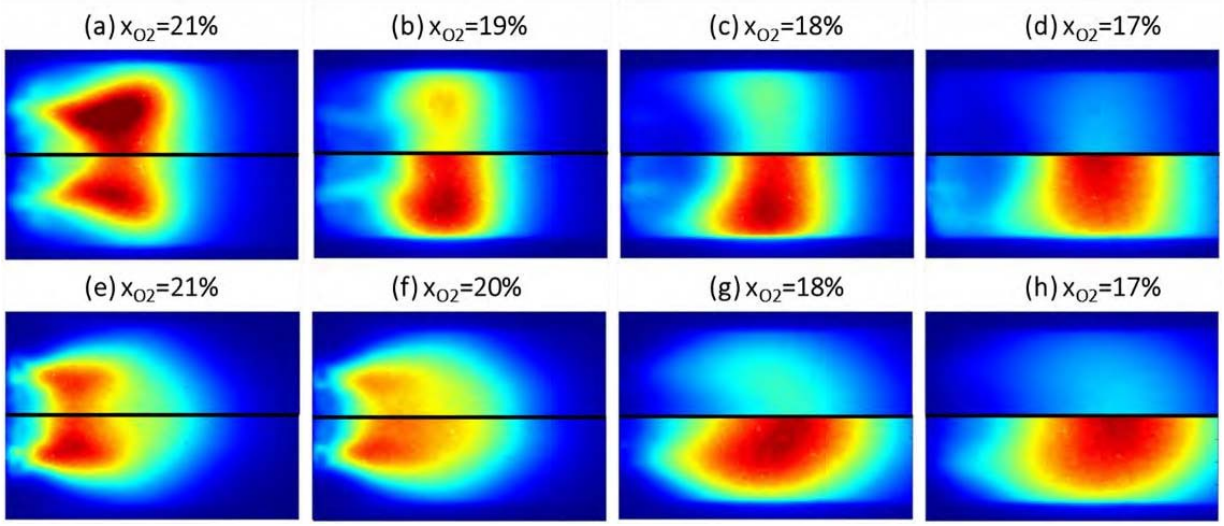

Figure 2. Time-averaged OH* chemiluminescence images at Tflame=constant for PLT/PLT_{ref}=1 (a-b-c-d) and PLT/PLT_{ref}=0.3 (e-f-g-h). (Upper halves: absolute OH* intensity, lower halves: normalized with each own maximum)

Considering at first the results with standard air, fuel split significantly influence the flame shape: when the fuel split is fully diffusive the flame stabilizes in correspondence of the pilot jets, which are clearly distinguishable near the burner exit (Fig 2a). As the fraction of fuel injected with the premixed line increases the flame "closes" toward the centerline, and OH* intensity decreases. Looking at the absolute OH* intensity CO_2 addition significantly lowers the flame reactivity. The flame lifts off from the burner exit and shifts downstream. The oxygen content depletion leads to a slowdown of the reaction process. Indeed, the reaction zone becomes more widespread, reaching an extension that almost covers the whole combustion chamber (Fig 2c-d-g-h).

The significant reduction of the flame reactivity is confirmed by emission levels.

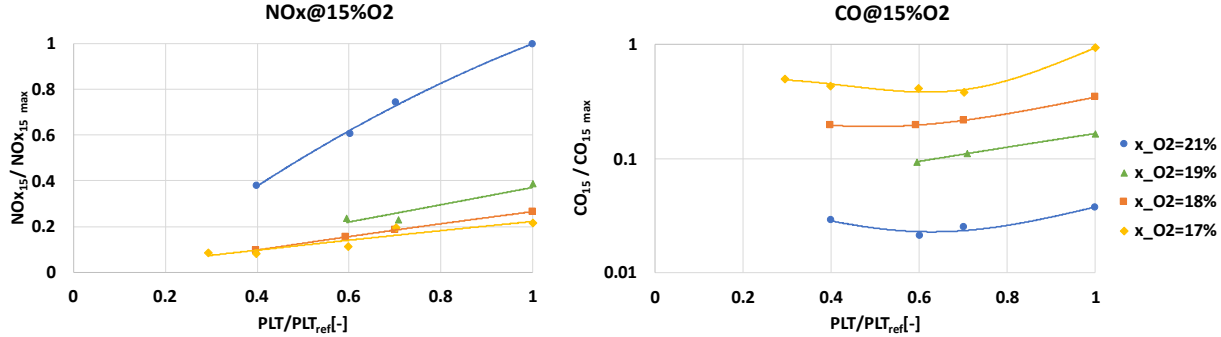

Figure 3. NOx and CO emission measurements at Tflame=constant

Figure 3 shows the results of NOx and CO emission measurements, which have been corrected with the following expression in order to take into account the lower inlet oxygen content [1] (same for CO). Values were then scaled with the maximum emission level for proprietary reasons.

$$NO_{x\,15} = NO_{x\,dry} \cdot \frac{0.2095 - 0.15}{2 - 0.2095} \frac{2 - x_{O2\,inlet}}{x_{O2\,inlet} - x_{O2\,dry}}$$

As expected, simulated EGR strongly reduces NOx emissions, but at the same time CO levels are extremely high. Despite the fact that all the points have the same adiabatic flame temperature, OH* images showed that the flame reactivity strongly decreases with lower oxygen content of the oxidizer. CO increase could also be linked with the downstream shift of the reaction zone, which doesn't allow the reaction to be completed at the probe location (about 2.5 diameters downstream of the burner exit). CO_2 addition reduces the effect of fuel split on NOx emissions, which, however, remain growing with pilot split. After an important drop of NOx levels with the first level of oxygen reduction, a further decrease has a limited effect on NOx, while CO continues to increase.

During the reactive tests strong tonal pressure oscillations have been observed as soon as the oxidizer composition changes from standard air. The amplitude of these oscillations quickly grows with the CO_2 fraction in the oxidizer, reaches a maximum, and eventually decreases, going back to the levels corresponding to standard air, or even lower in some cases. This last condition is near the flame extinction, as showed by very high CO levels. This behavior has been observed for all the tested fuel splits, but the oscillation amplitude increases with the fraction of fuel supplied with the premix line. Figure 4a shows this trend, while Figure 4b reports the frequency spectrum of these pressure oscillations. The peak frequency is around 330 Hz and decreases with lower oxygen inlet content, as the mixture composition changes, and the reaction becomes more widespread.

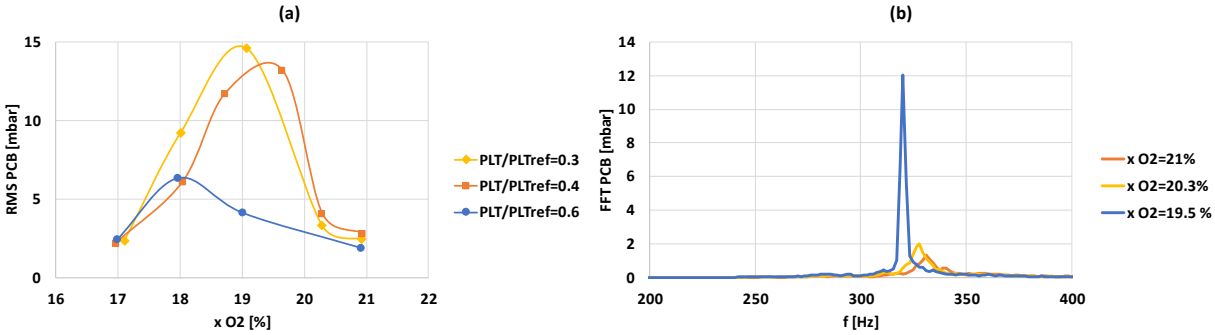

Figure 4. Amplitude of pressure oscillation as a function of inlet oxygen molar fraction (a) and frequency spectrum of pressure oscillation at PLT/PLT_{ref}=0.4 (b)

Thermoacoustic instabilities triggered by CO_2 have also been detected with OH* chemiluminescence: the frequency spectrum of the OH* intensity averaged over the whole measurement area captures the pressure oscillation peaks detected with the PCB. Figure 5a reports some instantaneous OH* images, where it can be seen the flame subjected to intense longitudinal fluctuations. Figure 5b shows the standard

deviation of the OH* intensity over time in comparison to the corresponding case with standard air (upper half). The fluctuation of OH* emission is much more intense in the case with CO_2 addition, and the area where these fluctuations occur extends further downstream.

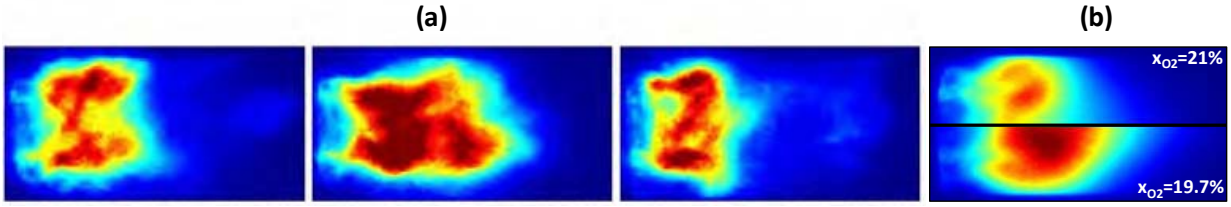

Figure 5. Instantaneous OH* images (f=1000 Hz) (a) and standard deviation of OH* intensity (b) for PLT/PLT_{ref}=0.4 x_{O2}=19.7% compared with case with standard air (x_{O2}=21%, upper half)

Conclusion

In the present work the experimental characterization of an industrial burner operated at ambient pressure with reduced inlet oxygen level caused by the dilution of standard air with CO_2 has been presented. Emission measurements revealed very high CO levels (correlated to both air vitiation and the reduced residence time of the rig), progressively increasing with CO_2 addition, while NOx emissions decrease. OH* chemiluminescence images showed very different flame structures varying the fuel split and oxidizer composition. The outbreak of thermoacoustic instabilities with CO_2 vitiated air strongly limits the burner operating window at intermediate EGR-like conditions, pointing out to the necessity of finding a different strategy to help the flame to stabilize in such conditions.

Acknowledgement

Funded by the European Union

This project has received funding from the European Union's Horizon Europe research and Innovation program under Grant Agreement No 101069665

References

[1] ElKady, A. M., Evulet, A., Brand, A., Ursin, T. P., Lynghjem, A. "Exhaust Gas Recirculation in DLN F-Class Gas Turbines for Post-Combustion CO2 Capture". *Proc ASME Turbo Expo*, pp. 847–854 (2008)

[2] G. Babazzi, N. Giannini, R. Meloni, P. C. Nassini, G.Lemmi, A. Andreini, "On the impact of the EGR on to the operability of a heavy-duty GT combustor: a CFD investigation". Proc. of the 11th European Combustion Meeting, Rouen, France, 2023

[3] Tabbi Wilberforce, A.G. Olabi, Enas Taha Sayed, Khaled Elsaid, Mohammad Ali Abdelkareem, "Progress in carbon capture technologies", Science of The Total Environment, Vol 761, 2021

[4] Cerutti, M., Roma, M., Picchi, A., Becchi, R., and Facchini, B., 2019. "Improving Emission and Blow-Out Characteristics of Novel Natural Gas Low NOx Burners for Heavy Duty Gas Turbine". Proceedings of the ASME Turbo Expo, 4B-2019

[5] M. Cerutti, N. Giannini, G. Ceccherini, R. Meloni, E. Matoni, C. Romano, G. Riccio, "Dry low NOx emissions operability enhancement of a heavy-duty gas turbine by means of fuel burner design development and testing", Proc of ASME Turbo Expo, GT2018-76587, Oslo, Norway, 2018

AMMONIA/HYDROGEN COMBUSTION IN A GAS TURBINE: UNCERTAINTY QUANTIFICATION TO CALIBRATE THE CRN MODELING

R. Lamioni*, A. Mariotti*, M.V. Salvetti*, C. Galletti*
rachele.lamioni@unipi.it
* Dipartimento di Ingegneria Civile e Industriale, University of Pisa, Pisa 56126, Italy

Abstract
To tackle climate change, we need to incorporate renewable energy sources on a large scale. One potential solution is the use of hydrogen, which can be produced from excess wind and solar power, as an alternative energy vector that can be burnt in existing devices with little modification. In this context, ammonia, as a hydrogen carrier, is very appealing as it can be easily liquified and distributed through the existing infrastructure.
This study aims to explore the feasibility of using ammonia-hydrogen mixtures in industrial settings. This exploration is made using a network of chemical reactors (CRN) to reproduce a gas turbine system that can improve our understanding of the energy conversion process involving hydrogen, ammonia, and their mixtures. The study aims also to propose a novel methodology to identify the most significant parameters of the CRN model and calibrate the network, leveraging uncertain quantification techniques. This will enable the development of a CRN model that can accurately predict gas turbine system emissions under varying operating conditions, such as pressure, temperature, equivalence ratio, and mixture.

Introduction

The quest for cleaner gas turbine combustion technologies has gained traction in recent years. One of the potential solutions is the adoption of premixed combustion of ammonia-hydrogen blends; this promises to reduce carbon emissions while maintaining high combustion efficiency. Indeed, the use of NH_3-H_2 blends seems to be effective in overcoming the drawbacks related to these green energy vectors. Indeed, ammonia combustion presents some challenges, including low reactivity and high NOx emissions compared to conventional hydrocarbon fuels. On the other hand, hydrogen has a higher reactivity with high flame speeds which can favor the flashback phenomenon. The challenge, therefore, is to develop combustion technologies suitable for NH3, H2, and their blends. Previous experimental and numerical works have demonstrated the potential of NH_3-H_2 mixtures in reducing NOx emissions in rich conditions (ϕ>1) [1]. For instance, Pug et al. [2] showed that multistage NH3 combustion, where rich and lean combustion is performed sequentially, results in lower NO emissions. However, studying new fuel mixtures

through experiments or full-scale numerical simulations is prohibitively expensive due to the need to analyze a wide range of operating conditions, such as mixture, equivalence ratio, injection pressure, and temperature as well as the possibility to devise novel geometrical configurations. To address this problem, simplified-order models such as chemical reactor networks (CRNs) can represent a valuable tool for quickly analyzing a broad range of operational parameters. CRN models have already been used to characterize emissions in combustion processes and are useful as detailed kinetic simulations of practical systems [3-4]
In this study, we use Uncertainty Quantification (UQ) techniques to calibrate the parameters of a CRN model emulating a premixed gas turbine system operating with NH_3-H_2 blends. Such techniques are necessary since the behavior of these new mixtures in the operating conditions of gas turbines is not known. The NOx emissions predicted through the kinetic simulations of the CRN model will be compared with the experimental data of the system. The calibrated model, with quantified uncertainty, can then be employed to study a broad spectrum of operating conditions and identify a robust optimum operating point that minimizes pollutant emissions.

Case study

The case study is the high-pressure generic swirl burner (HPGSB), housed within the high-pressure optical chamber (HPOC) [5]. The HPGSB uses quartz windows and a cylindrical quartz burner confinement to provide optical access to the flame. The HPGSB is modular and can be operated with a wide range of swirl numbers. Previous works [5-6] include further information on the design and operation of this high-pressure combustion rig test facility.

Chemical Reactor Network model

The CRN model comprises a Perfectly Stirred Reactor (PSR) [7] and a Plug Flow Reactor (PFR) [8]. The PSR represents the primary combustion zone, while the PFR mimics the secondary combustion zone.
Figure 1 shows a schematic diagram of the CRN model constructed using five reactors: one mixer into which our blend enters, three PSRs that represent the flame zone, and two recirculation zones due to the swirl burner configuration. Finally, the last reactor characterizes the uniform zone of the system (PFR).

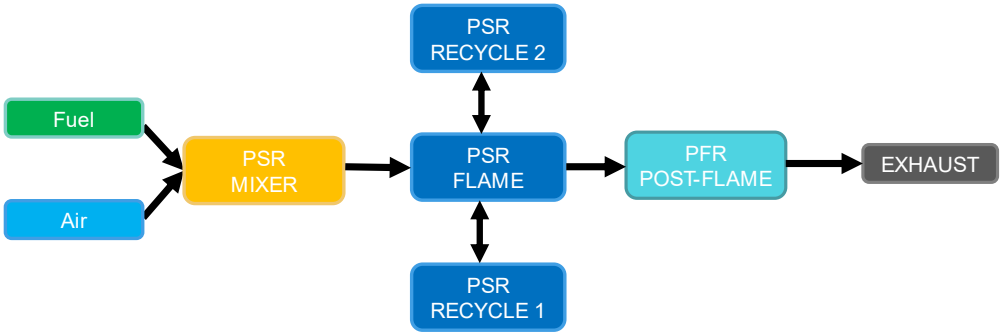

Figure 1: Chemical Reactor Network.

The CRN code is written in Python using Cantera [9], an open-source software for thermodynamics and reaction kinetics.
The CRN is tested against the experimental data from the Gas Turbine Research Center of Cardiff University that refer to a 50%H_2-50%NH_3 [5] blend with an equivalence ratio of $\phi = 0.52$ and atmospheric pressure. In the CRN we use the kinetic mechanism from Stagni et al. [10] with 31 species and 203 reversible reactions. The reactor volumes represent a fundamental parameter for a correct estimate of the emissions in terms of NOx as the volumes impact the residence time in each zone of the system. Hence, uncertainty quantification is employed here to help identify these volumes by calibrating the CRN. More specifically, three ratios between the volumes of the reactors involved are considered:

- V_{PSR}/ V_{PFR}, with the PSR volume represented by the contributions of the flame (V_f) and two recirculation (V_{r1} and V_{r2}) reactors. $V_{PSR} = V_f + V_{r1} + V_{r1}$.
- V_{r1}/V_f, the ratio between the first recirculation and the flame volumes reactors.
- V_{r2}/V_f the ratio between the second recirculation and the flame volumes reactors.

To quantify NO_x emissions from the combustion process, the molar fractions of NO and NO_2 are measured in the PFR reactor.

Uncertainty Quantification procedure

A stochastic sensitivity analysis is carried out, using the generalized Polynomial Chaos (gPC) in its non-intrusive form, to investigate how the reactor volumes of the CRN affect the NOx emissions. This analysis allows us to obtain continuous and accurate response surfaces in the parameter space, with an affordable number of deterministic simulations.
In the gPC approach, the dependence between a quantity of interest, $Z(\varepsilon)$, and the vector of independent uncertain parameters, $\boldsymbol{\zeta}(\varepsilon)$, is expressed using of a polynomial expansion [11]. The uncertain parameters are considered as random variables with a given probability density function (PDF). So, employing term-base indexing:

$$Z(\varepsilon) = \sum_{j=0}^{\infty} b_j \Psi_j \left(\boldsymbol{\zeta}(\varepsilon)\right)$$

where ε is an aleatory event, $\Psi_j\left(\boldsymbol{\zeta}(\varepsilon)\right)$is the j-th gPC polynomial and b_j is the corresponding projection coefficient.

The response surface is truncated to the limit O that can be calculated as follows:

$$O = \prod_{k=1}^{N} (T_k + 1) - 1$$

where N is the dimension of $\boldsymbol{\zeta}(\varepsilon)$, the index k identifies the k-th element of that vector, and T_k is the maximum order of the corresponding polynomial. The coefficients b_j of the expansion can be computed as follows:

$$b_j = \frac{\langle Z, \Psi_j \rangle}{\langle \Psi_j, \Psi_j \rangle} = \frac{1}{\langle \Psi_j, \Psi_j \rangle} + \int_\zeta Z\, \Psi_j \omega(\zeta) d\zeta$$

where $\omega(\zeta)$ is the weight function connected to $\Psi_j(\zeta)$. In this work, the integral above is approximated using a Gaussian quadrature formula and the optimal polynomial family Ψ_j is related to the shape of the PDFs of the uncertain parameters. Since we assumed uniform PDFs, Legendre polynomials are used. The same range of variation is selected for the three parameters, i.e. [1/5,5]. The total volume of the gas turbine system is $V_{TOT} = V_f + V_{r1} + V_{r2} + V_{PFR} = V_{PSR} + V_{PFR}$. The polynomial expansion is truncated to the 3rd order in each dimension. Thus, 4 quadrature points are needed for each variable (Gauss-Legendre points), whose values are summarized in **Table 1** and, using a tensor grid 64 simulations are carried out to evaluate the stochastic response surfaces.
The variability of the output quantities is described in terms of total variance as $\sigma^2 = \sum_{j=1}(b_j^*)^2$,with $b_j^* = b_j|\Psi_j|$, $|\Psi_j|$ being the norm of the j-th polynomial. The partial sensitivity of the quantities of interest to a single input parameter or a combination of them is computed using the variance decomposition method proposed by [12]. The related Sobol indexes I_i is defined as the ratio between the partial variances σ_i^2 i.e., the variance only due to the i-th uncertain input parameter, and the total variance σ^2, as $I_i = \sigma_i^2 / \sigma^2$.

Table 1: Quadrature points for the three input parameters.

Quadrature Points	1st	2nd	3rd	4th
V_{PSR}/V_{PFR}	0.534	1.786	3.414	4.666
V_{r1}/V_f	0.534	1.786	3.414	4.666
V_{r2}/V_f	0.534	1.786	3.414	4.666

Results: effect of the PSRs and PFR volumes

Figure 2 shows the emissions in terms of NOx predicted by the 64 CRN simulations with different flame (PSR) volume values. The black dashed line is the experimental data for the test case considered with 50%H_2 and 50%NH_3 ($\phi = 0.52$, $p = 1.0$ atm and $T = 288$ K). With $V_f = 0.13\ V_{tot}$ the estimated NOx value agrees with the experimental data, which corresponds to 7 ms of the flame residence time.

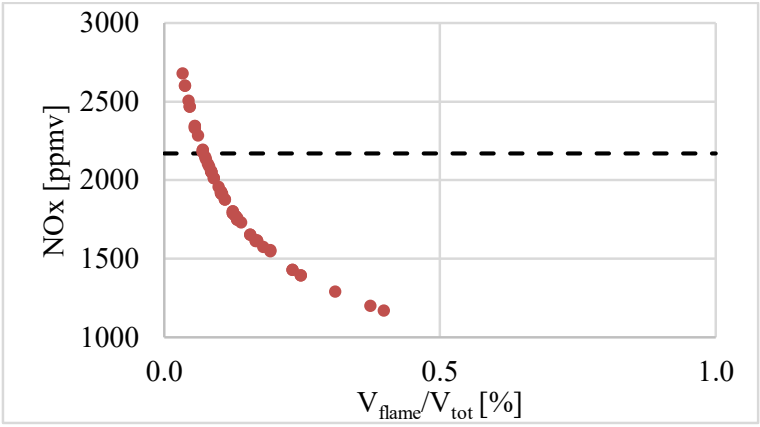

Figure 2: NO_x emissions with respect to the PSR (flame) residence time compared with experimental data from [3] (dashed line).

Errore. L'origine riferimento non è stata trovata. shows the Sobol indices representing the sensitivity to the choice of PSR and PFR volumes on the prediction of NOx emissions. The contributions of the interaction between the three selected parameters (the ratios V_{r1}/V_f, V_{PSR}/V_{PFR}, and V_{r2}/V_f) are negligible (<1%). The greatest contribution (43%) is given by the A/B ratio which represents the ratio between the volume of PSR and PFR. This result confirms that to have a good estimate of NOx emissions it is essential to correctly estimate the residence times, in particular, the one of the PSR of the flame as can be seen from the equal importance of the ratios V_{r1}/V_f and V_{r2}/V_f (28%).

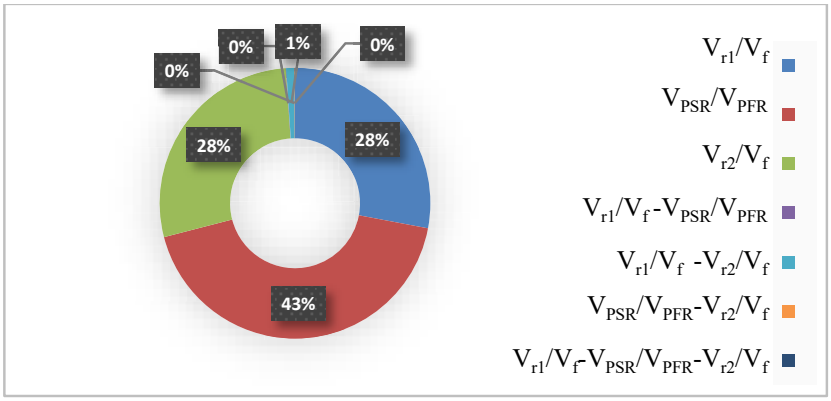

Figure 3: Sobol indexes for NOx emissions.

Conclusion

In this work, a chemical reactor network is developed and implemented to emulate a gas turbine system fueled with an ammonia-hydrogen mixture using the Cantera software. The uncertainty quantification techniques are used for the network calibration, by assessing in detail the effect of the volume of each individual reactor. Indeed, the volumes are a fundamental parameter affecting the correct estimation of NOx emissions. It is found that the parameter which has the main impact is the volume of the flame zone.

This work provides a first step for a CRN model that can be further employed to

devise combustor geometry modification, as well as to evaluate the effect of operating parameters such as temperature, pressure, and mixture composition on combustion efficiency and emissions.

Acknowledgment

This research is supported by the Ministry of University and Research (MUR) as part of the PON 2014-2020 “Research and Innovation” resources - Green/Innovation Action – DM MUR 1062/2021.

References

[1] Valera-Medina A. et al. "Premixed ammonia/hydrogen swirl combustion under rich fuel conditions for gas turbines operation." *J. Hydrog. Energy* 44 2019.

[2] Pugh D. et al. "Emissions performance of staged premixed and diffusion combustor concepts for an NH_3/air flame with and without reactant humidification. " *J Eng Gas Turbine Power* 143.5 2021.

[3] Yousefian, S. et al. "Review of hybrid emissions prediction tools and uncertainty quantification methods for gas turbine combustion systems. "*Turbo Expo: Power for Land, Sea, and Air*, 508 American Society of Mechanical Engineers 2017.

[4] Andreini A et al. "Gas turbines design and off-design performance analysis with emissions evaluation." *J. Eng. Gas Turbines Power* 126, 83-91 2004.

[5] Valera-Medina A. et al. “Preliminary study on lean premixed combustion of ammonia-hydrogen for swirling gas turbine combustors”. *Int. J. Hydrog. Energy* 42.38 2017.

[6] Runyon J. et al. "Lean methane flame stability in a premixed generic swirl burner: Isothermal flow and atmospheric combustion characterization." *Exp. Therm. Fluid Sci.* 92 2018.

[7] Chen J-Y. "Stochastic modeling of partially stirred reactors." *Combust Sci Technol* 122 1997.

[8] Turns S. R. Introduction to combustion. 287 New York, USA McGraw-Hill Companies, 1996.

[9] D. G. Goodwin et al. Cantera: An object-oriented software toolkit for chemical kinetics, thermodynamics, and transport processes, https://www.cantera.org 2022.

[10] Stagni A. et al. "An experimental, theoretical and kinetic-modeling study of the gas-phase oxidation of ammonia." *React. Chem. Eng.* 5.4 2020.

[11] Xiu D. et al. "The Wiener--Askey polynomial chaos for stochastic differential equations." *SIAM J. Sci. Comput.* 24.2 2002.

[12] Sobol I. M. "Global sensitivity indices for nonlinear mathematical models and their Monte Carlo estimates." *Math Comput Simul* 55.1-3 2001.

LES validation of an industrial burner flame extinction operated with highly vitiated oxidizer

R. Meloni*, G. Babazzi*, S. Galeotti, A. Picchi**, R. Becchi**,S. Castellani**, A. Andreini****
roberto.meloni@bakerhughes.com
*Baker Hughes, Via F. Matteucci 2, 50127, Florence, Italy
**Department of Industrial Engineering, University of Florence, Italy

Abstract
In this paper an enhanced Thickened Flame Model (TFM) is leveraged to reproduce the extinction limit of an industrial burner operated at atmospheric pressure along a vitiated oxidizer: CO_2 is employed to dilute the air and mimic an Exhaust Gas Recirculation (EGR). It is found that the TFM is able to reproduce the Lean Blow-Out (LBO) at exactly the same oxidizer composition detected experimentally. Additionally, approaching the extinction limit, the numerical model manifests the same dynamics observed during the test with the flame propagating backward to the burner from an extremely elongated position.

Introduction
The EGR technology in GT power plants doesn't find application because of the high installation costs that do not justify the benefit in terms of NO_x reduction. Moreover, a high EGR content can strongly compromise the flame stability that can lead to undesired emissions of CO/UHC [1-3]. Nevertheless, if the LBO resistance of the combustor is enhanced and the rate of EGR consequently increased, such technology can pave the way for a more efficient capture of the CO_2. Increasing the carbon-dioxide content could not only reduce the total energy consumption of standard amine-based carbon capture units but even enable the adoption of new capture processes (adsorption or membrane separation [4]). The enlargement of the operability window can be achieved in several ways. The first one can be done through an optimization of the premixer design [5]. The second could be represented by the doping of the fuel gas with H_2 able to increase the extinction strain rate and/or its injection in controlled quantities through a pilot line. In this context, this paper will show the experimental findings characterizing the LBO resistance without any H_2 addition of an industrial burner when it is operated with an oxidizer having a high CO_2 content. The vitiation of the oxidizer through CO_2 to mimic EGR is due to storage limitations of the experimental facility. Despite that, since operating with CO_2 dilution is a more severe condition in terms of combustion stability, the findings are fully representative and still valid in case the same design is operated with EGR. These results will allow to plane an optimization of the design to further extend its extinction limits. The optimization can be performed through a dedicated CFD

models whose validation will be here presented as well. The manuscript is organized as follows: the next section describes the test facility while the numerical model is introduced in the following paragraph. The experimental sequence leading to the LBO and reproduced numerically will introduce the results and discussion section.

Test Rig and Measurement Techniques

Figure 1-a) shows a sketch of the rig where the tests are executed. The facility is able to run at a maximum pressure of 10 bar delivering up to 1 kg/s of the oxidizer. An electric heater of 600 kW rises the temperature of the oxidizer up to 300 °C after that the same is filtered and the humidity removed. When the CO_2 is used to dilute the air, it mixes before entering the heater such that a homogeneous temperature and composition of the mixture can be assumed at the combustor inlet. The facility has up to three independent fuel gas lines (up to 90 Nm^3/h at 16 bar of pressure).

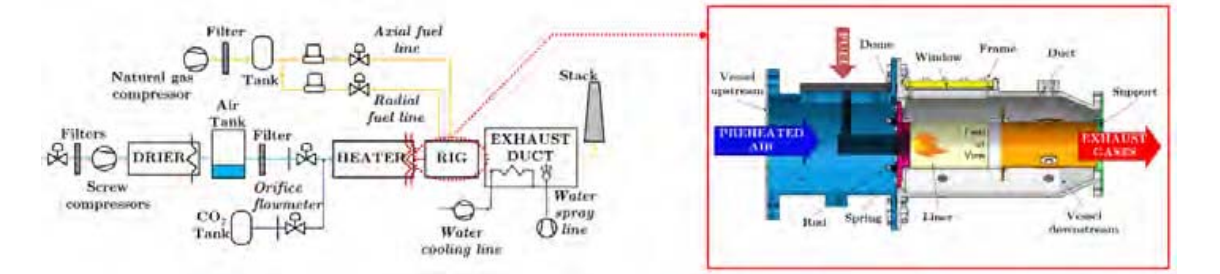

Figure 1. Combustion test rig (a) and close-up of the combustor set-up (b).

Figure 1-b) side shows a close-up of the combustor with the external casing that, in the flame region, is equipped with two perpendicular optical accesses allowing to visualize the 2.5 mm thick quartz liner. The latter is cooled by a fraction of the oxidizer passing through the dome and entering the annulus between the external casing and the flame tube. The dome plate is instead cooled by effusion holes fed through a second fraction of the oxidizer coming from the upstream vessel. Regarding the standard instrumentation, the rig counts on thermocouples monitoring the temperature of the dome and the liner downstream the quartz and static pressure probes to quantify the pressure drop across the burner. A dynamic pressure probe is used to detect any thermoacoustic instability may rise. The flue gas is sampled at the end of the metal liner for the measure of the pollutant emissions through a HORIBA PG300: the sample is kept at 150 °C before reaching the gas analyzer and then cooled to remove the water vapor. A Phantom MIRO M340 camera coupled with an intensifier is used for OH* recording; the intensifier is equipped with a Nikon UV lens with a bandpass filter set at 310±2 nm; the gain and the acquisition frequency are fixed to 5 and 500 Hz. Concerning the burner, it is composed by two counter-rotating swirlers ensuring a good mixing of the main fuel gas that is injected at the tip of the inner swirler. The pilot line delivers the fuel into the primary zone of the combustor through circumferentially equally spaced holes for flame stability. In this study, the burner is operated injecting the entire fuel from the pilot line. More information about the fuel nozzle and its flame stabilization can be found in [5].

Enhanced-Thickened Flame Model and Numerical Settings

The application of the TFM, theoretically valid for premixed and partially premixed flames, is here justified by the lifted nature of the piloted flames [6-7]. This is even more effective when the oxidizer is vitiated through CO_2 leading to a high lift-off. Nevertheless, where the flame is characterized by a diffusive regime (especially when the air is the oxidizer) the original formulation of the combustion model [9] is modified such that the chemical source term of each species-related transport equation is a function of the local flame index. For positive flame-index (premixed regime), the original TFM formulation is applied; when it is negative, the thickening of the flame is not applied, a finite rate closure is adopted and the species diffusivity not altered. Being φ the vector of the species mass fractions (a 19 species-62 reactions skeletal mechanism calculated ad-hoc is used), the corresponding transport equations can be written as:

$$\frac{\partial \bar{\rho}\,\widetilde{\varphi_\alpha}}{\partial t} + \frac{\partial \bar{\rho}\,\widetilde{u_j}\,\widetilde{\varphi_\alpha}}{\partial x_j} = \frac{\partial}{\partial x_j}\left(\bar{\rho}(EFD_\alpha + (1-\Omega)D_t)\frac{\partial \widetilde{\varphi_\alpha}}{\partial x_j}\right) + \frac{E}{F}\dot{\omega}_\alpha(\tilde{\varphi}) \qquad (1)$$

with E, F and Ω the efficiency function, the dynamic thickening factor and the flame sensor, respectively [9]. The dynamic thickening factor F is a function of the number of points N in the flame thickness δ_{th}. Since the latter parameter changes along the different oxidizer compositions, N is dynamically accommodated to maintain an almost constant thickening factor along the entire flammability range and equal to 5 at stoichiometric conditions. Regarding the mentioned computational grid, Figure 2 shows a longitudinal cut with a resolution inside the flame tube equal to 0.6 mm and 0.2 mm where the pilot jets enters the combustor (important mainly when the oxidizer is air and the flame stabilizes primarily around the pilot jets).

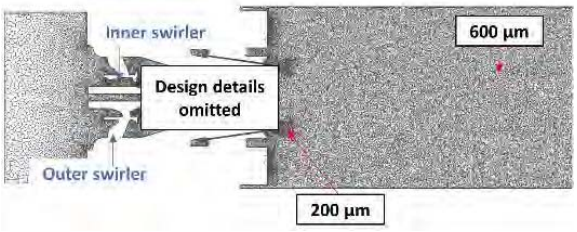

Figure 2. Mesh size at the main locations of the computational model.

As for the quartz thermal boundary conditions, a heat transfer coefficient equal to 35 W/m^2-K and a bulk temperature of 577 K is used to model the heat loss. Discrete Ordinate is adopted for radiation with semi-transparent boundary for the quartz and the gas modelled as optically thick. Regarding the numerical setting, the Dynamic-Smagorinsky closure is used to model the sub-grid scale turbulent structures along the LES. All the transport equations are resolved at the second discretization order as well as the bounded time step advancement.

Results and Discussion

Experimentally, the LBO limit is found increasing the CO_2 content through several

steps. Numerically, the same process is simplified considering two steps of CO_2 rising, summarized in Figure 3. The investigation starts with pure air and then the CO_2 is increased to have 18.6% O_2 vol. and eventually16.2% O_2 vol, respectively.

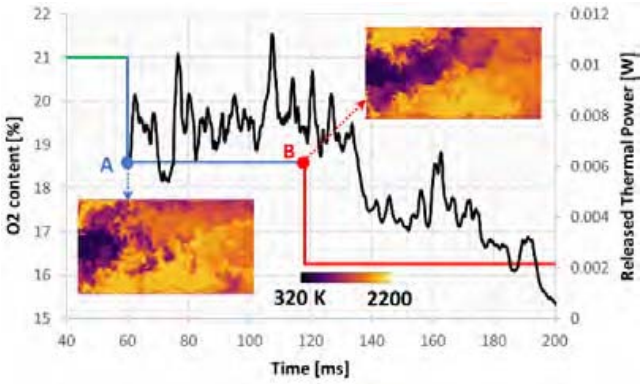

Figure 3. O_2 reduction steps and the volume-average released power till LBO.

The same Figure 3 reports the trend of the volume-average released thermal power from the combustor. It can be seen that the first oxygen reduction doesn't have an impact onto the global fuel consumption rate with the thermal power remaining approximately constant, as demonstrated by the contour plot of the temperature field at the beginning and at the end of the first step. Conversely, once the second oxygen reduction starts interacting with the pilot flames (at135 ms, after about 15 ms from the beginning of its injection in the domain), the heat release drops. The simulation takes approximately 60 ms to completely push the flame outside the combustor.
Focusing the attention on the time window between 60 ms and 120 ms, it is useful to compare the numerical results with the experiments in terms of CO and combustion instability, whose main finding are summarized in Figure 4. Regarding the CO, it can be observed that an excellent prediction is achieved working with pure air while an overprediction is achieved with O_2 at 18.6%. At the same time, the TFM model is able to predict the higher instability recorded experimentally if compared with the operation with air (not shown here): experimentally only the L=2 tone is triggered, while numerically also a lower frequency tone (150 Hz) is observed, denoting a propensity through LBO related to colder spot release from the flame [6].

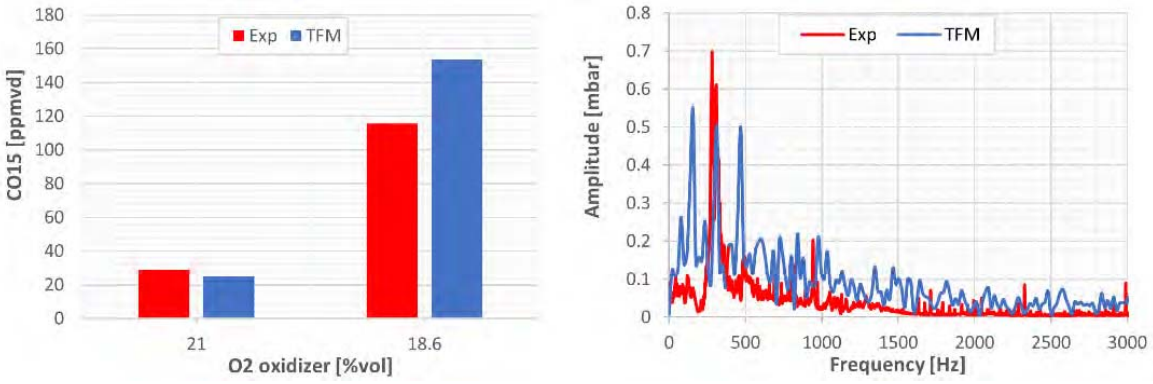

Figure 4. CO (left) and FFT of the acoustic pressure inside the combustor (right).

Focusing on the transitory phase leading to the flame extinction (numerically $\tau > 135\ ms$), Figure 5-a shows the experimental sequence of the last 3.5 seconds before

the flame out and Figure 5-b the numerical highlights. During the test, the flame moves cyclically from an extremely detached position toward the pilot jets. A similar behavior can be observed numerically: for example a backpropagation is detected at 0.15 s and 0.18 s after that the flame presents a significant lift-off with the heat release rate region placed even in the middle of the liner.

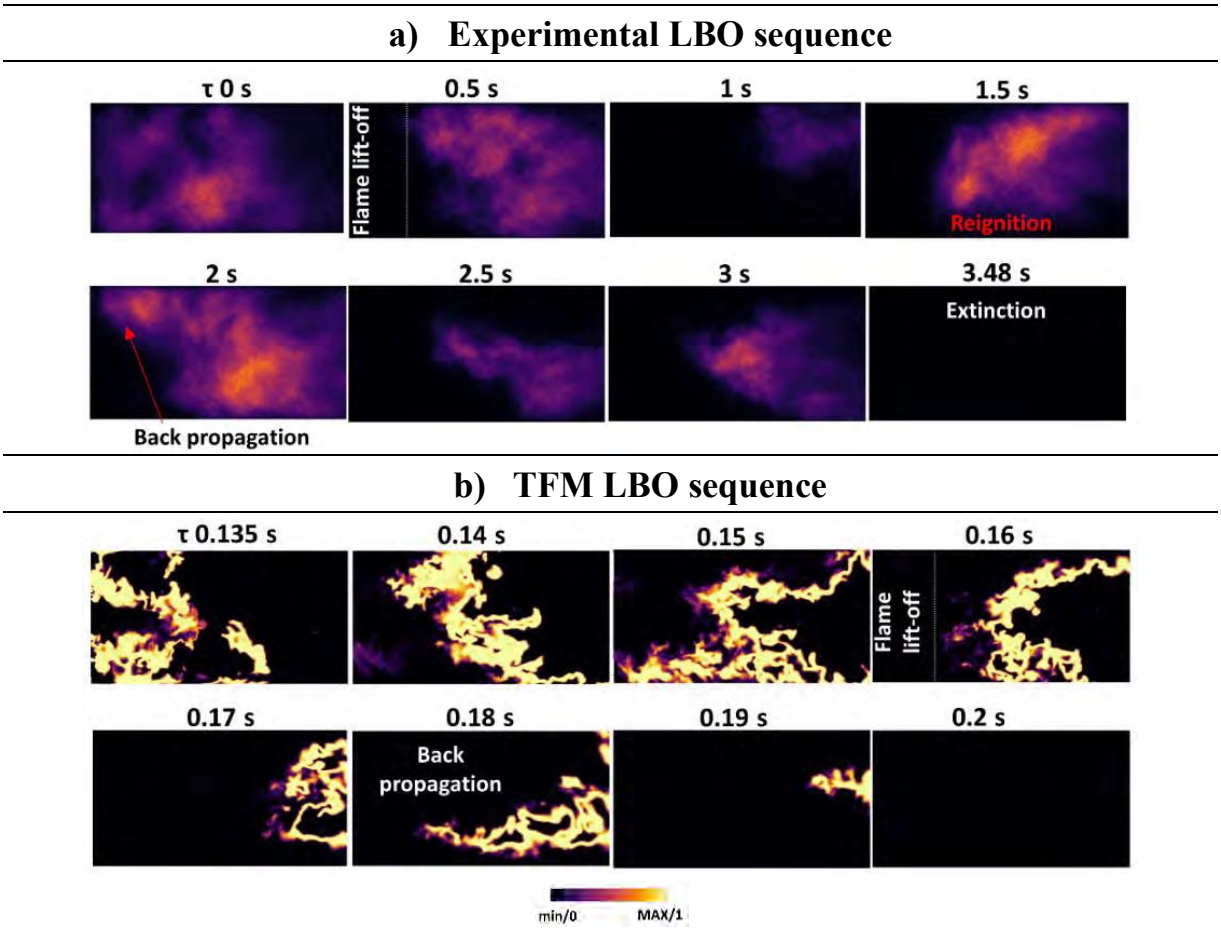

Figure 5. Experimental Line of Sight OH* (a) and numerical Ω sensor [0-1] (b).

In order to provide an insight of the complex mechanism leading to the extinction, Figure 6 correlates the flow field (through its vectors) with the radical OH at four instants after the O_2 final depletion. As a general result, it can be observed that the

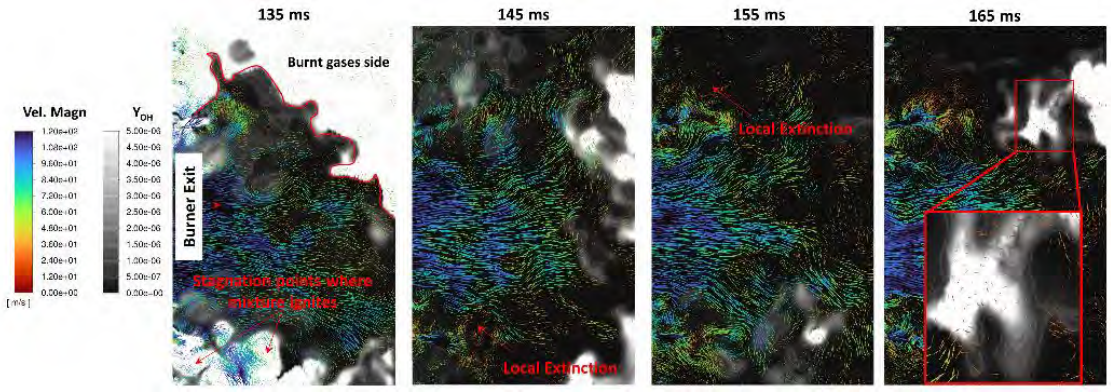

Figure 6. Velocity magnitude vectors for stagnation point detection overlapped to the OH mass fraction (gray scale) right downstream the burner exit.

flame gets preferentially anchored in the outer recirculation zones and in particular where the stagnation points are located. Those stabilization locations are lost quite immediately once the CO_2 rate is increased (i.e., at 145 ms) causing local extinctions. Even if localized ignition events are still present, like the one depicted by the close up at 165 ms, such events happen quite far from the pilot line where the regime is leaner and consequently the laminar flame speed can't sustain the flame stabilization.

Nomenclature

CFD	*Computational Fluid Dynamics*	*LES*	*Large Eddy Simulation*
EGR	*Exhaust Gas Recirculation*	*LBO*	*Lean Blow-Out*
FFT	*Fast Fourier Transform*	*TFM*	*Thickened Flame Model*
GT	*Gas Turbine*	*UHC*	*Unburnt Hydro-Carbon*
Subscripts			
F	Fuel	*ox*	Oxidizer

Conclusion

The present work reports the findings of a TFM-based combustion model in predicting the flame extinction of an industrial burner experimentally operated with a highly-CO_2 vitiated oxidizer. The model reproduces quite accurately the behavior of the burner during a first O_2 reduction, with similar CO emission and acoustic fluctuations. Also the phenomenology leading to the LBO seems to be captured by the numerical model showing a back-propagation behavior toward the pilots.

References

[1] ElKady, A. M., Evulet, A., Brand, A., Ursin, T. P., Lynghjem, A. "Exhaust Gas Recirculation in DLN F-Class Gas Turbines for Post-Combustion CO2 Capture". *Proc ASME Turbo Expo*, pp. 847–854 (2008)

[2] Evulet, A. T., ELKady, A. M., Branda, A. R., Chinn, D. "On the Performance and Operability of GE's Dry Low NOx Combustors utilizing Exhaust Gas Recirculation for PostCombustion Carbon Capture". *Energy Procedia*, 1(1) (2009), pp. 3809–3816

[3] G. Babazzi, N. Giannini, R. Meloni, P. C. Nassini, G.Lemmi, A. Andreini, "On the impact of the EGR on to the operability of a heavy-duty GT combustor: a CFD investigation". Proc. of the 11th European Combustion Meeting, Rouen, France, 2023

[4] Tabbi Wilberforce, A.G. Olabi, Enas Taha Sayed, Khaled Elsaid, Mohammad Ali Abdelkareem, "Progress in carbon capture technologies", Science of The Total Environment, Vol 761, 2021

[5] M. Cerutti, N. Giannini, G. Ceccherini, R. Meloni, E. Matoni, C. Romano, G. Riccio, "Dry low NOx emissions operability enhancement of a heavy-duty gas turbine by means of fuel burner design development and testing", Proc of ASME Turbo Expo, GT2018-76587, Oslo, Norway, 2018

[6] P.C. Nassini, D. Pampaloni, R. Meloni, A. Andreini, "Lean blow-out prediction in an industrial gas turbine combustor through a LES-based CFD analysis", *Combustion and Flame*, Volume 229, 2021

[7] O. Colin , F. Ducros , D. Veynante , T. Poinsot, "A thickened flame model for large eddy simulations of turbulent premixed combustion", *Phys. Fluids 12* (2000) 1843-63

WORK IN PROGRESS POSTERS


THE COMBUSTION INSTITUTE
1954

NUMERICAL BASELINE ANALYSIS OF THE T100 MICRO GAS-TURBINE (MGT) COMBUSTOR

G. Generini*, A. Andreini*, E. Bianchi**
giulio.generini@unifi.it
*Heat Transfer and Combustion group
University of Florence
50139, Via S.Marta 3, Florence, Italy
**Ansaldo Green Tech,
16152, Via Nicola Lorenzi, 8, Genoa, Italy

Abstract
In the last decades, micro Gas Turbines (mGTs) have gained interest in distributed power generation, over other technologies, due to their characteristics. The low emissions and noise level, their compact sizes, the fuel flexibility and in general, their high-efficiency combustion became key factors for their affirmation in the energy production horizon. mGTs are small-scale gas turbines that operate on a regenerated Brayton cycle characterized by a power output below 500 kW and are used in various applications, such as Combined Heat and Power (CHP) and cogeneration systems. Despite their technological potential, the harsh operating conditions lead to the necessity for the development of high-performance components. The mGT combustion chamber is exposed to high temperatures and pressures, which can cause thermal stresses and material degradation, and the use of different fuels can affect the mGT durability. From this point of view, the necessity for a careful analysis of these aspects became significant.
A numerical study of the methane-powered Ansaldo T100 mGT tubular, single-can, reverse-flow combustion chamber was defined. Starting from a kinematic analysis of the flame in Cantera, 3D CFD RANS simulations were run to evaluate both the adiabatic and non-adiabatic case through a complete conjugate heat transfer (CHT) analysis: the latest were carried out using the commercial Navier-Stokes solver ANSYS Fluent. Moreover, a CFD run of the full domain, considering the distribution air volute at the combustor inlet, was performed to better discretize and evaluate the air split between the dilution holes and the combustor inlet. The turbulent combustion is modelled using the Flamelet Generated Manifolds (FGM) formulation using both the standard Zimont's Turbulent Flame Closure (TFC) and an Extended Turbulent Flame Closure (ETFC) model to introduce the stretch and heat loss effects on the flame. The ETFC uses a look-up table for the laminar flame speed defined in a pre-processing step where the heat loss was applied on both the fresh gas and burned mixture through an enthalpy-based parameter. The preliminary analysis brought showed non-uniform temperature distributions, which affect the flame symmetry and NOx emissions.

Quantification of Heat Loads for Rotating Detonation Combustor with GT Conditions

Shreyas Ramanagar Sridhara*, Pier Carlo Nassini, Myles D Bohon**, Antonio Andreini****

shreyas.ramanagarsridhara@unifi.it
*Heat Transfer and Combustion Group – University of Florence
** Heat Transfer and Combustion Group – University of Florence
** Hermann-Föttinger-Institute – Berlin Institute of Technology
** Heat Transfer and Combustion Group – University of Florence

Abstract

Rotating Detonation Combustors (RDC) offer a very high-power density compared to other engines. Although they must overcome many challenges to be integrated into a gas turbine (GT), it is certainly a promising solution for increasing cycle efficiency. Among the many challenges, cooling the RDC is one of the most predominant, due to the high heat loads generated by the combustion process. Most of the available numerical and experimental data in the literature about RDC heat loads are obtained for laboratory conditions (i.e. at atmospheric pressure). However, in order to design a cooling system for an RDC that allows for its sustainable operation and aids its integration to GT engines, a quantification of the heat loads of an RDC with GT conditions is necessary. The presence of a detonation wave/boundary layer interaction and a small annulus width leads to a very high heat transfer when compared to a conventional GT combustor.

This paper describes the numerical models and tools to estimate the heat flux and heat transfer coefficient of an RDC with GT conditions. Since the flow in most part of the RDC is supersonic, the compressible boundary relations are used to model the heat transfer. Integral boundary layer methods are employed to build a tool which uses 2D distributions of integral quantities to obtain the heat flux. The simulations are conducted using Ansys fluent utilizing a single step reaction mechanism. The heat transfer in RDC is mainly governed by the strength of detonation which is dependent on the operating conditions and many other parameters.

TOWARDS A DATA-DRIVEN MODEL FOR THERMAL CHARACTERIZATION IN ROCKET COMBUSTION CHAMBERS FIRING PLATES

A. Remiddi*, P.E. Lapenna*, G. Indelicato*, R.C. Pellegrini, E. Cavallini**, M. Pizzarelli**, M. Valorani*, F. Creta***
arianna.remiddi@uniroma1.it
*Sapienza University of Rome, Via Eudossiana 18, 00184 Rome, Italy
**Italian Space Agency (ASI), Via del Politecnico snc, 00133 Rome, Italy

Abstract
Thermal characterization is an aspect of paramount importance in the design process of propulsion systems for space transportation. Liquid Rocket Engines (LREs) are, in particular, characterized by the interplay of a plethora of physical pheno-mena ranging from the turbulent mixing and combustion to the convective and radiative heat transfer, representing the ideal problem to be efficiently tackled by numerical investigation through Computational Fluid Dynamics (CFD). The pre-sent contribution proposes a data-driven model for the heat transfer characte-rization of a generic multi-injector firing plate in LRE-like operating conditions. The approach is based on two databases of two-dimensional axis-symmetric simu-lations of single-injector combustors with variable confinement length, i.e. transverse dimension, mimicking respectively the flame-wall interaction and the flame-flame interaction between neighbouring injectors [1]. The database is built using a unsteady RANS (uRANS) solver developed in the context of OpenFOAM and OpenSMOKE++ [2], based on a flamelet approach for turbulent non-premixed combustion accounting for non-adiabatic and non-equilibrium effects [3] and on a wall-modeled description of the boundary layers [4]. The heat transfer data collected from such a database are mapped on a generic multi-injector geometry on the basis of geometric criteria and then interpolated, resulting in a topological reconstruction of the faceplate that is found to be well-representative of the main morphological features of the three-dimensional heat flux field. The proposed algorithm is applied to a 37-injector chamber, featuring a plate geometry based on the layout of a real-existing subscale combustor [5]. A three-dimensional simu-lation of the same geometry is eventually presented and used for comparison.

References
[1] A. Remiddi et al, J. Propuls. Power 39 (2), 176-189 (2023)
[2] A. Cuoci et al, Comp. Phys. Commun. 192, 237-264 (2015)
[3] P.E. Lapenna et al, AIAA 2018-4872. Joint Propulsion Conference. (2018)
[4] G. Indelicato et al, Int. J. Heat Mass Transf. 169, 120913 (2021)
[5] S. Silvestri et al, Trans. Jpn. Soc. Aeronaut. Space Sci. 16(5):374-381 (2018)

A TABULATED LARGE EDDY SIMULATIONS FRAMEWORK FOR COMPLEX FLOWS IN REALISTIC GEOMETRIES

C. Matteucci*, D. Schintu*, D. Molinaro*, D. Cavalieri*, A. Remiddi*, F. Creta*
chiara.matteucci@uniroma1.it; davide.cavalieri@uniroma1.it
**Sapienza University of Rome, Via Eudossiana 18, 00184 Rome, Italy*

Abstract
The development of a reliable and accurate numerical framework to aid in the computation of turbulent reactive flows through Large Eddy Simulations (LES) is of the utmost importance in combustion chamber design. This paper proposes a numerical framework based on the OpenFOAM open-source environment, which allows the adoption of unstructured grids for the creation of realistic geometries. A tabulated chemistry (flamelet) approach is employed [1]: turbulent flamelets are generated before run-time and stored in tables to be addressed during the fluid dynamics computational process, leading to a highly efficient computation at run-time. This approach is implemented through the OpenSMOKE++ framework [2], which was modified and improved to allow for a variable number of inputs in the tables, so as to account for the physical characteristics of each case. In particular, non-adiabatic, real-gas, and thermodiffusive instability effects are among the physical processes that can be accounted for. The resulting LES framework is generated and adapted from an unsteady RANS (uRANS) framework [3].
In this contribution, the proposed framework is implemented in several applications, ranging from cold flows to premixed and diffusive flames. The canonical case of the Sydney burner [4] is simulated, presenting a non-premixed turbulent swirled flame at atmospheric pressure. A premixed jet flame is computed through the simulation of a Bunsen burner, characterized by grid generated turbulence. A reference flame for rocket applications is simulated in the TUMrig single injector chamber [5], defined by a non-premixed oxycombustion. The Ruiz case [6] is computed as a reference for mixing layers in real fluids. Finally, the capability of the framework is evaluated by comparing the results with the available experiments.

References
[1] N. Peters, Prog. Energy Combust. Sci. 10-3, 319-339 (1984)
[2] A. Cuoci et al., Comp. Phys. Commun. 192, 237-264 (2015)
[3] A. Remiddi et al., Proc. Combust. Inst (2022)
[4] P. A. M. Kalt et al., Proc. Combust. Inst. 29, 1913-1919 (2002)
[5] M. P. Celano et al., Progress in Propulsion Physics 8, 145-164 (2016)
[6] A. M. Ruiz et al., AIAA J. 54-5, 1445-1460 (2016)

Large Eddy Simulations of hydrogen combustion in a reverse flow micro gas turbine burner

E. Stendardo[1,2,4], M. Muhammad Kamal[3,4], A. Coussement [3,4], A. Parente [3,4], J. Blondeau[1,4], L. Bricteux[2], K. Bioche[5]

Elisa.stendardo@vub.be
[1] Thermo and Fluid Dynamics (FLOW), Vrije Universiteit Brussel (VUB), Pleinlaan 2, 1050 Brussels, Belgium
[2] Université de Mons (UMONS), Belgium
[3] Université Libre de Bruxelles (ULB), Belgium
[4] Brussels Institute for Thermal-fluid systems and clean Energy (BRITE), Vrije Universiteit Brussel (VUB) and
Université Libre de Bruxelles (ULB), Belgium
[5] INSA Rouen Normandie, CORIA lab, France

Abstract

Hydrogen is gaining more and more interest in future power generation and heating systems. The current need for decarbonization of the energy sector puts hydrogen forward as a suitable energy carrier.

This research aims to perform numerical simulations of the combustion process of hydrogen and hydrogen-derived fuels in innovative micro-Gas Turbines (mGT) combustors using three-dimensional Large Eddy Simulations (LES) to predict combustion efficiencies and pollutant emissions. The study analyzes the performances of a reverse flow mGT combustor designed for domestic fuel-flexible applications to minimize pollutant emissions. The LES simulations were performed using the YALES2 research code developed at French lab CORIA. Given the challenges in simulating this combustor type, a two-step modeling approach was used. Firstly, the fuel mixing problem in a non-reacting flow was solved before moving on to the multi-species reacting flow between air and hydrogen. The study includes a comprehensive model for simulating multi-species reacting flow, which requires further experimental data validation. The preliminary simulations indicate that the model accurately captures the flame structure, providing confidence in the accuracy of the approach. The results of this study will have a positive impact on the development of advanced and decarbonized energy conversion systems. Having reliable computational models for the combustion of hydrogen and its derivatives is a crucial step toward achieving this goal.

Bimetallic Fe-Cu catalysts supported on Ceria for CO_2 valorization by reverse water gas shift reaction

G. Sorbino*, S. Scognamiglio*,, G. Ruoppolo*, A. Di Benedetto***, G. Landi****

stefano.scognamiglio@stems.cnr.it
*Istituto di Scienze e Tecnologie per l'Energia e la Mobilità Sostenibili - CNR
**Politecnico di Torino
***Dipartimento di Ingegneria Chimica, dei Materiali e della Produzione Industriale – Università degli Studi di Napoli Federico II

Abstract

The reverse water-gas shift (rWGS) reaction represents a direct route and a promising approach for CO_2 conversion, in order to mitigate CO_2 emissions by producing value-added chemicals using carbon dioxide as a carbon pool. The generated CO, combined with hydrogen, acts as a feedstock to valuable fuels such as methanol and dimethyl ether (DME). The aim of this study is to evaluate the performance of novel bimetallic Fe-Cu catalysts supported on ceria towards rWGS. In fact, despite the long commercial application of WGS, there is a need for novel catalysts characterized by higher intrinsic activity (especially at relatively low temperatures), good thermal stability, and high conversion and selectivity rates.

In this work, bimetallic Fe-Cu catalysts supported on ceria, characterized by a very low active phase content (Fe_2O_3+CuO < 5 wt.%), were prepared, characterized, and tested. Additionally, bare Fe_2O_3/ceria and CuO/ceria and commercial Clariant ShiftMax® 120 HCF catalysts were tested for comparison. Fresh and used samples were characterized by ICP-MS, XRD, N_2 physisorption, SEM-EDS, to relate physico-chemical features and catalytic activity.

The sample with Fe/Cu ≈ 1 and 4 wt.% active phase content showed the best catalytic properties in terms of turnover frequency, no methane formation, stable performance, and conversion rates. Its unique properties were due to both a strong Fe-Cu interaction and a strong metal-support interaction, leading to outstanding redox behavior.

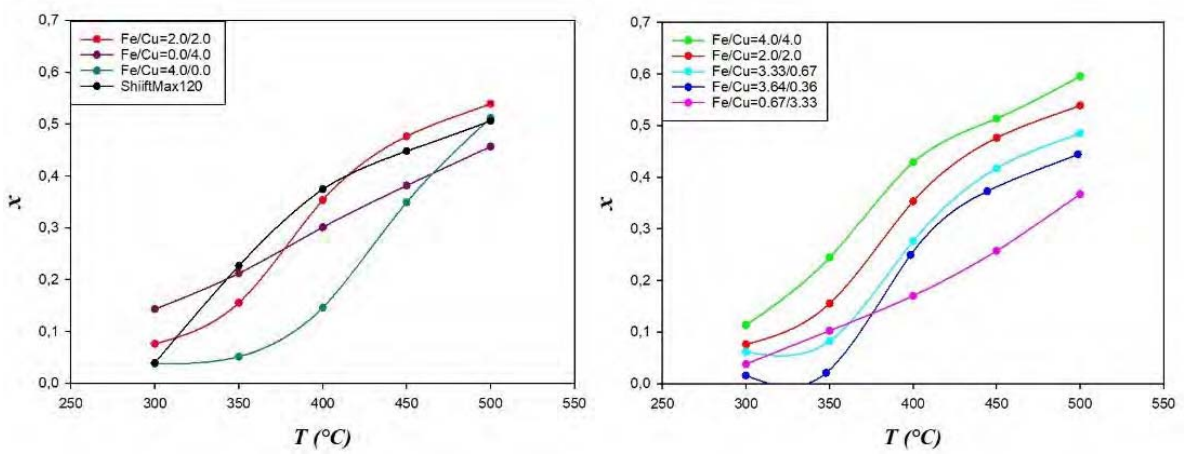

Automated adaptive chemistry for LES of turbulent flames

R. Amaduzzi*, **, G. D'Alessio*, **,*, P. Pagani*,**,A. Cuoci***, R. Malpica Galassi*, **, A. Parente*, ****

alessandro.parente@ulb.be

*Aero-Thermo-Mechanics Department, École Polytechnique de Bruxelles, Université Libre de Bruxelles, Avenue F.D. Roosevelt 50, Brussels 1050, Belgium

**Brussels Institute for Thermal-fluid systems and clean Energy (BRITE), Université Libre de Bruxelles and Vrije Universiteit Brussel, Belgium

***CRECK Modeling Lab, Department of Chemistry, Materials and Chemical Engineering, Politecnico di Milano, Piazza Leonardo da Vinci 32, 20133 Milano, Italy

Abstract

Large Eddy Simulations (LES) of turbulent flames carried out with detailed kinetic mechanisms have a key role for the discovery of the physical and chemical processes occurring in combustion systems, and are essential for the development of efficient, stable, and non-pollutant technologies. Nevertheless, these simulations require huge computational resources, making their utilization for large-scale systems, such as industrial burners and gas turbines, impractical.

In this work, we combine state-of-the-art machine learning algorithms and model reduction methods to deliver a fully automated strategy for performing LES with adaptive chemistry. This strategy is based on the Sample-Partitioning Adaptive Chemistry (SPARC) algorithmic procedure, which consists of four steps: the generation of a training dataset, its partitioning in clusters, the generation of a set of reduced chemical mechanisms specifically tailored to each cluster and, lastly, the numerical simulation of the case of interest with adaptive chemistry enabled by an *on-the-fly* classification of every grid point. The SPARC approach has already been demonstrated to substantially reduce the computational effort of reactive flows simulations. However, a non-negligible level of user interventions is needed, upon which the method's success critically depend. Therefore, with the goal of boosting the performance of this workflow and minimise the user-specified degrees of freedom, we plug in and exploit the Local Principal Component Analysis augmented with an automated Bayesian-optimised search for optimal clustering solutions, and the Computational Singular Perturbation method with an additional layer of automation based on the Tangential Stretching Rate for minimally-sized reduced mechanisms. We employ a cheap and easy-to-generate 1-dimensional-flames training database and we demonstrate the efficiency, accuracy and robustness of this strategy with an application to LES of the Adelaide Jet in Hot Coflow (AJHC) burner, a turbulent reacting flow exhibiting intense turbulence-chemistry interactions.

A combined experimental and numerical approach for the characterization of temperature distribution in a MILD combustion furnace

M. Lubrano Lavadera*, M.M. Kamal*, S. Sharma*, L. Donato*,, G. Bellacima**, A. Coussement*, C. Galletti**, A. Parente***

marco.lubrano.lavadera@ulb.be

*Aero-Thermo-Mechanics Department, Université Libre de Bruxelles, 1050 Bruxelles, Belgium.

**Dipartimento di Ingegneria Civile e Industriale, Università di Pisa, 56122 Pisa, Italy.

Abstract

The complexity of MILD combustion reactive structures has pushed the development of a number of different approaches for CFD simulations, which are usually validated using temperature measurements. To this end, the availability of experimental data in MILD conditions is crucial. Simplified configurations that mimic MILD conditions, such as jet in hot co-flow, make it possible to implement optical diagnostics and deliver high-fidelity experimental data crucial for model validation. However, in industrial MILD configurations, the distributed conditions result from the internal aerodynamic recirculation and the modification of the local mixing timescales. The availability of experimental data in furnace configurations operating in MILD conditions is generally limited to exhaust gas emissions due to the presence of an enclosure. The few experimental data on temperature fields are acquired with intrusive techniques such as suction pyrometers or thermocouples. Several authors have analyzed the influence of the selection of the combustion model, chemical and mixing time scales, turbulence model, and kinetic mechanism on temperature fields. Discrepancies between experimental and numerical temperatures have been found and are often attributed to limitations in the modeling approaches. Hence, the aim of this work was to implement the non-intrusive Rayleigh scattering technique to measure the temperature field in a semi-industrial MILD combustion furnace and compare the results with those obtained using an intrusive suction pyrometer. The temperature trends obtained with the two measurement techniques were consistent. However, laser-based measurements brought somewhat higher temperature values. CFD simulations were used to shed light on the disturbances induced by the suction pyrometer and their impact on the fluid dynamics and thermochemical field. It was found that the presence of the suction pyrometer disrupts the flow inside the furnace and shifts the reactive zone upstream. In addition, the probe results in a cooling effect caused by removing non-negligible amounts of the reactants from the reactive zone. The present analysis can be helpful to reconcile inconsistencies found in CFD modeling in which probe sampling measurements are used for validation.

CHARACTERIZATION OF THE CARBON PRODUCED BY METHANE CRACKING IN A MOLTEN TIN REACTOR

Emmanuel Busillo, Maria Paola Bracciale, Paolo De Filippis, Benedetta de Caprariis
Department of Chemical Engineering Materials Environment, Sapienza University of Rome

Abstract
Experimental tests of non-catalytic thermal methane cracking have been conducted at a fixed temperature (1070 °C) in a cylindric quartz reactor (i.d.= 1,5 cm, L= 20 cm) with capillary injection (d_{cap}= 0,25 mm) in homogenously gas phase and in the presence of molten tin (bubble column system). The use of molten tin can be an effective solution for methane cracking feasibility due to its high thermal conductivity which makes the gas heating faster and to its high density which can considerably simplify the carbon recovery operations. The effect of the presence of molten metals in the carbon formation and morphology has not been deeply investigated yet. Carbon morphology is a key parameter for the determination of its value. Aim of this study is to compare properties and morphology of carbon produced in homogeneous and molten tin methane cracking. Carbon samples were produced in different conditions: in the empty reactor and in the presence of molten bed for different tin heights (7 – 20 cm). Carbons were characterized by RAMAN spectroscopy, SEM and surface area measurements. The Raman spectra were acquired paying attention to the D, G, and 2D vibration bands pointing out that the amorphous structure was predominant carbon produced in homogeneous gas phase, while an increase in the crystallinity of the graphitic domains was obtained increasing the tin height. SEM images were obtained by a high-resolution AURIGA Zeiss scanning electron microscope equipped with an energy dispersive X-ray analyzer. As a result, the micro-structure of the carbon collected from the reactor in the absence of molten media was characterized by spherical stacked carbon particles (∼200–500 nm). In contrast, sheet-like structures with tin traces were observed in all the carbon samples produced in the molten media. According to the literature, this morphology seemed to be related to the bubbling configuration, since carbon particles were formed in the bubbles preferably at the liquid-gas interface. Methane decomposition likely took place at the gas-tin surface contact, which likely led to the formation of spherical sheets of carbon so that, once the bubbles broke up on the top surface of the tin bath, flat sheets overlaid.

Assessment of flamelet-tabulated approaches for LES analysis of swirl non-premixed flames

G. Indelicato*, C. Matteucci, P. E. Lapenna**, D. Mira*, F. Creta****
giuseppe.indelicato@bsc.es
*Barcelona Supercomputing Center, Plaça d'Eusebi Güell, 1-3, 8034, Barcelona, Spain
**Sapienza University of Rome, via Eudossiana 18, 00184, Rome, Italy

Abstract

As of today, a substantial interest still revolves around the understanding of swirled turbulent flames of typical aero-engine combustors, despite the progresses of the last twenty years. Although a number of LES studies on flame stability, transitions into unsteady behavior and swirl induced vortex breakdown already exist on experimental configurations, less is established in terms of tabulated combustion modeling of unsteady effects such as localised extinction experienced by highly swirling flames. This contribution presents work-in-progress analysis on a hybrid swirl/bluff body burner [1] envisaging unconfined, turbulent, swirled flames at atmospheric pressure and providing simple yet well-defined boundary conditions [1]. Swirl is introduced into the primary air stream by three tangential inlets positioned up-stream of the burner exit plane. In the present work only part of the burner is considered as computational domain, restricting to the outlet of the injector element and to a portion of the surrounding environment. This choice is justified by the unconfined nature of the investigated flames and by previous studies on the selected configuration. As a consequence swirl is imposed as an inflow boundary condition. A validation of the proposed simplified setting is carried out in terms of averaged radial profiles of axial and tangential velocity, temperature and selected species for the cold case and for a methane/air swirled non-premixed flame with a geometric swirl number of 0.5 (denoted as SM1). Simulations are performed both with the multi-physics finite element code Alya [2] and with an in-house developed solver based on OpenFOAM [3], providing a comparison between steady and unsteady flamelet approaches. A good reproduction of the main flow field and flame characteristics is found for SM1 with the steady approach. Questions arise when the analysis is moved to SM2, where localized extinction phenomena downstream the first central recirculation zone are observed.

References

[1] P. A. M. Kalt et al., Proc. Combust. Inst. 29, 2002/pp. 1913–1919
[2] M. Vázquez at al. J. Comput. Sci. 14, 2016/pp. 15–27
[3] G. Indelicato et al. Int. J. Heat Mass Transf. 169-120913, 2021

WETTABILITY OF CNP NANOFILM OBTAINED WITH DIFFERENT HARVESTING PROCESS

R. Griffo[*], F. Di Natale[**], A. Parisi[**], G. De Falco[**], M. Sirignano[**], R. Dondè[***], F. Migliorini[***], S. De Iuliis[***], C. Carotenuto[*]
e-mail of principal author: raffaella.griffo@unicampania.it
*University of Campania L. Vanvitelli, Via Roma 29, 81031, Aversa (CE) - ITALY
**University of Naples Federico II, P.le Tecchio 80125 Napoli- ITALY
***CNR-ICMATE, Via R. Cozzi 53, 20125, Milan, Italy - ITALY

Abstract
Flame synthesis methods allow producing engineered thin films of carbon nanoparticles (CNPs) with tuneable properties that derives from the high capability of modern techniques used to control combustion and particle harvesting processes. Thin films of carbon particles are usually produced starting from carbon black (CB) particles and are superhydrophobic. Such superhydrophobicity derives from the chemical structure of the CBs and their arrangement on the film.
Flame synthesis allows producing CNPs that are with size significantly smaller than CBs, from few tens of nanometers down to few nanometers and also potentially with higher oxygen content that helps increasing their hydrophilicity. This peculiarity can help tuning CNP nanofilm wettability from superhydrophilic to superhydrophobic behaviors. However, the wettability of the film is not only a function of the particles properties, but also of the harvesting technique.
This poster reports preliminary results on the hydrophilic/hydrophobic response of CNP films produced by flame synthesis in a premixed ethylene/air flame (C/O = 0.67) generated with a McKenna burner, using two harvesting methods. The first one (named Hot Flame Harvesting, HFH) involves pure thermophoretic and electric-field assisted harvesting of CNPs by insertion of a cold substrate directly in a hot flame. The second one (named Cold Flame Harvesting, CFH) makes use of a dilution probe that extract particles from the flame and deposit them over the plates of a cold electrostatic precipitator.
The films and the substrates are analyzed using sessile drop methods, adopting both distilled water and water-based solutions to exploit different surface tensions, γ. The experiments reveal that the CFH film is phobic until γ remains above 0.036 N/m, where a transition from phobic to philic behavior occurs in a few seconds. The HFH films exploit such a fast transition also with the surface tension of pure water (γ = 0.073 N/m). This indicates that the harvesting process substantially alters the properties of the CNP films, due to particle dynamics from flame transportation to film deposition and the rearrangement of particles on the CNP deposits.

Acknowledgments: This work is funded by the Italian PRIN Project 2017PJ5XXX: MAGIC DUST.

Numerical modelling of combustion stability prediction in a dual mode ramjet with a cavity flameholder

M. Riis*, A. Piscopo*,, A. Coussement***

Mehdi.riis@ulb.be

*Université Libre de Bruxelles and Vrije Universiteit Brussel, Brussels Institute for Thermal-Fluid Systems and Clean Energy (BRITE), Brussels, Belgium.

**Univesity of Mons, Thermal Engineering & Combustion Unit, Mons, Belgium.

Abstract

The renewed interest of the aeronautics industry in hypersonic propulsion systems led to a relaunch in dual mode ramjets (DMR) research. These engines operate at sensitive inlet conditions and must be combined with low-speed propulsion systems such as turbojets. The transition between supersonic and hypersonic regime shows an oscillating behavior as the combustion shifts from subsonic to supersonic. Recent studies use hydrogen as a fuel given its high specific impulse. The most common engines use either a strut injection or cavity-based ones. Nevertheless, the experimental campaigns of these propulsion systems are quite expensive and difficult to reproduce, thus limited to reduced-scale test facilities. Computational Fluid Dynamics (CFD) represents a viable alternative to emulate the behavior of such engines. Still, where cold flow simulations can precisely predict the air passing through the DMR, the combustion process and stabilization is difficult to study numerically. In this initiative, the Partially Stirred Reactor (PaSR) model seems promising in describing the interactions between the chemistry and turbulence as it showed its ability in describing combustion in different regimes. This work aims at implementing the PaSR model in DMR to assess the stability of the combustion process so as its limits. To this end, 2D and 3D RANS simulations are performed on a jet in crossflow with cavity flameholder using Ansys Fluent. The effects of inlet stagnation temperature and equivalence ratio on the flame stability and changes in backpressure in the isolator are assessed in this work. Finally, the PaSR model is compared to the other reactor-based model, namely the Eddy Dissipation Concept (EDC) model. The results of the simulations are validated with the available experimental data.

VALORIZATION OF PLASTIC ELEMENT OF DECOMMISSIONED PHOTOVOLTAIC PANELS

R. Migliaccio*, M. Urciuolo*, Andrea Mieli **, G. Ruoppolo*
renata.migliaccio@stems.cnr.it
*Istituto di Scienze e Tecnologie per l'Enrgia e la Mobilità Sostenibili, Piazzale V. Tecchio, 80- 80125 Napoli- Italy
**La mia Energia Scarl 03043 Cassino (FR) Via Cerro Antico s.n.c.

Abstract
The world is moving more and more toward the use of renewable energy sources, alternatives to fossil fuels, among which, for example, the power generation from solar energy by means of photovoltaic panels. The latter are typically made up of a series of solar cells connected together, called photovoltaic cells, which are semiconductors, generally of doped silicon, placed between two rigid plastic elements consisting mainly of EVA (Ethylene-vinyl acetate-$(C_2H_4)_n(C_4H_6O_2)_m$) and Tedlar (polyvinyl-fluoride-$(CH_2CHF)_n$)). The lifetime of photovoltaic panels is on average 22 years; after which they need to be disposed of. All PV panel components are recycled with the exception of plastic polymers in which the fluorine is a critical element in terms of energy valorization; it is, therefore, necessary to identify alternative techniques for reusing the plastic waste from decommissioned panels (PV plastic waste), avoiding their unsustainable disposal. In this context, thermochemical conversion processes and, in particular, pyrolysis offer a suitable solution. In this work, an investigation on the potential of pyrolysis in the valorization of PV plastic waste was performed by carrying out a preliminary batch test (2 repetitions) with the aim to study the composition of the output streams. The experiments were performed in a micro-reactor (26mm), under a pure nitrogen flow (60 Nl/h) at the final temperature of 580 °C (i.e., the temperature of complete material devolatilization). The characterization of the raw feedstock was carried out in terms of proximate and ultimate analyses as well as calorific value determination. The fluorine content was instead, measured using an ion chromatograph. All the gaseous, condensable, and solid products of the process were also analyzed. Preliminary results highlight that, in gaseous products, the most abundant compound was CO_2 followed by propylene and ethylene. The condensate streams from both experiments consists of an oily wax made up mainly of linear aliphatic hydrocarbons, both saturated and unsaturated, with a carbon number between C_8 and C_{12}; aromatic hydrocarbons were also identified (such as benzene, toluene, styrene, and phenols). No fluorinated compounds were detected in the condensed products, so this suggests that probably the most of fluorine in the PV plastic waste was confined either in the solid or the gas products. Therefore, future studies will focused on analysis of char and permanent gas to confirm the possible presence of fluorinated compounds.

INFLUENCE OF GAS CARRIER AND TEMPERATURE ON THE PYROLYSIS OF CONTAMINATED BIOMASS

C. M. Grottola*, P. Giudicianni*, D. Amato, R. Ragucci***
Corinnamaria.grottola@stems.cnr.it
* STEMS-CNR, Naples, Italy
** DICMaPI-UNINA, Naples, Italy

Abstract
Pyrolysis is considered as a suitable thermochemical treatment when the biomass sources are contaminated by potentially toxic elements (PTEs). More than the type of the feedstock, the pyrolysis operating conditions are the key parameters affecting the transformation of PTEs during the thermal treatment and the migration and distribution to the pyrolysis end-products. By a proper choice of the pyrolysis conditions allow to concentrate the PTEs in the solid product (biochar) leaving the vapor phase (bio-oil) free of heavy metals thus enabling its use as a fuel[1]. Pyrolysis temperature is the main variable affecting PTEs concentration and recovery in the biochar in a more thermally stable form than those found in the original biomass. At lower temperature PTEs are confined in the biochar, and their concentration increases with the temperature, whereas 550-700°C is the optimal range for producing biochar with both high porosity but less PTEs concentration. Moreover, high porosity and surface area are the most relevant properties for biochar application involving solid–fluid interface phenomena in different application fields [2] (fertilizer, activated carbons precursor, filler in wood and polymer composites, contaminants adsorbent in wastewater and soil, floating cover). A key aspect for the enriched PTEs biochar application is the assessment of its toxicity related to the PTEs mobility and bioavailability. To the best of our knowledge, temperature and heating rate are already faced out for the PTEs behavior, but there is still a knowledge gap concerning their fate under different pyrolysis reaction environments. To this aim, in the present study lignocellulosic biomass (populus nigra) contaminated by Pb is tested under slow pyrolysis conditions (HR=5 °C/min), and the effect of temperature (465, 550, 700 °C) and gas carrier (N_2, CO_2, H_2O and mixture of them) are investigated on biochar properties and PTEs behavior. The risk assessment of the biochar is also performed based on the sequential extraction procedure defined by the European Community Bureau of Reference (BCR) that allows for the classification of metals in the biochar in different chemical categories.

[1] Grottola, C. M., Giudicianni, P., Pindozzi, S., Stanzione, F., Faugno, S., Fagnano, M., Ragucci, R. Steam assisted slow pyrolysis of contaminated biomasses: Effect of plant parts and process temperature on heavy metals fate. Waste Management; 2019; 85, 232-241.
[2] Qian K., Kumar A., Zhang H., Bellmer D., Huhnke R., Recent advances in utilization of biochar. Renewable and Sustainable Energy Reviews; 2015, 42, 1055–1064.

FATE OF LEAD DURING PYROLISIS OF LIGNOCELLULOSIC BIOMASS

D. Amato*,, P. Giudicianni*, C. M. Grottola*, F. Stanzione*, R. Migliaccio*, R. Ragucci***

davide.amato@stems.cnr.it

* STEMS-CNR, Naples, Italy

** DICMaPI-UNINA, Naples, Italy

Abstract

In recent years, lignocellulosic biomass role as an alternative energy source to fossil fuels gain interest among the scientific community. Both its direct use and, even more, the use of biofuels produced after upgrading chemical and thermo-chemical processes, among which the pyrolysis, have been analyzed in the scientific literature and demonstrated in selected cases. To address the rising demand for lignocellulosic biomass, required to this aim, while mitigating iLUC (indirect land use change) related concerns, a viable solution could be the use of biomasses produced on marginal lands and contaminated soils. However, the biomasses produced on contaminated soils may be as a consequence contaminated by pollutants contained in the soils, like heavy metals (HMs). The presence of heavy metals in the biomass structure could hinder both its processing through pyrolysis and the subsequent use of the potentially contaminated pyrolysis products.

In the above-mentioned framework, the aim of this work is to evaluate the fate of lead (Pb) during contaminated lignocellulosic biomass pyrolysis in terms of lead distribution between pyrolysis products; moreover, it has to be considered that the presence of HMs can also modify the yields and properties of pyrolysis products. The experimental campaign tested a variety of combinations of pyrolysis final temperatures (from 450 up to 800 °C) and biomass pretreatments (i.e. untreated or doped with HMs salts). The employed biomass is a poplar (*Populus nigra*); the poplar biomass was doped via wet impregnation with two different lead salts, lead acetate and lead nitrate, to achieve a concentration of lead of 1000 ppm. Moreover, by using two different salts, information can be gained on the effect of the starting chemical form of lead on its fate during pyrolysis. All the pyrolysis products, as well as the untreated and doped biomass, were characterized in their yields and composition. In particular, the ICP-MS (Induced Coupled Plasma Mass spectroscopy) represents a key tool for the purpose of this work, since it detects HMs in the biomass and pyrolysis products at ppm levels, granting the possibility to track lead displacement during pyrolysis.

In summary, the present work aims to shed light on the basics of heavy metals behaviors during the pyrolysis of HMs contaminated lignocellulosic biomass. Moreover, the possible effects of HMs on pyrolysis products yield and properties are also analized.

A REDUCED KINETIC MECHANISM FOR JET-A1 COMBUSTION IN VITIATED AIR

M. V. Manna*, R. Ragucci*, M. de Joannon*, P. Sabia*
mariavirginia.manna@stems.cnr.it
* Institute of Science and Technology for Sustainable Energy and Mobility - Consiglio Nazionale delle Ricerche, Napoli, Italy

Abstract
Understanding the fundamental oxidation properties of jet fuels is essential for the development of aircraft engines and the improvement of aeronautical propulsion systems, in particular for non-conventional applications, like vitiated air-conditions (i.e. afterburner chamber conditions). The presence of non-negligible concentrations of CO_2 and H_2O in the combustion chamber can affect the combustion properties, as largely demonstrated in literature for the oxidation of hydrogen and other hydrocarbons. However, few studies have been carried out to date to investigate the effects of vitiated air on aviation fuels. Given this framework, JetA1 oxidation experiments were carried out in a Jet Stirred Flow Reactor (JSFR) as a function of the inlet temperature, at fixed dilution level (in N_2 and N_2-CO_2 as diluent species), residence time and equivalence ratio, at nearly-atmospheric pressure. Temperature and species concentrations were collected for different operative conditions, to outline a reference database for a kinetic model reduction.
The experimental tests suggested that CO_2 can affect the oxidation behaviour of JetA1. In particular, due to its high specific heat capacity, it reduces the maximum temperature increment of the system. CO_2 concentration equal to 20% has a slight promoting effect on system reactivity in the low-temperature range (950-1030 K), while at CO_2=50, 70%, the oxidation process is delayed, thus a higher inlet temperature is required to ignite the mixture.
At T<1000 K, the unburnt species formation is slightly affected by CO_2, while for higher temperatures, the mixture with 50% CO_2 oxidizes with the highest CO formation whereas the mixture with 70% CO_2 produces the lowest concentrations of H_2 and CO_2.
A two component fuel surrogate (20% C_7H_8, 80% $nC_{12}H_{26}$) was identified for the numerical investigations, based on the chemical analysis on the JetA1. Different kinetic mechanisms were tested against the obtained data, observing in general a good agreement with the experimental results. The smallest-size model was selected for a further mechanism reduction. A reduced scheme, consisting of 59 species and 591 reactions was obtained by a sequential use of different Direct Relation Graph (DRG) techniques. The reduced model reproduces well the target temperature and species profiles; nevertheless a further optimization is necessary to reproduce better the CH_4 concentration in the temperature range 950-1050 K.

Performance of biomass pyrolysis products MILD combustion in a cyclonic burner

G.B. Ariemma*, G. Sorrentino, P. Sabia, P. Giudicianni, M. de Joannon, R. Ragucci

1 Institute of Sciences and Technologies for Sustainable Energy and Mobility (STEMS-CNR), Naples, Italy

*corresponding author: giovannibattista.ariemma@stems.cnr.it

Abstract

Energy vectors play a key role in supporting the integration of alternative and renewable energy sources in the fast evolving concept of smart energy grid. They include many fuels, among which bio- or deriving from thermochemical conversion of biomass unquestionably occupies a relevant role. On the other hand, due to the high content of diluent, which varies case by case and depends on the conversion process from biomass and on the biomass itself, the direct utilization of these low-grade fuels requires combustion technologies able to ensure high combustion efficiency, fuel and thermal load flexibility. In this respect, MILD combustion [1] is one of the most attractive. In fact, MILD combustion is suitable for the direct conversion of low calorific values, as gases deriving from bio- or thermochemical degradation of biomass are. With this background, in this work combustion performances of several model gas surrogates were experimentally investigated in a cyclonic burner under MILD conditions. These fuels were identified as gaseous fraction of biomass pyrolysis products, obtained from different feedstocks and condition ($43<\%CO_2<71$, $16<\%CO<39$, $6<\%CH_4<9$, $2<\%C_2-<4$, $0<\%H_2<3$). In particular, combustion stability and pollutant emissions were analyzed with respect to fuel composition, preheating level, equivalence ratio and thermal power. In this respect, experimental results showed that the oxidation process can be stabilized in a wide range of equivalence ratios by means of an effective preheating strategy, due to the high CO_2 dilution characterizing the gas surrogates. In fact, operational temperatures decrease by increasing the CO_2 amount in the fuel mixtures, being always lower than 1400K for all the investigated conditions. With respect to the speciation, the mixture composition and considered operational parameters slightly affect NO_x emissions, that always keep lower than 10 ppm, whereas CO emissions depend on both CO-CO_2 ratio in the fuel mixture. In particular, lower CO emissions have been detected for the fuel mixture with the lowest $\%CO_2$, despite the highest %CO. This behavior is due to the slightly higher operative temperature detected for the identified case, that allow to stabilize the oxidation process in a wider range of equivalence ratios, thus converting all the CO to CO_2.

Reference

[1] Sabia P, Sorrentino G, Ariemma GB, Manna M V., Ragucci R, de Joannon M. MILD Combustion and Biofuels: A Minireview. Energy and Fuels 2021;35:19901–19.

INVESTIGATION ON THE EFFECT OF NITROGEN COMPOUNDS ON THE OXIDATION OF SURROGATE GASEOUS FRACTION OF BIOMASS PYROLYSIS COMPOUNDS

M. V. Manna*, K. P. Shrestha, F. Maußß**, R. Ragucci*, M. de Joannon*, P. Sabia***

mariavirginia.manna@stems.cnr.it

* Institute of Science and Technology for Sustainable Energy and Mobility - Consiglio Nazionale delle Ricerche, Napoli, Italy

** Thermodynamics and Thermal Process Engineering - Brandenburg University of Technology, Cottbus, Germany)

Abstract

The use of gas deriving from bio- or thermochemical conversion of biomass (i.e. biogas) for energy production occupies a relevant role in addressing several issues in the reduction of the environmental impact of the whole carbon cycle. In the framework of efficient conversion of biomass to biogas, the main problem is the very low calorific values with respect to standard fuels due to the high content of diluent. Moreover, the presence of small concentrations of nitrogen compounds could be a further issue, since these species can boost the formation of nitrogen oxides.

In this work, the oxidation of a model gas surrogate for the gaseous fraction of biomass pyrolysis products containing C1-C2 species, CO, CO_2 and H_2 was experimentally and numerically studied over a wide range of temperatures in the presence of small concentrations of NH_3 and NO.

The experiments were carried out in a Jet Stirred Flow Reactor. The fuel oxidation chemistry was studied for fixed dilution level of 90%, equivalence ratio of 0.8 and residence time of 0.3 s. The pressure was nearly atmospheric. The study was realized as a function of the mixture pre-heating temperature. Combustion regimes (low- and high-temperature) and instabilities were identified as a function of the temperature for the reference mixture. Therefore, to analyse the influence of nitrogenated species in fuel oxidation, the investigation was carried out doping fuel blend with NO and NH_3 separately. At first, the fuel mixture was doped with 225 and 380 ppm of NO. For the second experimental campaign, fuel mixture was seeded with 5 and 7% (by mole) of NH_3. The results showed that the onset of reactivity for the biogas mixture is at around 950 K, while doping the mixture with NO promotes the reactivity, shifting the onset of ignition of about 100 K. Also for the mixtures doped with NH_3, a slightly promoting effect was observed, since the onset of ignition of is anticipated of about 40 K. The obtained experimental data were simulated with a detailed kinetic model. The simulations showed that the selected model was in reasonable agreement with the present experimental data.

INVESTIGATION OF PREMIXED LAMINAR SOOTING FLAME BY INFRARED PYROMETRY

L. Basta*, M. Commodo, C. Allouis**, A. D'Anna***
luca.basta@unina.it
*Dipartimento di Ingegneria Chimica, dei Materiali e della Produzione Industriale, DICMAPI Università degli Studi di Napoli Federico II, 80125 Napoli, Italy
**Istituto di Scienze e Tecnologie per l'Energia e la Mobilità Sostenibili, STEMS-CNR, 80125 Napoli, Italy

Abstract
The comprehension of soot formation in combustion processes relies on crucial parameters such as soot temperature, emissivity, and concentration. Moreover, the evolution of carbonaceous nanoparticles within the flame environment, undergoing a transformation from nascent to mature soot through coagulation and coalescence processes, alters their physical and chemical properties as their residence time increases.[1]
In this work, two-color – or ratio – pyrometry performed with a science-grade infrared camera, after a preliminary calibration of the spectral response of the camera in the measuring setup, allows to reconstruct the two-dimensional temperature field of a premixed laminar sooting flame.[2] The use of infrared narrow bandpass filters in the wavelength regions where the emission of the combustion gases is minimal guarantees that the measured radiance predominantly originates from the soot particles. Finally, a two-dimensional mapping of the soot emissivity is obtained, providing insight about the particles evolution within the flame.

References
[1] G. De Falco et al. / Proceedings of the Combustion Institute 36 (2017) 763–770
[2] Y. A. Lavendis et al. / Rev. Sci. Instrum. 63 (1992) 3608–3622

ENVIRONMENTAL IMPACT OF FIREWORKS ON AEROSOL CHEMICAL CHARACTERISTICS DUE TO CHAMPIONSHIP-WINNING CELEBRATION

F. Picca*, F. Sasso, A. Pignatelli†, M. Commodo‡, P. Minutolo ‡, A. D'Anna****

francesca.picca@unina.it

* Centro Servizi Metrologici e Tecnologici Avanzati, Università degli Studi di Napoli Federico II, Napoli, 80146, Italy

** Dipartimento di Ingegneria Chimica, dei Materiali e della Produzione Industriale, Università degli Studi di Napoli Federico II, Napoli, 80125, Italy

†Dipartimento di Fisica, Università degli Studi di Napoli Federico II, Napoli, 80125, Italy

‡ Istituto di Scienze e Tecnologie per l'Energia e la Mobilità Sostenibili, CNR, Napoli, 80125, Italy

Abstract

In this work, a seven-day intensive in situ measurement campaign was carried out using a high-resolution aerosol mass spectrometer (HR-ToF-AMS) to detect changes or alterations in air quality in Naples.

Indeed, in the first week of May 2023, there were huge celebration events in the city related to winning the Italian Soccer championship. As a means of celebration, citizens heavily used fireworks and smoke bombs.

In particular, two days proved significant: 4th May 2023 and 7th May 2023 on the occasion of the mathematical victory and the subsequent first game played in Naples, respectively.

As a definition, fireworks and smoke bombs are a mix of chemical substances that give rise to combustion and then to the generation of compounds that, after the effect of light, explosion and heat, release into the atmosphere some particles that almost immediately alter the air quality and also create more or less serious health problems. In addition, the same particles could remain in the atmosphere and generate adverse future issues.

From in situ measurements, it was possible to detect the presence of species related to and derived from the activity of fireworks/smoke bombs, such as chlorates, nitrates, and organic compounds and assert the concentration of which shows a significant increase in the hours associated with the festivities. Moreover, these measurements also allow evaluation of their behaviour on the atmosphere in the subsequent days.

Bayesian Inference for the Development of Conventional and Alternative Jet Fuel Surrogates

J. Liberatori*, D. Cavalieri*, R. Malpica Galassi*, M. Valorani*, P.P. Ciottoli*
jacopo.liberatori@uniroma1.it
*Department of Mechanical and Aerospace Engineering, Sapienza University of Rome, Via Eudossiana 18, Rome, 00184, Italy

Abstract
The endorsement of mid- and long-term climate neutrality policies by governments and other institutions in the last decade strengthens the ambition to identify sustainable alternatives to fossil fuels for any category of transportation systems. In this context, the aviation industry is one of the most impacted sectors, with precise climate neutrality targets to be achieved by mid-century. One potential solution for transitioning towards a low-carbon future is blending conventional and alternative jet fuels. Among the latter sustainable aviation fuels (SAFs) constitute the most practical way forward, given their "drop-in" nature, with their use being expected to increase in the coming years. However, the impact of unusual physical and chemical properties of SAFs may deeply impact the performance and operability of engines, e.g., in terms of altitude relight, lean blow-out, and cold start. In this respect, adequate characterization of alternative jet fuels is a necessary step toward the application of large-scale computational fluid dynamics (CFD) aimed at assessing the performance of SAF-fueled combustion devices. Thus, several approaches have been proposed to formulate surrogate fuels that emulate the physicochemical properties of real hydrocarbon mixtures. These strategies typically hinge on genetic optimization algorithms, which address objective functions combining specific fuel properties, e.g., the liquid-phase viscosity and the cetane number, and provide a single optimal surrogate composition. In the present work, we illustrate a novel strategy that resorts to the Bayesian inference framework to statistically characterize the possible surrogate fuel composition based on available experimental data, the intrinsic uncertainty of which is naturally considered. Moreover, the Bayesian framework fosters employing polynomial chaos expansion (PCE) representations of the major chemical observables, e.g., the ignition delay time, characterizing the real fuel, which could not be easily incorporated into standard optimization algorithms. This way, a comprehensive probability description of the surrogate composition is returned instead of a single set of optimal components' proportions and paves the way toward the cost-effective use of ad-hoc surrogate mixtures in CFD codes.

Modelling of Wildland-Urban-Interface wind-driven fires with slope effects

S. Gkantonas*, G. Efstathiou, A. Giusti**, E. Mastorakos***
E. Mastorakos: em257@eng.cam.ac.uk
*Engineering Department, University of Cambridge
**Mechanical Engineering, Imperial College London

Abstract
Recently, a new framework for modelling fires in terrains with strong inhomogeneities, such as those in the Wildland-Urban-Interface (WUI), has been proposed [1,2]. It has been applied so far to fires in flat terrains and fires that are propagating by firebrands. The model gives good predictions of the fire scar (the outline of the burnt region) and offers high-resolution information on the burn probability.
In this paper, the model is further used for two fires in Athens suburbs, in June and July 2022. One of these was going upslope, the other downslope, and both were at the interface between the built space and wildland with shrubs and low trees. The model's parameters were estimated for these situations and the inclination angle was included explicitly, based on previous CFD results [3]. The model gave fairly good predictions of the overall fire behaviour.
In the final poster, the results will be presented in detail, links to movies will be given, and a discussion on the model's strengths and weaknesses will be included.

1. Mastorakos, E., Gkantonas, S., Efstathiou, G. & Giusti, A. (2022) A hybrid stochastic Lagrangian - cellular automata framework for modelling fire propagation in inhomogeneous terrains. To appear in *Proceedings of the Combustion Institute* **39**. https://doi.org/10.1016/j.proci.2022.07.240

2. Efstathiou, G., Gkantonas, S., Giusti, A., Mastorakos, E., Foale, C.M. & Foale, R.R. (2023) Simulation of the December 2021 Marshall fire with a hybrid stochastic Lagrangian-cellular automata model. *Fire Safety Journal* **138**, 103795. https://doi.org/10.1016/j.firesaf.2023.103795

3. Eftekharian, E. et al. (2019) Investigation of terrain slope effects on wind enhancement by a line source fire. *Case Studies in Thermal Engineering* **14**. 100467. https://doi.org/10.1016/j.csite.2019.100467


THE COMBUSTION INSTITUTE
1954


THE COMBUSTION INSTITUTE
1954


THE COMBUSTION INSTITUTE
1954


THE COMBUSTION INSTITUTE
1954

Joint Meeting of the Belgian and Italian Sections of The Combustion Institute

45th Meeting of the Italian Section of The Combustion Institute

Organizing and Scientific Committee:

Dr. Mario Commodo (CNR-STEMS)
Prof. Alessandro Parente (Université Libre de Bruxelles)
Prof. Antonio Andreini (Università degli Studi di Firenze)
Dr. Giancarlo Sorrentino (CNR-STEMS)
Prof. Ward De Paepe (Universitè de Mons)
Dr. Gianluigi De Falco (Università degli Studi di Napoli Federico II)
Dr. Antonio Tregrossi (CNR-STEMS)

Local Organizer:

Dipartimento di Ingegneria Industriale
Università degli Studi di Firenze
Via S. Marta, 3 – Firenze, Italy
website: www.dief.unifi.it

Consiglio Nazionale delle Ricerche
STEMS
Istituto di Scienze e Tecnologie per l'Energia e la Mobilità Sostenibili

UNIVERSITÀ DEGLI STUDI FIRENZE

DICMaPI
Dipartimento di Ingegneria Chimica, dei Materiali e della Produzione Industriale
Università degli Studi di Napoli Federico II

Secretariat:

Ilaria Giorgi
E-mail: ilaria.giorgi@unifi.it

Under the auspices of:

REGIONE TOSCANA

ASICI

Associazione Sezione Italiana del Combustion Institute
P.le V. Tecchio, 80
80125 Napoli – Italia
ASICI website: www.combustion-institute.it
E-mail: secretary@combustioninstitute.it
Telephone: +39 081 7682256

Belgian Section of the Combustion Institute


THE COMBUSTION INSTITUTE
1954

ISBN 978-88-88104-27-0